

TECHNISCHE UNIVERSITÄT MÜNCHEN
Physik Department
Lehrstuhl für Biomedizinische Physik

Ptychographic X-ray Microscopy and Tomography

Martin Johannes Dierolf

Vollständiger Abdruck der von der Fakultät für Physik der Technischen Universität München zur Erlangung des akademischen Grades eines

Doktors der Naturwissenschaften (Dr. rer. nat.)

genehmigten Dissertation.

Vorsitzender: apl. Prof. Dr. Norbert Kaiser

Prüfer der Dissertation:

1. Univ.-Prof. Dr. Franz Pfeiffer
2. Prof. Pierre Thibault, Ph.D.,
University College London, UK
3. Univ.-Prof. Dr. Reinhard Kienberger

Die Dissertation wurde am 05.03.2015 bei der Technischen Universität München eingereicht und durch die Fakultät für Physik am 17.03.2015 angenommen.

Abstract

This thesis presents contributions to X-ray ptychography that enable its use as a versatile X-ray phase-contrast microscopy and tomography technique. Instead of relying on high-resolution X-ray optics, ptychography reconstructs the investigated specimens from their coherent diffraction signals by employing iterative computer algorithms. While in this way ptychography allows to overcome the limits of classical optics-based X-ray microscopy, it is also superior to most other iterative schemes used for coherent diffractive, or also “lensless”, imaging. This thesis first introduces the basic algorithmic and experimental concepts of X-ray ptychography and puts them in context with existing techniques for X-ray microscopy with and without lenses. Furthermore, by means of simulations and experimental results, several innovations are discussed that improve sensitivity and spatial resolution in two-dimensional ptychographic X-ray imaging. The final part focuses on the pioneering combination of ptychography and computed tomography and presents applications of this novel phase-contrast nanotomography technique in bone research.

Zusammenfassung

Diese Dissertation präsentiert Beiträge zur Weiterentwicklung der Röntgenptychographie, die deren Anwendung als vielseitige Technik zur Phasenkontrast-Röntgenmikroskopie und -tomographie ermöglichen. Statt sich auf hochauflösende Röntgenoptiken zu verlassen, rekonstruiert Ptychographie die zu untersuchenden Proben mittels iterativer Computeralgorithmen aus ihren kohärenten Streusignalen. Während sie auf diese Weise die Limitierungen klassischer optikbasierter Röntgenmikroskopie umgeht, ist Ptychographie zudem den meisten anderen iterativen Verfahren zur kohärenten (beugungsbasierten), oder auch „linsenfreien“, Bildgebung überlegen. Die vorliegende Dissertation führt zunächst in die grundlegenden algorithmischen und experimentellen Konzepte der Röntgenptychographie ein und setzt sie in Bezug zu bestehenden, sowohl linsenbasierten wie auch linsenfreien, Röntgenmikroskopiemethoden. Mittels Simulationen und experimenteller Ergebnisse werden darüberhinaus mehrere Neuerungen erörtert, die die Sensitivität und das räumliche Auflösungsvermögen in der zweidimensionalen ptychographischen Röntgenbildgebung verbessern. Schließlich wird ein Schwerpunkt auf die wegweisenden Kombination von Ptychographie und Computertomographie gelegt und Anwendungen dieser neuartigen Phasenkontrast-Nanotomographiemethode in der Knochenforschung werden präsentiert.

Es ist nicht das Wissen, sondern das Lernen, nicht das Besitzen, sondern das Erwerben, nicht das Dasein, sondern das Hinkommen, was den größten Genuss gewährt.

Carl Friedrich Gauß

Contents

I	Methods and Instrumentation	15
1	X-ray microscopic imaging	17
1.1	Linear imaging systems	17
1.1.1	Superposition in linear systems	17
1.1.2	Shift-invariant systems	18
1.1.3	Coherent and incoherent imaging systems	19
1.2	Contrast generation: X-ray interaction with matter	22
1.3	X-ray sources	23
1.4	Free-space propagation	25
1.5	X-ray optics	29
1.5.1	Refractive optics	29
1.5.2	Reflective optics	29
1.5.3	Diffractive optics	30
1.6	X-ray detectors	32
1.6.1	Detector parameters	33
1.7	Full-field microscopy	37
1.7.1	Transmission X-ray microscopy	37
1.7.2	Cone-beam projection microscopy	38
1.8	Scanning microscopy	39
1.8.1	Analysis of STXM data	41
2	Coherent diffractive imaging	45
2.1	The phase problem	45
2.2	Coherent X-rays	46
2.2.1	Transverse coherence	47
2.2.2	Longitudinal coherence	48
2.3	Sampling	50
2.3.1	The sampling theorem	50
2.3.2	Sampling requirements in far-field phase retrieval	52
2.4	Iterative phase retrieval in CDI	56
2.4.1	Phase retrieval as an optimization problem	56

2.4.2	Projections	58
2.4.3	Common iterative projection algorithms	59
2.4.4	Limitations of single-pattern CDI with common algorithms	70
2.4.5	Advanced iterative CDI techniques	73
3	Ptychographic coherent diffractive imaging	75
3.1	Ptychography: from crystals to iterations	75
3.1.1	The original concept of ptychography	75
3.1.2	Generalized definition of ptychography	76
3.1.3	Wigner-distribution deconvolution	78
3.1.4	The Ptychographical Iterative Engine (PIE)	82
3.2	Ptychography with probe retrieval	88
3.2.1	First concepts for probe refinement	89
3.2.2	The difference map ptychography algorithm for simultaneous probe retrieval	91
3.2.3	Validity of the wave factorization assumption	94
3.2.4	Uniqueness of solution	96
3.2.5	Maximum-likelihood refinement	101
3.2.6	Inclusion of additional <i>a priori</i> knowledge	107
3.3	Evaluating the resolution of PCDI reconstructions	109
3.3.1	Separation of features in test patterns	109
3.3.2	The concept of “knife edges”	110
3.3.3	Phase retrieval transfer function	111
3.3.4	Resolution estimate based on photon statistics	112
3.3.5	Fourier ring and shell correlations	113
4	Computed tomography	117
4.1	Radon transform and Fourier slice theorem	117
4.1.1	Definitions	117
4.1.2	Consequences of Fourier slice theorem for angular sampling	118
4.2	Filtered backprojection	119
4.2.1	Basic algorithm	119
4.2.2	Filtering	121
4.2.3	Filtered backprojection from derivatives of projections	122
5	Experimental realization of ptychographic CDI	125
5.1	Ptychographic CDI at the cSAXS beamline of the Swiss Light Source	125
5.1.1	Description of beamline	125

5.1.2	Set-up for two-dimensional scanning (diffraction) microscopy	131
5.1.3	Tomography set-up	134
5.2	Ptychographic CDI at ID22NI at the ESRF	137
5.2.1	Source and beam conditioning	138
5.2.2	Kirkpatrick-Baez focusing system	138
5.2.3	Scanning set-up	139
5.2.4	Detectors	140
5.3	General considerations on PCDI experiments and their limiting factors	141
5.3.1	Incident beam	142
5.3.2	Detector	144
5.3.3	Scanning overhead	146
5.3.4	Stability	149
5.3.5	Sample environment	151
5.3.6	Sample preparation	157

II Advanced developments for two-dimensional ptychography 161

6	Density “resolution”: weak-object imaging	163
6.1	Challenges of imaging weakly scattering objects	163
6.2	Description of demonstration experiment	165
6.3	Evaluation of scattering power	167
6.4	Reference reconstruction	168
6.5	Ptychographic reconstruction of a biological specimen	170
7	Ptychography with information sharing between data sets	173
7.1	Motivation	173
7.2	Concepts	174
7.2.1	Reconstruction with a shared probe	174
7.2.2	Reconstruction with a shared object	177
7.2.3	Hybrid approach	181
7.3	Simulations	183
7.3.1	General parameters	183
7.3.2	Sharing the probe with an empty object	183
7.3.3	Shared-object reconstruction in the presence of inter-scan sample drift	184
7.4	Application to experimental data	188

7.4.1	Shared-probe reconstruction of a high-resolution test object	188
7.4.2	Shared-object reconstruction in cellular imaging	192
8	Broad-bandwidth PCDI: towards high spatial resolutions	201
8.1	Motivation	201
8.2	Demonstration experiments at ID22NI	202
8.2.1	Experiment in July 2009	202
8.2.2	Experiment in March 2011	204
8.3	Results of test experiment in July 2009	205
8.4	Results of improved experiment in March 2011	208
8.4.1	Investigation of background-induced artefact in probe .	208
8.4.2	Estimation of detector PSF based on background-induced artefact	216
8.4.3	Reconstructions with post-processed diffraction data .	222
8.5	Conclusions	230
8.6	Outlook	231
8.6.1	Hardware improvements	232
8.6.2	Algorithmic improvements: mixed-state reconstructions	233
III	Ptychographic nanotomography	237
9	Development of ptychographic nanotomography	239
9.1	Demonstration experiment	239
9.1.1	Sample preparation	239
9.1.2	Data collection	240
9.2	Data analysis	242
9.2.1	Ptychographic reconstruction	243
9.2.2	Phase ramp removal and offset correction	245
9.2.3	Phase unwrapping	247
9.2.4	Alignment of projections	250
9.2.5	Tomographic reconstruction	253
9.2.6	Conversion to quantitative electron density	255
9.3	Results of demonstration experiment	256
9.3.1	Complex transmission functions: qualitative and quantitative information	257
9.3.2	Quantitative bone density results	260
9.3.3	Visualization of bone morphology	264
9.3.4	Spatial resolution	272
9.3.5	Dose estimation	274

9.4	Conclusions and outlook	281
10	Applications of ptychographic nanoCT in bone research	285
10.1	Quantitative mapping of mineralization gradients	286
10.1.1	Motivation: Do osteocytes remodel bone?	286
10.1.2	Sample preparation	289
10.1.3	Experiment	290
10.1.4	Data processing	292
10.1.5	Results	293
10.2	Visualization of collagen fibril patterns	306
10.2.1	Motivation: structure-function relationships in bone	306
10.2.2	Data set	309
10.2.3	Extraction of collagen fibril orientations	309
10.2.4	Results and discussion	312
10.3	Outlook: flat bone samples	316
10.3.1	Motivation	316
10.3.2	Experiment	316
10.3.3	Reconstruction results	320
IV	Conclusions and Outlook	323
11	Conclusions	325
12	Outlook	329
12.1	Experimental developments	329
12.2	Algorithmic and software developments	331
12.2.1	Algorithms for ptychographic nanotomography	333
V	Appendix, Bibliography and Indices	335
A	The Fourier transform and its properties	337
A.1	Definition and properties	337
A.2	Fourier-Bessel transform for circularly-symmetric functions	339
A.3	Discrete Fourier transform	339
	Bibliography	341
	List of Figures	384

Contents

Index of cited authors	389
Subject index	397
Nomenclature	401
List of Publications	403

Part I

Methods and Instrumentation

Chapter 1

X-ray microscopic imaging

This chapter introduces the basic principals of X-ray microscopic imaging based on X-ray optical elements. After a discussion of the origin of contrast in X-ray imaging in the first section, the second section covers the most important types of X-ray optical elements. The third section dealing with the detectors used for X-ray imaging is followed by two sections discussing the two major methods of X-ray microscopy, the full-field and the scanning case.

1.1 Linear imaging systems

Optical imaging set-ups can be conveniently described using linear systems theory. This section presents the basic ideas of this approach, focusing on those most relevant in the context of this thesis. The description here is based on section 2.3 of the book by GOODMAN (1996), to which the reader is referred for a more complete treatment of the subject. Further details on the topic can also be found in the books by JÄHNE (2002, section 7.6), ERSOY (2006, section 2.2) and BORN AND WOLF (2006, section 9.5).

1.1.1 Superposition in linear systems

A two-dimensional (imaging) system is assumed to be fully characterized by the operator \mathcal{S} , which maps the input signal $g_1(x_1, y_1)$ to the output signal $g_2(x_2, y_2)$:

$$g_2(x_2, y_2) = \mathcal{S} \{g_1(x_1, y_1)\} \quad , \quad (1.1)$$

where (x_1, y_1) and (x_2, y_2) are the respective transverse coordinates in the input and output plane of the system. The operator S is linear if the super-

position principle

$$\mathcal{S}\{af(x_1, y_1) + bg(x_1, y_1)\} = a\mathcal{S}\{f(x_1, y_1)\} + b\mathcal{S}\{g(x_1, y_1)\} \quad (1.2)$$

is fulfilled for all input functions f and g and all complex constants a and b . If the input is decomposed into a set of elementary functions, according to (1.2) the total response of the system can be described as the sum of responses for these elementary inputs. With the Dirac δ -distribution (MEYBERG AND VACHENAUER, 1999), the input $g_1(x_1, y_1)$ can be expressed as

$$g_1(x_1, y_1) = \iint g_1(\xi, \eta)\delta(x_1 - \xi, y_1 - \eta) d\xi d\eta . \quad (1.3)$$

In the case of imaging, this can be interpreted as decomposing an input image into individual point sources represented by the δ -peaks, where amplitude and phase at each point source are given by the weighting factor $g_1(\xi, \eta)$. First inserting (1.3) in (1.1) and then applying the superposition principle (1.2) yields

$$g_2(x_2, y_2) = \iint g_1(\xi, \eta)\mathcal{S}\{\delta(x_1 - \xi, y_1 - \eta)\} d\xi d\eta , \quad (1.4)$$

i.e. the output is obtained as the weighted sum of system's response to a point-like input. With the definition

$$h(x_2, y_2; \xi, \eta) \equiv \mathcal{S}\{\delta(x_1 - \xi, y_1 - \eta)\} , \quad (1.5)$$

input and output of the system are related by

$$g_2(x_2, y_2) = \iint g_1(\xi, \eta)h(x_2, y_2; \xi, \eta) d\xi d\eta . \quad (1.6)$$

$h(x_2, y_2; \xi, \eta)$ is the response of the system at output point (x_2, y_2) to a δ -shaped input at (ξ, η) , called the *impulse response*.

1.1.2 Shift-invariant systems

If a shift of a δ -peak (point source) in the input plane only causes a shift of the output, but not a change of its functional form, the system is called *shift invariant* or *space invariant*. In this case, $h(x_2, y_2; \xi, \eta)$ depends only on the transverse distances of source and output coordinates:

$$h(x_2, y_2; \xi, \eta) = h(x_2 - \xi, y_2 - \eta) . \quad (1.7)$$

With this, (1.6) simplifies to

$$g_2(x_2, y_2) = \iint g_1(\xi, \eta)h(x_2 - \xi, y_2 - \eta) d\xi d\eta , \quad (1.8)$$

i.e. the output g_2 of a linear, shift-invariant system is obtained as the two-dimensional convolution of the input g_1 with the impulse response h :

$$g_2 = g_1 \otimes h . \quad (1.9)$$

Taking the Fourier transform of both sides¹ and applying the convolution theorem (A.5), the spectrum $\tilde{g}_2(q_x, q_y)$ of the system output is linked to the spectrum $\tilde{g}_1(q_x, q_y)$ of the system input by

$$\tilde{g}_2(q_x, q_y) = \tilde{g}_1(q_x, q_y) \cdot \tilde{h}(q_x, q_y) , \quad (1.10)$$

i.e. by a simple multiplication with the *transfer function* $\tilde{h}(q_x, q_y)$, which is the Fourier transform of the impulse response.

1.1.3 Coherent and incoherent imaging systems

1.1.3.1 Impulse responses

If a given optical imaging system is illuminated with coherent light², the system is linear in amplitude and the input and output (complex) wavefields $\psi_1(x_1, y_1)$ and $\psi_2(x_2, y_2)$ are related by

$$\psi_2 = \psi_1 \otimes h . \quad (1.11)$$

In this fully coherent case, the impulse response h of the system is called the *amplitude-spread function (ASF)*. If the same system is used with fully incoherent radiation, input and output are intensities $I_1(x_1, y_1)$ and $I_2(x_2, y_2)$, which are linked through (compare GOODMAN, 1996, section 6.1.3, pp. 132–134, ERSOY, 2006, section 10.7, or BORN AND WOLF, 2006, section 9.5, pp. 545–547)

$$I_2 = I_1 \otimes |h|^2 \equiv I_1 \otimes PSF , \quad (1.12)$$

i.e. the system is linear in intensity. The impulse response $|h|^2$ of such an incoherently-illuminated imaging system is known as the *point-spread function (PSF)* and is the squared magnitude of the complex-valued coherent ASF of the system. However, as most imaging systems like microscopes are operated with incoherent radiation and the detectors for the visible light and X-ray regime can only measure intensities, the PSF is of far more practical importance: typically, it will characterize how the imaging system blurs the input I_1 . Therefore, deconvolution of the PSF from the output image

¹Definitions and fundamental properties of the Fourier transform are summarized in Appendix A starting on page 337.

²For more details on coherence properties of wavefields, see section 2.2 on page 46.

I_2 is frequently used to obtain the actual incident intensity distribution I_1 , compare e.g. BANHAM AND KATSAGGELOS (1997).

Typically, the total PSF of a complex imaging system is composed of the contributions of the individual components. In an X-ray microscope, e.g., one typically has to consider the effects of the X-ray source, the optics, and the detector:

$$I_2 = I_1 \otimes PSF_{\text{source}} \otimes PSF_{\text{optics}} \otimes PSF_{\text{detector}} \equiv I_1 \otimes PSF_{\text{system}} . \quad (1.13)$$

1.1.3.2 Transfer functions

By Fourier transforming the ASF, one obtains the *amplitude transfer function* or *coherent transfer function*, which characterizes the frequency response of the system for coherent illumination according to (1.10). While in the incoherent case also the Fourier transform of the PSF could be used as a transfer function, one usually works with normalized quantities. According to ERSOY (2006, section 10.8.2, p. 167), this is done to account for the fact that “the visual quality of an image is largely determined by the contrast of the relative intensity of information-bearing details of the image to the ever-present background”. With the normalized intensities

$$I'_1(x, y) = \frac{I_1(x_1, y_1)}{\iint I_1(x_1, y_1) dx_1 dy_1} , \quad I'_2(x, y) = \frac{I_2(x_2, y_2)}{\iint I_2(x_2, y_2) dx_2 dy_2} , \quad (1.14)$$

one obtains for the relation between their Fourier transforms:

$$\tilde{I}'_2(q_x, q_y) = \tilde{I}'_1(q_x, q_y) \cdot \mathcal{H}(q_x, q_y) , \quad (1.15)$$

where the *optical transfer function* (OTF) is given by

$$\mathcal{H}(q_x, q_y) = \frac{\mathcal{F} \{ |h(x, y)|^2 \}}{\iint h(x, y) dx dy} . \quad (1.16)$$

The OTF is also the normalized autocorrelation of the amplitude transfer function (ERSOY, 2006, section 10.8.2, p. 168). The *modulation transfer function* (MTF) is defined as the modulus $|\mathcal{H}(q_x, q_y)|$ of the OTF (GOODMAN, 1996, section 6.3.1, p. 139). The MTF plays an important role in the characterization of imaging systems. Their spatial resolution, for instance, is often given as the value for which the MTF falls below a certain threshold like, e.g., 0.1.

1.1.3.3 Experimental characterization of point-spread and optical transfer functions

OTFs and PSFs are often measured indirectly using the concept of “knife edges” (compare also section 3.3.2 on page 110): In this case, one records an image of an object (edge) which can be assumed to resemble a step function without the influence of the PSF one wants to determine. A line-out orthogonal to the blurred edge is sometimes referred to as *edge-spread function (ESF)* (compare e.g. CLOETENS, 1999, section 3.4.1.3). By taking the derivative of the ESF, the *line-spread function (LSF)* is obtained,

$$LSF(x) = \frac{d}{dx} ESF(x) , \quad (1.17)$$

which is defined as (GRUNER ET AL., 2002b)

$$LSF(x) = \int PSF(x, y) dy . \quad (1.18)$$

The one-dimensional Fourier transform of the LSF with respect to x yields the OTF along the q_x axis:

$$\mathcal{H}(q_x, 0) = \mathcal{F} \{ LSF(x) \} . \quad (1.19)$$

This is a consequence of the *Fourier slice theorem* (KAK AND SLANEY, 1988, chapter 3), see section 4.1.1 and in particular (4.4).

An important special case are imaging systems with a radially-symmetric impulse response, for instance detectors whose PSF is larger than a single pixels. Then also the system’s transfer function exhibits radial symmetry. When expressing the OTF in radial Fourier space coordinates ($|\mathbf{q}|, \theta$), $\mathcal{H}(|\mathbf{q}|, \theta) = \mathcal{H}(|\mathbf{q}|, 0)$ is fulfilled for all θ . Through obtaining with (1.19) the one-dimensional radial component of the OTF as the Fourier transform of the LSF,

$$\mathcal{H}(|\mathbf{q}|, 0) = \mathcal{F} \{ LSF(x) \} , \quad (1.20)$$

the full two-dimensional OTF $\mathcal{H}(q_x, q_y)$ can thus be directly constructed. The PSF can then be obtained as the inverse two-dimensional Fourier transform of this full OTF. When exploiting the radial symmetry once again, the radial component of the PSF can also be obtained directly as the one-dimensional *Fourier-Bessel transform*³ of the radial OTF.

³Also known as *Hankel transform of zero order*, see Appendix A.2 and CHAMPENEY (1973) for definition and properties.

1.2 Contrast generation: X-ray interaction with matter

This section is largely based on [ATTWOOD \(2000, chapter 3\)](#). At the length scales accessible by X-ray microscopy, the interaction of X-rays with matter can be described by a continuous, complex refractive index distribution

$$n(\vec{r}, \lambda) = 1 - \delta(\vec{r}, \lambda) + i\beta(\vec{r}, \lambda) , \quad (1.21)$$

which is a function of both the spatial coordinate $\vec{r} = (x, y, z) = (\mathbf{r}, z)$ as well as the X-ray wavelength λ . While β is linked to the photoelectric⁴ linear attenuation coefficient μ by the relation

$$\beta(\vec{r}, \lambda) = \frac{\lambda}{4\pi} \mu(\vec{r}) , \quad (1.22)$$

δ is related to the electron density $n_e(\vec{r})$ of the material as follows: For a material in which N different atomic species are present, δ depends on the real parts $f_{1,j}^0(\lambda)$ of their complex atomic scattering factors in forward scattering approximation as

$$\delta(\vec{r}, \lambda) = \frac{r_e \lambda^2}{2\pi} \sum_{j=1}^N n_{a,j}(\vec{r}) f_{1,j}^0(\lambda) \quad (1.23)$$

where $r_e = 2.818 \cdot 10^{-15}$ m is the classical electron radius and $n_a(\vec{r})$ the number density of the atoms. If the X-ray energy is higher than the binding energies of core level electrons, i.e. the absorption edges, $f_1^0(\lambda)$ reduces to the total number of electrons Z . With $n_e = Z \cdot n_a$ one obtains

$$\delta(\vec{r}, \lambda) = \frac{r_e \lambda^2}{2\pi} n_e(\vec{r}) . \quad (1.24)$$

where n_e represents the total electron density of the material constituted of the sum of the electron densities of the different atomic species present.

The wave $\psi(\mathbf{r})$ exiting an object with a refractive index distribution $n(\vec{r})$ for an incoming wave $\psi_0(\mathbf{r})$ propagating along the z -direction of the Cartesian coordinate system $(x, y, z) = (\mathbf{r}, z)$ is given by

$$\psi(\mathbf{r}) = O(\mathbf{r}) \cdot \psi_0(\mathbf{r}) , \quad (1.25)$$

⁴At the typical X-ray energies (below 20 keV) used for the work presented here, photoelectric absorption is the dominant effect of X-ray attenuation and other contributions can be neglected, e.g. Compton scattering, which only becomes relevant at energies of several tens of keV.

if the incoming wave field is sufficiently constant over the distance corresponding to the thickness of the object along the propagation direction. The validity of this projection approximation is further discussed in section 3.2.3. The complex object transmission function⁵

$$O(\mathbf{r}) = T(\mathbf{r}) e^{i\Phi(\mathbf{r})} \quad (1.26)$$

combines the projections along the propagation direction z of both the absorbing

$$T(\mathbf{r}) = \exp\left(-\frac{2\pi}{\lambda} \int \beta(\mathbf{r}, z) dz\right) \quad (1.27)$$

and the phase shifting part

$$\Phi(\mathbf{r}) = \frac{2\pi}{\lambda} \int \delta(\mathbf{r}, z) dz \quad (1.28)$$

of the complex refractive index distribution $n(\mathbf{r}, z)$.

In the case of a weak phase object, which shows basically no absorption and only small phase shifts, the complex object transmission function (1.26) becomes

$$O(\mathbf{r}) \approx 1 + i\Phi(\mathbf{r}) . \quad (1.29)$$

1.3 X-ray sources

Although high-resolution microscopy has also been demonstrated with conventional laboratory X-ray sources (FESER ET AL., 2008), the discussion here will be limited to synchrotron radiation obtained from undulators which was exclusively used for the work reported in this thesis. Undulators at large storage ring facilities or free-electron lasers are currently the only sources providing a sufficient amount of photons for practical applications of coherent X-ray imaging techniques. However, further developments in accelerator science may provide access to X-ray beams of similar quality on the laboratory scale in the future (FUCHS ET AL., 2009).

At modern ‘third-generation’ synchrotron sources, insertion devices – undulators or wigglers – are placed in straight sections of the electron storage

⁵ $O(\mathbf{r})$ is often also called the object’s exit wave, as it is the wave one would detect directly behind the object for a plane wave illumination with unit amplitude, which is the common case in standard coherent diffractive imaging (CDI). However, here the term (complex) transmission function is preferred to avoid confusion with the general exit waves $\psi(\mathbf{r})$ in (1.25) which have to be used in in ptychographic CDI.

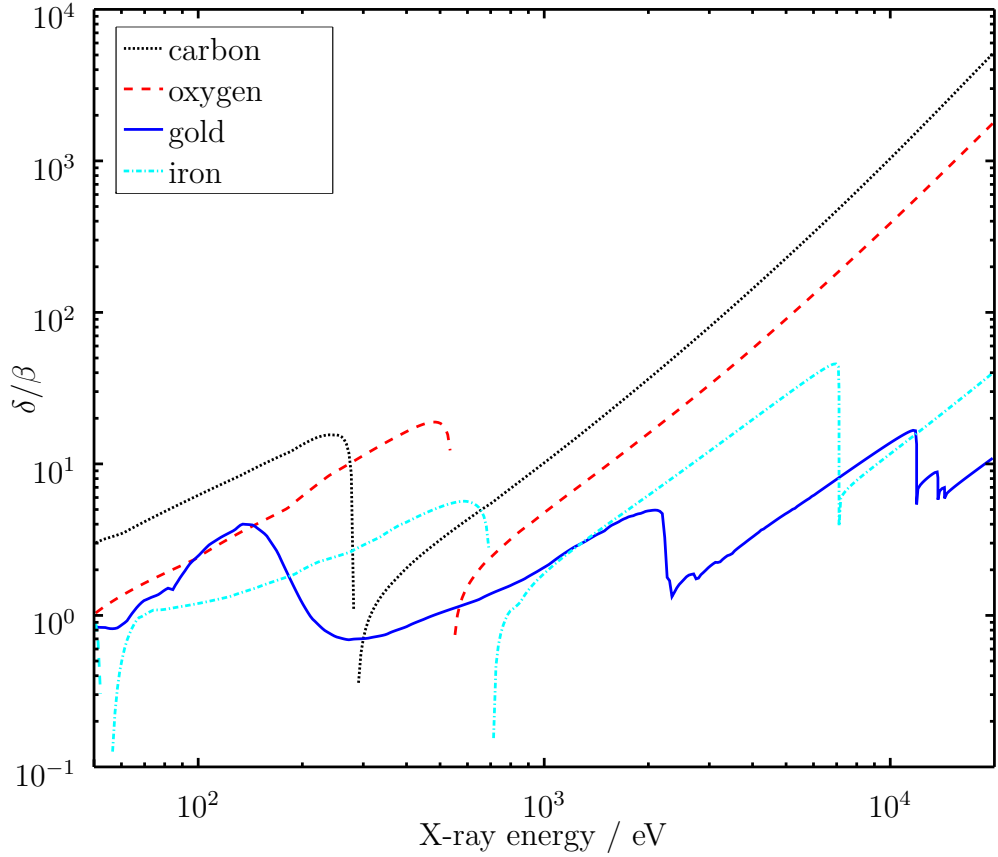


Figure 1.1: Comparison of the ratios δ/β for four different materials for X-ray energies ranging from 30 eV to 20 keV. In the soft X-ray region below 1 keV X-ray microscopy usually relies on absorption contrast, in particular in the so-called “water window” between the K-absorption edges of carbon at 284 eV and oxygen at 543 eV. For hard X-rays with energies above 5 keV, δ is usually one to two orders of magnitude larger than β . So especially for the lighter elements, phase sensitive techniques potentially provide better contrast in this energy range. Plots are based on tabulated values by HENKE ET AL. (1993) using the online-interface to the database available at http://henke.lbl.gov/optical_constants/.

ring. Insertion devices consist of two long arrays of periodic magnetic structures (period length λ_u) causing small transverse oscillations of electrons passing through the gap in between which therefore radiate. The amplitude of these oscillations depends mainly on the flux density B_0 of the magnetic field inside the insertion device and is quantified with the parameter (ATTWOOD, 2000, chapter 5)

$$K = \frac{eB_0\lambda_u}{2\pi m_e c^2} \simeq \gamma \cdot \theta_{e,max} , \quad (1.30)$$

where $\theta_{e,max}$ is the maximum angular deviation of the electron beam from the

forward direction and $\gamma = E_e/m_e c^2$ is given by the ratio between the energy E_e of the accelerated electrons and the electron rest energy $m_e c^2$. In wigglers with $K \gg 1$ the amplitude of these oscillations is larger than in undulators ($K < 1$) so that radiation intensity emitted at different oscillations adds up incoherently. In contrast, undulators are designed in a way that the oscillating electrons stay inside the cone of radiation, which for a relativistic electron has an opening angle $2\theta_{rad} \simeq 1/\gamma$. Therefore, the radiation emitted by an electron bunch at one oscillation is in phase with the radiation from the following oscillations for certain wavelengths λ_n of the emitted radiation, the so-called undulator harmonics (ATTWOOD, 2000, chapter 5):

$$\lambda_n = \frac{\lambda_u}{2\gamma^2 n} \left(1 + \frac{K^2}{2} + \gamma^2 \theta^2 \right), \quad (1.31)$$

where the angle θ quantifies the effects of off-axis observation of the X-ray beam. As the even harmonics have their intensity maxima off-axis, usually only the odd harmonics are used. The wavelengths of the harmonics can be shifted by changing the K -parameter of the undulator, usually done by changing the gap size between the magnetic structures.

1.4 Free-space propagation

For image formation processes in X-ray microscopy, it is important to be able to calculate from a complex wave field $\psi(x, y, z = 0) = \psi_0(x, y)$ in a given plane⁶ the diffracted complex field $\psi(x = x', y = y', z = Z) \equiv \psi_Z(x', y')$ formed at a distance Z in vacuum. Therefore, this section briefly reviews some basic concepts of free-space wave propagation. More details on the topic can be found, e.g., in the textbooks by LAUTERBORN AND KURZ (2003, section 9.1) and PAGANIN (2006, chapter 1), which are the main sources for the discussion below. The section is partly based on previous work in DIEROLF (2007, section 2.2.2).

According to the *Huygens-Fresnel principle*, the wave field at any point in space can be calculated as a superposition of the spherical wavelets emerging from all points of the original wave front (BORN AND WOLF, 2006). A more rigorous mathematical treatment starting from the inhomogeneous scalar wave equation leads to the *Fresnel-Kirchhoff diffraction integral*, which includes an additional direction dependent factor that cannot be derived from the mere Huygens-Fresnel principle (LAUTERBORN AND KURZ, 2003, section

⁶As $\psi(x, y, z = 0) \equiv \psi_0(x, y)$ is often the object's exit wave (see section 1.2), the plane $z = 0$ is also referred to as object plane in this section.

9.1):

$$\psi_Z(x', y') = \frac{1}{i\lambda} \iint \psi_0(x, y) \frac{e^{ikR}}{R} \cos(\angle(\hat{n}, \hat{R})) \, dx \, dy. \quad (1.32)$$

The wave is assumed to be monochromatic with a wave number $k = 2\pi/\lambda$. The distance R from a point in the object plane to a point on the screen is given by $R = \sqrt{(x - x')^2 + (y - y')^2 + Z^2}$. $\cos(\angle(\hat{n}, \hat{R}))$ is the said directional factor where \hat{n} is the unit normal vector of the object plane and \hat{R} the unit vector along the connection of $(x, y, z = 0)$ and (x', y', Z) .

In the *paraxial approximation*, the extent of object and diffraction pattern are considered to be small compared to the distance Z between the two planes, i.e. $Z \gg |x|, |y|, |x'|, |y'|$. As this means that all light rays can be considered to travel almost parallel to the optical axis, one can set $\cos(\angle(\hat{n}, \hat{R})) = 1$. Furthermore, the paraxial approximation allows to expand

$$R = \sqrt{(x - x')^2 + (y - y')^2 + Z^2} = Z \sqrt{1 + \frac{(x - x')^2}{Z^2} + \frac{(y - y')^2}{Z^2}} \quad (1.33)$$

around Z , which – up to the second order term – yields

$$R \approx Z + \frac{(x - x')^2}{2Z} + \frac{(y - y')^2}{2Z}. \quad (1.34)$$

The zeroth-order term is used to replace the factor $1/R$ in (1.32) by $1/Z$. In the exponent, also the higher order terms have to be considered, resulting in the *Fresnel approximation* of the diffraction integral:

$$\psi_Z(x', y') = \frac{e^{ikZ}}{i\lambda Z} \iint \psi_0(x, y) e^{\frac{ik}{2Z}[(x-x')^2 + (y-y')^2]} \, dx \, dy. \quad (1.35)$$

If one defines the Fresnel propagator in real space as

$$P_Z(x, y) = \frac{e^{ikZ}}{i\lambda Z} e^{\frac{ik}{2Z}(x^2 + y^2)}, \quad (1.36)$$

(1.35) can be rewritten into

$$\psi_Z(x, y) = \psi_0(x, y) \otimes P_Z(x, y), \quad (1.37)$$

i.e. the propagated wave field is obtained as the convolution of the original wave field with the Fresnel propagator. For numerical evaluation, (1.37) can be conveniently expressed using Fourier transforms as discussed at the end of this section, see (1.50). By expanding the quadratic terms in (1.34) such that

$$R \approx Z \left(1 - \frac{xx' + yy'}{Z^2} + \frac{x^2 + y^2}{2Z^2} + \frac{x'^2 + y'^2}{2Z^2} \right), \quad (1.38)$$

the Fresnel integral (1.35) can also be expressed in a different form:

$$\psi_Z(x', y') = \frac{e^{ikZ}}{i\lambda Z} e^{\frac{ik}{2Z}(x'^2+y'^2)} \iint \psi_0(x, y) e^{-ik(xx'+yy')/Z} e^{ik(x^2+y^2)/(2Z)} dx dy . \quad (1.39)$$

The quadratic phase factor contributed by the last exponential can be neglected for large distances from the object to the diffraction plane and for a finite size of the diffracting object, i.e.

$$k \frac{x^2 + y^2}{2Z} \ll \pi . \quad (1.40)$$

For an object with largest extent a , this can be rewritten into the so-called *far-field condition*

$$Z \gg \frac{a^2}{\lambda} . \quad (1.41)$$

Defining the dimensionless *Fresnel number* f_n , the far-field condition becomes

$$f_n \equiv \frac{a^2}{\lambda Z} \ll 1 . \quad (1.42)$$

In this case, the wave field in the diffraction plane can be expressed in the *Fraunhofer approximation*

$$\psi_Z(x', y') = A_Z(x', y') \iint \psi_0(x, y) e^{-ik(xx'+yy')/Z} dx dy , \quad (1.43)$$

with the abbreviation

$$A_Z(x', y') = \frac{e^{ikZ}}{i\lambda Z} e^{\frac{ik}{2Z}(x'^2+y'^2)} \quad (1.44)$$

for the pre-factor. Identifying the integrand in (1.43) as the two-dimensional Fourier transform of the exit wave $\psi_0(x, y)$ with respect to reciprocal space coordinates $(q_x, q_y) = (kx'/Z, ky'/Z)$, see Info box 1.1, (1.43) can be rewritten into

$$\psi_Z(q_x, q_y) = A_Z \left(q_x \frac{Z}{k}, q_y \frac{Z}{k} \right) \mathcal{F} \{ \psi_0(x, y) \} (q_x, q_y) . \quad (1.45)$$

Also Fresnel propagation can be conveniently expressed in terms of one or two applications of the Fourier transform and multiplication with quadratic phase factors: Comparison of (1.45) with (1.39) shows that the latter can also be written as

$$\psi_Z(q_x, q_y) = A \left(q_x \frac{Z}{k}, q_y \frac{Z}{k} \right) \mathcal{F} \left\{ \psi_0(x, y) e^{ik(x^2+y^2)/(2Z)} \right\} (q_x, q_y) , \quad (1.49)$$

i.e. in the Fresnel approximation the wave field in the diffraction plane can be obtained by multiplying the exit wave with a quadratic phase factor and

In small-angle approximation, $\mathbf{q} = (q_x, q_y)$ are the transverse components of the scattering vector $\vec{q} = (\mathbf{q}, q_z)$. It is defined as

$$\vec{q} = \vec{k}_s - \vec{k}_0, \quad (1.46)$$

with the wave vectors \vec{k}_0 for the incident and \vec{k}_s for the scattered wave, which enclose the scattering angle 2θ . In the case of elastic scattering, the condition $|\vec{k}_0| = |\vec{k}_s| = k = 2\pi/\lambda$ allows to express the absolute value of the scattering vector as

$$|\vec{q}| = 2k \sin \theta = \frac{4\pi}{\lambda} \sin \theta. \quad (1.47)$$

In small-angle approximation, this simplifies to $|\vec{q}| \approx \frac{4\pi}{\lambda} \theta$. For hard X-ray energies and small angles, the component q_z of the scattering vector along the beam can usually be neglected, i.e. the *Ewald sphere* is approximated as a plane and we have $|\vec{q}| = |\mathbf{q}|$. With $x'/R = \sin 2\theta_x \approx 2\theta_x$ and accordingly $y'/Z \approx 2\theta_y$, this leads then to the relations

$$q_x = k \frac{x'}{Z}, \quad q_y = k \frac{y'}{Z}, \quad (1.48)$$

which were used in (1.45).

Info box 1.1: Derivation of the relations between the transverse components of the scattering vector and the experimental geometry.

then taking the Fourier transform. The second expression is obtained by applying the Fourier convolution theorem (A.5) to the convolution form (1.37) of Fresnel propagation, which can then be rewritten as

$$\psi_Z(x, y) = \mathcal{F}^{-1} \left\{ \tilde{\psi}_0(q_x, q_y) \tilde{P}_Z(q_x, q_y) \right\}. \quad (1.50)$$

Here, $\tilde{\psi}_0(q_x, q_y) = \mathcal{F} \{ \psi_0(x, y) \} (q_x, q_y)$ is again the Fourier transform of the exit wave and the Fresnel propagator in Fourier space, obtained by Fourier transforming (1.36), is (PAGANIN, 2006, section 1.4.1)

$$\tilde{P}_Z(q_x, q_y) = e^{ikZ} e^{-\frac{iZ}{2k}(q_x^2 + q_y^2)}. \quad (1.51)$$

When implemented numerically, formulation (1.49) of Fresnel propagation is more suitable for larger propagation distances Z , while (1.50) is better suited for small Z (GIEWEKEMEYER, 2011): Small Z in (1.49) would result in a rather steep parabolic phase profile, so it would be hard to represent it accurately with discrete sampling points. The same is true if the Fourier space Fresnel propagator (1.51), which is used in (1.50), is evaluated for large Z .

1.5 X-ray optics

1.5.1 Refractive optics

Due to the fact that the real part of the refractive index is smaller than unity for X-ray wavelengths, focusing optics based on refraction have to be of concave shape in contrary to the convex lenses used in visible light. However, as refraction effects are very small such is the focusing effect of a single lens. Thicker lenses cannot be employed due to dominance of absorption effects. To circumvent these problems, compound lenses consisting of rows of refractive lenses have been introduced by [SNIGIREV ET AL. \(1996\)](#). They are mainly used for (pre-)focusing in beamline optics. Smaller focal spot sizes require higher curvatures of the individual lenses which are achieved by modern nanostructuring techniques ([SCHROER ET AL., 2003](#)). For two-dimensional focusing, usually a pair of crossed 1-D focusing lenses is used. The main applications of these nano-focusing lenses are in scanning (spectro-)microscopy. Compound refractive lenses show chromatic aberration and their efficiency (the ratio of focused photons to incoming photons) is limited by the absorption in the lens material. The minimal focal spot sizes are limited by the available nanostructuring techniques which prevents them from reaching the theoretical limit ([SCHROER AND LENGELER, 2005](#)).

1.5.2 Reflective optics

Reflective optics are based on the total external reflection of X-rays at material surfaces: If absorption is neglected, the condition $n < 1$ for the refractive index together with the small-angle approximation of Snell's law results in a critical angle $\theta_c \simeq \sqrt{2\delta}$ with the surface ([ATTWOOD, 2000](#)). All radiation incident with a smaller angle will be totally reflected. Focusing is achieved by giving a mirror surface an elliptical shape, typically either by polishing or by bending flat crystals. A special case are glass capillary optics whose surface is machined to form part of an rotational ellipsoid around the optical axis and which can provide a point-focus down to a few hundred nanometres diameter ([THIEL ET AL., 1992](#)). In contrast, two-dimensional focusing to even smaller focal spots is mostly done with a pair of crossed mirrors, usually referred to as Kirkpatrick-Baez (KB) mirrors ([KIRKPATRICK AND BAEZ, 1948](#)), but is also possible with a single mirror if special multilayer coatings are applied ([WOHLSCHLÖGEL ET AL., 2008](#)). Such multilayers are also added to increase the angular acceptance of reflective optics beyond the limit of the critical angle ([HIGNETTE ET AL., 2005](#)), which in turn allows to reduce the length of the mirrors.

While single-bounce mirrors operated close to the critical angle are used for suppression of higher harmonics from crystal monochromators, sometimes also with the option for slight focusing, and capillaries are mainly used as pre-focusing or condenser systems, 2D-focusing for microscopy applications is usually done with dedicated KB-systems: As reflective optics, they not only have the benefit of being achromatic, which allows to use a broader bandwidth beam in applications where no high monochromaticity is required. Furthermore, they also reach very high efficiencies as only total reflections at surfaces are employed. The focal spot sizes are limited by surface roughness building up in the production process, but may be further improved by use of adaptive optics (MIMURA ET AL., 2009). Currently, focal spot sizes down to $60 \text{ nm} \times 60 \text{ nm}$ (FWHM) are routinely used in imaging applications (MARTÍNEZ-CRIADO ET AL., 2012).

1.5.3 Diffractive optics

Diffraction effects are not only used for imaging or focusing optics respectively, but also for **spectral filtering** of X-ray beams. This is usually based on diffraction by crystals as described by Bragg's law

$$n \cdot \lambda = 2d_{hkl} \sin \theta_{hkl} , \quad (1.52)$$

where the integer n is the diffraction order, d_{hkl} the distance between crystal planes with Miller indices (hkl) and θ_{hkl} the angle between incident beam and scattering planes. For practical purposes, often two successive Bragg reflections are combined to keep the exit beam parallel to the incident one. The spectral bandwidth $\Delta\lambda/\lambda$ depends on the crystal used, e.g. for Si-111 it is about $1.4 \cdot 10^{-4}$ (ALS-NIELSEN AND MCMORROW, 2011, chapter 6). In addition to crystals, also artificially created diffracting structures like multilayers or – in the soft X-ray regime – gratings are used for spectral filtering.

For focusing applications in general and imaging in particular, **Fresnel zone plates** (FZPs) have been designed for X-ray energies (BAEZ, 1961): They can be understood by considering the first-order diffraction of a circular grating structure for which the periods become shorter for farther distances from the optical axis. For smaller grating periods, the diffraction angles become larger so that for the right choice all first-order diffraction peaks can be made to coincide in a focal spot, see Fig. 1.2. Mathematically, this results in the condition

$$r_n^2 = n\lambda f + \frac{n^2\lambda^2}{4} \simeq n\lambda f , \quad (1.53)$$

for the radius r_n of the n -th Fresnel zone to get a focal length f . The approximation on the right is valid for $f \gg n\lambda/2$. The higher diffraction

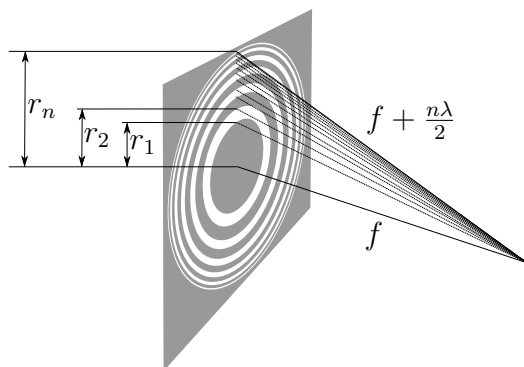


Figure 1.2: Sketch of a Fresnel zone plate which illustrates the constructive interference in the first-order focus: In the circular grating structure, the sequential zones of radius r_n are designed such that the path to the focal point is $f + n\lambda/2$, where f is the focal length. The zones are alternately transmissive or opaque and thus the waves from the former interfere constructively at the focal point. Opaque zones may also be replaced by ones exhibiting a phase shift of π , which is easier to realize for hard X-rays and also increases the diffraction efficiency, i.e. the fraction of the incident intensity focused into the first order.

orders η of the grating structures produce focal spots at the fractional focal lengths of f/η . Usually, higher order focusing can only be observed for odd values of η as in the discussed zone plate construction even orders with $\eta \geq 2$ cancel out due to destructive interference. However, even-order foci may start to appear already due to slight alterations of the design (VILA-COMAMALA ET AL., 2011b). Starting from (1.53), the focal length f can be also be expressed as (ATTWOOD, 2000, section 9.2)

$$f \simeq \frac{4N(\Delta r)^2}{\lambda}, \quad (1.54)$$

with $\Delta r \equiv r_N - r_{N-1}$ being the width of the outermost of the N Fresnel zones. Δr is clearly the most important parameter in zone plate design as it also determines the **size of the focal spot** and thus the **resolution** one can achieve: Due to the Fourier relationship between the circular entrance aperture and the focal plane, the intensity distribution in the latter is described by an Airy pattern (ATTWOOD, 2000, sections 9.3 and 9.4). The radius of its first intensity minimum is given by

$$\Delta r_{\text{Rayl.}} = 1.22 \cdot \Delta r. \quad (1.55)$$

When using a FZP for point-to-point imaging, $\Delta r_{\text{Rayl.}}$ is thus also the minimum distance between two mutually incoherent point sources so that in an image they are still discernible according to the *Rayleigh criterion* (GOOD-

MAN, 1996, section 6.5.2). Therefore, the resolution of a zone plate is ultimately limited by nanostructuring technology, in particular the ability to produce small zones with high enough aspect ratios to provide good diffraction efficiencies. However, (1.54) shows that smaller zones in turn result in smaller focal lengths and thus reduced working distances.

Production of zone plates typically uses a combination of electron beam lithography and electroplating with a highly-absorbing material, see e.g. JEFIMOV ET AL. (2007a). Due to the spread of the electron beam at higher penetration lengths, writing of small spatially-dense structures is not easily possible. In order to reduce the need for highest pattern densities, CHAO ET AL. (2005) have developed a double-exposure technique while JEFIMOV ET AL. (2007b) have doubled the number of zones by overcoating a less dense pattern of low-absorbing material with a uniform highly-absorbing iridium layer.

As typically at best only about 10 to 20% of the incoming intensity are diffracted into the first diffraction order (ATTWOOD, 2000, section 9.2) and thus contribute to the focal spot, a different way to fabricate diffractive optics with higher aspect ratios and thus higher diffraction efficiencies has been developed: the so-called **multilayer Laue lenses** (KANG ET AL., 2006) are produced by alternately growing absorbing and transmitting layers on a substrate to form a one-dimensional Fresnel zone plate with a large thickness along the optical axis. While the high precision of thin-film growth techniques allows for very small zone widths and thus very small focal sizes, again two optical elements have to be combined in a crossed geometry in order to achieve two-dimensional focusing.

1.6 X-ray detectors

As the last step in an X-ray microscopy set-up, the X-ray photons have to be detected in a way which in the end allows to convert the recorded information into images. While this is nowadays mostly achieved using two-dimensional position-sensitive pixelated detectors, also simpler options like proportional counters still play a role, e.g. in scanning transmission X-ray microscopes (see section 1.8 on page 39). The current section provides a summary of important general detector parameters. The detectors used for the experiments presented in this thesis are discussed in section 5.1.1.6 on page 130 and in section 5.2.4 on page 140. The primary sources for this section are the review by YAFFE AND ROWLANDS (1997) and section 3.6 of the book by PAGANIN (2006). More details on the physics of various detector types can be found, e.g., in the books by KNOLL (2000) and LOWE AND

SAREEN (2013), where the latter focuses on semiconductor X-ray detectors.

1.6.1 Detector parameters

Detectors as linear imaging systems Detectors are typically treated as linear (incoherent) imaging systems to which the formalisms introduced in section 1.1 can be applied. Of particular importance are the relations for the point-spread function (1.12) and the optical transfer function (1.15), as both PSF and OTF (or its magnitude, the MTF) are frequently used to characterize detector systems. These parameters are, e.g., determined following the procedure described in section 1.1.3.3 on page 21.

Detector geometry Detector geometry strongly depends on the specific application. For imaging, the most relevant parameters are the size of the active area, which determines the field of view or solid angle covered, and the pixel size, whose implications on resolution and modulation transfer are discussed under the point “Spatial resolution”.

Quantum efficiency Detection of X-rays is based on their interaction with the detecting medium. If this medium has a thickness d and a linear attenuation coefficient $\mu(E)$, the probability of interaction, or *quantum efficiency*, for photons with energy E is

$$\eta = 1 - e^{-\mu(E)d} . \quad (1.56)$$

As pointed out in section 1.2, photoelectric absorption is the dominant interaction at the energies of a few keV relevant in the context of this thesis. In the ideal case where η approaches unity, already a single incident photon is absorbed and can thus produce a detectable signal.

Dynamic range The dynamic range is typically defined as

$$DR = \frac{\text{largest detectable signal}}{\text{smallest detectable signal}} . \quad (1.57)$$

Often, it is expressed in terms of information bits as $\log_2(DR)$. This value cannot exceed the limit set by the digitization electronics (analog-digital converters, counters), which is typically 14 bit to 16 bit, sometimes also 20 bit (KRAFT ET AL., 2009a). This limiting case is only reached if the detector is sensitive to single photons, i.e. if noise levels are very low. A high dynamic range is especially important for typical diffraction experiments to measure simultaneously both the usually

very intense central beam and the surrounding scattering signals, which are many orders of magnitude weaker.

Linearity and uniformity The output signal of a detector element should be proportional to the number of incident photons. Deviations from this linear behaviour in the detection process itself, e.g. as an effect of dead time at high incident fluxes (KNOLL, 2000, chapter 4, section VII), have to be corrected in the read-out process (KRAFT ET AL., 2009a). The response of area detectors should also be spatially uniform, i.e. a uniform illumination should produce the same output signal for all pixels. However, non-uniformities can also be corrected in software by dividing the detector frames by a *gain map* in which the inhomogeneous pixel responses are stored. In full-field imaging, typically the same is done with *flat fields*, i.e. images of the illumination without sample. While the main purpose of this is to correct for inhomogeneities of the incoming beam, it also removes those of the detector.

Noise Random deviations of a detector's output signal from the actual number of incident photons can have various sources: The quantum nature of X-rays results in fluctuations of the detected intensities which are independent of the specific detector design. This is known as *shot* or *Poisson noise*, as the fluctuations can be described by a Poisson statistics with a variance

$$\sigma^2 = N_0\eta , \quad (1.58)$$

where N_0 is the mean number of photons falling on a detector element and η the quantum efficiency defined in (1.56).

Other sources of noise decidedly depend on the particular detector system: In cases where a conversion or amplification process with a mean gain \bar{g} and a variance σ_g^2 follows the initial detection step, the output signal becomes (YAFFE AND ROWLANDS, 1997, section 3.5)

$$N_g = N_0\eta\bar{g} , \quad (1.59)$$

with a variance

$$\sigma_g^2 = N_0\eta(\bar{g}^2 + \sigma_g^2) . \quad (1.60)$$

In many systems, the read-out procedure adds noise to the signal. This *read-out noise* is strongly influenced by the design parameters of the specific detector, e.g. its read-out speed. Furthermore, detectors often record a signal even in the absence of incident X-rays, the *dark noise*. Both dark and read-out noise can be reduced by cooling the detector, which suppresses thermally-induced fluctuations in its electronics. In

practice, dark frames without X-ray irradiation are recorded to determine the background noise which is then subtracted from the recorded images.

As the measure of the quality of an obtained image, often the *signal-to-noise ratio* (SNR) is used:

$$SNR = \frac{\langle S \rangle - \langle B \rangle}{\sigma}, \quad (1.61)$$

where $\langle S \rangle$ is the average of the investigated signal over a uniform area, $\langle B \rangle$ the mean background, and σ the noise.

Detective quantum efficiency (DQE) The DQE is a measure how the signal-to-noise ratio SNR_{in} of an input signal is affected by the detector system, i.e. what the output signal-to-noise ratio SNR_{out} will be. It is defined as (GRUNER ET AL., 2002b, p. 2838)

$$DQE = \frac{SNR_{out}^2}{SNR_{in}^2}. \quad (1.62)$$

For $DQE = 1$, SNR_{out} equals SNR_{in} , i.e. the detector adds no additional noise. For a quantum efficiency $\eta = 1$, according to (1.58) the variance σ_{in}^2 of a Poisson-distributed input signal with mean N_0 is also N_0 and thus $SNR_{in} = N_0/\sigma_{in} = \sqrt{N_0}$. With (1.62), the output SNR which can be expected for a given photon number can be calculated if the DQE is known: $SNR_{out}^2 = DQE \cdot N_0$. However, as the DQE combines the information about the propagation of both signal and noise through all stages of the detection, GRUNER ET AL. (2002b) point out that “the DQE will be seen to be functionally dependent upon practically every aspect of the detector and the measurement [...]”. As a result, the DQE will often not only depend on the detector parameters, like read-out and dark noise, but also the specific experimental conditions, like the incident flux or the spatial frequencies present in the input signal. This is expressed by the fact that the DQE can also be related to the MTF $|\mathcal{H}(q_x, q_y)|$ of the detector system (CUNNINGHAM AND SHAW, 1999; RABBANI ET AL., 1987; SHAW, 1978):

$$DQE(\mathbf{q}) = \frac{N_0 MTF^2(\mathbf{q})}{NPS(\mathbf{q})}, \quad (1.63)$$

where $NPS(\mathbf{q})$ is the *noise power spectrum* or *Wiener spectrum* of the output signal’s noise and $\mathbf{q} = (q_x, q_y)$ the coordinate in two-dimensional

Fourier space. If this noise is described by the function $\Delta S(\mathbf{r})$ with $\mathbf{r} = (x, y)$ in an image area ΔA , the NPS is defined as (SHAW, 1978, section 2.3)

$$NPS(\mathbf{q}) = \lim_{\Delta A \rightarrow \infty} \left\langle \frac{1}{4\Delta A} \left| \iint_{\Delta A} \Delta S(\mathbf{r}) e^{-i\mathbf{q}\cdot\mathbf{r}} d\mathbf{r} \right|^2 \right\rangle, \quad (1.64)$$

where $\langle \rangle$ signifies an ensemble average. With the relation for the Fourier transform of an autocorrelation given in (A.7) on page 338, one finds the *Wiener-Khinchin theorem* (SHAW, 1978, section 2.3)

$$NPS = \mathcal{F} \{ \Delta S \star \Delta S \}, \quad (1.65)$$

i.e. the NPS can be calculated by Fourier transforming the autocorrelation of the real-space noise function.

Spatial resolution As X-ray imaging is nowadays dominated by digital detectors, it is their (effective) pixel size that imposes the fundamental limit on the resolution. Assuming a pixel has a side-length Δs , the position of a photon cannot be determined with better accuracy, i.e. the smallest possible PSF takes the shape of one single pixel. The corresponding MTF is a absolute value of a two-dimensional sinc-function which has its first zero along each axis at the momentum transfers $q_{x,y} = 2\pi/\Delta s$. Furthermore, the pixel size also determines the *Nyquist frequency* $f_{\text{Nyq}} = 1/(2\Delta s) = q_{\text{Nyq}}/(2\pi)$, which is the highest spatial frequency that can be sampled unambiguously. More details on sampling are discussed in section 2.3 starting on page 50. If the intensity pattern falling on the detector contains higher frequencies than f_{Nyq} , *aliasing* occurs, i.e. the intensity of these higher frequencies is incorrectly attributed to lower frequencies.

In most cases, however, a detector has a PSF extending over several pixels. As even complex point-spread functions are often expressed as a sum of multiple two-dimensional Gaussian functions (HOLTON ET AL., 2012), a single Gaussian may already provide a good approximation in simple cases. With such an extended PSF, signals originating from neighbouring point-like inputs can only be distinguished if their separation is large enough to show a visible dip in intensity. For instance, one could require a reduction to 63% of the peak intensity, as this is the typical value observed at the Rayleigh distance for two overlapping Airy patterns, compare page 31 and GOODMAN (1996, section 6.5.2). For two Gaussians of width σ , the distance between their maxima has

to be approximately 3σ to fulfil this 63%-criterion⁷. For a Gaussian $PSF(\mathbf{r})$ with width σ_r , $MTF(\mathbf{q})$ is also a Gaussian (compare ALS-NIELSEN AND MCMORROW, 2011, Appendix E.2) with a sigma-width of $\sigma_q = (\sigma_r)^{-1}$ (or $\sigma_f = (2\pi\sigma_r)^{-1}$ when expressed in terms of spatial frequency f).

Frame rate and readout time The frame rate of a detector becomes important when a rapid succession of exposures is required, e.g. for time-resolved full-field imaging or in a scanning-based technique. The frame rate is constrained by the minimum possible exposure time, for instance limited by a mechanical shutter, and the time it takes to read out each frame. Depending on the detector system, readout times are between a few milliseconds up to several seconds. Most common are values of a few hundred milliseconds. In particular if exposure times are in the sub-second regime, readout times may constitute up to 50% or more of the total acquisition time. It is thus desirable to keep them as short as possible.

1.7 Full-field microscopy

1.7.1 Transmission X-ray microscopy

A full-field transmission X-ray microscope (TXM) is the direct X-ray equivalent of a classical visible light microscope:⁸ With a condenser optics the sample is illuminated uniformly such that the objective can produce a magnified image of it on a two-dimensional detector. For the condenser in principle any type of optics discussed in section 1.5 can be used. Due to their higher efficiency and robustness compared to the traditional condensers based on zone plates (compare, e.g., the first TXM set-up at a synchrotron by NIEMANN ET AL., 1976), glass capillaries are nowadays quite frequently employed (ZENG ET AL., 2008). The objective lenses, however, are typically Fresnel zone plates. Using their first⁹ diffraction order, the same point-to-

⁷For comparison: The full width at half maximum (FWHM) of a Gaussian function is approximately 2.355σ .

⁸Details on the technical implementation of a TXM and its applications beyond the brief overview given here can be found e.g. in the textbook by ATTWOOD (2000, section 9.7) and the reviews by SAKDINAWAT AND ATTWOOD (2010) and KIRZ ET AL. (1995), which are also the primary sources for this paragraph. Descriptions of the history of X-ray microscopy can be found as part of a detailed review by KIRZ ET AL. (1995), or in the short historical overview by KIRZ AND JACOBSEN (2009).

⁹Although it has been demonstrated (REHBEIN ET AL., 2009; SCHNEIDER ET AL., 2012) that higher resolutions can be reached by employing higher diffraction orders of the

point imaging behaviour is achieved as with a classical thin lens for visible light. According to (1.55) on page 31, their outermost zone width is then the main limiting factor for the resolution of a TXM. By matching the numerical apertures of condenser and objective, the spatial resolution can be increased even beyond this Rayleigh limit of the objective lens (JOCHUM AND MEYER-ILSE, 1995, or section 9.6 of ATTWOOD, 2000) However, due to the rather low efficiency of zone plates, even at best conditions about 80 to 90% of the radiation that passes through the sample does not contribute to the imaging process. As both this efficiency and the resolving power of the available Fresnel zone plates decrease at hard X-ray energies, the TXM instruments with the highest resolutions, routinely reaching about 15 nm, are operated at soft X-ray energies. They are frequently used for biological imaging – often in a tomographic mode – employing absorption contrast in the water window between 284 eV and 543 eV (compare Fig. 1.1 on page 24). A summary of some recent applications in this field is given in the review by LARABELL AND NUGENT (2010). As in biological imaging radiation damage is a major concern, most of this latest work has been done with instruments that allow cryogenic cooling of the specimens during acquisition.

Phase contrast, which is of more interest in the hard X-ray regime where absorption-based imaging is less sensitive, is also realized analogue to the case of visible light, i.e. following the approach of ZERNIKE (1942, 1955), an annular phase ring is inserted in the back focal plane of the objective (NEUHÄUSLER ET AL., 2003; SCHMAHL ET AL., 1994).

1.7.2 Cone-beam projection microscopy

In laboratory-based X-ray imaging, high magnifications are frequently realized by placing the specimen in the conical beam emanating from a small source point, which COSSLETT AND NIXON (1953) called “shadow microscopy” in one of the first proposals. If z_1 is the distance between specimen and source and z_2 the one between sample and detector, the (shadow) image on the detector will be magnified by a factor $(z_2 + z_1)/z_1$ compared to the original object. COSSLETT AND NIXON (1953) already pointed out the two major limitations of the approach in a laboratory setting: The resolution which can be reached with such a set-up is limited by the size of the X-ray source spot. As the heat dissipation in the target of an X-ray tube is the main factor limiting the X-ray flux, reducing the source size is only possible with lower electron beam currents. This directly results in the second limitation, namely that high-resolution (micro-focus) cone-beam laboratory set-ups typ-

objective zone plates, most instruments are designed to use the first order.

ically provide only rather low X-ray fluxes and thus very long exposure times are required.

Higher resolutions at shorter exposure times can be achieved by nano-focusing a synchrotron beam with suitable X-ray optics and thus creating a virtual source point for cone-beam projection microscopy (BLEUET ET AL., 2009; MARTÍNEZ-CRIADO ET AL., 2012). Compared to a TXM where a lot of photons are lost due to the objective lens, such a set-up is more dose-efficient. While propagation-based phase contrast employing the partial coherence of the X-ray beam can in principle also be realized at laboratory installations (WILKINS ET AL., 1996), it is more readily achieved at third-generation synchrotron sources (CLOETENS ET AL., 1996). Furthermore, the adaptation of advanced phase-retrieval techniques like holotomography (CLOETENS ET AL., 1999) to cone-beam geometry allows to obtain quantitative results in the latter case. However, imperfections in the beam introduced by the focusing optics cannot always be completely removed by the usual so-called flat-field correction, in which an image with sample is divide by one without. As a result, the quality of the retrieved images may suffer in these cases (MOKSO ET AL., 2007).

1.8 Scanning microscopy

Although already HOROWITZ AND HOWELL (1972) built a Scanning Transmission X-ray Microscope (STXM), it was the last of the lens-based X-ray microscopy concepts to be implemented for regular user operation (KIRZ ET AL., 1990; RARBACK ET AL., 1988): In such a set-up, the sample is raster-scanned in the focal plane of a focusing optics and the transmitted intensity is detected. Each pixel of the resulting image thus encodes the average transmission of the area illuminated by the focal spot during the corresponding acquisition. As a consequence, the lateral extent of the focus is the main factor limiting the spatial resolution. However, if the scanning set-up fails to provide the required stability and positioning accuracy on the nanometre scale, the resolution may be degraded further. While in principle any type of X-ray focusing optics discussed in section 1.5 can be used to construct a STXM, Fresnel zone plates play again the leading role. Even at hard X-ray energies, zone plates still excel at achieving the highest resolution (VILA-COMAMALA ET AL., 2011b), although low efficiencies, chromatic aberrations and too short working distances of FZPs have also led to the construction of KB-based scanning microscopes (MARTÍNEZ-CRIADO ET AL., 2012). To reach the diffraction-limited focal spot size of a FZP as given in (1.55) on page 31, the illumination should be sufficiently spatially coherent.

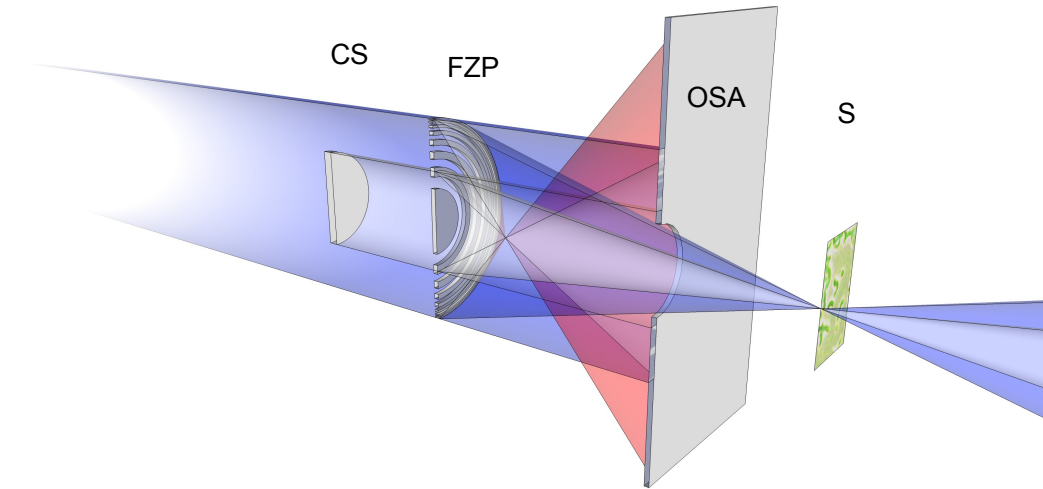


Figure 1.3: Schematic (not to scale) of a Scanning Transmission X-ray Microscope (STXM) with a Fresnel zone plate as focusing device. For better visualization, the model has been cut along the optical axis and is only shown in one half-space. The incident beam is focused by the Fresnel zone plate **FZP** onto the sample **S** located in the first-order focal plane. The undiffracted beam is rejected through a combination of a central stop **CS** and an order-sorting aperture **OSA** of smaller diameter than the former. Furthermore, the OSA filters out the higher diffraction orders of the FZP, as depicted for the third-order beam drawn in red. For data acquisition, the sample **S** is raster-scanned and the transmitted beam is collected either with a simple intensity monitor or a two-dimensional area detector (not shown). In the latter case, not only absorption images can be obtained, but also phase-contrast and dark-field signals (see section 1.8.1 for more details). For X-ray fluorescence mapping, an energy dispersive detector can be placed close to the sample, typically in the horizontal plane forming an angle of close to 90° with the optical axis.

This can be achieved by spatial filtering of synchrotron radiation (see section 2.2.1 on page 47). Therefore, STXMs have often been installed at undulator beamlines (already since the early days, see KIRZ ET AL., 1990), as they provide high coherent fluxes. The necessary illumination conditions can also be formulated as the requirement that the de-magnified image of the source at the focal plane should be smaller than the diffraction-limited focus.

When used in a STXM, the higher diffraction orders of the FZP as well as the undiffracted beam have to be prevented from hitting both the sample and the detector. As sketched in Fig. 1.3, this is achieved by combining a central stop and an order-sorting aperture (OSA). As a consequence, a STXM is more dose-efficient than a TXM: only the radiation contributing to the imaging process reaches the sample and there are no optics of limited efficiency between specimen and detector. However, the necessary scanning process still makes data acquisition in a STXM slower than in the other types

of X-ray microscopes. On the other hand, raster scans of an object with a small X-ray probe enable the application of various spectroscopic methods (compare also section 3.4 of the review by [KIRZ ET AL., 1995](#)): these include, e.g., near-edge absorption spectroscopy ([ADE ET AL., 1992](#)), X-ray fluorescence ([RIVERS ET AL., 1991](#)), photoemission ([ADE ET AL., 1990](#)), visible-light luminescence ([JACOBSEN ET AL., 1993](#)), or micro-diffraction ([KAPISHNIKOV ET AL., 2012](#)). Each of the latter three of course requires an additional dedicated detector. While for the detection of the transmission signal in principle a simple proportional counter is sufficient, installation of more sophisticated detection systems can also be beneficial in the forward direction: in addition to the transmission, also differential phase-contrast (DPC) and dark-field signals can be obtained with position-sensitive detectors, either by using a dedicated segmented design ([DE JONGE ET AL., 2008](#); [FESER ET AL., 2003](#); [HORNBERGER ET AL., 2008](#)) or standard pixelated solutions, like CCDs ([CHAPMAN ET AL., 1995](#); [GIANONCELLI ET AL., 2006](#); [MORRISON ET AL., 2003](#)) or fast hybrid pixel detectors ([MENZEL ET AL., 2010](#)). The analysis of STXM data for these contrast modalities is discussed in section 1.8.1. Alternatively, phase contrast may also be generated by placing a phase ring upstream of the focusing optics such that this scanning set-up is equivalent to a full-field Zernike set-up with reversed propagation direction ([HOLZNER ET AL., 2010](#)).

1.8.1 Analysis of STXM data

As ptychographic data sets provide sets of diffraction patterns recorded by scanning a localized illuminating probe across the sample, analysis schemes for STXM data can be readily applied to obtain low-resolution images of the investigated objects. This allows to get a fast on-line visualization of the scanned area and is thus especially useful to check sample alignment. Furthermore, upsampled versions of these low-resolution images may be used as starting guesses for the ptychographic phase-retrieval algorithms.

Fig. 1.4 illustrates the three different types of contrast which can be obtained when using segmented or pixelated detectors (compare also [KIRZ ET AL., 1995](#) for the basic concepts and [CHAPMAN ET AL., 1995](#) for the analysis in case of a pixelated detector):

Attenuation contrast The incoherent bright-field transmission image is constructed by assigning the total photon count in each detector frame to the position it was recorded at, compare Fig. 1.4(b). Mathematically, this corresponds to calculating the zeroth moment of the recorded pattern ([THIBAUT](#)

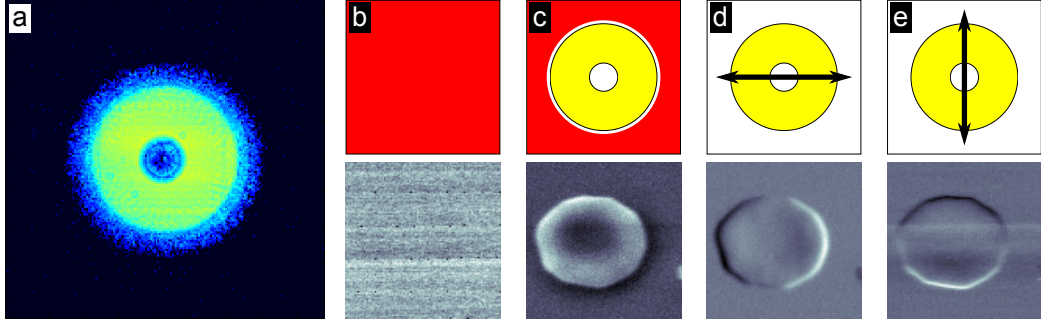


Figure 1.4: Analysis of STXM data: (a) Example for a typical signal recorded with a pixelated detector in a FZP-based STXM. In general, the detector in the far field shows an image of the effective entrance pupil of the focusing optics, which results in this annular shape for a FZP with a central stop (compare Fig. 1.3). In the top row of columns (b)–(e), a schematic representation of this pattern is used to illustrate the analysis options leading to the different contrast modalities shown in the bottom row. (b) To obtain an incoherent bright-field transmission image, the total sum of all pixel values in the respective detector frame is assigned to each pixel of the STXM map. In this case, however, the absorption of the sample – a human erythrocyte – is too weak to generate a meaningful image. (c) For dark-field contrast, only the signals outside the annulus are summed up by applying an appropriate mask to the recorded images. (d) Detecting the horizontal shifts of the annulus yields differential phase contrast in the horizontal direction (compare also Fig. 1.5). (e) Analogously, the vertical phase gradient of the object is obtained by assigning the corresponding vertical beam displacement to each point of the STXM map.

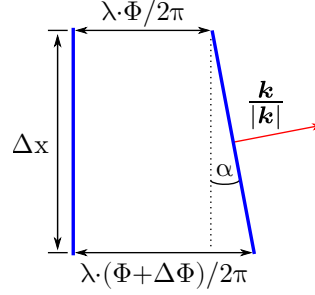
ET AL., 2009b)

$$M_0(\mathbf{r}_j) = \int |\Psi_j(\mathbf{q})|^2 d\mathbf{q} , \quad (1.66)$$

where \mathbf{r}_j is the current scan position, \mathbf{q} the detector plane coordinates, and $\Psi_j(\mathbf{q})$ the wave field in the detector plane (obtained by propagation of an exit wave (1.25)).

Dark-field contrast In analogy to visible light microscopy, dark-field contrast is obtained by only considering that part of the recorded photons which lies outside the bright-field cone. While CHAPMAN ET AL. (1995) used an annular mask, it can be beneficial to use a circular mask without a central hole like in Fig. 1.4(c): At higher X-ray energies, there may still be some residual transmission through the central stop which should not be assigned to the dark-field signal. The choice of a circular mask also resembles the first experimental realizations of dark-field contrast in a STXM by MORRISON AND BROWNE (1992), who blocked the unscattered bright-field cone by a circular beamstop in front of the detector. In principle, also directional information can be obtained if the detector frame is further divided into angular segments like in scanning small-angle X-ray scattering (BUNK ET AL.,

Figure 1.5: Relation of beam deflection angle and phase gradient: Assume that a wavefront (top blue line) accumulates a path-length difference of $\lambda \cdot \Phi / 2\pi$ compared to vacuum (bottom blue line) upon passing through a sample at a given position, while at a lateral distance of Δx the path-length difference amounts to $\lambda \cdot (\Phi + \Delta\Phi) / 2\pi$. If the change in phase can be considered to be linear over Δx , the result is a tilted wavefront, i.e. the propagation direction is changed by an angle $\alpha \approx \frac{\lambda}{2\pi} \frac{\Delta\Phi}{\Delta x}$ (in small-angle approximation).



2009).

Differential phase contrast As depicted in Fig. 1.5, a measurement of beam deflection α along a given direction allows to obtain the mean derivative $\Delta\Phi/\Delta x$ of the phase shift in the illuminated region with linear extent Δx . As according to (1.28) the phase shift depends both on the refractive index and the thickness of the material, a phase gradient may be caused by the change of either. A beam deflection can be trivially measured by calculating the difference of the signals detected in the corresponding half-planes (top and bottom, left and right) of the detector. Another option is to calculate in each image the centre-of-mass of the intensity along a given axis. Or, in other words, the first moments of the recorded intensity (THIBAULT ET AL., 2009b):

$$M_\chi(\mathbf{r}_j) = \int q_\chi |\Psi_j(\mathbf{q})|^2 d\mathbf{q}, \quad \chi = x, y. \quad (1.67)$$

A more rigorous investigation of the relation between the moments M_χ and the physical parameters of the object reveals some limitations (THIBAULT ET AL., 2009b): Only when the object is uniformly absorbing and the probe is centrosymmetric, the first moments are directly proportional to the gradient of the phase. In general, however, the measured differential contrast also depends on the gradient of the absorption, leading to an additional differential amplitude contrast (DAC). The contributions of DAC can usually be neglected when working in focus (DE JONGE ET AL., 2008), but have to be considered at a distance Δz out of focus (THIBAULT ET AL., 2009b):

$$M_\chi(\mathbf{r}_j) \propto k \frac{\partial}{\partial \chi} \left(t\delta - t\beta \frac{\Delta z}{z_{\text{DOF}}} \right), \quad \chi = x, y, \quad (1.68)$$

where t is the thickness of the sample, z_{DOF} the depth of focus, and δ and β the components of the refractive index according to (1.21). As a practical consequence of (1.68), the contrast inversion of the differential signal does

not occur at the focal plane, contrary to what one would intuitively expect from simple geometrical considerations.

Fig. 1.4 shows two examples obtained with the momentum analysis of the detected intensities: in Fig. 1.4(d), the horizontal shift of the beam has been assigned to each pixel of the STXM map, while in Fig. 1.4(e) vertical deflections are considered. From such orthogonal differential images, absolute phase maps can be calculated through integration (DE JONGE ET AL., 2008; KOTTLER ET AL., 2007; MENZEL ET AL., 2010):

$$\Phi(\mathbf{r}) = i\mathcal{F}^{-1} \left\{ \frac{q_x \tilde{\Phi}_x(\mathbf{q}) + q_y \tilde{\Phi}_y(\mathbf{q})}{q_x^2 + q_y^2} \right\}, \quad (1.69)$$

where $\tilde{\Phi}_x(\mathbf{q})$ and $\tilde{\Phi}_y(\mathbf{q})$ are the Fourier transforms of the DPC images. As a constant global phase shift is lost in the DPC signal, additional knowledge is required to fix this remaining free parameter and get fully quantitative results. Typically, an empty region in the vicinity of the specimen is employed. Assuming that the phase shift of the support structure, e.g. a silicon-nitride membrane, is the same for both this area and the object's location, the phase shifts of the specimen relative to this reference are equal to the absolute values.

Chapter 2

Coherent diffractive imaging

2.1 The phase problem

In the X-ray regime, a detector measures only the intensity of a wavefield incident upon it. If the electromagnetic field has the complex scalar amplitudes E_0 and H_0 , this intensity is given by the magnitude of the time-averaged Poynting vector (ATTWOOD, 2000)

$$I = \langle |\mathbf{S}| \rangle_t = \frac{1}{2} E_0 H_0^* = \frac{n}{2} \sqrt{\frac{\epsilon_0}{\mu_0}} |E_0|^2, \quad (2.1)$$

where n is the refractive index of the medium. As a result, the phases of the wavefield E_0 are lost in the measurement. This is known as the *phase problem*. Reconstruction of the lost phases and thereby finding a solution to the phase problem is called *phase retrieval*. While phase retrieval is also done in the Fresnel near-field regime (compare e.g. CLOETENS ET AL., 1999), the discussion in this thesis is limited to phase retrieval from Fraunhofer far-field diffraction patterns. According to (1.45) on page 27, the wavefields in the detector plane and directly behind object are then related by a Fourier transform. Reconstruction of the phases in the diffraction plane thus allows – together with the measured diffraction amplitudes – to obtain the object’s exit wave O via an inverse Fourier transform.

From a mathematical point of view, half of the information originally contained in the diffracted wavefield is lost when just its intensity is recorded. As a consequence, additional constraints have to be imposed to get a unique reconstruction. The phase (retrieval) problem of coherent diffractive imaging can thus also be re-formulated as follows:

Definition 2.1 (The phase problem). Find the unique reconstruction of the object’s exit wave which reproduces the measured diffraction amplitudes and

satisfies the additional constraints.

BATES (1982) has proven that such “Fourier phase problems are uniquely solvable in more than one dimension”. However, several **ambiguities** are inherent to the phase-retrieval problem from a single diffraction pattern: far-field intensities do not change if the object’s exit wave is multiplied by a constant phase factor or if the object is shifted within the field of view (causing a phase gradient in the diffraction plane, compare (A.3) on page 338). Furthermore, also the so-called *twin image*, which is related to the true solution via complex conjugation and rotation by 180° , is a valid solution. The Fourier transform of the twin image has the same magnitude as the original image, but the phase has the opposite sign. In literature (BATES, 1982), all these results are typically treated as equivalent manifestations of the same unique solution, also called its “trivial characteristics” (BATES, 1982; MIAO ET AL., 1998), as they are irresolvable without additional constraints. The twin image ambiguity, e.g., can be solved by breaking the symmetry of the problem, compare also section 3.1.4.3 on page 86, while both constant phase terms typically have to be removed using *a priori* knowledge about the imaged object.

2.2 Coherent X-rays

The coherence of waves is characterized by their spatio-temporal correlations. For a wave field $E(\vec{r}, t)$, the *mutual coherence function* (MANDEL AND WOLF, 1965) is defined as the correlation of the wave field at positions $\vec{r}_j = (x_j, y_j, z_j)$ ($j = 1, 2$) for a time separation τ :

$$\Gamma(\vec{r}_1, \vec{r}_2, \tau) = \langle E^*(\vec{r}_1, t)E(\vec{r}_2, t + \tau) \rangle_T . \quad (2.2)$$

Usually (2.2) is normalized, which yields the *complex coherence factor*

$$\gamma(\vec{r}_1, \vec{r}_2, \tau) = \frac{\Gamma(\vec{r}_1, \vec{r}_2, \tau)}{\sqrt{\Gamma(\vec{r}_1, \vec{r}_1, 0)\Gamma(\vec{r}_2, \vec{r}_2, 0)}} = \frac{\Gamma(\vec{r}_1, \vec{r}_2, \tau)}{\sqrt{I(\vec{r}_1)I(\vec{r}_2)}} . \quad (2.3)$$

It is also called *complex degree of coherence* as its modulus $|\gamma|$ gives the ratio of coherent intensity to total intensity (BORN AND WOLF, 2006, section 10.3). The wave field is said to be *coherent* if the modulus takes its maximum value $|\gamma| = 1$, whereas it is *incoherent* for $|\gamma| = 0$. *Partial coherence* is characterized by a degree of coherence $|\gamma|$ in the range $0 < |\gamma| < 1$. (VAN CITTERT, 1934; ZERNIKE, 1938)

In practice, one is usually interested in the characteristic length scales over which the degree of coherence is high for a given source, the so-called

coherence lengths: While the temporal coherence could also be quantified by the maximum time separation τ_{coh} in (2.3) for which $|\gamma(\vec{r}_1, \vec{r}_1, \tau)|$ first drops to zero, usually the *longitudinal coherence length* $\xi_l = c \cdot \tau_{\text{coh}}$, i.e. the distance a light wave at speed c would travel during the coherence time τ_{coh} , is used. The spatial coherence is typically characterized with the *transverse coherence length*, i.e. the distance $|\vec{r}_1 - \vec{r}_2|$ for which $\gamma(\vec{r}_1, \vec{r}_2, 0)$ falls to zero. $|\gamma|$ can be directly determined from interference experiments, e.g. with a Young's double-slit arrangement as in Fig. 2.1: If the two beams have equal intensity, one finds for the fringe contrast or *visibility* (VAN CITTERT, 1958; MANDEL AND WOLF, 1965, p. 239; BORN AND WOLF, 2006, section 10.4):

$$\mathcal{V} = \frac{I_{\text{max}} - I_{\text{min}}}{I_{\text{max}} + I_{\text{min}}} = |\gamma| . \quad (2.4)$$

2.2.1 Transverse coherence

For an X-ray CDI experiment, the illumination of the area from which the signal is collected has to be spatially coherent. Therefore, it is usually convenient to be able to calculate the relevant transverse coherence length from the experimental geometry. For the derivation of such a simple geometrical expression, let us consider a Young's double slit arrangement like in Fig. 2.1 (VAN DER VEEN AND PFEIFFER, 2004): An incoherent light source of one-dimensional transverse extent a illuminates small slits of separation d located in a plane perpendicular to the optical axis at a distance R from the source. The diffraction from the double slit is visualized on a screen located at a distance L behind it. Using relation (2.4), we define the transverse coherence length ξ_t as the separation of the slits d for which the fringe visibility in the diffraction pattern becomes zero. This means, that the minima of the diffraction pattern from the double slit illuminated by a point source at the centre of the extended source coincide with the maxima of the diffraction for a point source being placed at the edge of the extended source. In small-angle approximation, one gets $\alpha_{\text{max},n} = n\lambda/d$ for the angle to the n -th maximum and $\alpha_{\text{min},n} = (n + \frac{1}{2})\lambda/d$ for the n -th minimum for illumination with the central point source. For an element at the edge of the source, all extrema are shifted by an angle $\Delta\alpha = a/(2R)$. Thus the maxima of this pattern coincide with the minima of the other and vice versa, if $\frac{1}{2}\frac{\lambda}{d} = \frac{a}{2R}$ is fulfilled. Solving for d yields the transverse coherence length

$$\xi_t = \frac{\lambda R}{a} . \quad (2.5)$$

Realistic two-dimensional sources often have asymmetric Gaussian intensity distributions in the source plane, so that one can find different coherence

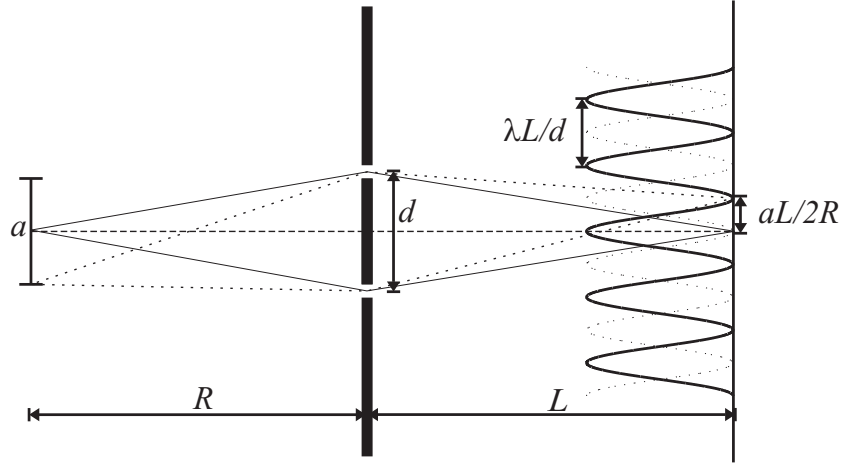


Figure 2.1: A Young's double-slit arrangement showing the interference patterns from two narrow slits (separation d) illuminated from elements at the central part (solid line) and the edge (dotted line) of the source (size a). The slit distance for which the patterns are in antiphase corresponds to the transverse coherence length $\xi_t = \lambda R/a$. From DIEROLF (2007), originally adapted from VAN DER VEEN AND PFEIFFER (2004).

lengths along the vertical ($\xi_{v,\sigma}$) and horizontal ($\xi_{h,\sigma}$) direction:

$$\xi_h = \frac{\lambda R}{2\pi\sigma_h} \quad \xi_v = \frac{\lambda R}{2\pi\sigma_v}, \quad (2.6)$$

where σ_h and σ_v are the sigma widths of the Gaussian source. These transverse coherence lengths represent the sigma widths of the complex coherence factor as introduced in (2.3) (SANDY ET AL., 1999). In many cases, the extent of a source is given as its full width at half maximum (FWHM), which for a Gaussian is related to the sigma widths by

$$\sigma = \frac{\text{FWHM}}{2\sqrt{2 \ln 2}} \approx 0.424 \cdot \text{FWHM}. \quad (2.7)$$

Accordingly, one can use $\xi_{\text{FWHM}} = 2\sqrt{2 \ln 2} \cdot \xi_\sigma \approx 2.355 \cdot \xi_\sigma$ to convert the coherence lengths in (2.6) to FWHM values.

2.2.2 Longitudinal coherence

For determination of the longitudinal coherence length ξ_l , two co-propagating waves with wavelengths λ and $\lambda + \Delta\lambda$ are considered (VAN DER VEEN AND PFEIFFER, 2004). ξ_l is then defined as the distance over which these two waves develop from being in phase to being in antiphase as illustrated in Fig. 2.2. This means that for N oscillations of the first wave, the second

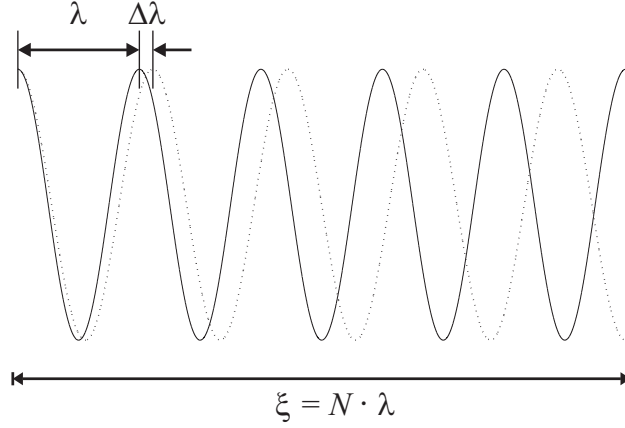


Figure 2.2: Two waves of wavelengths λ and $\lambda + \Delta\lambda$ starting simultaneously at the same point in time and space. At the longitudinal coherence length ξ_l the phase difference has become π . From [DIEROLF \(2007\)](#), originally adapted from [VAN DER VEEN AND PFEIFFER \(2004\)](#).

completes only $N - \frac{1}{2}$ oscillations. Solving the resulting condition $N\lambda = (N - \frac{1}{2})(\lambda + \Delta\lambda)$ for N and using $\xi_l = N\lambda$ one obtains

$$\xi_l = \frac{1}{2} \frac{\lambda^2}{\Delta\lambda} . \quad (2.8)$$

In CDI, the longitudinal coherence length puts a limit on the maximum observable diffraction angle and thus the resolution: For waves scattered at an angle 2θ from the centre and the edge of a sample with lateral extent a the path length difference is $\Delta s_{path}(\theta) = a \sin \theta$. As the condition for coherent interference is $\xi_l > \Delta s_{path}(\theta)$, this results in

$$\frac{\lambda^2}{\Delta\lambda} > a \sin \theta \approx a \frac{q_{max}}{k} , \quad (2.9)$$

where q_{max} is the largest momentum transfer detected and $k = 2\pi/\lambda$ the wave number. Using the relation $\Delta x = 2\pi/q_{max}$ between q_{max} and the resolution element Δx in real space (compare also section 2.3), one obtains the condition

$$\frac{\Delta\lambda}{\lambda} < \frac{\Delta x}{a} . \quad (2.10)$$

Considering additionally the thickness l of the sample along the beam yields the second condition

$$\frac{\lambda^2}{\Delta\lambda} > 4l(\sin \theta)^2 . \quad (2.11)$$

A crystal monochromator using a Si(111) Bragg reflection has a spectral bandwidth $\Delta\lambda/\lambda \simeq 1.4 \cdot 10^{-4}$ (ALS-NIELSEN AND MCMORROW, 2011, chapter 6). For a sample (or localized illumination) of lateral extent $a = 10 \mu\text{m}$, which is a size matching the typical transverse coherence lengths, (2.10) then gives a resolution limit of $\Delta x > 1.4 \text{ nm}$.

2.3 Sampling

Like other digital image processing techniques, phase-retrieval algorithms operate on images formed by arrays of discrete pixels using discretized versions of mathematical operations, like e.g. the discrete Fourier transform (DFT, see Appendix A.3 on page 339). Therefore, the sizes of sampling intervals have to be chosen such that the original continuous functions are still completely determined when sampled only at discrete points on finite grids. The conditions for this to be true are established by the *sampling theorem* (SHANNON, 1949), which is briefly reviewed in subsection 2.3.1. Based on this, the specific sampling requirements for phase retrieval from far-field diffraction data are discussed in subsection 2.3.2.

2.3.1 The sampling theorem

When a DFT is applied to an array which has N_{pix} samples of size Δx along a dimension in direct space, the relation to the sampling step size Δq along the corresponding dimension of size N_{pix} in Fourier space is given by (BUTZ, 2006)¹

$$\Delta x \cdot \Delta q = \frac{2\pi}{N_{\text{pix}}} . \quad (2.12)$$

The largest Fourier space component q_{max} contained in a DFT is

$$q_{\text{max}} = \frac{N_{\text{pix}}}{2} \Delta q = \frac{\pi}{\Delta x} . \quad (2.13)$$

Thus, if the continuous Fourier transform $\tilde{g}(q)$ of a continuous function $g(x)$ contains momentum transfers larger than q_{max} , the chosen sampling interval Δx is too coarse. In this case, spatial frequencies with $q > q_{\text{max}}$ are wrapped in Fourier space upon application of the DFT and create additional intensity

¹Analogous relations can be given for the other dimensions of an array. However, as multi-dimensional Fourier transforms can be expressed as consecutive applications of one-dimensional Fourier transforms with respect to each coordinate, all relations are given in a one-dimensional notation in what follows.

at lower frequencies. This behaviour, known as *aliasing*, is due to the periodicity of the DFT, compare (A.12) on page 340. A function with an infinitely broad Fourier spectrum can thus never be sampled unambiguously. However, aliasing does not occur if a continuous function $g(x)$ is bandwidth-limited, i.e.

$$\tilde{g}(q) = 0 \quad \forall |q| > q_{\text{Nyq}} , \quad (2.14)$$

and the condition

$$q_{\text{Nyq}} \leq q_{\text{max}} \quad (2.15)$$

is fulfilled for the chosen sampling interval. The value $f_{\text{Nyq}} = q_{\text{Nyq}}/(2\pi)$ is called the *Nyquist frequency* or sometimes also *cut-off frequency*. With (2.13), condition (2.15) can be rewritten into

$$\Delta x \leq \frac{2\pi}{2q_{\text{Nyq}}} = \frac{1}{2f_{\text{Nyq}}} , \quad (2.16)$$

i.e. the minimum sampling interval is inversely proportional to twice the Nyquist-frequency. If at least the equality in condition (2.16) is fulfilled, the continuous function $g(x)$ is completely determined by its sampled version $g_m \equiv g(m\Delta x)$ with $m \in \mathbb{Z}$. Mathematically, this means that the original function can be constructed as the sum of sinc-functions which are centred at the sampling points $m\Delta x$ and have amplitudes g_m (BUTZ, 2006; SHANNON, 1949):

$$g(x) = \sum_{m=-\infty}^{\infty} g_m \frac{\sin q_{\text{Nyq}}(x - m\Delta x)}{q_{\text{Nyq}}(x - m\Delta x)} = \sum_{m=-\infty}^{\infty} g_m \text{sinc} \frac{\pi}{\Delta x}(x - m\Delta x) . \quad (2.17)$$

This is often called the *Shannon sampling theorem*² and discretization according to the case of equality in (2.16) is also referred to as *Shannon sampling*. Sampling with finer steps does not add any additional information about $g(x)$.

In practice, the function g has not only to be band-limited, but usually should also be fully contained in the coordinate range covered by the real-space sampling array. However, SHANNON (1949) also pointed out that a function cannot be both band-limited and of finite extent in direct space. Nevertheless, he stated that keeping a band-limited function very small outside a given region is possible and sufficient. In this case, one can assume $g_m \approx 0$ for $m \notin [-N_{\text{pix}}/2, N_{\text{pix}}/2 - 1]$ and the infinite sums in equation (2.17) can be replaced by a finite sum over all sampling points, i.e. $m \in [-N_{\text{pix}}/2, N_{\text{pix}}/2 - 1] \cap \mathbb{Z}$.

²This is due to the fact that SHANNON (1949) first published this form of the sampling theorem. As he cites earlier work by Nyquist and Whittaker in his article, also the terms *Nyquist-Shannon sampling theorem* and *Whittaker-Shannon sampling theorem* are frequently used.

2.3.2 Sampling requirements in far-field phase retrieval

2.3.2.1 From crystallography to coherent diffractive imaging

Two articles by SAYRE (1952, 1980) are often referred to as the first major conceptual milestones in the development of X-ray coherent diffractive imaging of non-crystalline specimens through the application of phase retrieval³. One of the first connections between solving the phase problem and sampling of the diffraction data – in this case still for the crystallographic case – was made in the article “Some implications of a theorem due to Shannon” (SAYRE, 1952): Consider a function $g(x)$ that is non-zero only on an interval of finite size a in real space. In Sayre’s article, this extent a is the size of a crystal’s unit cell. To determine the rate necessary to unambiguously sample the Fourier transform of g , a can be considered as the direct-space analogue of twice the Nyquist frequency. According to (2.16), the Fourier transform $\tilde{g}(q)$ then has to be sampled with a step size of at least $\Delta q = 2\pi/a$. Therefore, $\Delta q = 2\pi/a$ is also the length scale of the smallest features in the typical grainy structure (“speckles”) of coherent diffraction patterns (compare LAUTERBORN AND KURZ, 2003, chapter 6), which is always inversely proportional to the largest extent a of the illuminated object. However, the intensity pattern $|\tilde{g}(q)|^2$ measured in an X-ray diffraction experiment is not the Fourier transform of the original object $g(x)$, but rather of its autocorrelation⁴ $g(x) \star g(x)$ (compare (A.7) on page 338). As the maximum extent of $g(x) \star g(x)$ is twice that of $g(x)$, the intensity pattern also has to be sampled with at least twice as fine steps, i.e. with $\Delta q = 2\pi/(2a)$, to unambiguously determine the autocorrelation. SAYRE (1952) concluded that sampling diffraction patterns this way would thus allow to solve the phase problem, at least for centrosymmetric crystals. In standard crystallography, however, this higher sampling rate cannot be achieved as the diffraction patterns consist only of discrete Bragg peaks appearing at spacings of $\Delta q = 2\pi/a$ (reciprocal lattice constant). As a result, the idea had only rather limited practical consequences at first. But three decades after he had published these first implications, SAYRE (1980) proposed that the approach could instead be applied to the continuous diffraction patterns of non-crystalline

³In his review “X-Ray Crystallography: The Past and Present of the Phase Problem”, SAYRE (2002) gives an overview on various techniques on solving the phase problem and their historical development. In addition to a discussion of various approaches to solve the crystallographic phase problem, Sayre also describes his personal perspective of the work (e.g. SAYRE, 1952, 1980; SAYRE AND CHAPMAN, 1995) which paved the way towards the first demonstration of X-ray CDI (MIAO ET AL., 1999).

⁴In the context of crystallography, like in Sayre’s original work (SAYRE, 1952), this autocorrelation is also called the Patterson function.

specimens. Instead of the unit cell's size, the quantity a then just represents the extent of a localized non-crystalline object. Based on some earlier work by BRUCK AND SODIN (1979) going in the same direction, BATES (1982) shortly afterwards proved that adequately high sampling allows to uniquely⁵ solve the phase problem in two or more dimensions. Based on the historical origins and the higher sampling rate compared to crystallography, the technique was later coined “oversampling method to retrieve the phase” (MIAO ET AL., 1998).

2.3.2.2 Sampling of two-dimensional diffraction patterns

Let us assume that two-dimensional diffraction patterns are recorded with a pixelated detector with $N = N_x \times N_y$ pixels (without loss of generality: N_x, N_y even) which is positioned at a distance Z behind the sample plane. Each pixel covers an area of $\Delta s_x \times \Delta s_y$. In small-angle approximation, a position difference of Δs on the detector corresponds to a scattering angle of $2\theta \approx \Delta s/Z$. Inserting this in (1.48) on page 28 reveals that the sampling intervals in reciprocal space depend solely on the experiment's geometry:

$$\Delta q_x = \frac{2\pi}{\lambda Z} \Delta s_x, \quad \Delta q_y = \frac{2\pi}{\lambda Z} \Delta s_y. \quad (2.18)$$

As the planes of sample and detector are related by a discrete Fourier transform, the size of the real-space image is also $N_x \times N_y$ pixels. The corresponding real-space sampling intervals Δx and Δy are given by (2.12) on page 50. The linear extent of the field-of-view in direct space along the Cartesian axis is thus

$$L_x = N_x \Delta x = \frac{2\pi}{\Delta q_x}, \quad L_y = N_y \Delta y = \frac{2\pi}{\Delta q_y}. \quad (2.19)$$

Inserting (2.18) into (2.19), allows to calculate the pixel size in real space for a given experimental geometry:

$$\Delta x = \frac{\lambda Z}{N_x \Delta s_x}, \quad \Delta y = \frac{\lambda Z}{N_y \Delta s_y}. \quad (2.20)$$

It is now assumed that the scattering object is represented by a density function $g(x, y)$ with a finite support S , i.e.

$$g(x, y) = 0, \quad \text{if } (x, y) \notin S. \quad (2.21)$$

⁵In the context of CDI, a unique solution is always to be understood as being unique apart from the inherent ambiguities, or “trivial characteristics”, discussed in the last paragraph of section 2.1.

If $S_x \times S_y$ is the smallest rectangle in which the support S is fully contained, sufficient sampling of its Fourier transform according to Shannon is achieved for⁶

$$\Delta q_x \leq \frac{2\pi}{S_x}, \quad \Delta q_y \leq \frac{2\pi}{S_y}. \quad (2.22)$$

However, like in the one-dimensional case discussed by SAYRE (1952) and in the previous section, the correct Shannon sampling intervals of the diffraction intensity $|\tilde{g}(q_x, q_y)|^2$ have to be determined from the larger support of this pattern's Fourier transform, the autocorrelation $g(x, y) \star g(x, y)$. As for this support of the autocorrelation the size of the minimum containing rectangle is $2S_x \times 2S_y$, the maximum size for the sampling intervals in reciprocal space reduces by a factor of two:

$$\Delta q_x \leq \frac{\pi}{S_x}, \quad \Delta q_y \leq \frac{\pi}{S_y}. \quad (2.23)$$

If the intensity is sampled according to these conditions, no aliasing in the autocorrelation occurs. The minimum sampling rate enforced by (2.23) is a factor of two higher than that of (2.22). Therefore, the diffraction pattern is often said to be *linearly oversampled* by a factor of two, although (2.23) just states the condition for proper Shannon sampling. When comparing the total minimum number of sampling points in the two cases, one arrives at a factor of four. For two and more dimensions and in the absence of noise, oversampling by this factor “almost always” (BATES, 1982) guarantees the existence of a unique solution for the corresponding phase problem.

2.3.2.3 Sampling and degrees of freedom

By comparing the number of unknowns to the amount of measured values, MIAO, SAYRE, AND CHAPMAN (1998) concluded that also lower oversampling factors can allow for unique solutions: In the sampled images, the pixel coordinates are $(q_{x,n}, q_{y,m}) = (n\Delta q_x, m\Delta q_y)$ in reciprocal space and $(x_n, y_m) = (n\Delta x, m\Delta y)$ in real space, with integer factors $n \in [-N_x/2, N_x/2 - 1]$ and $m \in [-N_y/2, N_y/2 - 1]$. The Fourier magnitude, i.e. the square-root of the measured intensity value, at a given pixel $(q_{x,n}, q_{y,m})$ is linked to the object function in real space by the discrete Fourier transform:

$$|\tilde{g}(q_{x,n}, q_{y,m})| = \left| \frac{1}{N_x N_y} \sum_{\nu=-N_x/2}^{N_x/2-1} \sum_{\mu=-N_y/2}^{N_y/2-1} g(x_\nu, y_\mu) e^{i2\pi(n\nu/N_x + m\mu/N_y)} \right|. \quad (2.24)$$

⁶As already pointed out in section 2.3.1 on the sampling theorem, smaller intervals than those given by the equality do not increase the information content of the sampled pattern.

Considering all $N = N_x \times N_y$ pixels of $|\tilde{g}(q_x, q_y)|$, this leads to set of N equations to reconstruct the N pixels of $g(x, y)$. If $g(x, y)$ is real-valued, N unknowns have to be calculated. However, according to Friedel's law (compare (A.8) in page 338), the corresponding diffraction pattern is centrosymmetric in this case, i.e. $|\tilde{g}(q_x, q_y)| = |\tilde{g}^*(-q_x, -q_y)|$. The measured data therefore provides only $N/2$ independent equations. Due to the breakdown of Friedel's law for a complex-valued object $g(x, y)$, $|\tilde{g}(q_x, q_y)|$ then has N independent values. But as in this case both the real and imaginary part for each pixel of $g(x, y)$ have to be reconstructed, one still has twice as many unknowns as the number of equations. For both real-valued and complex-valued object functions $g(x, y)$, the phase problem is thus underdetermined by a factor of two. To uniquely solve the phase problem, the number of unknowns therefore has to be reduced by at least a factor of two by introducing additional constraints based on *a priori* knowledge. With the ratio

$$\sigma = \frac{\text{total pixel number}}{\text{unknown-valued pixel number}} \quad (2.25)$$

introduced by MIAO ET AL. (1998), this can be expressed as the necessary condition $\sigma \geq 2$. If $g(x, y)$ has a finite support as defined in (2.21) and this support contains N_S pixels, (2.25) becomes the *oversampling ratio* (MIAO AND SAYRE, 2000)

$$\sigma = \frac{N}{N_S} . \quad (2.26)$$

For a rectangular support and Shannon sampling according to (2.23), this oversampling ratio is $\sigma \geq 4$, so at least two times higher than the minimum value necessary to constrain all degrees of freedom. This leads to the conclusion cited at the beginning of this paragraph (MIAO ET AL., 1998): unique reconstructions from two-dimensional diffraction patterns are also possible with oversampling factors lower than four.

2.3.2.4 Experimental implications

When preparing a CDI experiment, typically Shannon sampling according to (2.23) on page 54 is used for planning the geometry of the set-up: By replacing $\Delta q_{x,y}$ in (2.18) on page 53 with condition (2.23), one can deduce either the minimum required distance Z between sample and detector for a given object,

$$Z \geq \frac{2}{\lambda} \max(\Delta s_x, \Delta s_y) \cdot \max(S_x, S_y) , \quad (2.27)$$

or the maximum extent $\max(S_x, S_y)$ of the support or a localized illumination for a given geometry,

$$\max(S_x, S_y) \leq \frac{\lambda Z}{2 \max(\Delta s_x, \Delta s_y)}. \quad (2.28)$$

As an example, we consider some standard settings for CDI experiments at the cSAXS beamline of the Swiss Light Source (compare section 5.1 starting on page 125): With a wavelength $\lambda = 2 \text{ \AA}$ and a maximum distance of $Z = 7.2 \text{ m}$ for the Pilatus 2M detector with its pixels of $\Delta s_x \times \Delta s_y = 172 \mu\text{m} \times 172 \mu\text{m}$ size, one obtains the condition $\max(S_x, S_y) \leq 4.2 \mu\text{m}$ for the maximum size of sample or illumination.

2.4 Iterative phase retrieval in CDI

Additional constraints have been introduced as an integral part of the phase problem already in its Definition 2.1 on page 46. Their role in reducing the number of unknowns to allow for a unique reconstruction has been further detailed in section 2.3.2.3, in particular for the case of a finite support in real space. Additional information beyond a simple binary support is included in other common direct-space constraints, e.g. non-negativity of a real-valued object (FIENUP, 1982), constraints on the object's histogram (ELSER, 2003a), or a known illumination (FIENUP, 2006; QUINEY ET AL., 2005). These usually improve the convergence behaviour of the iterative algorithms which are typically employed to solve the system of equations defined by (2.24) on page 54. Most of these algorithms can be mathematically expressed in terms of iterative projections onto constraint sets. This section gives a brief introduction to this concept, mainly adapted from ELSER (2003a) and BAUSCHKE ET AL. (2002), as well as to some small extent also from MARCHESINI (2007) and THIBAUT (2007). A detailed description of the mathematical basics of iterative phase retrieval can be found e.g. in the review by LUKE ET AL. (2002). After introducing the projection formalism, the section discusses some phase-retrieval algorithms commonly used in CDI and their limitations. The section is partly based on previous work in DIEROLF (2007, section 2.2.3).

2.4.1 Phase retrieval as an optimization problem

Any image with N complex-valued pixels can be represented as a vector \mathbf{x} with complex components x_ν , $\nu \in [1, N] \cap \mathbb{N}$, in an N -dimensional Euclidean vector space V_N . If the image is Fourier transformed, the resulting image

can again be expressed as a vector $\tilde{\mathbf{x}}$ in V_N , i.e. the Fourier transform just changes the components of the vector \mathbf{x} . However, its norm is preserved due to Parseval's theorem (see (A.4) on page 338). The Fourier transform is thus *unitary* and can be interpreted as a rotation of the N -dimensional vector \mathbf{x} . Within this vector formalism, constraints both in real and reciprocal space can be expressed as the sets of all points in V_N for which the corresponding images satisfy the respective constraint. In CDI, one of these sets has of course to contain all images fulfilling the **Fourier modulus constraint** which is determined by the square root of the measured diffraction intensities. Representing these measured Fourier amplitudes by the vector \mathbf{m} , the corresponding constraint set is defined as

$$C_F = \{\mathbf{y} \in V_N \mid |\tilde{y}_\nu| = |m_\nu|, \forall \nu \in [1, N]\}, \quad (2.29)$$

where the \tilde{y}_ν are the components of the Fourier transform of \mathbf{y} . As pointed out in the introductory paragraph of this section, several types of *a priori* knowledge may be used to construct a direct-space constraint set. For simplicity, the following discussion uses the **support constraint** introduced in section 2.3.2.2. Based on the expression for the finite support in (2.21) on page 53, we define C_S as the set of all image vectors \mathbf{y} for which the values y_ν are non-zero only for the pixels inside the support, i.e. $\nu \in S$. In our vector space terminology, this means that any vector of the set is orthogonal to the basis vectors of the outside components (the basis vectors of the complement of C_S), i.e. their dot product vanishes. For these two constraints, the phase (retrieval) problem stated in Definition 2.1 on page 46 can be formulated as

$$\text{find } \mathbf{x} \in C_S \cap C_F. \quad (2.30)$$

For this phase problem to be uniquely solvable, the two constraint sets thus have to overlap and this intersection should furthermore consist of just one single point (image vector).

Convex and nonconvex sets A set D is convex, if for any two points $\mathbf{x}_1, \mathbf{x}_2 \in D$ also any point on the connecting line is part of the set, i.e. $\mathbf{x} = \eta\mathbf{x}_1 + (1 - \eta)\mathbf{x}_2 \in D$ is fulfilled for all $\eta \in [0, 1] \cap \mathbb{R}$. Optimization problems analogous to (2.30) in which the constraint sets are convex are well understood in terms of their convergence behaviour (BAUSCHKE ET AL., 2002). Unfortunately, phase retrieval turns out to be a nonconvex optimization problem. While the support constraint set C_S is convex (BAUSCHKE ET AL., 2002; ELSER, 2003a), it can be easily shown that the Fourier modulus constraint generates a nonconvex set (BAUSCHKE ET AL., 2002): If we

pick $\mathbf{x} \in C_F$, also $-\mathbf{x} \in C_F$. The vector $\frac{1}{2}\mathbf{x} + \frac{1}{2}(-\mathbf{x}) = 0$ lies on their connecting line but does not belong to the set C_F which is thus nonconvex⁷. As a result, the methods developed for convex optimization cannot be readily applied to the phase-retrieval problem. Or, as BAUSCHKE ET AL. (2002) put it, “[...] the mathematical theory remains unable to completely analyse the convergence behaviour of these algorithms in nonconvex settings [...]”. In particular, stagnation of iterative algorithms can occur, see the discussion in subsection 2.4.3.2 on the error-reduction algorithm and Fig. 2.5.

2.4.2 Projections

To create update rules for iterative algorithms, we have to establish a mapping between any possible image vector $\mathbf{x} \in V_N$ and the ones contained in the corresponding constraint sets. This is done by introducing projections:

Definition 2.2 (Projection onto constraint set). The projection $\pi_D(\mathbf{x})$ onto a given constraint set $D \subset V_N$ is the operator which maps every $\mathbf{x} \in V_N$ to $\pi_D(\mathbf{x}) = \mathbf{y} \in D$ such that the distance $\|\mathbf{x} - \mathbf{y}\|$ is minimized.

In other words, the projection selects the image \mathbf{y} fulfilling the constraint which is closest – in terms of Euclidean distance – to the current guess \mathbf{x} . If the input vector is already part of the constraint set, the projection obviously does not change it and is thus an *idempotent* mapping, i.e. $\pi_D(\pi_D(\mathbf{x})) = \pi_D(\mathbf{x})$. Again, we restrict our discussion to the projections onto the constraint sets C_F and C_S discussed in the previous section. The projection π_S for the support constraint can be obtained rather straightforward from the mathematical formulation of the support in (2.21) and is defined as (see also, e.g., BAUSCHKE ET AL., 2002)

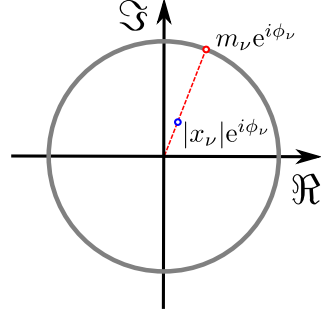
$$\pi_S(x_\nu) = \begin{cases} x_\nu & \text{if } \nu \in S, \\ 0 & \text{otherwise.} \end{cases} \quad (2.31)$$

The projection onto the Fourier modulus constraint is most conveniently applied to the Fourier transform $\tilde{\mathbf{x}}$ of the input vector \mathbf{x} , i.e. π_F is usually expressed as

$$\pi_F = \mathcal{F}^{-1} \tilde{\pi}_F \mathcal{F}, \quad (2.32)$$

⁷Note that the constraint set could be made convex by replacing $|\tilde{y}_\nu| = |m_\nu|$ with $|\tilde{y}_\nu| \leq |m_\nu|$ in (2.29), generating the so-called submodulus constraint. However, this modified constraint is typically not strong enough to produce reasonable phase retrieval results (BAUSCHKE ET AL., 2002).

Figure 2.3: Visualization of the Fourier modulus projection. A measured Fourier amplitude m_ν defines a circle in the complex plane. The projection replaces the amplitude of a complex number $x_\nu e^{i\phi_\nu}$ (blue marker) with this measured value by picking the closest point on this circle (red marker), which means the phase ϕ_ν is left unchanged. For $x_\nu = 0$, this operation is not well defined and any point on the circle has the same distance. The Fourier modulus projection is thus multi-valued, as characteristic for nonconvex constraint sets.



where the projection $\tilde{\pi}_F$ acting on the Fourier components is defined as

$$\tilde{p}_M(\tilde{x}_\nu) = \begin{cases} m_\nu \frac{\tilde{x}_\nu}{|\tilde{x}_\nu|} & \text{if } \tilde{x}_\nu \neq 0, \\ m_\nu e^{i\alpha} & \text{otherwise.} \end{cases} \quad (2.33)$$

For a non-zero component $\tilde{x}_\nu = |\tilde{x}_\nu| e^{i\phi_\nu}$, this projection is unique and replaces $|x_\nu|$ with the measured diffraction amplitude m_ν while keeping the original phase ϕ_ν . This is illustrated in Fig. 2.3. However, for zero-valued pixels the phase ϕ_ν is not defined and the phase α in the projected component may take any value. Or, in other words, all points on the circle defined by the modulus constraint of course have the same distance from an $x_\nu = 0$ located in the origin (compare Fig. 2.3), therefore no single closest point exists. In practice, the problem is often addressed by setting $\alpha = 0$. However, fact is that the Fourier modulus projection is not unique in all cases. According to BAUSCHKE ET AL. (2002), such *multi-valued projections* occur for all known examples of nonconvex sets and thus hinder predictions about convergence behaviour of algorithms using them.

2.4.3 Common iterative projection algorithms

The common iterative projection algorithms only differ in the choice of the update function G_{π_S, π_F} , which determines how the projectors π_S and π_F have to be applied to the current iterate $\mathbf{x}^{(n)}$ in order to construct the next one,

$$\mathbf{x}^{(n+1)} = G_{\pi_S, \pi_F}(\mathbf{x}^{(n)}) . \quad (2.34)$$

Some examples of update functions for common algorithms are given in the following subsections. Where appropriate, the iteration rules are not only expressed in this functional style, but also using a simplified operator notation,

$$\mathbf{x}^{(n+1)} = (G_{\pi_S, \pi_F}) \{ \mathbf{x}^{(n)} \} . \quad (2.35)$$

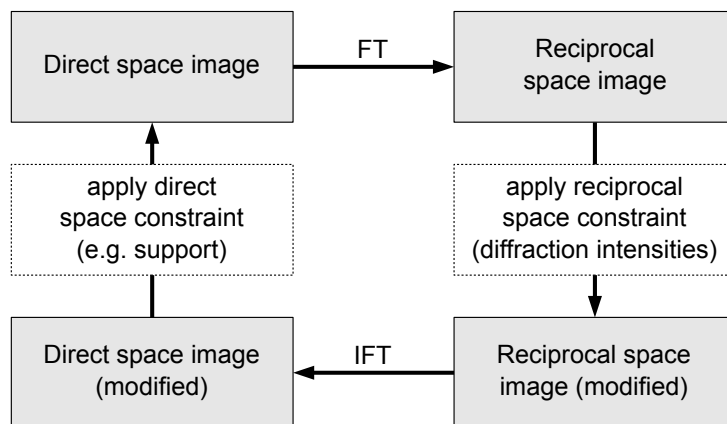


Figure 2.4: Schematic representation of the Gerchberg-Saxton or error-reduction algorithm (FIENUP, 1978; GERCHBERG AND SAXTON, 1972). The algorithm can be started with a random complex-valued input at any of the four different image states occurring during the cycle (grey boxes). It then iterates between direct and reciprocal space using the Fourier transform (FT) or its inverse (IFT) respectively. After each transform, the appropriate projection is carried out, i.e. the upwards arrow on the left corresponds to application of π_S given in (2.31) (or a different real space projection), while the downwards arrow on the right signifies the Fourier space projection $\tilde{\pi}_F$ defined in (2.33). From DIEROLF (2007).

Such a projection algorithm has converged, once the update procedure has reached a fixed point $\mathbf{x}_{fp} = G_{\pi_S, \pi_F}(\mathbf{x}_{fp})$ for which the iterates do no longer change upon repeated application of G_{π_S, π_F} . Depending on the update function used, this fixed point does not necessarily have to be the solution \mathbf{x}_{sol} of the phase retrieval problem (2.30). In general, there are usually many different fixed points associated with the same unique solution (ELSER ET AL., 2007). In the event of $\mathbf{x}_{fp} \neq \mathbf{x}_{sol}$, the latter thus has to be calculated in an additional step after completion of the actual iterative algorithm. As the unique solution is part of both constraint sets, it has to be invariant under application of either projection, i.e.

$$\mathbf{x}_{sol} = \pi_S(\mathbf{x}_{sol}) = \pi_F(\mathbf{x}_{sol}) . \quad (2.36)$$

The difference between $\pi_S(\mathbf{x}_{sol})$ and $\pi_F(\mathbf{x}_{sol})$ can be used to monitor convergence and also to assess whether the reached fixed point corresponds to a local minimum in the optimization problem, which may occur for certain update functions.

2.4.3.1 Gerchberg-Saxton algorithm

The *Gerchberg-Saxton algorithm* (GERCHBERG AND SAXTON, 1972) was the first algorithm used for diffractive imaging. Its iteration scheme is shown in

Figure 2.5: Error-reduction algorithm and projections onto constraint sets: Starting from a random image vector \mathbf{x}_0 , the error-reduction algorithm alternately applies projections onto the Fourier modulus constraint set C_F and the direct space (support) constraint set C_S . This way the algorithm constantly minimizes the distance between the points it picks on the respective sets. It is thus prone to getting caught in local minima of this distance, as seen for the initial guess at the bottom. For the one at the top, the true solution \mathbf{x}_{sol} at the intersection of the constraint sets is reached.

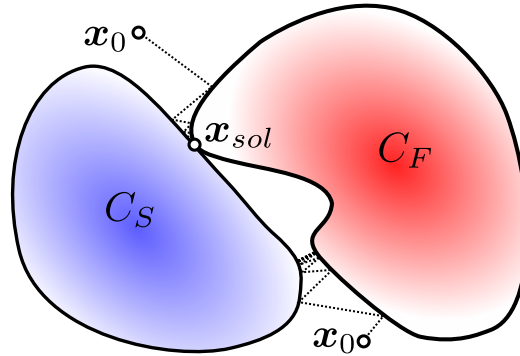


Fig. 2.4 and is the same as for the error-reduction algorithm which is discussed in the next subsection. But as the real space constraint, the Gerchberg-Saxton algorithm uses a direct image of the object instead of the support constraint discussed in previous sections⁸. Such an image can be easily obtained in transmission electron microscopy, where one can simply switch between imaging and diffraction mode. In a visible light imaging setup, the same can be achieved by an appropriate choice of lenses. Therefore, the main objective of this algorithm is to obtain phase-contrast images, rather than performing lensless imaging in cases where high-resolution direct space images are hard to get. The latter, however, is an important aspect in X-ray CDI, so that in this context the work of Gerchberg and Saxton is mainly interesting as a predecessor of later algorithms.

2.4.3.2 Error-reduction algorithm

The *error-reduction algorithm* (ER) was designed by FIENUP (1978, 1982), who generalized the work of GERCHBERG AND SAXTON (1972) by introducing the new real-space constraints non-negativity and finite support⁹. While non-negativity and a finite support are usually implicitly enforced by GERCHBERG AND SAXTON’s (1972) original use of a direct-space image, removing the need for this second measurement was an important step for the further development of iterative phase retrieval. In particular, it paved the way

⁸However, it should be kept in mind that the algorithm was developed almost a decade before the general conceptual work on CDI and the role of sampling by SAYRE (1980) and BATES (1982) discussed in section 2.3.2.1 starting on page 52.

⁹As the update rules are the same and only the direct space constraints differ, “error-reduction algorithm” and “(generalized) Gerchberg-Saxton algorithm” are sometimes used as synonyms, see also FIENUP (1982).

towards the reconstruction of an object from just its diffraction pattern as further discussed in section 2.4.3.6.

For the error-reduction algorithm, the update rule (2.34) has the form (BAUSCHKE ET AL., 2002)

$$\mathbf{x}^{(n+1)} = \pi_S \left(\pi_F \left(\mathbf{x}^{(n)} \right) \right) , \quad (2.37)$$

or, in operator notation,

$$\mathbf{x}^{(n+1)} = (\pi_S \pi_F) \{ \mathbf{x}^{(n)} \} , \quad (2.38)$$

so the algorithm is just based on alternately applying the two projections. The **behaviour of the algorithm** is schematically depicted in Fig. 2.5: A reconstruction run is usually started with an arbitrary guess \mathbf{x}_0 for the image in direct space. Already after the first application of either projection, any intermediate image vector reached during the remainder of the iterative procedure will be part of one of the two constraint sets. Any further projection always picks the closest point of the other constraint set, so the distance between the images selected from the two sets is constantly minimized. However, this behaviour makes the algorithm very prone to getting caught in local minima of this distance. In this case, the solution \mathbf{x}_{sol} is not simultaneously part of both constraints and will thus not fulfil condition 2.36. Therefore, typically many independent reconstructions have to be carried out with different random starting guesses.

Fig. 2.4 schematically shows the algorithm as a four-step cycle, which is obtained from (2.37) by considering that the projection π_F is actually a three-step procedure involving one Fourier transform and its inverse.

2.4.3.3 Input-output algorithms

Being aware of the stagnation problems of the error-reduction algorithm, FIENUP (1978, 1982) developed so-called *input-output algorithms*. In this, “input” is the image $\mathbf{x}^{(n)}$ to which the Fourier modulus projection is applied, producing the “output” $\pi_F(\mathbf{x}^{(n)})$. The next input $\mathbf{x}^{(n+1)}$, however, is no longer just obtained by executing the direct space projection on the output. It is rather calculated with a feedback function based on the difference between the output $\pi_F(\mathbf{x}^{(n)})$ and the input $\mathbf{x}^{(n)}$ which produced it. This mismatch between input and output is minimized by the new class of algorithms, instead of reducing the difference between images which respectively fulfil one of the two constraints as done in error-reduction. In the *basic input-output algorithm* (FIENUP, 1978), the input is only modified at pixel

indices $\nu \notin S$ where it violates the object domain constraints, which are in our case the pixels outside the support S :

$$x_\nu^{(n+1)} = \begin{cases} x_\nu^{(n)} & \text{if } \nu \in S , \\ x_\nu^{(n)} - \beta \pi_F(x_\nu^{(n)}) & \text{if } \nu \notin S , \end{cases} \quad (2.39)$$

where β is a real-valued constant feedback parameter, according to FIENUP (1987) best chosen in the range between 0.5 and 1.0. In another variant, which FIENUP (1982) dubbed the *output-output algorithm*, all occurrences of the input are replaced by the output, i.e.

$$x_\nu^{(n+1)} = \begin{cases} \pi_F(x_\nu^{(n)}) & \text{if } \nu \in S , \\ (1 - \beta) \pi_F(x_\nu^{(n)}) & \text{if } \nu \notin S . \end{cases} \quad (2.40)$$

For $\beta = 1$, this reduces to the error-reduction iteration formula.

Hybrid input-output algorithm One of the most widely-used algorithms in past and present X-ray CDI is Fienup's *hybrid input-output algorithm* (HIO), which in his tests (FIENUP, 1982) showed the best convergence behaviour. Its name is due to the combination of the upper line of (2.40) with lower line of (2.39) yielding the new update rule

$$x_\nu^{(n+1)} = \begin{cases} \pi_F(x_\nu^{(n)}) & \text{if } \nu \in S , \\ x_\nu^{(n)} - \beta \pi_F(x_\nu^{(n)}) & \text{if } \nu \notin S . \end{cases} \quad (2.41)$$

In the multiple reported applications of HIO, β has often been chosen closer to the upper limit of the interval $[0.5, 1]$ given by FIENUP (1987), with $\beta = 0.9$ being a rather common choice (CHAPMAN ET AL., 2006b; MARCHESINI ET AL., 2003). With the support constraint projection π_S , the two cases of (2.41) can be combined into a single recursive update rule for the image vector \mathbf{x} :

$$\mathbf{x}^{(n+1)} = \mathbf{x}^{(n)} + (1 + \beta) \pi_S(\pi_F(\mathbf{x}^{(n)})) - \pi_S(\mathbf{x}^{(n)}) - \beta \pi_F(\mathbf{x}^{(n)}) , \quad (2.42)$$

or, when expressing the difference to $\mathbf{x}^{(n)}$ as an operator,

$$\mathbf{x}^{(n+1)} = \mathbf{x}^{(n)} + ((1 + \beta) \pi_S \pi_F - \pi_S - \beta \pi_F) \{ \mathbf{x}^{(n)} \} . \quad (2.43)$$

By design of the algorithm, this iterate – the new input in the input-output scheme – is not a current guess of the object. When a true fixed point \mathbf{x}_{fp} is reached, the solution \mathbf{x}_{sol} can be calculated by applying a single Fourier modulus projection (ELSER, 2003a):

$$\mathbf{x}_{sol} = \pi_F(\mathbf{x}_{fp}) . \quad (2.44)$$

This relation can be easily derived based on the fact that HIO can be considered a special case of the difference map, compare section 2.4.3.5. HIO therefore also shares the properties of the difference map, in particular the global search behaviour that avoids local minima. For details, see the corresponding paragraph on the properties of the difference map in section 2.4.3.5.

Combination of HIO with ER Following the early example given by FIENUP (1982), HIO is often combined with ER in an alternating fashion. However, FIENUP (1982) introduced some additional ER steps mainly due to the observation that during HIO his error metric did not always correlate well with the visual quality of the output image, i.e. the output significantly improved while the error got barely lower or even increased. When adding the additional ER steps in these cases, (FIENUP, 1982) observed that “the visual quality of the output image changes very little, but E_0 [his error metric] decreases rapidly until it becomes more consistent with the visual image quality.” The final application of ER therefore seems to have served somewhat just as a sort of numerical trick to decrease error levels. In particular, FIENUP’s (1982) original studies do not appear to support the claim that alternating HIO and ER significantly speeds up convergence, which is often given as the reason for using this scheme (MARCHESINI, 2007). THIBAUT (2007, section 3.3.2) pointed out that ER just descends into the local minimum closest to the result of the previous HIO iterations. If this local minimum is not the global solution, the iterates will again move away from it during the subsequent application of HIO (compare discussion on fixed points of the difference map following (2.57) on page 67). It is therefore quite questionable, how this frequent probing of local minima, which HIO would otherwise pass, is supposed to improve the overall convergence towards the global solution.

Another motivation to use ER at the end of a run might be the fact that – unlike in HIO – the current iterate of ER is always the current guess of the object. Assuming that really the global minimum has been reached, the result of the final ER run in an alternating scheme thus directly yields the solution \mathbf{x}_{sol} . However, ELSER (2003a) emphasized that it is not necessary from an algorithmic point of view: for any fixed point of HIO, the true solution can be easily obtained with (2.44). CHAPMAN ET AL. (2006b), e.g., used HIO without combining it with ER.

2.4.3.4 Relaxed averaged alternating reflection algorithm

The *relaxed averaged alternating reflection algorithm* (RAAR) was developed by LUKE (2005) based on the earlier *hybrid projection reflection algorithm* (HPR) by BAUSCHKE ET AL. (2003). Both algorithms make use of reflection

operators. Instead of projecting onto a constraint set D , a reflection operator R_C moves twice the distance along the projection direction, i.e.

$$R_C(\mathbf{x}) = 2\pi_C(\mathbf{x}) - \mathbf{x} . \quad (2.45)$$

For our constraint sets C_S and C_F , the update function of RAAR takes the form

$$\mathbf{x}^{(n+1)} = \frac{1}{2}\beta \left(R_S \left(R_F \left(\mathbf{x}^{(n)} \right) \right) + \mathbf{x}^{(n)} \right) + (1 - \beta)\pi_F \left(\mathbf{x}^{(n)} \right) , \quad (2.46)$$

or in operator notation

$$\mathbf{x}^{(n+1)} = \left(\frac{1}{2}\beta (R_S R_F + \mathbb{I}) + (1 - \beta)\pi_F \right) \{ \mathbf{x}^{(n)} \} , \quad (2.47)$$

where \mathbb{I} is the identity operator. With (2.45), (2.46) can be expressed purely in terms of projections as

$$\mathbf{x}^{(n+1)} = \beta \left[\pi_S \left(2\pi_F \left(\mathbf{x}^{(n)} \right) - \mathbf{x}^{(n)} \right) - \pi_F \left(\mathbf{x}^{(n)} \right) + \mathbf{x}^{(n)} \right] + (1 - \beta)\pi_F \left(\mathbf{x}^{(n)} \right) , \quad (2.48)$$

or

$$\mathbf{x}^{(n+1)} = (\beta [\pi_S (2\pi_F - \mathbb{I}) - \pi_F + \mathbb{I}] + (1 - \beta)\pi_F) \{ \mathbf{x}^{(n)} \} , \quad (2.49)$$

which can be rewritten into

$$\mathbf{x}^{(n+1)} = \mathbf{x}^{(n)} + (\beta [\pi_S (2\pi_F - \mathbb{I}) - \pi_F] + (1 - \beta)(\pi_F - \mathbb{I})) \{ \mathbf{x}^{(n)} \} . \quad (2.50)$$

In this notation it can be easily seen that for $\beta = 1$ the update rules (2.50) for RAAR and (2.43) for HIO coincide (compare also MARCHESINI, 2007). RAAR is one of the algorithms implemented in the open-source CDI reconstruction software *Hawk*¹⁰ (MAIA ET AL., 2010), which was used, e.g., by SEIBERT ET AL. (2011) for the reconstruction of CDI data taken at an X-ray free-electron laser.

2.4.3.5 Difference map

Probably the most general projection-based algorithm used in CDI is the *difference map* (DM) by ELSER (2003a). Besides its application in phase retrieval (THIBAUT, 2007; THIBAUT ET AL., 2006), the difference map can be used for general optimization problems which can be formulated in terms of two constraints, e.g., protein folding problems or Sudoku puzzles (ELSER

¹⁰ Available for download on <http://xray.bmc.uu.se/hawk>.

ET AL., 2007). For CDI with a support constraint, its update rule has the form

$$\mathbf{x}^{(n+1)} = \mathbf{x}^{(n)} + \beta \left(\mathbf{y}_S^{(n)} - \mathbf{y}_F^{(n)} \right) , \quad (2.51)$$

where β , like in the other algorithms, is a real-valued feedback constant. The n -th support estimate $\mathbf{y}_S^{(n)}$ and the n -th Fourier estimate $\mathbf{y}_F^{(n)}$ are given by

$$\mathbf{y}_S^{(n)} = \pi_S \left((1 + \gamma_F) \pi_F \left(\mathbf{x}^{(n)} \right) - \gamma_F \mathbf{x}^{(n)} \right) , \quad (2.52a)$$

$$\mathbf{y}_F^{(n)} = \pi_F \left((1 + \gamma_S) \pi_S \left(\mathbf{x}^{(n)} \right) - \gamma_S \mathbf{x}^{(n)} \right) . \quad (2.52b)$$

The name support estimate for $\mathbf{y}_S^{(n)}$ originates from the fact that π_S is always the last applied operation, therefore $\mathbf{y}_S^{(n)} \in C_S$ is fulfilled at any iteration $n \in \mathbb{N}_0$. Analogously, we have $\mathbf{y}_F^{(n)} \in C_F$ for all $n \in \mathbb{N}_0$, making $\mathbf{y}_F^{(n)}$ a Fourier estimate. Geometrically, the parenthesis in (2.52a) can be interpreted as a general point on the line connecting $\mathbf{x}^{(n)}$ and $\pi_F(\mathbf{x}^{(n)})$ (ELSER, 2003a). (2.52b) features a corresponding term based on the support projection. The positions along the connecting lines are determined by the real-valued tuning parameters γ_S and γ_F . An in-depth analysis of the optimum choice of these two parameters can be found in ELSER (2003b), who also calls them “relaxation parameters”. Based on the simplifying assumption that the constraint sets are orthogonal in the vicinity of the solution, ELSER (2003a) had earlier found what THIBAUT ET AL. (2006) called a “near-optimal choice”:¹¹

$$\gamma_S = -\beta^{-1} , \quad \gamma_F = \beta^{-1} . \quad (2.53)$$

When inserting this in (2.52), the difference map only has the single tuning parameter β and the estimates become

$$\mathbf{y}_S^{(n)} = \pi_S \left((1 + \beta^{-1}) \pi_F \left(\mathbf{x}^{(n)} \right) - \beta^{-1} \mathbf{x}^{(n)} \right) , \quad (2.54a)$$

$$\mathbf{y}_F^{(n)} = \pi_F \left((1 - \beta^{-1}) \pi_S \left(\mathbf{x}^{(n)} \right) + \beta^{-1} \mathbf{x}^{(n)} \right) . \quad (2.54b)$$

If we set $\gamma_S = -1$, but leave $\gamma_F = \beta^{-1}$ as a free parameter, (2.54b) simplifies to $\mathbf{y}_F^{(n)} = \pi_F \left(\mathbf{x}^{(n)} \right)$. When inserting this in (2.51), the iteration rule becomes identical to (2.42), the update rule for HIO. Therefore, HIO is just a special

¹¹Here we use the convention of ELSER (2003a,b). In THIBAUT ET AL. (2006), γ_1 and γ_2 have the opposite sign. The reason is that the estimates in the difference map definition (2.51) are exchanged in THIBAUT ET AL. (2006), i.e. the parenthesis reads $\mathbf{y}_F^{(n)} - \mathbf{y}_S^{(n)}$. This can also be interpreted as a switch of the projectors π_S and π_F . For this “near-optimal” choice of γ_1 and γ_2 , such a projector switch corresponds simply to a change of the signs of the tuning parameters in (2.54).

case of the difference map¹². According to the condition 2.53 for the optimal choice of the relaxation parameters, $\gamma_S = -1$ also implies $\beta = 1$. As pointed out by ELSER (2003a), FIENUP (1982) observed the best performance of HIO just near $\beta = 1$ in his tests, so at the optimal settings according to the difference map formalism. Another popular parameter choice, e.g. applied by THIBAUT ET AL. (2006) in the reconstruction of a yeast cell (SHAPIRO ET AL., 2005), is to use (2.53) with $\beta = -1$. Then the estimates become

$$\mathbf{y}_S^{(n)} = \pi_S \left(\mathbf{x}^{(n)} \right) , \quad (2.55a)$$

$$\mathbf{y}_F^{(n)} = \pi_F \left(2\pi_S \left(\mathbf{x}^{(n)} \right) - \mathbf{x}^{(n)} \right) , \quad (2.55b)$$

and the full update rule reads

$$\mathbf{x}^{(n+1)} = \mathbf{x}^{(n)} + \pi_F \left(2\pi_S \left(\mathbf{x}^{(n)} \right) - \mathbf{x}^{(n)} \right) - \pi_S \left(\mathbf{x}^{(n)} \right) . \quad (2.56)$$

This is also the iteration rule applied in the algorithm forptychographic CDI based on the difference map, which is introduced in section 3.2.2 on page 91.

Properties of the difference map From the general definition (2.51) of the difference map, we can deduce that a fixed point is reached when

$$\mathbf{y}_S^{(n)} = \mathbf{y}_F^{(n)} . \quad (2.57)$$

For a given problem, the difference map typically has many such fixed points (ELSER, 2003a). But, as pointed out earlier, the design of the estimates implies $\mathbf{y}_S^{(n)} \in C_S$ and $\mathbf{y}_F^{(n)} \in C_F$ for all iterations n . Therefore, a fixed point only occurs when the estimates on the two constraints coincide, which is only the case for the unique solution $C_S \cap C_F$. For a local minimum of the distance between the constraints, in contrast, we have $\mathbf{y}_S^{(n)} \neq \mathbf{y}_F^{(n)}$ and thus no fixed point of the algorithm, i.e. the difference map (and its variants like HIO) does not get trapped in such local minima and moves away from them (ELSER, 2003a)¹³. Based on this behaviour, it is convenient to monitor convergence by means of the *difference map error*

$$\epsilon = \left\| \mathbf{x}^{(n+1)} - \mathbf{x}^{(n)} \right\| = |\beta| \left\| \mathbf{y}_S^{(n)} - \mathbf{y}_F^{(n)} \right\| , \quad (2.58)$$

¹²The basic input-output algorithm (2.39) and the output-output algorithm (2.40), however, can not be expressed in terms of the difference map (ELSER, 2003a). Also HPR, the algorithm preceding RAAR, has been found to coincide with the difference map for a certain choice of parameters (LUKE, 2005; MARCHESINI, 2007). For RAAR itself, the same is only true for $\beta = 1$. However, the algorithm can not be derived from the difference map for a general $\beta \neq 1$ (LUKE, 2005).

¹³However, THIBAUT (2007, section 3.2) pointed out that a sort of trapping may still occur if the algorithm gets again attracted by the same local minimum after moving away from it. He furthermore suggests that the occurrence of *phase vortices* (PEELE ET AL., 2004) in the reconstructed image may be an example for such a case. Forptychographic

where $\epsilon/|\beta|$ is the current geometrical distance between the two constraint sets. The behaviour of the difference map error often allows to draw some conclusions on the strength of the constraints: If the error drops to a very small value right at the beginning and does not show any fluctuations, this may be a sign of too weak constraints, e.g., a support which is not tight enough (ELSER, 2003a). In such a case, there are many valid solutions which fulfil the given constraints. In the opposite case, the constraints are incompatible, which means a fixed point with $\mathbf{y}_S^{(n)} = \mathbf{y}_F^{(n)}$ does not exist. Strictly speaking, the phase problem according to (2.30) no longer possesses a unique solution in this case. In practice, such incompatibilities are mainly caused by noise in the experimental data. If the distance between the constraint sets does not get too big, the error just shows tiny fluctuations around a small constant value. A unique, reproducible solution can then be obtained by averaging multiple of these near-solutions from this plateau region of the error (THIBAUT ET AL., 2006). In contrast, the error tends to show a strongly oscillating behaviour if the constraints are too far apart. In this case, it does not settle on the near-solutions but moves away from what it considers just another local minimum. While this wandering behaviour has sometimes been considered undesirable (LUKE, 2005), it is just a logical consequence of the design of the algorithm to avoid local minima. In particular, it stresses the fact that no reliable solution exists for the given constraint sets. A common measure in this case is to relax the constraints until the error does no longer show the strong oscillations but rather again settles on a plateau corresponding to a set of near-solutions. Reconstructions in the presence of noise and relaxation of the Fourier constraint is further discussed in section 3.2.4.1 starting on page 96.

2.4.3.6 Algorithms with dynamic support refinement

As pointed out in subsection 2.4.3.2, the introduction of the support constraint made phase retrieval also applicable to cases, where a direct image of the object, which would be required for the Gerchberg-Saxton algorithm, is not necessarily easily obtainable. While this on the one hand enables truly lensless imaging techniques, it also raises the question how to best determine the exact shape of the support just from the diffraction data. While a first guess can be done based on the object's autocorrelation, which is the inverse Fourier transform of the recorded intensity pattern (FIENUP ET AL., 1982),

phase retrieval using the difference map, e.g., it has been observed that the convergence slowed down when non-physical phase vortices appeared in the object iterates. The reconstructions would usually make barely any progress until these vortices annihilated with ones of the opposite helicity or moved out of the field of view.

this will usually result in a rather loose support. However, especially when the object is complex-valued (FIENUP, 1987; SPENCE ET AL., 2002), good reconstructions require a tight support which is accurate on the scale of the desired resolution. Therefore, the initial support guess has to be further refined during the reconstruction, typically using thresholding approaches. In most of these cases, the actual update function G_{π_S, π_F} remains that of a standard phase-retrieval algorithm, e.g. HIO or RAAR, but the projection π_S is modified during the reconstruction run. Although it is in principle possible to directly define the projection π_S in a dynamic way (THIBAUT, 2007), the change of the support is usually done in a separate step outside of the usual phase-retrieval iterations.

Rather widely used is the *Shrinkwrap algorithm* by MARCHESINI ET AL. 2003, which dynamically updates the support in a fully automated procedure: In the presented example, the first guess for the support was obtained by thresholding the autocorrelation at 4% of the maximum intensity. After every 20 iterations of a standard HIO algorithm, the image of the object was convolved with a Gaussian and thresholded at 20% of its maximum to create the new support. The width of the Gaussian was reduced between its applications. Shrinkwrap is rather popular for the reconstruction of CDI data taken at X-ray free electron lasers and was used, e.g., by CHAPMAN ET AL. (2006a) and SEIBERT ET AL. (2011). Although the threshold value of 20% is frequently reported, the Shrinkwrap parameters usually should be adjusted for each data set individually. In addition to automated threshold techniques, visual inspection of repeated reconstruction attempts may be used to manually refine the support, as e.g. done by THIBAUT ET AL. (2006).

Finally, it should also be mentioned that the support must not get too small in order not to truncate the object during reconstruction. In their description of the support update procedure, THIBAUT ET AL. (2006) pointed out: “Excessively tight supports were avoided by noticing sharp upturns in the difference-map error.” This demonstrates that a too tight support on the one hand has deteriorating effects on the reconstruction process, but on the other hand these effects also easily allow to identify this issue. As such problems were already observed by FIENUP (1982), he suggested to actually start with a very tight support and slightly relax it later in the reconstruction run.

2.4.4 Limitations of single-pattern CDI with common algorithms

Several problems may be encountered upon phase retrieval from a single diffraction pattern using one of the standard algorithms presented in the previous section. The following paragraphs describe these limitations and potential workarounds to overcome them.

Requirement of finite sample support For the discussion of different phase-retrieval algorithms in the previous section, we have used the constraint that the object has a finite support. The sampling requirements related to this constraint limit the maximum extent of the object according to (2.28). Even if an experiment’s geometry would be adapted to allow for very large samples, another fundamental limit exists: As in plane-wave CDI all information is collected in a single exposure, the size of the object must not exceed the transverse coherence length of the illumination. Preparation of perfectly isolated samples can be extremely challenging. As a first major requisite, the specimen has to show a well-defined, sharp border in order to be able to define a tight support. Furthermore, already small scatterers outside the support may negatively affect the reconstruction, as their signal is not considered in the algorithmic model. An example can be found in the work of THIBAUT ET AL. (2006), who discussed the effect of small dust particles which were located next to the yeast cell under investigation.

Instead of isolating the sample, constraining the origin of the scattering signal to a well-defined region in the object plane may also be achieved with a **localized illumination**. This can be realized, e.g., by putting an aperture upstream of the object or by placing the sample in the focal plane of X-ray focusing optics. However, such an “illumination pattern constraint” (FIENUP, 2006) typically has rather smooth edges. As it therefore does not provide the tight support required especially in the case of complex-valued objects, the standard algorithms do not work properly (FIENUP, 2006). Even though modified versions (FIENUP, 2006) of the algorithms may perform sufficiently well, the reconstruction of an extended object remains tedious: after collecting diffraction patterns at different relative lateral positions of sample and illumination, each of them would have to be reconstructed separately. The final result would be obtained by combining the individual reconstructions using standard image processing methods. As it typically takes several thousand iterations to reconstruct an object from its experimental CDI pattern (CHAPMAN ET AL., 2006a; SHAPIRO ET AL., 2005), this approach seems to be limited to a small number of positions.

Convergence issues As mentioned in the previous paragraph, reconstruction of experimental data typically requires a large number – several thousand – of iterations. This might be a problem in cases where a quick first feedback is desirable, e.g., when trying to identify a specific region of interest on an unknown extended sample. However, modern implementations like the *Hawk*¹⁴ reconstruction package often make use of parallel computing, either employing multiple processor cores, or harnessing the vast parallel computing power of graphics processing units (GPUs). Therefore, the time required for a single reconstruction run is getting less and less of a limitation.

More important are cases of stagnation in which the algorithm does not reach the solution. One example would be ER getting caught in a local minimum, but this can easily be avoided with the more sophisticated algorithms like HIO. However, also these algorithms may show stagnation (FIENUP AND WACKERMAN, 1986), e.g. when a superposition of the image and its twin image is reconstructed, which is common for centrosymmetric supports. Yet, FIENUP AND WACKERMAN (1986) also suggested how to reduce such problems: the previous example of the superimposed images, for instance, may be avoided by using a non-symmetric support – either in the experiment or during the first iterations of the reconstruction run. As the preferable experimental solution may not always be feasible, one should nevertheless be aware of this potential limitation.

Reconstruction of complex-valued objects In the case of objects that exhibit both absorption and phase shift, the strong non-negativity constraint (FIENUP, 1982) in direct space can no longer be applied. As pointed out already in section 2.4.3.6 on dynamic support refinement, very tight supports are required to get good reconstructions of such complex-valued objects (FIENUP, 1987; SPENCE ET AL., 2002). Preferably, these supports are in addition highly asymmetric or consist of several disconnected parts. To define the necessary tight real-space constraint, the object area has to feature a sharp outline. As mentioned before, this is in particular not the case for localized illuminations and prevents their use in combination with standard CDI algorithms (FIENUP, 2006).

Defocus ambiguity The support is also the only information constraining the position of the plane of the object reconstruction along the beam direction, as Fraunhofer patterns are insensitive to small-scale changes of this longitudinal position. Therefore, it may easily happen that the CDI algorithm produces a Fresnel-propagated version of the object’s exit wave, which

¹⁴Available for download on <http://xray.bmc.uu.se/hawk>.

provides the user only with a defocused image of the specimen (SPENCE ET AL., 2002). Numerical propagation of the retrieved wavefield often allows to get a sharp image, but it may be hard to identify the correct propagation distance in the case of an unknown specimen.

Experimental noise Even for perfect conditions, noise is always present in any CDI experiment in the form of Poisson noise, see (1.58) on page 34. Typically, experimental shortcomings like non-ideal detection add further uncertainties. As a result, the constraints of the phase-retrieval problem may become incompatible preventing the algorithm from converging to a unique solution. To compensate for the influence of the experimental uncertainties, the usual constraints have to be adapted accordingly. A typical approach would be a relaxation of the Fourier constraint (compare e.g. CHAPMAN ET AL. 2006b and the discussion in section 3.2.4.1 starting on page 96). Some details on the behaviour of the difference map in the presence of noise have already been discussed in the paragraph on its properties starting on page 67.

Ambiguities due to the “trivial characteristics” As pointed out already in the paragraph following the definition of the phase problem on page 46, the solution obtained by phase retrieval from a single diffraction pattern is only unique with respect to its “trivial characteristics” (BATES, 1982; MIAO ET AL., 1998): results showing an additional constant phase offset, a translation of the object, the twin image, or combinations of all these, are considered equivalent manifestations of the unique solution. While they can usually be corrected in post-processing steps, these ambiguities may still be undesirable, especially in cases where one wants to obtain quantitative information.

Partial coherence As, except for free-electron lasers, the emission processes of X-ray sources are not coherent, transverse coherence in CDI experiments has to be ensured by placing the sample at a sufficiently large distance from a small X-ray source according to (2.5). But even if one ensures that the resulting transverse coherence length is substantially greater than the specimen’s extent, some degree of partial coherence will remain. However, the discussed CDI algorithms assume fully coherent settings. WILLIAMS ET AL. (2007) have found that already small violations of this prerequisite degrade the reconstruction results. These problems are avoided in more recent algorithmic developments by WHITEHEAD ET AL. (2009), which allow to include *a priori* knowledge about the coherence properties of the illumination directly

in the reconstruction.

2.4.5 Advanced iterative CDI techniques

In our discussion of the various limitations in the previous section, we have already introduced possible workarounds to overcome them or at least reduce their importance. However, it is more desirable to avoid these problems in the first place. Therefore, advanced CDI techniques have been developed which are intrinsically more robust. During the last years, two main approaches have been successfully demonstrated through several experiments:

Fresnel Coherent Diffractive Imaging (FCDI) This technique is based on calculations and simulations by [NUGENT ET AL. \(2003, 2005\)](#) and [QUINEY ET AL. \(2005\)](#), who suggested to use a known illumination with a well-defined curved wavefront instead of the usual plane wave employed in CDI. They found that this approach removes the need for a tight support and leads to a much faster convergence. Furthermore, the ambiguities with respect to defocus, object translation and the twin image are suppressed ([PITTS AND GREENLEAF, 2003](#)). According to [WILLIAMS ET AL. \(2007\)](#), it is slightly more tolerant to partial-coherence effects than standard plane-wave CDI. [QUINEY ET AL. \(2005\)](#) reported another intriguing effect: with a curved wave front the error-reduction algorithm can be used for the reconstruction without showing the usual stagnation problems. [WILLIAMS ET AL. \(2006\)](#) coined the term FCDI when presenting their experimental demonstration of the concept, which then became the typical set-up for the later experiments. In this usual implementation, the sample is put downstream of a Fresnel zone plate's focus. This diverging beam features the desired curved wavefront. However, it may deviate from its ideal shape due to experimental imperfections. Therefore, a crucial step to get high-quality reconstructions – also already included by [WILLIAMS ET AL. \(2006\)](#) – is to retrieve also the illuminating wavefield via a phase-retrieval scheme ([QUINEY ET AL., 2006](#)). Employing the same experimental concept, [ABBEY ET AL. \(2008\)](#) used FCDI to image extended samples. As FCDI does no longer require a tight support, the localized illumination, which would be to soft-edged for a classical support constraint, allows to define the area of the object which is reconstructed. An extended object can thus be imaged by reconstructing diffraction data from multiple relative positions of the sample with respect to the beam and combining the individual results afterwards using standard image processing tools. [ABBEY ET AL. \(2008\)](#) called this approach *keyhole imaging*. To remove the need for this post-processing step and rather reconstruct the whole scanned area in a

common algorithm, [VINE ET AL. \(2009\)](#) combined FCDI with ptychographic ideas.

Ptychographic Coherent Diffractive Imaging (PCDI) While FCDI was originally developed for phase retrieval from a single diffraction pattern, PCDI by design employs multiple diffraction patterns. These are taken at different relative lateral positions of a localized illumination with respect to the object ([FAULKNER AND RODENBURG, 2004](#)). In principle, there are no further prerequisites in terms of the shape or structure of the incident wavefield, although some settings show beneficial properties (compare, e.g., [GUIZAR-SICAIROS ET AL., 2012](#)). In particular, a wavefront curvature is not mandatory. However, the areas illuminated on the object by adjacent exposures have to partially overlap. PCDI is the phase-retrieval scheme employed for all the work presented in this thesis and is therefore discussed in detail in [chapter 3](#). The background of the technique is presented in [section 3.1](#), while [section 3.1.4](#) introduces the first iterative ptychographic phase-retrieval algorithm. The main part of the chapter focusses on the discussion of PCDI with simultaneous retrieval of the illumination in [section 3.2](#) and how to evaluate resolution in [section 3.3](#).

Chapter 3

Ptychographic coherent diffractive imaging

3.1 Ptychography: from crystals to iterations

The evolution of ptychography from its origins in electron diffraction to the emergence of the first iterative algorithms has been reviewed by [RODENBURG \(2008\)](#), the technique's strongest advocate through many years and developer of many milestones. This review forms a major source of this section. Also the corresponding section 2.3.4 in [DIEROLF \(2007\)](#) has served as a loose basis for a few parts.

3.1.1 The original concept of ptychography

Like standard CDI employing a single far-field diffraction pattern (compare section [2.3.2.1](#)), also ptychographic CDI has its origin in a concept developed to solve the crystallographic phase problem: [HOPPE \(1969a\)](#) pointed out that if one can make the Bragg peaks of crystalline diffraction patterns interfere, information about their relative phases can be obtained. He dismissed that this could be achieved with X-rays, as the mosaicity of real crystals prevents the successful generation of interference. The stronger interaction of electrons, however, allows to collect diffraction data from much smaller areas which may be considered ideal crystallites. Furthermore, electron beams can be easily manipulated with electric and magnetic fields. [HOPPE \(1969a\)](#) therefore discussed his approach for experiments on thin crystals done with a transmission electron microscope in diffraction mode. But as for X-rays, the Bragg peaks are also highly localized in the standard implementation of electron crystallography. [HOPPE \(1969a\)](#) therefore suggested to use a finite coherent illumination instead of the usual extended plane wave. Due

to the Fourier convolution theorem (compare [A.5](#) on page [338](#)), the crystal's diffraction peaks in the resulting far-field pattern are then convolved with the Fourier transform of the localized illumination. If the extent of the illumination is shrunk to about the same order of magnitude¹ as the crystalline unit cell, this leads to overlap between the patterns of adjacent Bragg peaks and thus the desired interferences. While these interferences already allow to determine the relative phases, an ambiguity between the solution and its complex conjugate remains. [HOPPE \(1969a\)](#) showed that an unambiguous result can be obtained by recording another diffraction pattern at a slightly shifted position of the localized illumination.

[HEGERL AND HOPPE \(1970\)](#) later introduced the name *ptychography* for the technique. The term contains the Greek word for “fold”, $\pi\tau\upsilon\xi$, which alludes to the convolution of the Fourier transforms of illumination and crystal. Ptychography can thus be translated as “convolution imaging”.

In a second article accompanying his original proposal, [HOPPE \(1969b\)](#) even discussed already the extension of ptychography to non-periodic objects, e.g. by inserting different phase-shifting plates in the illuminating wavefield. Furthermore, he discussed the possibility of scanning transmission electron diffraction microscopy in two and three dimensions based on his ideas. However, apart from a few proof-of-principle studies (e.g. by [NELLIST ET AL., 1995](#)), ptychography has gotten rather little interest for almost four decades. In 1982, Hoppe even called it one of his two “nearly forgotten ideas” ([HOPPE, 1982](#)). During the following decades, mainly John Rodenburg continued to work on the implementation and further development of the technique as described in his review ([RODENBURG, 2008](#)) and below.

3.1.2 Generalized definition of ptychography

Reserving “ptychography” solely for Hoppe’s original approach for crystalline specimens has some appeal, as it would allow to more clearly distinguish it from later developments. In recent years, however, the term has also been used for the emerging combinations of ptychographic principles with iterative phase-retrieval algorithms, although also other names have been introduced to tell these techniques apart from ptychography in its original sense: “ptychographical iterative phase retrieval” ([FAULKNER AND RODENBURG, 2005](#)), “ptychographic coherent diffractive imaging” ([DIEROLF ET AL., 2010b](#); [GIEWEKEMEYER ET AL., 2010](#)), and “scanning X-ray diffraction microscopy” ([THIBAUT ET AL., 2008](#)) are some examples. Therefore,

¹In a companion article, [HOPPE AND STRUBE \(1969\)](#) demonstrated the approach by illuminating a two-dimensional diffraction grating with a localized visible-light illumination about five times the size of the lattice constant.

the generalized definition of ptychography by RODENBURG (2008, section II.C) more accurately reflects the actual use of the name in the X-ray imaging community:

Definition 3.1 (Ptychography). According to RODENBURG (2008, section II.C), the term *ptychography* refers to a method with the following characteristics:

- (a) In the experimental set-up, which is typically designed for transmission geometry, a localized illumination impinges on the object and the resulting diffraction intensities are recorded (usually, but not necessarily, in the far field).
- (b) At least two such diffraction patterns are recorded for different relative lateral positions of illumination and object. The shift between the positions is usually known. Instead of shifting, also the structure of the illumination function may be a changed.
- (c) A calculation involving at least two of the patterns is used to obtain all phases in the diffraction plane, or, which is equivalent, the object's exit wave in real space.
- (d) If the illumination on the object is only changed by means of relative lateral shifts, a nonperiodic object of theoretically unlimited size can be imaged by processing a large number of diffraction patterns.

In our case, the required change of the illumination conditions according to Definition 3.1(b) is achieved exclusively through relative lateral shifts of object and illumination function. We thus adapt the general Definition 3.1(b) of a ptychographic data set accordingly:

Definition 3.2 (Ptychographic data set). A ptychographic data set consists of far-field diffraction patterns I_j measured by illuminating an object $O(\mathbf{r})$ at N_j different positions $\mathbf{r}_j = (x_j, y_j)$ with a localized illumination function, the “probe” $P(\mathbf{r})$. The probe is the full wavefield incident on the object, which in turn is represented by the complex object transmission function $O(\mathbf{r})$ as introduced in (1.26) (page 23):

$$I_j(\mathbf{q}) = |\mathcal{F} \{P(\mathbf{r} - \mathbf{r}_j) \cdot O(\mathbf{r})\}|^2 . \quad (3.1)$$

Experimentally, the relative displacements \mathbf{r}_j of probe and object are in most cases realized by scanning the object with respect to a fixed illumination. Nevertheless, formulation (3.1), which corresponds to a (small) probe moving to different locations on a static (large) object, is an equivalent way to describe the problem mathematically and provides a more intuitive approach in terms of numerical implementations. The goal of any such implementation is of course the reconstruction of $O(\mathbf{r})$:

Definition 3.3 (Ptychographic phase-retrieval problem with known illumination). To reconstruct an image of an object on which a ptychographic data set according to Definition 3.2 has been recorded, one has to numerically find the function O that satisfies (3.1) for all scan points j , assuming the illumination function P is known.

The *a priori* knowledge of the probe, which is assumed in this definition, has been a common requirement of most ptychographic imaging techniques. Because of their importance for the development of X-ray ptychography, two of these methods are briefly introduced below, starting with an analytic approach in section 3.1.3, which is followed by a discussion of the first iterative algorithm in section 3.1.4.

3.1.3 Wigner-distribution deconvolution

Probably the next important milestone in ptychography development besides the already mentioned successful experimental demonstration of Hoppe's original ideas (NELLIST ET AL., 1995), was the introduction of the Wigner-distribution deconvolution by BATES AND RODENBURG (1989), which allows to reconstruct a non-crystalline object.

3.1.3.1 Reconstruction procedure

In this subsection, the theory of this approach is just briefly summarized, please refer to the article by RODENBURG AND BATES (1992) or the review by RODENBURG (2008) for more details: If we express the relative positions of probe and object by the coordinate $\mathbf{R} \in \{\mathbf{r}_j \mid 1 \leq j \leq N_j\}$, the entirety of a ptychographic data set according to (3.1) is given as the four-dimensional function

$$I(\mathbf{q}, \mathbf{R}) = |\mathcal{F}\{P(\mathbf{r} - \mathbf{R}) \cdot O(\mathbf{r})\}|^2 = |\mathcal{F}\{P(\mathbf{r} - \mathbf{R})\} \otimes \mathcal{F}\{O(\mathbf{r})\}|^2, \quad (3.2)$$

where the rightmost expression is of course based on the Fourier convolution theorem (A.5). With the Fourier transforms \tilde{P} and \tilde{O} of probe and object,

this can also be written as (RODENBURG, 2008)

$$I(\mathbf{q}, \mathbf{R}) = \left| \left(\tilde{P}(\mathbf{q}) e^{i\mathbf{R}\cdot\mathbf{q}} \right) \otimes \tilde{O}(\mathbf{q}) \right|^2, \quad (3.3)$$

as, according to the Fourier shift theorem (A.3) on page 338, a translation in real space corresponds to a phase ramp in Fourier space. Expanding the convolution in (3.3) results in

$$I(\mathbf{q}, \mathbf{R}) = \left| \iint \tilde{P}(\mathbf{a}) \tilde{P}^*(\mathbf{b}) \tilde{O}(\mathbf{q} - \mathbf{a}) \tilde{O}^*(\mathbf{q} - \mathbf{b}) e^{i\mathbf{R}\cdot(\mathbf{a}-\mathbf{b})} d\mathbf{a} d\mathbf{b} \right|^2, \quad (3.4)$$

where \mathbf{a} and \mathbf{b} are dummy variables. For further analysis, the two-dimensional Fourier transforms of this intensity function with respect to $-\mathbf{R}$ and \mathbf{q} are calculated:

$$H(\mathbf{r}, \mathbf{S}) = \iint I(\mathbf{q}, \mathbf{R}) e^{i(\mathbf{R}\cdot\mathbf{S} - \mathbf{q}\cdot\mathbf{r})} d\mathbf{q} d\mathbf{R}. \quad (3.5)$$

Using the explicit expression (3.4) for $I(\mathbf{q}, \mathbf{R})$, one can show that $H(\mathbf{r}, \mathbf{S})$ can be factorized such that one factor contains only the contributions of the illumination P , while the other factor depends solely on O (RODENBURG AND BATES, 1992):

$$H(\mathbf{r}, \mathbf{S}) = \chi_P(\mathbf{r}, -\mathbf{S}) \cdot \chi_O(\mathbf{r}, \mathbf{S}), \quad (3.6)$$

where the Wigner distribution functions, or also “ambiguity functions”, of P and O are defined as

$$\chi_P(\mathbf{r}, \mathbf{S}) = \int P^*(\mathbf{a}) P(\mathbf{a} + \mathbf{r}) e^{i\mathbf{a}\cdot\mathbf{S}} d\mathbf{a} \quad (3.7a)$$

$$\chi_O(\mathbf{r}, \mathbf{S}) = \int O^*(\mathbf{a}) O(\mathbf{a} + \mathbf{r}) e^{i\mathbf{a}\cdot\mathbf{S}} d\mathbf{a}. \quad (3.7b)$$

If the probe P is known, χ_P can be easily calculated using (3.7a). We can then easily deconvolve the contributions of probe and object in (3.2) by applying a suitable method on the intensity’s Fourier transform $H(\mathbf{r}, \mathbf{S})$. For example, a Wiener filter can be used to obtain an estimate χ_O^e of the object’s Wigner distribution function (see, e.g., CHAPMAN, 1996):

$$\chi_O^e(\mathbf{r}, \mathbf{S}) = H(\mathbf{r}, \mathbf{S}) \frac{\chi_P^*(\mathbf{r}, -\mathbf{S})}{|\chi_P^*(\mathbf{r}, -\mathbf{S})|^2 + \alpha}, \quad (3.8)$$

where the small constant α is introduced to avoid division by zero. Different routes exist to obtain an estimate of the object from χ_O^e (BATES AND RODENBURG, 1989; MCCALLUM AND RODENBURG, 1992; RODENBURG AND

BATES, 1992). Here, we continue with the Fourier transform of $\chi_O^e(\mathbf{r}, \mathbf{S})$ with respect to \mathbf{r} ,

$$D(\mathbf{q}, \mathbf{S}) \equiv \mathcal{F}_r \{ \chi_O^e(\mathbf{r}, \mathbf{S}) \} = \tilde{O}(\mathbf{q}) \tilde{O}^*(\mathbf{q} - \mathbf{S}) . \quad (3.9)$$

The absolute phase of a wavefield cannot be retrieved in a diffraction measurement and has to fixed to a value. A typical choice is to assign to $\tilde{O}(0)$ a purely real value equal to $\sqrt{D(0,0)}$. For $\mathbf{q} = 0$ in (3.9), one is able to solve for the Fourier transform \tilde{O} of the object,

$$\tilde{O}(\mathbf{S}) = \frac{D^*(0,0)}{\sqrt{D(0,0)}} , \quad (3.10)$$

from which the complex object transmission function can be obtained via an inverse Fourier transform.

3.1.3.2 Impact of the Wigner-distribution deconvolution

Experimental results The Wigner-distribution deconvolution was the first ptychographic technique which yielded reconstructions of non-crystalline specimens. Rodenburg and co-workers successfully applied it to data taken with an optical test set-up (McCALLUM AND RODENBURG, 1992) and a scanning transmission electron microscope (RODENBURG ET AL., 1993). Just shortly afterwards, X-ray ptychography was demonstrated for the first time by (CHAPMAN, 1996, 1997), who used the Wigner-distribution deconvolution to obtain a reconstruction from data taken with a scanning transmission X-ray microscope. However, the technique has not seen regular applications beyond these proof-of-principles experiments.

Resolution Unlike in classical scanning microscopy, the size of the localized illumination does no longer limit the resolution of the reconstruction (McCALLUM AND RODENBURG, 1992). The Wigner-distribution deconvolution can thus be used to obtain super-resolution images with existing scanning microscopes. Alternatively, it may also be implemented as a lensless technique, e.g. by using a pinhole to shape the illumination. However, the steps between the probe positions \mathbf{r}_j have to be equal to or smaller than the size of a resolution element in the reconstruction. As high-resolution imaging of extended areas therefore requires the collection of huge amounts of diffraction patterns, this makes the approach rather impractical in many cases. This may also be a main reason why the technique has not seen more applications.

Illumination: known or unknown? The standard reconstruction procedure described in section 3.1.3.1 requires a known probe as input in order to perform the eponymous deconvolution of the Wigner distributions. This is in accordance with our current Definition 3.3 of the ptychographic phase problem, where we have stated the same prerequisite. Consequently, one has to either fully characterize the illuminating wavefield by an independent measurement or model it. Both is in the best case tricky and in the worst one impossible. Typically, probes obtained either way still show deviations from the actual illumination function, which in turn degrades the corresponding object reconstructions.

To avoid the need to know the probe *a priori*, MCCALLUM AND RODENBURG (1993) suggested a way to directly reconstruct it also from the ptychographic data set: They showed that by replacing (3.8) with a *blind deconvolution*, both probe and object can be obtained simultaneously. A discussion of various existing approaches to perform blind deconvolution can be found, e.g., in the review by KUNDUR AND HATZINAKOS (1996). Another way to retrieve the illumination has been suggested by CHAPMAN (1996), who used the interchangeability of the roles of P and O in ptychography in general and in (3.6) in particular. Instead of deconvolving an known probe to get an unknown object, he used a known object to obtain a better estimate of his illumination function. This has of course the drawback that in this case the object has to be perfectly known, including the same difficulties as already mentioned for the probe. Nevertheless, CHAPMAN (1996) reported improved reconstruction results after having updated the illumination this way. Furthermore, he also pointed out that this approach can be employed to characterize the wavefields of X-ray focusing optics, which is nowadays indeed an important application of iterative ptychography with probe retrieval (KEWISH ET AL., 2010a,c; SCHROPP ET AL., 2010; VILA-COMAMALA ET AL., 2011a).

Partial coherence Already RODENBURG AND BATES (1992) extended the theory of the Wigner-distribution deconvolution to the case of a partially coherent illumination. For this, they derived equivalent relations to the ones used in section 3.1.3.1, but now including the mutual coherence function Γ according to (2.2). They found that the effects of partial coherence are fully separable from $H(\mathbf{r}, \mathbf{S})$ in (3.6), as the generalized version contains just an additional factor $\Gamma(-\mathbf{S})$. Like for the other two factors of $H(\mathbf{r}, \mathbf{S})$, it is thus possible to deconvolve $\Gamma(-\mathbf{S})$ from the data set. Or, like CHAPMAN (1996) demonstrated, it can be retrieved by using a known object or probe. RODENBURG (2008) pointed out that even if the mutual coherence function is not deconvolved before determining the object, the quality and resolution

of the obtained result are not limited by partial coherence.

The inclusion of and robustness with respect to partial coherence effects is a quite remarkable feature of the Wigner-distribution deconvolution. Most CDI approaches by default assume fully-coherent illumination conditions. As real-life electron or X-ray sources are typically not perfectly coherent, not considering this in the reconstructions leads to a reduced quality of the results (WILLIAMS ET AL., 2007). Only in 2009, WHITEHEAD ET AL. developed an approach which allowed them to successfully reconstruct data taken with partially coherent X-rays.

Importance as closed-form approach for ptychography Compared to the Wigner-distribution deconvolution, the more recent iterative algorithms for ptychography require much less diffraction data to produce the same reconstruction result. Because in their case, the lateral separation of the probe positions \mathbf{r}_j no longer limits the achievable resolution. So for the limiting case of small scan steps on the scale of a single resolution element, the closed-form solution of the ptychographic reconstruction problem can be obtained, which is the Wigner-distribution deconvolution.² Therefore, it continues to play an important role to gain insights into fundamental properties of ptychography. One recent example is the study by GUIZAR-SICAIROS ET AL. (2012) on the role of the length scales present in the probe's wavefront structure on the reconstruction quality. The Wigner-distribution convolution also demonstrated the possibilities to include partial coherence or retrieve an unknown probe and thus provided an indication that this might also be feasible in iterative ptychographic reconstructions. And indeed, the latest iterative schemes implement both probe retrieval (GUIZAR-SICAIROS AND FIENUP, 2008; MAIDEN AND RODENBURG, 2009; THIBAUT ET AL., 2009a, 2008) and partial coherence (THIBAUT AND MENZEL, 2013).

3.1.4 The Ptychographical Iterative Engine (PIE)

3.1.4.1 Basic concept of iterative ptychography

FAULKNER AND RODENBURG (2004) presented the first application of an iterative algorithm to (simulated) ptychographic data. As the localized illumination, they used the exit wave of a perfect circular aperture, i.e. an ideal

²One can also find an analogy to computed tomography (CT) here: CT as well has an analytic solution in the form of the filtered backprojection algorithm (compare section 4.2 on page 119). And also in the case of CT, one major benefit of alternative iterative reconstruction techniques lies in the possibility to significantly reduce the amount of input data, i.e. less projection images from different angles have to be recorded.

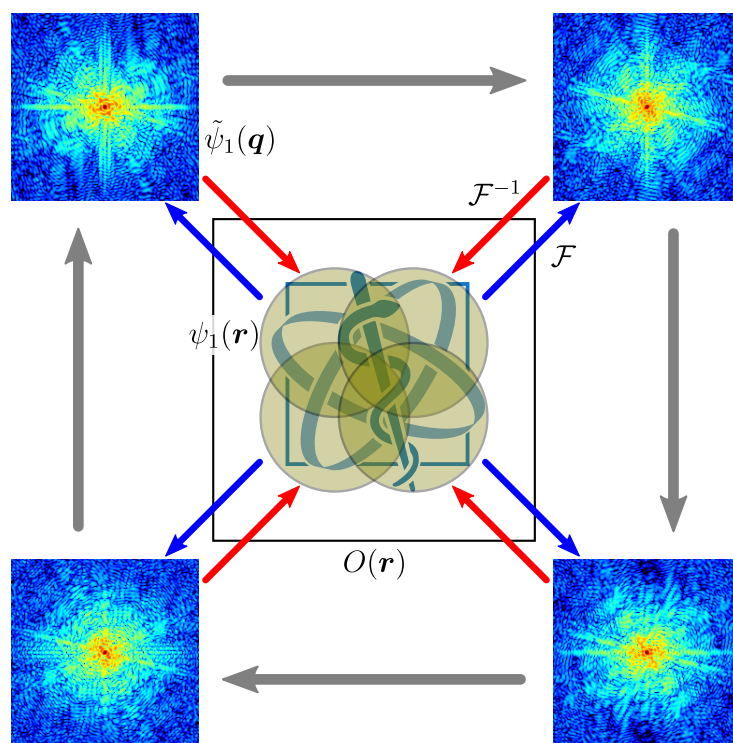


Figure 3.1: Schematic representation of an iterative reconstruction algorithm (PIE) applied to a ptychographic data set consisting of diffraction patterns collected at four overlapping positions of the probe, a circular aperture. The diffraction patterns are displayed on a colour-coded logarithmic scale (arbitrary units) and were calculated with the given test object by assigning brightness (value) to amplitude and hue to phase. The algorithm iterates over the scan positions in an outer loop (grey arrows). At each position j , the current guess of the exit wave $\psi_j(\mathbf{r}) = P(\mathbf{r} - \mathbf{r}_j) \cdot O(\mathbf{r})$ is constructed by multiplying the object O with the known probe P shifted to the respective position. An updated guess of this exit wave is obtained after application of the measured diffraction data in the Fourier constraint (blue and red diagonal arrows). From this new exit wave, a refined guess of the current object region is calculated and the algorithm moves to the next scan position. Due to the overlap between the probes, the result at the previous position directly improves also the exit wave guess at this adjacent scan point, leading to a faster convergence. Schematic is based on a similar sketch in RODENBURG ET AL. (2007b).

top-hat function. Fig. 3.1 schematically depicts an experiment like this, showing four calculated diffraction patterns for the corresponding position of a circular probe on the given test object (a logo). From an algorithmic point of view, multiplying the object with such a sharp-edged and perfectly homogeneous probe is just an application of a support constraint. Consequently, the algorithm reduces to HIO (compare section 2.4.3.3 on page 62) when using only one probe position (FAULKNER AND RODENBURG, 2004). If multiple diffraction patterns are used but the illuminated areas do not

overlap, an independent HIO reconstruction is performed for each position. For probes with partial overlap, however, the reconstruction highly benefits from the redundancy in the data: Consider a region of the object which is illuminated for several different probe positions, e.g. the centre of the object in Fig. 3.1. The reconstruction of this area has to be consistent with all the diffraction patterns to which it contributed, in our example with all four patterns of the ptychographic data set. So the updates of the object at the different illuminated patches are no longer independent. When the algorithm iterates through the scan positions, each subsequent object update benefits from the improvements already achieved at other overlapping scan points. This leads not only to a fast convergence, but also overcomes many of the other limitations mentioned in section 2.4.4 as further elaborated in section 3.1.4.3.

RODENBURG (2008) pointed out that the very first conceptual study of FAULKNER AND RODENBURG (2004) with a sharp-edged probe could not be extended straight away to smoother illuminations like a focused beam, as the iterations at the individual scan positions are just HIO updates which require a tight support. An important development was thus the introduction of a modified update function by RODENBURG AND FAULKNER (2004), thereby generating the algorithm which became known as the Ptychographical Iterative Engine (PIE) and is described in the next section.

3.1.4.2 Description of the PIE algorithm

The PIE algorithm is designed to solve the ptychographic phase-retrieval problem as given in Definition 3.3 on page 78, i.e. assuming perfect knowledge of the complex-valued two-dimensional probe function $P(\mathbf{r})$. According to RODENBURG ET AL. (2007a), this probe may be bandwidth-limited, have soft edges, or even an infinite spatial extent. It just has to be “substantially localized” (RODENBURG ET AL., 2007a), like e.g. a focal spot of an optics, such that the diffraction patterns are still appropriately sampled according to the conditions found in section 2.3.2.2 starting on page 53.

In addition to the known probe and the measured Fourier amplitudes, the iterative reconstruction receives an arbitrary guess $O^{(0)}(\mathbf{r})$ for the object function as input. This guess can be, e.g., an array of random complex number. The updated object $O^{(n+1)}(\mathbf{r})$ after $n + 1$ iterations is then calculated according to the following steps (FAULKNER AND RODENBURG, 2005; RODENBURG AND FAULKNER, 2004), compare also Fig. 3.1 and DIEROLF (2007):

1. Calculate a new guess for the exit wave (or “view”) $\psi_j^{(n)}(\mathbf{r})$ from the

current guess of the object $O^{(n)}(\mathbf{r})$ and the known probe $P(\mathbf{r})$ shifted to position \mathbf{r}_j :

$$\psi_j^{(n)}(\mathbf{r}) = P(\mathbf{r} - \mathbf{r}_j) \cdot O^{(n)}(\mathbf{r}) . \quad (3.11)$$

2. Apply the Fourier constraint by replacing the magnitude $|\tilde{\psi}_j^{(n)}(\mathbf{q})|$ of the view's Fourier transform with the square root of the measured intensity (blue and red arrows in Fig. 3.1):

$$\psi_{j,\text{new}}^{(n)}(\mathbf{r}) = \mathcal{F}^{-1} \left\{ \sqrt{I_j(\mathbf{q})} \frac{\tilde{\psi}_j^{(n)}(\mathbf{q})}{|\tilde{\psi}_j^{(n)}(\mathbf{q})|} \right\} . \quad (3.12)$$

3. Update the guess of the object in the currently illuminated region:

$$O^{(n+1)}(\mathbf{r}) = O^{(n)}(\mathbf{r}) + \beta U(\mathbf{r}) \left(\psi_{j,\text{new}}^{(n)}(\mathbf{r}) - \psi_j^{(n)}(\mathbf{r}) \right) , \quad (3.13)$$

where the function³ $U(\mathbf{r})$ is defined as

$$U(\mathbf{r}) \equiv \frac{|P(\mathbf{r} - \mathbf{r}_j)|}{\max(|P(\mathbf{r} - \mathbf{r}_j)|)} \frac{P^*(\mathbf{r} - \mathbf{r}_j)}{|P(\mathbf{r} - \mathbf{r}_j)|^2 + \alpha} . \quad (3.14)$$

4. Move to next scan position \mathbf{r}_{j+1} (grey arrows in Fig. 3.1) and repeat the previous steps. The illuminations $P(\mathbf{r} - \mathbf{r}_j)$ and $P(\mathbf{r} - \mathbf{r}_{j+1})$ at neighbouring points overlap partly. The object update at position \mathbf{r}_{j+1} thus benefits from the previous update at position \mathbf{r}_j .
5. Repeat the previous steps for the whole number N_j of scan positions \mathbf{r}_j to complete one update $O^{(n)} \rightarrow O^{(n+1)}$ for the full scanned object area.
6. Monitor convergence using an error metric, for instance the sum squared error between the measured intensities and the squared Fourier magnitudes of the current views (LINFOOT, 1964):

$$S_n = \frac{\sum_j \sum_{\mathbf{q}} \left(I_j(\mathbf{q}) - |\tilde{\psi}_j^{(n)}(\mathbf{q})|^2 \right)^2}{\sum_j \sum_{\mathbf{q}} I_j(\mathbf{q})^2} . \quad (3.15)$$

³We adapt here the notation of RODENBURG ET AL. (2007a), but do not use their term “update function” for $U(\mathbf{r})$ to avoid confusion with an iteration or update rule like (3.13).

Repeating steps 1 to 4 once for all N_j scan patterns is commonly referred to as one PIE iteration (compare, e.g., FAULKNER AND RODENBURG, 2005). Typically, a PIE reconstruction converges within just 10 to 30 PIE iterations to a state where no more changes can be perceived by eye. However, one should keep in mind that n PIE iterations correspond to $N_j \times n$ applications of the update rule (3.13). In single-pattern CDI algorithms, one iteration typically comprises one application of such an update rule. The parameter β plays the same role as the feedback parameter of the same name in the HIO update rule, see (2.41) on page 63. It is therefore chosen to be in the same range, typically one uses $\beta \in [0.9, 1]$.

Let us now take a look at the heart of the PIE update rule, the function $U(\mathbf{r})$: Its first term, $|P|/\max|P|$, is a weighting factor. In those areas of the object where the current probe has a strong amplitude $|P(\mathbf{r} - \mathbf{r}_j)|$, it leads to a maximum effect of the difference term in (3.13) on the updated object guess. In contrast, the object is only slightly modified in weakly-illuminated regions, where otherwise high errors would be observed (RODENBURG AND FAULKNER, 2004). If the probe P is a just binary mask, the first term of $U(\mathbf{r})$ corresponds to the application of a support constraint. The second factor in $U(\mathbf{r})$, $P^*/(|P|^2 + \alpha)$, removes the contribution of the probe from an exit wave, leaving an object function. Division-by-zero at pixels \mathbf{r} where $P(\mathbf{r}) = 0$ is avoided by adding the small positive real-valued constant α , which for a probe normalized to unity amplitude is typically in the order of 10^{-3} . In analogy to (3.8) on page 79, the factor $P^*/(|P|^2 + \alpha)$ can be considered as the deconvolution step in PIE which also takes the form of a Wiener filter.

3.1.4.3 Properties of the PIE algorithm

Benefits compared to standard CDI Iterative ptychography using the PIE algorithm provides superior performance compared to standard single-pattern CDI concerning many of the issues discussed in section 2.4.4 on page 70: It has already been pointed out that the convergence of iterative ptychography is faster than for common CDI algorithms due to the high redundancy of the data for adjacent scan positions. In addition, this enforced consistency of neighbouring illuminated object patches in overlapping regions does not allow that one of these patches is rotated by 180° and thereby suppresses convergence to the twin image. Furthermore, the lateral relative translation of probe and object produces a data set which allows a consistent reconstruction only at one defocus distance (RODENBURG ET AL., 2007a). However, this is the plane which fits best with the fixed input probe. So if for instance the propagation of the probe is not modelled correctly, the result will

be a propagated (defocused) object reconstruction. With the definition of the update rule (3.13) according to RODENBURG AND FAULKNER (2004), iterative ptychography does not require a sharp-edged illumination, neither for fixing this defocus distance nor for reliable reconstructing complex-valued objects (FAULKNER AND RODENBURG, 2004). According to investigations by FAULKNER AND RODENBURG (2005), the algorithm shows a remarkable tolerance to experimental noise. Altogether, these properties make PIE well-suited for the imaging of extended specimens without requiring *a priori* knowledge of the sample.

Limitations due to required *a priori* knowledge PIE relies on the two major assumptions that both the probe $P(\mathbf{r})$ and its positions \mathbf{r}_j are perfectly known on the length scale of the aspired resolution. It is therefore not particularly surprising that the algorithm turns out to be very sensitive to any errors in either of these (FAULKNER AND RODENBURG, 2005). However, such incomplete knowledge will typically be the case in an experiment: For one, it is extremely challenging to characterize or model an experimental illumination function flawlessly. As in addition the probe is considered to be the same for a whole ptychographic data set, potential fluctuations during a scan are not taken into account. And while we have pointed out that PIE eliminates defocus ambiguities and reconstructs the object at a well-defined focal plane, the latter is also the plane which fits best with the given input probe. So if for instance the propagation of this probe is not modelled correctly, the result will be a propagated (defocused) object reconstruction. Independently of all these potential issues with the characterization of the localized illuminating wavefield, also insufficient knowledge of its shifts \mathbf{r}_j is frequent. This shortcoming can be caused, e.g., by inaccuracies of the employed systems for scanning or position metrology, but may also be created by long-term drifts.

The other face of illumination overlap Under certain circumstances, even the basis of the beneficial properties of ptychography – the overlap of probes at adjacent positions – may be considered a limitation. In particular for radiation-sensitive specimens, the required multiple illumination of object regions may make it hard to define the dose that provides the optimal trade-off between low damage and high resolution. In the extreme case, radiation damage can be so large that the object no longer remains unaltered in overlap areas, making ptychography impossible. One example is diffractive imaging with an unattenuated X-ray free-electron laser beam, which typically destroys the sample with a single shot (compare, e.g., the

CDI demonstration by CHAPMAN ET AL., 2006a). At XFELs, ptychography is therefore restricted to special cases in which a sort of virtual overlap can be constructed due to translational symmetry of the specimen, e.g. two-dimensional crystals (KEWISH ET AL., 2010b). Also if radiation damage is not an issue, the chosen amount of overlap still has an influence on the performance of PIE. More overlap leads to a higher redundancy in the data and thus to an improved convergence behaviour. In the extreme case where the scan step size equals the resolution, even the closed-form reconstruction through the Wigner-distribution deconvolution (compare section 3.1.3) becomes possible. However, high overlap also reduces the field-of-view which can be covered in a given time and increases the total amount of diffraction patterns required to do so. In practice, positioning and detector read-out often create significant overheads, so a too high number of scan points may lead to an inefficient usage of limited beamtime. The influence of the overlap on the quality of a PIE reconstruction has thus been investigated in sections 3.1.4 and 4.4 of DIEROLF (2007), compare also the publication based on these results by BUNK ET AL. (2008): For the specific case of a pinhole illumination with diameter $2R$ being moved on a square scan grid with step size a , the linear relative overlap was defined as $o = 1 - a/2R$. It was found that a value of $o \approx 60\%$ provides high-quality reconstructions at still reasonable total acquisition times (doses). For this overlap, not only the nearest-neighbour probes overlap, but information is also shared with the next-but-one scan positions.

3.2 Ptychography with probe retrieval

In the previous section we have already seen that the requirement of perfect *a priori* knowledge of the probe can be a major limitation for the application of PIE to experimental data. The best results with PIE have therefore been achieved with visible laser light (BUNK ET AL., 2008; DIEROLF, 2007; RODENBURG ET AL., 2007a), where the shape of the illumination can be controlled with very precise pinholes. While the application to X-ray data has also been successfully demonstrated (RODENBURG ET AL., 2007b), these experiments are much more prone to imperfections in the illumination. These make it hard to define the probe for PIE with the required accuracy which often results in degraded reconstructions. In order to establish ptychography as a real alternative to standard X-ray microscopy techniques, it is thus mandatory that methods are available for the reliable and exact retrieval of the illuminating wavefronts. Ideally, these approaches should directly utilize the recorded ptychographic data sets instead of relying on additional mea-

surements. In this thesis, the term *ptychographic coherent diffractive imaging* (PCDI) is used to refer to these algorithms with probe retrieval in order to distinguish them more clearly from other types of ptychography, in particular from PIE.

3.2.1 First concepts for probe refinement

While all the results in [DIEROLF \(2007\)](#) were still obtained with PIE and a modelled probe, also two possibilities to overcome the associated disadvantages were already investigated at this time.

3.2.1.1 Probe retrieval using standard CDI

For testing this method, a diffraction pattern of the probe alone was used as the Fourier constraint and the known shape of the pinhole as the support in an HIO reconstruction. [QUINEY ET AL. \(2006\)](#) had earlier employed a similar approach to reconstruct the wavefield of a Fresnel zone plate. However, in our tests the quality of the PIE reconstructions using a probe retrieved this way was poorer than with a modelled probe. This was attributed to the effect of noise in the diffraction data, which the algorithm interpreted as genuine signal of the pinhole. Too much noise thus resulted in a degraded probe guess containing unphysical features. Furthermore, there is the limitation that very precise knowledge of the aperture is required to form a tight support constraint. In summary, the approach thus does not provide the means to perform model-independent ptychography reconstructions.

3.2.1.2 PIE with probe refinement

This method is based on the observation that in ptychography the roles of probe and object can easily be exchanged, as the exit waves are just given by the product $\psi_j = P_j \cdot O$. So instead of updating the object guess with a fixed probe, one can also iterate the probe while keeping the object fixed. If a specimen's complex transmission function is perfectly known, this can be used to reconstruct the probe using ptychography. As already mentioned on page 81, [CHAPMAN \(1996\)](#) has applied exactly this approach to the Wigner-distribution deconvolution to better characterize his illumination function. Independently of this work, an iterative scheme was suggested in [DIEROLF \(2007\)](#) in which probe and object are updated in an alternating fashion. The basic idea of this algorithm is sketched in Fig. 3.2: First, a normal PIE run is performed with a modelled probe to retrieve a good guess of the object. Then, the PIE algorithm is inverted, i.e. the object is kept fixed while the

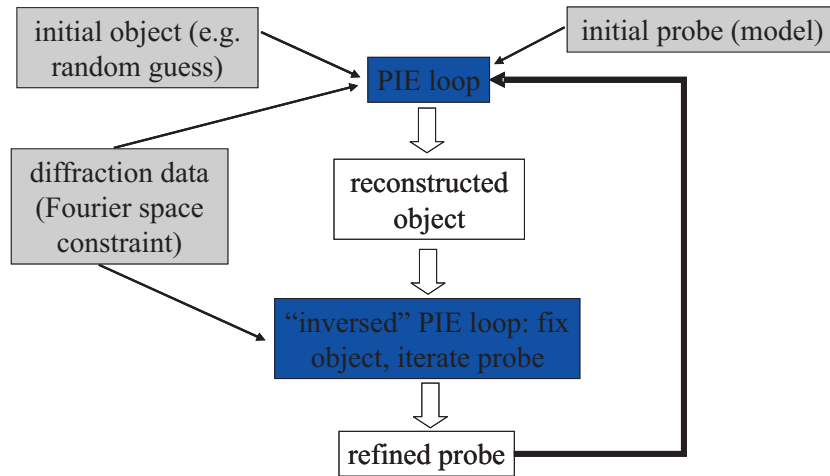


Figure 3.2: PIE algorithm with feedback loop for probe refinement: At first, a standard PIE reconstruction with a modelled probe is performed. The resulting object is then used as the fixed input for an “inversed” PIE loop, in which instead the probe is updated. From [DIEROLF \(2007\)](#).

probe is updated. This whole procedure is repeated several times. Unlike the probe refinement used by [CHAPMAN \(1996\)](#), this alternating approach can be carried out with an unknown object. And instead of retrieving the probe in an independent CDI step like discussed above, it is refined directly in the ptychographic reconstruction itself. Some first tests of the approach were carried out on visible laser data in August 2007. It was observed that some additional, plausible features appeared in the probes, but no general conclusions could be drawn for the quality of the object reconstructions. Further, more systematic studies of the method were not carried out as shortly afterwards a superior algorithm for ptychography with simultaneous probe retrieval was developed by [THIBAUT ET AL. \(2009a, 2008\)](#), which is described in section [3.2.2](#). Therefore, little is known about the performance and the optimal choice of parameters for the proposed alternating scheme, e.g. concerning the best amount of iterations between switching from probe to object updates and vice versa. Nevertheless, the validity of the general idea can be inferred from the later work of [MAIDEN AND RODENBURG \(2009\)](#), who introduced the *extended Ptychographical Iterative Engine* (ePIE) with two alternately applied update functions for probe and object. Both update rules take the some form, just the roles of illumination and object are simply exchanged. But in contrast to the proposed scheme of alternating PIE runs, in ePIE both P and O are updated at each scan position. So the alternation happens directly inside the PIE loop and at much higher frequency.

3.2.2 The difference map ptychography algorithm for simultaneous probe retrieval

A few years after the development of PIE, some new algorithms for iterative ptychography have been proposed which allow to simultaneously reconstruct both object and probe from the same ptychographic data set. In the previous section, it has already been mentioned that ePIE (MAIDEN AND RODENBURG, 2009) added this capability to the original PIE algorithm. Even before, GUIZAR-SICAIROS AND FIENUP (2008) had presented a conjugate-gradient approach for PCDI, whereas THIBAULT ET AL. (2008) had successfully demonstrated their iterative-projection PCDI algorithm based on the difference map on X-ray data. For the reconstructions presented in this thesis, mainly this difference map (DM) ptychography algorithm by THIBAULT ET AL. (2009a, 2008) was employed. It is therefore the focus of the discussion for the remainder of this section on ptychography with probe retrieval. However, in subsection 3.2.5 starting on page 101, an additional PCDI algorithm based on maximum-likelihood (ML) optimization (THIBAULT AND GUIZAR-SICAIROS, 2012) is introduced as an optional refinement step following a DM-based PCDI run. THIBAULT AND GUIZAR-SICAIROS (2012) also identified the earlier algorithm of GUIZAR-SICAIROS AND FIENUP (2008) as a special case of their method.

3.2.2.1 Ptychography as a two-constraint problem

To be able to apply the framework of projections onto two constraint sets used by the difference map, the ptychographic phase-retrieval problem has to be reformulated accordingly. Definition 3.3 for ptychography with a fixed probe was centred on the retrieval of the complex object transmission function O . In contrast, the generalized problem for the case of an unknown illumination is instead formulated in terms of the exit waves, or views, ψ_j :

Definition 3.4 (Generalized ptychographic phase-retrieval problem). Find the exit waves $\psi_j(\mathbf{r})$ which for all scan points j are consistent with the *Fourier constraint* enforced by the measured diffraction intensities

$$I_j(\mathbf{q}) = |\mathcal{F}\{\psi_j(\mathbf{r})\}|^2 \equiv |\tilde{\psi}_j(\mathbf{q})|^2, \quad (3.16)$$

and which at the same time fulfil the *overlap constraint*

$$\psi_j(\mathbf{r}) = P(\mathbf{r} - \mathbf{r}_j) \cdot O(\mathbf{r}), \quad (3.17)$$

i.e. for all j can ψ_j be factorized into the object $O(\mathbf{r})$ and the common probe $P(\mathbf{r})$ in the plane of the specimen shifted to the position \mathbf{r}_j .

As in standard CDI, the solution of this problem can be found as the intersection of the two constraint sets using suitable optimization methods. While in this generalized definition the probe no longer has to be known, exact values for the scan positions \mathbf{r}_j still have to be provided as input alongside the measured diffraction data. Also detailed information on the physical parameters and geometry of the experiment is required to calculate the actual physical size of the sampling intervals. As the pixel sizes in real and reciprocal space are coupled according to (2.12) on page 50, either the former can be calculated with (2.20) on page 53, or the latter using (2.18) on page 53. Therefore, also the wavelength λ , the detector pixel size Δs , and the sample-to-detector distance Z become mandatory input parameters for a PCDI reconstruction. The first two also have to be known accurately in a PIE reconstruction, while the distance Z may also be obtained by adjusting the scaling of a modelled diffraction pattern of the known probe until it matches a measured one. For PCDI with an unknown or complicated probe, this option does no longer exist. Yet, the importance of the exact determination of this distance is obvious to most ptychography practitioners, who are well aware of the severely degrading effects that mismatches in Z have on PCDI reconstruction results (for an illustration, compare e.g. BURDET ET AL., 2014). Luckily, direct or indirect measurement of Z is usually possible with the required accuracy.

3.2.2.2 Description of the difference map PCDI algorithm

The generalized Definition 3.4 introduced in the previous section allows to use the concept of projections onto constraint sets for the iterative reconstruction, in this case by employing the difference map algorithm. The description of the resulting PCDI algorithm given here is based on THIBAUT ET AL. (2008, supporting online material) and THIBAUT ET AL. (2009a): Iterations take place on the high-dimensional state vector $\Psi = (\psi_1(\mathbf{r}), \psi_2(\mathbf{r}), \dots, \psi_N(\mathbf{r}))$ embedded in the search space which is the direct product of the spaces of each individual view. This state vector is projected onto the constraint sets such that the distance $\|\Psi - \Pi(\Psi)\|^2$ between the current state Ψ and the project state $\Pi(\Psi)$ is minimal.

In this formalism the projection Ψ_F derived from the Fourier constraint (3.16) is given by

$$\Pi_F(\Psi) : \psi_j \rightarrow \psi_j^F = \pi_F(\psi_j) , \quad (3.18)$$

where π_F is the *Fourier modulus projection* for a single diffraction pattern, which replaces the current Fourier amplitudes with the measured ones but

keeps the phases:

$$\pi_F : \tilde{\psi}_j(\mathbf{q}) \rightarrow \tilde{\psi}_j^F(\mathbf{q}) = \sqrt{I_j(\mathbf{q})} \frac{\tilde{\psi}_j(\mathbf{q})}{|\tilde{\psi}_j(\mathbf{q})|}. \quad (3.19)$$

It should be pointed out that (3.18) is always decoupled in the views j , i.e. the individual Fourier projections do not influence each other and thus can be implemented as parallel code without the need for message passing. To exclude detector pixels for which no valid signal has been measured, e.g. insensitive inter-module gaps as well as dead pixels or randomly fluctuating “hot pixels”, a valid pixel mask $w_j(\mathbf{q})$ is introduced which may be adapted individually for each diffraction pattern j . It is equal to 0 for areas of the measured data to be excluded and to 1 for valid pixels. The projection operation (3.18) is then implemented in the form

$$\pi_F : \tilde{\psi}_j(\mathbf{q}) \rightarrow \begin{cases} \tilde{\psi}_j^F(\mathbf{q}) & , \mathbf{q} \in \{\mathbf{q} : w_j(\mathbf{q}) = 1\} \\ \tilde{\psi}_j(\mathbf{q}) & , \mathbf{q} \in \{\mathbf{q} : w_j(\mathbf{q}) = 0\} . \end{cases} \quad (3.20)$$

The overlap projection is computed by minimizing the distance $\|\Psi - \Psi^O\|^2$ while ensuring the constraint (3.17) is fulfilled. For this, one has to find the functions \hat{O} and \hat{P} that minimize

$$\|\Psi - \Psi^O\|^2 = \sum_j \sum_{\mathbf{r}} |\psi_j(\mathbf{r}) - \hat{P}(\mathbf{r} - \mathbf{r}_j) \cdot \hat{O}(\mathbf{r})|^2. \quad (3.21)$$

So the *overlap projection* can be formulated as

$$\Pi_O(\Psi) : \psi_j \rightarrow \psi_j^O(\mathbf{r}) = \hat{P}(\mathbf{r} - \mathbf{r}_j) \cdot \hat{O}(\mathbf{r}). \quad (3.22)$$

As the minimization of (3.21) can not be carried out analytically, a numerical approach is required. The roots of the derivative of (3.21) with respect to \hat{P} and \hat{O} give the solution as a system of equations:

$$\hat{P}(\mathbf{r}) = \frac{\sum_j \hat{O}^*(\mathbf{r} + \mathbf{r}_j) \psi_j(\mathbf{r} + \mathbf{r}_j)}{\sum_j |\hat{O}(\mathbf{r} + \mathbf{r}_j)|^2}, \quad (3.23)$$

$$\hat{O}(\mathbf{r}) = \frac{\sum_j \hat{P}^*(\mathbf{r} - \mathbf{r}_j) \psi_j(\mathbf{r})}{\sum_j |\hat{P}(\mathbf{r} - \mathbf{r}_j)|^2}. \quad (3.24)$$

In cases where the probe is known *a priori*, the overlap projection is given by (3.22) with \hat{O} being calculated with (3.24). This corresponds essentially to the original PIE algorithm.

If both \hat{P} and \hat{O} are to be retrieved, (3.23) and (3.24) have to be solved simultaneously. As an analytical decoupling is not possible, the equations

are applied in turns for a few steps in an iterative procedure, which was observed to be an efficient means to obtain the solution. Reconstruction is started with a rough model of the probe \hat{P} . Any subsequent iteration uses the results for \hat{P} and \hat{O} calculated in the previous iteration as initial guesses.

With the projections (3.18) and (3.22) the reconstruction is implemented using the *difference map algorithm* (ELSER, 2003a), for details see section 2.4.3.5 starting on page 65. With a standard choice of parameters (ELSER, 2003a,b), the update rule for the $n+1$ iteration then takes the form (compare also (2.56) on page 67)

$$\Psi_{n+1} = \Psi_n + \Pi_F [2\Pi_O(\Psi_n) - \Psi_n] - \Pi_O(\Psi_n) , \quad (3.25)$$

for the whole state vector Ψ , or

$$\psi_j^{(n+1)}(\mathbf{r}) = \psi_j^{(n)}(\mathbf{r}) + \pi_F \left[2\hat{P}(\mathbf{r} - \mathbf{r}_j)\hat{O}(\mathbf{r}) - \psi_j^{(n)}(\mathbf{r}) \right] - \hat{P}(\mathbf{r} - \mathbf{r}_j)\hat{O}(\mathbf{r}) , \quad (3.26)$$

if formulated for an individual view ψ_j . In between these difference map iterations, \hat{P} and \hat{O} are iteratively refined in a nested loop using (3.23) and (3.24) as described above. Iteration of (3.25) is continued until a fixed point is reached, i.e. $\Psi_{n+1} = \Psi_n$. From (3.26) it becomes clear, that this is equivalent to $\hat{P}(\mathbf{r} - \mathbf{r}_j)\hat{O}(\mathbf{r})$ satisfying the Fourier constraint for all j and therefore being solutions of the ptychographic phase retrieval problem at hand.

Convergence is monitored with the difference map error

$$\epsilon_{n+1} = \|\Psi_{n+1} - \Psi_n\| . \quad (3.27)$$

While in the ideal case this error would become zero if a fixed point had been reached, this is usually not the case in practice, as discussed in more detail in section 3.2.4.1.

For the initial views in the initial state vector Ψ_0 , arrays of random numbers are a typical choice. However, convergence can be sped up with better initial estimates, see also section 3.2.6. It has been observed that using the starting guess of the probe also as initial views, i.e. the object is assumed to be completely transparent, helps to avoid formation of phase singularities and results in faster convergence.

3.2.3 Validity of the wave factorization assumption

The assumption that the exit wave ψ behind the object can be factorized into two independent functions P and O according to (3.17) is fundamental for ptychography. Qualitatively, this means that the changes of the probe should be negligible when propagated on the scale of the object's thickness. A

quantitative measure can be derived by a wave optical treatment (THIBAUT ET AL., 2008, supporting online material): The inhomogeneous wave equation in the presence of a specimen with the complex refractive index $n(x, y, z)$ is given by

$$\nabla^2 \Upsilon + k^2 n^2 \Upsilon = 0 , \quad (3.28)$$

with the wave field Υ given by the factorization ansatz

$$\Upsilon(x, y, z) = T(x, y, z) \Upsilon_0(x, y, z) , \quad (3.29)$$

where $\Upsilon_0(x, y, z)$ is the incident wave field produced by the apparatus. The specimen is of finite extent L along the propagation direction, i.e. $n = 1$ outside of $0 < z < L$. For (3.29) to be a valid solution of (3.28) one has to assess the conditions under which the transfer function T is independent of Υ_0 throughout the specimen's depth. Substituting (3.29) in (3.28) using $\Upsilon_0 = v_0 \exp(ikz)$ yields

$$\left(\nabla^2 T + 2ik\partial_z T + k^2(n^2 - 1)T \right) v_0 + 2\nabla v_0 \cdot \nabla T = 0 . \quad (3.30)$$

If the rightmost term can be neglected, T can be independent of v_0 and then $T \exp(ikz)$ satisfies the wave equation

$$\nabla^2 [T \exp(ikz)] + k^2 n^2 T \exp(ikz) = 0 . \quad (3.31)$$

The last term of order k^2 in the parenthesis of (3.30) is always dominant. A sufficient condition for the approximation to be valid is

$$k|v_0 \partial_z T| \gg |\nabla v_0 \cdot \nabla T| . \quad (3.32)$$

Scaling arguments can be used to get a general estimate of this equality based on the experimental geometry. In the scalar product, the longitudinal terms along z can be ignored since $|\partial_z v_0| \ll k|v_0|$. An upper bound for the transverse gradient of T can be given using the inverse resolution $(\Delta x)^{-1}$ of the experiment: $|\nabla T| \sim (\Delta x)^{-1} |T|$. Along the propagation direction, $L^{-1} |T|$ is a lower limit of $|\partial_z T|$. Substituting in (3.32) gives

$$\frac{\Delta x}{L} \gg \frac{\lambda}{a} , \quad (3.33)$$

where a is the maximum extent of the illumination v_0 in the specimen plane.

In practice, one is typically interested in an upper limit L_{max} in terms of specimen thickness for specific experimental parameters such that the wave factorization assumption still holds true. It is roughly given by

$$L_{max} < \frac{a \Delta x}{\lambda} . \quad (3.34)$$

As the probe is assumed to be constant for all points of a ptychographic scan, the whole scanned region of the specimen has to lie entirely within this depth. This also imposes a limit on the tilt a flat sample can have with respect to the beam. As an example, consider a typical pinhole-based ptychography experiment, with $\Delta x = 10 \text{ nm}$, $a = 2 \mu\text{m}$ and $\lambda = 2 \text{ \AA}$: in this case, the maximum thickness of the specimen should stay below $100 \mu\text{m}$.

It should be pointed out that when (3.33) is fulfilled, T solves the wave equation, without any limitation on the scattering regime. The specimen neither has to be a weak phase object, nor has the Ewald sphere curvature to be negligible. Also dynamical scattering does not affect the validity of the reconstruction. L_{max} can also be understood as the focal depth of a ptychographic reconstruction.

3.2.4 Uniqueness of solution

3.2.4.1 Convergence in the presence of noise

In practical applications, one typically observes that the value of the difference map error (3.27) does not reach zero. This indicates that there is no state vector Ψ that perfectly fulfils both constraint sets, i.e. noise and other experimental imperfections make them incompatible. As a result, there is typically a whole set of near-solutions which are – in the multi-dimensional search space of the state vector – in close proximity around the true solution one would get with a perfect imaging system. When comparing such near-solutions, they will typically show the biggest differences in the high resolution features for which the signal-to-noise ratio in the corresponding diffraction data is lowest. In the following paragraphs, several approaches used in CDI to nevertheless get to unique solutions are discussed.

Averaging based on random starting guesses Some basic iterative phase-retrieval algorithms, like the error reduction algorithm (FIENUP, 1982; GERCHBERG AND SAXTON, 1972), by design pick only one of these near-solutions: they correspond to local minima of the distance between the two constraint sets in search space in which these algorithms get stuck. So convergence is in this case not a sign of success in terms of finding a unique solution as it completely ignores the inherent experimental uncertainties. In particular, retrieved high-resolution features may not be very reliable. To cope with these issues, reconstructions obtained using several random starting guesses are typically averaged to form reliable and reproducible results.

Averaging based on quasi-ergodic steady-state regime More sophisticated algorithms like the difference map, or the hybrid input-output algorithm (FIENUP, 1982) as one of its special cases, will be unstable when the constraint sets are not compatible. If they are too far apart, these algorithms will never converge and reconstruction will fail (unless the constraints are adapted accordingly, see next paragraph). However, typically a final steady-state regime is reached in which the difference error fluctuates slightly around a small, non-zero plateau value. Due to the chaotic behaviour of the algorithm, the set of all allowed solutions is then covered quasi-ergodically (THIBAUT ET AL., 2006). A unique reconstruction can therefore be obtained by averaging the solution attempts from this steady-state regime. As the algorithm described in 3.2.2 is also based on the difference map, this is also the method used in the implementations employed for this work.

Incorporation of noise model in Fourier constraint To avoid failure in the presence of excessive noise, one tries to adapt the constraints by incorporating a noise model. In our case, the simple and efficient – but also approximate – approach of a relaxed Fourier projection (CHAPMAN ET AL., 2006b) has been adapted for PCDI. The details have first been documented in the article by GIEWEKEMEYER ET AL. (2010, supporting information). In the relaxed projection the Fourier amplitudes are not reset to the measured ones if they already lie within a small range around the latter. The extent of this range is proportional to the relaxation parameter D . In this case, the Fourier projection (3.19) becomes

$$\pi_F : \tilde{\psi}_j(\mathbf{q}) \rightarrow \tilde{\psi}_j^F(\mathbf{q}) = \begin{cases} \left[\sqrt{I_j(\mathbf{q})} + \frac{D}{d_j} \left(|\tilde{\psi}_j(\mathbf{q})| - \sqrt{I_j(\mathbf{q})} \right) \right] \frac{\tilde{\psi}_j(\mathbf{q})}{|\tilde{\psi}_j(\mathbf{q})|} & , d_j > D \\ \tilde{\psi}_j(\mathbf{q}) & , d_j \leq D, \end{cases} \quad (3.35)$$

where d_j is the average distance for the j -view given by

$$d_j^2 = \frac{1}{N_q} \sum_{\mathbf{q}} w_j(\mathbf{q}) \left| |\tilde{\psi}_j(\mathbf{q})| - \sqrt{I_j(\mathbf{q})} \right|^2. \quad (3.36)$$

Here N_q is the number of pixels in one diffraction pattern and $w_j(\mathbf{q})$ the respective valid pixel mask. Using the latter, the relaxed Fourier projection (3.35) is usually also implemented according to (3.20) such that the Fourier amplitudes are only changed at values of \mathbf{q} for which $w_j(\mathbf{q})$ is 1 and left unaltered otherwise. In the limit $D \rightarrow 0$ the relaxed formulation (3.35) converges to the standard Fourier projection (3.19). While for diffraction patterns fulfilling Poisson statistics an expectation value $\langle d^2 \rangle \simeq \frac{1}{4}$ would give a theoretical relaxation parameter $D_{th} \simeq \frac{1}{2}$ (GIEWEKEMEYER ET AL., 2010),

it has been observed that smaller values of D may be more favourable: Too loose constraints may lead to stagnation or even prevent a unique solution. If the difference map error in the steady-state regime stays perfectly constant without the tiniest fluctuations, this is typically a sign of stagnation and thus a too large D . If on the other hand relaxation is chosen too small to successfully compensate the mismatch of constraints, the algorithm may not reach a steady-state regime at all, which shows up as oscillation with rather large amplitudes in the difference map error.

3.2.4.2 Constant phase terms

Phase retrieval reconstructions based on far-field intensity patterns are insensitive to constant phase terms as they do not affect the measured data and thus remain undetermined. Therefore, if $O(\mathbf{r})$ is a complex object transmission function and solution to the phase retrieval problem at hand, also $O'(\mathbf{r}) = O(\mathbf{r}) \cdot \exp(ia)$ is a valid solution, with a being a real-valued constant coefficient. So a calibration is necessary if absolute phase values are required.

3.2.4.3 Linear phase terms

According to the Fourier shift theorem, a shift in Fourier space corresponds to multiplication with a linear phase in real space. Therefore small errors in the determination of the centre of the diffraction patterns can result in a linear phase ramp in the corresponding CDI reconstructions.

When a ptychographic modality with simultaneous probe retrieval is used, reconstruction of linear phase terms becomes ambiguous: If the illumination function $P(\mathbf{r})$ and the complex object transmission function $O(\mathbf{r})$ are solutions to a ptychographic phase retrieval problem, the functions

$$P'(\mathbf{r}) = P(\mathbf{r}) \cdot \exp[i(\mathbf{g} \cdot \mathbf{r})] \quad (3.37a)$$

$$O'(\mathbf{r}) = O(\mathbf{r}) \cdot \exp[-i(\mathbf{g} \cdot \mathbf{r})] \quad (3.37b)$$

result in the exit waves

$$\psi'_j(\mathbf{r}) = P'(\mathbf{r}) \cdot O'(\mathbf{r} - \mathbf{r}_j) = \psi_j(\mathbf{r}) \cdot \exp[i(\mathbf{g} \cdot \mathbf{r}_j)] , \quad (3.38)$$

and

$$I'(\mathbf{q}) = |\mathcal{F}\{\psi'_j(\mathbf{r})\}|^2 = |\mathcal{F}\{\psi_j(\mathbf{r})\}|^2 = I(\mathbf{q}) . \quad (3.39)$$

As discussed earlier, the reconstruction is insensitive to the constant phase offset in (3.38), thus equations (3.37) will satisfy the constraints (3.17) and (3.16) for any value of the phase ramp's slope $\mathbf{g} = (g_x, g_y)$ (GUIZAR-SICAIROS

ET AL., 2011). Correction for linear phase terms is performed in a post-processing step using a object region which is supposed to have a flat phase as reference. Alternatively, *a priori* knowledge about flat areas of the object may also be incorporated as an additional constraint directly in the reconstruction process. This effectively prevents the built-up of an artificial phase ramp in the object transmission function. Details on this concept are given in section 3.2.6.2 on page 108.

3.2.4.4 Phase wrapping

As the reconstructed phase is computed from the retrieved complex-valued transmission, it is only known modulo 2π , so for larger phase shifts wrapping occurs. Typically, phase unwrapping is possible in these cases by applying the correct offsets with an absolute value 2π at the phase discontinuities in order to obtain a continuous phase function again. Mathematically, this means that the phase $\phi(\mathbf{r})$ at some point \mathbf{r} can be obtained from the path integral

$$\phi(\mathbf{r}) = \int_{\mathcal{C}} \nabla\phi \cdot d\mathbf{r} + \phi(\mathbf{r}_0), \quad (3.40)$$

if both the phase gradient⁴ $\nabla\phi$ and the phase at some initial point \mathbf{r}_0 are known and \mathcal{C} is any path connecting \mathbf{r} and \mathbf{r}_0 (compare also GHIGLIA AND PRITT, 1998). However, the phase signal may suffer from true discontinuities or dislocations, noise-corrupted phase gradients or aliasing due to undersampling of the phase signal, i.e. a phase jump larger than π radians for two neighbouring pixels. These are the sources of so-called “phase residues” (GHIGLIA AND PRITT, 1998): a closed-path integral around such a residue has a non-zero value of either $+2\pi$ (“positive residue charge”) or -2π (“negative residue charge”). Thus the integral in (3.40) becomes path dependent and the choice of the correct integration path a non-trivial problem. Various phase-unwrapping algorithms offer different approaches to nevertheless obtain consistent unwrapping (GHIGLIA AND PRITT, 1998). Details on the ones employed in the work with tomographic data can be found in section 9.2.3 (p. 247).

3.2.4.5 Raster grid pathology

If the illuminating probe $P(\mathbf{r})$ and the object $O(\mathbf{r})$ are reconstructed simultaneously solving a ptychographic phase-retrieval problem, there is an inherent

⁴ The phase gradient is of course not defined at the phase discontinuities themselves. Correct phase unwrapping is achieved by a continuous continuation of the gradient at these points.

unconstrained degree of freedom: The two functions

$$P'(\mathbf{r}) = \frac{1}{f(\mathbf{r})}P(\mathbf{r}) , \quad (3.41a)$$

$$O'(\mathbf{r}) = f(\mathbf{r})O(\mathbf{r}) , \quad (3.41b)$$

are also valid solutions to the phase problem at hand if and only if

$$f(\mathbf{r}) = f(\mathbf{r} - \mathbf{r}_j) \quad \forall j . \quad (3.42)$$

Apart from the trivial solution $f = \text{const.}$, this condition is also fulfilled if the scan points \mathbf{r}_j form a regular two-dimensional lattice. The latter is very common in practical applications, where raster scans are frequently used, therefore the effect has been termed “raster grid pathology” (THIBAUT ET AL., 2009a).

There are two general approaches to avoid raster grid artefacts in the reconstructed object:

1. In the case of a regular raster scan, use additional constraints to suppress the development of grid artefacts.
2. Break the symmetry of the scan pattern to make sure condition (3.42) is not fulfilled.

For the first approach, the fluctuations in an object region which is known to be flat are constrained to a level at which no grid imprints can develop in this area. As this breaks the periodicity of f as introduced in (3.42), the effect of the raster grid is suppressed effectively on the whole object. The drawback of having to rely on the presence of sufficiently large flat areas in the specimen can be circumvented by creating an additional artificial empty area from diffraction data of the probe alone.

For the second approach, it is best to completely abandon standard raster scanning. However, where a rectangular grid is required due to experimental constraints, the symmetry can be at least partly broken by using incommensurate grid spacings for the two scan directions. In our experiments we have been mostly using a scan pattern based on concentric circles which was termed “round scan” (DIEROLF ET AL., 2010b). While it does not show translation symmetry, it is still easy to describe analytically. As an additional benefit, the central part is measured first and thus – compared to a raster scan – less influenced by drift effects. If a rectangular field of view is required, a round scan can be cropped accordingly by just dropping scan points in the outside area. A round scan can be conveniently described by the three parameters radial step size Δr , number of concentric circles (shells) N_r ,

and the number of points in the first shell N_θ . To ensure a uniform density of scan points, the number of points in the j th shell is fixed to $j \cdot N_\theta$.

$$x_{j,m} = \Delta r \cdot j \cdot \cos \left((m-1) \frac{2\pi}{j \cdot N_\theta} \right), \quad (3.43a)$$

$$y_{j,m} = \Delta r \cdot j \cdot \sin \left((m-1) \frac{2\pi}{j \cdot N_\theta} \right). \quad (3.43b)$$

3.2.5 Maximum-likelihood refinement

3.2.5.1 Motivation

A relaxed Fourier constraint has been introduced in (3.35) on page 97 to be able to account for experimental noise when using algorithms like the difference map that are based on projections onto constraint sets. However, it can be difficult to properly include such statistical information into these formalisms which are ultimately based on Boolean expressions, i.e. whether a current state fulfills a constraint or not. Being a standard method for the estimation of probabilistic quantities (MYUNG, 2003), a maximum-likelihood (ML) approach for the ptychographic reconstruction process has been suggested by THIBAUT AND GUIZAR-SICAIROS (2012) as a way to properly include statistical models into it. While most results presented in this dissertation are based on the difference map algorithm, additional maximum-likelihood refinement starting from a previous difference map reconstruction has been applied in some cases. Therefore, the basic ideas presented by THIBAUT AND GUIZAR-SICAIROS (2012) are repeated in this section, however, the original publication should be consulted for a more detailed description. In particular, as it is the one used in the practical applications, only a Gaussian likelihood model is discussed here, whereas additionally also Poisson and Euclidean models are introduced in the original article.

3.2.5.2 Ptychographic maximum-likelihood estimation problem

Starting point is again the formulation of the ptychographic phase-retrieval problem according to equations (3.16) and (3.17), which establish the functional relation between the measured intensities $I_j(\mathbf{q})$ at scan positions \mathbf{r}_j , the object $O(\mathbf{r})$ and the probe $P(\mathbf{r} - \mathbf{r}_j)$ shifted to the corresponding positions on the object. In the next step, a statistical model has to be established which links P and O to the measured data, i.e. which defines the probability to measure a certain number of photon counts $n_j(\mathbf{q})$ for given $P(\mathbf{r} - \mathbf{r}_j)$ and

$O(\mathbf{r})$. The goal of the reconstruction process is to estimate the solutions $P(\mathbf{r})$ and $O(\mathbf{r})$ that – for all scan positions j – best explain the measured values $n_j(\mathbf{q})$ based on the underlying statistical model. Assuming a Gaussian distribution of measurement errors with the spatially-dependent uncertainties $\sigma_j(\mathbf{q})$ results in a weighted sum of squares for the negative log-likelihood:

$$\mathcal{L}(P(\mathbf{r}), O(\mathbf{r})) = \sum_j \sum_{\mathbf{q}} \frac{w_j(\mathbf{q})}{2\sigma_j^2(\mathbf{q})} (I_j(\mathbf{q}) - n_j(\mathbf{q}))^2 . \quad (3.44)$$

Here $w_j(\mathbf{q})$, the respective valid pixel mask at position j as introduced in (3.20) on page 93, restricts the sum over \mathbf{q} to include only valid measurements. However, the maximum likelihood formulation offers the possibility to assign customized weights to specific pixels in the data and thus allows to deviate from the usual definition of $w_j(\mathbf{q})$ as a binary mask. This can be useful in cases in which the signal is less reliable in certain regions of the diffraction patterns than in others. Ptychographic reconstruction is equivalent to minimizing \mathcal{L} with respect to the probe $P(\mathbf{r})$ and the object $O(\mathbf{r})$. For this one has to keep in mind that $I_j(\mathbf{q})$ is a function of both as defined in (3.16) and (3.17).

3.2.5.3 Implementation using conjugate gradient minimization

Calculation of gradient The numerical implementation done by Pierre Thibault, which has been used for the refinement of some reconstructions presented in this dissertation, employs a non-linear conjugate gradient minimization. Therefore, one has to calculate the gradient $g = (g_P, g_O)$ of function (3.44) with respect to P and O . In THIBAUT AND GUIZAR-SICAÏROS (2012) this is done using the Wirtinger derivatives

$$g_P = \frac{\partial \mathcal{L}}{\partial P(\mathbf{r})} = \sum_j O(\mathbf{r} + \mathbf{r}_j) \chi_j^*(\mathbf{r} + \mathbf{r}_j) , \quad (3.45)$$

$$g_O = \frac{\partial \mathcal{L}}{\partial O(\mathbf{r})} = \sum_j P(\mathbf{r} - \mathbf{r}_j) \chi_j^*(\mathbf{r}) , \quad (3.46)$$

where $\chi_j^*(\mathbf{r})$ is the complex conjugate of $\chi_j(\mathbf{r}) = \mathcal{F}^{-1} \{ \tilde{\chi}_j(\mathbf{q}) \}$ with

$$\tilde{\chi}_j(\mathbf{q}) = w_j(\mathbf{q}) \frac{I_j(\mathbf{q}) - n_j(\mathbf{q})}{\sigma_j^2(\mathbf{q})} \tilde{\psi}_j(\mathbf{q}) . \quad (3.47)$$

Here $\tilde{\psi}_j(\mathbf{q})$ is the Fourier transform of the views $\psi_j(\mathbf{r})$ as introduced in (3.16) and (3.17). In cases where Poisson statistics is the only source of

measurement uncertainties, one can set $\sigma_j(\mathbf{q}) = n_j(\mathbf{q})$ and rewrite (3.47) into

$$\tilde{\chi}_j(\mathbf{q}) = w_j(\mathbf{q}) \left(\frac{I_j(\mathbf{q})}{n_j(\mathbf{q})} - 1 \right) \tilde{\psi}_j(\mathbf{q}) . \quad (3.48)$$

However, this is only possible for moderately large photon counts for which the Poisson distribution approaches a Gaussian one.

Update procedure Conjugate gradient minimization is an iterative process in which the new search direction $\Delta^{(n)} = (\Delta P^{(n)}, \Delta O^{(n)})$ for the n -th step is generally not parallel to $-g^{(n)} = -(g_P^{(n)}, g_O^{(n)})$ but instead points into a conjugate direction defined by the function's local curvature, e.g. using the update rule

$$\Delta^{(n)} = -g^{(n)} + \beta^{(n)} \Delta^{(n-1)} . \quad (3.49)$$

Here $\beta^{(n)}$ is calculated using the Polak-Ribière formula

$$\beta^{(n)} = \frac{\langle g^{(n)}, g^{(n)} \rangle - \langle g^{(n)}, g^{(n-1)} \rangle}{\langle g^{(n-1)}, g^{(n-1)} \rangle} , \quad (3.50)$$

where \langle , \rangle is the scalar product in the (P, O) space. It can be written as

$$\langle g, g \rangle = g_P^\dagger g_P + g_O^\dagger g_O , \quad (3.51)$$

the dot product between the column vectors g_P, g_O and their Hermitian transposed versions g_P^\dagger, g_O^\dagger , where the indices run over all positions \mathbf{r} . The minimization of \mathcal{L} in the given search direction completes the iteration step. For the Gaussian model, it turns out that the problem can be reformulated as finding the relevant root of a polynomial of order eight,

$$\mathcal{L}(P + \alpha \Delta P^{(n)}, O + \alpha \Delta O^{(n)}) = \sum_{m=0}^8 c_m \alpha^m , \quad (3.52)$$

with the real-valued path parameter α . The calculation of the coefficients c_m is discussed in Infobox 3.1.

Modified metric for improved convergence The definition of the scalar product, i.e. the definition of the metric of the embedding space, has a strong influence on the efficiency of the line minimization procedure. Deviating from the standard definition (3.51) for improving the convergence behaviour is generally referred to as “preconditioning”. THIBAUT AND GUIZAR-SICAIROS (2012) have mentioned two different *ad hoc* preconditioners, based on a general change of variables in the form

$$\hat{\mathcal{L}}(\hat{P}(\mathbf{r}), \hat{O}(\mathbf{r})) = \mathcal{L}(UP(\mathbf{r}), VO(\mathbf{r})) , \quad (3.56)$$

Introducing a displacement in direction $(\Delta P(\mathbf{r}), \Delta O(\mathbf{r}))$ in (3.44) gives

$$\mathcal{L}(P + \alpha\Delta P^{(n)}, O + \alpha\Delta O^{(n)}) = \sum_j \sum_{\mathbf{q}} \frac{w_j(\mathbf{q})}{2\sigma_j^2(\mathbf{q})} \left(\sum_{n=0}^4 A_{n,j}(\mathbf{q}) \alpha^n \right)^2 . \quad (3.53)$$

The expansion of the square results in nine terms. Summing them over j and \mathbf{q} allows to obtain the coefficients c_m introduced in (3.52). The arrays $A_{n,j}(\mathbf{q})$ are given by

$$A_{0,j}(\mathbf{q}) = |\tilde{\psi}_j(\mathbf{q})|^2 - I_j(\mathbf{q}) , \quad (3.54a)$$

$$A_{1,j}(\mathbf{q}) = 2\Re \left\{ \tilde{\psi}_j(\mathbf{q}) a_j^*(\mathbf{q}) \right\} , \quad (3.54b)$$

$$A_{2,j}(\mathbf{q}) = 2\Re \left\{ \tilde{\psi}_j(\mathbf{q}) b_j^*(\mathbf{q}) \right\} + |a_j(\mathbf{q})|^2 , \quad (3.54c)$$

$$A_{3,j}(\mathbf{q}) = 2\Re \left\{ a_j(\mathbf{q}) b_j^*(\mathbf{q}) \right\} , \quad (3.54d)$$

$$A_{4,j}(\mathbf{q}) = |b_j(\mathbf{q})|^2 , \quad (3.54e)$$

with

$$\tilde{\psi}_j(\mathbf{q}) = \mathcal{F} \{ P(\mathbf{r}) O(\mathbf{r} - \mathbf{r}_j) \} , \quad (3.55a)$$

$$a_j(\mathbf{q}) = \mathcal{F} \{ P(\mathbf{r}) \Delta O(\mathbf{r} - \mathbf{r}_j) + \Delta P(\mathbf{r}) O(\mathbf{r} - \mathbf{r}_j) \} , \quad (3.55b)$$

$$b_j(\mathbf{q}) = \mathcal{F} \{ \Delta P(\mathbf{r}) \Delta O(\mathbf{r} - \mathbf{r}_j) \} . \quad (3.55c)$$

Info box 3.1: This infobox repeats the details given by THIBAULT AND GUIZAR-SICAIROS (2012) on the calculation of the polynomial coefficients in (3.52) for the line minimization. THIBAULT AND GUIZAR-SICAIROS (2012) pointed out, that “computation of the polynomial coefficients is preferable to other line search approaches because of the larger number of fast Fourier transforms (FFT) required for a repeated computation of the gradient”.

where U and V are invertible affine operators. Then the scalar product of the gradient $\hat{g} = \nabla \mathcal{L}$ is transformed to

$$\langle \hat{g}, \hat{g} \rangle = g_P^\dagger U U^\dagger g_P + g_O^\dagger V V^\dagger g_O , \quad (3.57)$$

For the reconstructions presented in this dissertation, only one of the two preconditioners described by THIBAULT AND GUIZAR-SICAIROS (2012) is relevant: It is based on the fact that the relative multiplicative scaling of $P(\mathbf{r})$ and $O(\mathbf{r})$ is an unconstrained degree of freedom. This can be expressed by setting $U = s$ and $V = 1$, with s being a positive scalar. The update rule (3.49) is then slightly different for the two components of the vector

$\Delta^{(n)} = (\Delta P(\mathbf{r})^{(n)}, \Delta O(\mathbf{r})^{(n)})$:

$$\Delta P(\mathbf{r})^{(n)} = -s^2 g_P^{(n)} + \hat{\beta}^{(n)} \Delta P(\mathbf{r})^{(n-1)}, \quad (3.58a)$$

$$\Delta O(\mathbf{r})^{(n)} = -g_O^{(n)} + \hat{\beta}^{(n)} \Delta O(\mathbf{r})^{(n-1)}, \quad (3.58b)$$

with

$$\hat{\beta}^{(n)} = \frac{s^2 g_P^{(n)\dagger} g_P^{(n)} + g_O^{(n)\dagger} g_O^{(n)} - s^2 g_P^{(n-1)\dagger} g_P^{(n)} - g_O^{(n-1)\dagger} g_O^{(n)}}{s^2 g_P^{(n-1)\dagger} g_P^{(n-1)} + g_O^{(n-1)\dagger} g_O^{(n-1)}}. \quad (3.59)$$

THIBAULT AND GUIZAR-SICAIROS (2012) have observed improved convergence – in particular for weakly-scattering objects – if the gradients of probe and object in the new metric are forced to be equal, i.e.

$$|\hat{g}_P|^2 = |\hat{g}_O|^2, \quad (3.60)$$

which defines s as a function of the current gradients and thus the current estimates for P and O :

$$s^2 = \frac{|g_O|^2}{|g_P|^2}. \quad (3.61)$$

Regularization THIBAULT AND GUIZAR-SICAIROS (2012) also reported that they “have observed a tendency to amplify high spatial-frequency noise, probable indication of a mild ill-conditioning” in maximum-likelihood reconstructions. This means that the noise power spectrum deviates from the expected behaviour at spatial frequencies for which only very little signal has been recorded in the diffraction patterns. As additionally their “maximum likelihood formulation is probably formally ill-posed” like many inverse problems, THIBAULT AND GUIZAR-SICAIROS (2012) suggested to add a regularization term to the negative log-likelihood function:

$$\mathcal{L}_R(P(\mathbf{r}), O(\mathbf{r})) = \mathcal{L}(P(\mathbf{r}), O(\mathbf{r})) + \frac{\mu}{K} R(P(\mathbf{r}), O(\mathbf{r})), \quad (3.62)$$

where $\mathcal{L}(P(\mathbf{r}), O(\mathbf{r}))$ is the original definition according to (3.44) on page 102. The choice of the adjustable parameter μ and the renormalization constant K are discussed below. In Pierre Thibault’s Python implementation of the ptychographic maximum-likelihood reconstruction, the regularizer acts only on the object and is chosen to be proportional to the squared gradient of the latter, i.e. $R(O(\mathbf{r})) \sim |\nabla O(\mathbf{r})|^2$. This term enforces some degree of smoothness in the final reconstructions by penalizing rapid fluctuations in the image and therefore efficiently suppressing the amplification of high frequency noise. In our discrete case, the term takes the form

$$R(O(\mathbf{r})) = \sum_{\mathbf{r}} |(O(\mathbf{r} + \Delta x) - O(\mathbf{r}))|^2 + |O(\mathbf{r} + \Delta y) - O(\mathbf{r})|^2, \quad (3.63)$$

where Δx and Δy are the linear dimensions of the pixels in the object array. In the update procedure of the algorithm, the derivative of $R(O(\mathbf{r}))$ with respect to $O(\mathbf{r})$, i.e.

$$\frac{\partial R}{\partial O(\mathbf{r})} = 4O^*(\mathbf{r}) - O^*(\mathbf{r} + \Delta x) - O^*(\mathbf{r} - \Delta x) - O^*(\mathbf{r} + \Delta y) - O^*(\mathbf{r} - \Delta y) , \quad (3.64)$$

has to be added to g_O as introduced in (3.58b) on page 105.

The renormalization constant K is obtained by order of magnitude calculations comparing the scaling behaviour of likelihood term \mathcal{L} and regularization term R : For the likelihood term \mathcal{L} one calculates the expectation value

$$\begin{aligned} \langle \mathcal{L} \rangle &= \sum_j \sum_{\mathbf{q}} \frac{w_j(\mathbf{q})}{2\sigma_j^2(\mathbf{q})} \langle (I_j(\mathbf{q}) - n_j(\mathbf{q}))^2 \rangle \\ &= \sum_j \sum_{\mathbf{q}} \frac{w_j(\mathbf{q})}{2\sigma_j^2(\mathbf{q})} \sigma_j^2(\mathbf{q}) \\ &= \frac{1}{2} N_m , \end{aligned} \quad (3.65)$$

where N_m is the total number of valid pixels in the measurement. For the expectation value of the regularization term R , although dependent on the actual object $O(\mathbf{r})$, one can find an upper limit given by the variance ΔO^2 originating from noise propagation:

$$\begin{aligned} \langle R \rangle &= 4 \sum_{\mathbf{r}} \langle |O(\mathbf{r}) - \langle O(\mathbf{r}) \rangle|^2 \rangle \\ &\leq 4N_{\text{pix}} \Delta O^2 . \end{aligned} \quad (3.66)$$

Here N_{pix} is the total number of pixels of the reconstructed object $O(\mathbf{r})$. The lower limit for the variance is determined by the total number of photons N_{phot} measured, i.e. the sum of all photon counts over all diffraction patterns of the experiment. If one assumes a uniform fluence on the object area, $N_{\text{phot}}/N_{\text{pix}}$ are scattered in each pixel of the reconstruction which results in

$$\Delta O^2 \simeq \frac{N_{\text{pix}}}{N_{\text{phot}}} . \quad (3.67)$$

Defining the renormalization constant K as

$$K = 8 \frac{N_{\text{pix}}^2}{N_m \cdot N_{\text{phot}}} \quad (3.68)$$

thus results in $\langle \mathcal{L} \rangle$ and $\langle R \rangle / K$ having the same order of magnitude and scaling behaviour. Therefore, the parameter μ can be used to adjust the relative strength of the regularization term with respect to \mathcal{L} , completely independent of the specific experimental conditions. Typical choices for μ are in the order of 1%.

3.2.6 Inclusion of additional *a priori* knowledge

It has been observed that including additional *a priori* knowledge into the reconstruction process can increase convergence speed and in some cases even improve the quality of the results.

3.2.6.1 Initialization closer to solution

Initializing either probe or object or even both with guesses close to the actual solutions typically significantly speeds up convergence.

Initial probe guess A good initial guess for the probe can on the one hand be based on a very accurate model. On the other hand, a illumination function retrieved with the same experimental settings can be used. To obtain aforementioned illumination at a high quality, it is advisable to use strongly-scattering specimens. Especially in the case of very weakly-scattering specimens, the latter approach has been employed frequently, see also chapter 6 and in particular section 6.4 on page 168.

Low resolution image of object Low resolution images for both the amplitude and the phase part of the object's exit wave can be reconstructed by applying the analysis schemes used for STXM with 2D detectors (compare section 1.8.1 on page 41) to far-field diffraction patterns of any kind, even if the illumination is not formed with focusing optics: While the total number of counts detected gives the transmission at the corresponding scan point, the shift of the centre of mass of can be used to calculate the differential phase contrast along both Cartesian axes. The latter can then be integrated to obtain a phase image. As in classical STXM, the resolution is in all cases limited to approximately the typical extent of the illumination on the object.

It has been already pointed out in the last paragraph of section 3.2.2 that initializing the object array with ones instead of random numbers already results in faster convergence. In particular, the formation of point singularities in the phase (phase vortices) is avoided to a large extent. Using an even closer starting guess based on a low resolution image can result in a further speed-up. However, phase guesses obtained from the integration

of the DPC images often showed artefacts which took a very long time to disappear again in the course of the reconstruction process. The approach should therefore not be applied, at least not as the default option, in cases where such artefacts are observed.

3.2.6.2 Additional constraints applied during reconstruction

While in the options discussed above the *a priori* knowledge is only applied once at the beginning of the reconstruction procedure, this section introduces constraints which are applied several times during the ptychographic phase-retrieval process, typically once per iteration.

Probe mask In particular for data sets with highly oversampled diffraction patterns in which the illumination occupies only a comparatively small area inside the probe array, it has been observed in some cases that unphysically high amplitudes tend to develop in the corners of the probe array. This can be easily suppressed by forcing the amplitude outside a probe mask to zero during each iteration, compare also THIBAUT AND GUIZAR-SICAIROS (2012). The mask can either be defined dynamically by thresholding the probe's autocorrelation or statically at the beginning of the reconstruction. In the latter case, typically a circular mask with a diameter somewhere between the lengths of the side and the diagonal of the square probe array is used. To avoid any truncation effects, the mask should not be chosen too tight. The constraint may be turned off once the retrieved probe is no longer changing significantly between iterations.

Enforcing flat regions in the object Additional constraints on the object can be applied, if it is known to contain areas of constant phase shift and absorption, e.g. a totally empty region in which the X-rays only pass through air or a membrane of uniform thickness supporting the sample. In this case, the reconstruction may be improved if the flatness of aforementioned areas is actively enforced. This can be done for either the amplitude or the phase part, but also for both. For the amplitude, the constraint is implemented by setting all the pixel values in the respective pre-defined area to a specific or their average value after each iteration. Before the same operation can be applied to the phase part, one often has to remove a global phase ramp from the object (compare page 98 in section 3.2.4.3). Because the phase ramp can be precisely determined in the region which is known to be flat, this can be used to correct the phase ramps of probe and object, as introduced in (3.37) on page 98, already during each ptychographic iteration and thus can make the usual post-processing step unnecessary. The main application of

this flatness-enforcing constraint, however, is the suppression of the raster grid pathology, see page 99 in section 3.2.4.5.

Periodic boundaries This approach has been developed to address some inaccuracies observed in the cases where a strongly phase-shifting specimen running from top to bottom in the centre of the object array is surrounded by disconnected areas of air on both sides. This is a common setting in projection images taken during a tomographic scan (see also chapter 9) of a rod-like specimen. Especially when several strong phase jumps occur along a very small horizontal distance, e.g. if a straight edge is almost parallel to the beam, slight inaccuracies in the reconstructed phase may accumulate across the specimen. In this instance, the average phase values retrieved for the air on the left and right side do not match. When in contrast a direct connection between the air patches exists, e.g. if the very top of a rod-shaped sample is imaged, the redundancy due to the overlap of the respective illuminated areas of neighbouring scan positions ensures an equal average phase value on either side of the sample.

Introducing periodic boundaries establishes a direct connection between the otherwise disconnected air patches at the left and right edges of the object array. Practically, this is achieved by replacing the pixel values in stripes which cover the width of about one probe array on either side by their common average value.

3.3 Evaluating the resolution of PCDI reconstructions

While the theoretical resolution limit given by the radiation's wavelength is hardly ever of any importance in coherent diffractive imaging with hard X-rays, the fundamental instrumental limit is usually the solid angle covered by the detector. However, the actual resolution achieved in an experiment depends typically highly on the specimen itself, in particular its scattering behaviour and its radiation hardness. Some of the various methods that have been introduced for the evaluation of this resolution are discussed in this section. Parts of the thoughts presented in this section have been published in [DIEROLF ET AL. \(2010b\)](#).

3.3.1 Separation of features in test patterns

Resolution in microscopy in general is often demonstrated by the ability to resolve a structure consisting of lines and spaces of equal width, arranged

either as a single pair of lines (VILA-COMAMALA ET AL., 2009) or, more commonly, as a periodic grid structure (CHAO ET AL., 2005). The width of a single line, i.e. a half-period of the structure, for which one is still possible to distinguish the lines, is then typically said to be resolution of the imaging system. A criterion for when two lines are still well-separated could be defined analogue to the *Rayleigh criterion* for the separation of two Airy peaks created by two point sources: the dip in intensity between the two peaks is 26.5%, so the same value could be defined to be required for the dip between two lines of a resolution test object for these lines to be separated.

Another frequently used test structure is the so-called “Siemens star”: It is a radial grating obtained by dividing a circle into N equally-sized radial segments arranged as alternating lines and spaces. At a given radius r , the line separation is thus given as $d = 2\pi r/N$ and can be used as a resolution criterion analogue to the case of the standard grating introduced above.

While this method provides a direct and immediate feedback on the imaging resolution, its practical importance for diffraction microscopy is limited: On the one hand, the production of the required nanostructures suffers from the same technical limitations as the production of high-resolution X-ray optics (see section 1.5.3). Thus the smallest features of typically – also commercially – available test objects are usually only in the order of about 50 nm in size. On the other hand, a real-life specimen rarely contains structures that would allow to apply this method. This limits its use to benchmarking tests with artificially-created objects which give some hints on potential resolutions under ideal conditions but do not address the question of experiment-specific resolving power.

3.3.2 The concept of “knife edges”

The concept of determining the width of a focal spot by scanning it across a “knife edge” is a quite common method for the characterization of X-ray optics (ATTWOOD, 2000, section 9.4). Assuming a perfectly sharp edge, i.e. its profile resembles a step function, the shape of the focal spot is readily obtained as the derivative of the transmission curve measured behind the knife edge. In diffraction microscopy, resolution of an image is often determined by applying the same method to features of the sample which are supposed to have a perfect edge parallel to the projection direction. The blurring of such sharp boundaries is then taken as a measure of resolution, either again by taking the derivative or by fitting an error function to the step (see e.g. GIEWEKEMEYER ET AL. (2010) for an application of the latter approach).

The method has the obvious limitations that such mathematically exact edges are neither easy to produce with the required precision in the nanome-

tre range, nor naturally present in a lot of real-life samples. Even if reasonably sharp edges are present, a deviation from a perfect step function will add an error to the determination of the resolution. Where an iterative algorithm with a support constraint is used on an isolated object, application of this knife-edge approach on the specimen’s boundary should be avoided as the support constraint may lead to an unphysical sharpening of this edge – especially if a support-refining method like “shrinkwrap” (MARCHESINI ET AL., 2003) is used.

3.3.3 Phase retrieval transfer function

In this approach, the Fourier intensities of the averages of many reconstructions $|\mathcal{F}\{\langle\psi_j(\mathbf{r})\rangle\}|$ are compared with the measured diffraction intensities $\sqrt{I_j(\mathbf{q})}$ as a function of the scattering vector \mathbf{q} (SHAPIRO ET AL., 2005). As the way the ratio of these two quantities decays for larger values of $|\mathbf{q}|$ reminds of a modulation transfer function (MTF) in classical (incoherent) microscopy, it is often called “phase retrieval transfer function” (PRTF)

$$\text{PRTF}_j(\mathbf{q}) = \frac{|\mathcal{F}\{\langle\psi_j(\mathbf{r})\rangle\}|^2}{I_j(\mathbf{q})}. \quad (3.69)$$

The index j indicates that in ptychographic CDI the PRTF has to be calculated independently at each scan point. Like an MTF, the function is typically averaged over shells of constant $|\mathbf{q}|$ resulting in a one-dimensional curve. If the retrieved Fourier phases of the individual reconstructions at a given \mathbf{q} are highly consistent, the PRTF will be unity as the Fourier intensity of the averaged reconstruction matches the measured diffraction intensity. However, if these phases are completely random due to a too low signal-to-noise ratio of the underlying diffraction data, the corresponding average Fourier intensity and thus the PRTF will go to zero. However, if the reconstruction algorithm is not unbiased, i.e. strong real-space constraints or screening of initial conditions change its mixing dynamics or the average, this may result in artificially high PRTF values.

While the definition with intensities in (3.69) allows for direct comparison with MTFs of incoherent imaging systems (SHAPIRO ET AL., 2005), the PRTF is frequently also defined as ratio of amplitudes (CHAPMAN ET AL., 2006b), i.e. as the square root of (3.69), which then corresponds to descriptions of coherent imaging systems. Apart from determining the resolution by comparison with well-known MTFs, often the spatial frequency for which the PRTF falls below a certain threshold is used as a criterion. However, there seems to be no general consensus on this threshold: values of 0.1 (SCHROER

ET AL., 2008), $1/e \approx 0.37$ (CHAPMAN ET AL., 2006a), 0.5 (CHAPMAN ET AL., 2006b) and 0.6 (HUANG ET AL., 2009) have been used, in these cases as the threshold for the ratio of amplitudes.

The PRTF formalism was typically not used for resolution determination of the reconstructions presented in this work because it is quite arguable whether a global PRTF provides a reliable assessment of reconstruction quality and resolution in ptychographic CDI:

1. As for each scan position an individual PRTF is calculated each of them contains information on the local quality of the phase retrieval. In an extended specimen, however, it is quite likely that the signal-to-noise ratio in diffraction patterns varies with scan position. It is questionable, how a global PRTF which allows statements on the reconstruction as a whole can be obtained from this, as simple averaging will discard all position-dependent information.
2. As obvious from the fundamental constraints (3.16) and (3.17) of ptychographic CDI, both the measured intensities $I_j(\mathbf{q})$ and the reconstructed exit waves $\psi_j(\mathbf{r})$ contain contributions of both the object and the illuminating probe. Therefore, it is not clear whether the obtained PRTFs are describing the object or the probe. In this context it should be pointed out again that the reconstruction of the illumination function is based on all diffraction frames, whereas only a small subset of them contains information on a given part of the object. In particular in cases there the diffraction patterns are dominated by the signal from the probe, the PRTF is thus more likely to indicate the resolution of the probe rather than the object.

3.3.4 Resolution estimate based on photon statistics

How to estimate the resolution of a ptychographic reconstruction from photon statistics has been presented in DIEROLF ET AL. (2010b): It is based on precise knowledge of the total number of incident photons in the experiment at hand. According to Poisson statistics the variance on the contrast of a pixel in the reconstruction which receives N incident photons is N^{-1} . This real space picture can also be transferred to ptychographic measurements which take place in Fourier space. If one assumes a roughly uniform illumination of the imaged area, a variance

$$\text{var } \Phi \cdot A_{\text{pix}} \simeq \frac{A}{N_0} \quad (3.70)$$

on the reconstructed phase Φ is expected. Here A_{pix} is the area of one pixel and N_0/A the fluence, i.e. the total number N_0 of incident photons divided by the total illuminated area A . Relation (3.70), its left hand side being similar to the definition of photographic granularity introduced by Selwyn (O’NEILL, 2003; SELWYN, 1935), shows explicitly the trade-off between spatial resolution A_{pix} and contrast resolution $\text{var } \Phi$ for a given photon flux. Due to its derivation from fundamental photon counting statistics, (3.70) provides a strict upper bound for the resolution achievable in an experiment. If the variance $\text{var } \Phi$ of a reconstruction can be determined accurately and the incident fluence is known, (3.70) allows to calculate the corresponding “effective pixel size” which gives the actual spatial resolution of the reconstruction.

Numerical experiments with the difference map suggest that the usually applied averaging of many object guesses from the steady-state regime of a reconstruction run (compare section 3.2.4.1 on page 96) cancels the fluctuations caused by the algorithm itself and ensures convergence to a unique solution which differs from the “true” solution only because of the noise. So if the imaged region of the object is known to contain uniform areas, the remaining fluctuations within these directly reveal the value of $\text{var } \Phi$. While the absence of sufficiently uniform regions may make this approach unfeasible in certain cases, the situation is greatly simplified for a weakly scattering specimen with negligible absorption: If one uses the fact that the fluctuations of the complex-valued object are equally shared by its real and imaginary parts, it is sufficient to compute the variance of the absorption part after normalizing to a mean 1.

3.3.5 Fourier ring and shell correlations

The Fourier ring correlation (FRC) and its extension for volume data, the Fourier shell correlation (FSC), are nowadays standard methods for determining the resolution in cryogenic single-particle electron microscopy (VAN HEEL AND SCHATZ, 2005). They have first been applied to results of ptychographic CDI experiments by Manuel Guizar-Sicairos (compare GUIZAR-SICAİROS ET AL., 2012; HOLLER ET AL., 2012; VILA-COMAMALA ET AL., 2011a), whose Matlab implementation has been used for calculations.

These Fourier correlation approaches are similar to the PRTF discussed in the last but one section in the sense that both methods employ multiple reconstructions to provide a measure of how reliably certain spatial frequencies are retrieved. However, the PRTF is based on averaging many phased diffraction patterns from independent reconstruction runs on the same data. In contrast, Fourier ring correlations are typical measures to assess the similarity of two final images which are based on separate data sets but show the

Assuming a weak phase object $O(\mathbf{r}) \approx 1 + i\phi(\mathbf{r})$, for which the exit wave at a given scan position can be written as

$$\psi(\mathbf{r}) \approx P(\mathbf{r})(1 + i\Phi(\mathbf{r})) =: P(\mathbf{r}) + iQ(\mathbf{r}) , \quad (3.71a)$$

the number N_s of photons scattered by the sample is given by

$$N_s \approx \int |Q(\mathbf{r})|^2 d\mathbf{r} = \int |P(\mathbf{r})|^2 |\Phi(\mathbf{r})|^2 d\mathbf{r} \quad (3.71b)$$

$$= \lim_{\Delta A \rightarrow 0} \sum_k |P_k|^2 |\Phi_k|^2 \Delta A . \quad (3.71c)$$

For the variance of this expression one obtains

$$\text{var } N_s = \lim_{\Delta A \rightarrow 0} \sum_k \left(2 |P_k|^2 \Phi_k \Delta A \right)^2 \Delta \Phi_k^2 , \quad (3.72)$$

which with

$$|\delta\Phi(\mathbf{r})|^2 = \lim_{\Delta A \rightarrow 0} \Delta A \Delta \Phi_k^2 \quad (3.73)$$

can be rewritten into

$$\text{var } N_s \approx \int 4 |P(\mathbf{r})|^4 |\Phi(\mathbf{r})|^2 |\delta\Phi(\mathbf{r})|^2 d\mathbf{r} . \quad (3.74)$$

If one infers that $\delta\Phi$ is independent of \mathbf{r} (i.e. the error is uniform throughout the reconstructed phase), this results in

$$|\delta\Phi|^2 \propto \frac{\text{var } N_s}{\int |P(\mathbf{r})|^4 |\Phi(\mathbf{r})|^2 d\mathbf{r}} \quad (3.75a)$$

$$\approx \text{var } N_s \frac{A}{N_0 \int |P(\mathbf{r})|^2 |\Phi(\mathbf{r})|^2 d\mathbf{r}} \quad (3.75b)$$

$$= \frac{\text{var } N_s}{N_s} \frac{A}{N_0} , \quad (3.75c)$$

where (3.75b) uses the assumption, that the illumination is uniform over an area A , i.e. $|P|^2 \approx N_0/A$ (with the total number of incident photons N_0). Equation (3.75c) is then obtained with (3.71b). If N_s follows Poisson statistics the first fraction in (3.75c) is equal to 1. With $\delta\Phi^2 \approx \Delta A \Delta \Phi^2$, this results in the relation introduced in (3.70).

$$\text{var } \Phi \cdot A_{\text{pix}} \simeq \frac{A}{N_0} , \quad (3.76)$$

where the proportionality constant has been chosen as unity based on numerical simulations performed by Pierre Thibault.

same object (for a general discussion of multiple similarity measures including Fourier ring correlation see VAN HEEL, 1987). In the case of ptychographic data, this has the benefit that only reconstructed object functions $O(\mathbf{r})$ serve as input while the PRTF is defined for the exit waves $\psi_j(\mathbf{r})$ at the individual scan positions, compare (3.69). Thus the Fourier correlation approaches do avoid the problem that the resolution information of probe and object is mixed. The FRC may also be used to replace the PRTF for comparing independent reconstruction runs of the same data set, but this still requires further investigation.

The Fourier ring correlation was independently introduced by SAXTON AND BAUMEISTER (1982), who called it “spatial frequency correlation function”, and by VAN HEEL ET AL. (1982). The three-dimensional Fourier shell correlation was first presented by HARAUZ AND VAN HEEL (1986). In both cases, first the Fourier transforms $\tilde{O}_{1,2}(\mathbf{q}) = \mathcal{F}\{O_{1,2}(\mathbf{r})\}$ of the two independent object reconstructions (or parts of them) are calculated. Then the normalized cross-correlation coefficients are determined for corresponding shells (or rings for the FRC) in Fourier space. A shell (FRC: rings) contains all Fourier space voxels (FRC: pixels) whose reciprocal space vectors \mathbf{q} have a length corresponding to the given spatial frequency or frequency range q_m :

$$\text{FSC}_{12}(q_m) = \frac{\sum_{|\mathbf{q}| \in q_m} \tilde{O}_1(\mathbf{q}) \cdot \tilde{O}_2^*(\mathbf{q})}{\left(\sum_{|\mathbf{q}| \in q_m} \tilde{O}_1^2(\mathbf{q}) \cdot \sum_{|\mathbf{q}| \in q_m} \tilde{O}_2^2(\mathbf{q})\right)^{1/2}}. \quad (3.77)$$

In practical application, the FRC calculation is usually preceded by a sub-pixel registration step (GUIZAR-SICAIROS ET AL., 2008) to make that both selected input images show exactly the same view of the object. To allow for this alignment, in most cases not the full reconstructions but rather smaller regions-of-interest are used. However, one has to ensure that they contain a range of spatial frequencies typical for the whole object, as otherwise the FRC may depend highly on the actual features present. An example of the latter is given in Fig. 9.10 on page 272.

The resolution is defined by the intersection of the FSC with a threshold curve. VAN HEEL AND SCHATZ (2005) have pointed out that no fixed-value thresholds should be used as the actual values of the FSC depend strongly on the specific settings, in particular on the number of voxels $n(q_m)$ present in the Fourier shell at the spatial frequency q_m . Taking this into account, a threshold function $T(q_m)$ can be defined such that its value at each q_m provides a lower bound above which the FSC exceeds a predefined signal-to-

noise ratio SNR (VAN HEEL AND SCHATZ, 2005):

$$T(q_m) = \frac{\text{SNR} + 2/\sqrt{n(q_m)} \cdot \sqrt{\text{SNR}} + 1/\sqrt{n(q_m)}}{\text{SNR} + 2/\sqrt{n(q_m)} \cdot \sqrt{\text{SNR}} + 1} . \quad (3.78)$$

VAN HEEL AND SCHATZ (2005) define a threshold curve based on the signal SNR necessary to achieve an information content per voxel of minimum 1/2 bit which can be calculated from the relation (SHANNON, 1948)

$$1/2 \text{ bit} = \log_2 \sqrt{2} = \log_2(1 + \text{SNR}_{1/2 \text{ bit}}) , \quad (3.79)$$

resulting in

$$\text{SNR}_{1/2 \text{ bit}} = \sqrt{2} - 1 \approx 0.4142 . \quad (3.80)$$

VAN HEEL AND SCHATZ (2005) “propose the 1/2-bit information threshold curve as a standard” because its results are comparable to those produced by similar criteria used in X-ray crystallography. However, it should be pointed out that in the standard application scenario in electron microscopy, typically two halves of a tomographic data are compared which are later combined to a full volume, or two images are compared whose average is considered the final result. Therefore, VAN HEEL AND SCHATZ (2005) assume that the SNR in each half data set only has to reach half of the value given in (3.80) because the final combination step of the input data will lead to a doubled SNR in the result. This will typically not be the case for ptychographic experiments, e.g. if the input images for the resolution determination via FSC are the two independent projections at 0° and 180° of a tomographic scan. For the application to PCDI results thus usually the full SNR value of 0.4142 obtained in (3.80) has to be used to calculate the 1/2-bit threshold curve.

Chapter 4

Computed tomography

A short review on the principles of computed tomography in the parallel beam case is given in this chapter. Starting from the Radon transform and the associated Fourier slice theorem, tomographic reconstruction with filtered back-projection, as the main method used for analysis of the tomography results presented in this work, is introduced. In the parallel beam case, signals from two-dimensional slices of the object perpendicular to the axis of rotation do not mix in the tomographic reconstruction process. Therefore, the necessary theory is reviewed for the case of two-dimensional functions. A more detailed treatment can be found in the book by [KAK AND SLANEY \(1988, mainly chapter 3\)](#) on which the discussion here is based.

4.1 Radon transform and Fourier slice theorem

4.1.1 Definitions

The Radon transform of a two-dimensional function $f(x, y)$ is given by

$$P_{\theta}(t) = \int_{-\infty}^{\infty} \int_{-\infty}^{\infty} f(x, y) \delta(x \cos \theta + y \sin \theta - t) dx dy , \quad (4.1)$$

where the parametrization $x \cos \theta + y \sin \theta = t$ of the line of projection is used as the argument of a Dirac δ -distribution. This generates a parallel-ray projection for different positions t of the parallel rays at a given rotation angle θ with respect to the (x, y) -coordinate system fixed to the sample.

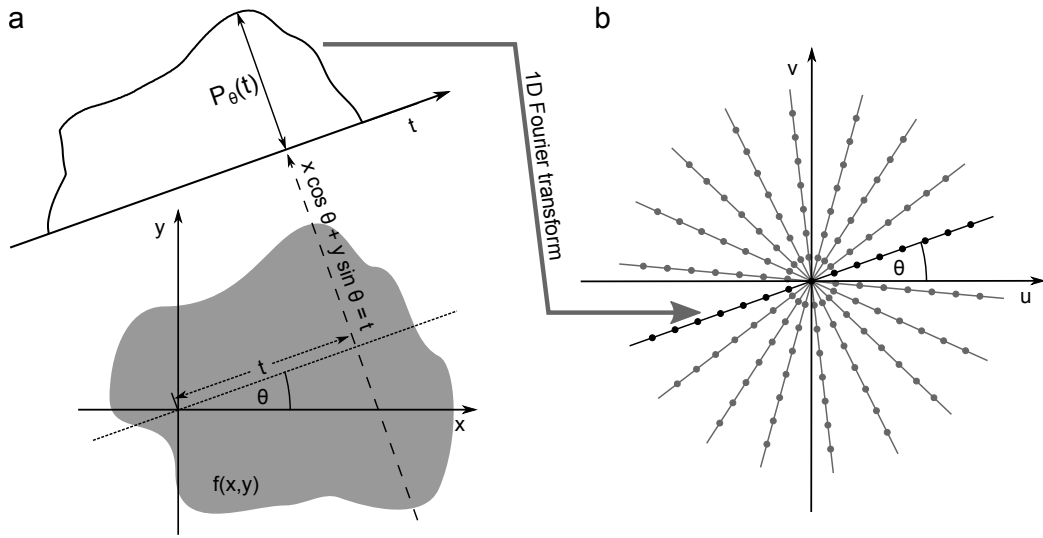


Figure 4.1: Radon transform and Fourier slice theorem.

The one-dimensional Fourier transform of such a projection with respect to t

$$\tilde{P}_\theta(w) = \int_{-\infty}^{\infty} P_\theta(t) e^{-i2\pi tw} dt, \quad (4.2)$$

is related to the two-dimensional Fourier transform of the object function $f(x, y)$

$$\tilde{f}(u, v) = \int_{-\infty}^{\infty} \int_{-\infty}^{\infty} f(x, y) e^{-i2\pi(xu+yv)} dx dy, \quad (4.3)$$

by the *Fourier slice theorem* (KAK AND SLANEY, 1988, chapter 3):

$$\tilde{P}_\theta(w) = \tilde{f}(w \cos \theta, w \sin \theta). \quad (4.4)$$

This means, that the values obtained by the one-dimensional Fourier transform of a projection of an object $f(x, y)$ rotated to an angle θ correspond to the values found along a line forming an angle θ with the u -axis and going through the origin of the two-dimensional Fourier transform of this object.

4.1.2 Consequences of Fourier slice theorem for angular sampling

According to (4.4), the Fourier transform of an object can be obtained by measuring projections covering an angular range of at least π rad. From this, the object can in principle be retrieved by an inverse Fourier transform, typically requiring interpolation onto a Cartesian grid first. However, as only a limited number of projection angles can be measured in practice, sampling

of Fourier space by the radial lines gets sparser for higher spatial frequencies, so some degradation for high-resolution features has to be expected (compare also KAK AND SLANEY, 1988, chapter 5). To achieve sufficient sampling of Fourier space at the maximum spatial frequency q_{\max} by means of the Fourier slice theorem, the distance between the radial lines at q_{\max} must not exceed the side length Δq of a pixel in reciprocal space. Thus the maximum angular step is $\Delta\theta \approx \Delta q/q_{\max} = \pi/N_{\text{proj}}$, where N_{proj} gives the number of equally-spaced projections over an angular range of π rad. With the relation $q_{\max} = \Delta q \cdot N_{\text{pix}}/2$ for projections of a width N_{pix} , one obtains

$$N_{\text{proj}} \approx \frac{\pi}{2} N_{\text{pix}} . \quad (4.5)$$

In practice, often less projections are used, e.g. $N_{\text{proj}} \approx N_{\text{pix}}$, as the gain from a larger number of projections is considered to be small (CLOETENS, 1999, page 50).

4.2 Filtered backprojection

4.2.1 Basic algorithm

Rewriting the inverse Fourier transform

$$f(x, y) = \int_{-\infty}^{\infty} \int_{-\infty}^{\infty} \tilde{f}(u, v) e^{i2\pi(ux+vy)} du dv , \quad (4.6)$$

with polar reciprocal space coordinates (w, θ) , i.e. $(u, v) = (w \cos \theta, w \sin \theta)$ with $w \in (-\infty, \infty)$ and $\theta \in [0, \pi)$, into

$$\begin{aligned} f(x, y) &= \int_0^\pi \left[\int_{-\infty}^{\infty} \tilde{f}(w \cos \theta, w \sin \theta) e^{i2\pi w(x \cos \theta + y \sin \theta)} |w| dw \right] d\theta \\ &= \int_0^\pi \left[\int_{-\infty}^{\infty} \tilde{P}_\theta(w) e^{i2\pi w t} |w| dw \right] d\theta , \end{aligned} \quad (4.7)$$

where the second line is using the Fourier slice theorem (4.4) and the definition of the parameter t . From (4.7), the *filtered backprojection algorithm* for tomographic reconstruction can be derived:

1. Measure the projections $P_\theta(t)$ (compare Fig. 4.2 (b)).
2. Filtering:
 - a) Obtain Fourier slices by calculating the 1D Fourier transforms $\tilde{P}_\theta(w)$ of the projections according to (4.2).

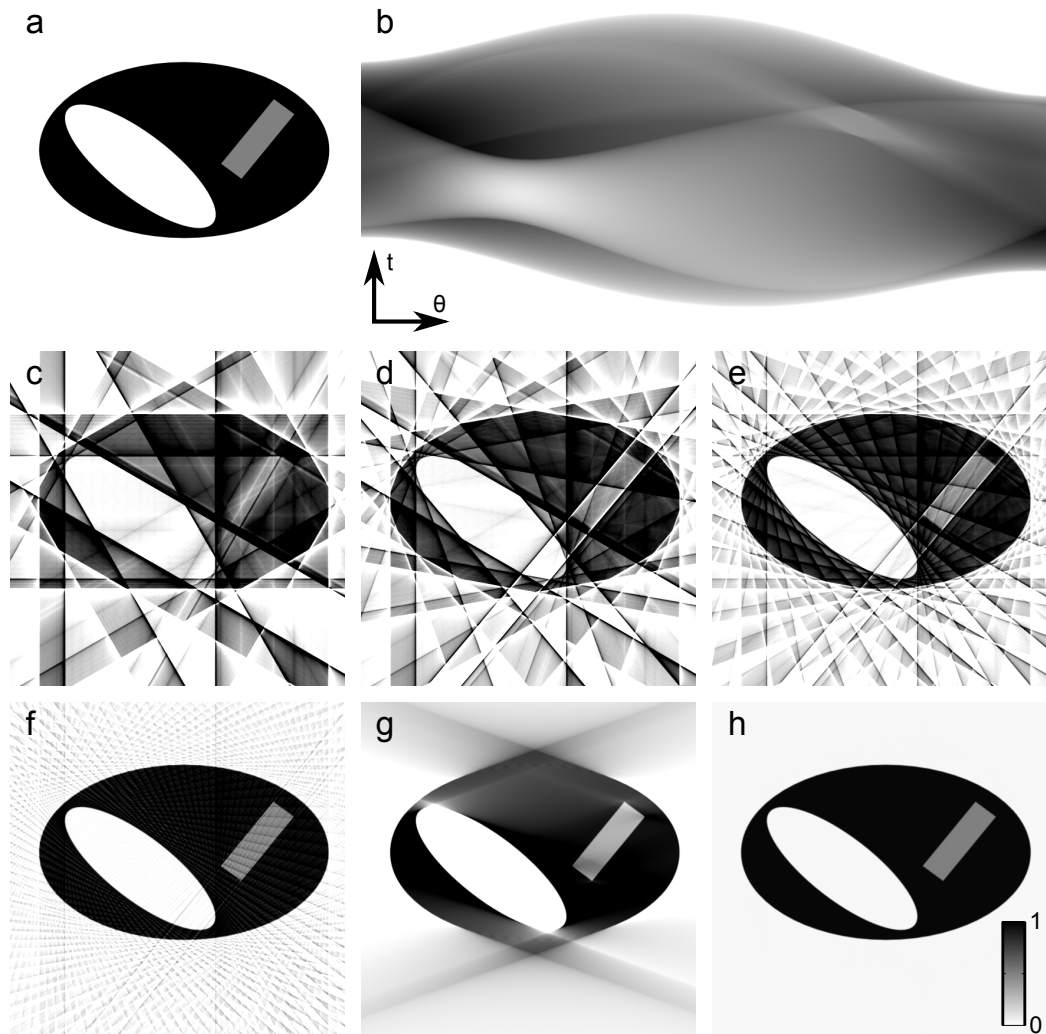


Figure 4.2: Filtered backprojection of a simulated phantom. **(a)** Phantom **(b)** Sinogram. Filtered backprojections covering an angular range of 180° unless stated otherwise: **(c)** 6 angles (30° steps), **(d)** 9 angles (20° steps), **(e)** 18 angles (10° steps), **(f)** 60 angles (3° steps), **(g)** 1400 angles in a limited angular range of $\pm 70^\circ$ (0.1° steps), and **(h)** 1800 angles (0.1° steps).

- b) Reciprocal space filtering: $|w|\tilde{P}_\theta(w)$ (or more general $\tilde{h}(w)\tilde{P}_\theta(w)$).
- c) Inverse Fourier transforms of filtered Fourier slice: inner integration in (4.7).

3. Backprojection: Sum in real space these inverse Fourier transforms of filtered Fourier slices for all angles θ , i.e. perform the outer integration in (4.7).

The result of step 2 can be understood as a filtered version of the projection that has been “smeared” across the real space image along the given projection angle. Doing this sort of backprojection in step 3 from various angles results in a tomographic reconstruction, as illustrated in Fig. 4.2 on page 120: In Fig. 4.2 (c) the “smearing” of the individual (filtered) projections across the image can be seen, as well as their adding up to a rough representation of the object in the central part. Fig. 4.2 (d)–(f) and (h) show the improvement in reconstruction quality as the number of projections that are summed up in the third step of the algorithm increases.

In practice, the backprojection step requires an **interpolation** from polar coordinates onto a discrete Cartesian grid. Frequently, a linear interpolation scheme is used, but also higher order interpolations, e.g. cubic, may be applied. According to KAK AND SLANEY (1988), interpolation in real space can typically be done with higher accuracy than in reciprocal space, which would be needed for a direct reconstruction with a 2D Fourier transform. As in addition implementations of the filtered backprojection are typically much faster than other tomographic reconstruction schemes, it is widely used.

4.2.2 Filtering

An additional benefit is offered by the separation of the filtering and the backprojection step: This allows to replace in (4.7) the simple ramp filter $|w|$, also referred to as *Ram-Lak filter*, with a different frequency response $\tilde{h}(w)$. While the ramp filter reduces the weight of low-frequency components to compensate for the lower density of sampling at higher spatial frequencies, it also makes the reconstruction sensitive to high-frequency noise. Thus for modified $\tilde{h}(w)$, the Ram-Lak filter is often multiplied with an apodization function such that the weight of the highest frequencies is again reduced and therefore the effects of noise are suppressed. The resulting filter functions differ by the choice of the respective apodization function, which can be, e.g., a sinc-function (*Shepp-Logan filter*), a Hann window, a Hamming window (*Hamming filter*), or a Parzen window (e.g. implemented in the code by GUIZAR-SICAIROS ET AL. 2011). The mathematical expressions for these filters are listed in Table 4.1 and follow the definitions used in the MATLAB implementation of the filtered backprojection (function “iradon”, see also MATLAB 2012b, page 9-29 and MATLAB 2012a, page 3-623). The corresponding frequency responses are shown in Fig. 4.3(a).

filter name	filter function $\tilde{h}(w)$ in Fourier space	
Ram-Lak	$ w $	(4.8a)
Shepp-Logan	$ w \frac{\sin\left(\frac{\pi}{2} w \right)}{\frac{\pi}{2} w }$	(4.8b)
Hann	$ w \cdot \frac{1}{2} \left[1 + \cos\left(\pi \frac{w}{w_{\text{Nyq}}}\right) \right]$	(4.8c)
Hamming	$ w \cdot \left[0.54 + 0.46 \cos\left(\pi \frac{w}{w_{\text{Nyq}}}\right) \right]$	(4.8d)
Parzen	$ w \cdot \begin{cases} 1 - 6 \left \frac{w}{w_{\text{Nyq}}} \right ^2 + 6 \left \frac{w}{w_{\text{Nyq}}} \right ^3, & 0 \leq \left \frac{w}{w_{\text{Nyq}}} \right \leq \frac{1}{2} \\ 2 \left(1 - \left \frac{w}{w_{\text{Nyq}}} \right ^3 \right) & , \frac{1}{2} \leq \left \frac{w}{w_{\text{Nyq}}} \right \leq 1 \end{cases}$	(4.8e)

Table 4.1: Definitions of Fourier space filters used in filtered backprojection. To generate the respective filters, the original linear frequency response of the Ram-Lak filter in (4.8a) is multiplied with different apodization functions, where w_{Nyq} is the Nyquist frequency. As a result, the higher spatial frequencies are damped and therefore the sensitivity of the tomographic reconstruction to noise is decreased. The frequency response of all five filters is depicted in Fig. 4.3(a). Definitions as used in the MATLAB Image Processing Toolbox (MATLAB, 2012b). Parzen filter as implemented in the code of GUIZAR-SICAIRIS ET AL. (2011) for ptychographic tomography.

4.2.3 Filtered backprojection from derivatives of projections

A filtered backprojection from the derivative $\frac{\partial}{\partial t} P_\theta(t)$ of a projection gives the same result as the backprojection of the original $P_\theta(t)$ if the condition

$$\tilde{k}(w) \mathcal{F} \left\{ \frac{\partial}{\partial t} P_\theta(t) \right\} (u) = \tilde{h}(w) \mathcal{F} \{ P_\theta(t) \} (u) \quad (4.9)$$

is fulfilled. With the Fourier theorem for the Fourier transform of derivatives

$$\mathcal{F} \left\{ \frac{\partial}{\partial t} P_\theta(t) \right\} (w) = i2\pi w \mathcal{F} \{ P_\theta(t) \} (w) , \quad (4.10)$$

one finds that this is the case with **redefined filter functions for differential data**

$$\tilde{k}(w) = \frac{\tilde{h}(w)}{i2\pi w} . \quad (4.11)$$

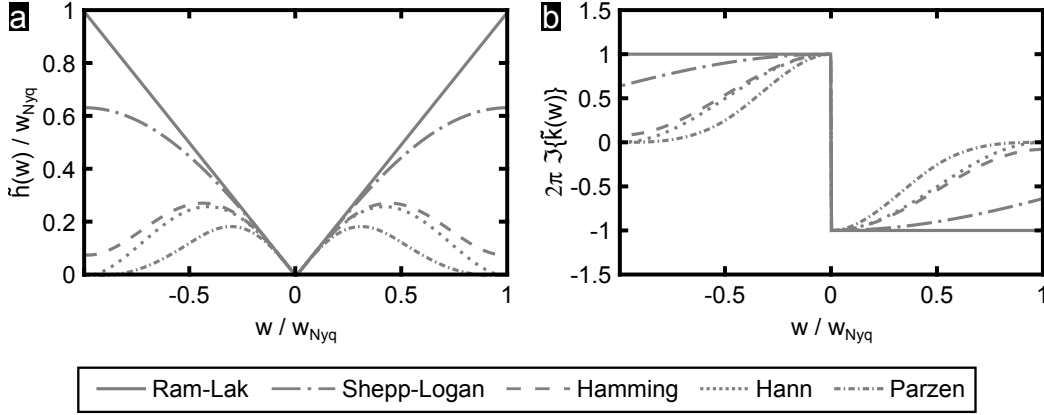


Figure 4.3: Frequency response of various filters used in filtered backprojection. (a) Various factors $\tilde{h}(w)$ (see legend) for weighting the spatial frequencies which can be used instead of the simple ramp weight $\tilde{h}_{\text{Ram-Lak}}(w) = |w|$ in (4.7). The frequency-axis is normalized to the Nyquist-frequency w_{Nyq} . The mathematical expressions are given in Table 4.1. Common to all filters is the damping of higher spatial frequencies which suppresses noise in the reconstruction. While the Shepp-Logan filter, compare (4.8b), remains very close to the original Ram-Lak filter for $|w| < w_{\text{Nyq}}/2$ and mainly affects the frequencies close to the cutoff, the other filters not only exhibit a stronger damping at the high frequencies but also affect the medium frequency range more. The Hamming filter, see (4.8d), still gives some weight to the Nyquist frequency, whereas the Hann filter (4.8d) and in particular the Parzen filter (4.8e) completely remove these Fourier components from the tomographic reconstruction. (b) Differential representations of the filters shown in (a) which are used for filtered backprojection reconstructions from the derivatives of projections.

Inserting the Ram-Lak filter $\tilde{h}(w)_{\text{Ram-Lak}} = |w|$ in (4.11), one obtains

$$\tilde{k}_{\text{Ram-Lak}}(w) = \frac{|w|}{i2\pi w} = \frac{\text{sgn}(w)}{i2\pi}, \quad (4.12)$$

which means that in all the definitions (4.8) on Table 4.1 in page 122 substituting the term $|w|$ with $\text{sgn}(w)/(i2\pi)$ yields the corresponding filter function for differential data.

This redefinition of the filter function for differential data has been introduced for beam deflection tomography (FARIS AND BYER, 1988) and for X-ray differential phase-contrast tomography (PFEIFFER ET AL., 2007). In the work presented here, typically ordinary phase-contrast or amplitude projections are retrieved to which standard filtered backprojection can be directly applied. However, as GUIZAR-SICAIROS ET AL. (2011) have pointed out, it may be beneficial to work nevertheless with the derivatives of projections, e.g. if the latter show strong phase wrapping.

Chapter 5

Experimental realization of ptychographic CDI

This chapter provides details on the experimental set-ups which were used to obtain the results presented in this dissertation. The first section gives a detailed record of the cSAXS beamline at the Swiss Light Source and the set-ups for two-dimensional and tomographic PCDI which have been constructed there and employed for most of the reported work. The second section introduces the nano-imaging endstation of beamline ID22NI at the European Synchrotron Radiation facility. In order to provide an overview what has to be considered when planning or performing PCDI experiments, a general discussion on their current status and limitations concludes the chapter.

5.1 Ptychographic CDI at the cSAXS beamline of the Swiss Light Source

5.1.1 Description of beamline

The cSAXS instrument, dedicated to coherent Small Angle X-ray Scattering, is an undulator beamline at the Swiss Light Source (SLS) located at the Paul Scherrer Institute near Villigen, Switzerland. As it was one of the first beamlines whose design was optimized for experiments with coherent X-rays and most of the experimental work presented in this thesis was performed there, a detailed description is given in this section. The information provided here, in particular the numerical values, is based on the cSAXS website ([cSAXS WEBSITE, 2015](#)) and the cSAXS beamline manual ([BUNK ET AL., 2011](#)).

5.1.1.1 Storage ring

The SLS is a 3rd generation synchrotron light source with a medium-sized storage ring with about 288 m circumference and 12 straight sections. The ring is typically operated at an electron energy of 2.4 GeV with the beam current kept constant around 400 mA by the so-called “top-up mode”, i.e. the usual decay of the beam current is compensated by short-period refills with new electrons. To achieve reasonable photon fluxes at beamlines working at hard X-ray energies in the range of 10 keV, these are equipped with in-vacuum insertion devices which allow for smaller gap sizes between the two magnet arrays resulting in higher magnetic fields.

5.1.1.2 Source

The source of the cSAXS beamline is an in-vacuum undulator with 96 periods of length $\lambda_u = 19$ mm. The minimum undulator gap is about 4.65 mm ($K_{\max} = 2.46$), for which the fundamental peak of the X-ray spectrum is located at about 1.24 keV. As the monochromator restricts the energy range that can be used to about 4 keV to 18.6 keV, the typical energies used in PCDI experiments are 6.2 keV (5th harmonic at minimum gap) and, more rarely, 8.7 keV (7th harmonic at minimum gap). PCDI tests at lower energies (around 4 keV) suggested that the gain in scattering signal typically does not compensate the increased absorption losses and the reduced incoming flux due to the non-optimal undulator gap settings. The source size is about $202 \mu\text{m} \times 18 \mu\text{m}$ (horizontal \times vertical, FWHM values, at 12.4 keV) with a divergence of $135 \mu\text{rad} \times 25 \mu\text{rad}$ (FWHM).

5.1.1.3 Beamline optics

The term beamline optics is used here to summarize all permanently installed beamline components that are used to precondition the beam before it exits the beamline vacuum at the first optical table of the experimental hutch. This table carries the dedicated experimental set-ups. Most of these optical components are placed in a separate lead hutch to ensure maximum stability during experiments. Their arrangement is shown schematically in Fig. 5.1. The elements of the beamline optics are used to control three main parameters of the X-ray beam: shape, energy and divergence (i.e. focusing).

Beam shaping by slits The shape of the beam is controlled by four pairs of slits, each allowing for horizontal and vertical confinement of the beam with four individually movable blades. Their distances from the source are listed in Table 5.1. Slit pair 1 defines the size of the incoming beam’s footprint

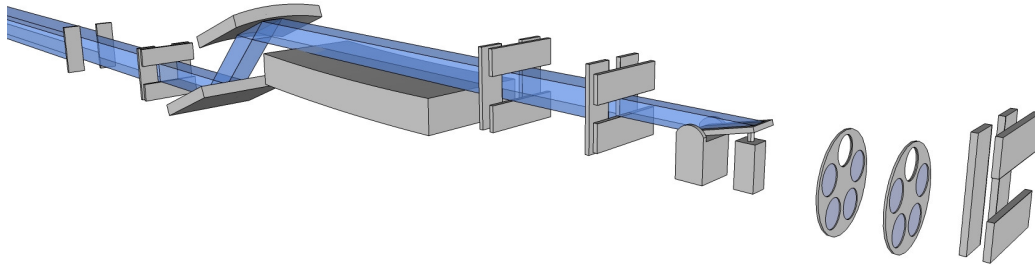


Figure 5.1: Sketch of cSAXS beamline optics (not to scale). Components from left to right: slit 0 (horizontal virtual source), slit 1, double-crystal monochromator, mirror, slit 2, slit 3, fast shutter, filter wheel 1, filter wheel 2, and slit 4. Their distances from the X-ray source are given in Table 5.1. At the beamline, all the sketched components are placed in vacuum. The components between and including slits 3 and 4 are housed in a common vacuum vessel, the so-called “exposure box” (label X in Fig. 5.2(a)), which is connected with a flexible bellow to the preceding vacuum path and can thus be moved along the beam. This way its exit window, which is mounted at the exit (label N in Fig. 5.2(b)) of a long thin tube protruding from the downstream end of the exposure box, can be placed as close as possible to the actual experimental setup.

Component	Distance from source / m
slit 0	12.1
slit 1	26.0
monochromator	28.6 (2nd crystal)
mirror	29.4
slit 2	30.7
slit 3	~33.4
fast shutter	~33.6
slit 4	~33.7
sample position	~34
detector position	up to ~41

Table 5.1: Distances of different beamline components at cSAXS from the source point (cSAXS WEBSITE, 2015). Compare also the schematic visualization in Fig. 5.1.

on the first monochromator crystal. Slit pair 2 is placed behind the vertically reflecting mirror which is directly downstream of the monochromator. The third and fourth slit pairs are situated at the very end of the evacuated beam path: they are used for the final definition of the beam shape before it enters a dedicated experimental set-up. In ptychographic imaging experiments, the beam incident upon the illumination-defining optical element (focusing optics or a pinhole aperture) is usually defined with the third slits and the fourth slit pair is only used to clean up parasitic scattering from the slit blades.

The single horizontal slit 0, which is significantly closer to the source point (compare Table 5.1), has a different role: it can be used to reduce the apparent horizontal source size and thus to improve transverse coherence of the beam by creating a secondary source. As it was only installed in the second half of 2010, this opportunity had not been available for most of the experiments reported here and so far no conclusions on its benefits or disadvantages can be drawn.

Monochromatization The X-ray energy is defined with a Si(111) double-crystal monochromator using a fixed-exit geometry. The resulting energy bandwidth $\Delta E/E$ is about $1.4 \cdot 10^{-4}$ (ALS-NIELSEN AND MCMORROW, 2011, chapter 6). The first crystal is cooled with liquid nitrogen which in this case, despite its lower heat capacity, is preferred to water. This is because the drastically reduced thermal expansion coefficient at liquid nitrogen temperatures makes the crystal lattice less prone to deformations caused by small variations in the heat load. The second crystal needs no cooling as it is only hit by the monochromatic beam. The accessible energy range is limited by mechanical constraints to about 4 keV to 18.6 keV. Higher-order Bragg reflections, which contain the contribution of the higher undulator harmonics, are rejected by a vertical total-reflection mirror downstream of the monochromator. This mirror consists of fused silica, a broad stripe of which is forming the reflecting surface together with two additional coatings of rhodium and platinum. Together with the possibility to change the incident angle, this allows to choose the energy dependent reflectivity such that over the whole energy range higher harmonics are efficiently suppressed.

Focusing The beamline optics offers possibilities to focus the beam both horizontally and vertically: Horizontal focusing is achieved by dynamical bending of the second monochromator crystal which allows to focus the beam by about a factor of 10 to approximately 20 μm FWHM. In the vertical direction, the total reflection mirror is equipped with a bending mechanism that allows to reduce the vertical beam size at the sample plane down to

5 μm FWHM. While focusing in the horizontal direction is usually not used in ptychographic experiments, the excess in transverse coherence along the vertical direction can be used to slightly prefocus the beam with the mirror. However, as the surface roughness of the mirror generates a pattern of horizontal stripes with vertically varying intensities inside the beam, a shift of this pattern with respect to the experimental set-up may lead to unwanted changes in the incoming wavefront. Focusing reduces the size of the stripes and thus makes it harder to select large enough flat regions within in the illumination which provide a stable enough wavefront even if vibrations or drift occur. Therefore, if at all, typically only mild vertical focusing is used for ptychographic imaging experiments.

5.1.1.4 Experimental set-ups

As a multi-purpose beamline, cSAXS has no permanently installed experimental set-up, i.e. sample manipulation equipment and – if required – further beam-defining elements are set up for each experiment individually. Common to all is the fact that around the sample the X-rays typically have to pass a short distance through air because the option of a fully evacuated beam path including the sample environment does not exist.

For CDI experiments, the coherence properties of the X-ray beam at the location of the experimental set-up are important: With a typical distance of 34 m from the source and the source size of $202 \mu\text{m} \times 18 \mu\text{m}$ (FWHM), one obtains with relation (2.6) at an X-ray energy of 6.2 keV ($\lambda \approx 2 \text{ \AA}$) transverse one-sigma coherence lengths of $\xi_{h,\sigma} \approx 13 \mu\text{m}$ in horizontal and $\xi_{v,\sigma} \approx 142 \mu\text{m}$ in vertical direction. For the energy bandwidth $\Delta\lambda/\lambda = 1.4 \cdot 10^{-4}$, a longitudinal coherence length of $\xi_l \approx 0.7 \mu\text{m}$ follows from (2.8).

During the course of the work presented here, there have been several iterations of dedicated set-ups for ptychographic CDI: By now, standard solutions for two-dimensional (discussed in detail in section 5.1.2) and for tomographic PCDI (see section 5.1.3) have been established, which are also offered in regular user operation.

5.1.1.5 Flight path

To prevent air scattering and absorption, the cSAXS beamline offers two flight tubes with lengths of 2.1 m or 7.0 m that can be inserted between sample and detector. For standard small-angle X-ray scattering applications (SAXS), these are typically evacuated. However, it has been observed that the required thick Mylar exit windows degrade the diffraction patterns in CDI applications due to their comparatively high absorption and more

importantly by adding parasitic scattering. Therefore, the flight tubes are typically equipped with much thinner polyimide (Kapton) exit windows for CDI experiments. As this does no longer allow to evacuate the tubes, they are flushed with Helium instead. Due to sampling requirements (compare condition (2.27) on page 55), typically the longer flight path has to be used for PCDI measurements.

5.1.1.6 Detectors

For the collection of all type of diffraction data, a PILATUS 2M detector is installed on an optical table which itself is placed on a rail system running along the beam. Details on the PILATUS II detector system are reported in the publications by KRAFT ET AL. (2009a,b), which are also the sources of the information on the PILATUS 2M in what follows.

The PILATUS 2M detector has 1475×1679 pixels of $172 \mu\text{m} \times 172 \mu\text{m}$ size which cover a total area of $253.7 \text{ mm} \times 288.8 \text{ mm}$. It is built from 3×8 individual detector modules with 487×195 pixels each. Every module has a monolithic $320 \mu\text{m}$ thick silicon sensor structured into the individual pixels each forming a separate p-n-diode. This sensor is bump-bonded to the 2×8 readout chips of the module. To avoid dead areas between the readout chips, the pixels next to these gaps have twice the width of normal ones. The counts detected by these larger pixels are distributed via software to three normal-sized pixels, i.e. a third virtual pixel is introduced at the gap. For digitization of the signal, each pixel has its own 20 bit counter. Because only events are counted for which the energy deposited in the sensor pixel lies above a certain adjustable threshold, the detector has no dark current, is insensitive to visible light and – to a large extent – X-ray photons of lower energy created by fluorescence. Due to the individual digitization of all pixels, there is also no readout noise. The detector therefore can be considered as noise-less and allows to obtain diffraction patterns in which Poisson noise, i.e. photon counting statistics itself, is the main source of errors. However, as for all detectors operated in single-photon counting mode, the maximum count rate is limited by the dead time after each event during which no new one can be detected. The detected rate N_{obs} thus has to be corrected to obtain the true incident rate N_0 . For a given dead time τ , the following relation (known as a *paralyzable model*, see KNOLL, 2000), is used (KRAFT ET AL., 2009a):

$$N_{\text{obs}} = N_0 \exp(-N_0\tau) \quad (5.1)$$

The maximum count rate is typically defined as $N_{0,\text{max}} = 1/\tau$. Depending on the amplifier gain settings used, it is between $0.9 \cdot 10^6$ photons/s/pixel (high gain) and $8 \cdot 10^6$ photons/s/pixel (low gain).

For complementary fluorescence measurements, an additional silicon drift detector (Amptek XR100-CR) can be installed close to the sample.

5.1.1.7 Control system

The standard command-line based user interface to all beamline functions including the motors of the customized experimental set-ups is based on the control software *spec* (Certified Scientific Software). The macro functionality of the software allows rather flexible applications, e.g. the definition of customized scan patterns like the round scan for PCDI introduced in section 3.2.4.5.

5.1.2 Set-up for two-dimensional scanning (diffraction) microscopy

Based on experiences with several earlier iterations, the set-up (see Fig. 5.2) for two-dimensional scanning techniques has been designed for maximum stability while still retaining enough flexibility for adaptations in geometry. To minimize vibrations, components with a high stiffness have been used for the construction of a very compact assembly with short lever arms. Therefore, all of the custom-made parts were produced in stainless steel instead of the aluminium used in previous iterations.

The X-ray beam at the cSAXS endstation has a vertical distance of about 50 cm from the surface of the optical table on which the sample environment is placed. The necessary vertical offset of the scanning set-up is achieved by mounting it on top of hexapod 6-axis parallel kinematics microrobot (model M850.11, Physik Instrumente (PI), label H in Fig. 5.2(a)) This hexapod does not only provide a very stable support, but also allows motorized fine-positioning in the micrometer range of the set-up as a whole. The actual scanning set-up is formed by up to four different three-axis motor stacks which carry the different optical components or the sample respectively (compare Fig. 5.2(b)). For maximum relative stability, in particular of the localized illumination with respect to the sample, they are mounted on a common base plate made of stainless steel (Fig. 5.2(a), label BP). Its hole pattern allows customized arrangements of the stages along the beam at two distances on either side of the optical axis. Each of the stacks consists of three stepper motor driven linear stages (model MFA-PP, Newport Corporation, minimum step size 242 nm, maximum range 25 mm) allowing independent movements along the three Cartesian axis. When looking along the beam through the scanning set-up, they carry the following components:

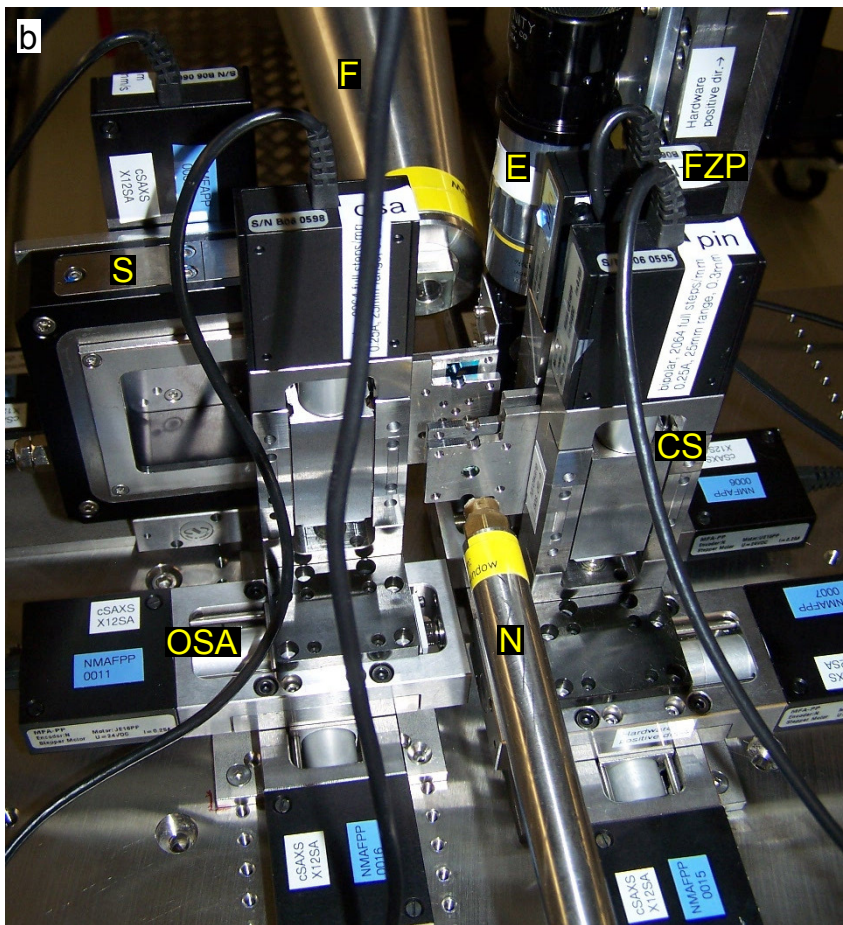
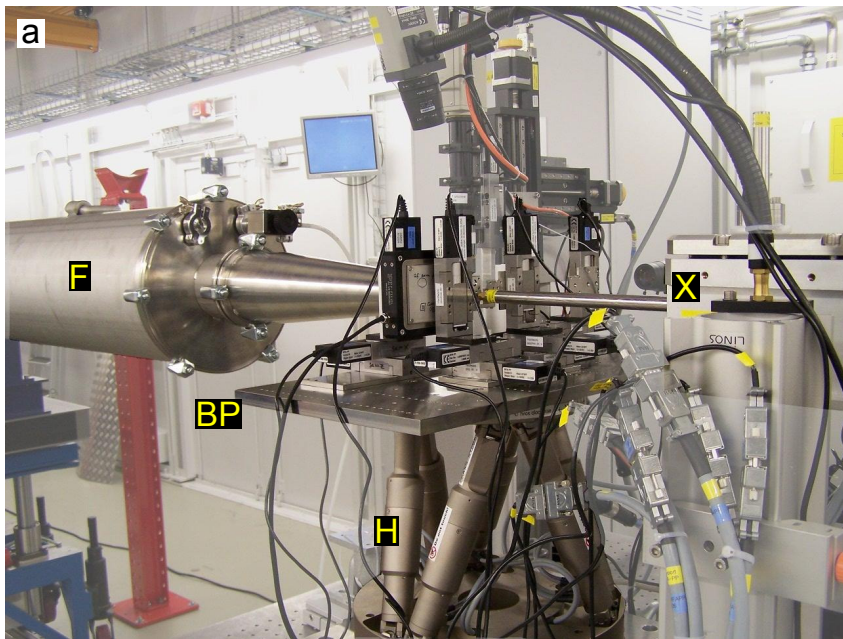
central stops or coherence-filtering aperture In a standard scanning microscopy application, the first stack of stages (Fig. 5.2(b), label CS) carries an assortment of central stops, which in combination with matching order-sorting apertures (OSAs) block the undiffracted beam. For coherent scanning microscopy, however, the transverse coherence may not be large enough to illuminate a whole Fresnel zone plate fully coherently. In this case, the first component is typically a coherence-defining aperture of significantly smaller diameter (in the range of 10 to 20 μm) than the zone plates. By putting this first aperture off-axis, the undiffracted beam passing through it is blocked by the OSA.

Fresnel zone plates The second holder (Fig. 5.2(b), label FZP) carries the Fresnel zone plate lenses used for focusing. Typically, a single silicon chip is used which carries several different lenses of various diameters between 30 μm and 200 μm and zone sizes between about 25 nm and 100 nm.

order-sorting apertures or illumination-defining pinholes The third holder (Fig. 5.2(b), label OSA) carries apertures of various sizes. If a focused beam is to be used, an order-sorting aperture can be chosen among several different pinholes with diameters between about 5 μm and 20 μm (Plano GmbH). For a ptychographic CDI experiment with a simple pinhole illumination, custom-made apertures with diameters from 1 μm to 4 μm are provided, which were specifically manufactured to fulfil the condition (2.27) on page 55 for sufficient diffraction-pattern

Figure 5.2 (following page): Photos of set-up for two-dimensional scanning (diffraction) microscopy at the cSAXS beamline: **(a)** Overview: Out of the so-called “exposure box” (X) on the right, the X-ray beam passes through the scanning set-up in the centre of the image into the flight tube (F) on the left. The different motorized stages of the scanning set-up are mounted on a steel base plate (BP), which is positioned by means of a high-load hexapod (H). **(b)** Close-up view of scanning set-up: The X-ray beam enters the set-up from the bottom, where a nozzle (N) holds the final beamline vacuum window, which is approached as close as possible to the set-up to reduce the air path. The scanning set-up itself consists in the most general case of four stacks of linear stages that allow to move each component independently along the Cartesian axes: The first stack (CS) holds either central stops or coherence-defining apertures, while the second one (FZP) positions the Fresnel zone plate focusing lenses in a focused-beam set-up. Order-sorting apertures are manipulated with the third stack (OSA). The fourth set of motors (S) is used for coarse positioning of a 2D piezo-electric scanning stage to which the sample holder is attached. The so-called “X-ray eye” (E) allows to use radiographs, obtained through a combination of a scintillator with an optical video-microscope, for alignment. The path through air to the flight tube’s (F) entrance is again kept as small as possible.

5.1. Ptychographic CDI at the cSAXS beamline of the Swiss Light Source



sampling. Placing all apertures on a common holder allows to quickly switch from a focused-beam to a pinhole-based geometry: the holders for the central stops and the zone plates are moved out of the beam path while on the OSA holder just one of the smaller pinholes is selected. If it is certain that a small pinhole will be the only required illumination defining element, the first two motor stacks can of course be completely left out.

2D piezo scanner with sample In the case of the sample stack (label S in Fig. 5.2(b)), the three stepper motors are only used for coarse positioning. The actual scanning in the plane perpendicular to the optical axis is done with a piezo-driven two-dimensional scanning stage (model P-733.2CL, PI), which has 0.3 nm nominal resolution, < 2 nm reproducibility and $100\ \mu\text{m} \times 100\ \mu\text{m}$ scan range. Most of the samples investigated with this set-up are typically prepared on silicon nitride membranes which provide high X-ray transparency and are usually directly glued onto the metallic mounting plate fixed to the piezo. The scanning of the sample has to be performed in stop-and-go mode for the collection of ptychographic data sets. Standard STXM acquisitions can be sped up by operating the piezo in a continuous translation mode. Recent algorithmic developments for mixed-state reconstructions (compare THIBAULT AND MENZEL, 2013) may allow to use this fast scanning mode also for PCDI in the future.

Another important component – although mechanically disconnected from the actual scanning set-up for stability reasons – is the so-called “**X-ray eye**” (Fig. 5.2(b), label E) which can be moved into the beam directly behind the sample when required: by imaging a scintillator screen with a microscope objective onto a CCD camera running at video frame-rates, it makes available online X-ray radiographs of the optical components and the sample with a resolution slightly better than $2\ \mu\text{m}$. These live images are mainly used for alignment or to find a region of interest within the sample.

5.1.3 Tomography set-up

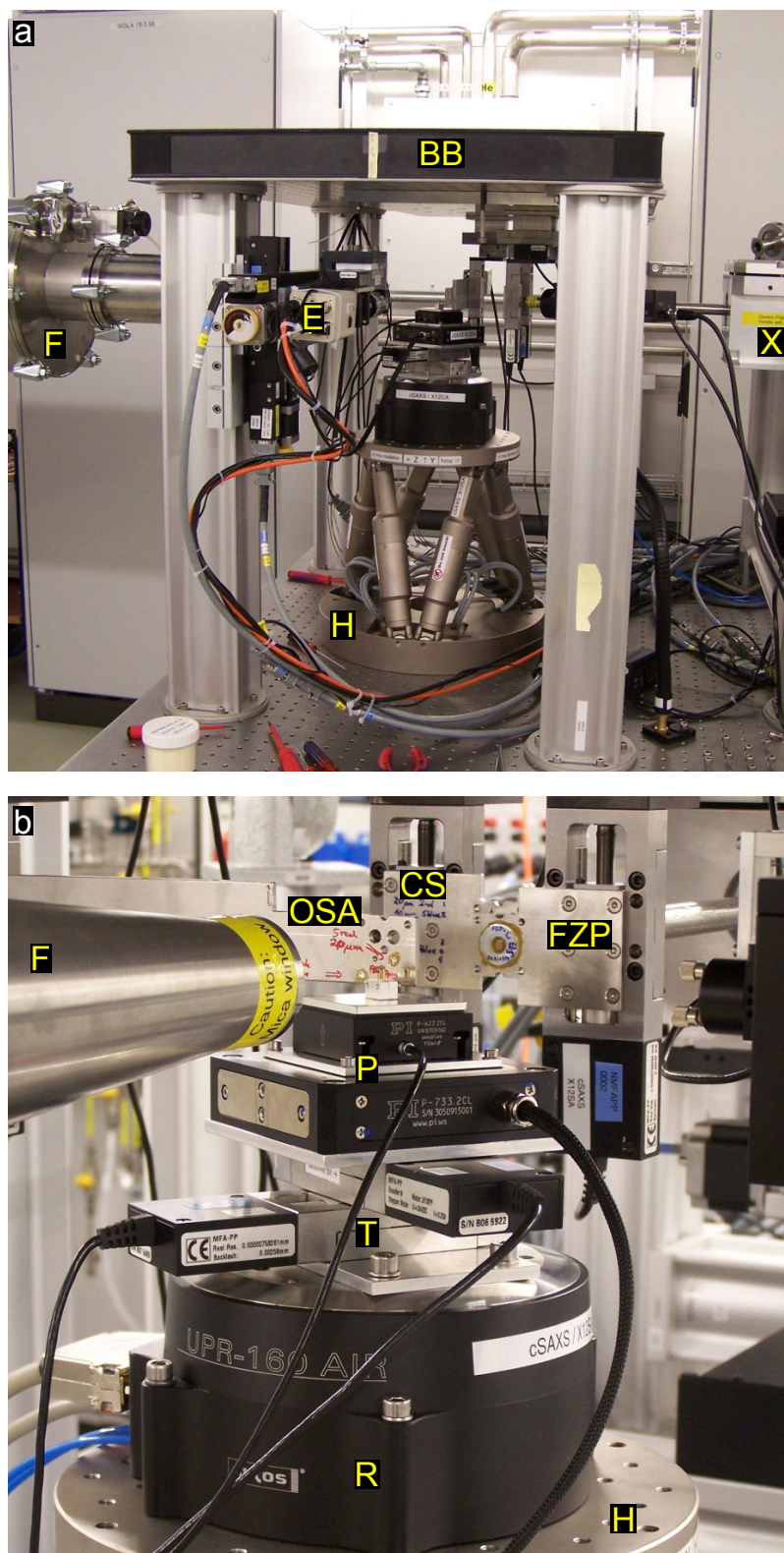
The sample rotation required for tomography makes it necessary to discard the common base plate used in the 2D set-up described in the previous section. The required relative stability of illuminating probe and object thus has to be ensured otherwise. For the cSAXS tomography set-up, geometrical constraints make it necessary to have the illumination-defining optical components hanging upside down from a sturdy support frame (see Fig. 5.3(a)),

while a stack of various stages carrying the sample (compare Fig. 5.3(b)) is rising from the surface of the optical table.

By reusing major parts of the 2D set-up, again both a focused-beam and a pinhole geometry are possible: The support plate of the scanning set-up is fastened on a heavy sand-filled breadboard (Newport) which is placed upside down on aluminium posts (Linos). Up to three of the stacks of stages discussed in detail in the section 5.1.2 are fixed to this plate as visible in Fig. 5.3(b): one for central stops or coherence-filtering apertures, the other for Fresnel zone plates and the last for the order-sorting apertures or the illumination-defining pinholes. The latter motor assembly always has to be used with a mounting plate with a long arm to allow for unhindered rotation of the sample stack.

The different components of the assembly of motorized stages carrying the sample are visible in Fig. 5.3(b): At the bottom, a hexapod 6-axis parallel kinematics microrobot (model M850.11, Physik Instrumente (PI), label H in Fig. 5.3(b)) is used for centring the rotation axis in the beam and for adjusting its tilt. Furthermore, it allows for coarse vertical translations along the rotation axis. Rotations are done with an air-bearing stage (UPR 160F, Micos, label R in Fig. 5.3(b)) on top of which two linear translation stages (model MFA-PP, Newport, label T in Fig. 5.3(b)) are installed for centring the specimen on the rotation axis. Samples are typically prepared on a brass pin of 3mm diameter and fixed with a clamping mechanism on top of the piezos used for scanning. To allow for highly precise stepping in all three dimensions, a 2D piezo scanner (P-733.2CL, PI, label P in Fig. 5.3(b)) in the horizontal plane is combined with a 1D piezo (P-622.2CL, PI) for vertical movements. With both the coarse translations and the piezos, movements

Figure 5.3 (following page): Photos of nanotomography set-up at the cSAXS beamline: **(a)** Overview: The X-ray beam passes from the exposure box (X) on the right to the flight tube (F) on the left. The stages carrying the illumination-defining optical components hang from a sturdy optical breadboard (BB). The X-ray eye (E) is attached to one of the aluminium posts supporting the breadboard. The stack of stages for sample positioning and rotation (see close-up view below) is placed on the hexapod (H). **(b)** Close-up view of scanning tomography set-up: Hanging from the top are the three stacks of linear stages for the optical elements: one for central stops or coherence-defining apertures (CS), another for Fresnel zone plates (FZP), and the last for order sorting apertures (OSA). For the latter, mounting on a longer arm is necessary to allow for free sample rotation. The sample is mounted centred on the top of stack: The hexapod (H) is used to centre the rotation axis of the air bearing rotation stage (R) on the optical axis and also to correct its tilt. Two coarse linear translations (T) allow to centre the sample on the rotation axis. Scanning along the Cartesian axis is done with a combination of a two-axis (horizontal) with a one-axis (vertical) piezo (P).



are always done along the fixed Cartesian axes of the laboratory frame by introducing software pseudo-motors that take the current rotation angle into account.

As in the 2D set-up, the radiographs provided at video frame rate by the X-ray eye installed downstream from the sample (label E in Fig. 5.3(a)) are used for alignment purposes.

The latest version of the tomography set-up at cSAXS (HOLLER ET AL., 2012) additionally provides a precise interferometric measurement for the relative position of sample and the illumination-defining element (e.g. zone plate or pinhole). As this option, however, only very recently became available, it has not been used for any of the work presented here.

5.2 Ptychographic CDI at ID22NI at the European Synchrotron Radiation Facility

Experiments were also performed at the European Synchrotron Radiation Facility (ESRF) in Grenoble. The ESRF storage ring (see ESRF WEBSITE, 2015 and LACLARE, 1994 for detailed parameters) is operated at about 6 GeV, which means that the peaks of the insertion devices' spectra are shifted to higher X-ray energies compared to smaller machines like the SLS. This is particularly interesting for materials science applications like imaging of integrated circuits or metallic pore structures. In these cases, an energy in the range of about 15 to 20 keV provides both the necessary penetration power and a sufficient scattering signal.

The **nano-imaging endstation of the ID22 beamline (ID22NI)** has been designed to employ a nano-focused X-ray beam for fluorescence mapping or phase-contrast projection microscopy using the holotomography approach (BLEUET ET AL., 2009). It has been chosen for the ptychographic experiments at ESRF because it offers a unique combination of five interesting characteristics:

1. High (coherent) flux in the energy range 15 to 20 keV.
2. "Pink" beam with a broad energy bandwidth.
3. Achromatic KB nano-focusing optics.
4. Permanently-installed dedicated nano-tomography set-up.
5. Option of simultaneous coherent diffractive and fluorescence imaging.

The parameters of the beamline ID22 and the nano-imaging endstation in the description below are taken from BLEUET ET AL. (2008) and MARTÍNEZ-CRIADO ET AL. (2012).

5.2.1 Source and beam conditioning

At ID22 the X-ray source consists of two independent undulators, a standard one (42 mm period) and an in-vacuum (23 mm period), which create a source point of $25\ \mu\text{m} \times 900\ \mu\text{m}$ (vertical \times horizontal, FWHM) size. For improved transverse coherence, a secondary source of typically $10\ \mu\text{m}$ to $20\ \mu\text{m}$ width can be created with a horizontal high-power slit located about 28 m from the undulator source. At 34 m, a horizontally deflecting Si mirror with stripes of Pd and Pt acts as an energy filter which blocks higher undulator harmonics.

5.2.2 Kirkpatrick-Baez focusing system

The KB system (HIGNETTE ET AL., 2005; ZHANG ET AL., 2010) is placed about 64 m from the source at the front of the massive stone table which is used as the common support for all components of the nano-imaging endstation in order to maximize mechanical stability. A nitrogen-flushed enclosure ensures the KB assembly stays clean and at a constant temperature. The entrance aperture of the mirror system is defined by a pair of slits. The two total-reflection mirrors are made out of silicon which is dynamically bent into the required elliptical shapes. The vertically-focusing first mirror is additionally coated with a graded-multilayer which acts as a monochromator with an energy bandwidth of $\Delta E/E \simeq 1.5 \cdot 10^{-2}$. This corresponds roughly to the spectral width of a full undulator harmonic. Said multilayer coating also increases the acceptance angle of the mirror. This specific system thus provides an X-ray flux in the focus of about 10^{12} photons/s in the energy range 15 to 20 keV (BLEUET ET AL., 2008). In the endstation's most recent development stage, the focal distances are 180 mm for the vertical and 83 mm for the horizontal focus. The set-up as of July 2011 is routinely operated with focal spots down to $60\ \text{nm} \times 60\ \text{nm}$. However, spots in ptychographic experiments are typically more about 120 nm to 180 nm in diameter, as the necessity to illuminate the entrance slits coherently results in a reduced numerical aperture. For CDI, the installation of an additional pinhole aperture (label PH in Fig. 5.5(a)) directly after the KB system to clean up parasitic scattering – in particular from the entrance slits – is highly beneficial. The effect of this pinhole is illustrated in Fig. 5.4.

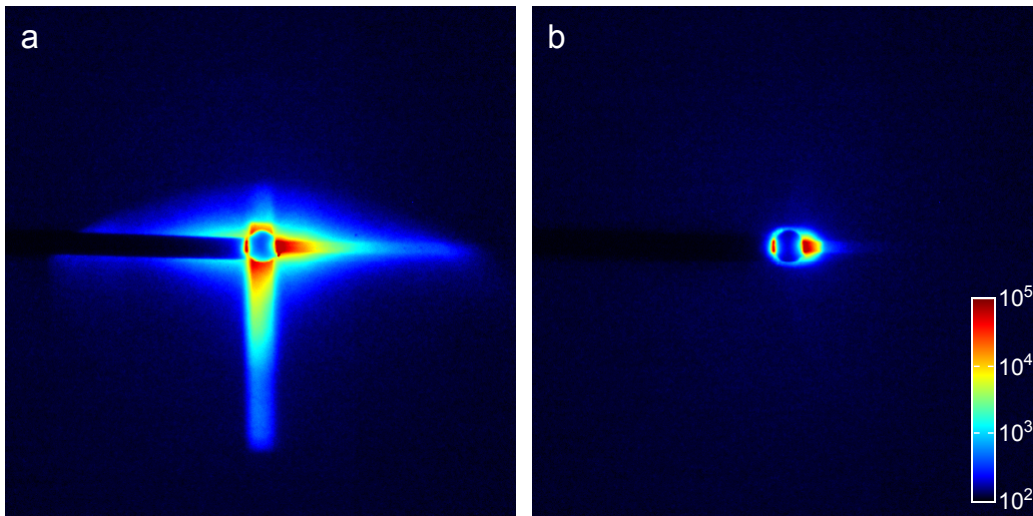


Figure 5.4: Effect of a clean-up pinhole on diffraction data quality at ID22NI. Both images show the central 512×512 pixels of far-field diffraction patterns measured with the FReLoN detector and using a beamstop to block the direct beam. (a) The signal without clean-up pinhole is dominated by strong streaks which are attributed to parasitic scattering from mirror imperfections and the entrance slits. (b) Placing a clean-up pinhole directly after the KB-system removes most of the parasitic scattering. The location of the pinhole is shown in Fig. 5.5(a).

5.2.3 Scanning set-up

The main set-up is based on a three-axis stage consisting of an air-bearing translation along the beam and two stepper motor driven stages for movements in the transverse plane. The rotation stage on top carries a magnetic disc which has a mounting mechanism for cylinders of 3 mm diameters. A pusher is used to move the magnetic disc with respect to the rotation axis in order to centre the sample. A piezo, which is usually employed for active position stabilization in the horizontal transverse direction during the standard holotomography applications of the endstation, is used for scanning in ptychographic tomography. However, as vertical scanning can only be done with the stepper motor, special scan patterns, like e.g. the “round scan” introduced in section 3.2.4.5, cannot be used.

In cases where one is only interested in 2D projection images, an additional platform with a 2D piezo scanner (P-733.2CL, PI, marked by label PZ in Fig. 5.5(a)) is mounted at the top of the stack of stages. The platform with the piezo is placed on a tripod construction which allows to keep the rest of the set-up unchanged.

An on-axis video microscope, which the beam passes through a hole in its 45° -mirror, is used for sample alignment (label VM in Fig. 5.5). It is placed

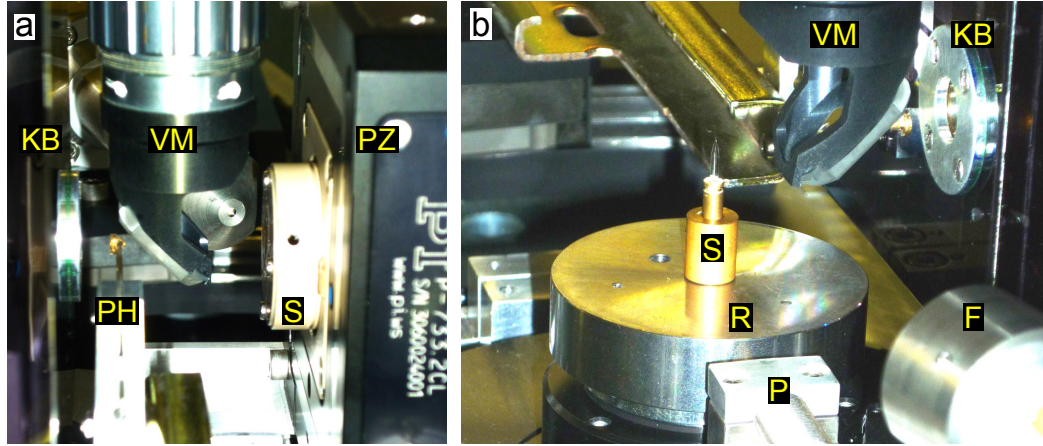


Figure 5.5: Photos of scanning set-up at ID22NI. **(a)** Set-up for two-dimensional scanning: The beam passes from the exit of the KB focusing system (KB) through a cleanup pinhole (PH) and the hole in the centre of the deflection mirror of the video microscope (VM) onto the sample (S), which is mounted on a two-axis piezo scanning stage (PZ). **(b)** Tomographic set-up, in which the sample (S) is mounted on top of a rotation stage whose top part (R) is a magnetically-coupled disc. A small actuator (P) can be used to change via pushing the position of the magnetic disc with respect to the rotation axis. X-ray fluorescence maps can be collected during ptychographic scans with the energy-dispersive detector (F).

behind the enclosure of the KBs in such a way that its focal plane coincides with that of the X-ray optics. This provides reliable means to place samples in the X-ray focus whose depth of focus is much larger than the microscope's.

5.2.4 Detectors

As ID22NI is mainly designed for holotomography and fluorescence mapping (BLEUET ET AL., 2009), it does not feature a permanently installed detector for collection of far-field diffraction data. However, the projection images obtained with the standard holotomography detector, which is based on a ESRF FReLoN charge-coupled device (CCD) with 2048×2048 pixels onto which the signal from a high-resolution scintillator is optically magnified, can be used for centring the sample on the rotation axis. While one of the two identical fluorescence detectors usually has to be removed to be able to mount the clean-up pinhole mentioned above, the remaining one may be operated simultaneously with the far-field detector. It is a collimated silicon drift diode (SDD) detector (SII Nanotechnology Vortex 50 mm^2), which is placed close to the X-ray focus forming an 75° angle with the incoming beam in the horizontal plane, compare Fig. 5.5(b), label F.

Diffraction patterns are collected with a FReLoN CCD system with a

fibre-optics taper. The detector is of the same principle design as the ones studied by COAN ET AL. (2006) and PONCHUT (2006), however with slightly varied taper dimensions and a different CCD chip. The system employs a gadolinium oxide scintillator that is fiber-optically coupled to a CCD chip (Kodak 4320) with 2048×2048 pixels. The resulting effective pixel size is $51 \mu\text{m}$. A rough estimate of the line-spread function (LSF) of the detector has been obtained from a radiograph of a regular grid of circular holes which was placed in close proximity to the scintillator. By taking the derivatives of lineouts across the edges of the holes, the FWHM values of the LSF were found to be about 2 to 3 pixels, i.e. about 100 to $150 \mu\text{m}$, which is consistent with the values reported for a similar taper-based system in the article by PONCHUT (2006, page 203). In this article it can also be seen that the LSF has very long tails which extend to a range of several millimetres. In particular when locally illuminated with a very intense beam, this will result in the detection of significant counts in non-illuminated pixels. Investigations of a similar detector by HOLTON ET AL. (2012) suggest that these long tails originate mainly from scattering in the fibre-optics taper of such systems and that scattering in the scintillator plays only a minor role in this case.

Data collection with the FReLoN can be sped up by reading out just a region-of-interest (LABICHE ET AL., 2007), in the case of our experiments typically the inner 1024×1024 pixels. To spread the intense undiffracted beam over as many pixels as possible, the detector is usually put to a distance of about 3 m, quite farther away from the sample than required by the sampling condition (2.27) on page 55. To allow for longer exposure times, a motorized beamstop can be inserted in front of the detector to block the direct beam.

5.3 General considerations on PCDI experiments and their limiting factors

Based on the experiences made with the experimental realization of ptychographic CDI, this section draws some conclusions what has to be considered in order to collect high-quality data sets. This at the same time provides an overview of the current experimental limitations ptychographic CDI is facing. The discussion on instrumentation focuses on the key points incident beam, detector, scanning overhead, stability, and – in a very broad sense – sample environment. The section concludes with some remarks on sample preparation.

5.3.1 Incident beam

5.3.1.1 Coherent flux

The coherent flux (photons per second) incident on the sample fundamentally limits both the spatial resolution and the sensitivity which are achievable in an experiment, compare also (3.70) on page 112. Furthermore, it also influences the acquisition time after which a given number of scattered photons is detected and thus the total area which can be scanned within a given time. In recent experiments at cSAXS, a coherent flux of about $1.2 \cdot 10^7$ photons/s at 6.2 keV was measured. However, even at this relatively low flux the beam had to be slightly attenuated to stay below the count rate limit of the detector (compare also section 5.3.2). Higher fluxes can typically be achieved at larger facilities, especially when it comes to higher photon energies: At ID22NI, from the incoherent flux of about 10^{12} ph/s about $5 \cdot 10^8$ ph/s were left in coherent imaging mode at about 16.96 keV mean energy. For the nanoprobe based on nano-focusing compound refractive lenses installed at beamline P06 of the PETRA III storage ring, values between $8 \cdot 10^8$ ph/s and 10^{10} ph/s have been reported at 20 keV (SCHROER ET AL., 2010).

Further gains in flux are to be expected with the advent of new sources, like energy recovery linacs (GRUNER ET AL., 2002a), and the upgrade of existing ones. However, current X-ray free-electron lasers (XFELs), which are optimized to deliver a very high peak flux within a few tens of femtoseconds, are not well suited for ptychographic CDI: Specimens are typically heavily damaged or destroyed by a single shot so that conducting several exposures with overlapping illumination positions is not feasible. Nevertheless, in the special case of periodic objects like two-dimensional nanocrystals, a ptychographic data reconstruction procedure may also be used for data taken at XFELs (KEWISH ET AL., 2010b).

The transverse coherence length at the location of the experiment is mainly determined by its distance from the source and the latter's size, either directly at the insertion device or at a secondary source, compare (2.5) on page 47. These parameters should therefore be considered when setting up or selecting an experimental station for ptychographic CDI. In order to use the full available coherent flux of the incoming beam, it should in particular be attempted to match the effective coherence lengths to the aperture of the illumination-forming system: In a typical pinhole-based ptychographic experiment, e.g., the transverse coherence lengths typically exceed the size of the pinhole by one to two orders of magnitude and therefore the beam may be pre-focused by this factor onto the pinhole without impairing the coherence of the illumination.

5.3.1.2 Localized illumination

A fundamental requirement of ptychographic imaging is that the illumination formed on the object, in the words of [RODENBURG ET AL. \(2007a\)](#), “must be ‘substantially’ localised”. Quite frequently, pinhole apertures have been used to accomplish this ([DIEROLF ET AL., 2010a,b](#); [GIEWEKEMEYER ET AL., 2010](#); [HOLLER ET AL., 2012](#); [RODENBURG ET AL., 2007b](#)). However, manufacturing pinholes with both small diameters (typically below 5 μm) and thicknesses which guarantee sufficient absorption at hard X-ray energies remains technologically challenging, even if advanced methods like focused-ion beam milling are available.

In various ptychographic experiments, the localized illuminations have been created by different types of X-ray focusing optics: This includes diffractive Fresnel zone plate optics ([THIBAUT ET AL., 2008](#); [VILA-COMAMALA ET AL., 2011a](#)), compound refractive lenses ([SCHROPP ET AL., 2010](#)), and Kirkpatrick-Baez ([KEWISH ET AL., 2010a](#)) or single-bounce reflective optics ([KEWISH ET AL., 2010c](#)). These examples in particular demonstrate the possibility of implementing ptychographic imaging using existing scanning microscopy set-ups.

While in principle any localized illuminating probe can be employed, our empirical observations suggest to use a illumination which has small-scale features: Reconstructions with very smooth probes have often shown slow and sometimes incomplete convergence behaviour. In contrast, the presence of higher spatial frequencies in the illumination has typically resulted in faster and better reconstructions. This empirical result has recently been confirmed in a study by [GUIZAR-SICAIROS ET AL. \(2012\)](#), who show that the presence of high-frequencies components in the probe leads to a higher signal-to-noise ratio and thus better reconstruction of high-resolution features. [GUIZAR-SICAIROS ET AL. \(2012\)](#) therefore conclude that “the spatial-frequency spectrum of the illumination probe, [...], should be a design parameter of a microscope based on ptychography”.

Another important parameter is the size of the localized illumination: On the one hand, it depends on the geometry of the set-up, i.e. the pixel size of the detector and its distance from the object plane, see also subsection [5.3.2.1](#). On the other hand, the probe’s extent determines the number of scan points required to cover a certain area. It thus strongly influences the total scanning overhead time. This is discussed in more detail on page [147](#) in section [5.3.3.1](#).

Different aspects of stability, which concern both the illumination itself as well as the accuracy of the relative positioning of probe and object, are considered in section [5.3.4.2](#) from page [149](#) on.

5.3.2 Detector

The detector is a crucial part of a ptychographic experiment. In order to achieve good results, several detector parameters (compare also section 1.6.1 starting on page 33) should be adapted to the specific requirements:

5.3.2.1 Geometry

The detector's pixel size and distance from the plane in which the specimens are scanned should be chosen according to (2.27) on page 55 such that the diffraction patterns are sufficiently sampled. Of course also the typical beam size at the sample has to be considered in this calculation. Furthermore, the total size of the detector directly determines the highest spatial frequencies for which diffraction signal can be detected. The area of the detector should therefore be large enough to be in principle able to reach the envisioned spatial resolution.

5.3.2.2 Incoming flux

First of all, the detector must not be damaged by the incoming photons, i.e. it must either be radiation hard (SOBOTT ET AL., 2009) or, e.g. in the case of a very intense undiffracted beam, the direct beam must either be blocked or, e.g. at free-electron laser sources, pass through a hole in the centre of the detector (GRAAFSMA, 2009). In the case of photon-counting detectors, like for instance PILATUS systems (KRAFT ET AL., 2009a,b) or the MAXIPIX based on the MEDIPIX II chip (PONCHUT ET AL., 2011), the maximum count rate – which is limited by the dead time after each event during which no new one can be detected – has been observed to be a major limiting factor: During several experiments the coherent beam had to be attenuated such that in forward direction the incident flux did not exceed the count-rate limit of the respective detector. As discussed in section 5.1.1.6, the limit for the PILATUS depends on the amplifier gain settings and lies between $0.9 \cdot 10^6$ photons/s/pixel (high gain) and $8 \cdot 10^6$ photons/s/pixel (low gain). According to RADICCI ET AL. (2012), the recent single-photon counting detector EIGER can cope with more than $2 \cdot 10^6$ photons/s/pixel already in its low-noise mode, which is the least favourable in terms of count rate. Furthermore, as the side length of one EIGER pixel is just $75 \mu\text{m}$, the photons that would hit one PILATUS pixel ($172 \mu\text{m} \times 172 \mu\text{m}$) are distributed over 4 to 5 pixels on the EIGER. Count rate is not an issue for integrating detectors like CCD-based systems or for detectors designed to be used at X-ray free electron lasers (GRAAFSMA, 2009).

5.3.2.3 Point-spread function

Reconstructions have been found to be strongly degraded (see the discussion in sections 8.4.1 and 8.4.3) by the rather extended tails of the FReLoN's point-spread function (compare PONCHUT, 2006, page 203). In contrast, when just a single pixel of a PILATUS detector is illuminated in a localized way, only this very pixel produces a signal, i.e. the PILATUS has a point-spread function of one pixel. This results in a higher quality of the retrieved images compared to scintillator-based systems.

5.3.2.4 Readout speed

As ptychographic data sets, in particular for tomographic investigations, may consist of more than 10^5 diffraction patterns, the time spent on detector readout plays a significant role when it comes to reducing the total duration of a scan. The actual readout time of modern detectors, i.e. the minimum time between subsequent exposures, can be as low as just a few milliseconds (for instance 2.85 ms for the PILATUS II readout chip, see KRAFT ET AL., 2009b). However, such high frame rates are typically only reached if the detector is operated in a non-interactive “burst mode”, in which a whole series of exposures is taken and directly written to disk without any further communication between detector software and control system. But it is exactly this communication which amounts for most of the total readout time observed in a PCDI experiment where each exposure is usually triggered individually by the control software. Among others, this total readout time constitutes a major contribution to scanning overhead, compare section 5.3.3. First demonstrations (GUIZAR-SICAIROS ET AL., 2014) show that this total time can be reduced with novel detector systems like, e.g., the EIGER (DINAPOLI ET AL., 2011; JOHNSON ET AL., 2014; RADICCI ET AL., 2012). This single-photon counting detector features dead times below 3 μ s, a large 2 GB RAM for temporary storing several frames directly on the readout board, and double buffering which allows to acquire another frame while the previous one is still being read out.

5.3.2.5 Noise

Scattering signals typically drop off pretty quickly towards higher momentum transfers $|\mathbf{q}|$, as e.g. illustrated by *Porod's law* for small-angle scattering from a colloidal system, which states an asymptotic relation $I(|\mathbf{q}|) \propto |\mathbf{q}|^{-4}$ for the intensity (POROD, 1951). To obtain high-resolution reconstructions, also the weak signals at large momentum transfers have to be recorded with high accuracy. In the ideal case, only Poisson noise due to the statistical

nature of the photon counting process is present in the recorded diffraction data. A detector may add additional noise which is mainly originating from two sources: Firstly, there is background or dark noise due to the charge generated – mostly thermally – in the pixels even when they are not illuminated. Secondly, additional noise is typically added during the readout process. On a CCD chip, e.g., usually the charge accumulated in the individual pixels is transferred to one analog-digital converter per line. The accuracy of the charge measurement and digitization is limited and gets worse at higher readout speeds. In hybrid-pixel detectors like the PILATUS (KRAFT ET AL., 2009a,b) or the MAXIPIX (PONCHUT ET AL., 2011) systems, each pixel has its own analog-digital converter which counts individual photons by directly comparing the charge generated in the pixel with a predefined threshold. By this, both dark and readout noise are eliminated.

5.3.2.6 Dynamic range

For the same reason as the noise, also the dynamic range of the detector is of utmost importance: The rapid drop of the scattering signal with growing spatial frequency requires that both very intense signals at the centre of the diffraction pattern and individual photons at high momentum transfers can be measured reliably within a single exposure. Within a single frame, the detector therefore has to be able to both accept and digitize differences in photon counts of several order of magnitudes. Typical CCD systems often digitize with 14 or 16 bit, i.e. if a photon increments the digital output signal by one, this allows to measure up to 16 384 or 65 536 photons in a single frame. In practice, the effective dynamic range is usually slightly lower than the nominal value determined by the electronics, as a signal first has to be above the level of the background noise to be detected. The PILATUS detector features a 20 bit counter (KRAFT ET AL., 2009b) and because there is also no background noise this allows to reliably measure photon counts between 0 and 1 048 576 in a single exposure. The upcoming EIGER system features a 12 bit counter which however can be extended to 32 bit by combination of multiple frames directly in the detector readout board (RADICCI ET AL., 2012).

5.3.3 Scanning overhead

In ptychographic experiments, the scanning overhead is often observed to be up to 30 % to 50 % of the total scanning time. It therefore becomes a major limiting factor in cases where a lot of diffraction patterns are taken, in particular in tomographic PCIDI. The factors that determine the total

overhead are the total number of scan positions and how much time is spent for each individual point in addition to the raw exposure time:

5.3.3.1 Total number of scan positions

The overhead per scan point, which is discussed in more detail in the next section, typically is a rather constant value which does not depend on the actual exposure time. If therefore a certain area is to be scanned in a given time, the ratio of total exposure time to total scan duration is higher the less points are used. This is illustrated by a numerical example: For an overhead of 0.2 s per position and a total scan time of 600 s, the accumulated time a given area is exposed amounts to 400 s if 1000 points are used. But if the same area is covered with only 100 points, the actual net exposure time is 580 s instead. So while in the first case the overhead amounts to 33 % of the total scan duration, it is only 3.3 % for the latter settings. Such a reduction of the number of scan points can be achieved if a larger illumination is used, e.g. a pinhole in the micrometer range instead of a nano-focused beam. However, also a larger beam still has to fulfil the sampling condition (2.27) on page 55, which also depends on other experimental constraints like the distance to the detector and its pixel size. It also has to be considered that the diffraction data may be easier degraded by instabilities during the longer exposure times which are required to deliver the same photon fluence with a more expanded beam.

5.3.3.2 Overhead per scan point

Ptychographic scans are typically done in “stop-and-go” mode which in addition to the major tasks of motor movement and detector readout requires a lot of interaction by the control software:

1. Send new position to motors.
2. **Motor movement.**
3. Wait for “position reached” feedback from motors.
4. Send exposure parameters and start command to detector or its specific control software.
5. **Detector readout.**
6. Wait for “exposure complete” or “file written” response from detector or its control software.
7. Write to screen and / or log file, often including additional information (like temperature sensors, storage ring current etc.).

The main contributions to the total overhead per point are discussed individually in more detail in the following paragraphs:

Motor movement The translations used for scanning are usually piezo-driven which means that the displacements happen on very short time scales. However, these actuators are typically operated in a closed-loop mode with their own digital controller and a position is only considered as “reached” when the controller reports so after a so-called settle-down time. This time it takes for the piezo to reach a certain position with a given accuracy depends heavily on the settings of the controller’s tuning parameters, which should thus be optimized accordingly.

Detector readout As discussed on page 145 in section 5.3.2, the actual time it takes to readout a single detector frame is as short as a few milliseconds for modern detectors and therefore only marginally contributes to the scanning overhead. The total exposure time includes the whole procedure of processing the exposure request of the control system, exposing, reading out, storing the frame and sending a confirmation to the control software. In this, everything apart from the actual exposure itself adds up to the total detector readout time.

Control software interaction Apart from a general optimization of the communication channels, the reduction of the delays due to interaction with the control system is not so straight forward: the stop-and-go mode cannot be easily replaced by schemes which require less interaction. For example, a continuous scan along a line with exposures at given, pre-programmed time intervals is often used for fast data acquisition in STXM. In ptychographic CDI, this may not be applied because unlike in the STXM case the required movement during the exposure would be much larger than the typical resolution element in the reconstruction. However, it has been demonstrated by PELZ ET AL. (2014) and DENG ET AL. (2015a) that the recent extension of PCDI to mixed-state reconstructions (THIBAUT AND MENZEL, 2013) allows to use such data.

A promising approach to reduce overhead times seems to be to execute the above-mentioned communication steps in parallel whenever possible. For instance, the detector could already send an “exposure complete” signal directly after the exposure is finished. The control system then immediately starts moving to the next scan position while the detector is still busy with reading and storing the last frame.

In general, one should try to keep the interaction with the control software and the communication caused by it at the minimum required level. In particular gathering a lot of additional information in step 7 on page 147 often causes significant delays. The amount of requests should therefore be

reduced as much as possible, e.g. it might be sufficient to record the values of the storage ring current not at each scan point but rather only at the beginning and the end of a scan.

5.3.4 Stability

Stability considerations affect many elements of a ptychographic experiment. The main aspects can be summarized as concerning the general experimental environment, the illumination, and the positioning stability and accuracy. They are discussed in more details in the following subsections.

5.3.4.1 Experimental environment

A fundamental prerequisite for all the other points is a general stability of the environmental conditions: Thermal fluctuations, strong changes in air flows and transmission of external vibrations through the ground should be avoided wherever possible. These aspects should not only be kept in mind during the design and construction phases of an experimental station, but also when conducting a ptychographic experiment. In the latter case, already simple measures, like e.g. minimizing the time the door of the experimental hutch is left open, can significantly improve stability.

5.3.4.2 Illumination

As typically only a small (coherent) portion of the incoming beam is used to form the illumination on the object, **fluctuations or movements of the beam** as such are usually not too critical: In the case of pinhole-based PCDI, e.g., when an incident beam with a non-uniform intensity distribution moves relative to the small pinhole, the illumination on the object will typically only change its overall intensity but not its structure. And as long as the wavefront of the actual illumination function is stable, the phase part of the reconstruction is not affected. Changes in the overall intensity affect only the absorption image, which is in most cases of less interest due to the higher sensitivity of phase-contrast imaging at hard X-ray energies.

Another aspect linked to the illumination is the **number of scan points** required to cover a given field of view, as this depends on the size of the beam on the object. In terms of stability, covering a given area either with few or with many points both has its advantages and disadvantages: In the first case, less movements are required which typically means less chance for positioning inaccuracies. However, if the accumulated exposure time is to be the same, the dwell time per point is higher so that the individual diffraction patterns

become more susceptible to drifts. In the second case, the situation is just reversed, i.e. while the shorter time spent at each position makes large drifts during the exposure less likely, the larger number of points increases the probability of positioning errors. However, as discussed on page 147 in section 5.3.3.1, the use of more scan positions to cover the same area results in a greater overhead. Nevertheless, sections 7.3.3 (simulations) and 7.4.2 (application to experimental data) show results of a new algorithmic scheme which allows to combine the data of many short, less drift sensitive scans of the same region into the reconstruction of a single object. The key point is that for each data set its own individual probe is reconstructed. This acts as a self-correction mechanism which can efficiently cope with changes of the illumination between scans, both in structure and position.

5.3.4.3 Positioning stability and accuracy

Most implementations of ptychographic reconstruction algorithms currently in use assume that the provided scan positions, which are obtained either as nominal values or as the measurements of position encoders, are accurate. This implies that their deviations from the actual positions are negligible on the scale of the retrieved image's resolution. Therefore, both accuracy and stability of the relative position of probe and object have to fulfil this requirement.

Relative movements of the sample with respect to the illumination are typically realized with standard commercial piezo-driven **scanning stages**. So far, their resolution and reproducibility proved to be sufficient to allow for high-resolution reconstructions, like e.g. the one described in section 7.4.1, without obvious effects of positioning inaccuracies. In the case of the set-up at the cSAXS beamline described in section 5.1.2, e.g., one has nominal values of 0.3 nm for the resolution and of < 2 nm for the reproducibility. Both are significantly smaller than the typical pixel sizes achieved in current ptychographic reconstructions. In practical applications, however, one should assure that the piezo system's parameters for motion and feedback are correctly adapted to the specific experiments. This is important in order to avoid that movements excite resonances of the scanning stage, which may degrade the measurement or even destroy the hardware.

To allow for tomographic imaging, an additional **rotation axis** has to be introduced like for instance in the set-up described in section 5.1.3. Although rotation stages show inaccuracies on much larger length scales, this does usually not affect the validity of the positions within two-dimensional ptychographic scans at individual projection angles. Typically, only the positioning of the retrieved projections with respect to each other suffers. Therefore,

among other post-processing steps, an additional alignment of the projections is necessary prior to tomographic reconstruction. This procedure is detailed in section 9.2.4 starting from page 250. As high-precision rotation stages are often air-bearing systems which have an active position feedback, vibrations may be introduced accidentally: a too strong pull of the connector cables of stages mounted on top of the rotation, e.g., may cause the rotation stage to slightly deviate from its target position once the motor is switched off. If the deviation appears again every time after the feedback loop has put it back to the target position, a periodic motion is induced which may cause significant errors in the relative position of probe and object during an individual ptychographic scan. An experiment should be tested for such effects and modified to avoid them if necessary.

To reach higher resolutions in ptychographic CDI, recently developed systems which interferometrically measure and actively stabilize the relative position of the illumination-defining elements with respect to the sample (HOLLER ET AL., 2012) are the most promising approach on the hardware side. Recently, an isotropic resolution of 16 nm in three dimensions was achieved with this type of set-up (HOLLER ET AL., 2014). On the software side, it has been demonstrated that a refinement of the probe positions within ptychographic reconstruction algorithms is possible (GUIZAR-SICAIROS AND FIENUP, 2008; MAIDEN ET AL., 2012b). While in some special cases position refinement may lead to ambiguous results (compare Fig. 12.1 on page 332), it is nevertheless expected to play an important role in future high-resolution imaging with ptychographic CDI.

5.3.5 Sample environment

This section discusses different aspects of the sample environment within a set-up for a ptychographic experiment. More specifically, requirements and limitations concerning the mounting, positioning and cooling of the sample are reviewed.

5.3.5.1 Sample mounting

To avoid mechanical drift during the scans, a rigid connection between the specimen and the scanning stages should be provided. For experiments in which only two-dimensional projection images are required, the specimens are best prepared on some sort of substrate transparent to X-rays like a silicon nitride membrane or a thin glass slide to be able to easily handle them. This support can then be fixed directly onto a holder, e.g. a metal plate with holes of several different sizes which is screwed onto the scanning stage.

While clamping is one possibility to fasten the substrates on the holder, good experiences were also made with directly gluing them in place. Glues with high viscosity or wax heated only slightly above its melting point provide sufficient control over the gluing process. Another option are glues which only harden after illumination with UV light. Compared to low-viscosity glue, which tends to creep also into the smallest gaps, the aforementioned options avoid unwanted contamination of the specimen and can significantly ease the process of removing it from the holder if necessary.

For tomographic PCDI, samples should be mounted free-standing whenever possible, i.e. such that a rotation of at least 180° can be completed without the sample holder blocking the field of view. So far, often cylindrical or rod-shaped samples have been attached to small metal tips, for instance of standard commercial needles. These are then fixed to the macroscopic sample supports, for which the scanning set-up provides a mounting mechanism, e.g. the brass pins described in section 5.1.3. While a focused-ion beam preparation of the sample allows to easily place it on top of a metal tip, mounting of isolated readily-prepared samples may prove challenging: With typical dimensions of a few millimetres in length and below $100\ \mu\text{m}$ in diameter, a controlled manipulation with tweezers or similar tools becomes close to impossible. The best mounting results were achieved with the following procedure: A tiny drop of glue is formed at the tip of a small injection needle by filling it from a syringe with cyanoacrylate-based adhesive, preferably of high viscosity and moderately fast hardening. This drop is then used to directly pick up the sample from a flat surface. If done carefully, the specimen is often already well-aligned with the long axis of the needle. However, small corrections to the orientation may be performed until the glue is fully hardened, given the sample is robust enough.

Future directions in sample handling may include kinematic couplings, also called kinematic mounts. Their construction allows for well-defined, highly-reproducible mounting, which e.g. results in a broad use in precision-positioning of synchrotron instrumentation (see e.g. OVERSLUIZEN ET AL., 1992; ZELENKA AND FLECHSIG, 2002, and references therein). An example for the specific application as a kinematic sample mount can be found in WARWICK ET AL. (1998, Fig. 5), in this case for a scanning transmission X-ray microscope. Such systems are of particular interest for correlative studies, in which regions investigated with another imaging modality have to be located precisely.

5.3.5.2 Sample positioning

Important aspects concerning the stability and accuracy of sample positioning have already been discussed on page 150 in section 5.3.4.3. The current section focuses on more general considerations which of the different degrees of freedom should be motorized and what are the best options to do so. In particular the decision where to put the rotation stage in a tomographic set-up strongly affects the requirements for the translations. The following paragraphs distinguish between the two major cases. It is assumed that the rotation axis points along the vertical direction and is perpendicular to the beam:

Rotation stage below scanning stages If the translations for scanning are mounted on top of the rotation stage and thus are rotated together with the sample, a three-axis system is the best choice. To ensure scanning is always done in a plane orthogonal to the beam direction, it is useful to configure pseudo-motors that consider the current angular position. As discussed before, the stages used for the ptychographic scanning have to provide a sufficiently high positioning accuracy. This is achieved with piezo-based translations which however offer only rather limited travel ranges in the order of 100 μm . While this is usually sufficient for ptychographic scans, the alignment of a sample with respect to the rotation axis or the selection of a region of interest may require larger motions. Some coarse horizontal translations, e.g. driven by stepper motors, can be mounted below the piezos to achieve this. Employing kinematic couplings for sample mounting can make coarse alignment for centring on the rotation axis obsolete. The rotation stage used in such a set-up will typically have to be rather big in order to carry all these components in a stable way. However, this also allows to employ air-bearing systems which provide a high accuracy. A horizontal translation perpendicular to the beam should be provided below the rotation stage to align the rotation axis with the beam. An additional coarse translation is required to adjust the vertical position of the specimen along the rotation axis. In most cases, it will probably be easier to also mount such a translation below the rotation stage rather than mounting an additional stage on top. The set-up at the cSAXS beamline, e.g., employs a hexapod microrobot not only to implement the two last-mentioned translations, but also to provide the necessary degrees of freedom to adjust the direction of the rotation axis: By design the rotation axis is parallel to the vertical scanning axis and perpendicular to the horizontal one within the accuracy provided when mounting different stages directly on top of each other. However, the orientation of rotation and scanning axes with respect to the detector pixels may have to

be adjusted.

In practice, an important aspect when constructing such a set-up is the aspect of the motor cables: as the motors are rotated during the measurements, one has to make sure that the cables do neither obstruct the beam nor create positional deviations by exerting too much force on the stack of motors. A negative example is the earlier-mentioned observation that a periodic motion of a rotation stage around the target value was created by a cable's slight pull which repeatedly triggered the position correction in closed-loop operation.

Rotation stage on top of scanning stages Several difficulties associated with rotating a whole stack of translation stages, in particular cabling issues and the requirement to define pseudo-motors, can be avoided if a rotation stage is scanned together with the specimen. This type of set-up may also show benefits in terms of stability, as a rather rigid construction can be employed for the combined translation stages which no longer have to be carried by the rotation stage. However, obtaining a rotation stage which is both light enough to be carried by a piezo scanner but nevertheless provides a high accuracy may not be straightforward, as e.g. most high-precision air-bearing rotation systems are way too heavy. Furthermore, also in this design a possibility to centre the sample on the axis of rotation is required, unless a very standardized and highly-reproducible way of sample preparation and mounting is devised.

In the scanning set-up at ID22NI introduced in section 5.2.3 on page 139, the components are arranged in the discussed way. The rotation axis is based on a commercial rotation stage, which was originally designed for very high revolution frequencies but nevertheless also at slow speed provides the necessary accuracy (Peter Cloetens, private communication). Centring on the rotation axis is achieved by pushing the magnetically-fixed top plate of the rotation stage into the right position with a small actuator.

In summary, both types of tomography set-ups have been observed to perform well in Ptychographic experiments. While in general the first type, where the translations are based on top of the rotation, seems to be more frequently implemented, the second option is worth some consideration if a suitable small rotation stage can be obtained.

In cases where only two-dimensional imaging is required, a two-axis high-precision scanner placed perpendicular to the optical axis – like in a standard STXM – is already sufficient. Some additional coarse translations may be introduced to facilitate centring of regions of interest within samples extending beyond the range of the scanner.

5.3.5.3 Sample cooling

Cooling of biological specimens to cryogenic temperatures can prevent structural changes due to radiation damage, mainly by reducing the mobility of the free radicals created by ionizing radiation (HENDERSON, 1990; MEENTS ET AL., 2010). Cryo-cooling has thus been established early in electron diffraction (TAYLOR AND GLAESER, 1974) and microscopy (DUBOCHET ET AL., 1988). In particular for electron tomography, also the additional aspect plays an important role that vitrification of water in a hydrated specimen makes the latter vacuum compatible without inflicting the structural changes other preparation techniques may cause (BAUMEISTER ET AL., 1999). Later, cryo-crystallography has been introduced in the X-ray regime for protein structure determination (HOPE, 1988), where it has now become the standard method to prevent radiation damage effects (HOLTON, 2009). Two typical approaches are used in these fields to realize cryo-cooling:

- 1. Cooling by heat conduction (typically used in electron microscopy):** The sample is kept in heat-conducting contact with a comparatively large cooled mass acting as a heat sink, e.g. by attaching the specimen to a metal sample holder which is cooled by a liquid-nitrogen reservoir. This has the benefit that cooling can be kept constant over long time spans and thus thermal stresses due to changing conditions can be avoided. That it can only be properly used in vacuum, as otherwise ice formation on the cooled components and thus also the sample would take place, is a major disadvantage of the technique. Furthermore, the requirement to ensure a good thermal connection all the time can complicate tomographic data collection.
- 2. Cooling by cold gas (typically used in protein crystallography):** The sample is put inside a laminar flow of cold gas, which is e.g. evaporating from a reservoir of liquid nitrogen. Such a set-up can be operated in air, as the gas flow prevents the direct contact of the specimen which humid air and thus ice formation. However, the cold flow may induce sample motions, both mechanically as well as thermally. The latter may be the case as with a gas flow the heat transport cannot be as well controlled as with a conductive connection.

The developments made in electron microscopy and protein crystallography have been adapted in various X-ray microscopy instruments to allow imaging of biological specimens:

Several X-ray microscopes use cryo-stages and holders manufactured for cryo-electron tomography, e.g. the TXM at BESSY II (SCHNEIDER ET AL.,

2012) or the Stony Brook cryo-STXM (MASER ET AL., 2000), with which also some systematic studies of radiation damage at the relevant soft X-ray energies have been performed (BEETZ AND JACOBSEN, 2002). Furthermore, this construction principle is also used in a dedicated apparatus for diffraction tomography, which is installed at beamline 9.0.1 of the Advanced Light Source (ALS) in Berkeley (BEETZ ET AL., 2005) and was used by HUANG ET AL. (2009) for coherent diffractive imaging of a frozen hydrated yeast cell. However, electron tomography cryo-stages have the major disadvantage that by design the specimen gets obstructed by the frame of the sample holder if the tilt angle relative to the surface normal gets too high, e.g. greater than about $\pm 80^\circ$ (BEETZ ET AL., 2005). Tomographic data sets taken with such a system will therefore always suffer from the “missing wedge” typical for limited-angle (electron) tomography (BARRETT, 1990).

Other X-ray microscopes keep the sample in a cryogenic gas atmosphere created by evaporation from a reservoir of liquid nitrogen. This approach is used e.g. by the group of Carolyn Larabell at the ALS beamline 6.1.2 (LE GROS ET AL., 2005), where it has enabled high resolution TXM-based tomography in the water window of full eukaryotic cells (PARKINSON ET AL., 2008). Also a previous version of the TXM at BESSY was constructed this way (SCHNEIDER, 1998).

At sufficiently high X-ray energies, where the sample can be measured in air, also a cryo-jet as typically employed in X-ray crystallography may be used, as LIMA ET AL. (2009) did for their first successful demonstration of cryogenic plane-wave CDI. Many of these cryo-jet systems sustain the gas flow by active pumping, which may induce vibrations in the specimen. In plane-wave CDI of an isolated specimen this does not affect the reconstruction as the recorded diffraction intensities are invariant with respect to translations of the object. In ptychographic CDI with its stringent requirements concerning the relative positioning stability of probe and object, however, such movements would degrade the reconstruction results. The successful cryo-PCDI experiments performed by GUIZAR-SICAIROS ET AL. (2012) and LIMA ET AL. (2013) at the cSAXS beamline thus employed a cryo-jet without active pumping, i.e. the gas pressure is maintained by the evaporation of the liquid nitrogen.

For in-air PCDI experiments at multi-keV energies, such a cryo-jet delivering a constant laminar flow so far seems to be the most promising option, whereas at soft X-ray energies the established set-ups of standard X-ray scanning microscopes may be employed.

5.3.5.4 Inspection system for alignment

A ptychographic set-up can greatly benefit from the installation of an inspection system that can be used for (coarse) alignment of the sample and to identify regions of interest. This can be achieved with an “X-ray eye” as at the cSAXS beamline (compare last paragraph of section 5.1.2), i.e. an X-ray detector providing a high-resolution online micro-radiographic image of the specimen preferably at video frame rate. While this approach has the benefit that the X-ray absorption contrast of the sample can be immediately assessed, it does for the same reason not work well for weakly-absorbing specimens. In the case of radiation-sensitive samples, the dose delivered during the inspection or alignment with an X-ray eye may already result in damage. Another important downside is that no diffraction data can be taken when such a system is in use, i.e. permanent monitoring of the sample during data acquisition is not possible.

These drawbacks are overcome by on-axis visible light microscopes, like e.g. the system at ID22NI described in section 5.2.3. Typically, the set-up consists of a digital video camera which is coupled to a microscope objective with a long working distance. Sample illumination and collection of the reflected light are realized with the help of a mirror which has an angle of 45° with the optical axes and a central hole that allows the X-ray beam to pass undisturbed. If the localized illumination on the specimen is created with optics with long focal lengths, such a set-up can be placed between the focusing elements and the sample. In the frequently used pinhole-based ptychographic set-ups, however, a location downstream of the sample should be considered if the sample is to be monitored also during data collection. In cases where the sample can also be illuminated from the back and is sufficiently transparent in the visible wavelength regime, the microscope may also be operated in transmission mode. If necessary, also various spectroscopic techniques can be implemented in this on-axis fashion (OWEN ET AL., 2009).

Compared with the previously discussed X-ray eye, the only major disadvantage may be in some cases the different contrast mechanism, e.g. if one has to find structures buried inside a material which is not transparent to visible light.

5.3.6 Sample preparation

In order to first identify whether a sample is in general suitable for ptychographic imaging, the following questions should be considered:

1. What sensitivity is required and does the sample show sufficient X-ray contrast at the selected energy?

2. What is the size of the interesting features?
3. Given the previous two numbers, what X-ray fluence is required (compare (3.70) on page 112)?
4. How large is the area / volume that has to be imaged to obtain a statistically significant result?
5. What is the total scan time which is required to satisfy all the constraints imposed by the previous points?
6. Is there another technique that allows to answer the specific scientific questions associated with the specimen, but is faster, cheaper, easier accessible, or less challenging to perform?
7. Can the sample be prepared in a suitable way in terms of size and shape, mechanical and thermal stability, and radiation hardness?

The actual preparation of the specimen in order to fit the requirements sketched in question 7 depends on the one hand on the specific type of sample to be investigated. On the other hand, also the actual ptychographic set-up imposes certain constraints, based e.g. on the maximum possible scan range or the X-ray energy. The required preparation steps can be grouped into two categories:

Fixation Samples for PCDI have to be rigid and mechanically stable, in particular while scanning them in stop-and-go mode. Especially biological samples with high water content, which are also very sensitive to radiation damage, will typically have to undergo a fixation procedure, which can either be chemical or cryogenic. Also for materials that come as powders, which can usually easily be spread onto a substrate transparent to X-rays, some additional adhesives may be required to fix the position of the particles.

Shaping An important criterion for the size and shape of the sample is the requirement that it has to be sufficiently transparent to the employed X-rays. This includes also any structures supporting the specimen that are in the beam path, like e.g. glass capillaries or silicon nitride membranes. Furthermore, the thickness should stay in the regime where the wave factorization assumption is valid, i.e. that the exit wave ψ behind the object can be factorized into the two independent functions probe P and complex object transmission O , compare section 3.2.3 on page 94. For a typical pinhole-based PCDI experiment at cSAXS, (3.34) has been used to estimate an upper limit for the sample thickness in the

order of $100\ \mu\text{m}$ on page 96. Thicker samples will have to be thinned down, e.g. with a focused-ion beam, mechanical polishing or by thin-sectioning in a microtome.

$100\ \mu\text{m}$ is also a typical lateral range which can be covered with piezo-driven axes in a single scan. For tomographic PCDI, which is introduced in chapter 9, it is also preferable if the sample's extent perpendicular to the rotation axis does not exceed this lateral range. This way, each projection contains information about exactly the same volume, i.e. in each reconstructed tomographic slice the sample is completely surrounded by air. As a result, the necessary alignment of the projection images during a post-processing step can be implemented in a rather simple and robust way, which is introduced in section 9.2.4. Furthermore, artefacts associated with local tomography are avoided.

Sample preparation in the broader sense also includes mounting the final specimens in a way that allows not only sufficiently easy handling during the experiment, but also fits with the specific set-up. Details have already been discussed in the paragraph "Sample mounting" at the beginning of section 5.3.5 on page 151.

Part II

Advanced developments for two-dimensional ptychography

Chapter 6

Density “resolution”: weak-object imaging

This chapter discusses ptychographic CDI of low-contrast specimens. After reviewing in the first section the main challenges involved when imaging this class of objects, a demonstration experiment on a biological specimen consisting of *Magnetospirillum gryphiswaldense* is presented: A description of the experiment itself (section 6.2) is followed by the introduction of a new strategy for evaluating the scattering power of weakly scattering specimens (section 6.3). After discussing reference reconstructions as a means to obtain reliable starting guesses for illumination functions in section 6.4, the chapter concludes with the results obtained for the biological specimen (section 6.5). Most of the work presented in this chapter has been published in [DIEROLF ET AL. \(2010b\)](#).

Although many of these low-contrast specimens could be treated as weak phase objects, neither the corresponding approximation (1.29) nor any other additional constraints derived from it are used in the reconstruction process.

6.1 Challenges of imaging weakly scattering objects

As in traditional CDI, the imaging of weakly scattering objects proves to be more difficult also in the ptychographic variant of the technique. While of course the typically reduced signal-to-noise ratio plays a significant role,

there are some specific challenges:

Dominating probe diffraction When working with a localized illumination, the far-field diffraction signal is typically dominated by the contribution of the probe. This may be less of an issue in the case of a focused beam, where the far-field diffraction usually has a finite extent resembling the entrance aperture of the optics. However, a pinhole illumination will generate an Airy pattern covering the entire detector area on which signal from the specimen is expected (compare Figure 6.1(c) on page 166). From the raw diffraction data, it is therefore often impossible to infer what the scattering contribution of a weak specimen is (compare Figure 6.1(d) on page 166). A method to disentangle the diffraction signals of probe and object allowing quantitative assessment of the specimen’s scattering is presented in section 6.3.

Occurrence of raster grid artefacts The so-called raster grid pathology has been introduced in section 3.2.4.5 on page 99 as an ambiguity inherent to the ptychographic phase-retrieval problem in cases where the probe is retrieved alongside with the object. While the effects of this are often negligible in the case of strong scatters, they can be severe in the case of a weak object: Raster grid artefacts are dominating the reconstruction or even cause it to fail completely. Several methods to suppress this ambiguity have been discussed in section 3.2.4.5. In practice, the alternative scanning scheme of the “round scan” has usually been employed for weakly-scattering specimens, see Figure 6.1(a) on page 166.

Weak constraints on probe defocus Correct reconstruction of low-order phase modes can be difficult in two-dimensional CDI (MARCHESINI ET AL., 2006). The location of the reconstructed plane along the propagation axis corresponds to a quadratic phase factor in Fourier space, which is the lowest problematic order. In traditional CDI, typically a tight support is required to successfully handle this “defocus ambiguity”. In PCDI, one has the benefit that the multiplication constituting the overlap constraint (3.17) is only valid in the sample plane, assuming of course that the thickness of the specimen is below the limit given by (3.34).

However, in the case of a weakly-scattering specimen, stagnation at a wrong defocus distance or “focal plane” is more likely to occur as the probe diffraction pattern is only slightly modified by the object, as illustrated in panels (c) and (d) of Figure 6.1. Using a very good initial guess for the probe can improve convergence in these cases: As the probe is already very close

to the solution, its further refinement – yielding the final defocus – converges faster profiting from a greatly reduced search space.

Modelling from a few key experimental parameters is one way to obtain an accurate initial estimate for the probe (GIEWEKEMEYER ET AL., 2010). In section 6.4, a more robust approach is presented: It relies on a reference reconstruction done with a strongly-scattering specimen (Figure 6.1), is therefore model-free and can also deal with more complicated illumination functions.

6.2 Description of demonstration experiment

The experiment was carried out at the cSAXS beamline at an X-ray energy of 6.2 keV with the pinhole-based set-up for two-dimensional PCDI described in section 5.1.2. The pinhole used in this case had a diameter of about 2 μm and had been milled into a tungsten foil of 20 μm thickness by focused ion beam. Next to the biological specimen, *Magnetospirillum gryphiswaldense* on a silicon nitride membrane, a nano-fabricated Fresnel zone plate was mounted on the same holder as a reference object for the reconstruction of an initial guess for the probe (see section 6.4). The zone plate was provided by the X-ray optics group of Christian David at the Paul Scherrer Institute. The biological specimen was prepared by Ilme Schlichting and Konstanze von König at the Max-Planck-Institute for Medical Research as described in DIEROLF ET AL. (2010b): “Liquid cultures (50 ml) of wild-type *Magnetospirillum gryphiswaldense* MSR-1 (DSM6361) were grown microaerobically (FSM medium in 250 ml flasks), similarly as described previously (HEYEN AND SCHÜLER, 2003). The cells were pelleted by centrifugation and stored as glycerol stocks at -80°C . Prior to deposition on the silicon nitride membranes (Silson Ltd., $1.5 \times 1.5 \text{ mm}^2$ window size with 1 μm thickness) the cells were washed several times in 25 mM ammonium acetate pH 7.5.”

Attached to a two-dimensional piezoelectric scanning stage, the sample was translated to positions given by the round scan formalism introduced in section 3.2.4.5 on page 99 as depicted in Fig. 6.1(a). For the biological specimen, a round scan with $N_r = 11$ shells covering a total diameter of 10 μm in radial steps of $\Delta r = 500 \text{ nm}$ was used. To increase the dynamic range of the diffraction data, two exposures of 0.7 s and 7 s duration were combined at each of the 330 scan points.

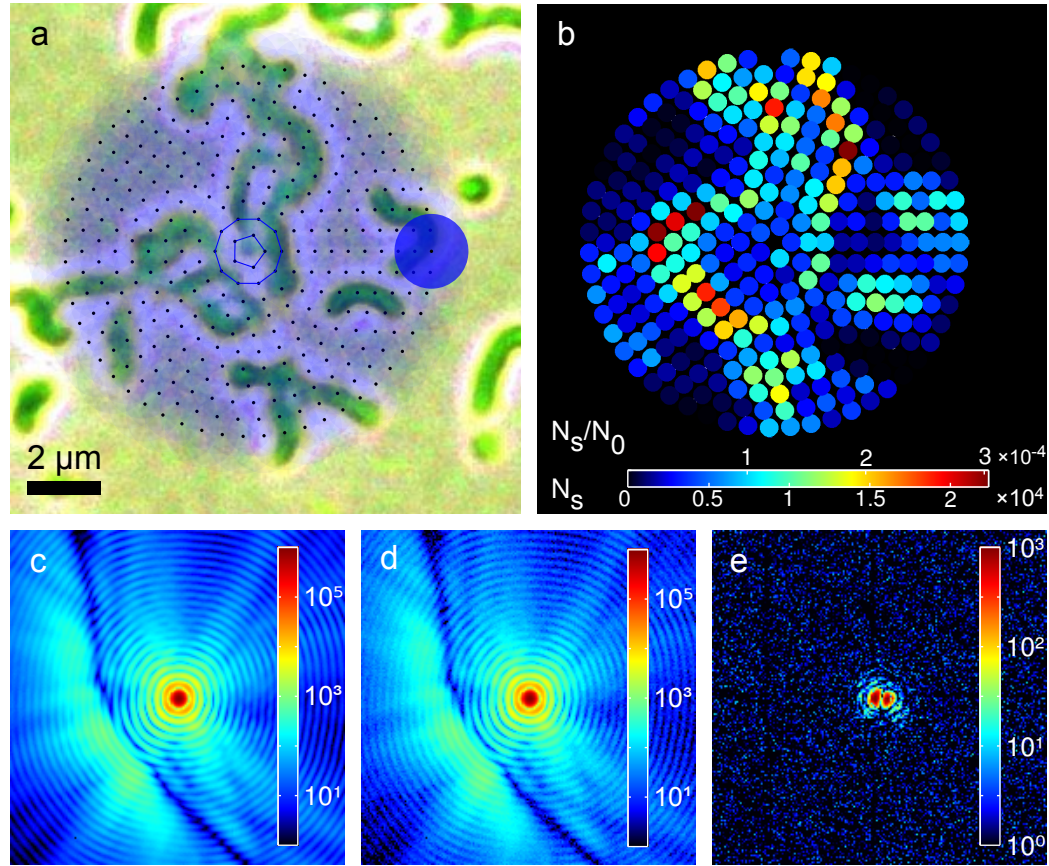


Figure 6.1: Evaluation of scattering power for a weakly interacting biological specimen. (a) Scan positions of the ptychographic data set overlaid on a visible light micrograph of the biological specimen (magnetotactic bacteria, *Magnetospirillum gryphiswaldense*). The circle on the right edge of the scan indicates roughly the extent of the illumination function. (b) Scattering power analysis: For each scan position, the number of scattered photons N_s and the ratio N_s versus N_0 are represented by the colour coding, where N_0 is the total number of photons incident upon the specimen. This analysis can provide an immediate online feedback on the location and scattering behaviour of the sample. The value of N_s at each position is calculated as follows: Low-noise diffraction data of the probe alone as shown in (c) is collected, here an average of 39 individual frames from empty areas of the specimen displaying the detected photon counts on a logarithmic scale. Together with the diffraction patterns at the respective scan positions – (d) shows one example at the location of a bacterium on logarithmic scale –, one obtains with (6.4) the signal distribution Ξ , shown in (e) on a logarithmic colour scale. From Ξ , N_s is obtained with (6.6). The prominent darker stripes running from top to bottom in panels (c) and (d) originate from a slight tilt of the illuminating pinhole with respect to the optical axis. The figure has been published in a modified version in DIEROLF ET AL. (2010b, © IOP Publishing Ltd and Deutsche Physikalische Gesellschaft, used with permission).

6.3 Evaluation of scattering power

If the diffraction of the probe is dominating the recorded diffraction patterns, the specimen can be treated as a weak phase object and its scattering contribution can be evaluated quantitatively: In this case, the exit waves can be approximated as

$$\psi(\mathbf{r}) \approx P(\mathbf{r})(1 + i\Phi(\mathbf{r})) =: P(\mathbf{r}) + iQ(\mathbf{r}) , \quad (6.1)$$

where the small effects of the phase shift Φ by the object on the incident wave field is represented as the perturbation Q . The scan point index j is omitted as the relations presented here have no j -dependence. Fourier transformation yields the corresponding far-field diffraction intensities

$$I(\mathbf{q}) \approx |\tilde{P}(\mathbf{q})|^2 + 2\Im[\tilde{P}^*(\mathbf{q})\tilde{Q}(\mathbf{q})] , \quad (6.2)$$

with \tilde{P} and \tilde{Q} representing the Fourier transforms of P and Q . A third term, quadratic in Φ , can be neglected. If one includes Poisson noise, the deviation from the probe diffraction intensity $I_0 = |\tilde{P}(\mathbf{q})|^2$ becomes

$$I(\mathbf{q}) - I_0(\mathbf{q}) \approx 2\Im[\tilde{P}^*(\mathbf{q})\tilde{Q}(\mathbf{q})] + \delta I(\mathbf{q}) . \quad (6.3)$$

We now assume that $\delta I(\mathbf{q})$ contains only the measurement error in $I(\mathbf{q})$, i.e. that the noise in the intensity pattern $I_0(\mathbf{q})$ of the probe can be neglected. This is based on the fact that the diffraction of the empty probe can be measured with very high precision as there are no limits to exposure times due to radiation damage.

If now the difference $I - I_0$ exceeds the expected noise level, this is interpreted as signal originating from the object. From the variance of the intensity $\text{var } I(\mathbf{q}) = I(\mathbf{q}) \approx I_0(\mathbf{q})$ this condition translates to $\Xi(\mathbf{q}) > 1$, with the “signal distribution” (see also Fig. 6.1(e))

$$\Xi(\mathbf{q}) = \frac{[I(\mathbf{q}) - I_0(\mathbf{q})]^2}{I_0(\mathbf{q})} . \quad (6.4)$$

Furthermore, this allows us to define a “local resolution” from the value q_{\max} of the maximum momentum transfer for which $\Xi(\mathbf{q}) > 1$ is observed. From that condition one can also derive an expression for calculating the number of photons scattered by the sample: Inserting (6.3) into the definition (6.4) and summation over all \mathbf{q} yields (see Infobox 6.1 for details)

$$\sum_{\mathbf{q}} \Xi(\mathbf{q}) \approx N_{\text{pix}} + 2 \sum_{\mathbf{q}} |\tilde{Q}(\mathbf{q})|^2 , \quad (6.5)$$

where N_{pix} is the number of pixels in a diffraction pattern. Solving for the number of photons scattered by the specimen $N_s = \sum_{\mathbf{q}} |\tilde{Q}(\mathbf{q})|^2$ one obtains

$$N_s \approx \frac{1}{2} \left[\sum_{\mathbf{q}} \Xi(\mathbf{q}) - N_{\text{pix}} \right]. \quad (6.6)$$

These calculations are not very demanding and can in principle be performed already during the measurements. So a direct feedback on the specimen’s scattering – and thus on the ‘local’ resolution via $\Xi(\mathbf{q}) > 1$ for $|\mathbf{q}| < q_{\text{max}}$ – is obtained already during data acquisition. This information may be used to directly adjust experimental parameters like exposure times accordingly. A plot of scattered photon numbers N_s as functions of scan positions provides a scattering map which allows to identify large features of the specimen and the scattering signal they produce. Comparison with the number of incident photons N_0 yields information on the local scattering cross-sections.

6.4 Reference reconstruction

As discussed in section 6.1 on page 164, reconstructions of weak scatterers are more prone to stagnation at a wrong propagation distance of the probe. To obtain an accurate initial guess of the illumination, which can greatly ease this problem, a strongly-scattering specimen is scanned in the same plane as the weak object. Most conveniently, this is achieved by mounting both samples on a common support. In the example presented here, a gold (Au) Fresnel zone plate had been mounted next to the biological specimen (magnetotactic bacteria). During data acquisition, both samples were scanned right after each other to make sure the probe guess obtained from the reference object was as close as possible to the actual illumination on the bacteria.

The test object was reconstructed from a ptychographic round scan with 140 points, combining always a short 0.7 s and a long 5 s exposure at each scan position to increase the dynamic range. Of each diffraction pattern – see Fig. 6.2(a) for an example – only the central $192 \text{ pixels} \times 192 \text{ pixels}$ were used in the reconstruction. This resulted in a pixel size for both the retrieved object (Fig. 6.2(c)) and the probe (Fig. 6.2(d)) of $43.5 \times 43.5 \text{ nm}^2$. As this only allows to barely resolve the zone plate structures, which are around 50 to 60 nm in size in this part of the specimen, one can infer that the main information on the probe is contained in the scattering arising from the two irregularly-shaped Au particles visible in Fig. 6.2(c). So very general strongly-scattering objects situated in the same plane as a weak object can be used as a reference. In particular, one could put such a reference scatterer

Inserting the intensity difference (6.3) into the definition (6.4) of the scattering distribution, one obtains

$$\begin{aligned}\Xi(\mathbf{q}) &= \frac{\left(2 \Im \left[\tilde{P}^*(\mathbf{q}) \tilde{Q}(\mathbf{q}) \right] + \delta I(\mathbf{q})\right)^2}{I_0(\mathbf{q})} \\ &= \frac{\delta I^2(\mathbf{q})}{\langle \delta I^2(\mathbf{q}) \rangle} + \frac{4 \left(\Im \left[\tilde{P}^*(\mathbf{q}) \tilde{Q}(\mathbf{q}) \right] \right)^2}{I_0(\mathbf{q})} + \frac{4 \delta I(\mathbf{q}) \Im \left[\tilde{P}^*(\mathbf{q}) \tilde{Q}(\mathbf{q}) \right]}{I_0(\mathbf{q})}.\end{aligned}\quad (6.7)$$

In the case of Poisson noise, it is by definition $\langle \delta I^2(\mathbf{q}) \rangle = I(\mathbf{q})$ and $\langle \delta I(\mathbf{q}) \rangle = 0$. So the first term on the right-hand side of (6.7) is on average equal to 1 and the last term averages to 0. Summation over all pixels N_{pix} in the diffraction pattern, i.e. over all scattering vectors \mathbf{q} , yields

$$\sum_{\mathbf{q}} \Xi(\mathbf{q}) \approx N_{\text{pix}} + \sum_{\mathbf{q}} 4 \left(\Im \left[\frac{\tilde{P}(\mathbf{q})}{|\tilde{P}(\mathbf{q})|} \tilde{Q}^*(\mathbf{q}) \right] \right)^2. \quad (6.8)$$

Expressing the Fourier transforms $\tilde{P}(\mathbf{q}) = |\tilde{P}(\mathbf{q})| \cdot \exp(i\chi_{\tilde{P}})$ and $\tilde{Q}(\mathbf{q}) = |\tilde{Q}(\mathbf{q})| \cdot \exp(i\chi_{\tilde{Q}})$ in terms of magnitude and phase, one gets

$$\sum_{\mathbf{q}} \Xi(\mathbf{q}) \approx N_{\text{pix}} + \sum_{\mathbf{q}} 4 \left| \tilde{Q}(\mathbf{q}) \right|^2 \sin^2 \left(\chi_{\tilde{P}} - \chi_{\tilde{Q}} \right). \quad (6.9)$$

When $\chi_{\tilde{P}}$ and $\chi_{\tilde{Q}}$ are treated as uncorrelated quantities, this results in $\langle \sin^2 \left(\chi_{\tilde{P}} - \chi_{\tilde{Q}} \right) \rangle = \frac{1}{2}$, and (6.9) can be simplified to

$$\sum_{\mathbf{q}} \Xi(\mathbf{q}) \approx N_{\text{pix}} + 2 \sum_{\mathbf{q}} \left| \tilde{Q}(\mathbf{q}) \right|^2. \quad (6.10)$$

Solving for $N_s = \sum_{\mathbf{q}} \left| \tilde{Q}(\mathbf{q}) \right|^2$, the total number of photons scattered by the specimen, gives (6.6).

Info box 6.1: Derivation of the term (6.6) for calculating the number of photons scattered by a weak phase object.

directly onto the substrate holding a biological specimen, e.g. in the form of colloidal gold.

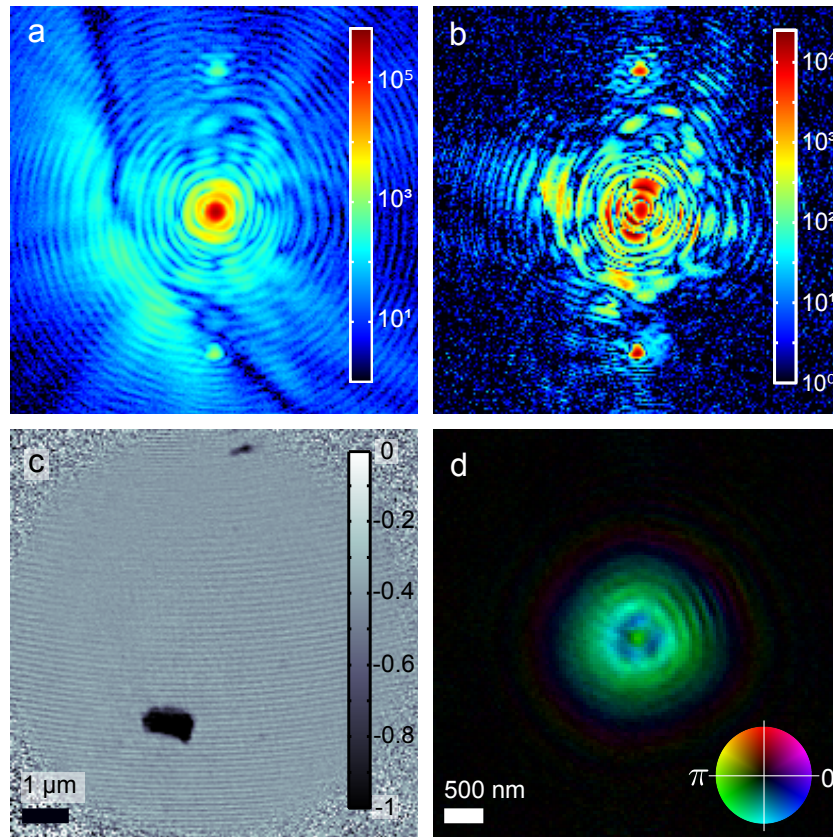


Figure 6.2: Imaging of a Au Fresnel zone plate structure as a reference for retrieval of the incident probe. **(a)** Exemplary diffraction pattern (logarithmic scale). **(b)** Calculation of the signal distribution according to (6.4) using the diffraction data in (a). Although the quantitative relations are not fulfilled for this strong scatterer, a qualitative comparison with Fig. 6.1(e) shows the large difference in signal strength. **(c)** Ptychographic phase reconstruction: In the imaged area, the Fresnel zones have widths of about 50 to 60 nm, thus the pixel size of $43.5 \times 43.5 \text{ nm}^2$ allows only barely to resolve them. The main information for the probe reconstruction originates from the two irregularly-shaped Au particles visible on top of the zone plate. **(d)** Reconstructed probe (colour-coded complex image, see colour wheel). In the reconstruction of the biological specimen (see Fig. 6.3), this probe was used as the initial guess for the illumination. This figure has been published in DIEROLF ET AL. (2010b, © IOP Publishing Ltd and Deutsche Physikalische Gesellschaft, used with permission).

6.5 Ptychographic reconstruction of a biological specimen

The scattering analysis in Fig. 6.1 showed that all the signal from the specimen was contained within the innermost 192×192 pixels of the diffraction patterns. As a starting guess, the probe obtained from the reference recon-

struction discussed in section 6.4 was used. However, the illumination was not fixed during the reconstruction process: the usual probe-retrieval scheme allowed it to adapt to any differences compared to the reference scan, in particular concerning the correct probe defocus. The final reconstruction of the illumination is shown in Fig. 6.3(a). The retrieved complex wavefield can be numerically propagated along the optical axis. Propagation to the plane of the pinhole aperture (Fig. 6.3(b)) reveals its slightly irregular shape. From a longitudinal cut through the propagated wave field (Fig. 6.3(c)), a distance of about 1.5 mm between pinhole and specimen is determined.

The phase shift Φ of the object itself is displayed in Fig. 6.3(d). This result was obtained after 200 iterations of the PCDI algorithm based on the difference map introduced in section 3.2.2. It is an average of 20 iterates chosen in-between iterations 100 and 200, i.e. from the steady-state regime of the difference map (compare section 3.2.4.1) which had been reached after 75 iterations. The maximum observed phase shift is about one order of magnitude smaller than for the reference object in Fig. 6.2. Although the assumption of a weak phase object was not at all enforced in the reconstruction, the bacteria are not visible in the retrieved amplitude which verifies that this assumption was sound.

Combining the relations (1.28) and (1.24) on page 23, the phase shift Φ can be converted into a map of the projected electron density $n_{e,\Delta z}$ (see second colour bar in Fig. 6.3(d)) using

$$n_{e,\Delta z}(x, y) = -\frac{\Phi_{\Delta z}(x, y)}{r_e \lambda}, \quad (6.11)$$

with the X-ray wavelength λ and the classical electron radius r_e . The index Δz was added to point out that at each point (x, y) of the reconstruction the measured phase shift – and thus also the calculated electron density – is an integrated value over the corresponding sample thickness Δz .

Resolution and dose For a first rough estimate of the maximal achievable resolution of the reconstruction, we use the signal distribution $\Xi(\mathbf{q})$ as defined in (6.4) on page 167. From Fig. 6.1(d) on page 166 it already becomes clear that the scattering contribution of the specimen drops to negligible signal-to-noise ratios much faster than the probe signal. Using the earlier introduced cut-off criterion $\Xi(\mathbf{q}) > 1$ for $|\mathbf{q}| < q_{\max}$ on the average of $\Xi(\mathbf{q})$ over all collected diffraction patterns results in $q_{\max} \simeq 0.4 \mu\text{m}^{-1}$, which corresponds to a half-period real space resolution of around 200 nm, about one tenth of the diameter of the illumination.

For a more precise evaluation of the upper bound of the resolution, the statistical approach employing relation (3.70) introduced on page 112 is used.

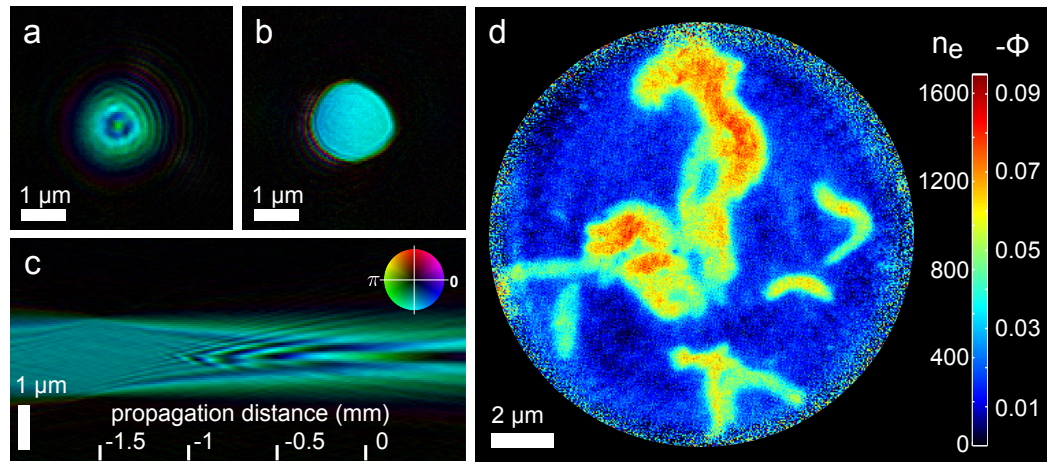


Figure 6.3: Ptychographic reconstruction of a *Magnetospirillum gryphiswaldense* sample. (a) Colour-coded representation (see colour wheel) of the complex probe reconstructed simultaneously with the object from the same ptychographic data set. (b) Numerical back-propagation of the probe to the plane of the pinhole, which reveals that the aperture was located around 1.5 mm upstream from the scanning plane. (c) Slice (parallel to the beam) through the wave field obtained by numerically propagating (a). (d) Phase part of the ptychographic reconstruction of the biological specimen. The colour bar indicates both the phase shift Φ and the projected electron density n_e (per \AA^{-2}). The pixel size of the reconstruction is again $43.5 \times 43.5 \text{ nm}^2$. This figure has been published in [DIEROLF ET AL. \(2010b\)](#), © IOP Publishing Ltd and Deutsche Physikalische Gesellschaft, used with permission).

From the variance of the absorption part (after normalizing to a mean of 1), a value of $\text{var } \Phi \simeq 2.56 \cdot 10^{-5}$ is determined. With a fluence estimate of $6.7 \cdot 10^5 \text{ } \mu\text{m}^{-2}$, this results in $\sqrt{A_{\text{pix}}} \simeq 242 \text{ nm}$ for the side length of an effective resolution element (half-period) in this reconstruction.

The total dose D absorbed by the specimen is estimated using an empirical protein model (see [HOWELLS ET AL. \(2009\)](#), chemical formula $\text{H}_{50}\text{C}_{30}\text{N}_9\text{O}_{10}\text{S}_1$, density 1.35 g/cm^3 , optical constants obtained from [HENKE ET AL. \(1993\)](#)) to be about $D \simeq 1.7 \cdot 10^3 \text{ Gy}$, well below the feature-destroying limit.

Chapter 7

Ptychography with information sharing between data sets

This chapter discusses reconstruction approaches based on sharing information between multiple ptychographic data sets which provide improved performance in certain cases. After discussing the motivation for such procedures in section 7.1, section 7.2 introduces three basic concepts of sharing. These are applied to simulated data sets in section 7.3 and experimental ones in section 7.4.

7.1 Motivation

As in all coherent diffractive imaging schemes, the resolution in ptychographic CDI is ultimately limited by the maximum solid angle for which diffraction data of still sufficiently high quality can be detected (compare section 3.3). However, collection of large-angle scattering signal often results in cases where diffraction data at certain spatial frequencies is missing in some data sets but present in others. One example is the use of multiple exposures of different durations taken at the same scan positions. If for the longer exposures a beam stop is required to protect the detector from the intense central part of the beam, it is usually impractical to do the multiple exposures right after another at each scan point as the movement of the beam stop would create too much overhead. Therefore, typically first the full scan has to be performed with the short exposure time and then the same scan has to be repeated with the longer exposures and the beam stop in place. The classical approach would be to replace the pixels shaded by the beam stop in the long exposures with the intensities of the same pixels in the short expo-

sure scaled with the ratios of the acquisition times. However, this method is sensitive to potential deviations in the illumination's position for repeated scans, which may either be caused by insufficient repositioning accuracy or drift of the specimen. To avoid this problem, a reconstruction approach with a single object shared by multiple data sets and an inherent mechanism for drift correction is introduced in section 7.2.2.

Another example are the insensitive areas in modern tiled detectors, e.g. the gaps between the modules of a PILATUS system. To collect data at all spatial frequencies, again multiple scans are required for each of which the detector is transversely translated to a different position with respect to the optical axis. Section 7.2.1 introduces a reconstruction scheme in which multiple data sets share a single probe, which not only avoids errors the direct combination of diffraction data may cause, but even allows to use scans taken on completely different areas of a specimen.

In practice, the achievable resolution in CDI is typically not only limited by the available coherent X-ray flux or the feasibility of long enough exposure times, which both determine the quality of the diffraction data. Often the most important constraint is radiation damage to the specimen (HOWELLS ET AL., 2009), in particular for biological samples. In PCDI, one additionally has to consider that the regions of the object which are illuminated multiple times during a ptychographic scan have to withstand radiation damage for all these exposures. This makes it very hard to assess the effects of very long exposures required for high resolutions on the specimen. Furthermore, also relative movements of the illuminating probe and the object during such long exposures may lead to degradation of the reconstructed image. Section 7.2.2 illustrates how these issues can be addressed by the approach of a shared object no longer relying on long-exposure scans or direct summation of diffraction patterns.

7.2 Concepts

7.2.1 Reconstruction with a shared probe

This approach has been developed in the context of high-resolution PCDI experiments at the cSAXS beamline: In order to make use of a large detector area, one has to address the problem of missing regions in the diffraction data due to the intermodule gaps (compare the description of the PILATUS 2M detector on page 130 in section 5.1.1.6). Data for the missing spatial frequencies is obtained by shifting the detector perpendicular to the optical axis by distances larger than the gap sizes. Being a very slow process, however,

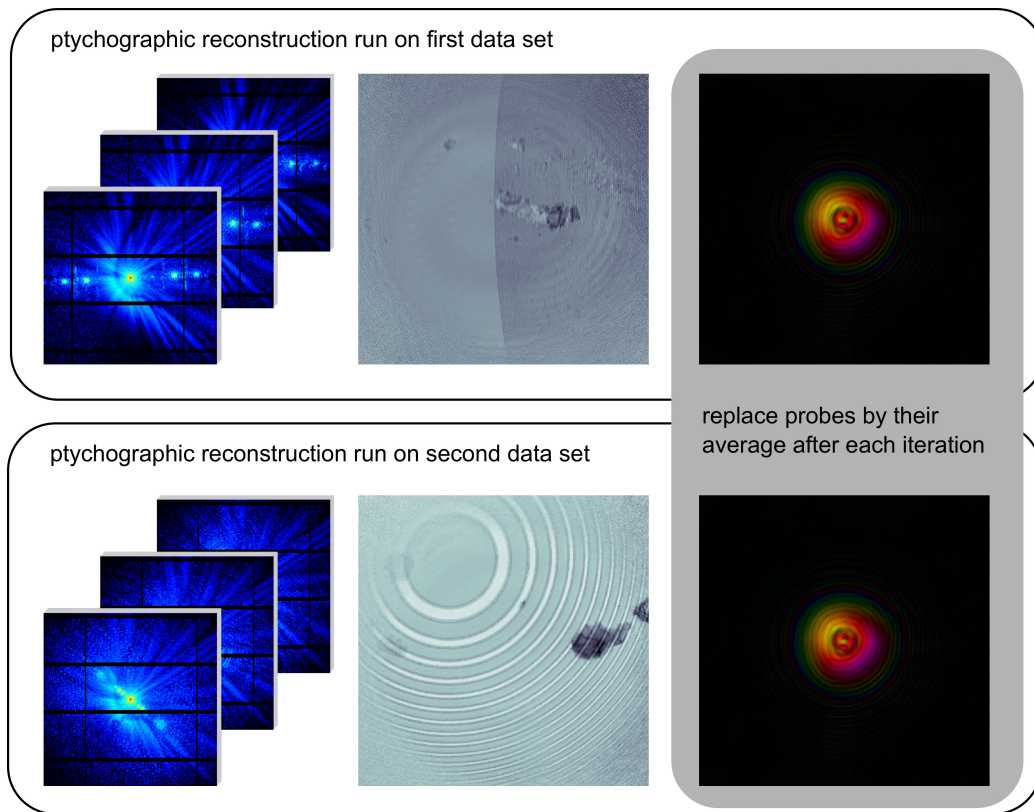


Figure 7.1: Implementation of ptychographic reconstruction with a shared probe. In this case, two reconstructions as indicated by the black frames run in parallel, but the approach can easily be scaled up to more parallel jobs. Each run works with its own diffraction patterns (left), object (centre) and probe (right). As shown here, different part of the objects can be scanned. In the diffraction data, certain spatial frequencies are missing as they fall into the gaps between detector modules, visible here as horizontal and vertical black lines. However, the missing frequencies are different for the two data sets as there is an offset of the detector position. Sharing of the probe is implemented using message passing: after each iteration, one of jobs collects all the probes broadcast by all the others, averages them and re-broadcasts the resulting average probe to all other jobs where it replaces the current probe. Probe sharing can also be implemented as a special case of the “hybrid approach” discussed in section 7.2.3, which is now the more frequently-used approach and also allows for a more flexible way of parallelization.

it is not feasible to repeat this for every scan point individually. Therefore, usually first a full scan is done at one detector position which is followed by one or more scans for which the detector has been shifted, quite similar to the procedure discussed in the previous section for cases in which a beam stop is used. Direct combination of the diffraction patterns from the different scans into new ones in which the respective missing gaps are filled with the pixels from one of the shifted frames is straightforward. But it requires

repositioning accuracy and drift stability better than the resolution one is aiming for. In particular for very high resolutions, this condition may easily be violated, leading to degradation of the fine details in the reconstruction. The concept of a shared probe is designed to avoid this problem.

Sharing of the probe amongst otherwise independent reconstructions of the data sets with multiple detector positions requires it to be stable during the whole data acquisition. In this context “stable” means, that the structure of the illumination must not change. Differences in the total intensity, however, may be tolerated, because they only affect the reconstruction of the absorption part but not of the phase shift. During various beamtimes at the cSAXS beamline, the assumption of the probe’s structure being stable was found to be valid on a scale of many hours, if the set-up and the beamline optics were in thermal equilibrium.

The prerequisite of a stable probe being met, multiple data sets are collected such that spatial frequencies missing in one are present in at least one of the others. For the PILATUS 2M, three data sets are required: During acquisition of the first, the beam is centred on the detector. For the other two, the detector is shifted along its diagonal once in positive and once in negative direction. Then ptychographic reconstruction runs are started in parallel on all these data sets. This is illustrated in Fig. 7.1, which for simplicity only shows two parallel jobs.

During every single ptychographic iteration, the probes in each of the runs are set to their common average. This is done by message passing between the parallel processes: one of the jobs collects the probes that the others broadcast, averages them and re-broadcasts this average probe to all other reconstruction runs where it replaces the respective current guess of the probe. Thus the average probe contains contributions of all spatial frequencies present in any of the diffraction patterns.

In ptychography, the latter are a convolution of the diffraction signals of probe and object. Because of this, retrieving the probe with a complete Fourier spectrum from multiple scans at once allows in turn to reconstruct each individual object just from a single scan despite the missing spatial frequencies: The convolution operation efficiently distributes the scattering contribution of certain length scales in the object, which would normally fall into one of the detector’s insensitive regions, to other areas of the diffraction patterns. However, for this the extent of the probe’s diffraction signal has to be larger than the size of the gaps, which is usually fulfilled in ptychographic CDI. So despite the presence of missing areas in the detector frames, the measured data still contains all information on the object. Complete knowledge of the probe allows an accurate separation of the respective contributions of illumination and object and therefore complete retrieval of the latter. This

has the practical implication that although one has to obtain three different scans with shifted detector positions, they can be performed on completely different parts of the specimen. In Fig. 7.1, e.g., the run in the upper frame employs data taken close to the edge of a Fresnel zone plate test specimen, while in the run below the central part of the same specimen is imaged. The multiple scans might even be done on completely different specimens under the condition that these are placed at exactly the same position along the optical axis, which in practice may only be achieved for objects of equal thickness mounted in close proximity on the same sample holder.

7.2.1.1 Special case: sharing the probe with an empty object

In a quite different context, the concept of probe sharing may also be used to prevent the built-up of arbitrary phase ramps (compare section 3.2.4.3, page 98) and of raster-grid artefacts (compare section 3.2.4.5, page 99). In this case, the data frames of one of the scans sharing a common illumination contain only the diffraction of the probe, i.e. signal taken without any object in the beam. These diffraction patterns can be associated with an artificial two-dimensional object, which has to fulfil the constraints that both its amplitude and phase are flat, i.e. the amplitude should be one everywhere and the phase must not show a ramp. If these are applied in a shared-probe reconstruction, on the one hand the phase ramp of the probe is fixed to the orientation by this empty scan which guarantees that empty areas around any object in the parallel reconstructions on real specimens would show no ramp. Thus these objects' phase ramps are automatically corrected during the reconstruction and there is no more need for empty reference regions within the individual reconstructions themselves as usually required for post-reconstruction phase ramp removal. On the other hand, forcing a flat amplitude and phase provides the necessary breaking of symmetry to suppress a possibly developing raster grid pathology. Potential refinements of the approach are still under investigation, e.g. forcing the object not to be completely flat but rather allow for some fluctuations of the amplitude and phase values around their fixed averages to account for noise in the data.

In section 7.3.2 on page 183 this approach is demonstrated with simulated data.

7.2.2 Reconstruction with a shared object

In this approach, many ptychographic data sets share the same object during the reconstruction while each has its individual probe. If a detector without readout noise is used, this can be employed to improve the statistics of a

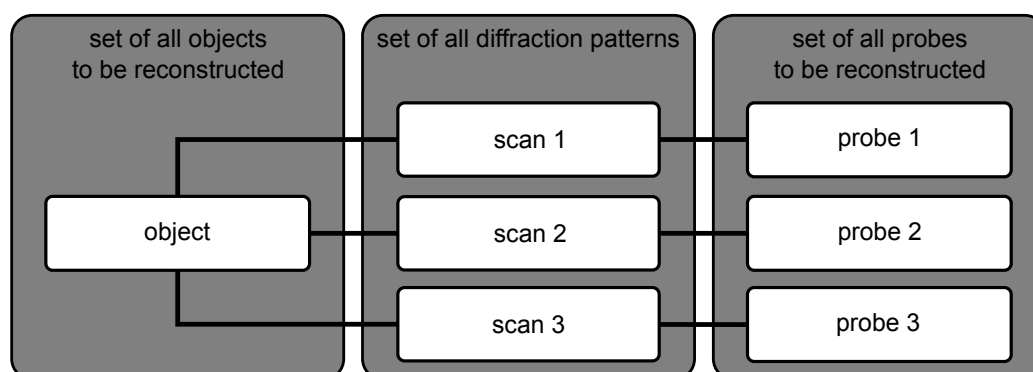


Figure 7.2: Ptychographic reconstruction scheme in which multiple data sets share the same object. In this example, three ptychographic scans of the same object are combined. While each scan is associated with the same object, a separate probe is assigned to each of them, which e.g. allows for the reconstruction to automatically compensate offsets in the relative positions of probes and object which might be introduced between the individual scans, see also section 7.3.3 for an example. Some details of the practical implementation of a shared-object reconstruction are discussed in the current section 7.2.2, but it is now typically treated as a special case of the “hybrid approach” detailed in section 7.2.3.

reconstruction: Instead of very long exposures at the individual scan points, one can combine the data of many short consecutive ptychographic scans of the same region on the specimen. This has several advantages:

- The sensitivity to drift and relative movements of probe and object during acquisition is reduced, as the individual ptychographic scans are quite short.
- By enforcing a shared object, inter-scan offsets in the scan positions are compensated by corresponding shifts of the probes such that the common object remains unaffected.
- As each of the short scans has its individual probe, long-term changes of the illumination have less effect than in a single scan of the same duration for which a stable probe is assumed for the whole scan.
- The individual scans may contain missing regions in the diffraction data, e.g. caused by the use of a beamstop, if in the entirety of all data sets all spatial frequencies of the common object are present.
- The approach is better suited for radiation sensitive samples: The requirement of overlap in PCDI results in sample regions being illuminated multiple times. If the exposures at individual scan positions are very long, the specimen may be damaged in the overlapping regions

before the scan can be completed. The multiple short scans can be used to slowly approach the radiation damage limit and discard data taken after the specimen has been damaged, similar to the approach used in X-ray crystallography, where radiation damage is often assessed by the fading of high-resolution Bragg peaks in repeated measurements (HOLTON, 2009).

A major disadvantage of the approach is the large increase in data volume: As more than 100 short scans may be used to replace a single long scan, the amount of diffraction patterns can easily increase by about two orders of magnitude. Therefore, an implementation like introduced in section 7.2.1 for the case of a shared probe for which each reconstruction is executed on an individual processor core would only be possible on rather large compute clusters. Again the processes would have to communicate by message passing. Also each of the cores would need to have enough memory attached to keep the respective ptychographic data set in RAM.

Given these constraints, one usually has to resort to different solutions which can also run on desktop machines or small compute clusters more widely available. If it is possible to hold all data in memory at once, an approach that no longer requires a one-to-one mapping of data sets to available processor cores can be used. As this increase in flexibility allows to also implement various combinations of probe and object sharing, this method is referred to as “hybrid approach” and further discussed in more detail in section 7.2.3. This implementation has also been used to obtain the results presented in sections 7.3.3 and 7.4.2.

7.2.2.1 Sequential approaches for shared object reconstructions

If the reconstruction cannot operate on the entirety of all ptychographic data at once, a sequential implementation with frequent hard drive access for reading and writing may become necessary. While the first applications of shared object reconstructions were still based on such a sequential approach, it has later been abandoned – upon availability of sufficient computing hardware – in favour of the implementation presented in section 7.2.3. However, as the sequential scheme is a good starting point for a generalized combination of shared-object and tomographic PCDDI, it is briefly introduced here.

To have the most benefit from the self-correction effects of using individual probes for each data set, one would also like to share the object between the individual reconstructions as frequent as possible, ideally once every ptychographic iteration. Taking all these aspects into consideration, a simple scheme for the reconstruction with a shared object in a fully sequential way

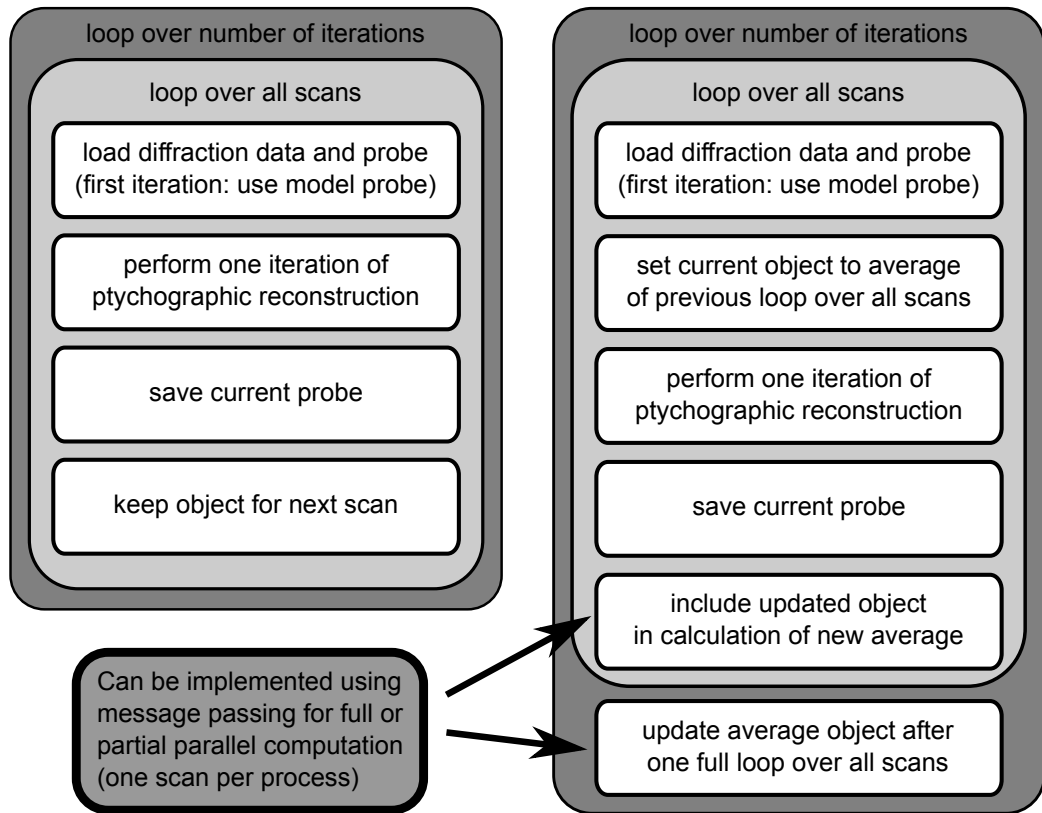


Figure 7.3: Proposals for sequential implementations of ptychographic reconstruction with a shared object. **Left:** The reconstructions of the individual data sets work with the same object sequentially: when it has been updated during a single ptychographic iteration using diffraction data and probe of one scan, this new version is used as the input object for the next scan’s iteration. **Right:** Modification of the sequential scheme which allows to run parallel reconstruction jobs on the individual scans: The parallel processes synchronize with an average of all objects only after all of the runs have completed their respective ptychographic iteration.

can be developed, see left part of Fig. 7.3. The basic idea is similar to the original PIE algorithm for ptychographic reconstructions: In PIE the object is updated sequentially following the scan position by iterating one-by-one through the diffraction patterns (compare section 3.1.4.2). The reconstruction approach here employs the same concept of a sequential object update not for multiple diffraction patterns but rather for multiple full ptychographic data sets.

The right side of Fig. 7.3 shows a slight modification of the algorithm which allows to make at least some use of distributed computing: All ptychographic iterations start from the same object which is the average of all objects retrieved for the individual scans in the previous iteration. There-

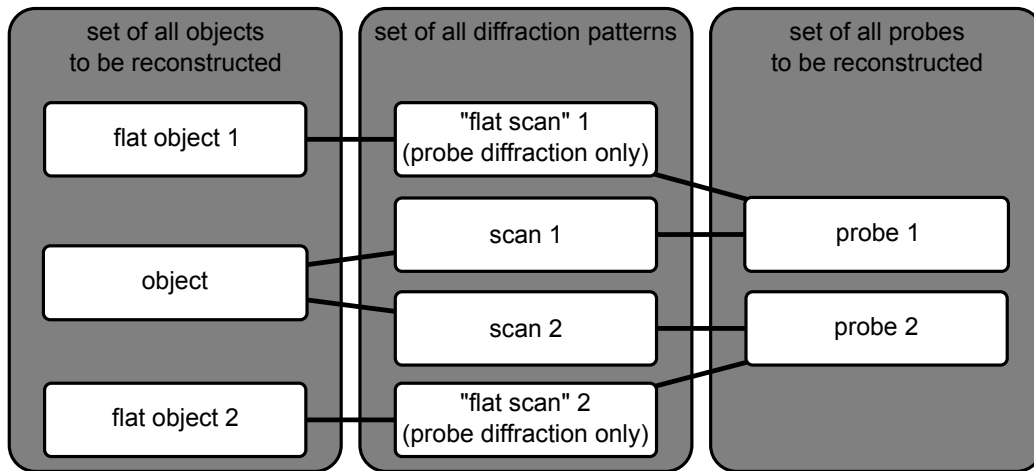


Figure 7.4: Scheme for an application of a hybrid approach for data set sharing in a ptychographic reconstruction illustrated for an example of two scans plus an “empty” one: Both scans share the same object, but have independent probes. The latter are both shared with an “empty” scan, which only contains diffraction patterns of the respective probe alone. The corresponding objects are constrained to be flat, i.e. reset to zero absorption and zero phase shift at each iteration.

fore, the reconstructions on the individual scans can run in parallel updating the common object, e.g. via message passing, only after for each scan the respective ptychographic iteration has been completed. Although the hardware limitations discussed above will still make frequent hard disc accesses necessary, at least a couple of data sets can be processed in parallel on a small cluster to improve speed compared to the fully sequential approach shown in the left part of Fig. 7.3.

The major drawback of any sequential implementation is the increase of time required for the reconstruction. In the implementations proposed here, a gain in speed could be achieved if more than one ptychographic iteration was done for each scan before continuing with the next data set or – in the second approach – averaging the object. The main benefit would be the reduction of the necessary hard disc accesses. However, as also the cross-talk between the data sets would decrease accordingly, effects on the convergence behaviour were to be expected.

7.2.3 Hybrid approach

In the recent implementation in the Python-Ptychography-toolbox by Pierre Thibault, multiple scans of the same type can share both probes and objects in various patterns, i.e. along with a list of scan numbers identifying the different data sets, an index-array is passed which determines the sharing

between these scans: By default, each scan has its own object and probe. Adapting the index-array accordingly, sharing of probe and object amongst multiple data sets can be tuned. In particular, combinations of the two approaches introduced in the previous sections are possible.

The **actual implementation** achieves this by no longer employing separate parallel reconstruction processes for the individual scans but rather using the diffraction data of all scans at once. The algorithm then initializes the required number of independent objects and probes and links them to the data of the different scans according to the data sharing settings defined in the index-array. How this approach enables a highly flexible intermixing of data sets is schematically shown in Fig. 7.4 for a set of two scans: Both scans share the same object while for each an individual probe is reconstructed. Each of the two probes is shared with a third data set, which contains diffraction patterns of the probe only and for which the corresponding object is constrained to full transmission and no phase shift. How this suppresses the built-up of raster grid artefacts and arbitrary phase ramps in the reconstructions has been discussed on page 177 in section 7.2.1.1. The need to treat the object for this “empty” scan according to these constraints is implemented by associating the corresponding part of the diffraction patterns with a “flat object”-flag, which not only links them to the flat object but is also used to modify the object update routines as required.

Limitations of the approach are mainly due to the fact that typically all data sets have to be kept in memory simultaneously. As discussed in section 7.2.2, this can be a major issue for shared-object reconstructions with many data sets.

Parallel computing is no longer implemented as an essential part of the shared-information approach using one reconstruction process per scan, but rather on a more global scale: Equal portions of all diffraction patterns are distributed on the available workers. Each reconstruction thread therefore works on a different part of the data. During each iteration, the so-called “all-reduce” command of the message passing interface (MPI) is used on the object and probe arrays. It combines the values of all parallel processes and re-distributes the result. By this, the MPI implementation behaves exactly the same as a standard single-thread PCDI reconstruction for any number of parallel jobs. As each job only loads its specific part of the whole data, this approach would even allow to reconstruct full shared-object data sets with more than 100 individual scans. This would require a sufficiently large cluster, such that the cumulative memory of all nodes used can hold the entire data, but each individual node only has to come with a moderate amount of memory.

7.3 Simulations

7.3.1 General parameters

The object used for the simulations presented here was obtained – in order to have it cover a wide range of spatial frequencies – from a fractal of the Julia set generated by 30 iterations of $z_{n+1} = z_n^2 + c$ with $c = -0.58 + 0.58i$ starting from the complex array $z_0 = x_0 + iy_0$ (2001×2001 pixels) with $x_0 \in [-1, 1]$, $y_0 \in [-1, 1]$. The amplitude of this procedure’s result was cropped to the range $[0, 2]$ and used to generate the complex object transmission function, in this case resulting in a amplitude in the range $[0.6, 1]$ and a phase shift in the range $[0, 0.4\pi]$ radians.

The ptychographic data was created from this object using parameters typical for experiments at the cSAXS beamline: 6.2 keV X-ray energy, 172 μm detector pixel size, 7.22 m distance from object to detector, 128×128 pixels diffraction pattern size and 2.5 μm diameter of illuminating pinhole. The actual probe incident on the object is generated by blurring a disc of this size with a Gaussian and propagating the result by 1.2 mm. For the respective simulations, this probe was scanned relative to the simulated object utilizing different scan patterns. The pixel values in the resulting diffraction patterns are rounded to integer values to account for the single-photon counting behaviour of the detector. Optionally, Poisson noise can be added to the data.

7.3.2 Sharing the probe with an empty object

This simulation was performed to demonstrate the approach introduced on page 177 in section 7.2.1.1. In this case, the fractal object introduced in the previous section was scanned with a 21×21 raster using a step size of 1.4 μm . In addition, 441 diffraction patterns of the probe alone were stored as the scan of a flat (empty) object. In both cases, no Poisson noise was applied to the diffraction data.

The generated data was processed with the Python ptychography package routinely used for the reconstruction of experimental data. 300 iterations of the difference map PCDI algorithm (see section 3.2.2) were followed by 100 iterations of maximum-likelihood refinement (see section 3.2.5). For the empty scan, the corresponding object during each iteration was set to a flat amplitude of one and zero phase shift while its probe was shared with the second scan containing the fractal object.

That the probe-sharing with a flat object efficiently suppresses both raster grid artefacts and arbitrary phase ramps can be seen in Fig. 7.5 on page 184.

7.3.3 Shared-object reconstruction in the presence of inter-scan sample drift

To avoid the need for additional constraints to suppress raster grid artefacts, round scans following the definition (3.43) on page 101 were used for this simulation. Two data sets were created, both with a radial step size $\Delta r = 1 \mu m$, $N_r = 13$ radial shells and $N_\theta = 5$ points in the first shell. This resulted in 455 diffraction patterns per scan. To model the effect of a drift of sample position between the two scans, their centres on the object were offset by 3 pixels vertically and 7 pixels horizontally. Three different types of ptychographic reconstructions were performed on the two data sets:

1. Individual reconstruction of each scan, i.e. a unique probe and a unique object for each scan.
2. Reconstruction of the averaged diffraction data: To model the approach of summing up multiple diffraction patterns for improved statistics, the average of the respective diffraction frames of the two scans at each scan position is used as input data. One obtains a single probe and a single object.
3. Reconstruction with a shared object: Following the ideas presented in section 7.2.2 on page 177, the two scans were reconstructed with a common shared object but two individual probes. By this, the phase retrieval process was given the freedom to compensate the object's shift between the scans by shifting the probes accordingly.

In each of the three cases, reconstructions were obtained with 300 iterations of the difference map PCDI algorithm and further refined by applying the maximum-likelihood implementation for another 300 iterations.

Figure 7.5 (following page): Simulation results illustrating the effects of sharing the probe with a second object which is forced to be flat. **(a)** The reconstructed amplitude obtained with the standard ptychographic reconstruction procedure shows strong artefacts due to the raster grid pathology. **(b)** The artefacts are efficiently suppressed if the probe is shared with a flat object, i.e. a ptychographic data set which only contains diffraction patterns of the probe alone. **(c)** In addition to the raster-grid artefacts, the reconstructed phase also shows a slight ramp in the standard case. **(d)** With the flat object approach, empty regions of the object are forced to be flat preventing the built-up of a phase ramp. **(e)** Close-up view (with adapted colour scale) of raster-grid artefacts in the region marked by the black frame in panel (a). **(f)** Close-up view of the same area on the object when using probe sharing with the flat object, see black frame in panel (b). Some traces of the raster grid pathology are still visible on an adapted colour scale. **(g)** The comparison of the profiles along the red lines in panels (e) (blue curve) and (f) (red curve) illustrates the reduction of the artefacts' amplitudes by about one order of magnitude.

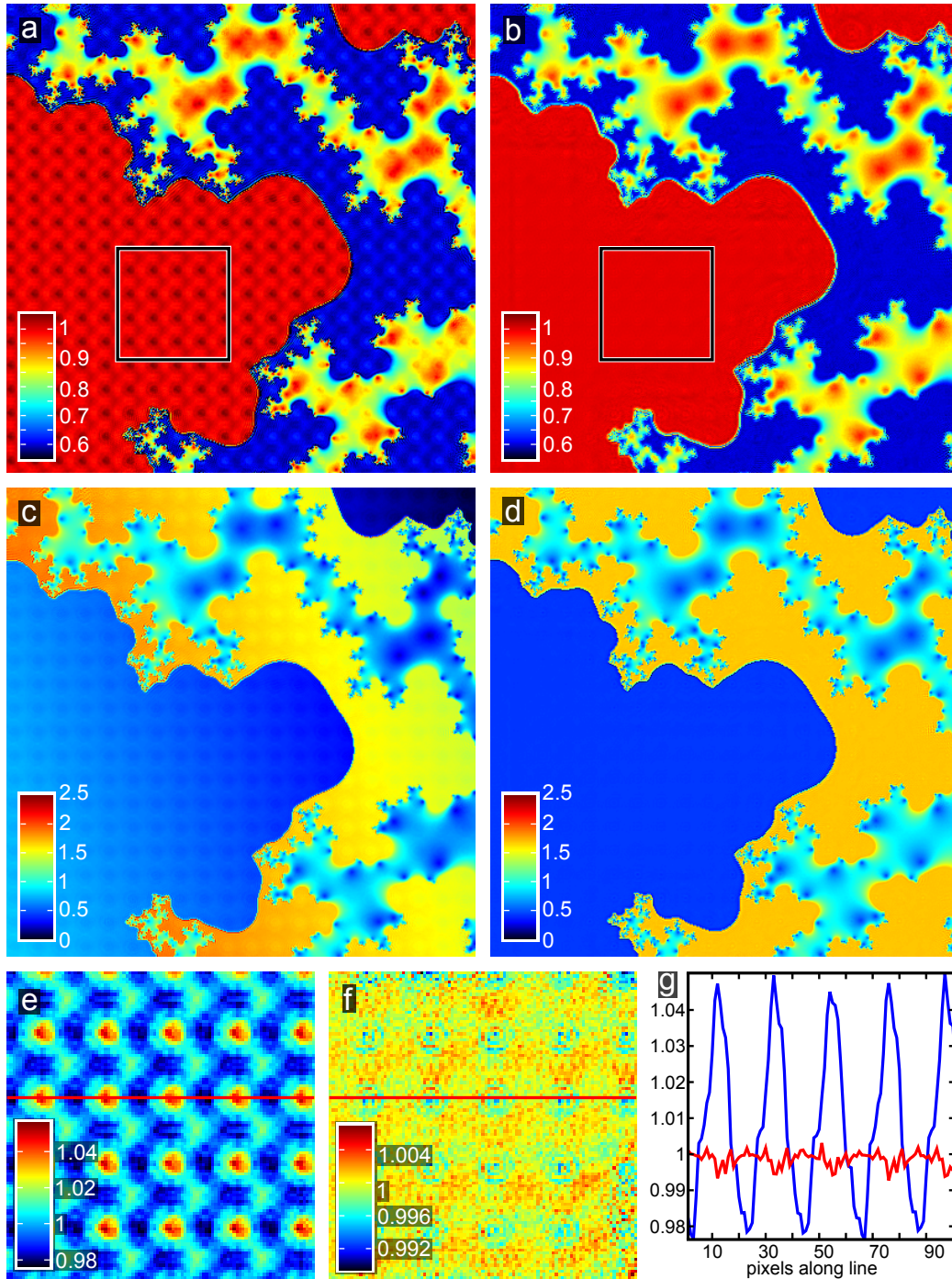
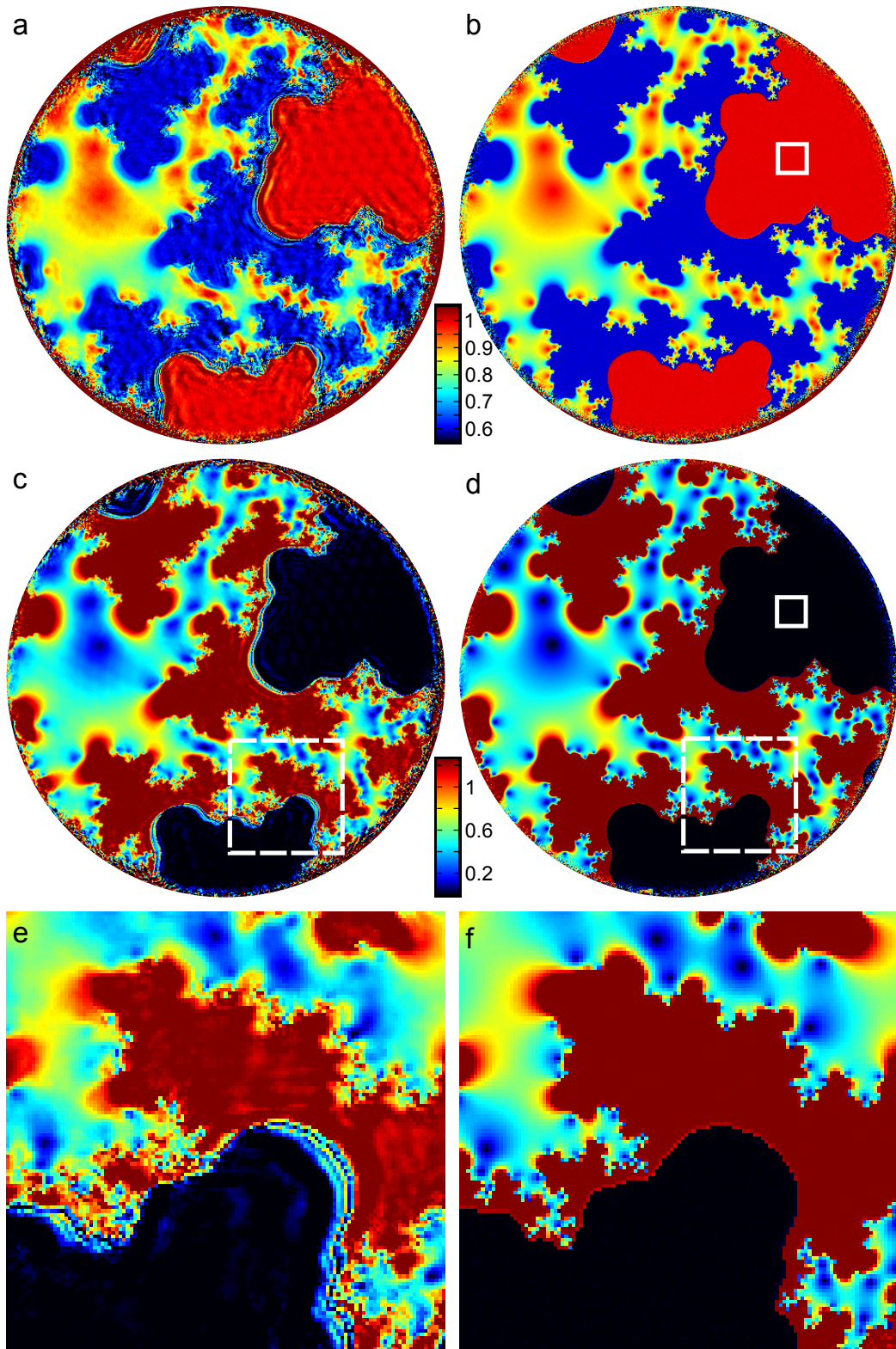


Fig. 7.6 on page 186 shows a comparison of the result obtained from the averaged data (left column) with the one from the shared-object approach (right column). It clearly demonstrates the ability of the shared-object method to correct for inter-scan drifts.

An individual reconstruction of a single scan is not shown as the result is indistinguishable by eye – down to the smallest visible features – from the case where the object is shared. However, as the number of contributing diffraction patterns and thus the incoming flux is doubled, one should be able to observe a difference in the variances of the reconstructed pixel values. To investigate this, the variances for an empty area of the object have been calculated for the phase and the amplitude part of both reconstructions. The selected region is marked by the white square with the solid border in panels (b) and (d) of Fig. 7.6. For the reconstruction of a single scan, one finds variances of $6.6 \cdot 10^{-6}$ for the phase and $5.6 \cdot 10^{-6}$ for the amplitude part. The shared-object result has variances of $3.3 \cdot 10^{-6}$ (phase) and $2.8 \cdot 10^{-6}$ (amplitude). The change in variance fits well with relation (3.70) on page 112 which links the incoming flux with both the size of the reconstructed pixels and their variance in value. As the pixel size in the reconstruction remains the same, the doubling of incident flux in the case of a shared object results in the observed reduction of the variance by a factor of two.

Figure 7.6 (following page): Comparing the result of reconstructing two simulated scans with a shared object (right column) to the one obtained from their averaged diffraction data (left column): **(a)** Amplitude reconstructed from the averaged data set. The large-scale structure of the object is successfully retrieved, but the reconstruction shows strong artefacts in areas that are supposed to be flat and fails for sharp edges and small features most affected by the offset between the scans. The colour-scale covers the range $[0.55, 1]$ as shown in the colour-bar between the two panels of the row. **(b)** The amplitude obtained with the shared-object approach. It does not suffer from artefacts in the flat areas and also small-scale features are reliably reconstructed in this case. The area marked by the white square has been used for comparing the variance of the retrieved values with the one obtained for the reconstruction of a single scan (see main text for details). **(c)** Phase part of the reconstruction from the averaged data set. Colour-scale covers the range of $[0, 1.25]$ radians, see colour-bar in the centre of the row. **(d)** Like the amplitude one, the phase image resulting from the shared-object treatment of the scans is of much higher quality than the one obtained with the averaged data, in particular concerning the high spatial frequencies. **(e)** Close-up view of the region marked by the dashed white square in (c) using the same colour-scale. **(f)** The enlarged view of the same part of the specimen for the shared-object reconstruction (dashed white square in (d)) illustrates the dramatic improvement compared to (e) in quality for both high-resolution features and uniform areas.



7.4 Application to experimental data

7.4.1 Shared-probe reconstruction of a high-resolution test object

7.4.1.1 Description of experiment

A damaged Fresnel zone plate structure was used as a high-resolution test specimen. It had been produced using the so-called “zone-doubling technique” (JEFIMOV ET AL., 2007b): A structure with twice the desired gap size between the lines is etched into silicon and overcoated by atomic layer deposition with a heavy element that covers all surfaces, in particular the side walls of the silicon structure, homogeneously. As a result, the line density is doubled compared to the silicon template which allows to obtain X-ray optics for very high resolutions. For the object presented here, the silicon substrate was structured with line widths going down to 25 nm in its outermost parts and then coated with an iridium layer of 25 nm thickness. Therefore, one finds a repetitive sequence: air gap, Ir wall, Si ring, Ir wall, air gap. Close to the edge of the zone plate, each of these elements has a well-defined width of 25 nm, which makes it ideally suited as a high-resolution test object.

The experiment was conducted at the cSAXS beamline of the Swiss Light Source using the set-up for two-dimensional PCDI as described in section 5.1.2 on page 131 at an X-ray energy of 4.8 keV. The illumination on the object was formed with a pinhole of about 2.7 μm diameter located about 1.7 mm upstream from the sample. Data was collected with the PILATUS 2M detector positioned 7.14 m behind the plane in which the specimen was scanned. Four independent round scans were done, each with 10 shells, 5 points in the first shell and 500 nm radial step size. Compared to the scan position definition (3.43) on page 101, one point per shell was left out by accident, but as the probe diameter was about five times the radial step size, the specimen was still completely covered. In addition, the radius of the first shell was artificially reduced to 350 nm instead of the 500 nm in the standard mode. Thus each of the scans covered a circular region of 9.7 μm diameter with 265 points. At every position, two subsequent exposures of 1 s and 30 s were taken. While one of the two different areas scanned was close to the centre of the Fresnel zone plate, the other was in its outer region which contained the smallest structures. The second and the fourth scan were done one the same regions of the sample as their respective predecessor but with the detector shifted diagonally by nominally $\sqrt{2} \cdot 10$ mm. This was done in order to also collect data at spatial frequencies coinciding at the detector’s standard position with its inter-module gaps, compare Fig. 7.7.

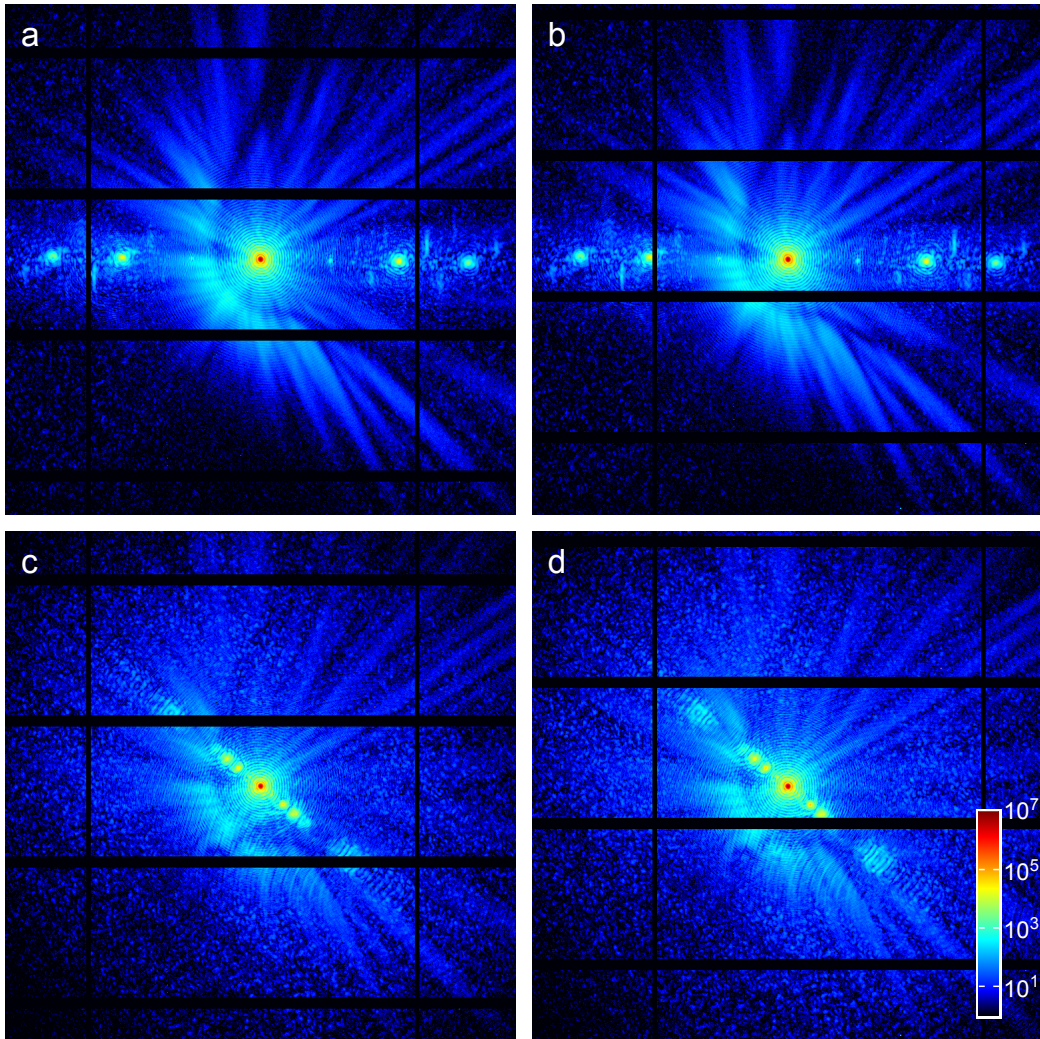


Figure 7.7: Examples of diffraction data used for the high-resolution reconstruction with a shared-probe approach. In each case, 768×768 detector pixels around the beam centre are shown on a colour-coded logarithmic scale which gives the photons counted in each pixel according to the colour-bar in panel (d). All patterns shown are merged from a short 1 s and a long 30 s exposure. **(a)** Diffraction pattern from first scan, taken in an outer area of the Fresnel zone plate. The Airy pattern created by the illuminating pinhole can be seen in the central part. For the diffraction orders originating from the zone plate's grating structure, the convolution of the diffraction signals of probe and object typical for ptychography can be seen. **(b)** Diffraction pattern from second scan, taken at the (nominally) same position but with the detector shifted diagonally. **(c)** Data measured close to the centre of the zone plate (third scan). Due to the structures in this region being larger, the separation of the diffraction orders is decreased. **(d)** Diffraction pattern from (nominally) same scan position, but taken from the fourth scan for which again the detector had been shifted.

7.4.1.2 Data processing

The data was processed using the shared-probe approach as described in section 7.2.1. Fig. 7.1 on page 175 illustrates it with examples from two of the four scans recorded in this experiment. The input data was preprocessed by correcting it for global intensity fluctuations in the incoming beam and by replacing the overexposed central pixels in each of the long-exposure diffraction patterns with the accordingly scaled values of the corresponding short exposure. Each of these frame was then cropped to the inner 768×768 pixels around the centre of the beam. Reconstruction was done with the difference map PCDI algorithm (see section 3.2.2) implemented in Matlab. Using Matlab's Distributed Computing Toolbox, the data was processed with four parallel reconstruction runs, one for each scan. After every iteration, the probe in each of the parallel processes was set to the average of the four runs' current probes using inter-process communication methods provided by the toolbox. In total, 500 iterations of the algorithm were done, which reached a steady state (see section 3.2.2) already after about 100 iterations. The final reconstructions were obtained by averaging the object guesses of 80 iterations from this steady-state regime.

7.4.1.3 Results

Together with the other experimental parameters discussed above, the diffraction pattern size of 768×768 pixels results in a pixel side length of 14 nm in the reconstructed images of probe and objects. Fig. 7.8 on page 191 shows the phase part of one of the four reconstructions. In this case, one of the two scans taken on the outer regions of the zone plate is shown¹. Probe sharing infers that the structure of the probe remains constant during all scans. Since each error in the probe would directly degrade the reconstruction of the object, the achieved high resolution in the presented scan, see Fig. 7.1(d) and the corresponding SEM image in (c), clearly indicates the validity of this assumption. It is also demonstrated that the relatively simple and inexpensive pinhole geometry can provide very high resolution in PCDI: The lines and spaces of 25 nm visible in the image correspond to a more than 100-fold improvement if compared to the 2.7 μm diameter of the pinhole, which would be the resolution of the system if used as a STXM.

¹A reconstruction of the second scanned area close to the centre of the Fresnel zone plate can be seen in the lower half of Fig. 7.1 on page 175

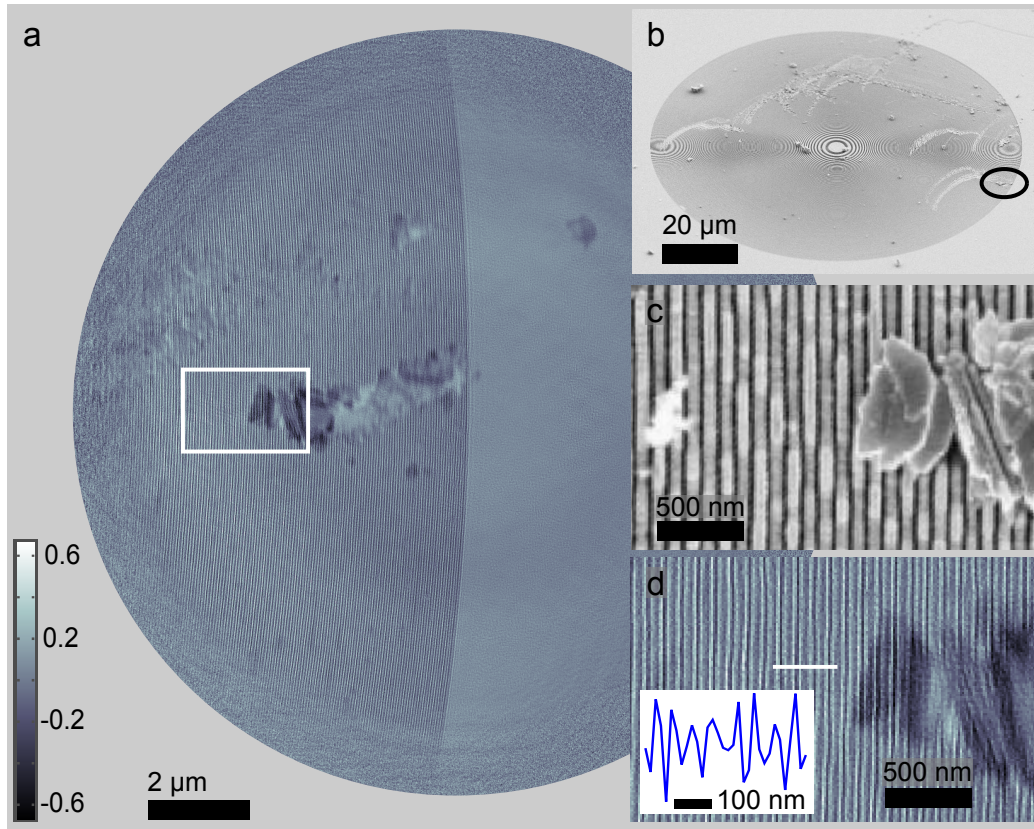


Figure 7.8: Result of a parallel reconstruction of four data sets sharing the same probe: A Fresnel zone plate structure etched into silicon and overcoated with a layer of 25 nm iridium which also has some some damaged areas was used as a high-resolution test object. **(a)** Reconstructed phase shift (in radians) obtained from a ptychographic round scan. To avoid problems with the dead areas of the detector, four scans with two different detector positions were reconstructed in parallel (see text for details), shown is one of the final object reconstructions. **(b)** Scanning electron micrograph (SEM) of the full Fresnel zone plate (tilted view). The black ellipse marks the location of the scan presented in (a). **(c)** SEM zoom-in on the region of interest indicated by the rectangle in (a). **(d)** Zoom-in on the reconstructed phase image, showing the rectangle marked in (a). The inset shows the line profile taken at the position of the white bar. It cuts through three overcoated silicon rings (visible as white structures in (c)), forming the following sequence of materials for each ring: gap, Ir wall, Si ring, Ir wall, gap. The pixel size of 14 nm allows to see the iridium walls and the air gaps, which are both 25 nm wide. The colour scale is the same as in (a), with the phase shift (in radians) adjusted to be around zero for the empty region of the specimen, resulting in negative phase shifts for the gaps etched into the silicon and positive phase shift for the iridium walls.

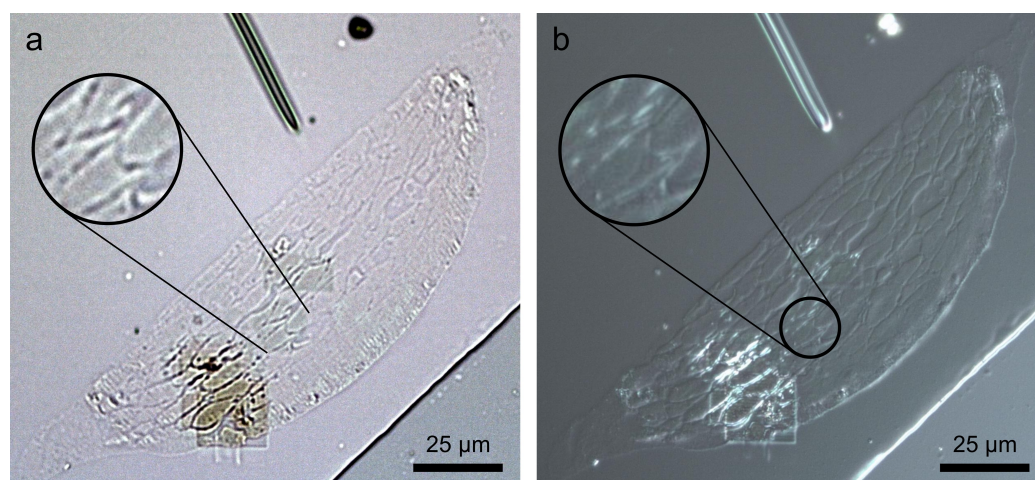


Figure 7.9: Visible-light micrographs of mouse liver slice used as specimen in the shared-object test experiment: **(a)** Transmission image (white balance adjusted in post-processing step) showing dark imprints at the location of different scans done on this specimen. The area covered by the multiple round scans of the experiment is visible as a disc of darker colour in the central part of the specimen and is also shown as a close-up view in the inset. The darker areas below and above have been raster-scanned with a zone plate focus, the lower ones using the full available flux. **(b)** Differential interference contrast image taken in reflection mode of the same region. Imprints are only visible for the STXM scans.

7.4.2 Shared-object reconstruction in cellular imaging

7.4.2.1 Description of experiment

The shared-object reconstruction was tested on a slice of a resin-embedded mouse liver prepared at the Electron Microscopy Center of the ETH Zürich (EMEZ). Visible light micrographs are shown in Fig. 7.9. The specimen had a thickness of $1\ \mu\text{m}$ and was supported on a silicon nitride windowed frame. The last-mentioned was glued to the sample holder of the cSAXS beamline's 2D scanning set-up, whose detailed description can be found in section 5.1.2 on page 131. At an X-ray energy of $6.2\ \text{keV}$, a pinhole of about $2.3\ \mu\text{m}$ diameter milled by focused ion beam into a $50\ \mu\text{m}$ thick tungsten foil was used to create the illuminating probe. The diffraction patterns were recorded with the PILATUS 2M detector which was placed $7.16\ \text{m}$ downstream from the sample. The same area of the object – compare inset in Fig. 7.9 – was covered by repetitive round scans with a radius of $6.4\ \mu\text{m}$ for the outermost of their eight shells and 5 points in the inner shell. The scan positions being calculated according to (3.43) on page 101, this resulted in 225 points per scan at each of which a 1 s exposure was taken. With the overhead for motor movements and detector communication, a single scan took about 10 minutes

to record. The repeated execution of the round scan was done in groups of three scans: for the first, the beam was centred on one of the central detector modules, while for the second scan the detector was shifted diagonally by means of shifting it 30 pixels horizontally and 30 pixels vertically. For every third scan, the same shifts relative to the detector position of the first scan were applied in the opposite directions. Motivation was again to collect spatial frequencies missing in some of the data sets in other ones. In total, 57 of these triple scans, i.e. 171 single round scans, were performed.

As for the mouse liver slice one faces the challenges associated with a weakly-scattering object described in section 6.1 on page 163, reference scans were done on a gold Fresnel zone plate mounted next to the mouse liver sample on the same sample holder. The reference scans were also performed as triplets with changing detector positions and with the same parameters as the ones on the mouse liver specimen.

7.4.2.2 Data processing

To evaluate the effects of data set sharing, three different types of ptychographic reconstructions were performed, in all cases using 150 iterations of the difference map algorithm described in section 3.2.2:

1. Individual reconstructions of all data sets. For nine of the scans the reconstructed objects and in particular the retrieved probes deviated strongly from the ones obtained for the majority of the data sets. In all the further reconstructions discussed below, the corrupt data sets identified this way were excluded.
2. Several reconstruction runs, each of which operated on an increased number of the input data sets while sharing the object. Starting from 5 scans, the number of data sets was incremented by 5 in each reconstruction run. Up until a total number of 55 data sets, only scans taken with the first detector position were used, because in this case the 192×192 inner pixels contained no insensitive PILATUS gap area. Starting from 55 data sets, their number was increased by 15 after each run until the maximum of 160 was reached. From 70 data sets on diffraction patterns taken at all three different detector positions had to be used. In total, 18 reconstruction runs using different amounts of data were performed.
3. Reconstruction using averaged diffraction patterns. The same 160 data sets as in the last shared-object reconstruction were used, but in this

case diffraction patterns taken at the nominally same scan points were simply averaged resulting in a single data set with 225 frames.

The individual reconstructions of point 1. were started with a simple probe model, i.e. a propagated disc. In both other cases, additionally the probe obtained from the reference scans on the gold Fresnel zone plate was used as an initial guess. For this, a scan triplet was reconstructed with a shared probe as described in section 7.2.1 using a diffraction pattern size of 512×512 pixels. To fit the size of the data in the reconstruction runs of the mouse liver, the retrieved probe was numerically downsampled to 192×192 in these cases.

7.4.2.3 Results

Shared-object reconstructions for an increasing amount of input data Out of the 18 shared-object reconstruction runs with an increasing number of input data, Fig. 7.10 on page 195 shows a comparison of the phase parts of nine retrieved objects. The figure shows the object reconstruction after the last iteration without application of the usual averaging procedure performed in the steady-state of the difference map procedure. This is done to avoid the effects of the averaging on the images' noise statistics, such that all changes can be fully attributed to the varying amount of input data. The increasing number of input round scans, given in the upper left corner of each panel, is clearly reflected in an increased quality of the reconstruction: an improved signal-to-noise ratio allows to better distinguish small-scale fluctuations in both density and spatial domain. However, for more than 70 input data sets the improvements become small and the results seem to be almost identical upon visual inspection.

By calculating the variances for the regions marked by the white frames for all 18 runs, the quantitative relation between the number of data sets and the reconstruction quality can be investigated. Again, these calculations are based on the last iterate of the reconstruction dropping the usual averaging of the object to avoid its effects on noise statistics. According to equation (3.70) on page 112, it is expected that the product of the reconstruction's variance and the area of one of its pixels is inversely proportional to the incoming X-ray fluence. In our case, the pixel size is fixed to $43.4 \text{ nm} \times 43.4 \text{ nm}$. For the weak scatterer investigated here, the number of incident photons is well approximated by the total number of photons N_D detected with the photon-counting detector. N_D is linearly related to the number N_{scans} of round scans: by linear regression one obtains $N_D = 1.2808 \cdot 10^6 \cdot N_{\text{scans}} + 1.3854 \cdot 10^6$ with a confidence coefficient of $R^2 = 0.9999$. Therefore, one can infer an inverse

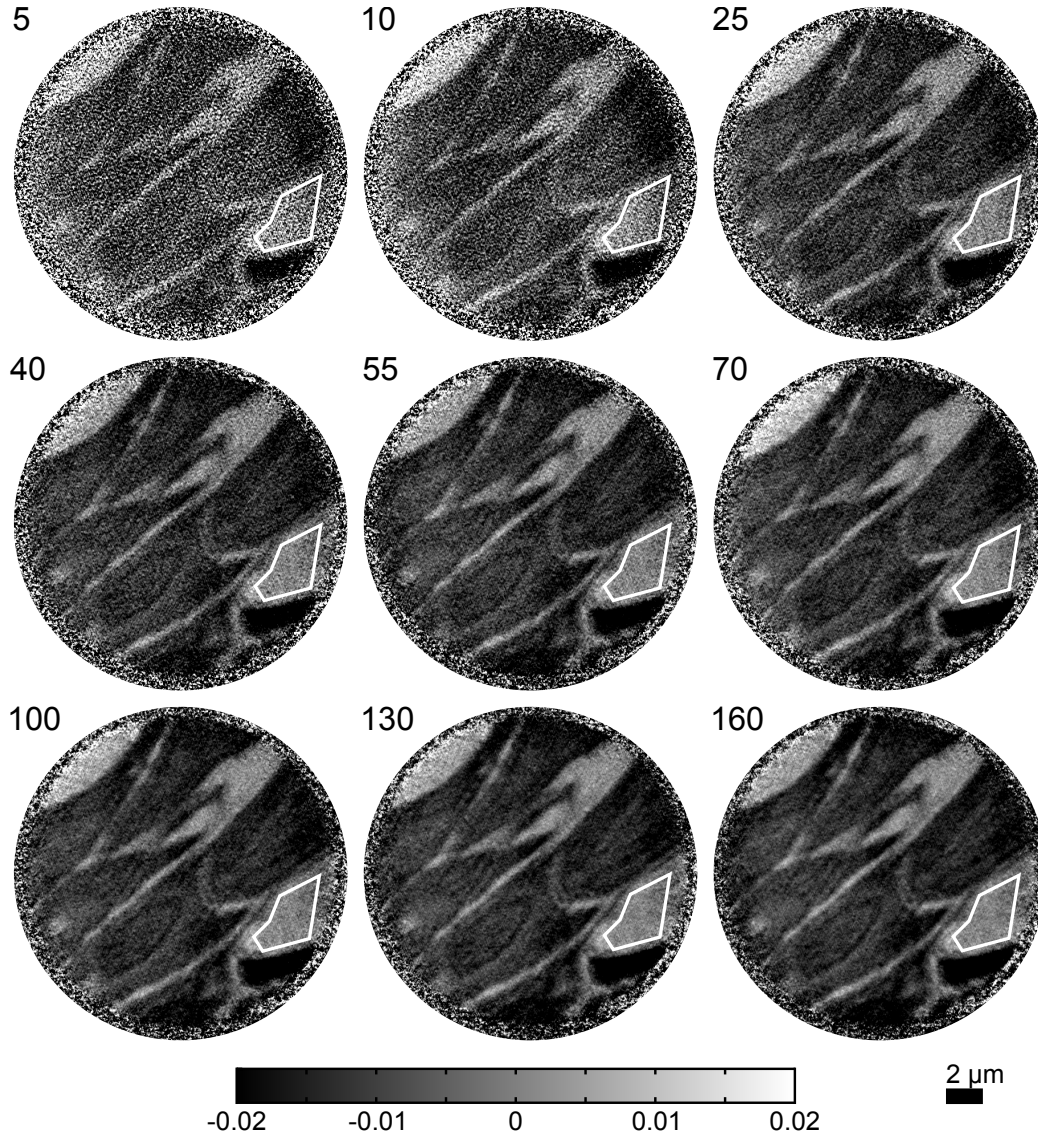


Figure 7.10: Comparison of shared-object reconstruction results (phase parts) for an increasing amount of input data. The labels in the upper left corners of each panel specify the number of identical round scans used for each reconstruction. While a significant improvement of the image quality is observed for up to 70 scans, the results seem to be identical on visual inspection when even more data sets are included. The white frames mark the regions used for the calculation of the variances (see Fig. 7.11 and main text for details). The average phase shift of these regions has been set as the origin of the phase colour scale (in radians).

proportionality between the variance and the number of data sets, which is the parameter being varied.

In Fig. 7.11 (a) and (b) on page 197 one finds the expected behaviour for the variances of both amplitude (left) and phase part (right) of the reconstructions. For the pixel size used in the reconstructions and with the given experimental parameters, the image quality is quickly improving with a growing number of data sets until about 50 scans are employed. For more than 50 data sets, the variance decreases only very slowly. However, both the time required for data acquisition and reconstruction scale linearly with the number of scans. If therefore only a specific resolution is required, relation (3.70) on page 112 may be used to estimate the number of scans necessary for the desired image quality.

Fig. 7.11 (c) for the amplitudes and (d) for the phases of the retrieved images clearly show the linear relation between the reciprocal variances and the amount of data used. However, one also observes deviations in the slopes for the first (less than 55 scans) and the second part (more than 70 scans) of the reconstruction runs. This fact is further illustrated in Fig. 7.11 (e) and (f) which shows the values obtained by dividing the reciprocal variance values by the corresponding number of data sets used. In contrary to a simple linear behaviour for which all these points should be scattered around the same mean value, one observes that the points for the first and the second part are located at different levels corresponding to two different slopes in the linear trend. The sudden change in noise behaviour can be explained by the fact that for the second group of reconstruction runs also diffraction data with missing regions has been used. The first group using up to 55 scans, however, is entirely based on data from the central detector position which does not include the detector gaps. The missing information in the second group of runs therefore leads to higher variances (lower reciprocal variances) than what would be expected upon extrapolation from the first group of values. Comparing the mean value of the second group of reciprocal variances per scan with the one of the first group, one finds a ratio of 0.83 for the amplitude and 0.72 for the phase part. When calculating the ratio of mean photons per scan for the same data sets, one obtains the significantly higher value 0.97, i.e. the simple decrease of photons does not directly explain the change of noise statistics. Neither does the reduced number of constrained pixels in the Fourier domain: as the missing areas due to the PILATUS gaps contain 192×17 pixels and about $2/3$ of the diffraction patterns in the second group of runs contain one of these, the ratio of valid pixels of second to first group is 0.94.

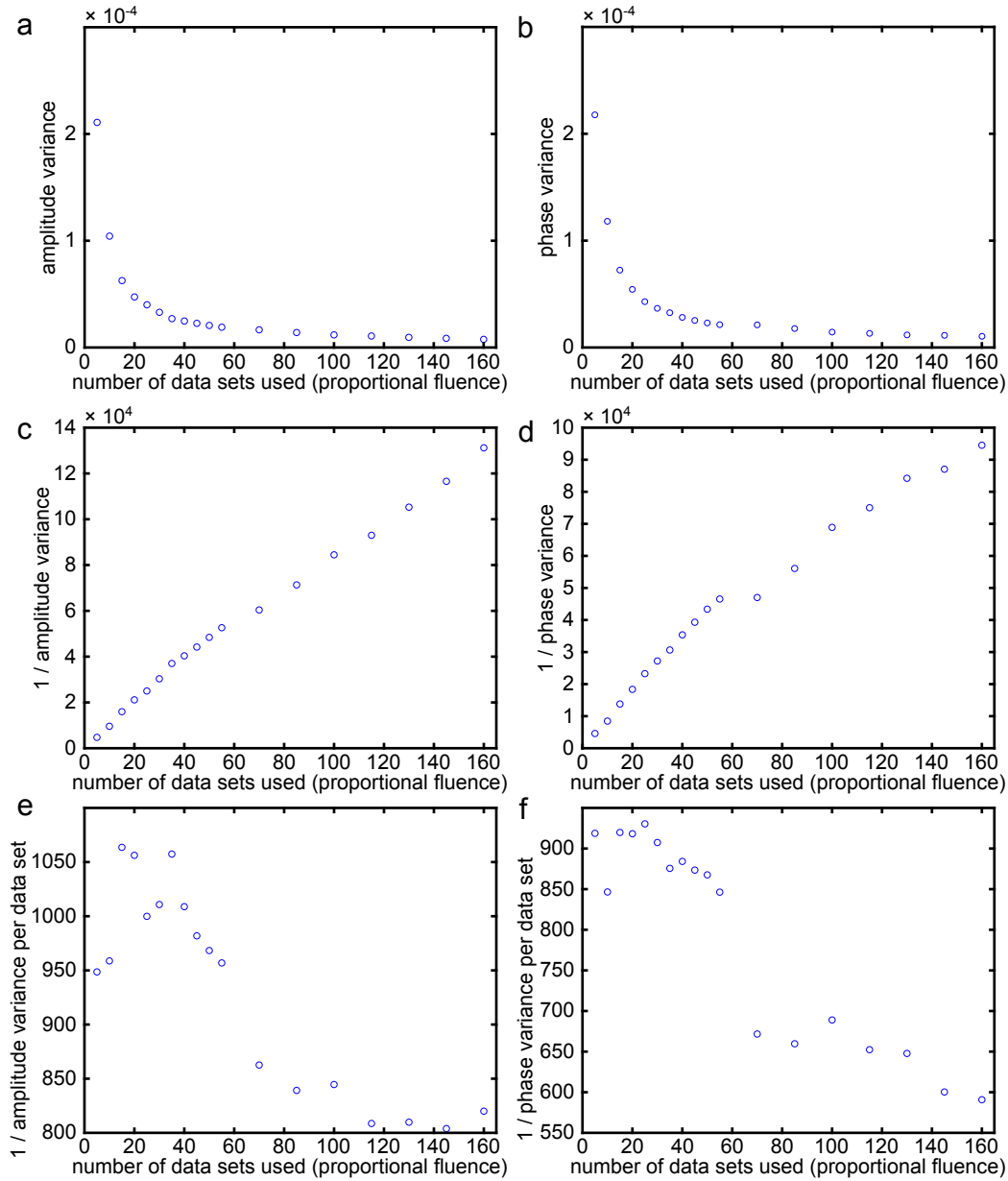


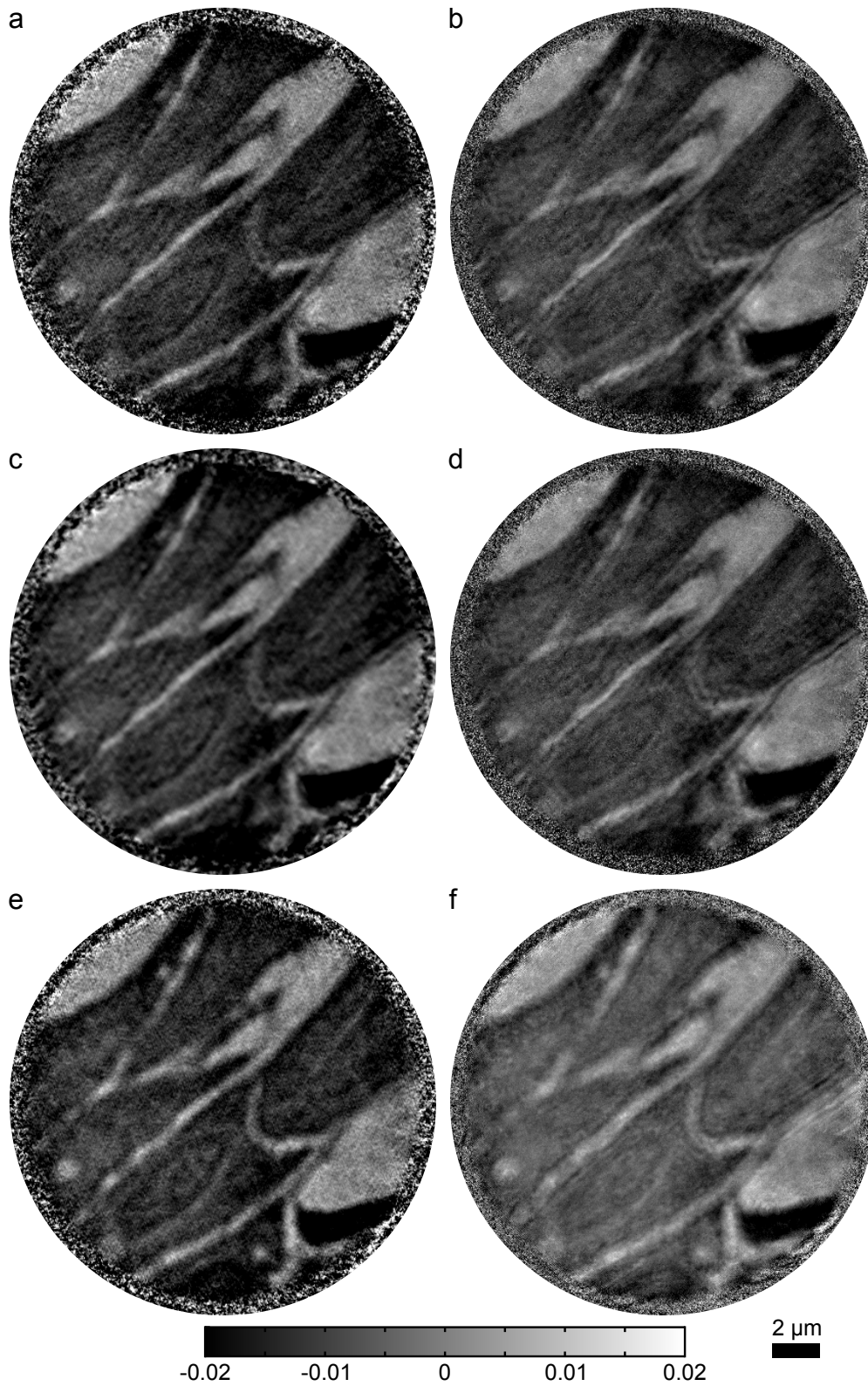
Figure 7.11: Dependence of variance in the reconstructed shared object on the number of data sets, i.e. the total fluence, used for the reconstruction. The plots in the left column are based on the variances of the reconstructed amplitudes, the right column uses the variances of the phase images. All have been calculated from an empty region of the respective object marked by the white frames in Fig. 7.10. In (a) and (b), the reduction of variance for an increasing number of data sets resembles the reciprocal relation predicted by equation (3.70) on page 112. In (c) and (d), one expects a linear behaviour for the reciprocal variances. However, the linear slopes differ for the first (up to 55 data sets) and the second part of the reconstruction runs. In (e) and (f) this fact is further illustrated by dividing the reciprocal variance values by the corresponding number of data sets used.

Comparison with reconstruction based on averaged diffraction data

Fig. 7.12 on page 198 compares the phase reconstructions obtained with a shared-object reconstruction of 160 individual round scans (left column) with the results based on a single round scan in which each diffraction pattern is the average of the 160 respective frames taken at the corresponding position in the individual scans (right column). The top row presents reconstructions using the probe obtained from the reference scan as an initial guess. The central row is based on the same phase-retrieval runs, but instead of showing just the final iterate of the object, the results displayed here are averages of ten object iterates from the steady-state regime of the difference map algorithm. The bottom row shows the results one gets if the probe is initialized with a simple model. However, no clear advantage of employing the shared-object approach in the case of this specific weakly-scattering object can be deduced from these reconstructions.

A close inspection of Fig. 7.12 (a) and (b) shows, that small features seem to be better resolved in the case of the averaged data, e.g. the thin line that is visible at the border of the bright patch on the right. A comparison of the variances for said bright area also favours the data averaging as the variance for the shared-object case is by factors of 1.3 (amplitude) and 1.6 (phase) larger. However, it should be pointed out again that single object iterates are compared here. If ten of these iterates are averaged, as done for the central row of Fig. 7.12, the smoothing effect in the shared-object case is much stronger than for the averaged data. Therefore the variances when sharing the object are now lower by factors of 0.53 (amplitude) and 0.65 (phase)

Figure 7.12 (following page): Comparison of shared-object results with reconstructions based on averaged diffraction data. **Top row:** Reconstructions using the probe obtained from the reference object as an initial guess for the illumination. Phase part of the last object iteration are shown in (a) for the shared-object case and in (b) for the the averaged diffraction data. Both reconstructions are based on the same set of 160 scans. Small features seem to be better resolved in (b), e.g. the thin line at the border of the bright patch on the right. However, also some localized high-frequency artefacts are visible, e.g. on top of the elliptic cell core in the lower left. **Central row:** Reconstructions obtained by averaging ten iterates from the steady-state regime of the reconstruction runs presented already in the top row. While for the shared-object approach shown in (c) a efficient suppression of the global high-frequency noise is observed, the result based on the averaged diffraction data in (d) hardly changes. In particular, the localized high-frequency artefacts remain visible. **Bottom row:** Reconstructions obtained when using a modelled probe as a starting guess. In this case, also a different diffraction pattern centring was used to avoid the build-up of phase ramps. The retrieved phase for the shared-object approach is shown in (e), for the averaged data in (f). The shared-object method obviously handles the case of a modelled initial probe better. The origin of the phase shift colour scale (in radians) has been set to the mean value of the empty brighter patch in the lower right.



than in the case of diffraction pattern averaging. This is because the high-frequency noise uniformly distributed over the whole image (a) is efficiently suppressed in (c). However, some localized high-frequency artefacts visible in (b), e.g. on top of the elliptical cell core in the lower left, remain also for the mean of several object iterates shown in (d). This can be attributed to the observation that the reconstruction of the averaged data very quickly converges the solution shown in (b) but then barely changes anymore.

The results based on a modelled initial probe shown in the bottom row of Fig. 7.12 suggest that the shared-object approach (e) is more robust than using averaged data in case no highly accurate initial guess of the illumination function is provided.

Chapter 8

Broad-bandwidth PCDI: towards high spatial resolutions

This chapter presents the results of two proof-of-principle PCDI experiments with broad-bandwidth or “pink-beam” synchrotron radiation. Following an introductory section motivating this approach, the experimental details for the two test experiments are given in section 8.2. Their results are treated in separate sections. Based on the conclusions in the section 8.5, an outlook for future improved results from broad-bandwidth experiments is given in section 8.6.

8.1 Motivation

At a higher incoming flux, a specimen can be imaged either with a better signal-to-noise ratio or at higher resolution: relation (3.70) on page 112 shows that the product of signal variance and resolution in a reconstruction is inversely proportional to the number of photons hitting the specimen area. The incoming flux can be optimized by fully exploiting the coherence properties of the beam: An excess in transverse coherence length, e.g. compared to the size of an illumination-defining pinhole, may be used to prefocus the beam onto the coherence-filtering aperture to benefit from the full coherent flux. Most beamlines at which coherent imaging experiments are conducted can be optimized in this respect.

The longitudinal coherence length, however, typically has a fixed value determined by the installed monochromator. In many cases, monochromators for the energy range 5 keV to 20 keV use a Si-111 Bragg reflection with a bandwidth $\Delta\lambda/\lambda \simeq 1.4 \cdot 10^{-4}$ (ALS-NIELSEN AND MCMORROW, 2011,

chapter 6). A broader bandwidth can for example be provided by using multilayer monochromators instead. This is done in many beamlines dedicated to applications in which high flux is more important than monochromaticity, e.g. X-ray microtomography (compare for instance [RAU ET AL., 2007](#)). In the case of CDI, however, an increase in bandwidth comes at the price of a reduction of the maximum spatial resolution which is achievable with a given geometry, see condition (2.10) on page 49. But (2.10) also shows that this reduction can be counteracted by reducing the extent of the illumination. While this typically requires achromatic X-ray optics which are capable of producing sub-micron focal spots, it in turn allows to fully benefit from the increased flux of a broad-bandwidth beam.

However, the broad-bandwidth beam also limits the density resolution which can be achieved: The phase shift observed for a given material (a given electron density) is proportional to the wavelength, which can be seen when inserting (1.24) in (1.28) on page 22. This means that a variation in wavelength causes a proportional variation of the observed phase shifts, i.e. the width $\Delta\Phi$ of the distribution of phase shifts produced by a homogeneous sample is proportional to the bandwidth $\Delta\lambda/\lambda$ of the illuminating wave field:

$$\Delta\Phi = \Phi \cdot \frac{\Delta\lambda}{\lambda} , \quad (8.1)$$

where Φ is the phase shift at the central wavelength λ of the spectrum.

8.2 Demonstration experiments at ID22NI

The nano-imaging endstation ID22NI at the ESRF offers a combination of an achromatically-focused broad-bandwidth beam with a dedicated set-up for nano-scale scanning and tomography. It is therefore ideally suited for ptychographic imaging with reduced longitudinal coherence: The spectral bandwidth of the beam is $\Delta\lambda/\lambda \simeq 1.5 \cdot 10^{-2}$ and the maximum extent of the focus in ptychographic imaging mode amounts to $a \simeq 180$ nm. With these values, the resolution is limited to $\Delta x > 2.7$ nm according to (2.10).

A detailed description of the ID22NI experimental set-up can be found in section 5.2 on page 137.

8.2.1 Experiment in July 2009

The first test for ptychographic imaging at ID22NI was carried out in July 2009. It allowed to identify various possibilities for improving the set-up, some of which could be readily implemented during the beamtime while others could only be considered in later experiments:

1. Quality of the incoming focused beam:

- (a) Some drift problems were caused by the mechanics of the KB system installed at this time. An approximately linear drift of the beam position in the vertical direction with a rate of about $0.8\ \mu\text{m}$ per hour could be observed. Before the second experiment in March 2011, the mechanics had been replaced with a more stable solution.
- (b) The collected diffraction patterns were to a large extent dominated by strong streaks which were attributed to parasitic scattering from mirror imperfections and the entrance slits, see Fig. 5.4(a) on page 139. To reduce this unwanted component in the signal, an additional clean-up pinhole was added directly downstream of the KB system during the last part of the beamtime, see Fig. 5.4(b) for its effect.

2. Collection of diffraction data:

- (a) The FReLoN detector (see section 5.2.4 on page 140 for details) had been placed about 1.58 m behind the scanning plane. As the high flux of the undiffracted beam was concentrated on only a modest amount of pixels in its central area, the detector quickly saturated despite the use of attenuators in the incoming undulator beam. Therefore, it is considered beneficial to place the detector as far behind the focal plane as possible. However, such a change of set-up could not be done during the course of this first experiment and has only been realized for later runs.
- (b) Given the fast saturation of the detector, installation of a motorized beamstop became necessary to be able to collect diffraction data with a high enough dynamic range.
- (c) The most important limiting factor of data collection was the time overhead created by detector readout and motor movements: in typical scans it accumulated to more than 0.47 s per diffraction pattern, whereas the exposure times were usually in the range of 0.035 to 0.8 s.

For the test experiment reported here, a Siemens star (compare also section 3.3 on page 109) was used, which formed part of a commercial resolution chart (XRadia Inc., model X50-30-2 with an increased thickness of 700 nm electroplated gold). Its smallest features have a size of 50 nm.

For the experiment, the high-power slits were set to a horizontal opening of $10\ \mu\text{m}$, while in the vertical direction the source size of $\sim 25\ \mu\text{m}$ in the undulator is relevant. The X-ray peak energy was adjusted to $17.5\ \text{keV}$. Considering the beamline's geometry introduced in section 5.2, from these values coherence lengths (FWHM) at the location of the KB optics of $\xi_{h,\text{FWHM}} \approx 160\ \mu\text{m}$ and $\xi_{v,\text{FWHM}} \approx 135\ \mu\text{m}$ are estimated. Therefore, the entrance slits of the KB system were closed to $75\ \mu\text{m}$ (horizontal) \times $100\ \mu\text{m}$ (vertical) opening. For these settings, the size of the focus was determined by fluorescence knife-edge scans to be about $90\ \text{nm} \times 130\ \text{nm}$ (horizontal \times vertical FWHM).

Diffraction patterns were collected with the 2D version of the ID22NI scanning set-up from a circular region of $2.4\ \mu\text{m}$ diameter close to the centre of the Siemens star. The scan points were located on concentric circles to suppress artefacts inherent to reconstructions from a rectangular scan grid (see page 99 in section 3.2.4.5). These round scans were done with 16 radial steps and 5 points in the first shell according to definition (3.43) on page 101, which resulted in 765 scan positions in total. A first scan was done without beamstop. Although the counting time was just $0.035\ \text{s}$, still $3\ \text{mm}$ of aluminium filters were required to avoid overexposure of the central detector area. The same scan was repeated for dwell times of $0.1\ \text{s}$ and $0.4\ \text{s}$, this time without the filters but with a beamstop protecting the detector from the direct beam. In addition to the diffraction patterns obtained with the FReLoN camera, Au- L_α fluorescence signals were recorded using the silicon drift detector, which partially contributed to the observed large time overhead. For background correction, sets of dark frames were collected for each exposure time.

8.2.2 Experiment in March 2011

The same Siemens star test object was again scanned during a second experiment in February 2011 which could take advantage of the improved stability of the upgraded KB system. Also the rest of the set-up already from the start included the improvements identified during the previous run, in particular the clean-up pinhole behind the KB mirrors and the beamstop directly in front of the detector. To spread the central part of the beam over as many pixels as possible, the FReLoN camera was installed at the very end of the sample table, i.e. about $2.89\ \text{m}$ behind the focus. The time required for detector readout was reduced to about $0.1\ \text{s}$ by using a region-of-interest of only the 1024×1024 innermost pixels and the FReLoN's so-called kinetic readout mode (LABICHE ET AL., 2007). The experiment was carried out using a mean X-ray energy of $16.9\ \text{keV}$ and with the entrance slits of the KB system set to $70\ \mu\text{m} \times 35\ \mu\text{m}$ (vertical \times horizontal) opening. Due to the different

focal lengths of vertical and horizontal mirror (compare section 5.2.2 on page 138) this should lead to a roughly symmetric focus. During this beamtime, however, the size of the focal spot was not measured independently of the ptychographic scans, e.g. using fluorescence knife-edge scans. Yet previous detailed characterization measurements by the beamline staff could be used to deduce a focal spot size of about $150 \text{ nm} \times 170 \text{ nm}$ (horizontal \times vertical FWHM).

The specimen was scanned using a raster grid of 73×73 points covering an area of $5.4 \mu\text{m} \times 5.4 \mu\text{m}$ with scan steps of 75 nm . First, a complete data set was taken with 0.03 s dwell time at each of the 5329 points (without beamstop and with 3 mm aluminium filters), while in a second scan an exposure time of 0.15 s (with beamstop and no filters) was used. The data sets were complemented by corresponding dark frames.

8.3 Results of test experiment in July 2009

As a first step, a STXM analysis according to section 1.8.1 was performed which allows to obtain **low-resolution images** directly after data acquisition. Fig. 8.1(a) on page 206 shows the transmission calculated by summing the counts in each diffraction pattern and assigning each result to one pixel per scan position. The values are normalized to the maximum total counts measured in an empty area of the sample, see left scale on colour-bar. While Fig. 8.1(a) is based on a short-exposure scan (no beamstop), only very little fluorescence counts are detected with these settings. Simultaneous **fluorescence imaging** therefore requires a higher incoming flux such as used in the scans with beamstop. In turn, this means that – under the condition that the incoming beam is sufficiently coherent – ptychographic imaging lends itself as a natural option to make use of the photons transmitted through the specimen during fluorescence mapping. Fig. 8.1(b) shows the $\text{Au-}L_{\alpha}$ fluorescence signal based on a long-exposure scan of the same area as in panel (a). The number of detected counts is colour-coded according to the right scale on the colour-bar. For both low-resolution images, the values at the round scan positions were interpolated linearly onto a raster of square pixels. While in the upper-left part of the images individual spikes of the Siemens star can still be distinguished, this is no longer possible when further approaching the test patterns centre. As expected for the focal size of about $90 \text{ nm} \times 130 \text{ nm}$ (horizontal \times vertical FWHM), already the structures with a half-period of 100 nm at the inner radius of the larger ring of segments are no longer resolved properly. A slight difference reflecting the asymmetric focus is observed between the resolutions in horizontal and vertical direction.

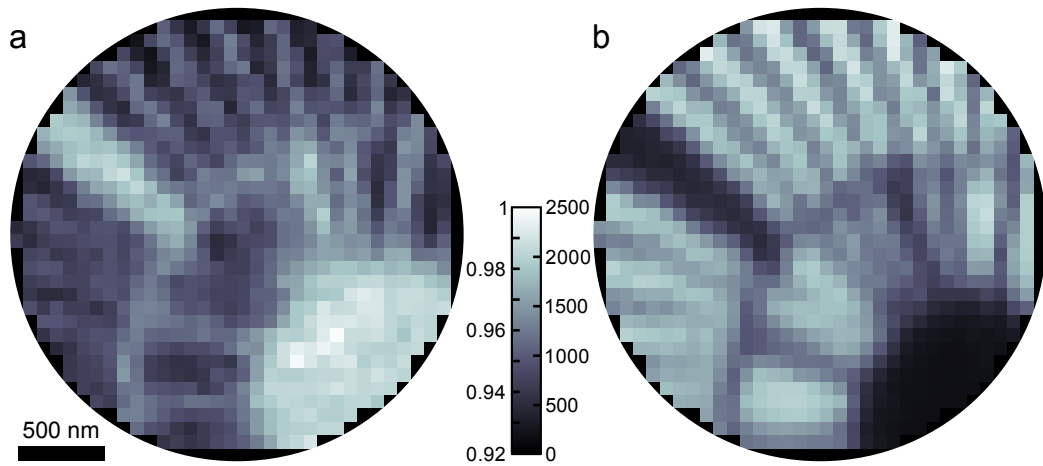


Figure 8.1: Low-resolution images of Siemens star test object scanned at ID22NI in July 2009: (a) Transmission image. The total counts in each diffraction pattern were normalized to the maximum total count value (left scale on colour-bar). (b) Au- L_{α} fluorescence signal (detected counts, see right scale on colour-bar) based on the long-exposure scan of the same area. Both images were obtained by linear interpolation of the values at the round scan positions onto a raster of square pixels.

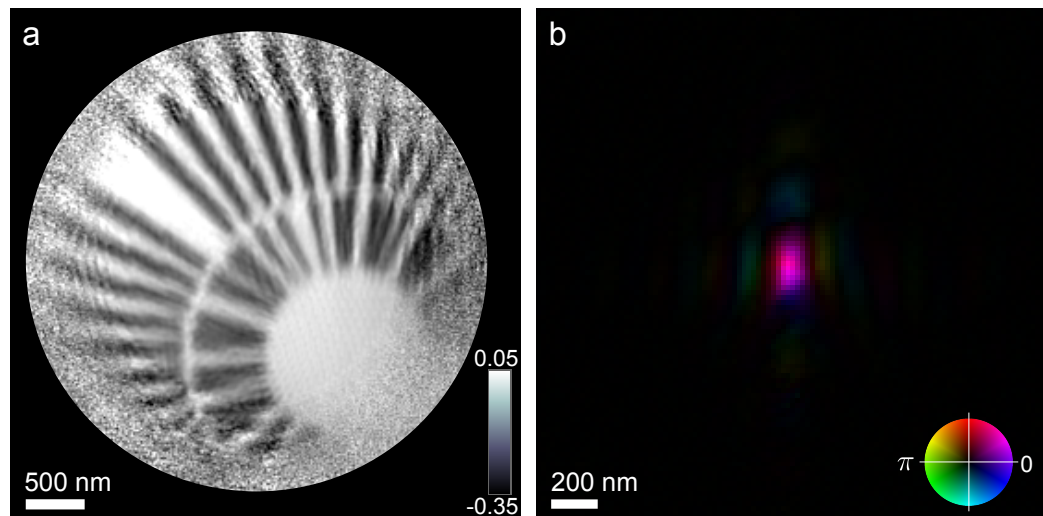


Figure 8.2: Results of PCDI reconstruction of test specimen. (a) Reconstructed phase shift of the object (linear colour scale in radians). Some of the structures of the innermost ring of spikes with structure sizes down to 50 nm are resolved, corresponding roughly to a two-fold improvement of resolution compared to the size of the focal spot. However, some distortions due to drift during the scan are visible. (b) Colour-coded representation (see colour-wheel) of the retrieved complex-valued illumination function showing the wave field produced by the KB system in the focal plane. The size of the focal spot, about $80 \text{ nm} \times 120 \text{ nm}$ (horizontal \times vertical FWHM of probe intensity), is consistent with the one obtained from fluorescence knife-edge scans if the effect of the side-lobes is taken into account (see text for details).

The **ptychographic reconstruction**, which is shown in Fig. 8.2, yields a significant gain in spatial resolution. In this case, the central 128×128 pixels of the diffraction patterns taken without a beamstop were used. Starting with a symmetric Gaussian model as the initial probe, a MATLAB implementation of the difference map algorithm (compare section 3.2.2) was applied for 300 iterations. The retrieved phase shift shown in Fig. 8.2(a) (colour-coded on a linear grey scale, in radians) was obtained by averaging 20 individual object iterates from the steady-state regime of the reconstruction run. In the resulting image, even some of the smallest structures at the tips of the innermost spikes become visible. There the pattern has a half-period of 50 nm, i.e. more than a factor of two smaller than the focal spot size.

However, the overall **quality of the reconstruction** is still quite poor: Firstly, resolution is lower in vertical than in horizontal direction, visible in particular in the lower left part of Fig. 8.2(a), where the reconstructed horizontal spikes additionally suffer from some distortions. Secondly, no part of the image shows the well-defined sharp edges one would expect for a lithographically structured specimen. The first point is attributed to vertical drift of the beam already mentioned in item 1a in section 8.2.1. A major cause of the second issue is a strong background in the diffraction patterns mainly attributed to the long tails of the detector's point-spread function. This background and its effects are discussed in more detail in section 8.4.1. As the quality of the reconstructions is mainly limited by the two discussed factors, data sets acquired with the beamstop and thus with longer dwell times were not included because no further improvements could be expected.

The simultaneously **retrieved illumination function** is displayed in Fig. 8.2(b) in a colour-coded representation which maps amplitude to value and phase to hue according to the colour-wheel in the bottom-right corner of the panel. The probe shows the asymmetric shape expected from the fluorescence knife-edge measurements of the focal spot, its vertical extent being a factor of about 1.5 larger than the horizontal one. In addition, one can observe side lobes along the horizontal and vertical directions resembling the proportionality to a sinc-function along each dimension: As effective entrance aperture and focal plane of the optics are related via a Fourier transform, this sinc is the result of the rectangular setting of the KB system's entrance slits. However, in this relation one also has to take the different focal lengths of the two mirrors into account.

The **size of the central peak** is measured in the intensity image, which is obtained as the absolute square of the reconstructed probe's amplitude. It is about $80 \text{ nm} \times 120 \text{ nm}$ (horizontal \times vertical, FWHM values). This is slightly lower than the approximately $90 \text{ nm} \times 130 \text{ nm}$ determined as the size of the focal spot in independent fluorescence knife-edge scans. The deviation

is attributed to the fact that in the latter case the intensity in the side lobes of the probe contributes substantially to the generation of fluorescence photons. Re-binning the reconstructed probe to a lower resolution was observed to reproduce this effect, i.e. the apparent width of the central peak increases at the expense of the higher orders.

8.4 Results of improved experiment in March 2011

As a result of the improved experimental set-up, the quality of the data collected in this second beamtime was significantly better than in the previous experiment. In the case of the Siemens star test object, this immediately manifests itself in substantially improved reconstructions, compare e.g. Fig. 8.2(a) on page 206 with Fig. 8.7(a) on page 228. However, the retrieved images are still degraded by a strong background which surrounds the undiffracted beam in all diffraction patterns. This background is attributed mainly to the extended point-spread function of the detector, in particular its long tails (compare also section 5.2.4 on page 140 and PONCHUT, 2006).

8.4.1 Investigation of background-induced artefact in probe

The ptychographically reconstructed probe shows an additional unexpected, highly-localized peak at its centre. It is located on top of the central maximum of the expected probe which is supposed to be proportional to a two-dimensional sinc-function. The latter assumption is again based on the Fourier relationship between the respective wave fields at a rectangular, uniformly-illuminated entrance aperture and at the focal plane of a KB system. As a highly-localized structure in real space hints at an extended corresponding Fourier signal, the artefact is suspected to be induced by the background signal in the diffraction pattern. This is further investigated in the current section.

8.4.1.1 Model for the illumination function

Fig. 8.3 on page 211 compares the amplitudes of the reconstructed probe in panels (a) and (b) with modelled ones in (d) and (e). For the model, the absolute value of a 2D sinc-function was multiplied with an additional

Gaussian damping factor:

$$|P(x, y)| = a |\text{sinc}(b_1(x + c_1))| |\text{sinc}(b_2(y + c_2))| \cdot e^{-(d_1(x+c_1)^2 + d_2(y+c_2)^2)}. \quad (8.2)$$

Here the normalized definition of the sinc-function is used, i.e. $\text{sinc}(x) \equiv \sin(\pi x)/\pi x$. The model (8.2) is adjusted using scaling a , stretching factors b_1 and b_2 , lateral offsets c_1 and c_2 , and damping constants d_1 and d_2 . While in the practical applications the six last-mentioned parameters were typically expressed in pixel units, they can be easily converted to metric units with the side length of one pixel in the reconstruction, here $\Delta x \approx 16.2 \text{ nm/px}$. With the coordinates being transformed according to $x[\text{m}] = x[\text{px}] \cdot \Delta x$, the conversion rules become

$$\begin{aligned} b_{1,2}[\text{m}^{-1}] &= b_{1,2}[\text{px}^{-1}]/\Delta x, \\ c_{1,2}[\text{m}] &= c_{1,2}[\text{px}] \cdot \Delta x, \\ d_{1,2}[\text{m}^{-2}] &= d_{1,2}[\text{px}^{-2}]/\Delta x^2. \end{aligned} \quad (8.3)$$

If the origin for the metric units is to be placed in the centre of the array, an additional offset of half the probe array's side length has to be subtracted from $c_{1,2}[\text{px}]$ before the conversion.

In many cases, the extent of the central maximum of the 2D-sinc is of major interest. It allows, for example, to conveniently compare the parameters of a ptychographically reconstructed illumination to the ones obtained with independent characterization methods. For our normalized sinc-definition, the first minima are located at $\pm 1/b_{1,2}$ from the centre of the pattern. The FWHM values of the central maximum in the intensity image along the Cartesian axis are of particular interest for a direct comparison with the expected extent of the focus. The required intensity image is calculated by squaring (8.2). A direct relation between FWHM values and $b_{1,2}$ is therefore obtained by numerically solving $|\text{sinc}(b_{1,2}x)|^2 = 1/2$:

$$\text{FWHM}_{h,v} \approx 0.88589/b_{1,2} \quad (8.4)$$

Damping factor in probe model The necessity of the damping factor in (8.2) is illustrated by the line-outs in Fig. 8.3(f): the decrease of the retrieved amplitude (red crosses) towards the edges of the array is stronger than in the case of a unmodified 2D $|\text{sinc}|$ (dashed curve) and is better represented by the solid curve based on the model in (8.2). The damping was first observed for reconstructions in which the initial probe guess was a simple 2D Gaussian representing only the central peak of the focus. However, the same behaviour

		A model (Fig. 8.3)	B fit start	C fit result
amplitude	a	12.6	25.2	13.93 ± 0.03
stretching	b_1/px^{-1}	0.094	0.06	0.0972 ± 0.0001
	b_2/px^{-1}	0.094	0.06	0.0930 ± 0.0001
centre	c_1/px	-64	-60	-64.03 ± 0.01
	c_2/px	-64	-60	-64.64 ± 0.03
damping	d_1/px^{-2}	$5 \cdot 10^{-4}$	$5 \cdot 10^{-4}$	$5 \cdot 10^{-4}$
	d_2/px^{-2}	$5 \cdot 10^{-4}$	$5 \cdot 10^{-4}$	$5 \cdot 10^{-4}$

Table 8.1: Parameters of fits to illumination function. The values are given in pixel units, see (8.3) for conversion to metric units. **(A)** Parameters for probe model shown in Fig. 8.3, panels (b),(c),(e) and (f). **(B)** Starting parameters for the least-squares fit. The values that were chosen differ significantly from the ones in the first row in order to test the robustness of the result for non-optimal starting guesses. **(C)** Result of least-squares fit of the probe model (8.2) to the retrieved probe with the area of the background-induced artefact excluded. A visualization of the fit can be found in Fig. 8.4(a). The fit result depends strongly on the amount and signal strength of these excluded pixels. However, the fit is very robust with respect to changes of the initial parameters listed in the second row with the exception of the parameters d_1 and d_2 defining the Gaussian apodization. It was observed that the damping tended to get too strong and the higher order maxima of the sinc were completely suppressed if d_1 and d_2 were left unconstrained. Therefore, these two parameters had to be confined to the interval $[-5 \cdot 10^{-4}, 5 \cdot 10^{-4}]$. The uncertainty of the fit coefficients is represented by the 95% confidence bounds. For d_1 and d_2 no confidence bounds can be given as they stayed at the upper bound of the interval to which they had to be constrained.

was exactly reproduced in runs where the probe had been initialized as an undamped 2D sinc. Therefore, the possibility can be ruled out that the initial Gaussian probe could be partly imprinting itself onto the retrieved probe in the form of a Gaussian damping factor.

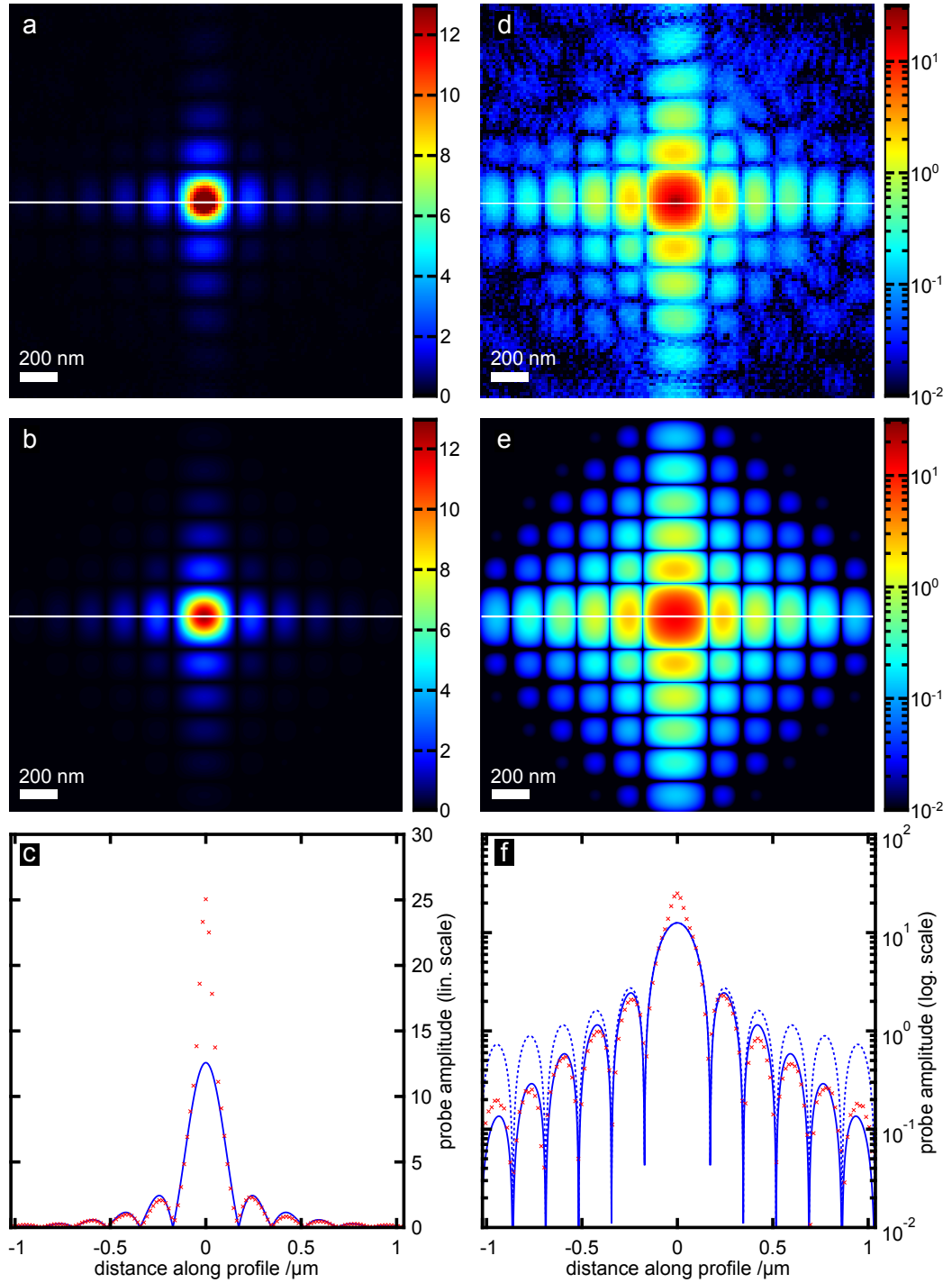
From a Fourier optics point of view, the wave field in the focal plane is proportional to the Fourier transform of the wave field incident on the optical system. In this picture, there are two possible explanations for the obvious reduction of high Fourier frequencies compared to what would be expected for a rectangular slit with perfectly sharp edges: Either these spatial frequencies were only present with reduced amplitudes already in the incident wave field, or they were damped by the optical system. The first may be the case, if the slit blades defining the incident beam have smooth edges. If such an edge can be described as a convolution of a perfect step-function with a Gaussian, the amplitude of the corresponding Fourier transform according to the convolu-

tion theorem is the observed product of an undamped $|\text{sinc}|$ and a Gaussian. Alternatively, an apparent smoothness of the slits' edges may also be caused by small vibrations. The second case, in which the high frequencies are damped by the optical system, may be caused by roughness of the reflecting surfaces which is known to lead to a frequency-dependent reduction of the reflectivity. Under the assumptions that the height variations are uncorrelated and their statistics are Gaussian, the reflectivity $R(q_{\perp})$ of a rough surface is the usual Fresnel reflectivity $R_f(q_{\perp})$ multiplied with a frequency-dependent Gaussian damping factor (ALS-NIELSEN AND MCMORROW, 2011, section 3.8; compare also SINHA ET AL., 1988), i.e. $R(q_{\perp}) = R_f(q_{\perp}) \exp(-\sigma^2 q_{\perp}^2)$, where σ is the root-mean-square roughness of the reflecting surface and q_{\perp} the component of the scattering vector normal to it.

Another influence could be the point spread function (PSF) of the detector: The reconstruction is based on the Fourier relation between the focal plane and the detector plane. In the latter the convolution of the impinging intensity with the detector's PSF is measured. For a PSF with Gaussian shape this again corresponds to a multiplication of the original field in the focal plane with a Gaussian.

As most likely a combination of all discussed factors causes the observed damping of the reconstructed probe at higher spatial frequencies, a quantification of their individual contributions is not easily possible. However, some implications of the values obtained for the damping are discussed alongside with the other quantitative results for the illumination on page 213 in the next but one subsection.

Figure 8.3 (following page): Manual modelling of ID22NI probe function. **(a)** Amplitude of reconstructed probe (colour-coded linear scale, maximum value restricted to 13, see colour-bar). **(b)** Amplitude of modelled probe shown on same colour scale. The probe model is based on a 2D sinc function – as the amplitude in the focal plane is proportional to the Fourier transform of the rectangular entrance aperture – which is multiplied with a 2D Gaussian damping factor, see (8.2) and main text. The parameters for the model as listed in the column A of Table 8.1 were chosen by visual comparison of the line profiles in panel (f). **(c)** Comparison of horizontal line-outs through the probe amplitudes at the positions marked by white lines in (a) and (b). The reconstructed values are marked with red crosses, while the model is represented by a solid blue curve. On this linear scale, a strong deviation from the expected behaviour can be seen in the central part of the retrieved probe. **(d)** Amplitude of reconstructed probe (colour-coded logarithmic scale, see colour-bar). **(e)** Amplitude of modelled probe shown on same colour scale. **(f)** Comparison of the horizontal line-outs on a logarithmic scale, see white lines in (d) and (e). In addition to the reconstructed (red crosses) and the modelled (solid blue curve) probe amplitudes, the dashed blue curve shows a profile through the 2D sinc function which is obtained if the probe is modelled without the Gaussian damping factor.



8.4.1.2 Least-squares fit of probe

For a first comparison of modelled and retrieved probe, the set of parameters listed in column A of Table 8.1 was chosen by visual comparison of the resulting line profiles, compare Fig. 8.3(f). Fig. 8.3(e) illustrates that the amplitude in the central maximum due to the background induced-artefact is about two times the expected value. Therefore, this intermediate step of interactive adjustment was necessary in order to identify the largest deviations and exclude these data points in the least-squares fitting process which otherwise failed to converge. For the fit result shown in Fig. 8.4(a) and listed in column C of Table 8.1, pixels with amplitude values larger than $0.67 \cdot \max_r |P(\mathbf{r})| = 17$ were excluded. They are marked by red crosses in Fig. 8.4(a). The remaining points served as input for the least-squares fit which was done with the standard surface-fitting routines provided by MATLAB. The latter use the trust-region concept (CONN ET AL., 2000) to solve this non-linear minimization problem (compare MATLAB 2012c, page 6-21 for details on the implementation). To confirm the reproducibility of the fit result, various starting guesses were used, which in some cases differed significantly from the parameters used for the first model (Fig. 8.3 and column A of Table 8.1). Table 8.1(B) lists the input parameters of the particular fitting run shown in Fig. 8.4(a), whose numerical result can be found in column C of Table 8.1. While the parameters' individual 95% confidence intervals are given as uncertainties in column C of Table 8.1, a coefficient of determination of $R^2 = 0.984$ and a root-mean-square error of $\text{RMSE} = 0.123$ quantify the overall goodness of the fit.

8.4.1.3 Quantification of illumination function

From the fitted parameters $b_1 = 0.0972 \text{ px}^{-1}$ and $b_2 = 0.0930 \text{ px}^{-1}$, one obtains with (8.3) and (8.4) the following FWHM values for the central intensity maximum in the focal plane:

$$\text{FWHM}_h \approx 148 \text{ nm} \qquad \text{FWHM}_v \approx 154 \text{ nm} . \qquad (8.5)$$

This result is in good agreement with the $150 \text{ nm} \times 170 \text{ nm}$ (horizontal \times vertical FWHM) deduced from older characterization measurements with similar experimental conditions. The deviations, in particular for the vertical direction, may be due to the fact that these interpolated sizes are not precise enough in this case. Furthermore, the initial calibration measurements probably also incorporate the effect of the strong side-lobes of the sinc-shaped focus: as discussed in the last paragraph of section 8.3 on page 207, the intensity in these side-lobes may increase the apparent size of the focus in fluorescence knife-edge scans.

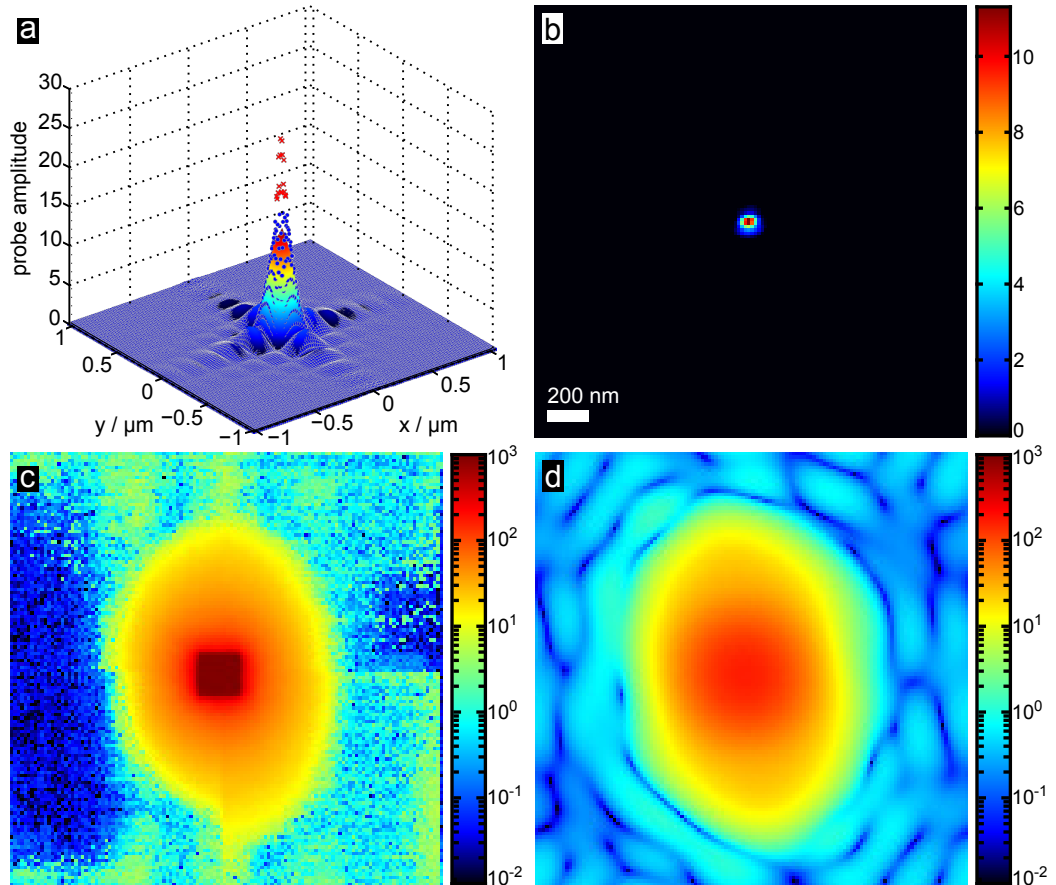


Figure 8.4: Isolation of background-induced artefact in probe by using a least-squares fit of the model (8.2) to the amplitude of the reconstructed probe. **(a)** Result of least-squares fit (colour-coded solid surface) compared to reconstructed amplitude (blue dots). The red crosses mark the points which have been excluded from the input data of the fit due to clearly belonging to the artefact. **(b)** Isolated background-induced artefact obtained by subtracting the result of the least-squares fit from the retrieved probe amplitude shown on a colour-coded linear scale. As only the difference in the central peak is of interest, deviations outside of this region have been suppressed by applying a mask. **(c)** Fourier magnitude of the retrieved probe displayed on a logarithmic scale (see colour-bar). As expected, a projection image of the effective entrance aperture of the KB focusing system shows up as a square with pretty uniform amplitude. Around the beam a rather extended halo is visible which is also present in the measured diffraction data and is attributed to the extended point-spread function of the scintillator-based detection system. **(d)** The Fourier magnitude of the isolated artefact shows that the latter accounts for most of the halo around the central beam. It can thus be concluded that in the reconstruction process the background halo in the diffraction patterns generates this artefact on top of the central peak of the probe which in turn degrades the quality of the reconstructed object.

From the parameters $d_{1,2}$ as defined in (8.2), the sigma widths $\sigma_{1,2}^f = (2d_{1,2})^{-1/2}$ of the **2D Gaussian damping factor** can be calculated. For $d_{1,2} = 5 \cdot 10^{-4} \text{ px}^{-2}$ one obtains $\sigma_{1,2}^f = 31.6 \text{ px} \hat{=} 512.8 \text{ nm}$, where the superscript f labels this as the value in the focal plane. The various potential sources of this damping factor have been discussed in the corresponding paragraph starting on page 210. To distinguish their respective effect the widths of the Fourier transforms of the Gaussian damping factor both at the detector and at the effective entrance aperture of the KB are of interest. In both cases, the sigma values can be calculated from $\sigma_{1,2}^f$ based on relation 2.20 on page 53 which becomes

$$\sigma_{d,e} = \frac{L_{d,e}\lambda}{\sigma^f}, \quad (8.6)$$

where $\lambda = 0.73 \text{ \AA}$ is the X-rays' wavelength and $\sigma^f = \sigma_1^f = \sigma_2^f$. The calculation uses the distances between focal plane and detector $L_d = 2.89 \text{ m}$ and between effective entrance aperture and focal plane L_e . The latter value is given by the focal length of the respective KB, which is $L_{e,h} = 83 \text{ mm}$ in the horizontal direction and $L_{e,v} = 180 \text{ mm}$ in the vertical one.

If the damping had been due to the smoothness of the entrance slits of the KB system, a sigma value for the corresponding Gaussian in the convolution kernel of $\sigma_{e,h} \approx 11.8 \mu\text{m}$ would be obtained with (8.6) and the values given above. This is rather large compared to the horizontal slit width of $35 \mu\text{m}$. Furthermore, the difference in focal lengths in the horizontal and the vertical direction has to be considered: If the damping was due to the slits' edges all being smoothed the same way either physically or just seemingly (i.e. by vibrations or due to the propagation to the mirror), one would expect the Gaussian damping function in the focal plane to be asymmetric. However, no asymmetry is observed. The value for $\sigma_{e,v}$ obtained with the same value of σ^f and the longer vertical focal length of 180 mm is also unrealistic for a smooth slit as it would be even larger than in the horizontal case: $\sigma_{e,v} \approx 25.8 \mu\text{m}$.

In the detector plane, the sigma widths of the Fourier-transformed Gaussian envelope are both $\sigma_d \approx 413 \mu\text{m}$. This corresponds two about 4 pixels of $102 \mu\text{m}$ effective size, where the latter results from the two-fold software binning applied to the diffraction data in this particular reconstruction run. According to (2.7) on page 48, this is a FWHM of about 9.5 pixels. This is significantly larger than the roughly 2 to 3 (unbinned) pixels FWHM which were estimated for the LSF of the detector in section 5.2.4 (see page 140) and which were also found to be consistent with values reported by PONCHUT (2006, page 203). However, an estimation (see section 8.4.2 starting on page 216) of the PSF based on the background-induced artefact also yields widths

which are significantly larger than expected, i.e. even about twice the size of the values obtained here.

In summary, both the sigma values obtained at the entrance plane and at the detector were found to be larger than expected. In turn, this means that the damping in the focal plane is stronger than it would be if just one of the discussed effects was the reason for it. The observed Gaussian factor thus probably contains the contributions of several sources. As the lack of asymmetry in the focal plane makes a strong influence of the entrance slits less likely, a combined effect of the mirrors' surface roughness and the detector's PSF seems to be the most reasonable explanation.

8.4.1.4 Isolation of background-induced artefact

As shown in Fig. 8.4(b) on page 214, the background-induced artefact on top of the central peak can be well isolated by subtracting the amplitude of the undistorted least-squares fit from the amplitude of the reconstructed probe. Mathematically, this corresponds to the assumption that the reconstructed probe P_{rec} can be described as the sum of the undistorted probe P and the artefact P' :

$$P_{\text{rec}}(\mathbf{r}) = P(\mathbf{r}) + P'(\mathbf{r}) \quad (8.7)$$

As the phase part of the retrieved illumination shows no artefact, it is further assumed that the reconstructed phase resembles the correct value and thus is the same for both additive components $P(\mathbf{r})$ and $P'(\mathbf{r})$. Fig. 8.4(c) shows the Fourier magnitude $|\tilde{P}_{\text{rec}}(\mathbf{r})|$ which is calculated from the reconstructed probe and corresponds to the square root of an intensity pattern obtained without any sample in the beam. As in all measured diffraction patterns, also here the background halo around undiffracted beam is present. Due to its close resemblance to the Fourier magnitude $|\tilde{P}'|$ shown in Fig. 8.4(d), this background is identified to be the main cause of the artefact P' .

8.4.2 Estimation of detector PSF based on background-induced artefact

Based on the assumption that the background around the central beam present in all diffraction patterns can be fully attributed to the detector's point-spread function (PSF), the previously isolated probe artefact P' is used in this section to obtain an estimate for this PSF.

8.4.2.1 Relation of PSF and previously isolated artefact

In what follows, the detector is described as a general linear imaging system (BORN AND WOLF, 2006; GOODMAN, 1996). The impulse response of such a system for fully coherent illumination is given by the amplitude spread function (ASF) h . In our case, it connects the actual diffracted wave field $\tilde{\psi}_j(\mathbf{q})$ to the Fourier transform $\tilde{\psi}_{j,\text{rec}}(\mathbf{q})$ of the reconstructed exit wave, i.e. the wave field in the detector plane retrieved by the reconstruction algorithm:

$$\tilde{\psi}_{j,\text{rec}}(\mathbf{q}) = \tilde{\psi}_j(\mathbf{q}) \otimes h(\mathbf{q}) , \quad (8.8)$$

at each scan position j . If the complex-valued amplitude-spread function of a linear imaging system when illuminated with fully coherent radiation is known, the point spread function (PSF) for fully incoherent illumination is the square of the magnitude of the ASF, compare e.g. GOODMAN (1996, section 6.1.3, pp. 132–134) or BORN AND WOLF (2006, section 9.5, pp. 545–547):

$$I_{j,\text{det}}(\mathbf{q}) = I_j(\mathbf{q}) \otimes |h(\mathbf{q})|^2 = I_j(\mathbf{q}) \otimes \text{PSF}(\mathbf{q}) . \quad (8.9)$$

According to the Fourier convolution theorem, the convolution with the amplitude spread function in the diffraction plane in (8.8) can be expressed as a multiplication in the object plane, which is the conjugated Fourier plane:

$$\psi_{j,\text{rec}}(\mathbf{r}) = \psi_j(\mathbf{r}) \cdot \tilde{h}(\mathbf{r}) , \quad (8.10)$$

where the Fourier transform \tilde{h} of the amplitude impulse response h is often called the amplitude transfer function (GOODMAN, 1996). It is now further assumed that this multiplicative factor, which is independent of the scan position j , can be considered to be fully absorbed in the reconstructed probe, i.e.

$$P_{\text{rec}}(\mathbf{r}) = P(\mathbf{r}) \cdot \tilde{h}(\mathbf{r}) . \quad (8.11)$$

The comparison with (8.7) shows, that $\tilde{h}(\mathbf{r})$ can be expressed in terms of the previously isolated artefact P' :

$$\tilde{h}(\mathbf{r}) = \begin{cases} 1 + \frac{P'(\mathbf{r})}{P(\mathbf{r})} & , \mathbf{r} \in \{\mathbf{r} : P'(\mathbf{r}) \neq 0\} \\ 1 & , \text{otherwise} \end{cases} \quad (8.12)$$

As the artefact is non-zero only within a small localized part of the central maximum of the 2D-sinc which forms the undistorted probe, one has $P(\mathbf{r}) \neq 0$ for all these pixels and the division in the first case is well-behaved. In the rest of the area, the artefact does not influence the probe at all, i.e. the amplitude transfer function is unity as stated in the second case of (8.12).

According to (8.9), the PSF is then obtained as the squared magnitude of the Fourier transform of (8.12):

$$PSF = |h(\mathbf{q})|^2 = \mathcal{F} \left\{ \frac{P'}{P} \right\} (\mathbf{q}) + \mathcal{O}(\delta(\mathbf{q})) . \quad (8.13)$$

In what follows, the contributions $\mathcal{O}(\delta(\mathbf{q}))$ originating from the constant term of $h(\mathbf{r})$, which results in its Fourier transform containing a Dirac- δ distribution as a summand, are not considered. The PSF is thus further characterized by means of a least-squares fit to the first term in (8.13), which is depicted on a colour-coded logarithmic scale in Fig. 8.5(b) on page 219.

8.4.2.2 Model used for fit to PSF

HOLTON ET AL. (2012) found that the PSF of a fibre-coupled CCD-based detector similar to the one employed here could best be “described by a Moffat function (MOFFAT, 1969), which is essentially the convolution of a Gaussian with a power law”. As they state that “this convolution cannot be expressed in closed form”, HOLTON ET AL. (2012) model the PSF as a sum of Gaussians, in their case adding up eight terms. Here, the number of summands has been restricted to two terms only, as for more terms the least-squares fit started to become unstable. As a result, there is one term that models the central, symmetric peak of the background while the second term accounts for the lower intensities and their asymmetric spatial distribution:

$$PSF_{\text{fit}}(u, v) = \sum_{j=1}^2 a_j \exp \left[-\frac{u_j'^2}{2\sigma_{u',j}^2} - \frac{v_j'^2}{2\sigma_{v',j}^2} \right], \quad (8.14)$$

where each component depends on its own set of rotated Cartesian coordinates u_j' and v_j' which are related to the unrotated pixel coordinates u and v (horizontal and vertical) by

$$\begin{pmatrix} u_j' \\ v_j' \end{pmatrix} = \begin{pmatrix} \cos \phi_j & -\sin \phi_j \\ \sin \phi_j & \cos \phi_j \end{pmatrix} \cdot \begin{pmatrix} u - u_{0,j} \\ v - v_{0,j} \end{pmatrix} . \quad (8.15)$$

As the pixel coordinate (u, v) is determined with respect to the lower-left corner of the image, the redefined coordinate system for the fit of the j -th Gaussian peak in (8.14) is not only rotated by angle ϕ_j . Before the rotation, the origin has to be shifted to the centre $(u_{0,j}, v_{0,j})$ of the corresponding peak.

8.4.2.3 Result of fit to PSF

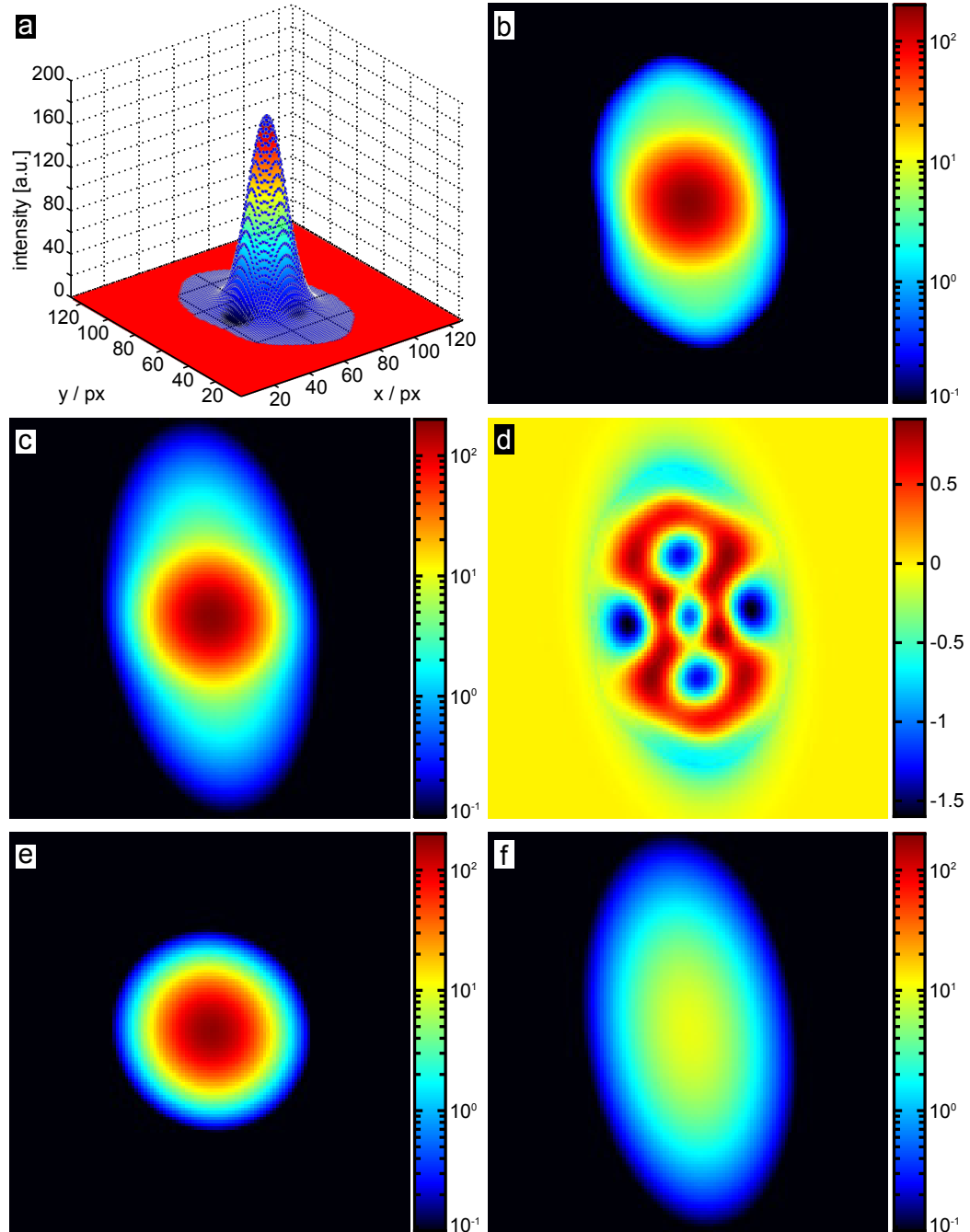
The result of the fit of the model (8.14) to the first term of (8.13) is depicted in Fig. 8.5 on page 219 and listed in Table 8.2. As for the fit of the probe

		$j = 1$ in (8.14)	$j = 2$ in (8.14)
amplitude	a_j	175.0 ± 0.4	9.8 ± 0.3
widths	$\sigma_{u',j}/\text{px}$	8.13 ± 0.01	11.20 ± 0.11
	$\sigma_{v',j}/\text{px}$	8.50 ± 0.01	20.94 ± 0.32
	$\sigma_{u',j}/\mu\text{m}$	829 ± 1	1142 ± 11
	$\sigma_{v',j}/\mu\text{m}$	868 ± 1	2136 ± 33
centre	$u_{0,j}/\text{px}$	65.0 ± 0.1	65.0 ± 0.1
	$v_{0,j}/\text{px}$	65.0 ± 0.1	65.0 ± 0.2
angle	$\phi_j/^\circ$	-39.2 ± 0.8	-7.5 ± 0.4

Table 8.2: Parameters obtained for the least-squares fit of the sum of two Gaussians in (8.14) to the PSF calculated from the Fourier transform of the background-induced artefact. The result of the fit is visualized in Fig. 8.5 and further discussed there and in the main text. While the 1st summand ($j = 1$) models the rather symmetric central peak, the 2nd summand ($j = 2$) accounts for the asymmetry of the surrounding lower intensities.

presented on page 213, also this fit was performed with the tools for non-linear surface fitting which MATLAB provides as part of its optimization toolbox (MATLAB, 2012c) and which employ a trust-region concept (CONN ET AL., 2000) for the actual minimization. In order to consider only the PSF itself and exclude the outer parts of the image from the fit, a threshold of 0.1, i.e. about 6‰ of the maximum value, was applied to the data. The excluded points are coloured red in Fig. 8.5(a) while the input data points used for the fit are marked by blue dots. The uncertainties in Table 8.2 correspond to the 95% confidence intervals of the individual parameters. Concerning the overall goodness of the fit, one finds a coefficient of determination of $R^2 = 0.9997$ and a root-mean-square error of $\text{RMSE} = 0.544$.

Figure 8.5 (following page): Least-squares fit of the sum of two Gaussians in (8.14) to the PSF obtained as the first term of (8.13) from the previously isolated background-induced artefact in the probe (compare Fig. 8.4(b)). (a) Result of least-squares fit (colour-coded solid surface) compared to input PSF (blue dots). The data points marked in red have values below 0.1 (about 6‰ of the maximum value) and have been excluded from the input data by thresholding. (b) Input PSF on a colour-coded logarithmic scale. (c) Result of least-square fit according to (8.14) shown on the same colour scale. The nearly-symmetric central Gaussian peak and the asymmetry for the lower values are well reproduced. (d) The difference image shows, that there are still some systematic deviations between input data and fit result for the simple model employed here. (e) First Gaussian summand of the fit (8.14) which accounts for the symmetric central peak. (f) Second term of the fit (8.14) modelling the asymmetry of the lower values.



For the first Gaussian summand of the fit, which models the central, symmetric peak of the PSF, sigma-widths of about 8.1 and 8.5 pixels are obtained. For the 2-fold binned pixel size of $102\ \mu\text{m}$, this corresponds to $830\ \mu\text{m}$ and $870\ \mu\text{m}$ (compare Table 8.2). PONCHUT (2006, page 203) reported a FWHM value 2 to 3 (unbinned) pixels FWHM for the line-spread function of a taper-based FReLoN system. A rough value estimated in section 5.2.4 (page 140) based on the image of a hole array lies in the same range. Therefore, the discrepancy to the significantly larger widths of the fitted surface, which definitely describes the observed background well, cannot be only attributed to deviations of the specific detector system from the one studied by PONCHUT (2006). Other possible reasons are:

- 1. The PSF is broadened due to a non-linear increase of the spread in the fibre-optics taper at high incoming intensities:** HOLTON ET AL. (2012) found for an X-ray detection system which relies on a fibre-optics taper that scattering in the latter is a major source of the PSF, in particular its long tails. Consider now a case, in which the detector is illuminated with a pencil beam significantly smaller than its (effective) pixel size. Any light detected by the CCD in non illuminated pixels will then be an effect of the PSF, i.e. the scattering in the taper. At a higher intensity of the incoming beam, also the intensity of the scattered light will increase. As long as this increase is proportional to the one of the incident intensity, the width of the PSF will not change. But if the amount of light scattered in the scintillator or the fibre-optics taper and detected by the CCD showed a non-linear dependence on the X-ray flux hitting the scintillator, this could lead to a broadening of the PSF for very high incoming intensities. This could for instance be the case, if the extra mural absorption, which is supposed to reduce the light transfer between the optical fibres (compare e.g. GRUNER ET AL., 2002b), became significantly less efficient in removing stray light. However, such effects have not been described or quantified elsewhere. Furthermore, the similar FReLoN camera studied by PONCHUT (2006) shows a linear detector response also for higher incoming intensities.
- 2. The background present in the diffraction patterns around the central beam contains contributions of multiple effects and is not only caused by the detector's PSF:** As the latter is usually symmetric, in particular the asymmetry of the second Gaussian term of the sum (8.14) suggests the presence of other influences. It seems unlikely that this is due to a symmetric effect upstream of the KB system which results in an asymmetric signal on the detector due to the different focal lengths of the two KB mirrors: any such signal, e.g. scattering from the several

meters of air the beam passes before entering the focusing device, is first spatially filtered by the KB system's entrance slits. As these apertures are asymmetrically set to create a symmetric beam footprint on the detector, also scattering that has passed them is expected to reflect their shape. Therefore, a signal on the detector created by such scattering should also not show a difference between horizontal and vertical direction. This leaves the KB system itself as the origin of the asymmetry, e.g. in the form of residual parasitic scattering which is not completely removed by the clean-up pinhole behind the mirror box (compare Fig. 5.4(a) on page 139 for the effect of this pinhole). A tilt of this rather thick aperture with respect to the optical axis could then explain both the asymmetric shape of the second Gaussian as well as deviation of its long axis from the vertical direction. A contribution which could be partly responsible for the broadening of the symmetric Gaussian term is the scattering in the almost 3 m air path between the KB system and the detector.

Considering the various possible factors influencing the recorded diffraction patterns, the second explanation seems to be most likely. In this case, the basic assumption that the background in the diffraction patterns can be fully described as an effect of the detector's PSF is too strong.

8.4.3 Reconstructions with post-processed diffraction data

The features of the original object reconstruction in Fig. 8.7(a) do not show the sharp boundaries one would expect for a lithographically-patterned test structure, but have rather smooth edges instead, compare also the blue line-outs in Fig. 8.7(c) and (d). In this section, it is shown that this effect can be attributed to the strong background around the central beam and the artefact it causes and that post-processing in which this background is removed from the diffraction data yields significantly improved ptychographic reconstructions. The section compares different correction approaches and concludes with a discussion of the obtained quantitative values.

All reconstructions discussed in this sections have been obtained with the difference-map PCDI algorithm. In particular in cases where the reconstructions still showed strong artefacts, no improvement could be observed when applying additional maximum-likelihood refinement.

8.4.3.1 Comparison of different correction approaches

Two major classes of correction approaches can be distinguished:

Reconstruction-based corrections These approaches rely on the assumption that ptychographic reconstructions of the untreated data allow to identify, characterize and isolate degrading components in the diffraction patterns. Even when this is possible, there remains the disadvantage that the processes required to obtain the necessary results may be rather involved and time consuming.

Data-based corrections This refers to direct corrections of the diffraction data employing no or only little *a priori* knowledge. While this typically allows to circumvent the lengthy characterization process of the reconstruction-based approaches, many of these methods share the problem that the correction of the direct beam's intensity remains unknown.

The next paragraphs discuss different approaches of both types which were investigated for the correction of the Siemens star data set:

Subtraction of wave fields This approach is based on the isolation of the background-induced artefact in the probe in section 8.4.1. As a consequence of (8.7) on page 216, also the reconstructed exit waves $\psi_{j,\text{rec}} = P_{\text{rec}}(\mathbf{r} - \mathbf{r}_j) \cdot O(\mathbf{r})$ at each scan point j can be expressed as the sum of the contributions of undistorted probe P and artefact P' :

$$\psi_{j,\text{rec}}(\mathbf{r}) = \psi_j(\mathbf{r}) + \psi'_j(\mathbf{r}) . \quad (8.16)$$

From this, one can obtain a corrected intensity in which the contribution leading to the artefact P' is removed:

$$I_{j,\text{corr}} = |\tilde{\psi}_j|^2 = |\tilde{\psi}_{j,\text{rec}} - \tilde{\psi}'_j|^2 , \quad (8.17)$$

where $\tilde{\psi}_j$ signifies the Fourier transform of ψ_j .

The phase part of the reconstructed object obtained after 600 iterations of difference-map PCDI with data corrected this way is shown in Fig. 8.7(e). While locally some minor improvements are observed, the overall smooth shape of the lithographic structures remains: Line profiles across the bars differ only marginally from the blue ones in Fig. 8.7(c) and (d), which are obtained with the uncorrected data. The line-outs for the case at hand are therefore not plotted separately. As anticipated from the way the data was corrected, the previously observed artefact is no longer present in the reconstructed probe amplitude (not depicted).

Deconvolution As pointed out in section 1.1.3, deconvolution is frequently used to remove the effects of an imaging system’s PSF from the measured intensity pattern $I_{\text{det}} = I_{\text{in}} \otimes \text{PSF}$ (compare (1.12) on page 19) in order to obtain the actual incident intensity distribution I_{in} . Standard deconvolution techniques require that a highly accurate input PSF is provided, compare e.g. the overview given by BANHAM AND KATSAGGELOS (1997). In contrast, iterative *blind deconvolution* techniques can start from a less precise PSF guess which is then further refined (see review by KUNDUR AND HATZINAKOS, 1996).

Blind deconvolution was applied to the Siemens star data employing the function `deconvblind` of MATLAB’s Image Processing Toolbox (see MATLAB 2012b, page 13-16 and MATLAB 2012a, page 3-131) at an early stage of this work. The diffraction patterns treated this way resulted in a slightly better quality of the reconstructed images. However, the improvement is not nearly as significant as for other investigated correction approaches. In addition, the iterative procedure also showed a rather unstable convergence behaviour, i.e. more iterations of the blind deconvolution algorithm would degrade the diffraction data rather than improve – or at least stay at – an already reasonable result. As a consequence, this approach was not pursued any further in the course of the current studies. Nevertheless, a more detailed future investigation of its applicability in this specific context might be worthwhile.

Subtraction of global pixel minimum For the scan investigated here, a lot of points lie in empty areas of the object. The corresponding diffraction patterns therefore contain only the combined signal of the background to be corrected and the direct beam. Apart from the area hit by the direct beam, the minimum value a given pixel $\mathbf{q} = (u, v)$ assumes when comparing its respective counts for all scan positions j should thus give a reasonable estimate of the sample-independent background intensity. With the further assumption that this background can be treated as an incoherent contribution, i.e. additive in intensity, the corrected diffraction pattern for scan point j is obtained as

$$I_{j,\text{corr}}(\mathbf{q}) = I_j(\mathbf{q}) - \min_j I_j(\mathbf{q}) , \quad (8.18)$$

where I_j is the original diffraction pattern recorded at position j . This method has the benefit that it can be directly applied to the diffraction data without any further pre-characterization steps. In cases where the object does not contain empty regions, a set of dedicated diffraction patterns taken without sample may be used to determine the background. However, the approach has the major disadvantage that it does not provide any infor-

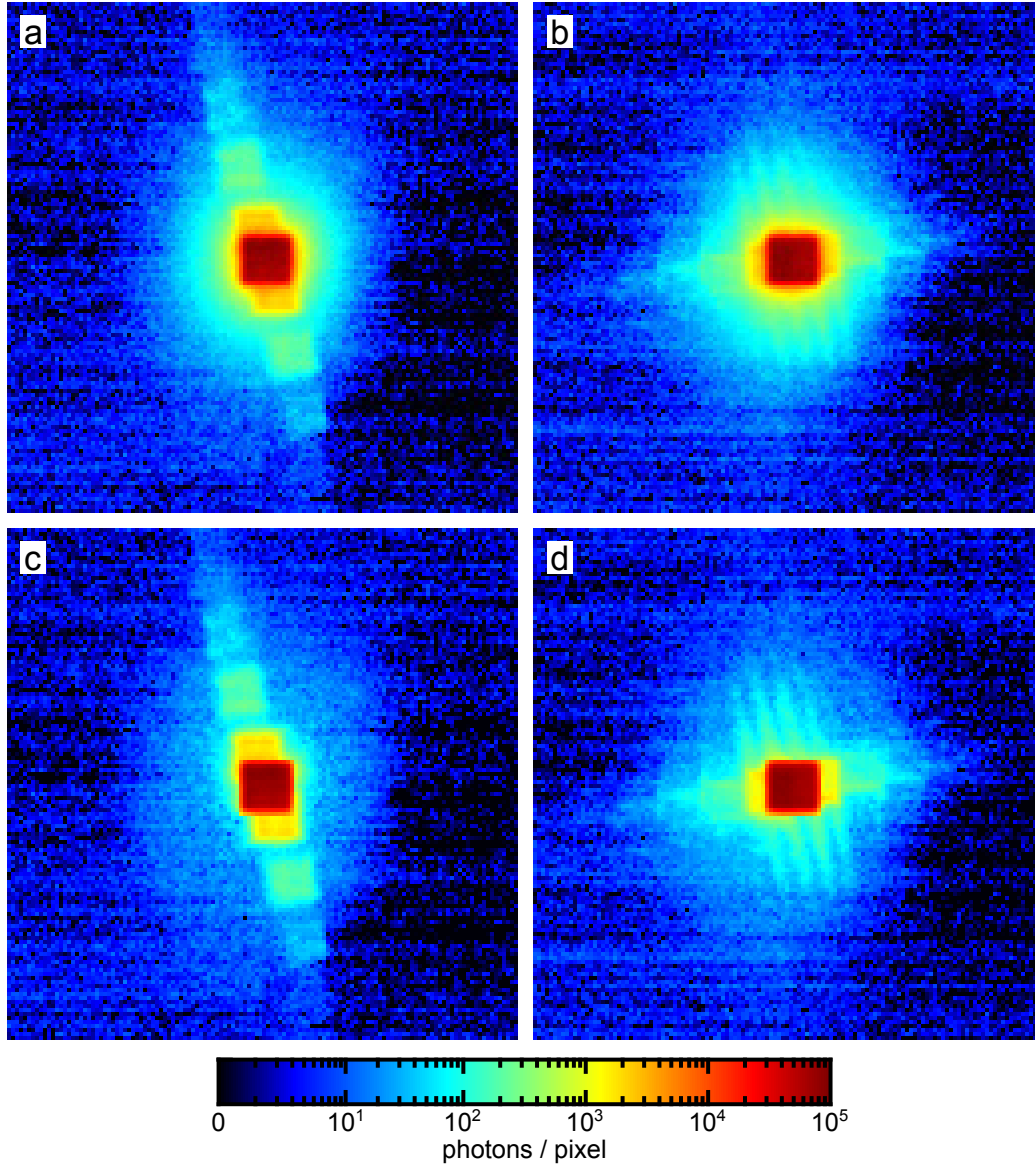


Figure 8.6: Comparison of original and post-processed diffraction patterns. (a),(b) Original diffraction patterns which have only been corrected for the dark current of the CCD. (c),(d) The same diffraction patterns after subtracting from each pixel the minimum value it recorded during the whole ptychographic scan according to (8.18). The visibility of the diffraction signal is greatly improved: the four vertical lines, e.g., which are nicely visible in (d) are barely discernible from the background in (b). All plots share the same colour-coded logarithmic scale defined by the colour-bar at the bottom.

mation on how to correct the pixels always covered by the direct beam. In the application to the Siemens star data set, two different ways have been investigated:

1. In area of the direct beam, the subtraction (8.18) is not applied and the reconstruction is done using the original, uncorrected pixel values in this area. Two examples for the diffraction patterns obtained this way are shown in the lower row of Fig. 8.6 on page 225, while the upper row of the figure displays the input data. The resulting reconstruction of the phase part of the complex object transmission function after 300 iterations of difference-map PCDI is shown in Fig. 8.7(b) on page 228. In comparison with the original reconstruction in (a), the features of the test structure have a much sharper appearance in the case of the background-corrected data. This is confirmed by the line-outs in Fig. 8.7(c), which are taken perpendicular to some of the radial bars in both the original image (blue plot) and the improved reconstruction (green plot). In the green plot in (c), the bars show the rectangular cross-section one would expect from their lithographic manufacturing process. The increased sharpness of the edges also allows to better distinguish the smallest features, as apparent from the line-outs in Fig. 8.7(d), even down to the minimum bar separation of 50 nm. This result thus already clearly demonstrates that the background in the diffraction patterns is indeed the main limiting factor for the quality of the ptychographic reconstructions. However, Fig. 8.7(b) also suffers from some grid-like artefacts which are visible in particular in the bright gaps. They are most likely due to the discontinuity introduced into the diffraction patterns by excluding their central part with the direct beam from the subtraction (8.18).
2. In the second case, the area of the central beam is excluded from the reconstruction, i.e. the mask defining the valid pixels in the Fourier projection, compare (3.20) on page 93, is set to 0 in this region. This allows the algorithm to freely adapt the Fourier magnitudes of these pixels in the way which fits best with the surrounding data. The latter is again corrected according to (8.18). As a result, Fig. 8.7(f) does no longer show the grid-like artefacts. However, it has to be pointed out that they still occur in the individual iterations of the object. As they strongly fluctuate while the reconstruction progresses, they are removed by the averaging step of the difference-map PCDI algorithm, which has been applied for 600 iterations in this case. Although a rather nice result is obtained this way, there is a fundamental drawback: due to the loss of all information about the central diffraction order, the relative scaling of the two components of this binary object is no longer constrained well. As a consequence, the

phase shift obtained for the gold structures is about a factor of two larger in Fig. 8.7(f) than for the other reconstructions in (a), (b) and (e). The result is thus no longer quantitative.

Direct fitting of background in diffraction data This approach is basically an extension of the subtraction of the global minimum discussed in the previous paragraph. As such, direct fitting of the background in the diffraction patterns also allows to avoid the intensive pre-characterization required for the reconstruction-based corrections. More importantly, replacing the global minimum by a fit adds the major benefit, that it also provides correction values for the direct beam area and a continuous transition to the surrounding pixels.

For the tests of this method, an estimate of the background which formed the basis of the fit was obtained by calculating the global minimum pixel map $I_{\min}(\mathbf{q}) = \min_j I_j(\mathbf{q})$. As a fit model a sum of Gaussians with up to two independent additive terms in analogy to (8.14) on page 218 was used. The pixels containing the direct beam were not considered for the least-squares fits, which were again performed with the tools provided by MATLAB's optimization toolbox (MATLAB, 2012c), which implement a trust-region minimization concept (CONN ET AL., 2000). The fitted surface was then used to correct the full diffraction pattern, again by simply subtracting it from the original diffraction frames. The resulting reconstructions are similar to Fig. 8.7(b). However, also in these retrieved images a lot of artefacts are present, most likely due to residual background structures which remain after subtracting the fit results. More importantly, the fit itself is rather unstable when it comes to the amplitude of the Gaussian peak which is supposed to model the background in the area of the central beam: this amplitude proves to be very dependent on the choice of initial parameters or small changes of the area of excluded pixels. The major goal of preserving the quantitiveness of the ptychographic reconstruction result by appropriate correction of the direct beam is therefore not achieved.

8.4.3.2 Discussion of quantitative results

The phase shift relative to a reference introduced by a $\Delta z = 700$ nm thick bar of pure gold is $\Phi = (2\pi/\lambda)\delta_{\text{Au}}\Delta z$, compare (1.28) on page 23. At the X-ray energy of 16.9 keV used in this experiment, the wavelength is $\lambda \approx 0.73$ Å and the real part of the refractive index becomes $\delta_{\text{Au}} = 1.0951 \cdot 10^{-5}$. The latter value has been calculated based on the data compiled by HENKE ET AL. (1993) using the online-interface to the database available at <http://henke>.

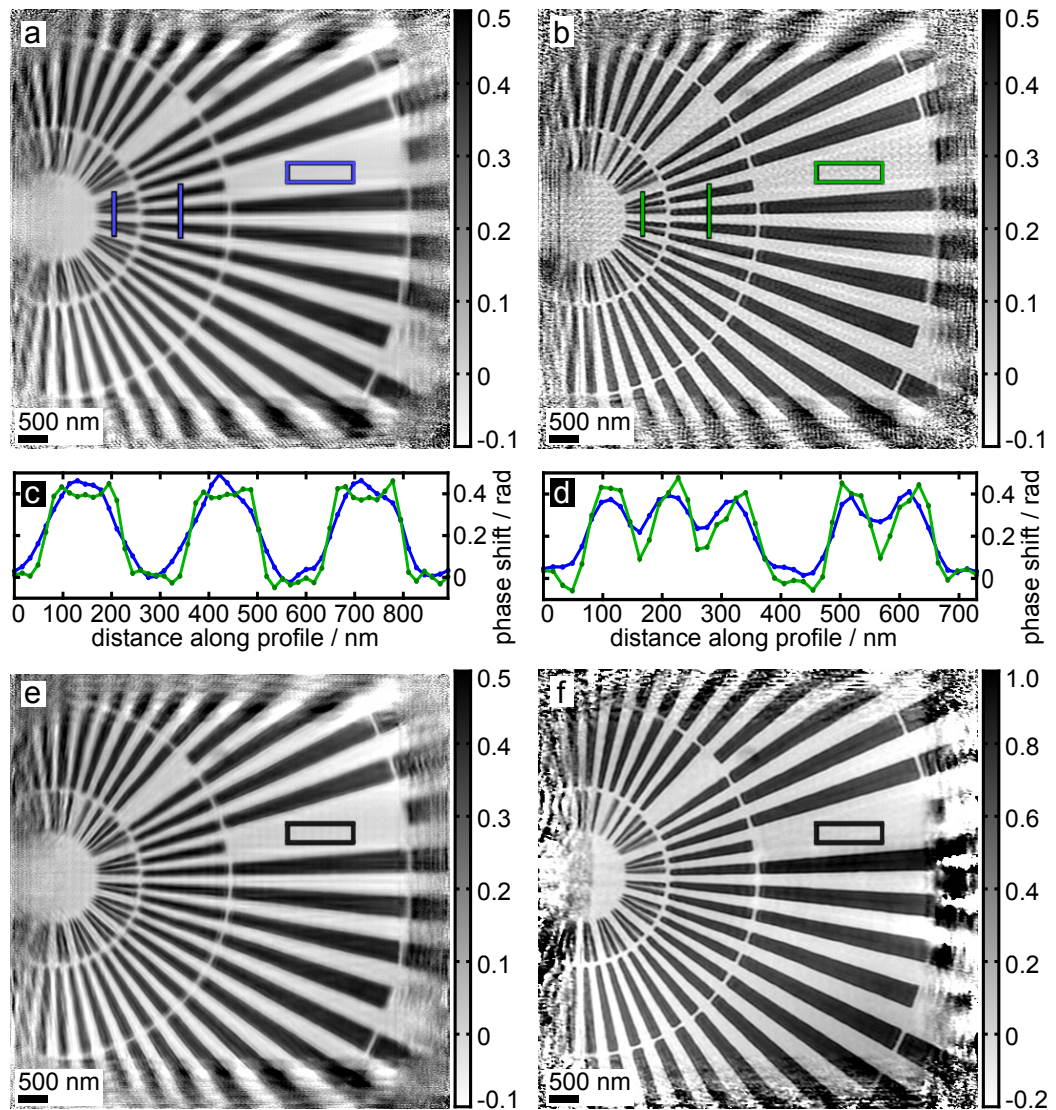


Figure 8.7: Comparison of ptychographic reconstructions of the Siemens star test pattern illustrating the effects of the background present around the central beam in all diffraction patterns. **(a)** Phase shift (in radians, see colour-bar) retrieved from the original data (200 iterations difference-map PCDI). **(b)** Reconstruction of the same data set after the diffraction patterns have been corrected to remove the background (subtraction of global pixel minimum, see main text). Already a visual comparison with **(a)** shows a improved sharpness of the retrieved structure. The gain in resolution is further illustrated by line-outs through bars in the second ring from the centre **(c)** or the inner one **(d)**, respectively, as marked by the vertical lines of the corresponding colour in **(a)** and **(b)**. While in **(c)** it is demonstrated how the rectangular shape of the lithographic structures is more accurately retrieved in **(b)**, **(d)** presents the improved separation of fine features. **(e),(f)** Further examples of phase reconstructions from corrected diffraction data (subtraction of wave field or global minimum, see main text). Note the different colour scale in **(f)**. The phase scale has been calibrated by setting the average in the marked rectangular regions to zero.

lbl.gov/optical_constants and the standard mass density of 19.3 g cm^{-3} provided there. From these value, a phase shift $\Phi_{\text{calc}} \approx 0.66 \text{ rad}$ is to be expected. In the reconstructed images, however, the phase shifts Φ_{rec} of the gold bars fluctuate around only about 0.4 rad . For the same mass density, this corresponds to a thickness $\Delta z_{\text{rec}} \approx 430 \text{ nm}$. Yet, previous measurements of this test pattern with other techniques have shown that this electroplated gold has a lower density, also because it contains a fraction of nickel, and thus exhibits a lower phase shift than pure bulk gold (Peter Cloetens, private communication):

If the material is assumed to be only gold, the proportionality between phase shift and mass density, which results from the linear relation between δ and the electron density in (1.24) on page 22, can be employed: The observed lower phase shift would then correspond to a density reduction to about 61 % of the nominal value, i.e. to roughly 11.8 g cm^{-3} .

If on the other hand the material is modelled as a binary mixture of Au and Ni in which each of the phases has the nominal mass density of the bulk material, the respective volume fractions can be estimated: From the reconstructed phase shift $\Phi_{\text{rec}} \approx 0.4 \text{ rad}$, a mean value $\bar{\delta} \approx 6.67 \cdot 10^{-6}$ is obtained for the real part of the refractive index with the relation

$$\bar{\delta} = \frac{\lambda}{2\pi\Delta z} \Phi_{\text{rec}} . \quad (8.19)$$

This $\bar{\delta}$ can be expressed as a weighted sum of δ_{Au} of bulk gold and δ_{Ni} of pure nickel:

$$\bar{\delta} = \xi \delta_{\text{Ni}} + (1 - \xi) \delta_{\text{Au}} , \quad (8.20)$$

where ξ is the volume fraction of Nickel in the material. Solving for ξ yields

$$\xi = \frac{\bar{\delta} - \delta_{\text{Au}}}{\delta_{\text{Ni}} - \delta_{\text{Au}}} . \quad (8.21)$$

With $\delta_{\text{Ni}} = 6.2511 \cdot 10^{-6}$ for Ni (with mass density $\rho_{m,\text{Ni}} = 8.9 \text{ g cm}^{-3}$) at an X-ray energy 16.9 keV (HENKE ET AL., 1993), one obtains $\xi \approx 0.91$. The knowledge of this volume fraction allows to calculate both a mean electron density $\bar{n}_e \approx 2.75 \text{ \AA}^{-3}$ and a mean mass density $\bar{\rho}_m \approx 9.8 \text{ g cm}^{-3}$ with relations corresponding to (8.20).

The obtained Nickel volume fraction of 91 % is most certainly too high and does not describe the composition of the sample correctly. However, it has to be considered that the reconstructed phase shift of the bars shows rather large variations of about 0.1 rad . Compared to such large fluctuations, the 1.5 %-spread in the phase shift distribution due to the broad bandwidth of the incident radiation, see (8.1), is only a minor influence. To better

quantify the effect of the phase uncertainties, a general expression for the volume fraction ξ depending only on the reconstructed phase shift Φ_{rec} can be obtained by replacing $\bar{\delta}$ in (8.20) with its definition in (8.19):

$$\xi \simeq -3.55 \cdot \Phi_{\text{rec}} + 2.33 . \quad (8.22)$$

A phase difference of ± 0.1 rad therefore changes the calculated volume fraction of nickel by about ∓ 0.355 . For $\Phi_{\text{rec}} = 0.5$ rad, e.g., one finds a significantly lower Ni content with $\xi \approx 0.56$. Furthermore, the fundamental assumption may be wrong that each of the components has the “density of the element in its naturally occurring form”, as stated in the online interface¹ to the tables of HENKE ET AL. (1993), which is the source for the mass density values of gold and nickel used in the previous calculations.

In conclusion, the observed discrepancy between the reconstructed and expected phase shift is most likely due to a combination of all three previously discussed sources of errors: a contamination of the gold bars with an unknown fraction of nickel, a deviation of the mass densities from the tabulated values, and the large uncertainty of the retrieved phase values.

8.5 Conclusions

The work presented in this chapter has proven the feasibility of ptychographic CDI with broad-bandwidth synchrotron radiation. This paves the way for high-resolution imaging enabled by the increased coherent flux compared to set-ups with standard crystal monochromators. Although this potential could not yet be fully exploited in the presented demonstration experiments, they allowed to identify and address several important problems: Based on the first test in July 2009, multiple questions of optimal experimental settings and data acquisition routines have been solved, compare the list on page 202 in section 8.2.1. While these issues therefore did no longer have a major impact on the results of the improved demonstration experiment in March 2011, in this second run the quality of the detected diffraction patterns proved to be the main limitation, namely the strong background observed around the undiffracted beam. The artefact in the probe reconstruction created by this background has been investigated in detail in section 8.4.1 on page 208. In section 8.4.2 starting on page 216, the detector’s point spread function has been characterized based on its relation to this artefact. This characterization, however, resulted in an estimate with a substantially larger width than expected from previously reported values.

¹http://henke.lbl.gov/optical_constants/pert_form.html

The strong negative influence of the background on the quality of the obtained images has been confirmed by results based on post-processed diffraction data sets in which the background had been removed prior to the ptychographic reconstruction. In section 8.4.3 starting on page 222, various approaches for background removal have been discussed. So far, subtracting from each pixel the global minimum value it assumes throughout the whole ptychographic scan has proven to yield the best results (see Fig. 8.7 on page 228). The improved reconstructions not only reproduce the rectangular cross sections of the lithographic structures but also allow to clearly resolve the finest features of the Siemens star test pattern, which have a size of 50 nm. However, the necessary background correction for the detector area always covered by the undiffracted beam cannot as easily be deduced from the data. The retrieved objects thus still either show some grid-like artefacts or the quantitative information concerning the offset between the two main phase values of the investigated binary structure is lost.

The quantitative values of the phase shifts obtained for the gold bars of the Siemens star test pattern have been discussed in the last subsection of 8.4.3 starting on page 227. They were found to be significantly lower than what would have been expected for a pure gold structure of the test pattern's nominal thickness. It has been concluded that this discrepancy is due to a combination of the presence of an unknown fraction of nickel within the gold bars, a deviation of the materials' densities from the tabulated values used in the calculations, and the retrieved phase values' large uncertainty manifesting as fluctuations of about 25 % around their mean.

Neither in terms of spatial resolution nor in terms of quantitative accuracy has the approach yet reached the fundamental limits imposed by the broad bandwidth of the synchrotron radiation. The main limiting factor has clearly been the detector, which could not cope with the full coherent flux and with its extended point spread function has been a major cause of the strong background degrading the diffraction patterns. If these problems can be solved, e.g. by the improvements discussed in the outlook section below, it will be possible to exploit the full potential of broad-bandwidth illuminations to achieve highest resolutions.

8.6 Outlook

This section introduces some improvements in terms of both hardware and reconstruction algorithms which are expected to allow to overcome some of the limitations discussed in the previous section.

8.6.1 Hardware improvements

The most promising option available at ESRF to avoid the strong background created by the fibre-optics taper of the FReLoN system is the **MAXIPIX detector** based on the MEDIPIX II chip (PONCHUT ET AL., 2011). In the standard design, however, the absorption in the silicon sensor at the typical working energies of ID22NI is not sufficient to protect the detector’s electronics from radiation damage. Only recently, the option of an CdTe sensor has enabled the use of the MAXIPIX at ID22NI (see e.g. CHMEISSANI ET AL., 2004 for an early demonstration of this technology). Although the technically-challenging production process currently still results in a lot of sensor defects, first tests have shown that the quality of the recorded diffraction data is nevertheless better than with the FReLoN. However, the high flux in the undiffracted beam easily exceeds the count rate limit of this detector, compare also the paragraph “Incoming flux” on page 144 in section 5.3.2.

In order to record in the same detector frame both low intensities at larger diffraction angles and high intensities in and around the direct beam, a **semi-transparent beamstop** has been tested: It consisted of a small rectangular piece cut from a metal sheet and mounted on a thin polyimide film (Kapton). Its size matched the footprint of the undiffracted beam on the detector in the specific experiment. As this significantly lowers the required dynamic range, an attenuation of the incident beam is no longer required and the full coherent flux can be exploited. For the reconstruction, the intensities of the respective pixels have to be rescaled to the unattenuated values. The rescaling factor can e.g. be determined from taking images with and without the beamstop at lower intensity which does not saturate the detector. Another option could be to measure the gain map of the modified detection system by illuminating it uniformly.

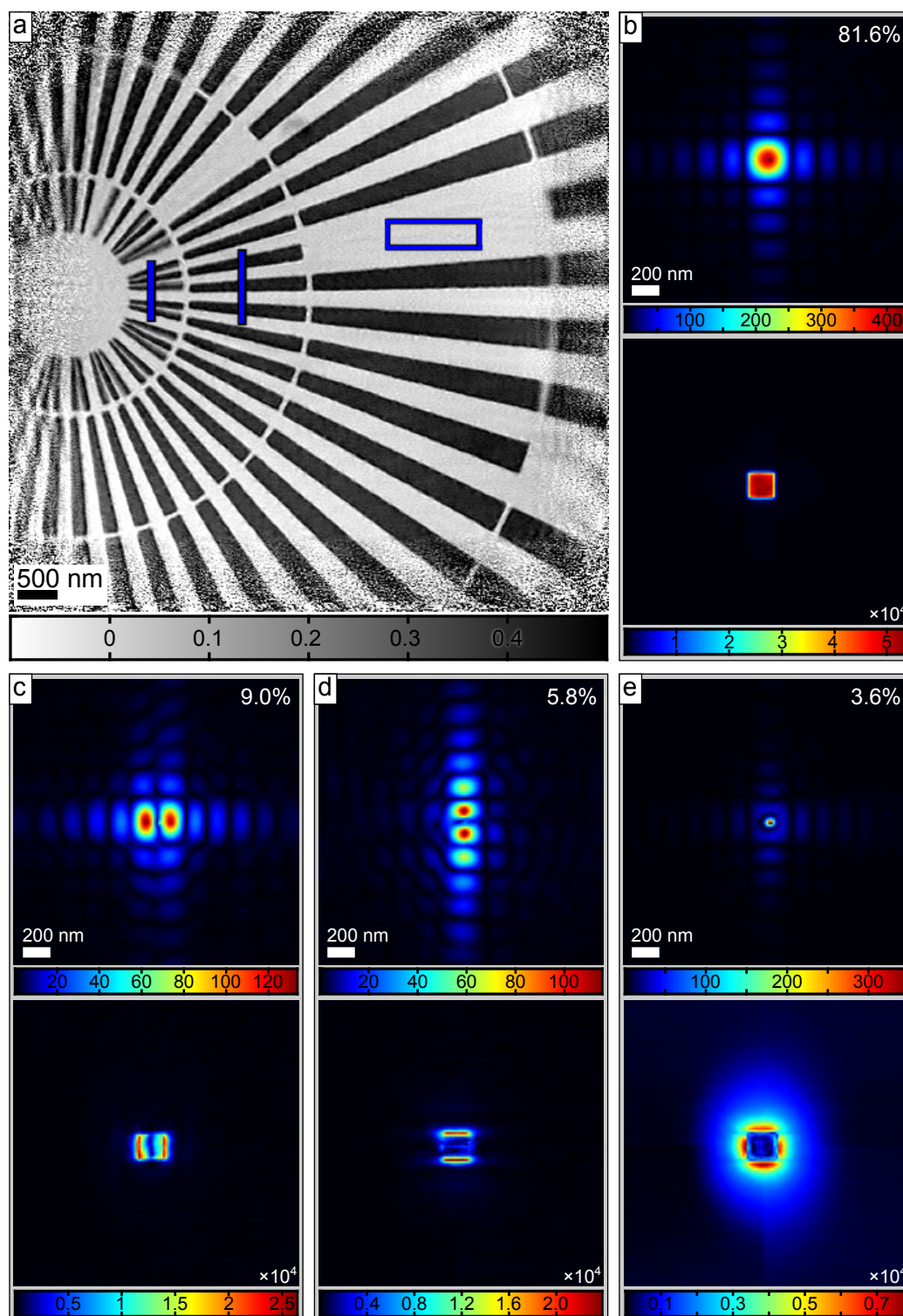
Further hardware improvements are to be expected at the long beamline NINA (**N**ano**I**maging and **N**ano**A**nalysis) which will be replacing ID22 as part of the ESRF upgrade program (CLOETENS, 2009): among other things, it is expected to provide a higher coherent flux, a scanning set-up with higher precision and an increased overall stability. As it is planned to offer ptychographic CDI in regular user operation at NINA, the project features some specific optimizations, most notably the plan to design a dedicated detector: it would handle the incoming high rate in the central direct-beam region through an integrating detection approach but still use single-photon counting for the low intensities at higher angles.

8.6.2 Algorithmic improvements: mixed-state reconstructions

Especially in the case of the strong background caused by the extended point-spread function of the detector, further improvements of the reconstruction algorithms can yield significantly better results already for the current data sets: The recent extension of ptychographic algorithms by THIBAUT AND MENZEL (2013) compensates for a detector's point spread by treating it as a mixed state: The probe is decomposed into several orthogonal modes. Each mode contributes a signal resulting from its interaction with the object to the total diffraction intensity such that the latter is the incoherent sum of all these contributions. This way, intensities which do not truly originate from the object itself are accounted for by higher order modes. The reconstruction of the object is thus no longer degraded by forcing it to account for all recorded intensity values in combination with just one unique probe.

More details on the application of mixed-state reconstructions to data recorded both with a broad-bandwidth and a detector of limited quality can be found in the recent article by ENDERS ET AL. (2014). A mixed-state reconstruction with four probe modes has been applied to the Siemens star data set which has been discussed in section 8.4. Apart from subtracting dark images and rebinning by a factor of two, no other corrections were carried out on the input diffraction data. In particular, no attempts to correct for the background around the central beam were made in this case. The input data thus was the same as for the reconstruction presented in Fig. 8.7(a). The mixed-state run used 600 iterations of difference-map PCDI followed by 400 iterations maximum-likelihood refinement. The retrieved phase shift

Figure 8.8 (following page): Reconstruction of Siemens star test pattern with four probe modes: **(a)** Phase shift of test object (in radians, see colour-bar) retrieved after 600 iterations of difference-map PCDI followed by 400 iterations maximum-likelihood refinement. The reconstruction is based on the same uncorrected input data as Fig. 8.7(a). The sharpness of the edges of the nano-structures resembles the results in Fig. 8.7(b) and (f), which were obtained with data in which the background had been removed prior to the reconstructions by post-processing. However, the result presented here does neither show the strong artefacts of Fig. 8.7(b) nor is the quantitiveness lost as in Fig. 8.7(f). The phase scale has been calibrated such that the average phase value in the marked rectangular region equals zero. Line profiles along the vertical blue bars are shown in Fig. 8.9. **(b-e)** Amplitudes of the four probe modes (top of the respective panel) and of their Fourier transforms (bottom). All values are displayed on colour-coded linear scales as encoded by the colour-bars below the individual images. The relative power of the respective mode, i.e. the percentage it contributes to the total probe intensity, is given in the top-left corner of each panel.



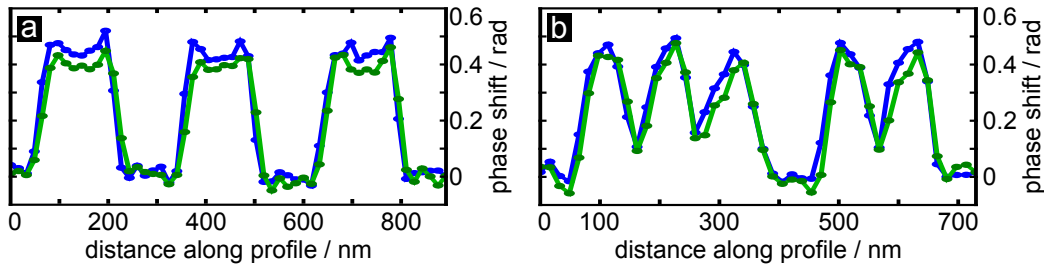


Figure 8.9: Line-outs across structures of Siemens star test pattern. The green plots show profiles along the green lines in Fig. 8.7(b), i.e. through a result obtained with background-corrected data. The blue plots are obtained for the reconstruction with uncorrected data and four probe modes which is shown in Fig. 8.8(a) and where the location of the line-outs is marked by the two vertical blue bars. (a) Line-outs through three bars in the second ring from the centre (marked by right vertical lines in phase images) which show the expected rectangular profile of the lithographic structures. (b) Line-outs across five bars in the ring closest to the centre (marked by left vertical lines in phase images) which allow to compare the contrast obtained for these small features.

of the object is shown in Fig. 8.8 together with the amplitudes of the four probe modes and their respective Fourier transform's amplitudes. As for the reconstructions in Fig. 8.7, also in Fig. 8.8(a) the object extends into the noisy border areas of the object array which are not touched by the central peak of the sinc-shaped probe but just by its side maxima. The object reconstruction is clearly the best result obtained so far for this data set: The edges are as sharp as in the results for the background-corrected data in Fig. 8.7(b) and (f). Profiles across the bars have the very same shape as the green lines in Fig. 8.7(c) and (d), only a slightly higher average phase offset between empty regions and bars is observed. Fig. 8.9 provides a direct comparison of these previous line-outs (green lines) with the ones across the phase image obtained with the four probe modes (blue lines).

The retrieved orthogonal probe modes, in particular their Fourier space amplitudes in Fig. 8.8(b) to (e), provide some valuable insights which parts of the diffraction patterns cannot be attributed well to signal coming from the object: The first mode in Fig. 8.8(a) contains 81.6 % of the total incident intensity and shows the expected sinc-shaped amplitude distribution in the focal plane, i.e. its Fourier amplitude reproduces the KB system's entrance aperture without any additional signal around. The modes in Fig. 8.8(c) and (d) however indicate that the illumination contains also strong contributions which are localized at the edges of the entrance apertures' image. This signal could thus be an effect of either slit scattering still passing the installed clean-up pinhole, or of spread in the fibre-optics taper at the edges of the undiffracted beam. Together the two modes amount to about 15 %

of the total intensity. The fourth mode in Fig. 8.8(e) accommodates for the background around the central beam (see Fourier amplitude) and thus in real space resembles the background-induced artefact investigated in section 8.4.1.

In combination with the hardware upgrades discussed in the previous section, mixed-state reconstructions like the example presented here are expected to play a major role in improving the results of future broad-bandwidth experiments.

Part III

Ptychographic nanotomography

Chapter 9

Development of ptychographic nanotomography

This chapter presents the development of nano-scale ptychographic X-ray computed tomography (PXCT) by means of a demonstration experiment on a murine bone previously published in [DIEROLF ET AL. \(2010a\)](#). Details on the experiment are given in the first section, while the second section introduces the various data analysis steps required to convert ptychographic data into a three-dimensional volume reconstruction. The third section discusses the results of the demonstration experiment. They are compared both to other imaging techniques in terms of their potential for bone research and to previous coherent X-ray imaging experiments concerning the applied doses and achieved resolutions. The last section provides conclusions on the current state and outlook on the future of the technique. Parts of the work present in this chapter has already been published in [DIEROLF ET AL. \(2010a\)](#).

9.1 Demonstration experiment

9.1.1 Sample preparation

For the demonstration experiment, a specimen was prepared from a mouse's femur bone (approved by the local animal ethics committee, the "Veterinärämamt des Kantons Zürich", Zürich, Switzerland). Preparation was carried out at the Center for Electron Microscopy at the ETH Zurich (EMEZ) by R. Wepf, M. Meier and P. Gasser. It followed the protocols established for the

investigation of this class of samples with serial focused ion beam / scanning electron microscopy (FIB/SEM) (compare SCHNEIDER ET AL., 2010). Here, the detailed description as published in the full Methods section of DIEROLF ET AL. (2010a) (available in the online version of the article) is quoted:

“Femora of twelve-week-old C57BL/6 (B6) mice were dissected and cleaned from soft tissue. After cutting the femora into halves using a scalpel, bone marrow was washed out using a 70% ethanol steam. Bones were stored in 70% ethanol and underwent an ethanol dehydrating series before further processing steps. Bones were infiltrated at four stages with a progressively increasing ratio of Lowicryl HM20 (from Polyscience, Chemie Brunschwig AG) to ethanol and a progressively decreasing temperature from 0 °C to −50 °C. The resin was subsequently polymerized for more than two days at −50 °C using ultraviolet radiation. The embedded specimens were then machined with a high-speed milling system (Leica EM TRIM2) to access a mid-diaphyseal cross-section. Finally, focused ion beam milling was performed on a CrossBeam workstation (NVision 40; Carl Zeiss SMT) to prepare a roughly cylindrical specimen of about 25 μm in diameter and 35 μm in height.”

While the last step of FIB milling required the specimen to be vacuum-compatible, this would in principle not have been necessary for the actual X-ray measurements in which the sample was placed in air. This possibility is exploited by a different preparation protocol which is introduced in section 10.1.2 on page 289. As it no longer relies on FIB milling, this approach allows to skip the complex dehydration and embedding steps.

9.1.2 Data collection

The details of the data collection in the course of the demonstration experiment have first been published in DIEROLF ET AL. (2010a, full Methods section in online version). The experiment was carried out at an X-ray energy of 6.2 keV (about 2 Å wavelength) at the cSAXS beamline of the Swiss Light Source (see section 5.1) using a tomography set-up developed in preparation of this specific run. A detailed description of the set-up and its individual components can be found in section 5.1.3 on page 134. This set-up offers the flexibility to use either a pinhole or the focus of a Fresnel zone plate to create a localized illumination on the specimen. In the case reported here, a pinhole of about 2.3 μm diameter was employed, which had been milled by focused ion beam into a tungsten foil of 50 μm thickness (K. Jefimovs,

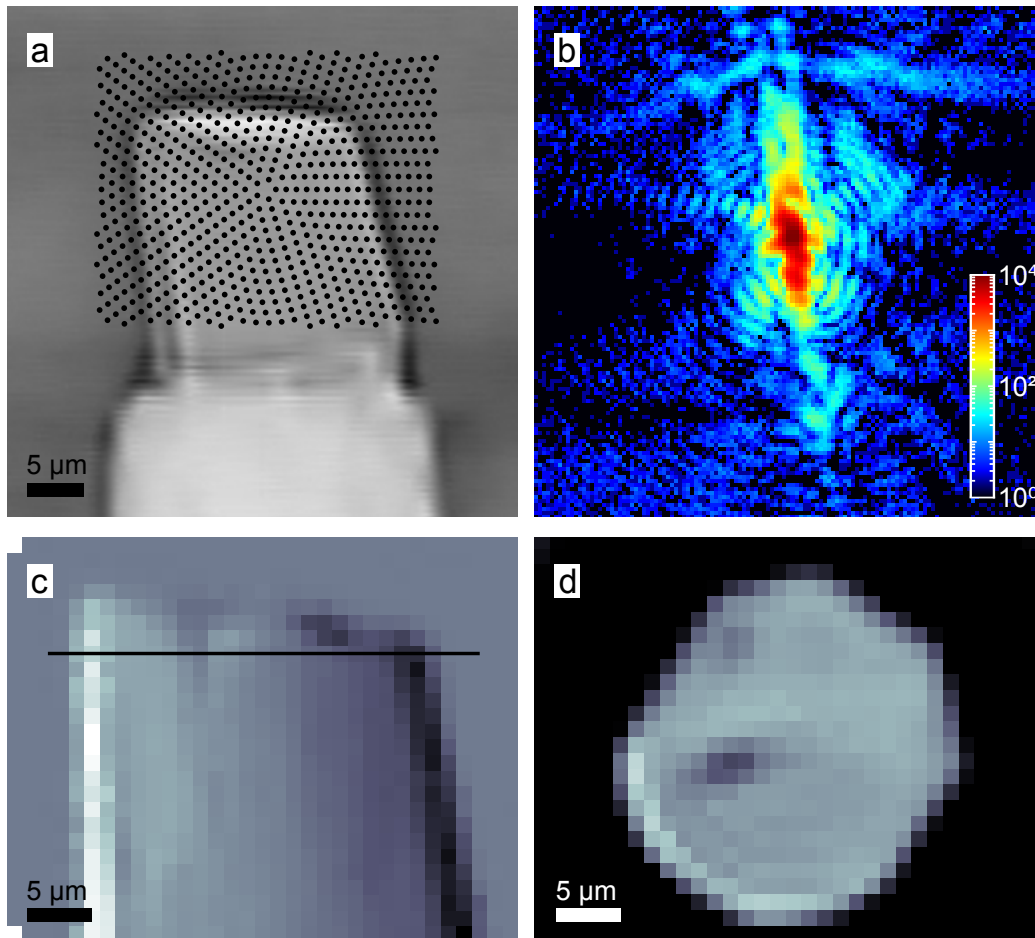


Figure 9.1: Data collection and online evaluation in demonstration experiment: (a) Projection radiograph of the specimen obtained using the so-called “X-ray eye”, in which a scintillator is imaged with a video microscope (see also section 5.1.2). During the experiment, these images were used for alignment and to define the scan range of $40\ \mu\text{m} \times 32\ \mu\text{m}$ (horizontal \times vertical) size. At each of the 180 projection angles, a ptychographic scan covers this area with 704 positions which are marked by the black dots. The pattern is a variant of the round scan introduced on page 101 in section 3.2.4.5, i.e. the scan points lie on concentric circles which are cropped to fill a rectangular field of view. (b) One of the 127424 collected diffraction patterns (photon counts on logarithmic scale, see colour-bar). (c) Low-resolution differential phase contrast image. Each pixel corresponds to one scan position with the grey value encoding the horizontal shift of the underlying diffraction pattern’s centre of mass. Linear interpolation was used to map the irregular scan pattern onto a Cartesian grid. That the left edge of the cylinder shows a positive phase gradient (white colour) while the right edge exhibits negative values (black colour) illustrates the differential character of the image. While a quantitative analysis (compare e.g. MENZEL ET AL., 2010) would be in principle possible, the main interest here lies in a quick online overview of the scanned area. (d) Tomographic slice obtained using the full set of low-resolution DPC projections and a filtered backprojection with a differential filter (PFEIFFER ET AL., 2007). The black line in panel (c) marks the vertical position of the slice. Parts of this figure were first published in DIEROLF ET AL. (2010a).

EMPA). Accurate manipulation of the sample was achieved by mounting it on a three-axis piezo-driven scanning stage which itself had been placed on top of a air-bearing rotation stage. Diffraction patterns were recorded with a PILATUS 2M detector located about 7.18 m behind the specimen. To reduce both absorption and scattering by air, this gap was bridged with a helium-flushed flight path.

Individual **ptychographic projection scans** were taken in an angular range from -90° to 90° for the tilt angle around the vertical axis at an angular increment of 1° . For each of the 181 projections, 704 diffraction patterns (see Fig. 9.1(b) for an example) were collected with an exposure time of 1 s per frame. The scan positions were determined according to the round scan definitions in (3.43) (see page 101) with $N_\theta = 5$ points in the first shell and an radial step $\Delta r = 1.2 \mu\text{m}$. However, the scan pattern was modified such that only the points inside a rectangular field of view of $40 \mu\text{m} \times 32 \mu\text{m}$ (horizontal \times vertical) were used, as illustrated in Fig. 9.1(a).

A **differential phase contrast analysis** following the basic ideas discussed in 1.8.1 on page 41 was employed to get first overview images directly after the corresponding diffraction patterns had been collected. Fig. 9.1(c) shows the result for one of the projections, while combining them all allows to obtain tomographic slices like presented in Fig. 9.1(d).

While the **cumulative exposure time** for all diffraction patterns is about 35.4 h, the total data collection process took about 43 h, due to an additional overhead of about 7.6 h for motor movements and detector read-out. However, it should be pointed out that in this case not the full coherent flux of the beamline was exploited as the illumination-defining pinhole was significantly smaller than the transverse coherence lengths of the beam (see paragraph “Experimental set-ups on page 129 in section 5.1.1 for a detailed discussion of the coherence properties of the beam). By prefocusing the beam with the beamline optics, this excess in transverse coherence can be used to reduce the exposure time per point by more than one order of magnitude, a possibility employed in later experiments.

9.2 Data analysis

Data analysis for ptychographic tomography follows the procedure described below, which was developed in the course of the first demonstration experiment (DIEROLF ET AL., 2010a):

1. Ptychographic reconstruction of individual projections from the diffraction data.

2. Removal of phase ramps in the reconstruction and correction for global phase offsets.
3. As the phase is obtained modulo 2π from the complex projections, phase unwrapping is necessary if phase shifts exceed 2π .
4. Alignment of projections with respect to each other to correct for inaccuracies of the rotation stage and drifts in general.
5. Tomographic reconstruction of the three-dimensional volume from the projection images by standard tomography algorithms (mainly filtered backprojection).
6. Conversion to a quantitative electron density map.

For later tomographic runs a Matlab implementation of this processing steps by [GUIZAR-SICAIROS ET AL. \(2011\)](#) – developed for users of the technique at the cSAXS beamline – was employed for steps 2 to 6. In what follows, a description of the individual processing steps is given in a general way. Their application in the demonstration experiment is discussed in detail and provides the examples to illustrate the practical use of the analysis procedures.

9.2.1 Ptychographic reconstruction

Each of the projections is reconstructed independently from the corresponding diffraction patterns using the algorithms for ptychographic CDI described in detail in section 3.2.2. For some data sets the projections were taken with relatively large point spacings, i.e. small illumination overlaps, in order to reduce the total exposure time. In these cases single scans with very high overlap values were used to get a good first reconstruction of the respective illumination. This reconstruction then acted as a starting guess for the actual projections resulting in faster convergence.

For tomographic data sets, a **lock-file mechanism** has been implemented in the reconstruction code. This allows to run several identical copies of the code in parallel, while making sure that each data set is only processed by one of the reconstruction jobs without the need for a more sophisticated message passing implementation. Usually, these multiple reconstruction processes were already started during data acquisition so that in the more recent experiments the projection images were typically available within a few hours after the corresponding tomographic scan had finished.

The **amplitudes** of the retrieved complex exit waves are typically of lower quality than the phase part, i.e. they exhibit lower signal-to-noise ratios and

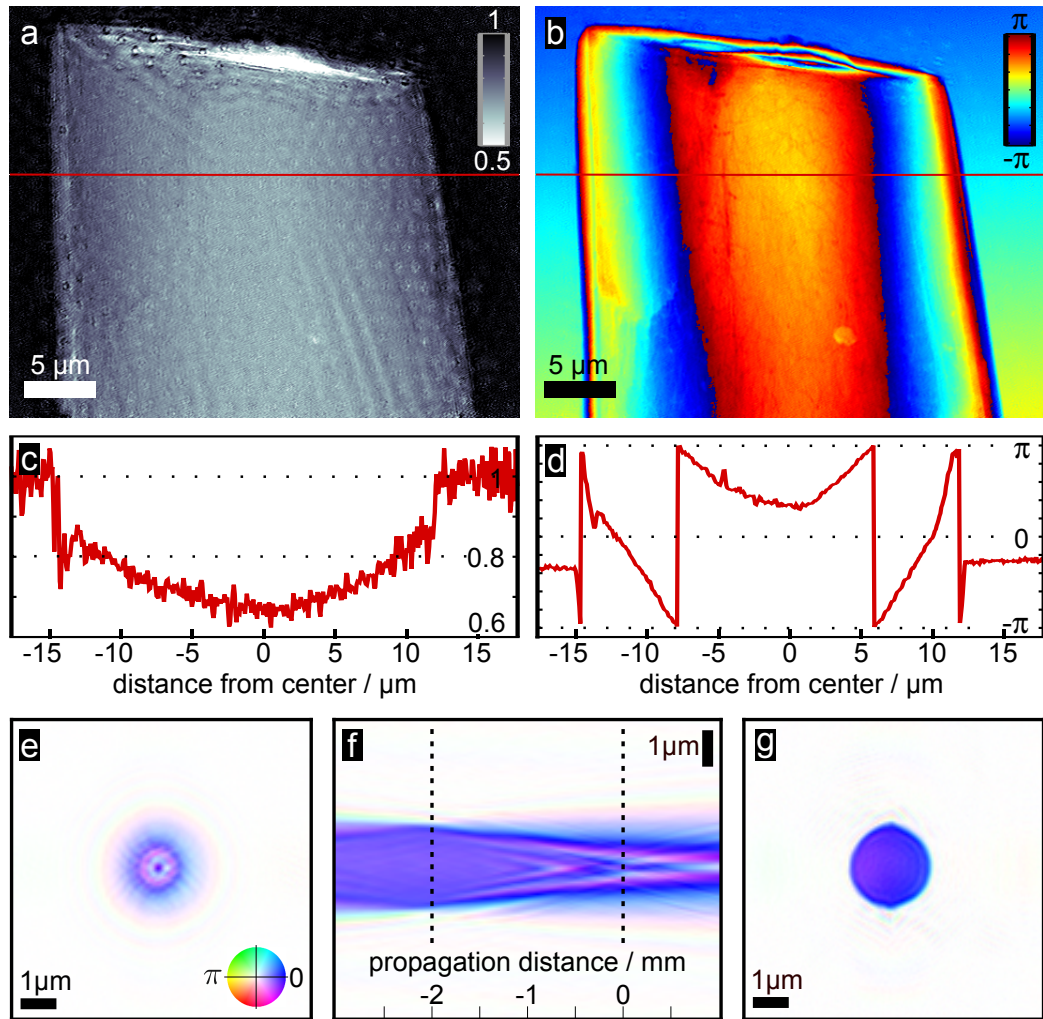


Figure 9.2: Ptychographic reconstruction results for a tomographic projection of the demonstration experiment. **(a)** Reconstructed amplitude of the complex object transmission function. Values are normalized with respect to air and displayed on a linear grey-scale (see colour-bar). As the amplitude is very sensitive to fluctuations of the incident intensity, it is more prone to artefacts. **(b)** Without any corrections, the phase part of the complex object transmission function (in radians, see colour-bar) shows both phase wrapping and a phase ramp, but not the strong artefacts of the amplitude. **(c)** Profile along the red line in panel (a) showing the low signal-to-noise ratio in the amplitude reconstruction. **(d)** This profile along the red line in panel (b) illustrates not only the higher signal-to-noise ratio in the phase part. Also the wrapping of the phase into the interval $[-\pi, \pi]$ rad is observed, as the maximum phase shift in this region of the specimen is more than 3π rad. **(e)** Reconstructed probe at the object plane (colour-coded complex representation, see colour-wheel). **(f)** Cut parallel to the beam direction through the propagated probe wavefield. From this, one can deduce that the pinhole (left dashed line) was located about 2 mm upstream from the object plane (right dashed line). **(g)** Probe in pinhole plane as obtained by numerical back-propagation. Parts of this figure were first published in DIEROLF ET AL. (2010a).

often significant reconstruction artefacts, compare Fig. 9.2(a). The first can be attributed to fact that at hard X-ray energies δ , the part of the refractive index responsible for the phase shift, is typically significantly larger than β , the imaginary part determining the absorption (compare Fig. 1.1). Artefacts show up frequently in the amplitude part as it is very sensitive to fluctuations in the incident intensity, which do not affect the retrieved object's phase as long as the phase structure of the illumination does not change. Therefore, typically only phase projections are used for further analysis, in particular as input for tomographic reconstructions.

Of the diffraction patterns taken in the **demonstration experiment**, the innermost 128×128 pixels were used for the reconstructions. With the experimental parameters stated in section 9.1.2 and (2.20) this results in a pixel size of about $65.2 \text{ nm} \times 65.2 \text{ nm}$ in both the retrieved object and probe, which are shown in Fig. 9.2. All projections were cropped to a size of 617×499 pixels (horizontal \times vertical) to remove the noisy areas close to the edges which are caused by the fact that the probe does not illuminate these regions sufficiently enough to produce a meaningful signal.

9.2.2 Phase ramp removal and offset correction

As discussed in section 3.2.4 on page 96, the projection images obtained by PCDI are ambiguous when it comes to constant phase offsets and linear phase ramps. Post-processing to remove these is typically based on the assumption that some – usually empty – region, that should show no ramp of its own and whose absolute phase shift is known, is present in each projection. This reference region may also consist of several disconnected areas on the sample. Typically, this reference area is picked from some air surrounding the specimen in the reconstructions.

For the correction itself different implementations have been used:

Least-squares fit For this, points from the aforementioned reference region are selected from the phase part of the reconstruction. To these points, a plane is fitted in a least-squares sense. Subtraction of this plane from the phase image corrects for the phase ramp. The constant phase offset is removed by setting the mean value of the corrected reference region to the desired value. However, this approach does not work if the slope of a phase ramp is so large that phase wrapping occurs within the selected reference region.

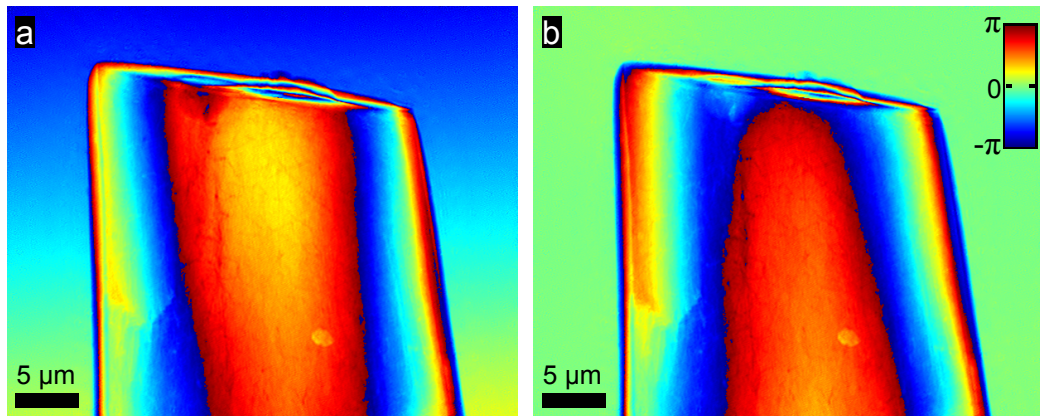


Figure 9.3: Phase ramp removal and offset correction: **(a)** Ptychographically reconstructed phase projection of a bone specimen (DIEROLF ET AL., 2010a) surrounded by air (linear colour scale, see panel b). The existence of a linear phase ramp along the vertical direction is indicated by the non-uniformity of the outer region. **(b)** Resulting phase projection after ramp removal and offset correction. As a least-squares fit does not work if phase wrapping occurs within the selected reference region, a first pass is done with the gradient-based ramp removal approach to avoid this. The reference region is in this case determined by thresholding the amplitude reconstruction. For the second pass, reference points close to each corner, the left edge and the top are selected. The values used for the least-squares fit are determined by averaging squares of 11×11 pixels centred on these reference points. See main text for details on the different approaches for phase ramp removal. Parts of this figure were first published in a modified version in DIEROLF ET AL. (2010a).

Gradient-based approach The mean two-dimensional gradient of the reference region is used to determine the slopes (compare (3.37b) on page 98) of the phase ramp. With this, a phase factor is constructed that is multiplied with the full complex image to remove the linear phase. Constant phase offsets are then corrected by again determining the mean phase value of the reference region in the such-treated image and setting it to the known absolute value.

Windowed Fourier transform GUIZAR-SICAIROS ET AL. (2011) introduce a method based on a windowed Fourier transform of the reference region: Detection of the position of the central peak of the Fourier transform gives the slopes of the ramp while its phase directly corresponds to the constant phase offset, where it is usually assumed the actual value in the reference region should be zero. The determination of the peak position has to be very precise, as already a one-pixel shift corresponds to a ramp that introduces a phase difference of 2π radians between opposite edges of the object. Therefore, the implementation by GUIZAR-SICAIROS ET AL. (2011) uses up-

sampling by typically a factor 100 to detect the peak with sub-pixel precision. Compared to the traditional least-squares fit and the gradient-based method, this approach is insensitive to discontinuities in the phase caused by phase wrapping.

The projections of the **demonstration experiment** were corrected with the gradient-based approach followed by a least-squares fit. While in the first case the empty outside area was determined by applying a threshold to the amplitude reconstruction, the second case used reference points close to the corners and the centres of the top and left edges. Each of the six reference points was attributed the average value of a square 11×11 pixels surrounding it. Fig. 9.3 shows an example for an original projection together with the result obtained after ramp removal and offset correction.

9.2.3 Phase unwrapping

Phase unwrapping is unproblematic if no phase residues (compare section 3.2.4.4, page 99) are present. Practical implementations, e.g. Matlab’s built-in “unwrap” function, in this case directly rely on a numerical integration of the phase gradient according to (3.40). In cases where this simple method failed due to the presence of phase residues, implementations of two more sophisticated path-following algorithms have been used:

Goldstein’s branch cut algorithm This approach is used in the Matlab processing package by [GUIZAR-SICAIROS ET AL. \(2011\)](#). The key point is the introduction of so-called “branch cuts” (a detailed discussion of the algorithm can be found in the book by [GHIGLIA AND PRITT \(1998, section 4.2\)](#)): Prior to the actual unwrapping step, pairs or clusters of positive and negative residues are connected by so-called branch cuts such that the “charges” of the connected residues neutralize each other in the end. The algorithm is designed to minimize the length of the branch cuts which is achieved by iteratively connecting always the nearest residues until the charges are balanced. Then it moves on to the next unbalanced residue and repeats the process. When all residues are balanced, unwrapping is done by evaluating the integral (3.40) while making sure that the integration path is not crossing any of the branch cuts and thus not encircling any unbalanced residues.

Problems may arise in cases where the branch cuts are completely isolating certain regions of the image from the rest or if connecting just nearest neighbour residues is not the optimal choice. Therefore, unwrapping becomes typically increasingly difficult, if many residues are present.

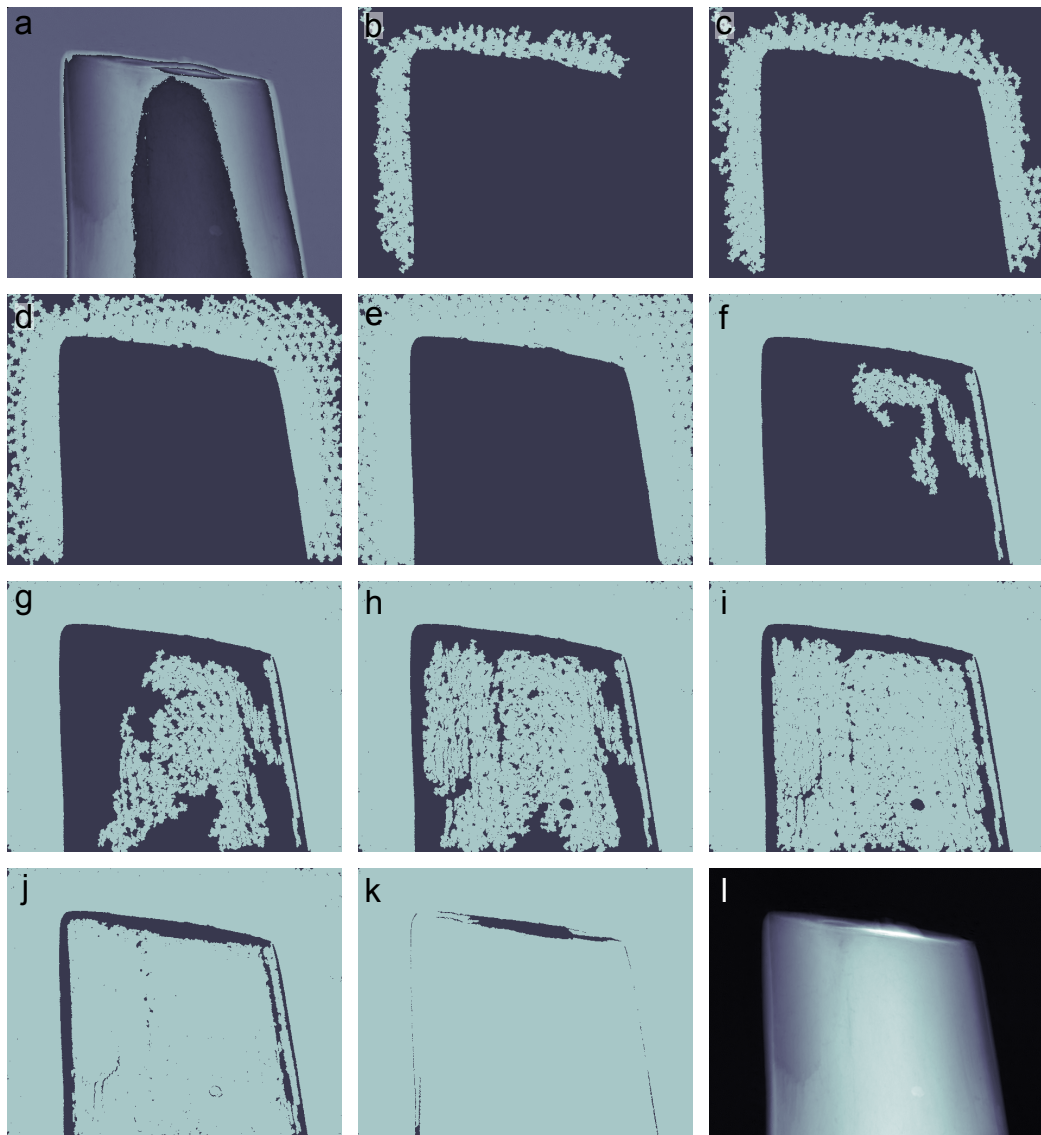


Figure 9.4: Illustration of phase unwrapping using quality-guided path following. Starting from the input projection (a), unwrapping progress is visualized in panels (b) to (k), there the brighter pixels are the already unwrapped ones. The quality map (see text for details) used in this case is proportional to the squared gradient of the input projection (a). Unwrapping starts with the pixel in the top left corner and in a region-growing approach always progresses to the neighbouring pixel with the highest quality, i.e. the smallest value of the squared gradient. For the bone specimen (DIEROLF ET AL., 2010a) shown here, the algorithm first processes the empty region outside the specimen and then the smooth regions in the centre of the cylindrical sample. Only at the very end, compare (k), the regions with steep edges – and thus strong phase wrapping – at the left edge and in particular at the top of the cylindrical specimen are addressed. The resulting phase image after unwrapping is shown in (l). The images of both the wrapped (a) and the unwrapped phase (l) were first published in modified versions in DIEROLF ET AL. (2010a).

Quality-guided path following This approach uses a “phase quality map”, which is calculated directly from the input data, to define the integration path. Typically, residues and corrupted phase signals have low-quality values. One assumes that with a suitable quality map the integration path, which follows the high-quality pixels, will not encircle any unbalanced residues. Although no branch cuts are used, this assumption seems to be quite valid in practice. See also GHIGLIA AND PRITT (1998, section 4.3) and LIM ET AL. (1995) for a more descriptions of the algorithm, as well as ZHAO ET AL. (2011) for a comparison of various quality maps. The iterative unwrapping process can be understood as a region-growing approach, as from a starting pixel with reliable phase value the area of unwrapped pixels is successively growing where the next pixel to be unwrapped is the neighbour with the highest quality value.

For unwrapping of the projections obtained from the first demonstration experiment (DIEROLF ET AL., 2010a), quality-guided path following was used with the squared gradient of the phase as a quality map. For this particular case, the progress of unwrapping is illustrated for one projection by snapshots at different points of the process in Fig. 9.4.

Refinement of unwrapping Some problems with unwrapping were frequently encountered if projections were perpendicular to very sharp edges of the sample: This resulted in very sudden strong phase jumps which could not be unambiguously unwrapped because of undersampling. This caused streak artefacts in the tomographic reconstructions. In these cases, some improvement can be achieved by taking also the phase data at adjacent angles of the tomographic tilt series into account. This is done by enforcing self-consistency in the sinograms: as the effect of ambiguous unwrapping at a sharp edge is constrained to very specific angles only, comparison with the neighbouring pixels along the angular axis of the sinogram typically allows to determine the correct phase values. In practice, the refinement starts from a tomographic reconstruction of the data. After blurring a slice by convolution with a Gaussian to suppress the artefacts caused by the incorrectly unwrapped pixels, an updated sinogram is calculated from this slice. Subtraction from the original sinogram yields the pixels of incorrect unwrapping and allows to determine their offset in multiples of 2π with respect to the values required to provide a smooth sinogram. The values are corrected right in the original sinogram and an updated slice is calculated by filtered back-projection. The procedure is repeated until no pixels with wrong phase are detected after the subtraction step.

While in the first demonstration (DIEROLF ET AL., 2010a) complete unwrapping of the projections was mandatory for both the alignment and the following tomographic reconstruction, the implementation of GUIZAR-SICAIROS ET AL. (2011) can work directly with the wrapped phase in the latter case, see section 9.2.5. Therefore, only a limited region of all projections has to be unwrapped for the alignment step. This allows to select an area for which unwrapping is expected to be well-behaved, i.e. a region with no or only few residues. The refinement step described in the previous paragraph is typically not necessary in this case.

9.2.4 Alignment of projections

This is a crucial step as any misalignment of projections with respect to each other substantially degrades the quality of the tomographic reconstruction or even creates artefacts. In particular, no incorrectly unwrapped pixels should be present in the unwrapped input data as these may lead to alignment errors.

In electron tomography, where the resolution also is much higher than the mechanical precession of the stages and thus realignment of the projections is mandatory, very often high-contrast fiducial markers are added to the specimen (NICKELL ET AL., 2005). For tomographic projections with perfect alignment, these markers should be moving on straight lines. By tracing the markers – either manually or in an automated way – for all images of an imperfect tilt series, the projections can be remapped into a common coordinate system (LAWRENCE, 1992). However, amount and distribution of the fiducial markers has to be well controlled and complicates sample preparation. Therefore, it has been decided not to use this approach for the experiments presented in this thesis.

Results obtained with alignment approaches based on two-dimensional cross-correlation of the images from adjacent projection angles (FRANK AND MCEWEN, 1992) were not sufficient and did not reach the accuracy achieved with the methods presented below. One problem is that as the computation of cross-correlation is done pairwise through the image stack, it may lead to accumulation of error (GUIZAR-SICAIROS ET AL., 2011; LAWRENCE, 1992).

Vertical alignment For vertical alignment, the sum of each projection along the horizontal direction is taken. When the sample always fully stays inside the horizontal field of view, this sum should be independent of the projection angle. Therefore, it can be used to detect shifts in the vertical direction. This is done by finding the shifts that maximize the correlation between the curves.

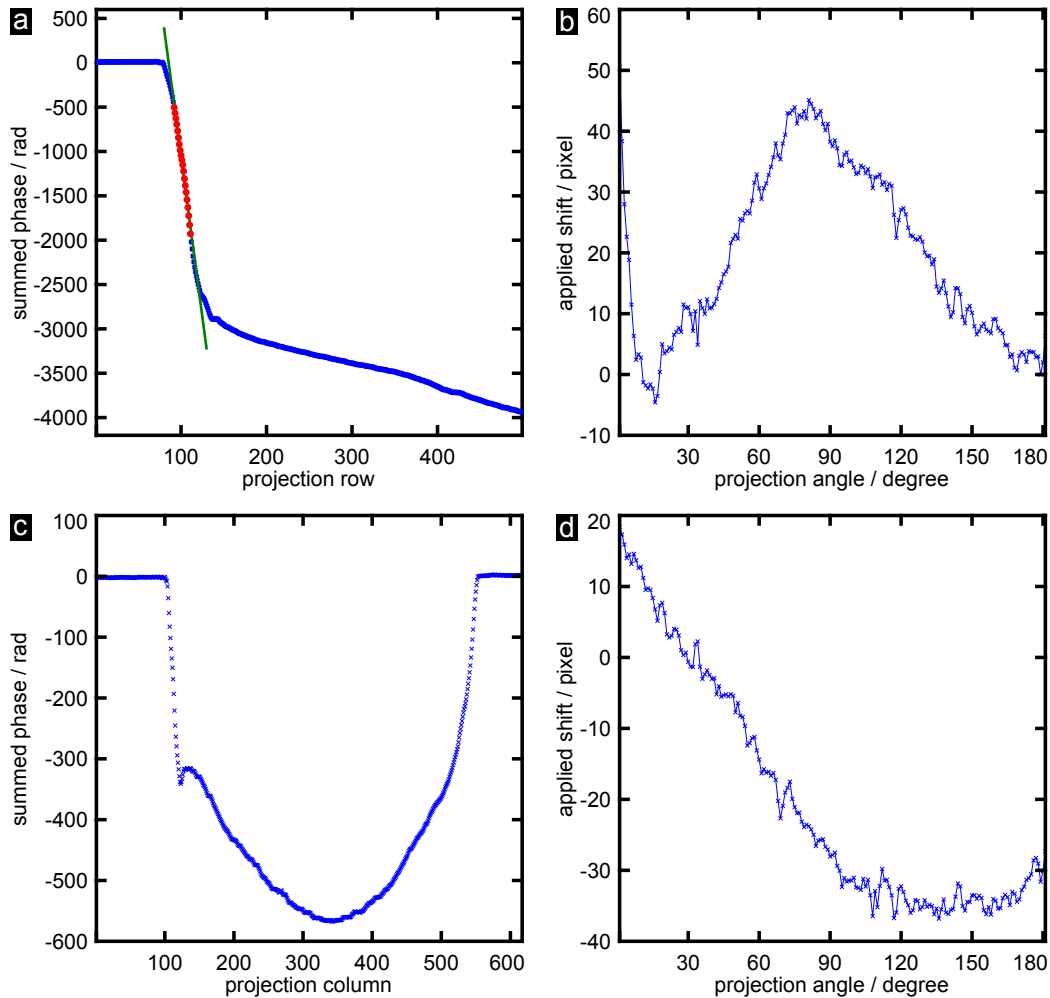


Figure 9.5: Alignment of PXCT projections. **(a)** Sum along the horizontal axis, the rows, of the unwrapped phase of the same projection as featured in Fig. 9.3 and 9.4. As always the full horizontal extent of the sample is within the field of view, the shape of this curve is – apart from deviations caused by noise or phase unwrapping errors – independent of the projection angle. The position of the edge, which is determined by the zero-crossing of the green linear fit, is used to detect the vertical shifts of the specimen. In each projection, the fit is based on the points (red circles) in the linear centre of the edge in the value range $[-2000, -500]$. **(b)** Vertical shifts of the specimen’s position as detected with the method illustrated in (a). The curve shows a slow vertical movement of the sample on a total scale of about 50 pixels ($\cong 3.26 \mu\text{m}$). Besides the limited accuracy of the rotation stage, also long-term thermal drift may contribute to this. The small scale fluctuations are in the order of 5 pixels. **(c)** Sum along the columns of a horizontal stripe which is 50 pixels high and spans the full width of the same unwrapped phase image. The centre of mass of these curves has to be the same for all projections. **(d)** Horizontal shifts determined with the approach presented in (c). A long-term sinusoidal movement of about 50 pixels total, indicating the centre of mass of the chosen area was not well-aligned with the rotation axis, is modulated with short-term fluctuations of about 5 pixels.

In cases like the demonstration experiment where the flat tip of a sample is measured, this creates a distinct edge in the horizontally summed phases, compare Fig. 9.5(a). Taking the derivative will give a peak whose position can be used to map vertical movements. For the data from the proof-of-principle experiment (DIEROLF ET AL., 2010a), it was first attempted to accurately determine the peak position by means of a parabolic fit. However, in the end it proved to be much more robust to detect the shift of the edge directly by means of a linear fit to its central part. The green line in Fig. 9.5(a) shows the extrapolated fit while red circles mark the points of the sum used for the fit. The shifts determined this way for all 181 projections are shown in Fig. 9.5(b).

For the more general cases, the implementation of GUIZAR-SICAIROS ET AL. (2011) was used: At first, constant and linear Legendre polynomial terms are removed from the summed projections, resulting in a one-dimensional function $\Upsilon_{\theta}(y)$ for each projection angle θ . The sum-squared error of these functions with respect to the average $\langle \Upsilon_{\theta}(y) \rangle_{\theta}$ over all angles is minimized. In an iterative procedure horizontal and vertical alignment are then applied alternately until the calculated shifts fall below a predefined threshold, typically one pixel in a first round and 0.1 pixels in a second sub-pixel alignment run. During the iterative position refinement, the average $\langle \Upsilon_{\theta}(y) \rangle_{\theta}$ starts of as a relatively smooth function which as alignment progresses is showing gradually more distinct features that in turn allow improved alignment. While the use of 1D curves $\Upsilon_{\theta}(y)$ makes the process relatively fast, employing the average $\langle \Upsilon_{\theta}(y) \rangle_{\theta}$ as a reference makes it very robust.

Horizontal alignment If in the retrieved images there is air on both sides of the specimen, the centre of mass in horizontal direction always has to stay at the same point for the projections to be well aligned. In the practical implementation, a stripe is cut out of each unwrapped phase image which covers the whole horizontal range but only part of the vertical one. Its vertical position and extent are chosen such that a region of well-behaved unwrapping is selected. The stripes are summed along their vertical axis, see e.g. Fig. 9.5(c) for a result obtained for one projection of the demonstration experiment. For each of these summed profiles the centre of mass is calculated. Fig. 9.5(d) shows the obtained values for the full tomographic data set of the demonstration experiment. All projections are then shifted, using nearest-neighbour interpolation to make these centre of masses coincide. If there are strong changes in the vertical position of the specimen, this will affect the obtained values for the centre of mass as always different parts of the

specimen are inside the selected stripe if there is no correction. Therefore, and if only a single alignment step is done for each direction, the vertical alignment should always come first.

However, this alignment method relies heavily on the assumption that air is present on either side of the specimen in all projection images. In more general cases, like local tomography applications or an extension to flat extended objects by means of either limited-angle tomography (BARRETT, 1990) or laminography (HELFEN ET AL., 2005), this prerequisite is not fulfilled. The use of fiducial markers or cross-correlation for alignment will have to be reconsidered for those applications.

9.2.5 Tomographic reconstruction

Reconstructions from unwrapped projections In cases where all the phase projections are completely unwrapped, like the example shown in Fig. 9.6(a) on page 254, standard parallel-beam filtered backprojection as introduced in section 4.2 on page 119 is used to reconstruct tomographic slices from the sinograms formed by the respective rows of the projection images. An exemplary sinogram from the murine bone data set of the demonstration experiment is shown in Fig. 9.6(b). For the reconstruction of the full murine bone data, filtered backprojection with a Hamming filter and linear interpolation was used slice-by-slice. The reconstruction – after conversion to quantitative electron density values, compare section 9.2.6 – of the slice corresponding to the sinogram in Fig. 9.6(b) is shown in Fig. 9.9(b) on page 263. From 180 input projections of 617×499 pixels (horizontal \times vertical) a volume of $617 \times 617 \times 499$ isotropic voxels with 65.2 nm edge length has been obtained.

Reconstructions from differential projections For later experiments, tomographic reconstructions have also been done from the derivatives of the obtained phase shift maps using the approach and Matlab code of GUIZAR-SICAIROS ET AL. (2011). As discussed in section 4.2.3 on page 122, filtered backprojections from the gradients of projections can be easily done by replacing the usual filter functions with their derivative versions according to (4.11). As input data, the derivatives of the projections along the horizontal coordinate axis (x) are calculated using the relation (GUIZAR-SICAIROS ET AL., 2011)

$$\frac{\partial}{\partial x} \Phi(x, y, \theta) \approx \frac{1}{h} \arg [\exp(i\Phi(x + h/2, y, \theta)) \exp(-i\Phi(x - h/2, y, \theta))] , \quad (9.1)$$

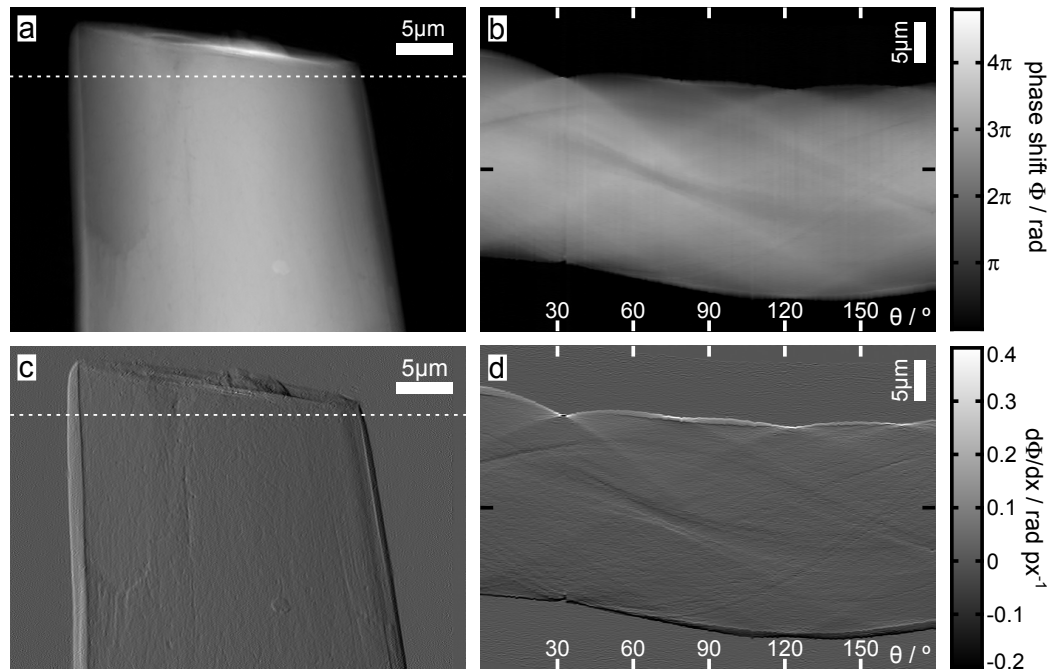


Figure 9.6: Examples for typical projections and sinograms serving as input for tomographic reconstructions. (a) Completely unwrapped phase projection represented on a linear grey scale, compare colour-bar on the very right. (b) Phase sinogram, in which each column shows the values of the specific pixel row marked by the dashed white line in (a) for each of the 180 projection angles θ . The rotation axis runs horizontally through the centre of the image as marked by the two black ticks on either side. This sinogram has been used as input of a filtered backprojection reconstruction to obtain the tomographic slice shown in Fig. 9.8(b) on page 261. (c) Derivative along the horizontal axis of the phase projection shown in (a) which has been calculated using (9.1). However, the formulation used in (9.1) is insensitive to phase wrapping and thus gives the same result if applied to a projection image which has not – or only partially – been unwrapped. The edges of the bone cylinder show the differential character of the image: a strong positive signal is observed for the left edge at which the material thickness increases towards the centre of the bone, whereas the decreasing thickness at the right edge yields negative values. (d) Differential phase sinogram of the same row as shown in (b), which is also marked by the dashed white line in (c). Again the contrast inversion for the left edge (at top of sinogram) and the right edge (bottom) of the specimen is visible. Furthermore, some imperfections can be observed at angles slightly above 30° , where the flat face of the specimen which is visible at the top left in Fig. 9.8(b) on page 261 was approximately parallel to the beam. The rapid phase changes observed at such a sharp edge lead to undersampling of the phase, i.e. there are phase jumps bigger than π rad for neighbouring pixels. In these cases, also differentiation according to (9.1) does not eliminate artefacts due to ambiguous phase wrapping.

where h is the step size of the numerical differentiation and is typically set to one pixel. As an example, Fig. 9.6(c) shows the derivative of the projection shown in Fig. 9.6(a) while the corresponding sinogram is shown in Fig. 9.6(d).

Differentiating according to (9.1) eliminates the need to completely unwrap the projections: As the complex exponential functions map the phase values onto the unity circle there are no more wrapping discontinuities and thus the derivatives are well-behaved. Therefore, unwrapping is only required for the parts of the projections used in the alignment process, but is no longer mandatory for the tomographic reconstruction itself. However, also differentiation according to (9.1) requires the phase to be sufficiently sampled, i.e. phase jumps from one pixel to the next must not exceed π rad. Otherwise, artefacts due to ambiguous phase wrapping may be observed despite the use of (9.1). In the differential sinogram in Fig. 9.6(d), for example, such an imperfection is visible slightly above 30° at top edge of the sinogram. At these angles, the flat face of the specimen which can be seen at the top left in Fig. 9.8(b) on page 261 was approximately parallel to the beam resulting in large phase jumps over short lateral distances.

9.2.6 Conversion to quantitative electron density

The average electron density n_e of a volume element with side length Δx is directly proportional to the real part δ of the refractive index (compare relation (1.24) on page 22). The value of δ is directly related to the phase shift $\Phi_{\Delta x}$ assigned to the respective voxel as the result of the tomographic reconstruction: from (1.28) on page 23 one obtains $\delta = \Phi_{\Delta x} \lambda / (2\pi \Delta x)$, which allows to calculate the electron density as

$$n_e = \frac{2\pi}{r_e \lambda^2} \delta = \frac{2\pi}{r_e \lambda^2} \frac{\lambda}{2\pi \Delta x} \Phi_{\Delta x} = \frac{\Phi_{\Delta x}}{r_e \lambda \Delta x}, \quad (9.2)$$

where $r_e = 2.818 \cdot 10^{-15}$ m is the classical electron radius and λ the X-ray wavelength used in the experiment. The origin of the electron density scale is calibrated by using the air surrounding the specimen as a reference, i.e. by shifting the air peak in a histogram like the one in Fig. 9.8(c) on page 261 to its correct position.

Conversion to mass density values For an element with atomic number Z and atomic weight A , the mass density ρ_m can be calculated by

$$\rho_m = \frac{A}{Z} u \cdot n_e, \quad (9.3)$$

where $u = 1.6605 \cdot 10^{-27}$ kg is the atomic mass unit and the relation $n_e = Zn_a$ between the atomic density n_a and the electron density n_e has been used. In a compound material, the electron density n_e reconstructed for a voxel is the average value of the electron densities of all the elements present in it. This results in a mean mass density of

$$\langle \rho_m \rangle_{\text{voxel}} = \frac{1}{N_{\text{elem}}} \sum_{j=1}^{N_{\text{elem}}} \xi_j \left(\frac{A}{Z} \right)_j u \cdot n_{e,j} , \quad (9.4)$$

for a total number of N_{elem} different elements with relative mass fractions ξ_j . Therefore, accurate knowledge of the elemental composition would be required to obtain a precise conversion. However, for elements with atomic numbers in the range between 5 (boron) and 20 (calcium), which includes all the main constituents of bone like calcium, phosphate and oxygen in the mineralized parts and carbon in the organic components, the approximation $A/Z \approx 2$ is valid within a few percent which is accurate enough for most practical purposes. With this, (9.4) simplifies to

$$\langle \rho_m \rangle_{\text{voxel}} \approx \frac{2u}{N_{\text{elem}}} \sum_{j=1}^{N_{\text{elem}}} \xi_j \cdot n_{e,j} = 2u \cdot n_e , \quad (9.5)$$

where n_e is the mean electron density of the material which is calculated with (9.2). As n_e is directly derived from the reconstruction without the need of the approximation just discussed, the results are usually presented as electron density values in this work. For the typical units used here, (9.5) can be written as

$$\langle \rho_m \rangle_{\text{voxel}} [\text{g cm}^{-3}] \approx 3.32 \cdot n_e [\text{\AA}^{-3}] , \quad (9.6)$$

i.e. an electron density of 1\AA^{-3} corresponds to a mean mass density of about 3.32 g cm^{-3} .

9.3 Results of demonstration experiment

The results in this section have been obtained from the data of the demonstration experiment described in section 9.1 by applying the analysis steps detailed in section 9.2. Most of the discussion presented here has already been published in [DIEROLF ET AL. \(2010a\)](#).

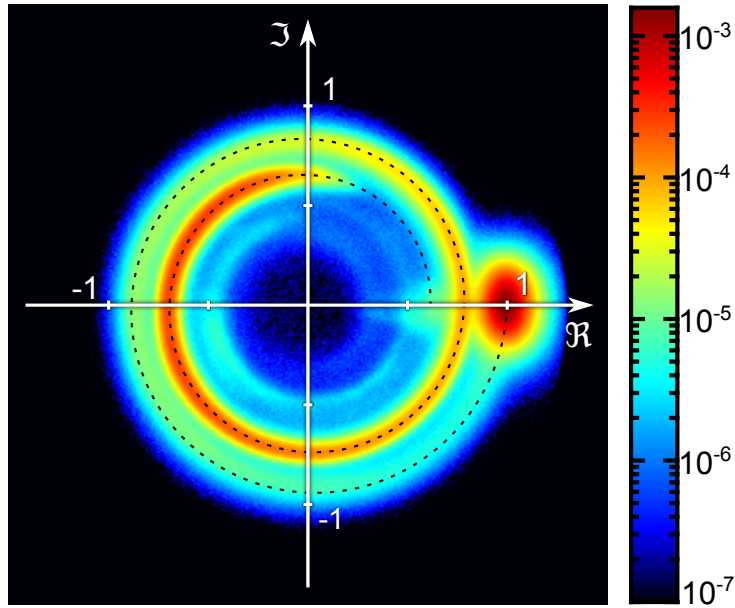


Figure 9.7: Complex-plane histogram plot encoding the relative frequency of each complex value within the data set on a colour-coded logarithmic scale. As input data, all 181 reconstructed complex transmission functions (projections) of the demonstration experiment are used. For a specific material, the distribution follows a logarithmic spiral in accordance with the projection approximation (1.26) on page 23: While the total phase shift is given by the angular component of the spiral, the decrease of its radius follows the usual exponential relation between attenuation and thickness given by Beer-Lambert law. The variance of the reconstructed projections, which is due to the measurement noise, and the chemical inhomogeneity of the sample lead to the broadening of the spiral. The dashed curve is based on a ratio $\delta/\beta \approx 25.8$ of real versus imaginary part of the material's complex refractive index, which is its most important input parameter. A calculation of δ/β requires precise knowledge of the chemical composition which cannot be provided for the mouse bone under investigation. Therefore, the ratio has been calculated for human cortical bone by combining the elemental composition available from ICRU (1989, Table 4.4 on page 22) with the X-ray interaction properties of HENKE ET AL. (1993), resulting in $\delta/\beta \approx 32.5$. The discrepancy is mainly attributed to the higher density of the mouse bone (JEPSEN ET AL., 2001) reflecting a different composition, but also to a systematic overestimate of the specimens absorption (see main text for details). Figure first published in a modified form in DIEROLF ET AL. (2010a, Supporting Online Material).

9.3.1 Complex transmission functions: qualitative and quantitative information

From all the retrieved complex transmission functions – after correcting for phase ramps and offsets according to section 9.2.2 – a two-dimensional his-

togram for the complex plane as shown in Fig. 9.7 can be constructed¹: Both real and imaginary axis span the interval $[-1.5, 1.5]$ in equally-sized bins of width 0.01. The relative frequency with which the complex values in the respective intervals appear in all reconstructed projections is given on a colour-coded logarithmic scale, see colour-bar in Fig. 9.7. The prominent peak around $(1 + 0i)$, i.e. no absorption and no phase shift, corresponds to the outside area where only air has been scanned. Its broadening is due to the variance of the retrieved values caused by noise in the measured data.

The plot is dominated by a **spiral curve** curling around the origin which consists predominantly of complex transmission values of bone material. For a better understanding of this behaviour, the material is assumed to be homogeneous and thus constant values are assigned to the components δ and β of the complex refractive index. Using this in (1.28) and (1.27), the value of the complex transmission function according to (1.26) depends only on the material thickness Δz at the respective position (x, y) :

$$O(\Delta z) = e^{i\frac{2\pi}{\lambda}(\delta+i\beta)\Delta z} . \quad (9.7)$$

Introducing the phase shift $\Delta\phi = \frac{2\pi}{\lambda}\delta\Delta z$ this can be rewritten into

$$\begin{aligned} O(\Delta\phi) &= e^{(i-\frac{\beta}{\delta})\Delta\phi} \\ &= (\cos \Delta\phi + i \sin \Delta\phi) \cdot e^{-\frac{\beta}{\delta}\Delta\phi} , \end{aligned} \quad (9.8)$$

where for the last line Euler's formula has been used. The real and imaginary parts of O

$$\Re \{O(\Delta\phi)\} = e^{-\frac{\beta}{\delta}\Delta\phi} \cdot \cos \Delta\phi , \quad (9.9a)$$

$$\Im \{O(\Delta\phi)\} = e^{-\frac{\beta}{\delta}\Delta\phi} \cdot \sin \Delta\phi , \quad (9.9b)$$

can be interpreted as the parametric form of a logarithmic spiral in the complex plane whose shape depends only on the value $-\beta/\delta$. Therefore, if a complex-plane histogram shows a distinct spiral curve for a major component like in Fig. 9.7, an estimate for the ratio δ/β may be obtained. While in the innermost part of Fig. 9.7 there are some faint traces of spirals with different parameters, the spiral formed by the values associated with projections through the bulk of the specimen dominates the image. Using the air peak as a starting point and the centre of the intersection with the imaginary axis

¹The Matlab implementation for this analysis makes use of the “hist2” function of Nedialko Krouchev, GRSNC, Université de Montréal, which is available on Matlab Central File Exchange (last visited August 2012): <http://www.mathworks.de/matlabcentral/fileexchange/12346-hist2-for-the-people>.

after 1.75 turns of the spiral as a second reference, a parameter $\delta/\beta \approx 25.8$ has been determined. This results in the logarithmic spiral according to (9.9) which is represented by the dashed black line on top of the histogram values. For the mouse bone investigated here, the precise chemical composition, which would be required for a calculation of δ/β , is not known. In order to establish at least some comparison with a closely-related material, the elemental composition for human cortical bone provided in ICRU (1989, Table 4.4 on p. 22) has been used. Calculation of the complex refractive index of this compound based on the tabulated values of HENKE ET AL. (1993) yields $\delta/\beta \approx 32.5$. Several factors contribute to the observed discrepancy:

- The difference of the chemical compositions of human and murine bone which manifests itself in a higher mass density of the latter, compare JEPSEN ET AL. (2001) and also the discussion in section 9.3.2. This is probably the most important factor, there is already a variability of up to more than 50 % between different mice strains (BEAMER ET AL., 1996).
- A systematic overestimation of the absorption in Fig. 9.7 when compared to the value of β obtained from the tomographic reconstruction of the bone volume. The most likely reason for this is the presence of a high-density surface layer on the cylindrical bone specimen, which is attributed to gallium implantation during the preparation process. In particular, a value $\delta/\beta \approx 26.7$ is obtained when β and δ are calculated from subvolumes of the tomographic reconstructions of phase and amplitude, which exclude the surface layer.
- Errors in the reconstructed amplitude values: As already discussed in section 9.2.1, the retrieved amplitude is both very prone to noise and reconstruction artefacts and its quantitative values may therefore not be very reliable. To this, also the averaging process during the difference map reconstruction may contribute, which reduces the amplitudes to means smaller than the maximum values. Furthermore, the amplitude part is also effected by truncation effects, i.e. any scattered photons that do not hit the inner part of the diffraction patterns used for the reconstructions make the specimen seem absorb stronger than it is actually the case.

Fig. 9.7 also illustrates benefits of imaging techniques which provide phase contrast: The amplitude signal is confined to the interval $0 < |O| \leq 1$ due to its exponential decay with the sample thickness according to the Beer-Lambert law. The phase shift, however, affects only the angular component

in the complex plane, compare Fig. 9.7. Therefore its sensitivity is not influenced by the sample thickness or a change of the overall incident intensity, as long as the absorption becomes not so high that the detected intensity values get too small.

The higher **signal-to-noise ratio** of the phase signal in comparison to the amplitude (see also the line-outs in Fig. 9.2) can be seen in Fig. 9.7 by relating the broadening of the spiral curve with the respective signal strengths: Compared to the change in radius, which encodes the absorption information, the relative size of the broadening is much more significant than for the phase signal of the same sample area, as the latter translates into a much longer distance along the spiral.

The **phase wrapping** occurring for thicker samples which exhibit phase shifts exceeding 2π rad can be observed in Fig. 9.7 as well: As a single turn of the spiral curve around the origin corresponds to 2π rad phase shift, the multiple turns visible here will cause the phase projections obtained as $\arg O$ to be heavily wrapped. In the picture of the spiral plot, unwrapping means that the phase value of a pixel is not just determined as $\arg O$ but it is additionally considered on which turn of the spiral the value of pixel is located. For each turn completed before reaching the given value, an offset of 2π rad has to be added. Unwrapping can therefore be imagined as uncurling the spiral to get from a periodic to a continuous phase axis. In practice, the determination to which part of the spiral a pixel belongs is done based on spatial correlations with the methods presented in section 9.2.3.

9.3.2 Quantitative bone density results

The result of the filtered backprojection of the phase projections, which is described in detail in section 9.2.5, was converted to a three-dimensional absolute electron density map of the bone specimen according to section 9.2.6. Fig. 9.8 shows two cuts through this volume, in (a) parallel to the rotation axis, in (b) perpendicular. The electron density is displayed on a linear grey scale in units of electrons per cubic ångstrom. Obviously, each value is the average over the density within one voxel of size $(65.2 \text{ nm})^3$. The histogram in Fig. 9.8(c) shows the relative frequencies of the respective electron densities within the full volume on a logarithmic scale. The different peaks can be associated with prominent structural features, which are marked with the same labels in Fig. 9.8(a):

- A** The dominating air peak has been used to calibrate the origin of the density scale while its broadening provides a measure for the uncertainty of the reconstructed densities: for the outside area a standard

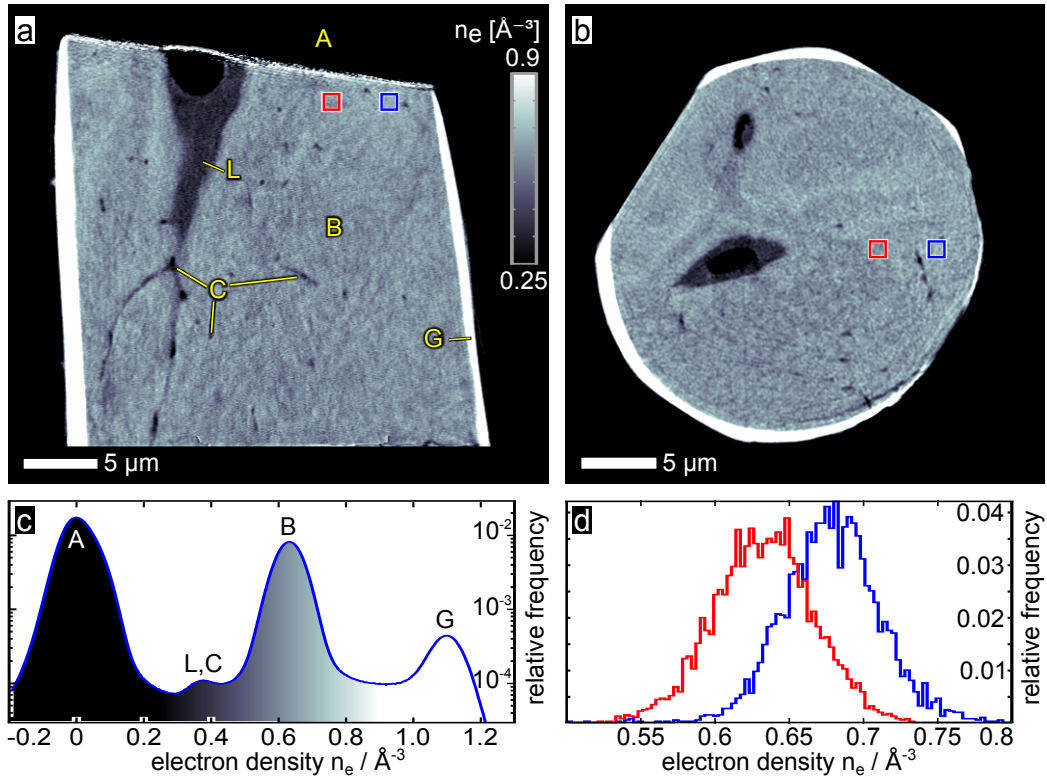


Figure 9.8: Quantitative electron densities n_e (linear greyscale, see colour-bar) for the murine bone specimen of the demonstration experiment obtained by converting the tomographic phase reconstruction according to relation (9.2) on page 255. (a) Cut through the reconstructed volume parallel to the rotation axis. Some typical structural features have been labelled: air (A), bone matrix (B), gallium coating (G) resulting from the focused-ion beam used for preparing the sample, canaliculi (C), and osteocyte lacuna (L). (b) Tomographic slice, i.e. a cut perpendicular to the rotation axis, from the top part of the volume (compare the position of the cubes marked by the red and blue squares in both panels). A section through the lacuna presented in panel (a) is visible close to the centre of the image, while a trace of an additional one shows up on top of it. Individual canaliculi show up as small dark dots. Within the bone matrix, variations of the grey values scan be observed, which indicate density fluctuations on a submicrometre scale. (c) Histogram showing the relative frequency of electron density values (500 equally-sized bins in the range -0.2 \AA^{-3} to 1.2 \AA^{-3}) on a logarithmic scale. The colours below the curve indicate the corresponding grey values in panels (a) and (b), while the labels are the same as used in (a) and link the peaks in the histogram to the structural features marked there. (d) Comparison of the bone peak's position (label B) in the histograms of two cubic sub-volumes of $1 \mu\text{m}^3$, whose location within the reconstructed volume is marked by the red and blue squares in (a) and (b). The position of the red cube has been chosen as to contain mainly voxels of the lower bone density visible as a darker shade of grey in (b), whereas the blue volume is located in one of the brighter areas. While the global bone peak in (c) did not allow to clearly quantify the different densities present in the bone matrix, they can be well distinguished at this micrometer level. For this type of analysis, the detection threshold for density fluctuations is slightly less than 0.001 \AA^{-3} which corresponds to about 0.2% of the mean bone density. First published in [DIEROLF ET AL. \(2010a\)](#).

deviation of 0.04 \AA^{-3} is computed.

- L,C** This smallest peak is formed around 0.37 \AA^{-3} by densities corresponding to material inside a partially-imaged *lacuna* (L) – a void inside the bone matrix which contains a bone cell, an osteocyte – and the little channels called *canaliculi* (C) forming a network between these voids. Visualization of these morphological features is discussed in section [9.3.3](#).
- B** The main part of the specimen consists of bone material, i.e. a mineralized collagen matrix, with an electron density fluctuating around 0.63 \AA^{-3} .
- G** The highest densities present in the volume are localized at the surface of the bone and are attributed to implantation of gallium during focused-ion beam preparation. The corresponding peak in the histogram is found at about 1.1 \AA^{-3} .

Although a visual inspection of slices through the reconstructed volume shows distinct density differences inside the bone matrix, visible in particular in Fig. [9.8\(b\)](#), these cannot be differentiated in the global histogram in Fig. [9.8\(c\)](#). Yet, when two subvolumes of $(1 \mu\text{m})^3$ are selected in parts of the bone reconstruction which show different grey levels, as marked by the red and blue boxes in Fig. [9.8\(a\)](#) and (b), their histograms show a clear shift of the respective bone peak's position, see Fig. [9.8\(d\)](#). The width of these peaks is consistent with the standard deviation of 0.04 \AA^{-3} calculated above from the empty part of the reconstruction. However, their positions may be determined with much higher accuracy of 0.001 \AA^{-3} on this $1 \mu\text{m}$ scale, which corresponds to about 0.2% of the mean bone density or a mass density variation of about 3.3 mg cm^{-3} according to [\(9.6\)](#). This behaviour - that a lower resolution allows to discern the (mean) reconstructed values with a higher accuracy - reflects the relation [\(3.70\)](#) on page [112](#) linking the total photon flux to the pixel size and variance of the reconstruction.

9.3.2.1 Comparison of obtained bone density with literature values

C57BL/6J (B6) mice are extensively studied in bone research, in particular due to the low mineral density of their bones, which can be more than 50% higher in other mouse lines ([BEAMER ET AL., 1996](#)). For the total mass density ρ_{wet} of wet femur diaphysis of C57BL/6J mice, [JEPSEN ET AL. \(2001\)](#) report $\rho_{\text{wet}} = (2.20 \pm 0.14) \text{ g cm}^{-3}$ with a water content of

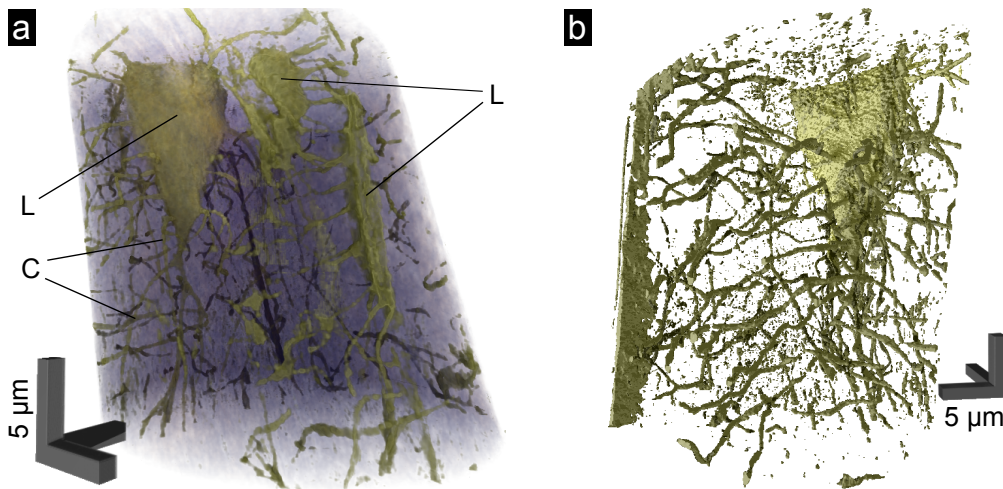


Figure 9.9: 3D rendering of the tomographic reconstruction of the murine bone specimen used in the first demonstration experiment. **(a)** Volume rendering in which the voxel values corresponding to the bone matrix are mapped to translucent colours. This shows that the sample volume is cutting through two or three osteocyte lacunae (L) and their connecting canaliculi (C). **(b)** Segmentation of the lacuno-canalicular network represented as an isosurface rendering. Voxels have been identified as belonging to the network based on the electron density values forming the corresponding peak in the histogram shown in Fig. 9.8(c). The obtained binary representation is independent of the measured densities and may, e.g., form the basis of a morphological analysis. First published in DIEROLF ET AL. (2010a).

(11.9 ± 2.9)%. Considering that in the specimen imaged here this water has been replaced by Lowicryl HM20 resin, which according to its safety data sheet has a density of about 0.9 g cm^{-3} , the density estimate reduces slightly to $\rho_{\text{dry}} \approx (2.19 \pm 0.14) \text{ g cm}^{-3}$. The electron densities associated with the bone matrix in the histogram in Fig. 9.8(c) fluctuate around 0.63 \AA^{-3} . With (9.6), this gives an estimate for the mass density of 2.09 g cm^{-3} , which is well within the uncertainty range of ρ_{dry} . In comparison, the density of human cortical bone is reported to be 1.92 g cm^{-3} in the literature (ICRU, 1989). It should be stressed once more that all these densities are averages taken over some larger volume, whereas on a smaller scale quite significant differences in the local bone density can be observed, as demonstrated in Fig. 9.8(d). The strength of PXCT lies in the ability to investigate such small density changes with combination of both high density sensitivity and high spatial resolution.

9.3.3 Visualization of bone morphology

9.3.3.1 The lacuno-canalicular network

During the formation of new bone, *osteoblasts*, which are the cells generating the bone material, get embedded inside the mineralizing bone matrix. They transform² into *osteocytes* and connect with their neighbouring cells through several long dendrites joined by gap junctions (KNOTHE TATE ET AL., 2004). The morphology of this cellular network can thus provide important information on the bone formation process (KERSCHNITZKI ET AL., 2011). The small channels within which the dendrites run through the bone material are called *canaliculi*, while the voids containing the osteocytes are referred to as *lacunae*. Together they form the *lacuno-canalicular network*, which is only partially filled by the interconnected osteocytes, but additionally contains bone fluid and a gel-like extra-cellular matrix. For more details on the lacuno-canalicular network, see e.g. SCHNEIDER ET AL. (2010) and references therein.

The basic shape of the lacunae is a flat elongated ellipsoid (BENO ET AL., 2006) whose orientation reflects the growth directions of the surrounding bone matrix (KERSCHNITZKI ET AL., 2011). The specific parameters of the individual voids as well as their density inside the bone differ significantly between species and additionally depend on various factors like age or anatomical location (SCHNEIDER ET AL., 2010). According to SU ET AL. (2006), the size of murine lacunae is in the order of 5 μm by 20 μm , while for the diameters of the canaliculi a value of about 50 to 100 nm is given. A slightly larger range of 50 to 150 nm can be found in the recent work by SCHNEIDER ET AL. (2011, Fig. 6), together with a distance of about 25 μm between neighbouring lacunae.

The interconnected osteocytes are considered to constitute the basic sensor network for translation of mechanical strains into biochemical signals (BURGER AND KLEIN-NULEND, 1999; KLEIN-NULEND ET AL., 2013, 1995) and therefore to play a crucial role in the bone remodelling process (KERSCHNITZKI ET AL., 2011). Imaging of the 3D morphology of the lacuno-canalicular network is therefore an actively pursued field in bone research and has been realized – with different degrees of success – with various methods which are discussed in the review by SCHNEIDER ET AL. (2010) and to some extent in the second to next paragraph.

²For details of this transformation process, see e.g. FRANZ-ODENDAAL ET AL. (2006).

9.3.3.2 Results of PXCT

The distinct differences in densities for the main structural features present in the murine bone specimen, which are observed in Fig. 9.8(c), allow to segment them with a histogram-based approach. Fig. 9.9 presents two 3D renderings obtained this way using the commercial VGStudio Max 2.0 visualization package (Volume Graphics GmbH). In panel (a), all pixels with values corresponding to the high-density surface layer are excluded, while the densities of mineralized the bone matrix are rendered semi-transparently to visualize the distribution of the lacunae (L) and canaliculi (C) within the full scanned bone volume. As a starting point for further quantitative analysis, a binary representation of the lacuno-canalicular network can be created by selecting only the values which form the corresponding peak in the histogram in Fig. 9.8(c). This segmentation has the benefit that the binary result becomes independent of the actual densities and thus may be treated more easily with general morphology analysis tools. Fig. 9.9(b) shows an isosurface rendering of the segmentation's result.

However, the reconstruction results may be affected by **partial-volume effects**: due to the technique's high density sensitivity, also tiny structures produce enough signal that even though they only occupy a small part of a voxel they substantially influence its resulting value, which is the density average over the voxel's volume. Therefore, the apparent size of such structures in the reconstruction may be bigger than their actual extent.

9.3.3.3 Comparison with other imaging techniques

The comparison of PXCT with other techniques employed for imaging the lacuno-canalicular network presented in this paragraph focuses on methods that provide true 3D volume reconstructions. A more complete overview including 2D imaging techniques is given by SCHNEIDER ET AL. (2010, 2011). The benefits and disadvantages are discussed here on the basis of four major criteria: sample preparation, compatibility with other techniques (e.g., if correlative studies with various imaging techniques are feasible), resolution, and typical volume imaged. The two last-mentioned characterize the ability of the respective method to handle the challenge of the multiple length scales present in the lacuno-canalicular network, which extend over three orders of magnitude from the sub-canalicular level to the distance between neighbouring lacunae. Unless stated otherwise, the comparisons by SCHNEIDER ET AL. (2010, 2011) and the references cited in the introductory paragraphs of the respective techniques are the sources of the different parameters given below.

1. X-ray nanotomography The lacuno-canalicular network has also

been investigated with classical X-ray tomography methods not relying on coherent imaging techniques (i.e. PXCT is discussed separately as point 4. on page 269): parallel-beam tomography with a high resolution detector also employing propagation-based phase-contrast effects (PACUREANU ET AL., 2012), and full-field transmission X-ray microscopy (TXM) with the option of Zernike phase contrast and the possibility to do tomography (ANDREWS ET AL., 2010). To achieve the high resolutions required for studying bone on the subcellular level, both methods are typically implemented at synchrotrons, but lab-based systems which provide similar resolutions are emerging (FESER ET AL., 2008). Current work (compare the outlook by PEYRIN, 2009) in this field aims at the application of holotomography based on a nano-focus set-up for full-field projection microscopy like available at ID22NI / ESRF (compare section 5.2).

Sample preparation As at X-ray energies of several keV the sample to be investigated can be placed in air, the bones can be left untreated apart from adapting their extent perpendicular to the rotation axis to the available field of view. For high-resolution parallel-beam tomography, this maximum size is about 0.5 to 1 mm and for TXM in the order of 50 μm . Samples can be bigger if local tomography (FARIDANI ET AL., 1992) is applied, which however may lead to artefacts in the resulting images.

Compatibility with other techniques Although radiation damage may occur for too long exposure, the technique is essentially non-destructive which in combination with the lack of sophisticated sample preparation paves the way for correlative studies. In particular, parallel-beam tomography may be used to gain an overview of the sample at a larger scale and define a volume of interest which is then further investigated at higher resolution with another technique.

Resolution The resolution in parallel-beam tomography is limited by effective pixel size of the detection system. The latter typically consists of a high-resolution, i.e. it has small grain sizes and is relatively thin, scintillator screen whose visible light output is imaged with magnifying optics onto a CCD chip. Effective pixel sizes down to few hundred nanometres can be achieved this way, e.g. 282 nm in the study by PACUREANU ET AL. (2012), which is just sufficient to image the canaliculi in human bone whose size is given as 300 to 600 nm by the authors.

As discussed in section 1.7 on page 37, the resolution of a TXM instrument is limited to few tens of nanometres – [ANDREWS ET AL. \(2010\)](#) e.g. report 30 to 40 nm – by the smallest structure sizes of its Fresnel zone plate objective lens. With nano-focus projection microscopy set-ups, where the size of the virtual source point of the diverging beam is the limiting factor, similar values can be achieved.

Typical volume imaged Parallel-beam tomography allows to obtain overviews of the structure of the lacuno-canalicular network in volumes of about $500 \times 500 \times 500 \mu\text{m}^3$ containing several hundred lacunae in less than 1 hour total acquisition time.

With a field of view of about $30 \times 30 \mu\text{m}^2$ per acquisition in TXM-based tomography, one often has to refrain to scanning the sample to different positions and combining the individual images into projection of larger areas. Typical volumes imaged that way are in the order of $50 \times 50 \times 100 \mu\text{m}^3$, i.e. covering several lacunae.

- 2. Serial focused ion beam / scanning electron microscopy (FIB / SEM)** While electron microscopy can in principle provide the highest resolution of about 1 nm or below, it is either limited to surfaces in the case of scanning electron microscopes (SEM) or to thin sections of a view hundred nanometre thickness for typical transmission electron microscopes (TEM). As a result, both techniques provide essentially only 2D information. Electron tomography with a TEM can in principle be used to obtain 3D reconstructions, but in addition to the small sample volumes allows only for limited-angle tomography ([BARRETT, 1990](#)), which is prone to artefacts. To image larger volumes in 3D, serial sectioning techniques are applied of which serial focused ion beam / scanning electron microscopy (FIB/SEM) is one variant used in bone research ([SCHNEIDER ET AL., 2010, 2011](#)): from the specimen's surface, a thin layer is milled away by FIB and the new surface imaged with the SEM present in the same instrument. Repeated application allows to collect volumetric data by combining the obtained cross-sections into an image stack.

Sample preparation As common in electron microscopy, also specimens for FIB/SEM imaging have to be made vacuum compatible by dehydrating and resin-embedding. In bone imaging, the resin also serves the additional purpose to fill the lacuno-canalicular network in order to have always smooth surface layers during the milling process ([SCHNEIDER ET AL., 2011](#)).

Compatibility with other techniques As it is inherently destructive, serial FIB/SEM always has to be the last technique applied in correlative studies. Apart from that, specimens prepared for one of the other imaging methods discussed here will in many cases have to undergo additional preparation steps to ensure vacuum compatibility.

Resolution With below 10 nm, FIB/SEM provides the highest resolution of the techniques presented here. The main limiting factor is in this case the accuracy of the FIB milling, as an SEM in general would be capable of even higher resolutions.

Typical volume imaged If sufficient time is available, the total volume that can be imaged with FIB/SEM is fundamentally limited only by the long-term stability of the instrument, e.g. with respect to drifts of the beam, the specimen or the focal length. The maximum dimension of typical volumes, however, is usually just some few tens of microns. SCHNEIDER ET AL. (2011) formulate a goal of $40 \times 40 \times 40 \mu\text{m}^3$ for the total imaged volume, as this “will be sufficient to capture two complete osteocyte lacunae”.

- 3. Confocal laser scanning microscopy (CLSM)** While standard full-field visible light microscopy allows to obtain two-dimensional images of internal structures of bone specimens, confocal laser scanning microscopy allows to investigate the lacuno-canalicular network in three-dimensional space (KAMIOKA ET AL., 2001; KERSCHNITZKI ET AL., 2011), due to its higher resolution along the optical axis: In CLSM, a specimen stained with fluorescent dyes is scanned in the focal plane of the microscope’s objective, which is also used to collect the resulting fluorescence light. By inserting a small pinhole aperture in the back-focal plane of the objective only signal originating directly from the focal plane reaches the detection system. This basic principle can be further refined to achieve even higher lateral and axial resolutions (HELL, 2007).

Sample preparation To account for the limited penetration of visible light, specimens are typically polished down to thicknesses of about $100 \mu\text{m}$ or below, but can have lateral sizes of several millimetres. Apart from this and the required staining with fluorescent dyes (KAMIOKA ET AL., 2001; KERSCHNITZKI ET AL., 2011), which attach to the surfaces of canaliculi and lacunae, the bone can be kept close to its native state.

Compatibility with other techniques As CLSM is non-destructive and the bone itself is not altered during the preparation process, it can be applied before any of the other techniques. Application of CLSM after X-ray tomography, both in its standard and its ptychographic implementation, is in principle possible, but in practice not advisable: to begin with, the sample volume is either smaller (PXCT) or thicker (nano-CT) than it has to be for CLSM. For another thing, the mounting used is typically incompatible with light microscopes and cannot be easily changed.

Resolution The resolution in CLSM is usually limited by the size of the volume of the focal spot inside which the intensity is high enough to excite the fluorescent dyes. This is about 200 to 300 nm in the lateral plane, there it is ultimately limited by the wavelength of the used light, and about 500 nm along the optical axis (HELL, 2007). Although the diameters of canaliculi may be smaller, this is sufficient to trace the whole lacuno-canalicular network in the volume imaged: the canaliculi are spatially well-separated and produce strong fluorescence signals which in combination allows to easily distinguish the individual channels. However, the resolution is too low to determine the actual diameters or the small-scale morphology of canaliculi.

Typical volume imaged While the vertical extent of the imaged volumes in CLSM is limited by the penetration depth of the light to some tens of microns, the lateral extent is typically in the order of some hundred microns, but can in principle be up to a few millimetres. The technique is therefore suited to obtain overviews on the general organization of lacuno-canalicular networks composed of several dozens up to several hundreds of cells.

- 4. Ptychographic nanotomography** The application of PXCT in bone research (DIEROLF ET AL., 2010a; SCHNEIDER ET AL., 2011) is revisited here once more, specifically considering the four criteria stated above in order to ease comparison with the other techniques.

Sample preparation The horizontal alignment approach presented in section 9.2.4 requires that the horizontal extent of the object under all projection angles does not exceed the width of the scanned area and that there is still some empty space left on either side. Therefore, specimens have to be prepared in the shape of cylindrical or cuboid rods which can be mounted with their long axis parallel to the rotation axis while their size in the perpendicular

direction stays below 100 μm . As the experiments are conducted in air, the samples can be left as close to the native state as the preparation method used for cutting them into their final shapes permits. In the case of the demonstration experiment, vacuum-compatibility of the murine bone specimen had to be ensured by resin embedding (compare section 9.1.1 on page 239) to allow focused ion beam milling. The samples are typically permanently glued to needle-like supports centred on top of metal pins with about 3 mm diameter, which allows easy handling and mounting on the rotating axis.

Compatibility with other techniques PXCT can be used to investigate a volume of interest cut as a thin rod out of a larger sheet which has been imaged with CLSM before. If the specimen is prepared in a vacuum-compatible way from the beginning, like the murine bone used here, a follow-up investigation with FIB/SEM is possible. Usually, also the mounting systems are compatible enough to make remounting unnecessary. However, although the technique is in principle non-destructive, some small-scale alterations due to radiation damage may occur.

Resolution The resolution obtained depends on the coherent flux delivered to the sample and therefore on both the parameters of the source and the total scan time. For typical settings, a resolution between 50 to 150 nm can be achieved. This is apparently a higher resolution than in both CLSM and X-ray micro-CT but lower than in FIB/SEM. It allows to resolve the canaliculi in murine femur whose diameters are in the range of 50 to 150 nm (compare e.g. Fig. 6 in SCHNEIDER ET AL., 2011), which is significantly smaller than the 300 to 600 nm reported for human bone (PACUREANU ET AL., 2012). However, as discussed earlier, the canaliculi may appear bigger than their actual size due to partial volume effects.

Typical volume imaged Compared to the first demonstration experiment described in this chapter, acquisition speed in PXCT could be increased by more than a factor of five, mainly by prefocusing the beam with the beamline optics which allows to use more of the available coherent flux. Therefore, a significantly larger volume than before can be imaged in a given time, although the number of projections is usually also doubled. For example, scanning a volume of $65 \times 65 \times 25 \mu\text{m}^3$ at 361 projection angles took about 12 h in recent experiments at cSAXS. The sampled volume is therefore typically larger than in FIB/SEM and comparable

technique	sample preparation	compatibility	resolution	volume throughput
nano-CT	native	good	low to medium	high
TXM	native, small	medium	medium to high	low
CLSM	native, fluorescent dyes	good	low	high
FIB/SEM	for vacuum	must be last	highest	lowest
PXCT	native, small	medium	medium to high	low

Table 9.1: Summary of the comparison presented in section 9.3.3.3 that assesses different techniques commonly used for imaging of the lacuno-canalicular network on the basis of four specific criteria. This table only lists a qualitative assessment of the respective method’s performance, while a detailed discussion, including also quantitative values e.g. for the resolution, can be found in the main text.

with TXM tomography, but still much smaller than what can be imaged with CLSM and parallel-beam nanotomography.

Conclusion of comparison From this comparison, which is also once more summarized in a qualitative way in Table 9.1, the conclusion can be drawn that the best option for imaging the morphology of the lacuno-canalicular network is a multimodal approach: in a first step, relatively large overview volumes can be obtained with CLSM or parallel-beam nanotomography. Detailed studies of the local morphology are then done on volumes of interest, selected from the results of the first measurements. In order to achieve high enough resolutions to properly resolve the features of individual canaliculi, FIB/SEM seems the most promising candidate for this second step. Currently, reconstructions obtained with PXCT do not provide sufficiently reliable information on the canaliculi. Instead, this would require higher resolution to avoid partial volume effects. However, with the other techniques it is either impossible (CLSM) or very difficult (nano-CT, TXM, FIB/SEM) to obtain similar high-sensitivity quantitative density results as presented in section 9.3.2 on page 260. Therefore, further applications of ptychographic nanotomography in bone research have mainly been focusing on investigations that strongly benefit from this aspect of the method, see chapter 10.

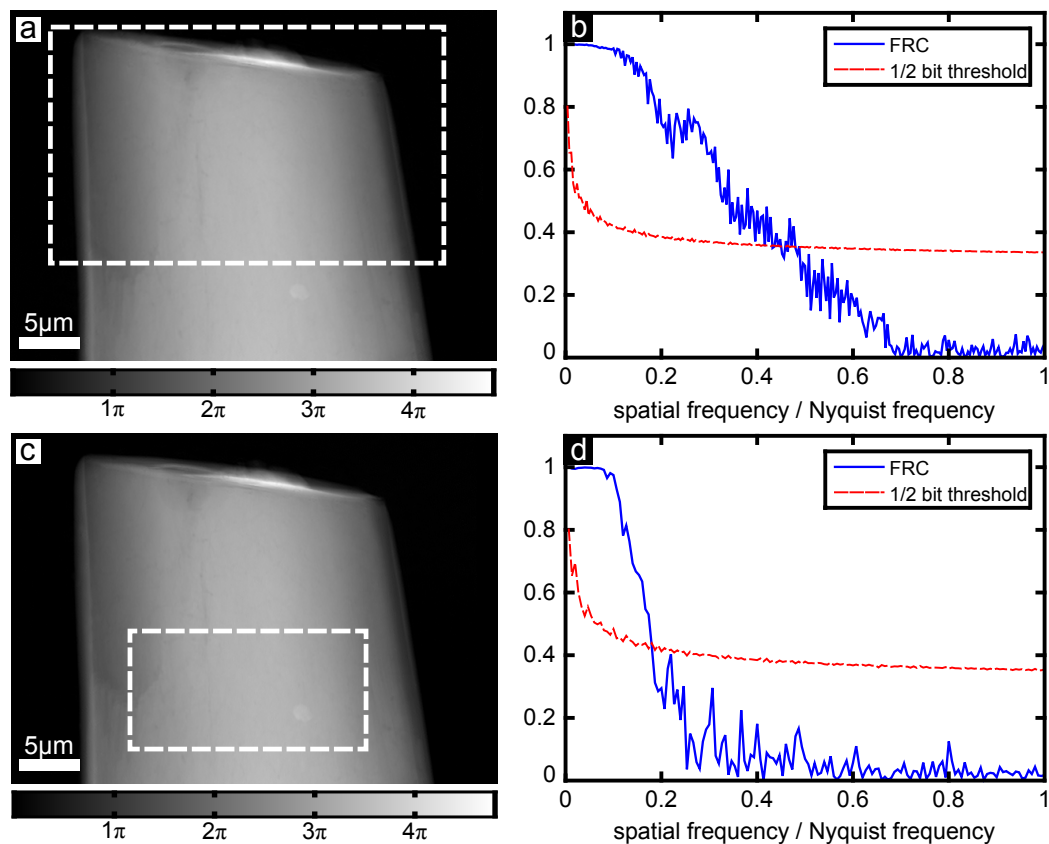


Figure 9.10: Assessment of spatial resolution by calculating Fourier ring correlations (FRC) between phase-contrast projections taken 180° apart. **(a)** Reconstructed phase image at 0° . The dashed white rectangle marks the area to calculate the FRC shown in **(b)**. The phase shift (in radians) is encoded on a linear grey scale (see colour-bar). **(b)** Fourier ring correlation calculated for the sub-images marked by the dashed white rectangle in **(a)**. The spatial frequency axis is normalized to the Nyquist frequency f_{Nyq} . The FRC falls below the 1/2-bit threshold curve at $0.48 \cdot f_{\text{Nyq}}$ which corresponds to a real space resolution of about 136 nm. **(c)** Projection image (phase part) at 180° flipped horizontally to match the orientation of the 0° -image. In order to demonstrate the dependence of the FRC on the actual features present in the region of interest, an area (dashed white rectangle) of the image which contains none the sample's sharp boundaries has been chosen for a second calculation whose result is shown in **(d)**. **(d)** Fourier ring correlation calculated using the interior region of interest marked in **(c)**. In this case a cutoff frequency of $0.18 \cdot f_{\text{Nyq}}$ is found which amounts to a spatial resolution of about 362 nm.

9.3.4 Spatial resolution

The resolution of the reconstruction is estimated based on the Fourier correlation approach introduced on page 113 in section 3.3.5. According to VAN HEEL AND SCHATZ (2005), the resolution of a tomographic volume would

be typically determined by splitting the projection data in two parts which are reconstructed separately and then calculating the Fourier shell correlation from the three-dimensional Fourier transforms of these two volumes. In the case of the murine bone data set, however, the number of projections is already less than half of the specimen's horizontal extent in pixels (compare also the relation (4.5) for angular sampling in tomography on page 119). A tomographic reconstruction with only half of the projections would therefore introduce additional artefacts which would influence the resolution determination. To avoid this, the Fourier ring correlation (FRC) of two projections 180° apart is used instead: when one of the projections is flipped horizontally, they provide two independently obtained images of the same object and can thus be used as input for a Fourier correlation method. More importantly, one can infer that in the current implementation of PXCT the resolution of the volume reconstruction can never exceed the value found for the projection images: Any high-resolution information which is present in the diffraction data but too weak to be successfully retrieved during the ptychographic reconstruction is no longer contained in the individual projections. Although the cumulative information content in the entirety of all diffraction patterns would be enough to get a meaningful high-resolution signal, the low-pass filtering effect of the PCDI algorithm prevents this information from reaching the tomographic reconstruction. Thus these spatial frequencies can also not benefit from tomographic dose fractionation (compare [HEGERL AND HOPPE, 1976](#)).

The resolution obtained in the test experiment on the murine bone specimen is estimated by comparing the phase part of the ptychographic reconstructions at projection angles 0° and 180°, which are shown in Fig. 9.10(a) and (b) respectively. For the calculations of the FRC, a Matlab implementation has been used which is part of the latest version of the processing package for ptychographic CDI coded by Manuel Guizar-Sicairos (a general description of the package – not including the FRC calculation – is given in [GUIZAR-SICAIROS ET AL., 2011](#)). To illustrate how the choice of the region of interest may affect the Fourier ring correlation, it is calculated for two different areas. The first, marked in Fig. 9.10(a), contains a significant part of the edges of the specimen, which show both a strong contrast and sharp features. The second, as shown in Fig. 9.10(b), is located in the interior of the specimen which exhibits only relatively smooth features and little variations in contrast. As a result, the FRC drops below the 1/2-bit threshold curve already at $0.18 \cdot f_{\text{Nyq}}$ in the latter case, while for the first region the cutoff is at $0.48 \cdot f_{\text{Nyq}}$. Here $f_{\text{Nyq}} = 1/(2 \cdot N_{\text{max}})$ is the respective Nyquist frequency of the Fourier transformed region whose maximum linear extent is N_{max} pixels. The 1/2-bit threshold curve is introduced on page 116 in

section 3.3.5, compare in particular (3.78). According to (3.79) and (3.80), one has a signal-to-noise ratio of about 0.4142 where the FRC intersects the 1/2-bit threshold curve. This is twice the value used in typical definitions of this curve (VAN HEEL AND SCHATZ, 2005), because in our case the final result is not an average of the two compared images and thus does not have twice the SNR of the input images. Considering the real space pixel size of 65.2 nm, the cutoffs determined above result in spatial resolution estimates of about 136 nm for the larger region of interest and about 362 nm for the smaller one. This illustrates once more the highly local aspect of resolution values and that a single number for the whole reconstruction conveys only limited information. For the murine bone result, the single characterizing value is 136 nm, which is the highest achieved resolution. This value is in good agreement with what can be expected for the dose delivered during the experiment. Dose aspects are discussed in more detail in the following section 9.3.5.

9.3.5 Dose estimation

The total radiation dose a specimen received is defined as the total energy it absorbed divided by its mass.

9.3.5.1 Estimation of absorbed energy

For the tomography scan of the murine bone, the total number of absorbed photons is estimated from the photons counted with the PILATUS detector: after summing the counts in each detector frame, the maximum value obtained for the 704 diffraction patterns constituting one projection is taken as the number of incoming photons $N_{0,\text{exp}}(\theta)$ during one exposure at the respective projection angle θ . The total number of incoming photons for each projection is then estimated to be $N_{0,\text{proj}}(\theta) = 704 \cdot N_{0,\text{exp}}(\theta)$. This approximation gives rather too high values for the amount of incident photons. By attributing this way any reduction in intensity not to fluctuations of the incoming beam but instead to absorption by the specimen, the calculated dose will be an upper estimate. For the whole tomography scan, one gets $N_{0,\text{tom}} = \sum_{\theta} N_{0,\text{proj}}(\theta)$. The average incoming coherent flux can be estimated by dividing $N_{0,\text{tom}}$ by 127 424 s, which is just the total number of diffraction patterns multiplied by the exposure time of 1 s. The total amount of absorbed photons is calculated by subtracting from $N_{0,\text{tom}}$ the sum of all photons measured by the detector. Each photon has an energy of 6.2 keV. The numerical results of the procedure just described are summarized in Table 9.2.

absorbed energy	total incoming photons $N_{0,\text{tomo}}$	$2.1 \cdot 10^{11}$
	mean coherent photon flux / s	$1.6 \cdot 10^6$
	total absorbed photons	$5.9 \cdot 10^{10}$
	total absorbed energy / J	$59 \cdot 10^{-6}$
specimen mass	specimen volume / px	$53 \cdot 10^6$
	specimen volume / m^3	$15 \cdot 10^{-15}$
	specimen mass / kg	$31 \cdot 10^{-12}$
dose	total dose / Gy	$1.9 \cdot 10^6$
	dose per projection / Gy	$11 \cdot 10^3$

Table 9.2: Numerical values related to the estimation of the radiation dose delivered to the murine bone specimen which is presented in section 9.3.5. The **first block** lists the figures related to the calculation of the absorbed energy based on the photon counts measured by the PILATUS detector. In the **second block**, the specimen mass is calculated based on a segmentation of the total specimen volume from the surrounding air in the reconstructed 3D data set and assuming a uniform mass density of 2.09 g cm^{-3} . The **third block** presents the results for the dose obtained by dividing the total absorbed energy by the sample's mass.

9.3.5.2 Estimation of specimen mass

For estimating the mass of the specimen, the total sample volume is obtained by excluding the surrounding air in the tomographic reconstruction and summing the remaining voxels. For the material in this volume, a uniform mass density is assumed, which corresponds to the value $\rho_{\text{bone}} = 2.09 \text{ g cm}^{-3}$ determined for the mineralized bone matrix on page 262 in section 9.3.2.1. As the actual specimen contains some significantly denser parts, in particular the Gallium-infused surface region, this simplification leads to a systematic underestimation of the actual mass density (the mean electron density of the specimen is about 0.66 \AA^{-3} , while it is 0.63 \AA^{-3} of the mineralized bone matrix). In turn, this results in higher calculated dose values as the same energy is absorbed in a supposedly smaller mass. As the main interest here is to obtain an upper estimate of the delivered dose, this mass calculation is not further refined: for more accurate mass density values, the chemical compositions of the compounds would have to be known precisely, because the simplified relation (9.5) on page 256 does not hold for heavy elements. The numerical values for volume estimates and the resulting specimen mass are listed in the second block of Table 9.2.

9.3.5.3 Comparison with calculated lower and upper dose limits

Using the values listed in Table 9.2 for total absorbed energy and specimen mass, which are obtained by the procedures described in the two previous paragraphs, a total radiation dose of approximately 1.9 MGy is estimated, or about 11 kGy per projection. In this section, these values are put in relation to numerical calculations of maximum tolerable and minimum required doses.

Maximum tolerable dose For this dehydrated specimen, the collagen forming the organic part of the bone matrix is expected to be most affected by radiation damage. For wet bone, significant alterations of the mechanical behaviour have been found by BARTH ET AL. (2010) for doses above 70 kGy. In small angle X-ray scattering investigations by FERNÁNDEZ ET AL. (2002), the degree of alignment of the collagen and the diffracted intensity have started to show changes at a dose of 100 kGy. It can therefore be concluded, that – like in standard synchrotron-based microtomography techniques (BARTH ET AL., 2010) – the dose in PXCT is too high to allow *in situ* mechanical testing. However, although the breaking of cross-links between collagen molecules quickly influences the mechanical properties, it does not automatically imply structural changes on the larger length scale of 50 to 150 nm which is the current resolution limit in ptychographic nanotomography of bone: using spot fading experiments on protein crystals, HOWELLS ET AL. (2009) have found that the maximum tolerable dose D_{\max} and the achievable resolution Δx , i.e. the size of the largest features not exhibiting radiation damage, are linked approximately by the linear relation

$$D_{\max}[\text{Gy}] \approx 10^8 \cdot \Delta x[\text{nm}] . \quad (9.10)$$

Although in the article by HOWELLS ET AL. (2009), (9.10) has been determined mainly from data for resolution of 10 nm and below, it is also considered to give a valid lower bound for lower resolutions, as e.g. the few measured values the authors provide for the range 10 to 100 nm stay clearly above this limit. The 1.9 MGy delivered to the murine bone specimen are therefore well below the feature-destroying dose.

Required imaging dose HOWELLS ET AL. (2009) also present calculations of the imaging dose D required to collect P photons on the detector from a resolution element (voxel) of size $d \times d \times d$, which is characterized by its mass density ρ_m , its complex refractive index $n = 1 - \delta - i\beta$ and the derived absorption coefficient $\mu = (4\pi/\lambda)\beta$:

$$D = \frac{PE_{\text{ph}}\mu}{\rho_m} \frac{\lambda^2}{4\pi^2|\delta + i\beta|^2d^4} , \quad (9.11)$$

	collagen	protein	gold
chemical formula	$C_{12}H_{24}N_3O_3$	$C_{30}H_{50}N_9O_{10}S_1$	Au
density / $g\text{ cm}^{-3}$	1.35	1.35	19.3
β at 6.2 keV	$2.869 \cdot 10^{-8}$	$4.577 \cdot 10^{-8}$	$1.246 \cdot 10^{-5}$
δ at 6.2 keV	$7.964 \cdot 10^{-6}$	$7.834 \cdot 10^{-6}$	$7.996 \cdot 10^{-5}$

Table 9.3: Material parameters used for the calculations of imaging doses required to reach a given resolution according to (9.11) which are depicted in Fig. 9.11 on page 278. For dry collagen a mass density of 1.3 to 1.4 $g\text{ cm}^{-3}$ is reported (PODRAZKÝ AND SEDMEROVÁ, 1966). Here a mean value of 1.35 $g\text{ cm}^{-3}$ has been used together with an empirical chemical composition published by (OMOKANWAYE ET AL., 2010). Chemical formula and density of the general empirical protein in the second column are taken from HOWELLS ET AL. (2009). All values of real (δ) and imaginary (β) parts of the refractive index at an X-ray energy of 6.2 keV have been calculated based on the tabulated values by HENKE ET AL. (1993) using the online-interface to the database available at http://henke.lbl.gov/optical_constants/.

where the incident radiation has the energy E_{ph} and the wavelength λ . Following the argumentation of HOWELLS ET AL. (2009), P is chosen as to match the Rose criterion, i.e. the signal-to-noise ratio (SNR) is larger than 5 (ROSE, 1948): if the signal is only limited by Poisson (or shot) noise, this leads to $P = 25$. It should be pointed out, that HOWELLS ET AL. (2009) have originally derived (9.11) for the case of a 2D projection image. For the extension to three dimensions, they have assumed perfect dose fractionation (compare HEGERL AND HOPPE, 1976): in order to reconstruct a voxel with the same statistical accuracy as its projection obtained in a 2D experiment, the same total dose given by (9.11) has to be applied in the corresponding 3D experiment.

Employing the parameters listed in Table 9.3 for collagen, a general empirical protein and gold, (9.11) has been used to calculate the required imaging doses at an X-ray energy of 6.2 keV for the resolution range 1 to 500 nm. The refractive index values correspond to measurements with respect to vacuum (or with good approximation also air), whereas the resulting dose would have to be about one order of magnitude higher to achieve the same contrast against a background of water. The results are plotted in Fig. 9.11 on page 278. In addition, the maximum tolerable dose for biological material according to (9.10) (see also HOWELLS ET AL., 2009) is shown. To ease comparisons, the average dose per projection (11 kGy) and the total dose (1.9 MGy) of the tomographic scan are marked with grey horizontal lines. The combination of all this information in Fig. 9.11 allows for the following observations:

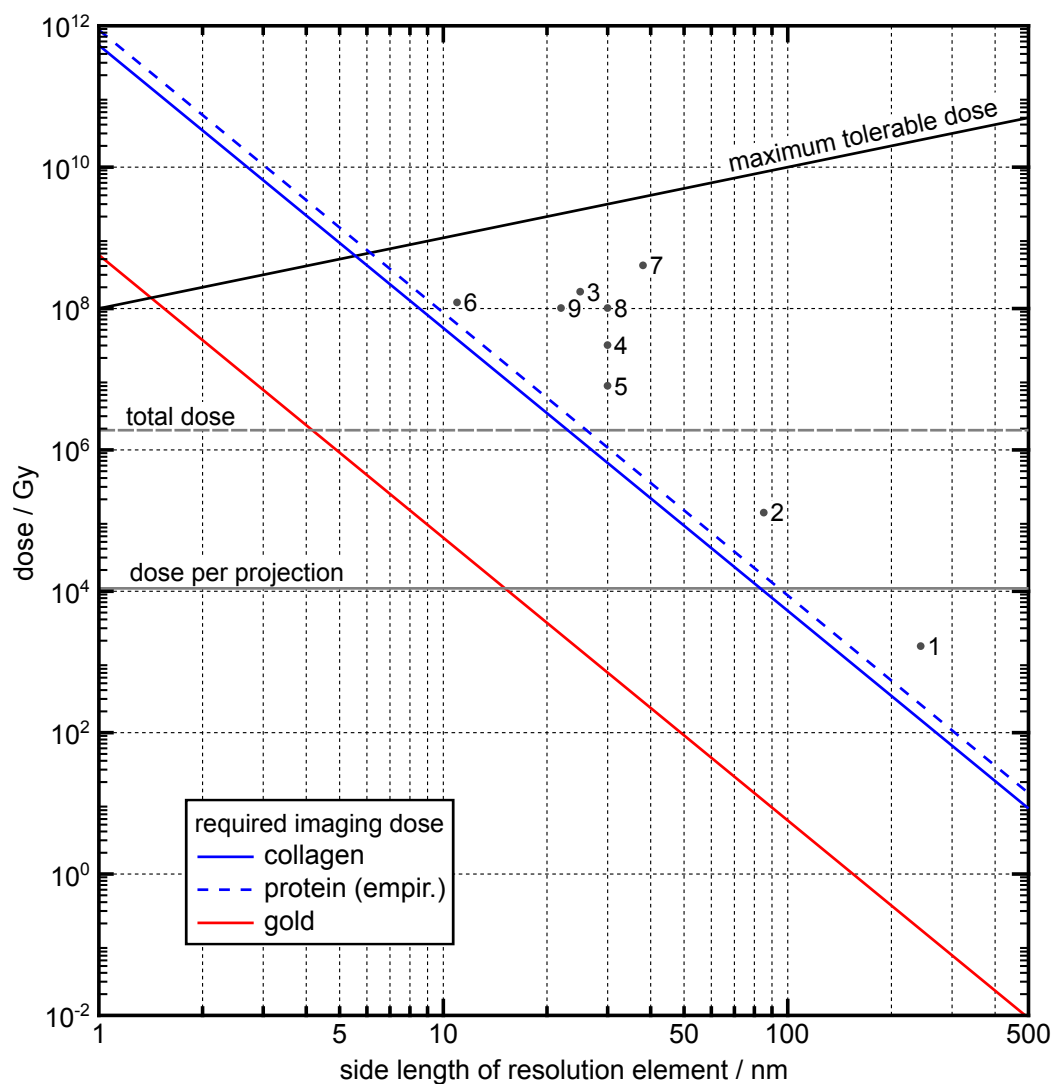


Figure 9.11: Doses required to collect a sufficient scattering signal against a background of vacuum (air) from a resolution element (pixel or voxel) of a given size, which consists either of collagen (solid blue line), a general empirical protein (dashed blue line) or gold (red line). The curves are calculated with relation (9.11) (compare also HOWELLS ET AL., 2009) using the material parameters listed in Table 9.3. The maximum tolerable dose for biological material according to (9.10) is shown as a solid black line. For collagen and the other protein, the allowed dose-resolution value pairs are therefore constrained to the triangular region between the curves marking the required minimum and the feature-destroying maximum dose values. The intersections of these curves mark the highest achievable resolutions for this type of samples in synchrotron-based CDI experiments. The doses for an individual projection and the total PXCT scan of the murine bone are marked by grey horizontal lines, whose intersections with the required dose curves allow to assess the experiment-specific resolution limits. The labeled dots mark pairs of dose and resolution values reported for other CDI experiments which are listed in Table 9.4 on page 282. See also the main text for a more detailed discussion.

Dose per projection Both proteins show a very similar behaviour, although the required dose for collagen with the parameters in Table 9.3 is slightly lower. For the calculated dose per projection, a maximum resolution of slightly below 100 nm is found.

Due to the much stronger interaction of X-rays with gold, the same dose would already allow to reconstruct resolution elements with side-lengths below 20 nm with the same statistical accuracy. This reflects the general relation (3.70) on page 112 linking the variance of the reconstructed values, the resolution and the incident photon fluence.

Total dose The total dose would in principle allow for resolutions below 30 nm in the case of the proteins or below 5 nm in the case of gold. However, the perfect dose fractionation assumed in the generalization of (9.11) to the 3D case is not given for PXCT: as discussed already in section 9.3.4, high-resolution information not retrieved in the ptychographic phase-retrieval process of the individual projections is not at all propagated to the subsequent filtered backprojection. In the current scheme, the resolutions of tomographic reconstructions can therefore not exceed the ones of the projection images.

The potential of dose fractionation could be fully exploited with an approach which integrates ptychographic and tomographic reconstruction in such a way that all diffraction patterns directly contribute to the 3D volume being retrieved.

Maximum tolerable dose The curve for the maximum tolerable dose presented in Fig. 9.11 has been determined for biological materials (HOWELLS ET AL., 2009) and therefore does not pose a limit in the case of gold. For the proteins, however, one finds that the highest resolution achievable in a CDI experiment³ is in the range of 6 to 7 nm. It is also clearly illustrated that the total dose the murine bone received in the demonstration experiment is well below the feature-destroying limit.

³ Not considering the latest developments at X-ray free electron lasers (CHAPMAN ET AL., 2006a; NEUTZE ET AL., 2000), in which this fundamental limit is circumvented by delivering the full photon flux in such a short time that radiation damage only takes effects after the X-ray pulse has passed the specimen. Therefore, the collected diffraction patterns are considered to be essentially unaffected by radiation damage.

9.3.5.4 Comparison with experimental doses reported in the literature

To put the dose values delivered to the murine bone specimen in the demonstration experiment in a wider context, they are compared with doses reported in the literature for CDI reconstructions of biological specimens. Some recent examples are summarized in Table 9.4 (alphabetically ordered by names of first authors). The locations of the corresponding dose-resolution value pairs in Fig. 9.11 are marked by grey dots labelled according to the first column of Table 9.4. In cases where a resolution range is given in the original publication, the lower bound is shown in Fig. 9.11. Apart from the first two entries, all these results were obtained with isolated objects which allowed to impose well-defined support constraints in real space during the reconstructions. Consequently, the respective input data consisted of just a single diffraction pattern, typically merged from multiple exposures to increase the dynamic range. As only the work of NISHINO ET AL. (2009) features a three-dimensional result, the values listed in Table 9.4 should be compared to the average dose per projection of 11 kGy calculated for the murine bone experiment. Upon closer inspection of Table 9.4 and Fig. 9.11, one can make the following observations:

- All the specimens are very similar and mainly consist of proteins. The empirical protein which HOWELLS ET AL. (2009) used for their calculations is therefore considered to be a valid model in these cases and also has been used in several of the publications to estimate the dose. For photon energies larger than about 2 keV, the required imaging dose in (9.11) becomes independent of the wavelength (compare HOWELLS ET AL., 2009, Fig. 2(b)). This dose is thus well approximated by the blue dashed curve in Fig. 9.11 for most of the cases, as only experiments 3, 4 and 8 were conducted at soft X-ray energies below 1 keV.
- If all the reported resolutions were fundamentally dose-limited, they would be expected to lie on or parallel to the blue dashed curve marking the required imaging dose for the empirical protein. Mathematically, this corresponds to

$$D_j \cdot d_j^4 = \text{const.}, \quad j = 1, \dots, 9, \quad (9.12)$$

i.e. the product of dose D and fourth power of the resolution element's side length d should be the same constant value for all experiments j . The dose-resolution pairs of experiments 1, 2 and 5 fulfil (9.12) within a few percent and as a result form a straight line in Fig. 9.11. Some

offset with respect to the theoretical curve is to be expected, as the latter is based on the idealized assumption of a vacuum background and also does not take into account that imperfect detection and the reconstruction algorithms may lead to some resolution degradation.

- The other experimental values show strong deviations from the fourth-power law described by (9.12). This may have several reasons, ranging from difficult experimental conditions to the way the resolution was determined. But even if the delivered dose would in principle allow for a higher resolution, a reconstruction with a lower value may have the benefit of better statistical accuracy.
- The results of 1, 2 and 5 do not only show the best correspondence with (9.12), but have also been obtained with exactly the same X-ray energy of 6.2 keV as the PXCT reconstruction. Therefore, they are used here to calculate a mean value for the constant on the right-hand side of (9.12) which is employed to estimate the resolution of the PCDI result from the previously determined dose value: For the average dose per projection of about 11 kGy, the average resolution calculated from (9.12) is 155 nm which fits well with the 136 nm obtained in section 9.3.4. As discussed earlier, the resolution of the tomographic reconstruction cannot exceed the one of the projection images. The 43 nm one estimates with (9.12) for the total dose of 1.9 MGy could only be reached in the case of perfect dose fractionation.

9.4 Conclusions and outlook

This chapter has introduced a combination of ptychographic CDI with standard tomography techniques. It enables quantitative volumetric phase-contrast imaging of non-isolated specimens, whose size can be much larger than the transverse coherence lengths of the incident X-ray beam.

The results of a first demonstration experiment on a murine bone specimen presented in section 9.3 show that the method provides a very high density sensitivity at a high spatial resolution. In section 9.3.2, the former has been identified as the technique's most promising feature when it comes to applications in bone science and forms the basis of the research activities reported in chapter 10.

At the cSAXS beamline, the technique is now available for regular users (compare, e.g., CHEN ET AL., 2013; DIAZ ET AL., 2014; ESMAEILI ET AL., 2013; TRTIK ET AL., 2013) while no longer requiring them to have expert

#	reference	specimen	dose / Gy (per projection)	resolution / nm (half period)
1	DIEROLF ET AL. (2010b)	<i>Magnetospirillum gryphiswaldense</i>	$1.7 \cdot 10^3$	242
2	GIEWEKE- MEYER ET AL. (2010)	<i>D. radiodurans</i> (freeze-dried)	$1.3 \cdot 10^5$	85
3	HUANG ET AL. (2009)	yeast cell (frozen-hydrated)	$1.7 \cdot 10^8$	25
4	LIMA ET AL. (2009)	<i>D. radiodurans</i> (frozen-hydrated)	$3 \cdot 10^7$	30 to 50
5	MIAO ET AL. (2003)	<i>Escheria coli</i>	$8 \cdot 10^6$	30
6	NELSON ET AL. (2010)	yeast cell (freeze-dried)	$1.2 \cdot 10^8$	11 to 13
7	NISHINO ET AL. (2009)	human chromosome	$4 \cdot 10^8$	38
8	SHAPIRO ET AL. (2005)	yeast cell (freeze-dried)	$\sim 10^8$	< 30
9	SONG ET AL. (2008)	herpes virus	$\sim 10^8$	22

Table 9.4: Overview of doses and resolutions reported for other CDI experiments conducted on biological specimens. Results are sorted alphabetically by names of first authors. The enumeration in the first column corresponds to the labels marking the corresponding dose-resolution values in Fig. 9.11. Entries 1 and 2 are based on ptychographic reconstructions, while for the remaining a single diffraction pattern and a support constraint in real space form the basis of the respective phase-retrieval process. Most experiments were performed at hard X-ray energies between 5 and 8 keV, only for 6, 8 (750 eV) and 3 (520 eV) soft X-rays were used. Abbreviation: *D. radiodurans* = *Deinococcus radiodurans*.

knowledge of CDI. The MATLAB implementation by Manuel Guizar-Sicairos of the data analysis procedures (GUIZAR-SICAIROS ET AL., 2011) described in section 9.2 plays a major role in this. At TUM, graphical user interfaces for Python implementations of both the ptychographic reconstruction and the post-processing steps are being developed.

However, the current standard alignment routine (see 9.2.4) requires that the specimen always stays fully within the field of view in the direction perpendicular to the rotation axis and is surrounded by sufficiently large areas

of air. More general schemes, which would then allow to integrate ptychographic CDI with digital tomosynthesis (see also section 10.3), laminography and local tomography, are an active field of current research. Similarly, other steps of the analysis procedure are continuously re-evaluated and improved, e.g. the replacement of the filtered backprojection with iterative tomographic reconstruction techniques, which are more suited for the typically relatively small number of projections.

A more fundamental idea aims at making several of the current processing steps obsolete, in particular the alignment procedures whose results tremendously affect the quality of the tomographic reconstructions: it is an extension of the shared-object reconstruction scheme introduced in section 7.2.2 to three dimensions, such that information is shared between the data sets through a combination of ptychographic and tomographic reconstruction steps. Similar to the 2D object sharing, this approach could most probably compensate automatically for the misalignment of projections by introducing probe shifts. More details are discussed in section 12.2.1 on page 333.

As discussed in sections 9.3.4 and 9.3.5, the current approach in which ptychographic and tomographic reconstruction are two subsequent but independent steps does not fully exploit the potential of dose fractionation. A method that would make best use of all detected information would therefore have to directly reconstruct the 3D volume from the diffraction data without the intermediate step of generating projection images in which high-frequency information may be lost. While this is in principle possible, e.g. through a generalization of the maximum-likelihood scheme introduced in section 3.2.5, the large amount of diffraction data which has to be processed at once complicates the practical implementation.

Chapter 10

Applications of ptychographic nanoCT in bone research

Bone is a biological material built from mineralized¹ collagen fibrils (FRATZL ET AL., 2004; WEINER AND WAGNER, 1998) in a highly hierarchical manner. WEINER AND WAGNER (1998), e.g., define seven hierarchical levels which are listed in Table 10.1 together with the typical length scales over which the respective structures extend. From the results of the demonstration experiment described in chapter 9, it can be inferred that PXCT is best suited for the investigation of levels 2 to 5: structures with sizes down to about 100 nm can be visualized in specimens with a transverse extent of at most 100 μm . In terms of the lacuno-canalicular network (compare also section 9.3.3.1), which is formed by cells (osteocytes) embedded in voids (lacunae) inside the bone matrix and their connecting cell processes (canaliculi), this field of view allows to cover several lacunae and their vicinity. The internal structure of the bone matrix in-between the cells, i.e. in particular the fibril array patterns (level 4), may be to some extent deduced from the morphology of the lacuno-canalicular network (KERSCHNITZKI ET AL., 2011). For a direct visualization, however, both resolution and sensitivity of the imaging technique have to be high enough to image the individual collagen fibrils which form the larger structures. As demonstrated in section 9.3.2, PXCT

¹The mineral in bone occurs as small platelet-shaped crystals of carbonated hydroxy(l)apatite (FRATZL ET AL., 2004; WEINER AND WAGNER, 1998). Compared to the original composition of hydroxyapatite, $\text{Ca}_{10}(\text{PO}_4)_6(\text{OH})_2$, some of the phosphate groups (PO_4^{3-}) are replaced by CO_3^{2-} , resulting in a chemical formula of $\text{Ca}_{10-x}[(\text{PO}_4)_{6-2x}(\text{CO}_3)_{2x}](\text{OH})_2$ (WOPENKA AND PASTERIS, 2005). The actual composition varies strongly depending on species and age, see e.g. the experimental studies by BILTZ AND PELLEGRINO (1983), where a range for x between roughly 0.1 and 0.6 can be found.

Level	description	typical scale
1	major components (collagen, bone mineral crystals)	< 100 nm
2	mineralized collagen fibril	100 nm
3	fibril array / bundle	< 1 μm
4	fibril array patterns	$\sim 10 \mu\text{m}$
5	cylindrical motifs: osteons	$\sim 100 \mu\text{m}$
6	spongy (trabecular) versus compact bone	< 1 cm
7	whole bone	$\sim 10 \text{cm}$

Table 10.1: The seven hierarchical levels of bone according to WEINER AND WAGNER (1998, compare in particular their Figure 1). In addition, the third column gives some rough values for the typical extent of the described structures. In the case of the fibrils, the given value is referring to the size perpendicular to the long axis. In particular, direct visualization of structures at levels 3 and 4 is typically only possible if the collagen fibrils (level 2) themselves can be properly resolved.

provides both nano-scale spatial resolution and quantitative electron density information with a high sensitivity.

As a consequence of the previously discussed points, feasibility studies whose first results are presented in this chapter have been focusing on potential applications of the technique in investigations of the intracellular bone matrix: on the one hand, the possibility to study bone density fluctuations in 3D on a sub-micrometer level is further explored in section 10.1. On the other hand, the direct visualization of collagen fibril arrays and their patterns is discussed in section 10.2. Tomosynthesis on flat extended bone slices, which provides the potential to extend the range of accessible samples and ease preparation procedures, is introduced by means of preliminary results in section 10.3.

10.1 Quantitative mapping of mineralization gradients

10.1.1 Motivation: Do osteocytes remodel bone?

Osteocytes as sensors The basic description of the lacuno-canalicular network in section 9.3.3.1 on page 264 has already pointed out the role of the interconnected osteocytes as a sensor network for mechanical loads (for a detailed review of the mechanisms, see e.g. KLEIN-NULEND ET AL., 2013). It is commonly accepted that this sensor information is used by the osteocytes to regulate of the activity of osteoblasts (bone-depositing cells) and osteoclasts

(bone-removing cells) through biochemical signalling pathways ([ATKINS AND FINDLAY, 2012](#)).

More than sensors? However, the bone research community has been debating for more than 40 years whether the osteocytes only have this passive role of “conductor of the bone orchestra” ([BONUCCI, 2009](#)), or if they can also actively remodel bone and thus contribute to mineral equilibrium. This idea is supported by the fact that in an adult the total surface area (about 1200 m²) of the lacuno-canalicular network is more than 100 times the surface area covered by osteoblasts and osteoclasts ([AARDEN ET AL., 1994](#); [BÉLANGER, 1969](#)). Therefore, the osteocytes have access to a huge reservoir of bone mineral in their closest vicinity. As a result, removal and deposition of mineral in order to regulate the levels of Ca and P (mineral homeostatis) could be achieved by the osteocytes without major changes of the bone’s structure or mechanical properties. Theories which propose active bone remodelling by osteocytes are generally referred to as “osteocytic osteolysis” ([BÉLANGER, 1969](#)), as mostly the removal of mineral has been studied.

The long debate on osteocytic osteolysis and facts in favour and against the concept have recently been summarized in reviews by [TETI AND ZALLONE \(2009\)](#), [QING AND BONEWALD \(2009\)](#) and [BONEWALD \(2011\)](#): The removal of mineral by osteocytes was first suggested more than 100 years ago ([RIGAL AND VIGNAL, 1881](#) as cited e.g. in [BÉLANGER, 1969](#); [VON RECKLINGHAUSEN, 1910](#)²). The concept gained significant momentum in the 1960s and 1970s, when it was used to interpret various experimental findings, like enlarged lacunae or rough lacunar walls (an overview over this work was compiled by [BÉLANGER, 1969](#)). Also bone formation by osteocytes was reported ([BAYLINK AND WERGEDAL, 1971](#)). In the late 1970s, however, osteocytic osteolysis was strongly opposed, especially due to its close connection to the “bone flow theory”: The latter states that new bone is produced by osteoblasts on the surfaces and continuously flows towards the osteocytes inside, which resorb it through osteocytic osteolysis ([PARFITT, 1977](#)). As the physical properties of bone make such a flow impossible, the theory was rejected in the end and with it osteocytic osteolysis. Among others, the rebuttal of ([PARFITT, 1977](#)) was most influential in this context. In this article and similar ones, the previous experimental observations for osteocytic oste-

²VON RECKLINGHAUSEN (1910) wrote e.g. on page 38 of his book that the observed growth of canaliculi and lacunae could be most easily explained, if one assumed that the solid embedding bone material had been somehow altered and thus softened: “Die Erweiterung der Knochenhöhlen und -kanälchen [...] erklärt sich am leichtesten, wenn wir uns vorstellen, daß dabei das feste Material der einbettenden Grundsubstanz nachgiebig und weich geworden, jedenfalls umgewandelt war.”

olysis were mainly attributed to sample preparation artefacts. Furthermore, it was pointed out that most of the data used as evidence was based on only two-dimensional cuts through osteocytes and thus can hardly provide a thorough understanding of the 3D lacunar morphology and its changes.

Renewed interest in the concept of osteocytic osteolysis has recently been triggered by new experimental evidence (compare reviews by QING AND BONEWALD, 2009; TETI AND ZALLONE, 2009). In this new work, however, osteocytes are attributed a more subtle role in bone remodelling than in the rejected bone flow theory: TETI AND ZALLONE (2009) conclude that normal physiological mineral control activity of osteocytes does not affect the size and shape of lacunae. Instead, they suppose that mineral exchange takes place on a sub-microscopical level in the perilacunar matrix³ in close proximity to the lacunar wall, as suggested by WASSERMANN AND YAEGER (1969, page 319): According to them, this process probably involves the so-called “coastal crystals” growing at the inner edge of the perilacunar matrix. Strong morphological changes of lacunar size and shape, however, are – according to TETI AND ZALLONE (2009) – only to be expected under pathological conditions. Such changes have also been reported for other times of unusually high calcium requirements like e.g. during lactation (QING ET AL., 2012; WYSOLMERSKI, 2013). Despite the recent evidence, further investigations are required to proof the theory.

Ptychographic X-ray nanotomography (PXCT) as introduced in chapter 9 provides a combination of features which make it an ideal tool for such further investigations of osteocytic osteolysis:

High spatial resolution The high spatial resolution of PXCT allows to resolve structural details of the lacuno-canalicular network and the surrounding bone matrix.

High density resolution The high sensitivity of PXCT (compare section 9.3.2 on page 260) allows to visualize subtle differences in the degree of mineralization of the bone matrix.

Three-dimensional volumetric imaging PXCT allows to obtain three-dimensional volumetric representations of samples with the aforementioned high spatial and high density resolutions. In contrast, histology-based methods or electron backscatter imaging, which have been fre-

³According to PARFITT (1977), *perilacunar matrix* or *perilacunar bone* is produced by osteoblasts that only recently became enclosed in bone. Before transforming into osteocytes, these cells continue to “line their lacunar and canalicular walls with a unique form of bone”. WASSERMANN AND YAEGER (1969) point out that one observes the perilacunar matrix to be “more heavily mineralized than the bulk of the interlacunar matrix”.

quently used in the past, provide only two-dimensional information. PXCT should therefore be less prone to potential misinterpretations due to the fact that only a 2D slice is used to interpret changes of lacunae with complex three-dimensional shapes.

For the first application of PXCT in the context of bone mineralization investigations, specimens with artificially-created mineralization gradients were used. **This experiment had two major objectives:**

1. To demonstrate that already a simple NaCl solution at physiological conditions can lead to significant bone demineralization. In particular, to show this way that mineral removal does not necessarily require the strong acidic environment which is created by active osteoclasts (BOYLE ET AL., 2003; ROODMAN, 1996).
2. To establish that PXCT allows to quantitatively image bone mineralization gradients in 3D together with the morphology of the lacuno-canalicular network in a single experiment.

10.1.2 Sample preparation

The ovine bone samples (femur) were prepared by Michael Kerschnitzki and co-workers at the Max-Planck-Institute for Colloids and Interfaces (MPIKG) in Potsdam-Golm. The bones were provided by the Julius Wolff Institute at Charité, Berlin, and originating from animals sacrificed as part of a study conducted in Berlin, Germany. This study had received an ethics permit issued by the appropriate committee of ethics in animal experiments at Charité. Several specimens for PXCT measurements were prepared according to the following protocol (compare also KERSCHNITZKI, 2012, p. 20):

1. Treatment with a non-ionic detergent (Nonidet P-40) to make samples permeable for NaCl solution by dissolving diffusion barriers (membranes) inside.
2. Immersion in NaCl solution (150 mM, pH 7) at room temperature on a shaker until Ca saturation was reached (72 hours).
3. Mechanical sectioning with a low-speed diamond saw (IsoMet, Buehler GmbH, Düsseldorf, Germany) followed by mechanical thinning with an automatic polisher (Logitech PM5, Logitech Ltd., Glasgow, UK; compare also KERSCHNITZKI ET AL., 2011, section 2.1) to sheets of thicknesses in the order of 40 to 70 μm .

4. Cutting of small sticks of $\sim 50\ \mu\text{m}$ width and $\sim 3\ \text{mm}$ length out of the thin sheets with a UV-laser microdissection system (P.A.L.M MicroBeam C, P.A.L.M Microlaser Technologies AG, Bernried, Germany; compare also GUPTA ET AL., 2006, page 17744). The direction of cutting was chosen such that the long axis of the respective stick was perpendicular to the surface exposed to the NaCl solution. As a result, the long axis of each stick should be roughly parallel to the expected mineralization gradient. A visible light micrograph of the specimen discussed in the following sections is presented in Fig. 10.1(a) on page 291.
5. Drying of samples in air.
6. Free-standing mounting with cyanoacrylate-based adhesive on top of metal needles (compare section 5.3.5.1 on page 151 for details). Orientation was chosen such that the long axis of the respective stick pointed along the (vertically aligned) axis of rotation and the region of strongest demineralization was located at the very top of the specimen.

While the first two steps are specific to the generation of samples with artificial gradients, specimens very close to the native state can be prepared when starting from step 3. Furthermore, the procedure is much less demanding – both in terms of protocol complexity and required equipment – than the preparation involving FIB milling discussed in section 9.1.1 on page 239.

10.1.3 Experiment

Experiments were performed at the cSAXS beamline of the Swiss Light Source with the tomography set-up described in section 5.1.3 starting on page 134. The energy of the incident X-rays was set to 6.2 keV. The illumination on the sample was created with a pinhole aperture of about $2.5\ \mu\text{m}$ diameter, which had been milled into a tungsten foil by focused ion beam (prepared by K. Jefimovs, EMPA). The excess in transverse vertical coherence length compared to the pinhole's diameter allowed to prefocus the beam with the beamline optics (compare section 5.1.1.3). As a result, the typical exposure time per point could be reduced to about 0.1 s, i.e. by a factor of ten compared to the first demonstration experiment (see section 9.1.2 for details of the latter), while counting statistics still remained slightly better. This increase in acquisition speed allowed not only to scan larger and more volumes, but in particular also to double the number of projections per tilt series.

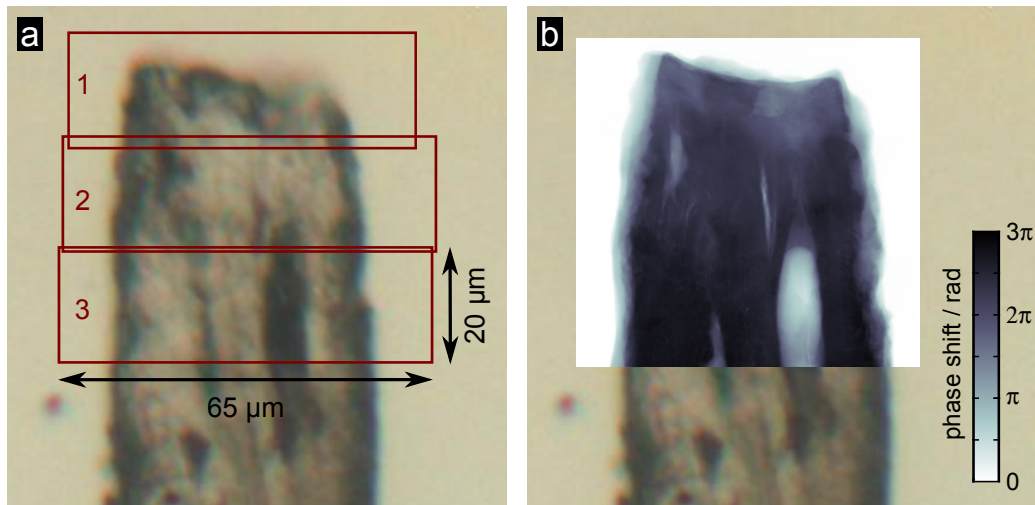


Figure 10.1: Visible light micrographs of ovine bone specimen with mineralization gradient indicating area covered by ptychographic scans. **(a)** Coverage of the top of the sample by the ptychographic projections of three subsequent tomographic scans. The slight vertical overlap between the three scanned volumes was chosen to allow for merging them into a single volume later. The first scan (1) at the top had a slightly smaller extent of $60\ \mu\text{m} \times 20\ \mu\text{m}$ (horizontal \times vertical) compared to $65\ \mu\text{m} \times 20\ \mu\text{m}$ of the lower two. The offset of the scans' centres is due to manual corrections of the area to be scanned between each of the tilt series. **(b)** The same visible light micrograph overlaid with a phase-contrast projection to illustrate the effective field of view of the combined scans. The projection image was calculated from the final volume merged from the result of all three tomographic reconstructions. Upon comparison with the radiograph, certain features visible in (a) can be more clearly identified, most prominently the big lacuna in the area covered by scan 3. As the surface exposed to the NaCl solution is at the top of the stick, a mineralization gradient along the vertical direction is to be expected in a more detailed analysis. Visible light micrograph provided by Michael Kerschitzki, MPIKG Potsdam-Golm.

Each tomographic scan consisted of 361 projections taken over an angular range of 180° with an angular step of 0.5° . To improve stability, these measurements were done as two consecutive interlaced scans with 1° steps and 0.5° offset in their angular positions. At each projection angle, ptychographic data was collected by scanning the sample perpendicular to the optical axis and recording far-field diffraction data with the two central modules of the PILATUS 2M detector. To avoid artefacts arising from the raster grid pathology (compare section 3.2.4.5), the points of the ptychographic scans were positioned on concentric circles (round scan) according to (3.43) with a radial step size of $1.5\ \mu\text{m}$. Data was only collected at points inside a pre-defined rectangular field of view. A typical tomographic scan with a field of view of $65\ \mu\text{m} \times 20\ \mu\text{m}$ (horizontal \times vertical extension) and 361 projections took about 12 hours (453 points per projection, each with an exposure

time of 0.1 s). At these settings, an overhead of about 0.1 s per scan point turned out to be the main limiting factor for further reduction of total scan times.

To visualize the artificially-induced mineralization gradient, a series of three such tomographic scans was collected, starting at the top of the specimen (strongest demineralization) and progressing into the less-demineralized lower parts. Fig. 10.1(a) shows the locations of three tomographic scans on the bone specimen, while Fig. 10.1(b) illustrates the effective field of view of the combined scans.

In order to obtain a bone volume which had certainly not been affected by the NaCl solution and could thus serve as a reference showing regular mineralization, a fourth tomographic scan was performed about 400 μm below the top of the specimen. While angular spacing (0.5°) and range (0° to 180°) remained the same, the individual projections covered a slightly larger field of view of $70 \mu\text{m} \times 28 \mu\text{m}$ (horizontal \times vertical) with 690 scan points.

To be able to relate the reconstructed electron-density values to the mineral content of the bone specimens, a single spherical particle taken from a hydroxyapatite powder was measured to obtain a reference value for the electron density of pure hydroxyapatite. In this case the scan area was $30 \mu\text{m} \times 36 \mu\text{m}$ (387 scan points) with otherwise unchanged parameters.

10.1.4 Data processing

Data processing followed the steps developed for the demonstration experiment in section 9.2:

1. The **ptychographic reconstructions** of the projection images were performed with a Matlab implementation of the difference-map-based PCDI algorithm with simultaneous probe retrieval described in section 3.2.2. As input, the central 128×128 pixels of each diffraction pattern were used. Considering the distance of 7.19 m between sample and detector and the latter's pixel size of $172 \mu\text{m} \times 172 \mu\text{m}$, this results with (2.20) in a pixel size of $65.3 \text{ nm} \times 65.3 \text{ nm}$ in both reconstructed object and probe. The projections were obtained after 400 iterations as the average of 25 object iterates from the steady-state regime of the difference map algorithm, i.e. by averaging every fifth of the last 100 object guesses.
2. For **alignment and related post-processing of the projections**, the methods described by [GUIZAR-SICAIROS ET AL. \(2011\)](#) (compare also the detailed descriptions in section 9.2.4) were used in form of a Matlab implementation provided by Manuel Guizar-Sicairos.

3. **Tomographic reconstructions** were done from differential projections (compare sections 4.2.3 and 9.2.5) employing again the specific approach and Matlab code of GUIZAR-SICAIROS ET AL. (2011). Reconstructions were done with the derivative version of the Parzen filter (compare Fig. 4.3(b) on page 123). To further suppress high-frequency noise, the filter was applied with a frequency-scaling of 0.8, i.e. the filter is compressed into the frequency range between 0 % and 80 % of the Nyquist frequency and is set to 0 for all frequencies above.
4. **Conversion to quantitative electron density values** according to (9.2) in section 9.2.6. The air surrounding the specimen was used to calibrate the origin of the electron density.
5. As an additional step compared to the standard processing procedure, **merging of the three overlapping subvolumes** from the gradient region was performed at sub-pixel accuracy (linear interpolation) with a least-squares optimization approach developed and implemented by Andreas Fehring in the course of his *Diplom* thesis (FEHRINGER, 2011).

10.1.5 Results

The final volume merged from the three scans close to the top of the sample consists of 854 tomographic slices. In these, the rectangular cross section of the sample is contained within a region of about 400×720 pixels. The volume has thus been cropped to $521 \times 902 \times 854$ cubic voxels of 65.3 nm side length. Given the extent of the specimen, the 360 projections recorded over 180° are not sufficient to fulfil the condition for angular sampling in (4.5). However, the absence of abrupt transitions or sharp edges prevents the generation of very pronounced streak artefacts. Therefore, the artefacts actually arising in the reconstructed slices have only small amplitudes and mainly just increase the overall noise level.

10.1.5.1 Visualization of mineralization gradient

A longitudinal cut through the volume, i.e. both parallel to the rotation axis and the main diffusion direction of the mineral-dissolving NaCl solution, is presented in Fig. 10.2(a). In addition to canaliculi (C) and lacunae (L), Fig. 10.2(a) allows to easily distinguish three different grey levels in the surrounding bone matrix itself, which have been labelled B_0 to B_2 . These different grey levels clearly indicate a decrease in mineralization closer to the top, which was part of the surface exposed to the NaCl solution. This

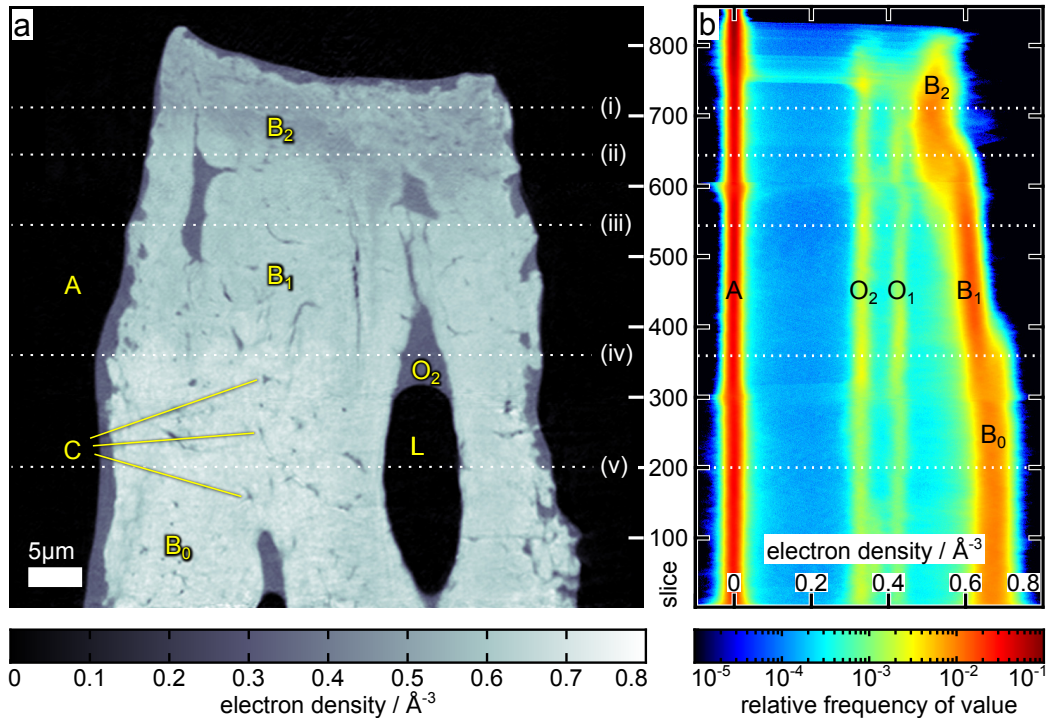


Figure 10.2: Result of tomographic reconstruction of an ovine bone which exhibits a mineralization gradient. (a) Exemplary longitudinal plane (cut parallel to rotation axis) of reconstructed volume. The grey values encode the electron density on a linear scale, see colour-bar. The bone had been chemically decalcified in the preparation process (see section 10.1.2 for more details), resulting in a mineralization gradient along the rotation axis. The gradient is visible as a change in the grey values of the bone matrix from darker ones at the top (less mineral, label B₂) via an intermediate range in the centre (label B₁) to brighter grey values at the bottom (full calcification, label B₀). The typical structural features like lacunae (L) and osteocytes (C) are also visible. Organic material with two different densities is found both inside the lacuno-canalicular network and on the surface of the specimen. This slice only shows the less dense material labelled O₂, the denser O₁ is visible in the histogram in panel (b) and in the tomographic slices presented in Fig. 10.3. (b) Change of histogram along gradient direction. Each row of the image is the histogram of the respective tomographic slice with the relative frequency of electron density values (500 equally-sized bins in the range -0.1\AA^{-3} to 0.8\AA^{-3}) within this slice represented on a colour-coded logarithmic scale, see colour-bar. The transitions between the three independent volumes merged here are visible around slices 300 and 600. The air peak A was used to calibrate the origin of the electron density scale. The density values of the two central peaks O₁ and O₂ representing the organic material are independent of the height within the sample. However, the peak on the right, which corresponds to the density of the bone matrix at the respective height, shifts to lower values closer to the surface. While there are smooth transition regions, one can also identify the three regions of relatively constant densities which are also labelled in panel (a): fully-mineralized bone at the bottom (B₀), a region of intermediate density in the centre part (B₁), and significantly de-calcified material at the top (B₂). Slices and histograms from these regions and the transition areas, whose positions are marked by the dashed white lines, are compared in Fig. 10.3.

result thus already demonstrates the possibility to generate substantial bone demineralization with NaCl solution at physiological conditions, which has been formulated as objective 1 of the experiment on page 289.

The presentation of all per-slice histograms in Fig. 10.2(b), where each line in the image colour-codes the relative frequency of the different electron density values in the respective tomographic slice, allows a more detailed investigation of the mineralization changes along the rotation axis:

- The rightmost peak in the histogram, which represents the bone matrix material, shifts from a value of about 0.68 \AA^{-3} at the bottom to about 0.52 \AA^{-3} close to the top of the specimen.
- The mineralization gradient is not constant: instead of a continuous change of bone density, one observes three extended areas with quite constant mineralization and smooth transitions between them. This can be explained by the complex morphology of the bone and in particular the lacuno-canalicular network, which is expected to give rise to strong local variations of the diffusivity. So far, the bone density has just been examined as a function of the distance from the specimen's top, which was part of macroscopic bone surface in direct contact with the NaCl solution. A more sophisticated analysis, however, has to consider all surfaces which had a direct connection to the reservoir of NaCl solution. The mineralization thus has to be investigated as a function of distance from the surfaces of the lacuno-canalicular network (compare e.g. [KERSCHNITZKI ET AL., 2013](#)). While the segmentation required for such an analysis works well for the reference bone volume (Fig. 10.6 on page 300), it fails for the canaliculi in the top part of the reconstructed volume because the contrast to the surrounding demineralized bone matrix gets too low. This manifests itself in the histogram in Fig. 10.2(b) as an overlap of peaks B_2 and O_1 .
- Apart from the air peak A, which has been used to calibrate the origin of the electron density axis, two more peaks O_2 and O_1 are visible. They are interpreted as originating from organic components in the specimen: While O_1 most likely resembles unmineralized (collageneous) bone matrix (compare also section 10.1.5.3), the origin of O_2 is not completely certain. There is a high probability that the material is some of the cyanoacrylate glue used for mounting the specimen, although a higher electron density was found for glue which was scanned together with the hydroxyapatite particle (see section 10.1.5.3 and Fig. 10.7).

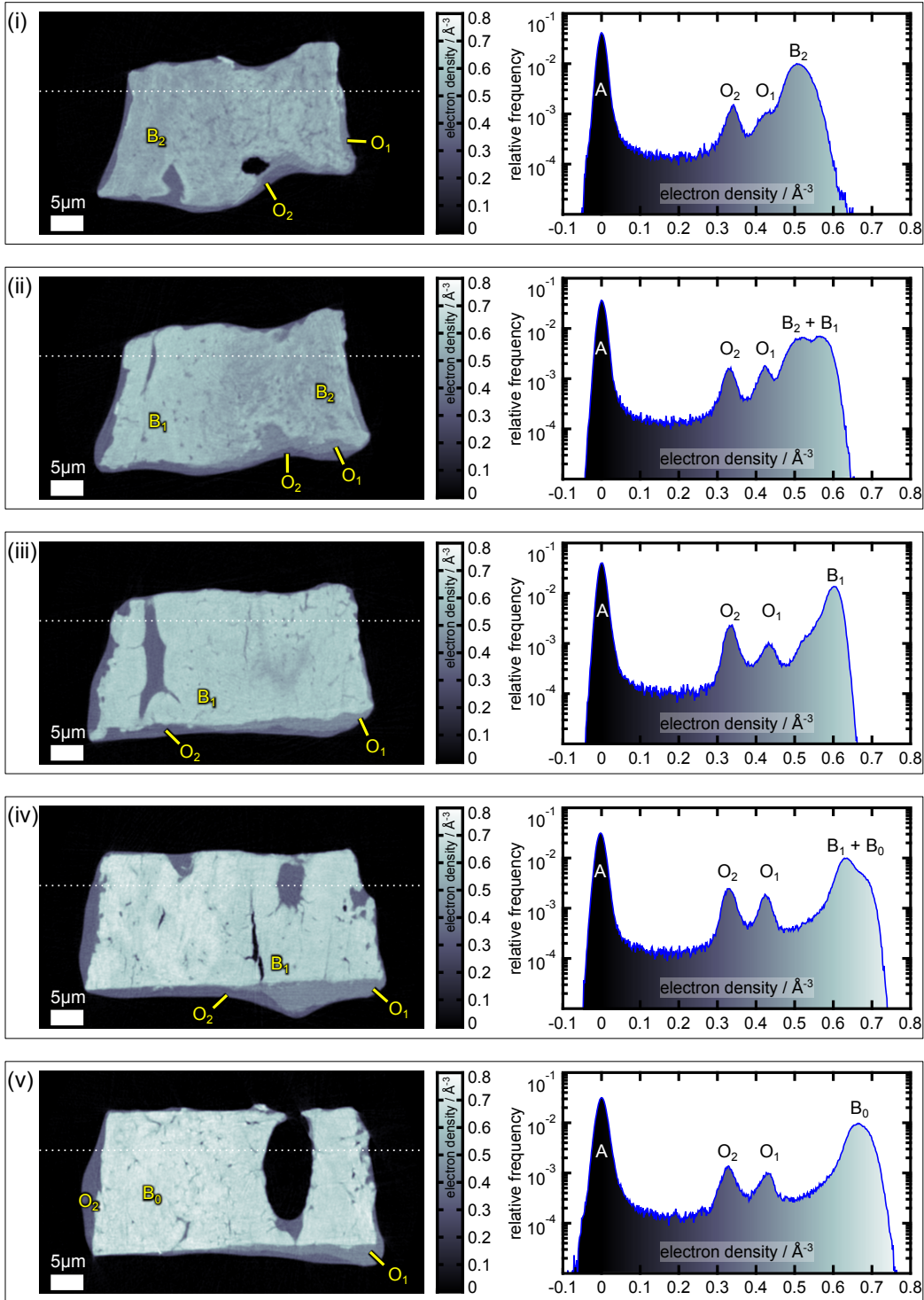
Further details are revealed in Fig. 10.3, which on the left-hand side presents tomographic (transverse) slices through the volume and on the right-hand

side their respective histograms. Their locations along the longitudinal axis of the specimen are indicated by the white dashed lines in both panels of Fig. 10.2. The slices were selected to represent each of the three regions with relatively constant bone densities previously identified in Fig. 10.2(b), as well as the two transition regions. Fig. 10.2 allows for three more important additional observations:

- The bone density in the transition regions (panels (ii) and (iv)) is neither homogeneous nor showing an intermediate mineralization value. Instead, the transition regions both show two distinct phases of bone with the respective mineralizations of the neighbouring regions (below and above) of nearly constant densities.
- The organic material O_2 shows very smooth surfaces and bulges in the centres of the specimen's edges, the latter visible in particular on the left edges in panels (iv) and (v). Both this can be interpreted as the result of a wetting process, which would be consistent with the assumption that O_2 is cyanoacrylate glue which covered the sample during the mounting process.

Figure 10.3 (following page): Tomographic slices at five different heights marked by the dashed white lines bearing the same labels in the longitudinal cut in Fig. 10.2(a). The respective histogram is shown on the right of each slice (relative frequencies of electron-density values for 500 equally-sized bins in the range -0.1 \AA^{-3} to 0.8 \AA^{-3}). Each of these corresponds to a lineout through the colour-coded histogram in Fig. 10.2(b), where their position is also marked by dashed white lines. As the direction of the artificially-induced mineralization gradient also points along the rotation axis, the slices represent different degrees of decalcification: **(i)** Strongly decalcified bone close to the sample's top, which was the surface exposed to the NaCl solution removing the mineral. The bone peak (B_2) approaches the value of the denser organic material (O_1). **(ii)** Transition area between the two regions of relatively constant bone densities B_2 and B_1 (compare also Fig. 10.2(b)), which can be nicely distinguished in the slice on the left. The non-uniformity in a cut perpendicular to the main diffusion direction of the mineral-dissolving solution can be attributed to the fact that the latter's local penetration depends highly on the bone morphology. As a result, the bone peak in the histogram is a double peak containing the contribution of both phases. **(iii)** Slice from the region of intermediate bone density B_1 , where the contributions of B_2 have largely vanished. **(iv)** Transition region between region with density B_1 and the part of the specimen in which no mineral was dissolved and thus the original density B_0 has been preserved. The histogram exhibits again a double peak with contributions of both densities. **(v)** Slice from lower part of the sample, in which no more changes of mineralization are observed and the bone peak stays at B_0 . In addition to the bone areas of different densities, also areas of the two sorts of organic material O_1 and O_2 are marked exemplary in each of the slices together with the corresponding peaks in the histograms. The dashed white lines indicate the position of the longitudinal cut orthogonal to these slices which is shown in Fig. 10.2(a).

10.1. Quantitative mapping of mineralization gradients



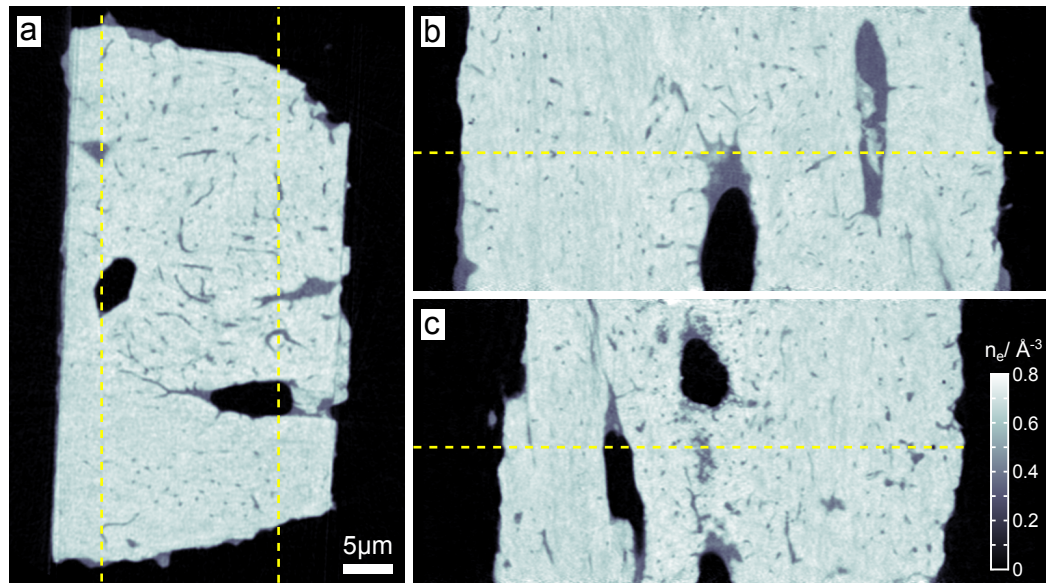


Figure 10.4: Reconstruction result for ovine bone with native mineralization. A linear grey scale colour codes the electron density values according to the colour-bar in panel (c). (a) Tomographic (transverse) slice. The bone’s growth direction is approximately parallel to the vertical axis of this image. The parallel flat surfaces on either side are an effect of the grinding processed used to thin down the specimen. Due to the abrupt phase jump the sample’s left edge produces then aligned parallel to the projection direction, some reconstruction artefacts are visible in the upper part of said edge. (b) Longitudinal slice (parallel to rotation axis), whose location is marked by the left of the dashed lines in (a). (c) Longitudinal slice marked by the right of the dashed lines in (a). The respective dashed line in (b) and (c) marks the location of slice (a). Examples for slices perpendicular to both of the directions presented here can be found in Fig. 10.10 and 10.11.

- In contrast, the denser organic material O_1 features some rather structured surface areas, e.g. on the lower edge of the specimen’s cross section in panel (iii). This supports the notion of O_1 being part of the original bone which got almost completely demineralized. However, the interpretation remains disputable as it is unclear why this material is found also abundantly on surfaces which were not supposed to be in direct contact with the NaCl solution. Due to the lack of accurate knowledge about the original morphology of the bone before polishing and laser cutting, a definite answer to this question can not be given.

10.1.5.2 Reference volumes

Slices through the reconstructions of the two reference volumes are presented on page 298: Fig. 10.4 shows cuts through the bone volume with native mineralization, which is referred to as “reference bone” in what follows. It

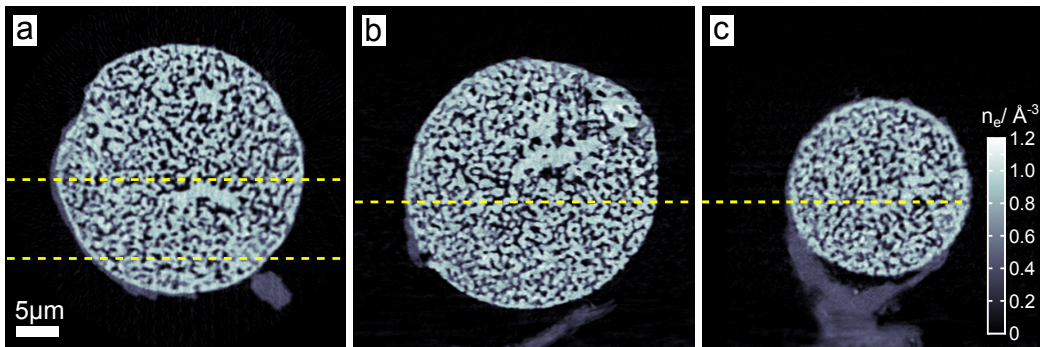


Figure 10.5: Slices through the tomographic reconstruction (electron density, see colour-bar in (c)) of the hydroxyapatite particle. They reveal that the shape of the particle is close to spherical as well as a highly-porous internal structure. The latter was not expected for this specimen and raises the concern that it affected the accuracy of the quantitative electron density values in an unknown way. (a) Tomographic (transverse) slice. (b) Longitudinal slice, in (a) marked by top dashed line. (c) Longitudinal slice, marked by the bottom dashed line in (a). At the bottom, the glue holding the specimen is visible.

also forms the basis for the visualization of collagen fibril patterns discussed in section 10.2 starting on page 306. Several lacunae are fully or partially contained within the imaged region, together with the canaliculi connecting them. The high contrast between canaliculi and surrounding bone material gives access to the morphological details of the network, see the volume rendering in Fig. 10.6. As visible in the tomographic (transverse) slice in Fig. 10.4(a), the specimen has two rather flat, parallel surfaces on either side, which are a result of the grinding process used to thin it down. Due to the large, abrupt phase jumps these surfaces produce in projections where they are parallel to the optical axis, some streak artefacts are visible at these edges of the specimen. However, they do not impair the overall reconstruction quality of the interior part of the volume.

The result obtained for the hydroxyapatite (HAP) particle is depicted in Fig. 10.5: The slices show a highly porous internal structure and not the anticipated compact particle of rather uniform density. A strong impact of this porosity on the validity of the quantitative results cannot be ruled out. Furthermore, also the noise level of the HAP particle reconstruction was significantly higher than for all the other volumes. It was reduced by per-slice application of an anisotropic diffusion filter (PERONA AND MALIK, 1990) such that the air peak has roughly the same width as in the other reconstructions, compare histogram in Fig. 10.7. As a consequence of these two issues, the calculated electron density of HAP has been used as a reference value in the end, compare the discussion in section 10.1.5.3.

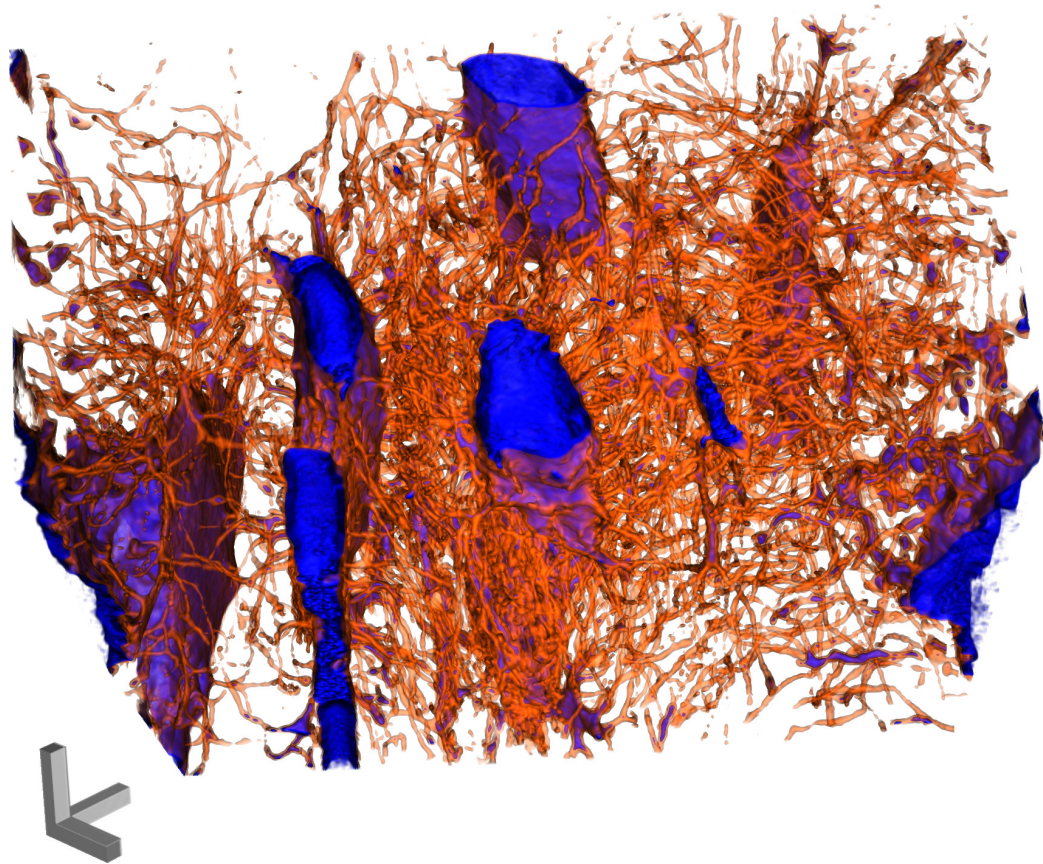


Figure 10.6: Volumetric rendering of the lacuno-canalicular network (LCN) in the reference bone volume, which has been segmented using histogram-based thresholding. Voids within the bone are shown in blue colour, while the canaliculi connecting them are visualized in red. Four lacunae can be identified unambiguously in the central part of the volume. Segmentation like presented here can be relevant for the study of osteocytic osteolysis if the mineralization is to be analysed as a function of the distance from the surfaces of the LCN. For the sample discussed here, however, segmentation fails for the canaliculi in the demineralized part at the top of the sample, as the contrast is insufficient to distinguish them unambiguously from the surrounding bone matrix. Long axes of tripod = 5 μm .

10.1.5.3 Discussion of quantitative results

For the discussion of the quantitative electron density values, the full histogram of the bone volume which exhibits the mineralization gradient (blue curve) is compared to the histograms of the reference bone volume (black) and of the hydroxyapatite sphere (red) in Fig. 10.7. Table 10.2 summarizes the electron density values n_e of the various peaks visible in the histograms. The uncertainty $\sigma_{n_{e,\text{air}}} = 0.01 \text{ \AA}^{-3}$ of the peak values is calculated from the FWHM of the air peak in the respective histogram. $\sigma_{n_{e,\text{air}}}$ provides an upper

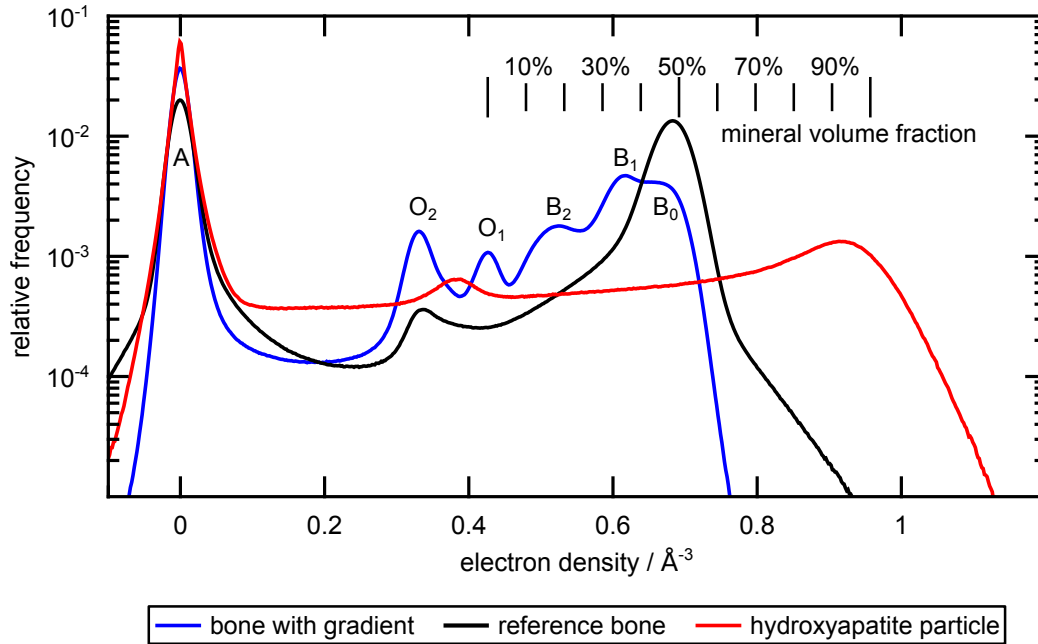


Figure 10.7: Comparison of the histogram of the bone with a mineralization gradient (blue) to the histograms of an unaltered reference bone volume (black) and a hydroxyapatite particle (red). The histograms give (on a logarithmic scale) the relative frequencies of electron density values for 722 equally-sized bins in the range -0.1 \AA^{-3} to 1.2 \AA^{-3} (which results in the same bin width as in Fig. 10.3). The scale for mineral volume fraction uses the O_1 peak of the bone with gradient, which is interpreted as fully-demineralized bone, and the mineral peak of the hydroxyapatite particle as reference points, see (10.2). The positions of the various peaks are listed in Table 10.2.

specimen	peak / material	$n_e / \text{\AA}^{-3}$	$\frac{V_{\text{HAP}}}{V_{\text{bone}}}$	$\frac{m_{\text{HAP}}}{m_0}$	$\frac{m_{\text{Ca}}}{m_0}$	
bone with gradient	bone	B_0	0.67(1)	0.45(2)	0.66(2)	0.26(1)
		B_1	0.62(1)	0.36(2)	0.57(3)	0.23(1)
		B_2	0.52(1)	0.17(2)	0.32(4)	0.13(2)
	organic	O_1	0.43(1)	0.00(3)	0.00(6)	0.00(3)
		O_2	0.33(1)			
reference bone	bone	B_{ref}	0.68(1)	0.47(2)	0.68(1)	0.27(1)
	organic		0.33(1)			
HAP particle	mineral		0.92			
	organic (glue)		0.38			
calculated values	hydroxyapatite		0.958(3)	1.000(8)	1.000(3)	0.399(1)
	collagen		0.444(16)			

Table 10.2: Peak positions in the comparison of histograms depicted in Fig. 10.7.

estimate for the noise level in the reconstruction of a completely homogeneous area. It contains the combined effect of the noise in the raw data and any additional uncertainties introduced by the reconstruction process. In order to compare the quantitative results to reference values, the electron densities of collagen – representing unmineralized bone matrix – and hydroxyapatite (HAP) were calculated:

- For collagen, an refractive index decrement at 6.2 keV photon energy $\delta_{\text{coll}} = 7.964(295) \cdot 10^{-6}$ was calculated based on the tabulated values by HENKE ET AL. (1993) using the online-interface to the database available at http://henke.lbl.gov/optical_constants/, the chemical composition $\text{C}_{12}\text{H}_{24}\text{N}_3\text{O}_3$ (OMOKANWAYE ET AL., 2010), and a mass density $\rho_{m,\text{coll}} = 1.35(5) \text{ g cm}^{-3}$ (PODRAZKÝ AND SEDMEROVÁ, 1966). With relation (1.24) between δ and electron density n_e (see page 22), one obtains $n_{e,\text{coll}} = 0.444(16) \text{ \AA}^{-3}$.
- Analogous calculations for hydroxyapatite, using a mass density of $\rho_{m,\text{HAP}} = 3.16(1) \text{ g cm}^{-3}$ (DOROZHKIN AND EPPLE, 2002) and the chemical composition $\text{Ca}_{10}(\text{PO}_4)_6(\text{OH})_2$ as input⁴, yield the values of $\delta_{\text{HAP}} = 1.719(5) \cdot 10^{-5}$ and $n_{e,\text{HAP}} = 0.958(3) \text{ \AA}^{-3}$.

A comparison of these calculated values to the peak positions listed in Table 10.2 shows that the O_1 peak of the NaCl-treated bone volume exhibits an electron density value $n_{e,\text{O}_1} = 0.43(1) \text{ \AA}^{-3}$, which lies within the uncertainty range of the value calculated for collagen. The material O_1 is therefore interpreted as completely-demineralized bone matrix, which mainly consists of collagen, and used as the origin of the mineral volume fraction scale. The calculated value for hydroxyapatite, $n_{e,\text{HAP}} = 0.958(3) \text{ \AA}^{-3}$, serves as the reference point for 100 % mineral content. This value is used instead of the mineral peak of the HAP particle which does not provide a sufficiently reliable reference point: As the particle shows an unexpectedly porous structure, the mass density even in areas that seem to be solid mineral may not reach the value given for HAP in the literature. This could be one reason for the discrepancy between calculated and measured HAP electron density. The porous structure might also be responsible for the rather broad distribution of mineral densities that is reconstructed.

⁴As mentioned earlier, the mineral in bone is actually mostly carbonated hydroxyapatite. However, calculations with the same mass density but a chemical composition $\text{Ca}_{9.75}[(\text{PO}_4)_{5.5}(\text{CO}_3)_{0.5}](\text{OH})_2$ gave (for the four significant digits used here) the same results for δ and n_e as for pure hydroxyapatite. Therefore, the discussion here is limited to the latter.

With these reference points, the mineral volume fraction is calibrated based on the assumption that the electron density n_e measured for a given voxel can be expressed as the weighted sum

$$n_e = \xi \cdot n_{e,\text{HAP}} + (1 - \xi) \cdot n_{e,\text{O}_1} , \quad (10.1)$$

where $\xi = V_{\text{HAP}}/V_{\text{bone}}$ is the volume fraction of hydroxyapatite within the bone. Solving for ξ yields

$$\xi = \frac{V_{\text{HAP}}}{V_{\text{bone}}} = \frac{n_e - n_{e,\text{O}_1}}{n_{e,\text{HAP}} - n_{e,\text{O}_1}} = 1.8940 \text{ \AA}^3 \cdot n_e - 0.814 , \quad (10.2)$$

where the uncertainty

$$\sigma_\xi = \sqrt{0.0014 \text{ \AA}^6 \cdot n_e^2 - 0.0026 \text{ \AA}^3 \cdot n_e + 0.0016} \quad (10.3)$$

of this value is calculated via propagation of uncertainties using the values listed in Table 10.2. As the main interest is the conversion of the values of the bone matrix, all relations for uncertainties presented here use the assumption $\sigma_{n_e} = \sigma_{n_{e,\text{air}}} = \sigma_{n_{e,\text{O}_1}}$. Equation (10.2) has been used to convert the measured electron densities n_e in Fig. 10.7 and Table 10.2 to mineral volume fractions.

Together with the mass densities $\rho_{m,\text{HAP}} = 3.16(1) \text{ g cm}^{-3}$ for hydroxyapatite and $\rho_{m,\text{coll}} = 1.35(5) \text{ g cm}^{-3}$ for collagen, which is the main constituent of unmineralized bone matrix, the volume fraction (10.2) allows to calculate the average mass density in a voxel from its electron density value n_e :

$$\rho_m = \xi \cdot \rho_{m,\text{HAP}} + (1 - \xi) \cdot \rho_{m,\text{coll}} , \quad (10.4)$$

which, using (10.2), can be rewritten into

$$\rho_m = (3.428 \text{ \AA}^3 \cdot n_e - 0.123) \text{ g cm}^{-3} . \quad (10.5)$$

Propagation of uncertainties yields with (10.2) and (10.3)

$$\sigma_{\rho_m} = \sqrt{0.0139 \text{ \AA}^6 \cdot n_e^2 - 0.0259 \text{ \AA}^3 \cdot n_e + 0.0134} \text{ g cm}^{-3} , \quad (10.6)$$

with ξ defined by (10.2) and σ_ξ by (10.3). Equation (10.5) shows some deviation from the general relation between mass density and electron density in (9.6) on page 256. However, the actual value used for the mass density of collagen strongly influences this relation. If, e.g., a density of 1.4 g cm^{-3} instead of 1.35 g cm^{-3} is chosen, (10.5) becomes

$$\rho_m = (3.333 \text{ \AA}^3 \cdot n_e - 0.083) \text{ g cm}^{-3} , \quad (10.7)$$

which more closely resembles (9.6). However, this larger mass density would also result in a higher electron density value for collagen and thus a larger deviation from the O₁-peak. To retain the latter as the lower reference of the volume fraction scale, (10.5) is used by default.

Relation (10.4) can also be employed to calculate the mass m_0 of a specific voxel (volume V_0) from its electron density value n_e , which determines the volume fraction ξ via (10.2):

$$m_0 = m_{\text{HAP}} + m_{\text{coll}} = \xi V_0 \cdot \rho_{m,\text{HAP}} + (1 - \xi) V_0 \cdot \rho_{m,\text{coll}} . \quad (10.8)$$

The mass fraction of hydroxyapatite is then obtained as

$$\begin{aligned} \frac{m_{\text{HAP}}}{m_0} &= \frac{\xi \cdot \rho_{m,\text{HAP}}}{\xi \cdot \rho_{m,\text{HAP}} + (1 - \xi) \cdot \rho_{m,\text{coll}}} \\ &= \frac{1.7459 \text{ \AA}^3 \cdot n_e - 0.7507}{1 \text{ \AA}^3 \cdot n_e - 0.0362} , \end{aligned} \quad (10.9)$$

with an uncertainty (if n_e is given in units of \AA^{-3})

$$\sigma_{m_{\text{HAP}}/m_0} = \frac{\sqrt{0.3235 \cdot n_e^4 - 0.8982 \cdot n_e^3 + 0.9154 \cdot n_e^2 - 0.4167 \cdot n_e + 0.0833}}{(3.4280 \cdot n_e - 0.1241)^2} . \quad (10.10)$$

The mass fraction of collagen can be calculated with $\frac{m_{\text{coll}}}{m_0} = 1 - \frac{m_{\text{HAP}}}{m_0}$. Based on the chemical composition of hydroxyapatite and the atomic weights of its constituents, one finds that calcium accounts for about 39.9% of the mass of hydroxyapatite. The mass fraction of calcium in bone can thus be calculated using

$$\frac{m_{\text{Ca}}}{m_0} = 0.399 \cdot \frac{m_{\text{HAP}}}{m_0} , \quad (10.11)$$

while the uncertainty is

$$\sigma_{m_{\text{Ca}}/m_0} = 0.399 \cdot \sigma_{m_{\text{HAP}}/m_0} . \quad (10.12)$$

The relations between the mass fractions in (10.9) and (10.11), the electron density, and the mineral volume fraction are visualized in Fig. 10.8.

Comparison to values reported in the literature Relation (10.11) is of particular importance as it allows to convert an electron density obtained by PXCT to a calcium weight percentage value (wt% Ca). The latter is the quantity determined with quantitative backscattered electron (qBSE) imaging (BLOEBAUM ET AL., 1997; ROSCHGER ET AL., 1998), which can thus be used to study bone mineralization changes on the subcellular scale. For ovine

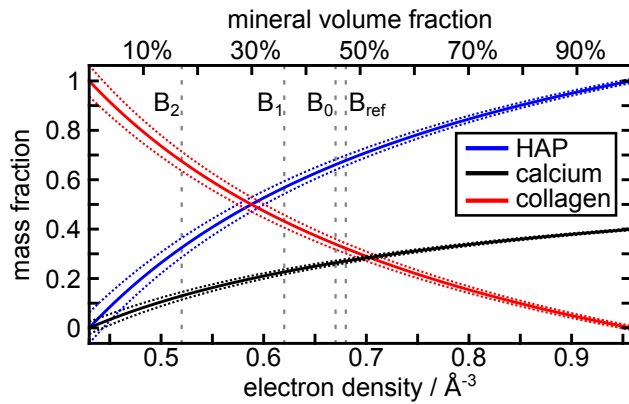


Figure 10.8: Conversion of mineral volume fractions or electron density values to mass fractions – calculated with (10.9) and (10.11) – of hydroxyapatite (blue), calcium (black), and collagen (red). The vertical lines mark the bone peak positions of the blue and the black curve in Fig. 10.7. The dotted curves give the uncertainties of the mass fractions, see (10.10) and (10.12).

bone, to the best of the author’s knowledge, so far no wt% Ca reference value measured by qBSE has been reported. In contrast, human bone has been studied frequently (compare e.g. ROSCHGER ET AL., 2008). The chemical composition of the mineral in ovine and human bone is basically identical (RAVAGLIOLI ET AL., 1996) and sheep are thus considered a valuable animal model in bone research (PEARCE ET AL., 2007). However, PEARCE ET AL. (2007) also point out significant differences in the respective mass densities and in total mineral content. The fact that the reference peak value of 22.94(39) wt% Ca used in human bone studies (ROSCHGER ET AL., 2008) is significantly lower than the 27(1) wt% Ca calculated for the untreated bone volume (see Table 10.2) may therefore just be an effect of inter-species variability. In order to allow for a reliable comparison of the actual numerical values, it would be ideal to perform PXCT and qBSE measurements on the same specimen. Furthermore, the accuracy of the calibration for the conversion of electron densities to maps of calcium content can still be improved by imaging well-defined standards. Nevertheless, PXCT can clearly provide the same information as qBSE in terms of bone mineralization, however in three dimensions and without the need for sample preparation compatible with electron microscopy requirements.

While qBSE has only been established during the last two decades, the older approach to determine calcium contents relies on analysing the composition of ashed bone, for which in the case of ovine bone MORENO AND FORRIOL (2002) report a value of 25(10) wt% Ca (for 21 specimens studied). The high standard deviation, however, indicates that very strong variations in calcium content occur also for individuals of the same species, even if they are of similar age. The 27(1) wt% Ca calculated from the retrieved electron density are thus considered a valid result. This is further supported by comparing the total mineral content m_{HAP}/m_0 obtained by PXCT to values

determined from bone ashes: SKEDROS ET AL. (1997), e.g., report a range of 67.5% to 73% for ovine bone, which includes the 68(1)% measured for the untreated reference bone volume.

10.2 Visualization of collagen fibril patterns

10.2.1 Motivation: structure-function relationships in bone

WEINER AND WAGNER (1998) classify the organization of the fibril arrays into various patterns as the fourth hierarchical level of bone, compare Table 10.1. They point out that while the structures of levels 1 to 3 show only little variations in different types of bone, striking differences in the arrangement of the fibril bundles appear to reflect the function of the respective bone. WEINER AND WAGNER (1998) illustrate this by a discussion of the four most common fibril array pattern types:

Arrays of parallel fibrils In this case, the mineralized fibrils are oriented parallel on the micron up to the millimetre scale. This can be found for instance in mineralized tendons (like e.g. in turkey legs) and in parallel-fibred bone, in which the fibres are usually parallel to the long axis of the bones, a structure characteristic for bovids. The anisotropy of such bones corresponds to a optimization of the elastic properties along a specific direction, i.e. the elastic modulus parallel to the aligned fibrils is typically around a factor of two higher than perpendicular to them (compare WEINER AND WAGNER, 1998, page 285).

Woven fibre structures Woven bone is constructed of fibril bundles of various sizes which are arranged in an unordered way and thus do not show a preferential orientation. Furthermore, this type of bone has an unusually high content of non-collagenous material. Woven bone can be found, e.g., in the skeletons of amphibia, reptiles and mammalian embryos. As it can be formed very rapidly, it is also the first type of bone formed after fractures and is only later replaced with the usual ordered structures, a process also observed during the development of embryos.

Plywood-like structures The name of this fibril array pattern type is derived from its resemblance to plywood or other types of laminated composites: It consists of stacked discrete layers of parallel fibrils, whose preferential orientation is different in adjacent layers. Several variants

of this structure, in which the angle between preferential orientations changes in different ways, have been described by BOULIGAND (1972) and GIRAUD-GUILLE (1988, 1994). In the simplest case, one finds orthogonal fibril orientations in alternating layers, which is e.g. typical for some fish scales. In contrast, lamellar bone – the most common type of bone in humans – is characterized by a more complex organization of the collagen fibril layers: *Lamellae* in general refer to planar sheets of mineralized collagen fibrils with a thickness of 3 to 7 μm (RHO ET AL., 1998). The most common occurrence is in secondary osteons (level 5 in Table 10.1), in which the lamellae form concentric layers around a central (Harvesian) channel (see also the schematic sketch in Fig. 10.9). This structure is a result of bone remodelling, during which osteoclasts remove bone and create circular tunnels which are then refilled by osteoblasts with new material in concentric layers starting from the outer edge till only a central channel containing the blood supply is left. The lamellae are thus reflecting the formation processes of osteons in a fashion similar to growth rings in trees.

Collagen fibril orientations inside and between these lamellae are still under investigation: Bright-dark contrast changes in polarized light microscopy reveal that the orientation is different for adjacent osteonal lamellae. GIRAUD-GUILLE (1988) interprets the typical patterns observed this way as a result of either orthogonal or twisted plywood. In the latter case, the bright-dark contrast in polarized light is still due to fibrils being orthogonal. However, their preferential orientation is not changing abruptly at the boundary of lamellae like in orthogonal plywood, but rather goes through several intermediate angles inside the lamellae themselves.

WEINER AND WAGNER (1998) point out that the mechanical properties of such a twisted – or rotated – plywood structure “may reflect the requirement for lamellar bone to withstand compressive forces in many directions” as this structure makes the material “more isotropic than the building block from which it is constructed”. Furthermore, this arrangement is believed to be beneficial in terms of protection of the blood vessels inside the Harvesian channels (WAGERMAIER ET AL., 2006) and more resistant to fractures (WEINER AND WAGNER, 1998).

Radial fibril arrays The inner part of teeth consists of dentin through which channels called tubules run. The latter are the tracks which odontoblastic cells form during dentin formation between the pulp chamber and the dentin-enamel junction (MARSHALL ET AL., 1997).

Tubule density and diameters are smaller at the larger dentin-enamel interface (about 1 % of area, tubule diameters about 0.8 μm) and higher (22 % of area, about 2.5 μm diameter) at the junction to the pulp chamber (MARSHALL ET AL., 1997). The collagen fibrils in dentin are arranged in planes roughly perpendicular to the tubules' long axis, i.e. they lie in planes “parallel to the surface at which dentin formation takes place in the pulp cavity” (WEINER AND WAGNER, 1998). Within these planes, however, the fibrils show no preferential orientations but rather surround the tubules in a tangential fashion. WEINER AND WAGNER (1998) thus conclude that “dentin is structured to withstand compressive forces in one prevailing direction”.

As the arrangement of fibril bundles yields information about mechanical properties of bone (WEINER AND WAGNER, 1998), various techniques are being employed to study it: Electron microscopy allows direct visualization of the fibrils at high resolution. Some illustrative examples can be found in the articles by BOULIGAND (1972) and GIRAUD-GUILLE (1988, 1994), who however also point out that due to the limitation to essentially two-dimensional samples (surfaces), misinterpretations of fibril array patterns may easily occur. This problem is circumvented in serial sectioning FIB-SEM recently employed for this type of studies (REZNIKOV ET AL., 2013, 2014), which allows to investigate volumes in the order of $10\ \mu\text{m} \times 10\ \mu\text{m} \times 10\ \mu\text{m}$ at a resolution of about 10 nm (compare also the more detailed discussion of FIB-SEM on page 267). In case larger volumes are to be investigated or one does not want to be restricted to specimens prepared in a vacuum-compatible way, X-ray techniques with their high penetration power can offer an alternative. Many studies of the orientation of the mineralized collagen fibrils employ scanning small-angle X-ray scattering (SAXS), in which the preferential orientation within the specimen volume illuminated by a focused X-ray beam is determined from the anisotropy of the recorded diffraction pattern (RINERTHALER ET AL., 1999). However, most of these experiments are done on thin bone slices (see e.g. WAGERMAIER ET AL., 2006) and thus provide essentially two-dimensional information. Tomographic reconstructions from scanning SAXS data, however, rely on the assumptions that the scattering from each volume element is either symmetric (fibre symmetry, see SCHROER ET AL., 2006; STRIBECK ET AL., 2008), or isotropic (JENSEN ET AL., 2011). Furthermore, the beam size and thus the spatial resolution in scanning SAXS is typically several microns or even tens of microns and thus too coarse to resolve e.g. the internal fibril orientations within individual bone lamellae.

Direct imaging of collagen fibrils in three dimensions requires a high-resolution tomography technique which very high sensitivity. Only recently,

LANGER ET AL. (2012) obtained reconstructions of a bone specimen with synchrotron phase-contrast nanotomography based on holotomography in a cone-beam geometry from which VARGA ET AL. (2013) extracted orientations of collagen fibril patterns.

Based on the features of ptychographic X-ray nanotomography discussed on page 288 in section 10.1.1, the **two major objectives** of the study presented in the following sections are:

1. To demonstrate that also ptychographic X-ray nanotomography provides the necessary spatial resolution and contrast to image collagen fibrils in real space.
2. To investigate the feasibility of determining the fibrils' preferential orientations from the obtained data.

10.2.2 Data set

The data set used for this study is the reference bone volume already presented in section 10.1. The corresponding tomographic scan was performed about 400 μm below the tip of the specimen in a region where the bone should be unaffected by the NaCl solution which had been used to dissolve the mineral in the top part. Each projection of the scan covered a field of view of 70 μm \times 28 μm (horizontal \times vertical). More details on sample preparation can be found in section 10.1.2, and a description of the experiment in section 10.1.3. The volume was reconstructed following the first four steps in section 10.1.4. A first discussion of the results can be found in section 10.1.5.2. This reconstruction serves as the basis for all further analysis presented in this section.

10.2.3 Extraction of collagen fibril orientations

A sequence of several processing steps was employed on the volume obtained by PXCT to identify collagen fibril arrays and their arrangement. Exemplary visualizations are shown in Fig. 10.10. The labels of the panels in Fig. 10.10 correspond to the individual steps of the workflow:

- (a) The long axis of the specimen's rectangular cross section in the transverse plane (see Fig. 10.4(a)) is presumed to point approximately along the radial direction of an osteon (see sketch in Fig. 10.9). Changes of fibril array orientations are thus most apparent when investigating longitudinal slices taken in a plane roughly perpendicular to the bone's growth direction, i.e. both parallel to the horizontal axis in Fig. 10.4(a)

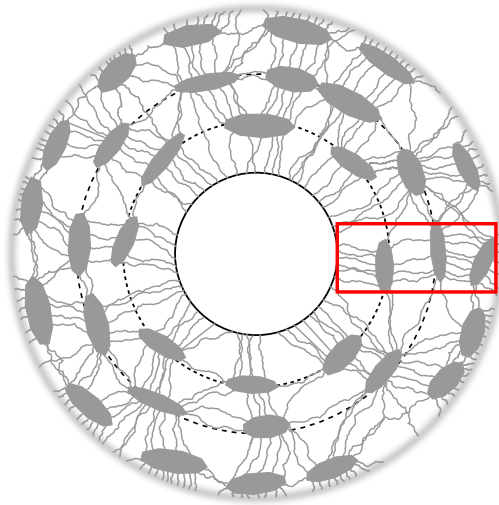


Figure 10.9: Schematic cross-sectional view of a secondary osteon. The lacuno-canalicular network is sketched in grey (for actual images of the LCN in osteons, compare e.g. [KERSCHNITZKI ET AL., 2011](#)) and reflects the concentric growth of the lamellar structure. In bone, the central hole – the Haversian channel – contains the blood supply. The red rectangular frame marks the presumed location of the specimen, represented by its cross section in the transverse (axial) plane (compare [Fig. 10.4\(a\)](#)), within such an osteonal structure. As depicted here, the long axis of the cross section is thus presumed to point approximately along the radial (growth) direction of an osteon.

and the rotation axis. On the usual colour-scale covering an electron density range from 0 \AA^{-3} to 0.8 \AA^{-3} , the fibril arrays manifest as slightly darker stripes in the bone matrix, which can also be identified in line-outs as shown in the inset in [Fig. 10.10\(a\)](#). In particular when played as a movie, already these unprocessed slices allow a human observer to identify changes in the fibril array patterns.

- (b) Restricting the colour-scale to only a small range around the electron density values associated with the fibril structures can greatly improve the latter's visibility in the slice images. In the case of [Fig. 10.10\(b\)](#), e.g., the colour-scale covers only a range from 0.5 \AA^{-3} to 0.72 \AA^{-3} .
- (c) For further processing, a binary representation of the fibril array structures was created: in the masks, all those pixels are set to unity which exhibit electron densities between 0.64 \AA^{-3} and 0.67 \AA^{-3} in the original slices.
- (d) In order to determine the local preferential orientation of the collagen patterns, a Fourier-based analysis was employed. The approach bears a resemblance to scanning SAXS, which is an important tool in the study of collagen arrangements in bone ([RINNERHALER ET AL., 1999](#)): In scanning SAXS, the preferential orientation in a far-field diffraction pattern is used to identify local ordering in the respective area of the specimen illuminated by a localized X-ray beam. Based on this idea, the following steps were used:

- 1) Each binary image was subdivided into small regions-of-interest (ROIs) of 32×32 pixels.
 - 2) The Fourier transform of each ROI was calculated after zero-padding it to a size of 128×128 pixels.
 - 3) The respective Fourier image was divided into 16 wedge-shaped angular segments each covering an angular range of $\pi/8$ rad (25°) and a radius > 1 pixel and < 64 pixel.
 - 4) As preferential orientation of the given Fourier pattern, the mean angle of the segment for which the summed-up pixel values were maximal was assigned. This direction is perpendicular to the dominant fibril direction in the underlying structure.
- (e) The orientation information obtained in the previous step was visualized as a field of indicators for each of the slices. The direction of each indicator was set to point along the dominant fibril direction and its length to reflect the magnitude of the summed-up pixel values in the corresponding angular segment.
- (f) Superimposing the indicators on the respective slice illustrates the preferential orientations of the underlying fibril array structures. The obtained results were found to provide objective evidence for the orientation changes a human observer can identify when examining a movie of the slices.

To verify the presumption in (a) that the selected slices are roughly perpendicular to the bone growth direction, the same analysis has also been applied to the slices of the perpendicular longitudinal direction. As expected, the fibrils have been found to be aligned along the longitudinal direction, i.e. parallel to the rotation axis. A slice-by-slice investigation is thus sufficient and it is not necessary to extend the Fourier analysis to determine the preferential orientation of the three dimensional Fourier transform of a cubic volume, as it is in principle possible. Furthermore, this restriction to quadratic regions allows to determine the orientation in each slice along the growth direction, while using cubic volumes would reduce the resolution along this axis.

In addition to the procedure described here, other approaches for extracting the orientation of the collagen fibrils have been explored: Anisotropic filtering to detect preferential directions of features (GEUSEBROEK ET AL., 2003) was applied both to the data in real space and its Fourier transform. Detecting preferential orientations in the autocorrelation of slices, as recently used by VARGA ET AL. (2013) for exactly the same purpose of identifying collagen fibril orientations, was also tested. However, none of them yielded

results which correlated well enough with the preferential directions a human observer can identify in an animated sequence of slices. Furthermore, while VARGA ET AL. (2013) limited their analysis to volumes without canaliculi or even lacunae inside, thresholding and binarization of the fibril signal allows to overcome this restriction.

10.2.4 Results and discussion

The result of the analysis procedure described in section 10.2.3 is shown in Fig. 10.11. The obtained preferential orientations of the collagen fibrils in the respective region-of-interests of 32×32 pixels are depicted as blue indicators overlaid at the corresponding positions of the slice images. The exemplary 64 slices depicted in Fig. 10.11 are equally spaced by 12 pixels or $0.78 \mu\text{m}$ along the long axis of the specimen's cross section. Several observations can be made:

1. Volumes with and without lacunae are alternating as expected along the radial direction of a secondary osteon (compare Fig. 10.9). Lacunae are cut by slices 01–08, 16–21, 26–36 (up to three lacunae), and 49–52.
2. Of the volumes between the lacunae, slices 09–16 and 53–60 are dominated by one or two relatively large regions of aligned fibrils, which cover up to one third of the total bone area. In terms of electron densities, these regions show a distinct dark grey colouring which also allows to trace the respective orientation.
3. In the third interlacunar space, i.e. in slices 37–48, the signal from the fibrils seems to be weaker and thus they appear in a lighter grey than the ones discussed in 2. Compared to these, the bone slices are also divided into more and smaller areas of aligned collagen. Altogether, alignment along the vertical axis seems to be the most frequent orientation in this subvolume.
4. In between the second and the third lacunar volume, i.e. in slices 21–26, the slices are dominated by canaliculi and the bone matrix shows very little ordering. To some extent, this is also true for the third lacunar volume (slices 27–34). However, also rather extended areas of aligned fibrils are observed in the presence of lacunae for instance in slices 01–08, so the decrease in alignment does not seem to be a general feature.
5. In general, when slices have small sub-regions with a high density of canaliculi, the degree of alignment detected for these areas is typically

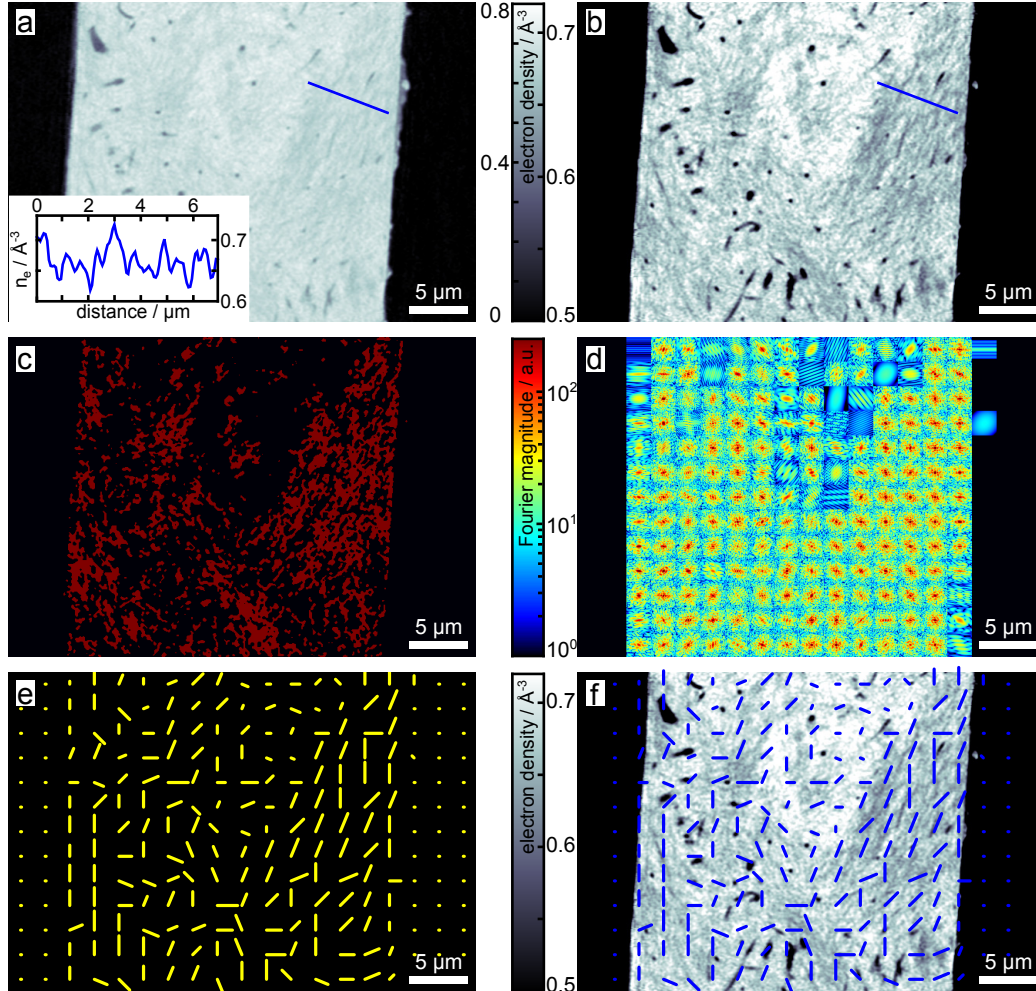


Figure 10.10: Analysis procedure employed to visualize the orientations of collagen fibril arrays. (a) Longitudinal slice taken in a plane roughly perpendicular to the bone's growth direction. Collagen fibril structures manifest as darker regions in the electron density (linear grey-scale, see colour-bar) of the bone matrix. The profile (see inset) taken along the blue line illustrates the density changes observed when crossing fibril bundles. (b) The same slice displayed on a colour-scale spanning only 0.5 to 0.72\AA^{-3} in order to increase the contrast of the collagen structures. (c) Binary representation obtained by setting all pixels with values between 0.64 and 0.67\AA^{-3} to unity (red) and all other pixels to zero (black). (d) Local Fourier magnitudes calculated for areas of 32×32 pixels of the binary image. (e) Field of indicators representing the preferential orientations deduced from the Fourier magnitudes. (f) Superimposing the indicators on the electron density map provides impartial evidence for the orientation of the underlying fibril array structures.

rather low, which manifests as very short and randomly oriented indicators. In these cases, however, the applied analysis might just be too insensitive to detect a preferred orientation even if one exists.

6. As discussed before, orientation analysis in the perpendicular slices suggested that the fibrils are aligned parallel to the rotation axis and thus the fibrils should lie in the planes of the slices in Fig. 10.11. However, some of the fibril patterns show a curved appearance, e.g. at the bottom of slice 13. According to BOULIGAND (1972) and GIRAUD-GUILLE (1988, 1994), only straight features should be observed in the fibril planes and they interpret such curvatures as an effect of inclined slices through a twisted plywood structure.
7. The most notable observation is the change of fibril orientations between close-by slices (in what follows, the preferential orientation of the fibrils is encoded as clock positions, where 12 o'clock corresponds to the vertical axis): On the right edge of slices 09–12, a change of about 90° from 1 o'clock to 4 o'clock occurs by passing through some intermediate orientations visible in slices 10 and 11. In slices 13–16, the orientation in the lower central area progresses from 9 o'clock to 12 o'clock. And in 57–60, again a transition of the dark collagen fibrils direction from 1 o'clock to 4 o'clock can be seen. In all three cases, the preferential orientations exhibit a clockwise rotation and the slices with orthogonal orientations are separated by 2.34 μm.

If one compares these results with the serial-sectioning electron microscopy work by REZNIKOV ET AL. (2013), parallels can be found to the three structural motifs which they identified in a lamella of a rat femur: Their “unidirectional sub-lamella”, in which “the preferred fibril orientation remains nearly constant” can be linked to observation 3 of a mostly vertical alignment in the third interlacunar volume. Observation 4, on the other hand, closely resembles what they call “disordered sub-lamella”, i.e. a volume in which “little or no preferred orientation can be seen”. Finally, “fanning sub-lamella” with “gradually changing preferred direction” is the same structure as described in observation 7, better known as *rotated* or *twisted plywood* (a description of “plywood structures” can be found on page 306, in WEINER AND WAGNER, 1998, or in the original articles by BOULIGAND, 1972 and GIRAUD-GUILLE, 1988, 1994).

Also VARGA ET AL. (2013) report volumes of little anisotropy (compare observation 4) and of twisted plywood (observation 7). For the latter they found both clockwise and counter-clockwise rotations with a rate of $24.6 \pm 2.6^\circ$ per μm, which corresponds to about 3.66 μm for a 90° rotation.

Furthermore, they identified regions of so-called “oscillating plywood” in which the preferential orientation of the fibrils oscillates sinusoidally around the vertical axis by about $\pm 15^\circ$ in one area and $\pm 33^\circ$ in another. However, some of these zones featured an “irregular oscillating plywood pattern”. This fits well with the observation **3** of a preferential overall alignment without obvious twisting.

10.3 Outlook: flat bone samples

10.3.1 Motivation

In previous PXCT applications, mainly cylindrical or rectangular rod like samples with an extension of at maximum $80\ \mu\text{m}$ perpendicular to the axis of rotation – which thus could be covered within the field-of-view of the projections – where imaged. This kind of sample preparation is beneficial for the necessary post-processing steps of the reconstructed projections. In particular, the alignment of projections required to correct for drifts or inaccuracies of the rotation stage is more robust if the projections have regions of air on both sides. However, the preparation of such free-standing specimens of just a few tens of microns in diameter typically is quite challenging, e.g. requiring focused ion beam milling, and not feasible for all classes of samples. Additionally, many specimens, like semiconductor elements or cells growing on flat substrates, already come in thin but laterally extended form. Also for other applications, e.g. for investigating bone specimens, having to thin down in just one dimension greatly facilitates preparation procedures.

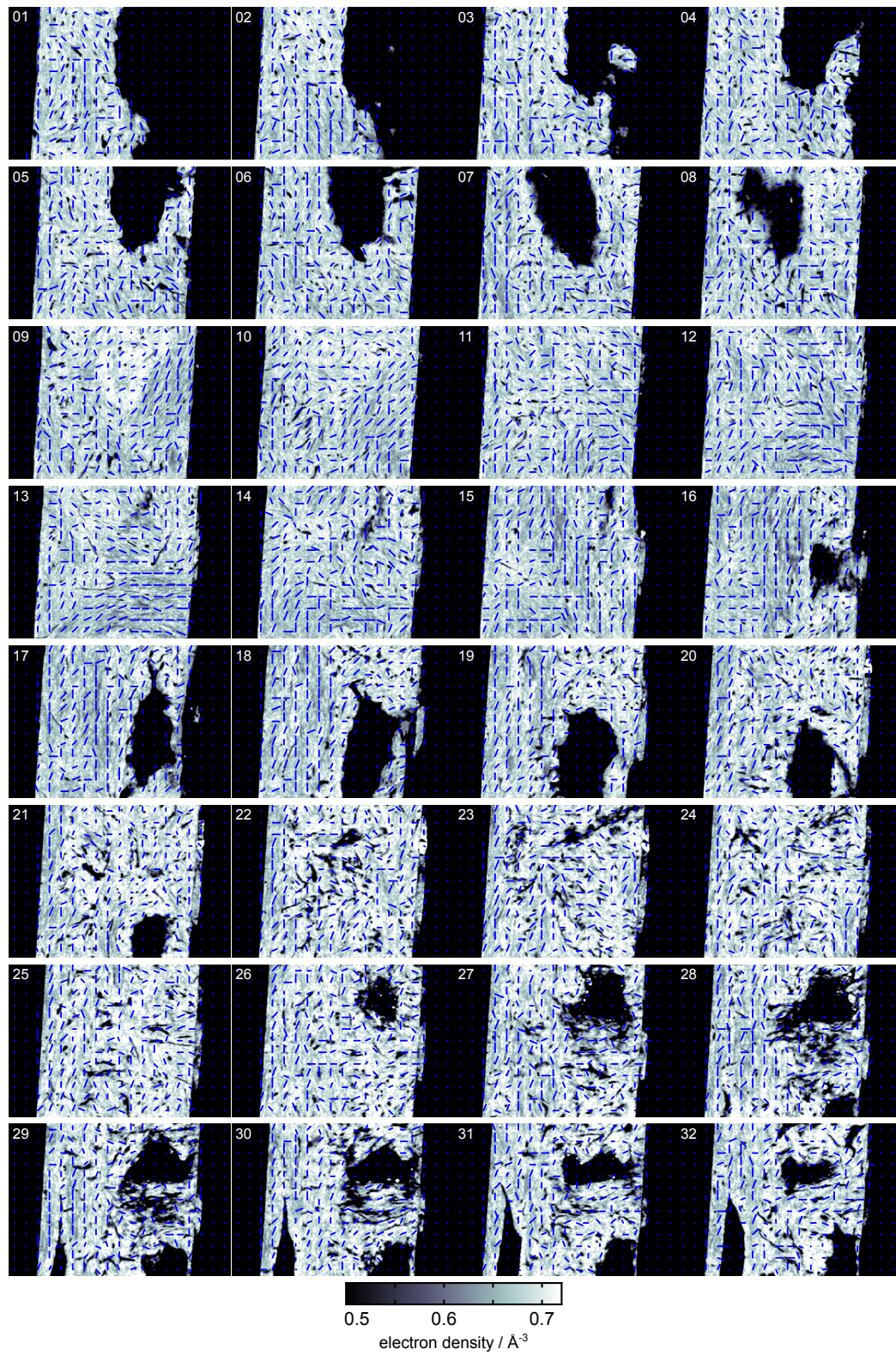
The test specimens for this methodological development were thin slices (thickness varying between $10\ \mu\text{m}$ to $50\ \mu\text{m}$) of ovine bone obtained by mechanical polishing.

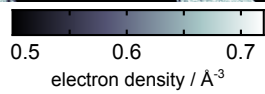
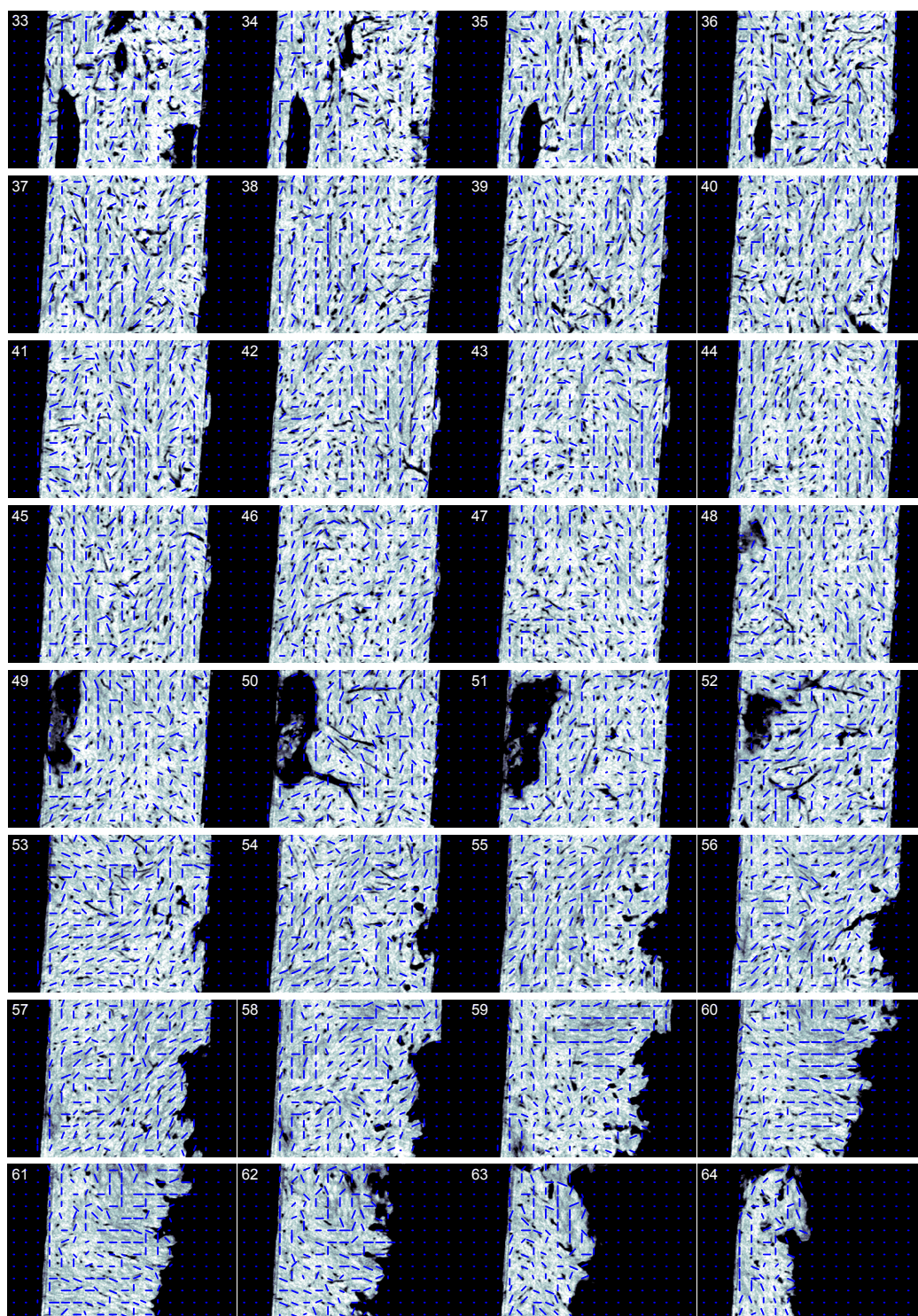
10.3.2 Experiment

Experiments were performed end of February 2011. Using the excess in transverse vertical coherence length, the incident X-ray beam (6.2 keV photon energy) was slightly focused with the beamline optics onto a pinhole with around $2.5\ \mu\text{m}$ diameter which defined the illumination on the specimen. Compared to the first demonstration experiment ([DIEROLF ET AL., 2010a](#)), the prefocusing allowed to reduce counting times by a factor of ten, resulting in an increase in acquisition speed and better counting statistics. Therefore, not only larger and more volumes could be scanned, but in particular the number of projections per tilt series could be doubled, resulting in improved quality of the tomographic reconstructions.

The sample was scanned in the plane perpendicular to the incoming beam with a three-axis piezo-driven nano-positioning system, which was placed on top of an air-bearing rotation stage. The scan points were located on concentric circles cropped in the outer regions to form rectangular scan fields. Each such ptychographic scan corresponds to one projection, while for a full tomographic scan of a free-standing rod typically an angular range of 180° would be covered with an angular step of 0.5° (361 projections total). In case of the

Figure 10.11 (following page): Visualization of collagen fibril array orientations in the reference bone sample. Depicted are 64 slices through the electron density in the plane both parallel to the rotation axis and to the small axis (corresponding to the horizontal axis in Fig. 10.4(a)) of the sample's cross section. The spacing between the slices is 12 pixels or 0.78 μm along the long axis of the specimen's cross section. The linear grey scale is restricted to a range between 0.5 \AA^{-3} to 0.72 \AA^{-3} (see colour-bars) to improve visibility of the collagen fibril arrays (compare also Fig. 10.10(b)). The overlaid blue indicators provide the preferential orientation of the fibrils in the underlying 32×32 pixels as obtained by the analysis procedure described in section 10.2.3. See main text for a discussion of the results.





flat samples, however, the exposure times had to be adapted according to the increase of the projected thickness. This limited the accessible angular range to $\pm 70^\circ$ which was again covered in 0.5° steps. Typically, two consecutive interlaced scans were done for stability reasons, each with an angular step of 1° and an offset of 0.5° between them. A typical such limited-angle tomographic data set covering a field of view of $65\ \mu\text{m} \times 28\ \mu\text{m}$ (637 scan points) took about 20 hours, with exposure times per point ranging between 0.1 s at normal incidence and 0.9 s at $\pm 70^\circ$. Data acquisition turned out to be very stable throughout all tomography scans. An overhead of about 0.1 s per scan point was observed whose reduction could further shorten total acquisition times.

10.3.3 Reconstruction results

Ptychographic reconstructions were already done right after the respective diffraction patterns of a projection. Typically, the central 128×128 pixels of the diffraction patterns contain data of sufficient quality, which for the employed experimental geometry leads to a pixel size of $65\ \text{nm} \times 65\ \text{nm}$ in the reconstructed projections. Some exemplary reconstructions are shown in Fig. 10.12. The 140° -scans require different approaches for the alignment of projections. Particularly at deviations from normal incidence larger than 60° , the preliminary new alignment routines did not yet provide sufficient reliability. Therefore, no high-resolution tomographic reconstructions have been obtained from these data sets. Further tests and improvements of the algorithms for alignment as well as for the tomographic reconstruction problem with a range of missing angles are in progress.

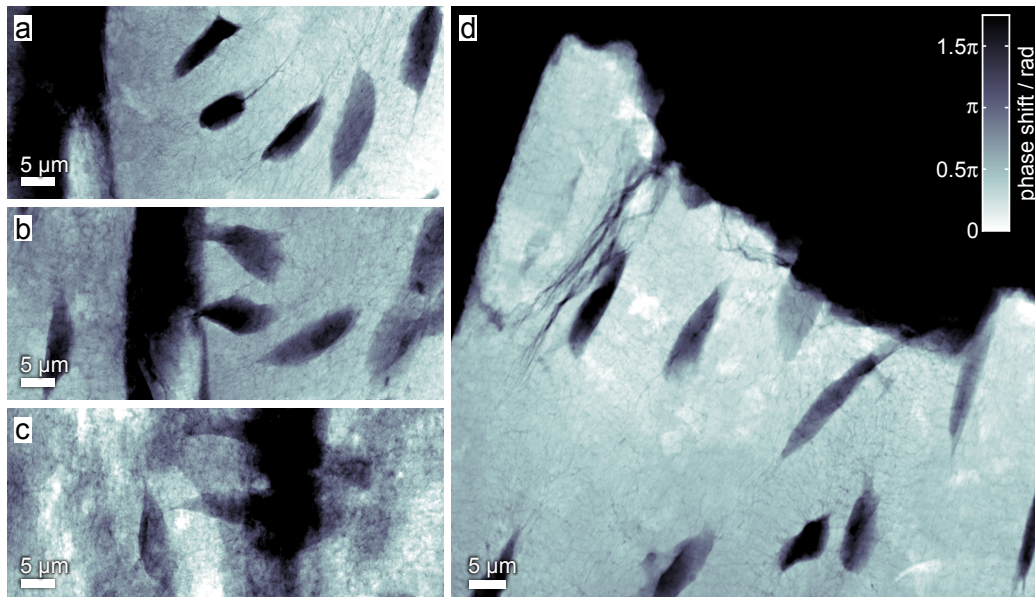


Figure 10.12: Ptychographically reconstructed phase-contrast projection images of regions on a slice of bone. For better visibility of the interior structures, the colour-scale in all images has been limited to the interval $[0, 1.75\pi]$ rad, whereas the maximum phase shift at normal incidence is about 5π rad. **(a)–(c)** The three images are part of one of the limited-angle tomographic scans and show the same region of the specimen for projection angles (relative to surface normal) of **(a)** 0° , **(b)** -35° and **(c)** -70° . The latter is the maximum tilt angle used. Not only the lacunae are visible as dark voids in these projection images, but also the small channels of the connecting canalicular network. The large dark stripe running from top to bottom is part of a blood vessel. **(d)** Result of a larger overview scan at normal incidence. It demonstrates the benefits of being able to work with flat, extended specimens: Interesting structures within a larger slice can be identified in medium or high resolution overview scans within short time and then further investigated with a tomographic scan. In contrast, in the case of the preparation of a free-standing rod-like specimen the regions of interest have to be identified beforehand.

Part IV

Conclusions and Outlook

Chapter 11

Conclusions

In the final session of the “International Workshop on Phase Retrieval and Coherent Scattering” (COHERENCE 2010) held in June 2010 in Rostock-Warnemünde, Janos Kirz, one of the pioneers of X-ray microscopy both with (KIRZ ET AL., 1990) and without lenses (MIAO ET AL., 1999), gave some concluding remarks on the status of CDI based on what had been presented during the days before. He pointed out that CDI in general yet had to live up to the great expectations which were raised in terms of providing a higher-resolution alternative to standard X-ray microscopy. He concluded that CDI was still not a user technique and would have to move away from “logo science” – the imaging of artificial test objects – and towards real applications to prove itself a truly useful X-ray microscopy technique.

About five years later, ptychographic coherent diffractive imaging has been successfully making the transition from pure methodological test experiments to application-driven studies, in which actual scientific questions concerning the imaged specimens are addressed. Many of the developments presented in this thesis have been playing an important role in this process:

The crucial prerequisite for all further contributions was our group’s successful demonstration of ptychography with simultaneous probe retrieval for data recorded with an X-ray scanning set-up (THIBAUT ET AL., 2008). In his perspectives introducing this article, CHAPMAN (2008) concluded that this approach “[...] should be implemented at every STXM at synchrotrons worldwide”. The importance of this development is also reflected by the fact that THIBAUT ET AL. (2008) is currently the most-cited article in the field of X-ray ptychography (with 340 citations¹, followed by RODENBURG ET AL. (2007b) with 256 citations, and DIEROLF ET AL. (2010a) with 180 citations). Chapter 3 has been largely dedicated to the discussion of this reconstruction

¹Citation numbers as of March 2, 2015, based on Thomson Reuters Web of Science, <http://www.webofscience.com>.

algorithm. Furthermore, we have seen the possibility of incorporating various types of *a priori* knowledge or of adding additional maximum-likelihood refinement. Reminiscent of Kirz appeal of meeting expectations in particular in terms of claimed resolutions, we have reviewed existing resolution measures regarding their applicability to ptychographic reconstructions in section 3.3.

The experimental realization of ptychographic CDI has been discussed in chapter 5, with a strong emphasis on the set-up constructed at the cSAXS beamline of the Swiss Light Source. Based on the experiences made at different instruments, the concluding remarks in section 5.3 have identified various factors which have to be considered to perform a good ptychography experiment. This section of “lessons learned” has thus also emphasized the limiting aspects of current set-ups, which should be the focus of future efforts. As especially crucial among these, one can single out the issues related to detectors, stability, and scanning overhead, which are also at the heart of ongoing and future experimental developments, compare section 12.1 in the Outlook.

In part II we have seen three methodological advances for two-dimensional PCDI which pave the way towards improved spatial resolution and sensitivity (or density resolution): In chapter 6 we have discussed the challenges associated with the imaging of weakly-scattering specimens and have introduced ideas to overcome them. Their successful application to a measurement on magnetotactic bacteria has demonstrated the potential of PCDI as a quantitative, highly-sensitive phase-contrast X-ray microscopy technique. The results of this chapter were published in DIEROLF ET AL. (2010b), which also plays a role as the article in which the concentric scan pattern, the “round scan”, was first employed. This pattern has been adapted rather widely in the community, compare, e.g., HUANG ET AL. (2014), who compared a new pattern to “the presently used mesh and concentric patterns”.

In chapter 7 we have investigated methods to perform ptychographic reconstructions using shared data sets. By means of simulations and experimental demonstrations, we have identified several important applications of this approach: In one case, a common probe is used for the reconstruction of several data sets taken with off-set detector positions. This allows to overcome the problem of missing areas in the diffraction patterns due to the gaps of modern tiled detectors. Another important approach is sharing the probe with a flat object, which has been demonstrated to suppress the raster grid pathology and phase ramps. Finally, we have seen the self-aligning effect when sharing the same, but off-set object among multiple scans. This may be used to reduce the influence of long-term drifts, to approach stepwise the damage limit of radiation sensitive samples, or to stitch large fields-of-view, which has recently been applied by GUIZAR-SICAIROS ET AL. (2014).

From the results presented in chapter 8, we can draw the conclusion that PCDI is in principle possible with relaxed requirements on the bandwidth of the incident radiation. As the detector employed for the demonstration experiments had an extended point-spread function which degraded the reconstruction results, we have investigated different options to compensate this. In the outlook section of chapter 8, we have seen a first glimpse of the power of the recently developed mixed-state ptychography (THIBAUT AND MENZEL, 2013), whose application to broad-bandwidth data ENDERS ET AL. (2014) have recently discussed in detail.

Part III has focused on the combination of ptychography and computed tomography, PXCT. In chapter 9, the first successful demonstration of this new phase-contrast nanotomography technique has been described. A processing pipeline has been established which allows to obtain a fully-quantitative three-dimensional reconstruction of a specimen's electron density from ptychographic data sets collected at many projection angles. This procedure has served as the basis for more generic implementations in Python (DAURER, 2013) and in Matlab (GUIZAR-SICAIROS ET AL., 2011). The latter has been employed in many successful PXCT applications at the cSAXS beamline. In addition, chapter 9 has also featured a comparison of PXCT, which in the demonstration experiment was applied to a murine bone specimen, to other techniques for bone imaging. We have reached the conclusion that although PXCT provides the necessary spatial resolution to visualize the lacuno-canalicular network, one of the other techniques is often a better choice for this sort of studies. However, ptychographic nanotomography provides a unique combination of both high spatial resolution and high density sensitivity. This has given rise to the idea to use the technique for studying tiny differences in bone mineralization on a sub-cellular level.

Chapter 10 has thus been focused on demonstrating the general feasibility of such bone studies. We have seen that PXCT has successfully retrieved artificially-induced mineralization gradients in ovine bone. In addition, it has been shown that also the orientations of collagen fibril patterns can be determined. Beyond their immediate implications for future applications of PXCT in bone science, the two demonstrations also signify the transition from pure methodological developments to more application-driven studies.

Among other factors, the development of PXCT – and probably also the fact that the first demonstration on a bone specimen already directly highlighted potential applications – has played a major role in enabling the recent success story of ptychography. The technique gets implemented at more and more instruments worldwide, in particular at almost every new STXM beamline as requested by CHAPMAN (2008). Furthermore, the use of PCDI is no

longer limited to the small coherent imaging community, as the techniques are being integrated into the regular user operation of beamlines. All this has led to a remarkable number of ptychography-based studies: [TRTIK ET AL. \(2013\)](#), e.g., have investigated density differences in cement. In-situ experiments have been carried out on silk fibres ([ESMAEILI ET AL., 2013](#)), wool ([ESMAEILI ET AL., 2015](#)), and a material for CO₂-capture ([HØYDALSVIK ET AL., 2014](#)). Other materials science applications include imaging of carbon fibres ([DIAZ ET AL., 2014](#)), paint ([CHEN ET AL., 2013](#)), and catalysts ([DA SILVA ET AL., 2015](#)). A recent biomedical study was performed on hair cell stereocilia ([PIAZZA ET AL., 2014](#)), which are important sensors for hearing and balance.

Characterization of X-ray focusing optics has become another important application of PCDI. Because with the reduction of the sizes of focal spots, investigating them with classical methods, like knife-edges, becomes increasingly harder or even impossible. The possibility to use PCDI instead has already been pointed out by [THIBAULT ET AL. \(2008\)](#) in our first demonstration of ptychography with probe retrieval. This experiment can also be considered as the first iterative ptychographic reconstruction of the full wavefield produced by a Fresnel zone plate. Another example of FZP characterization, where the experiment was carried out specifically for the purpose of optics metrology, is the work by [VILA-COMAMALA ET AL. \(2011a\)](#). The approach has also been used with reflective optics ([KEWISH ET AL., 2010a,c](#)) and refractive optics ([SCHROPP ET AL., 2010](#)). Since these first demonstrations, PCDI has been developing into a regular characterization tool in the X-ray focusing optics community.

Chapter 12

Outlook

12.1 Experimental developments

In this section, an outlook is given on ongoing and projected experimental developments. Some also address some of the limitations of current experimental implementations of ptychography which have already been discussed in section 5.3.

The requirement for highest positioning accuracy and stability presented in section 5.3.4.3, for example, is addressed by the OMNY project at the Swiss Light Source: Based on differential interferometric encoding of the relative position of illumination-defining optics and sample, the system allows for either precise tracking in open-loop or accurate positioning in closed-loop operation. The potential for ptychography has been demonstrated impressively by a PXCT result with 16 nm isotropic resolution (HOLLER ET AL., 2014).

Novel X-ray detectors address many of the issues raised in section 5.3.2. One example is the EIGER detector (DINAPOLI ET AL., 2011; JOHNSON ET AL., 2014; RADICCI ET AL., 2012), the successor of the PILATUS detector. GUIZAR-SICAIROS ET AL. (2014) have employed the faster readout and smaller pixel size of this system for a demonstration of PCDI with a very large field-of-view, with an effective dwell time of just 40 μ s per resolution element in the final reconstruction. Also in terms of count-rate limit, the EIGER supersedes the PILATUS, compare section 5.3.2.2. Another interesting development are detectors which combine photon-counting and integrating operation modes. These allow to record an intense central maximum while still retaining single-photon sensitivity in the outer regions of the diffraction pattern. GIEWEKEMEYER ET AL. (2014) have recently used a detector of this type, the MM-PAD, for ptychography. Energy-resolving imaging detectors

like the MEDIPIX 3 (BALLABRIGA ET AL., 2011) may also provide some interesting new opportunities.

Ptychography can of course also greatly benefit from the higher coherent flux of the newest 3rd generation synchrotron sources like PETRA III (BALEWSKI ET AL., 2004) or NSLS II (MURPHY ET AL., 2004). While it is unclear whether the intriguing concept of energy-recovery linacs (GRUNER ET AL., 2002a) will result in an operational machine any time soon, ptychography has already been used at an X-ray free electron laser (SCHROPP ET AL., 2013). However, full-power XFEL beams do not allow to illuminate sample areas several times in order to create the mandatory overlap. PCDI at XFELs will therefore probably remain limited to special settings, i.e. specimens with two-dimensional translation symmetry (KEWISH ET AL., 2010b). Exciting opportunities will arise with the upcoming diffraction-limited storage rings (ERIKSSON ET AL., 2014). As the coherent flux is expected to increase by more than two orders of magnitude compared to a conventional synchrotron ring, significant gains in quantity and quality of ptychographic results are envisioned (THIBAUT ET AL., 2014). Following up on the work of ENDERS ET AL. (2014), higher spatial resolutions are also possible at existing sources by employing broad-bandwidth beams or working only with partially-coherent beams (THIBAUT AND MENZEL, 2013).

In terms of applications, one can infer that the possibility of in-situ ptychographic imaging with hard X-rays (ESMAELI ET AL., 2013, 2015; HØYDALSVIK ET AL., 2014) will give access to a lot of interesting questions. A lot of emerging applications are now also done with soft X-rays, after the field has long been dominated by experiments in the multi-keV regime. Recent examples include the combination of ptychography and near-edge spectroscopy (SHAPIRO ET AL., 2014), or the simultaneous recording of fluorescence information (DENG ET AL., 2015b). Both approaches are expected to further grow in importance, as well as other multi-modal techniques and soft X-ray ptychography in general. Besides the studies on various classes of samples, also the characterization of focusing optics by PCDI (KEWISH ET AL., 2010a,c; SCHROPP ET AL., 2010; VILA-COMAMALA ET AL., 2011a) will remain an important application.

Recently, ptychography has also entered the field of full-field imaging through replacing the usual Fourier transform relation between object and diffraction plane with near-field propagation (STOCKMAR ET AL., 2013). The approach has demonstrated its potential to reconstruct data which is difficult or impossible to handle with the usual propagation-based near-field phase-contrast techniques (STOCKMAR ET AL., 2015). As near-field ptychography has lower coherence requirements and might even be used with laboratory sources, it will certainly remain an active field of research.

Finally, it should not be forgotten that ptychography is also actively developed for other types of radiation: Not too long ago, the iterative algorithms have finally successfully returned to their roots in electron microscopy (HUMPHRY ET AL., 2012; PUTKUNZ ET AL., 2012), after there had long been difficulties with the multiple scattering occurring in the case of electrons. As in the case of electrons, also PCDI with visible light is part of commercial efforts of Phase Focus Ltd.¹, a company which develops products based on ptychographic imaging.

12.2 Algorithmic and software developments

Like the experiments, also the software implementations for PCDI reconstructions strive to become more optimized and more user-friendly at the same time. With increasing data collection rates, parallel computing approaches get mandatory to obtain results with as little time delay as possible. More traditional CPU-based parallelization remains important, e.g. in the open-source package *ptypy* (ENDERS AND THIBAUT, 2014). Recently, also code harnessing the vast computing power of GPUs has emerged, e.g. in form of the open-source software *Sharp Camera* (SHARP CAMERA TEAM, 2014), developed by Filipe Maia and co-workers at the Advanced Light Source in Berkeley. More recently, also a group from the Advanced Photon Source near Chicago has published an article on GPU-accelerated ptychography (NASHED ET AL., 2014).

Another idea which also has the acceleration of ptychography in mind, is the recent successful use of on-the-fly scanning (DENG ET AL., 2015a; PELZ ET AL., 2014) instead of the usual stop-and-go mode. As the continuous scanning acts as a source of decoherence in the diffraction data, the data can be handled with the mixed-state reconstruction approach of THIBAUT AND MENZEL (2013). This extension of ptychography is probably the most important algorithmic development in the field since the introduction of simultaneous probe retrieval. It is therefore expected to continue to have an tremendous impact on the further development of the technique. ENDERS ET AL. (2014) have already demonstrated its potential for improving reconstructions from data collected with non-ideal detectors. A detailed study on the ability of the mixed-state approach to handle partial coherence has just recently been published by BURDET ET AL. (2015).

In usual PCDI, the scan position have to be provided as highly accurate *a priori* knowledge, but may easily suffer from inaccuracies and instabilities.

¹<http://www.phasefocus.com>

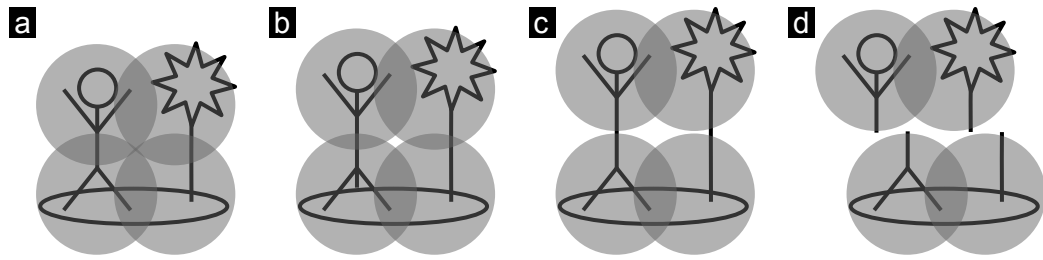


Figure 12.1: Illustration of ambiguous position refinement due to lack of translation diversity along one direction: A test object (black drawing) is assumed to be illuminated at four positions with a localized probe (grey discs). **(a)** Original shape of object, correct probe positions. **(b)** If the scan positions are refined, this result is equivalent to (a): as only horizontal shifts would cause changes in the diffraction data or inconsistencies in the overlapping areas, but not the vertical offset introduced here. **(c)** As the portion of the object covered at each probe position is still the same as in (a), also this result without any overlap in vertical direction is possible. **(d)** In a situation like shown in (c), the lack of overlap in the vertical direction also allows for horizontal shifts like the one shown here. It should be pointed out that this is not possible in case (b) where the overlap enforces the vertical lines to be continuous. Both (c) and (d) may be avoided by constraining the distances by which the refinement is allowed to change the positions.

Algorithmic position refinement is therefore highly desirable. The first approach in this respect has been published by [GUIZAR-SICAIROS AND FIENUP \(2008\)](#), who include an update of the probe locations in their conjugate-gradient optimization. [MAIDEN ET AL. \(2012b\)](#) suggested a method based on simulated annealing. Philipp Pelz (born Braun) used a expectation-maximization in his Bachelor’s thesis ([BRAUN, 2013](#)), whereas the approach of [ZHANG ET AL. \(2013\)](#) relies on the cross-correlation of object guesses from adjacent iterations of the ePIE algorithm. Despite all these options, one can still raise some concerns about their general applicability. Fig. 12.1 illustrates an example where the position refinement becomes ambiguous.

Also algorithms for the near-field case are being further developed, like, e.g., longitudinal ptychography utilizing reconstructions taken at different propagation distances ([ROBISCH AND SALDITT, 2013](#)).

There are several more recent algorithmic innovations, which have not yet found the way into mainstream applications. Examples are approaches exploiting the superresolution capabilities of ptychography ([MAIDEN ET AL., 2011](#)), or a multi-slice reconstruction method for thick specimens ([MAIDEN ET AL., 2012a](#)). In the future, high dissemination of such advances could be achieved through the timely addition to one of the emerging open-source ptychography libraries like *ptypy* ([ENDERS ET AL., 2014](#))

Finally, also Bragg ptychography ([GODARD ET AL., 2011](#)) has to be mentioned as a field of ongoing algorithmic developments.

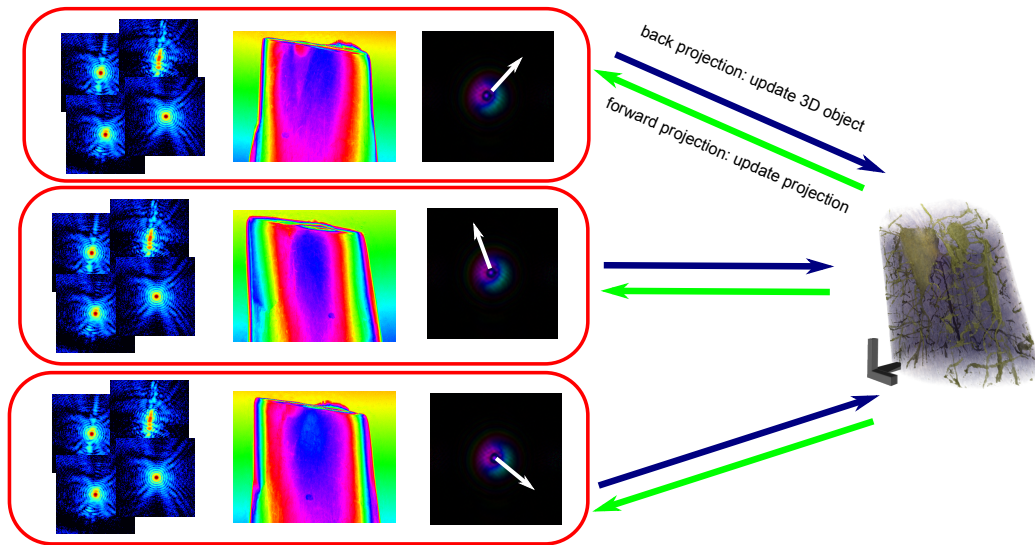


Figure 12.2: Information sharing via a tomographic volume. Ptychographic reconstructions are performed individually for the respective projection angle (red boxes). After a certain amount of ptychographic iterations, the three-dimensional volume is updated through a back-projection operation. If there is mutual misalignment between the projections, this volume will show a blurred appearance. Updated object guesses for each projection angle are then calculated by forward-projection of the volume. The projections will now also show a certain degree of blur. The working hypothesis is that, despite this blur, the averaging over the three-dimensional volume results in a projection with less misalignment from the global mean. The PCDI reconstructions are then expected to compensate for the ensuing shifts by moving the unconstrained probes accordingly (white arrows), similar to what has been observed for the two-dimensional case of a shared object in section 7.3.3 starting on page 184.

12.2.1 Algorithms for ptychographic nanotomography

Although we have seen in the chapter 11 of conclusions that ptychographic nanotomography has been successfully used in different applications, the processing procedure introduced in 9.2 starting on page 242 is rather tedious. The well-written processing packages by DAURER (2013), which also provides a graphical user interface, and GUIZAR-SICAIROS ET AL. (2011) have further streamlined the reconstruction process. However, they still rely on strong assumptions about the object, namely the presence of sufficiently empty areas on either side of the sample. As a result, PXCT in this form remains limited to free-standing specimens no thicker than the field-of-view. Local tomography or even tomosynthesis on limited-angle data sets (compare section 10.3) are not possible this way.

Inspired by the self-aligning effect observed when sharing a common object between scans with offset positions in section 7.3.3, this has been de-

veloped into an idea for self-consistent projection alignment. The details of this proposal are presented in Fig. 12.2. If the approach performs in the envisioned way, the alignment would no longer rely on *a priori* knowledge about the sample and could run almost unsupervised.

Another point where PXCT still has a lot of room for improvements is the tomographic reconstruction. So far, usually the filtered-backprojection (FBP) algorithm is used. However, due to the long acquisition times required, PXCT sinograms are typically angularly undersampled as not enough different projections are obtained. One can therefore expect to improve the quality of the CT reconstructions by using iterative algorithms (KAK AND SLANEY, 1988), which show a better performance for undersampled data than the FBP.

Part V

Appendix, Bibliography and Indices

Appendix A

The Fourier transform and its properties

Due to their paramount importance for far-field coherent diffractive imaging, this chapter provides a brief summary on the Fourier transform and its properties, which are frequently used throughout this thesis. The content of this chapter has been adapted from section 2.1 of [DIEROLF \(2007\)](#).

As a multi-dimensional Fourier transform can be understood as consecutive applications of independent one-dimensional transforms along each coordinate, all definitions are given in a one-dimensional notation. In what follows, x is a real-space coordinate and q the corresponding reciprocal coordinate in Fourier space (component of the scattering vector).

A.1 Definition and properties

In its continuous form, the complex Fourier transform $\tilde{f}(q)$ of a square-integrable function $f(x)$ is defined as ([BRACEWELL, 1986](#))

$$\tilde{f}(q) = \mathcal{F} \{f(x)\} = \int_{-\infty}^{\infty} f(x) e^{-iqx} dx, \quad (\text{A.1a})$$

with the corresponding inverse transform

$$f(x) = \mathcal{F}^{-1} \{\tilde{f}(q)\} = \frac{1}{2\pi} \int_{-\infty}^{\infty} \tilde{f}(q) e^{iqx} dq. \quad (\text{A.1b})$$

To express transformations between time and frequency domain in the same notation, x has to be replaced by the time t and q by the angular frequency

ω . The Fourier transform has several properties which can be easily derived from the definitions (A.1) (CHAMPENEY, 1973; GOODMAN, 1996):

1. Similarity theorem:

$$\mathcal{F}\{f(ax)\} = \frac{1}{|a|} \tilde{f}\left(\frac{q}{a}\right) . \quad (\text{A.2})$$

A coordinate “stretching” in direct space causes a contraction of the corresponding Fourier space coordinates.

2. Shift theorem:

$$\mathcal{F}\{f(x \pm a)\} = e^{\pm iqa} \tilde{f}(q) . \quad (\text{A.3})$$

A translation in direct space results in a linear *phase ramp* or *phase tilt* superimposed on the Fourier transform of the unshifted function.

3. Parseval’s theorem:

$$\int_{-\infty}^{\infty} |f(x)|^2 dx = \frac{1}{2\pi} \int_{-\infty}^{\infty} |\tilde{f}(q)|^2 dq . \quad (\text{A.4})$$

Apart from a constant pre-factor, the integral over the modulus squared in real and reciprocal space has the same value.

4. Convolution theorem:

$$\mathcal{F}\{f \otimes g\} = \mathcal{F}\left\{\int_{-\infty}^{\infty} f(x')g(x-x')dx'\right\} = \mathcal{F}\{f\} \mathcal{F}\{g\} . \quad (\text{A.5})$$

A convolution of two functions transforms to the product of their Fourier transforms.

5. Cross-correlation:

$$\mathcal{F}\{f \star g\} = \mathcal{F}\left\{\int_{-\infty}^{\infty} f(x')g^*(x'-x)dx'\right\} = \mathcal{F}\{f\} (\mathcal{F}\{g\})^* , \quad (\text{A.6})$$

with the important special case of the autocorrelation

$$\mathcal{F}\{f \star f\} = |\mathcal{F}\{f\}|^2 . \quad (\text{A.7})$$

6. Fourier transform of a real-valued function $f(x) = f^*(x)$:

$$\tilde{f}(q) = \tilde{f}^*(-q) , \quad (\text{A.8})$$

which is also known as *Friedel’s law* in diffraction physics (ALS-NIELSEN AND MCMORROW, 2011).

7. Fourier transform of derivatives:

$$\mathcal{F}\left\{\frac{d^n}{dx^n} f(x)\right\} = (iq)^n \tilde{f}(q) . \quad (\text{A.9})$$

A.2 Fourier-Bessel transform for circularly-symmetric functions

Optical set-ups often show circular symmetry with respect to the optical axis. If a function exhibits circular symmetry, this is also true for its Fourier transforms. The two-dimensional Fourier transform can thus be replaced by the one-dimensional *Fourier-Bessel transform*, which links the radial components in real and reciprocal space and is also known as *Hankel transform of zero order* (CHAMPENEY, 1973):

$$\tilde{g}(q) = \text{HT}_0 \{g(r)\} = 2\pi \int_0^\infty r g(r) J_0(rq) dr, \quad (\text{A.10})$$

where J_0 is the zeroth-order Bessel function of the first kind. Discrete versions of this transform utilize roots of the Bessel functions as sampling points, see YU ET AL. (1998) and GUIZAR-SICAIROS AND GUTIÉRREZ-VEGA (2004) for more details.

A.3 Discrete Fourier transform

To analysis discrete data sets like pixelated images, also the mathematical operations (transforms) have to be discretized. The one-dimensional Discrete Fourier Transform (DFT) maps an complex-valued vector \mathbf{f} of N elements to another vector space with the same dimension N . Then the n -th element of the transformed vector is (BUTZ, 2006)

$$\tilde{f}_n = (\mathcal{F}\{f\})_n = \frac{1}{N} \sum_{m=0}^{N-1} f_m e^{-2\pi i n m / N}, \quad 0 \leq n \leq N-1, \quad (\text{A.11a})$$

while the corresponding inverse transform is given by

$$f_n = (\mathcal{F}^{-1}\{\tilde{f}\})_n = \sum_{m=0}^{N-1} \tilde{f}_m e^{2\pi i n m / N}, \quad 0 \leq n \leq N-1. \quad (\text{A.11b})$$

The theorems introduced in section A.1 for the continuous case also hold for the DFT (for more details compare BRACEWELL, 1986; BUTZ, 2006; MEYBERG AND VACHENAUER, 1999). One important additional property is the *periodicity of the DFT* so that for all $n \in [0, N-1]$

$$f_{n+kN} = f_n, \quad \forall k \in \mathbb{Z}, \quad (\text{A.12a})$$

$$\tilde{f}_{m+kN} = \tilde{f}_m, \quad \forall k \in \mathbb{Z}. \quad (\text{A.12b})$$

Software implementations of discrete Fourier transforms typically rely on a *Fast Fourier Transform (FFT)* algorithm (COOLEY AND TUKEY, 1965)¹: The basic idea of such an algorithm is, to divide the vector \mathbf{f} of N elements into smaller sub-units, whose lengths are factors of N . The Fourier transforms of these sub-vectors can be calculated much faster, thus the total computation time scales only with $N \log(N)$ rather than N^2 as for a standard DFT. The method works best if N is “a highly composite number” (COOLEY AND TUKEY, 1965) which can be split into many factors. Therefore, the best performances are typically achieved when N is a power of two.

¹Although there are different FFT algorithms, the algorithm of COOLEY AND TUKEY (1965) is still the most popular one. As a result, “FFT” is sometimes used as a synonym for the Cooley-Tukey FFT algorithm.

Bibliography

- E. M. AARDEN, E. H. BURGER, AND P. J. NIJWEIDE. Function of osteocytes in bone. *Journal of Cellular Biochemistry*, 55(3):287–299, 1994. doi:10.1002/jcb.240550304. (Cited on page 287.)
- B. ABBEY, K. A. NUGENT, G. J. WILLIAMS, J. N. CLARK, A. G. PEELE, M. A. PFEIFER, M. DE JONGE, AND I. MCNULTY. Key-hole coherent diffractive imaging. *Nature Physics*, 4(5):394–398, 2008. doi:10.1038/nphys896. (Cited on page 73.)
- H. ADE, J. KIRZ, S. L. HULBERT, E. D. JOHNSON, E. ANDERSON, AND D. KERN. X-ray spectromicroscopy with a zone plate generated microprobe. *Applied Physics Letters*, 56(19):1841–1843, 1990. doi:10.1063/1.103064. (Cited on page 41.)
- H. ADE, X. ZHANG, S. CAMERON, C. COSTELLO, J. KIRZ, AND S. WILLIAMS. Chemical contrast in X-ray microscopy and spatially resolved XANES spectroscopy of organic specimens. *Science*, 258(5084):972–975, 1992. doi:10.1126/science.1439809. (Cited on page 41.)
- J. ALS-NIELSEN AND D. MCMORROW. *Elements of Modern X-ray Physics*. John Wiley & Sons, Inc., Hoboken, NJ, USA, 2011. doi:10.1002/9781119998365. (Cited on pages 30, 37, 50, 128, 201, 211 and 338.)
- J. C. ANDREWS, E. ALMEIDA, M. C. H. VAN DER MEULEN, J. S. ALWOOD, C. LEE, Y. LIU, J. CHEN, F. MEIRER, M. FESER, J. GELB, J. RUDATI, A. TKACHUK, W. YUN, AND P. PIANETTA. Nanoscale X-ray microscopic imaging of mammalian mineralized tissue. *Microscopy and Microanalysis*, 16(3):327–336, 2010. doi:10.1017/S1431927610000231. (Cited on pages 266 and 267.)
- G. J. ATKINS AND D. M. FINDLAY. Osteocyte regulation of bone mineral: a little give and take. *Osteoporosis International*, 23(8):2067–2079, 2012. doi:10.1007/s00198-012-1915-z. (Cited on page 287.)

- D. T. ATTWOOD. *Soft x-rays and extreme ultraviolet radiation: principles and applications*. Cambridge University Press, 2000. (Cited on pages [22](#), [24](#), [25](#), [29](#), [31](#), [32](#), [37](#), [38](#), [45](#) and [110](#).)
- A. V. BAEZ. Fresnel Zone Plate for Optical Image Formation Using Extreme Ultraviolet and Soft X Radiation. *Journal of the Optical Society of America*, 51(4):405–412, 1961. doi:[10.1364/JOSA.51.000405](#). (Cited on page [30](#).)
- K. BALEWSKI, W. BREFELD, W. DECKING, Y. LI, G. SAHOO, AND R. WANZENBERG. PETRA III: a new high Brilliance Synchrotron Radiation Source at DESY. In *Proceedings of EPAC*, pp. 2302–2304. Lucerne, Switzerland, 2004. (Cited on page [330](#).)
- R. BALLABRIGA, M. CAMPBELL, E. HEIJNE, X. LLOPART, L. TLUSTOS, AND W. WONG. Medipix3: A 64k pixel detector readout chip working in single photon counting mode with improved spectrometric performance. *Nuclear Instruments and Methods in Physics Research Section A*, 633(Supp. 1):S15–S18, 2011. doi:[10.1016/j.nima.2010.06.108](#). (Cited on page [330](#).)
- M. BANHAM AND A. KATSAGGELOS. Digital image restoration. *IEEE Signal Processing Magazine*, 14(2):24–41, 1997. doi:[10.1109/79.581363](#). (Cited on pages [20](#) and [224](#).)
- H. H. BARRETT. Limited-angle tomography for the nineties. *Journal of Nuclear Medicine*, 31(10):1688–1692, 1990. (Cited on pages [156](#), [253](#) and [267](#).)
- H. D. BARTH, M. E. LAUNEY, A. A. MACDOWELL, J. W. AGER, AND R. O. RITCHIE. On the effect of X-ray irradiation on the deformation and fracture behavior of human cortical bone. *Bone*, 46(6):1475–85, 2010. doi:[10.1016/j.bone.2010.02.025](#). (Cited on page [276](#).)
- R. H. T. BATES. Fourier phase problems are uniquely solvable in more than one dimension. 1. Underlying theory. *Optik*, 61(3):247–262, 1982. (Cited on pages [46](#), [53](#), [54](#), [61](#) and [72](#).)
- R. H. T. BATES AND J. M. RODENBURG. Sub-Angstrom transmission microscopy: A Fourier transform algorithm for microdiffraction plane intensity information. *Ultramicroscopy*, 31(3):303–307, 1989. doi:[10.1016/0304-3991\(89\)90052-1](#). (Cited on pages [78](#) and [79](#).)

- W. BAUMEISTER, R. GRIMM, AND J. WALZ. Electron tomography of molecules and cells. *Trends in Cell Biology*, 9(2):81–85, 1999. doi:10.1016/S0962-8924(98)01423-8. (Cited on page 155.)
- H. H. BAUSCHKE, P. L. COMBETTES, AND D. R. LUKE. Phase retrieval, error reduction algorithm, and Fienup variants: a view from convex optimization. *Journal of the Optical Society of America A*, 19(7):1334–1345, 2002. doi:10.1364/JOSAA.19.001334. (Cited on pages 56, 57, 58, 59 and 62.)
- H. H. BAUSCHKE, P. L. COMBETTES, AND D. R. LUKE. Hybrid projection-reflection method for phase retrieval. *Journal of the Optical Society of America A*, 20(6):1025–1034, 2003. doi:10.1364/JOSAA.20.001025. (Cited on page 64.)
- D. J. BAYLINK AND J. E. WERGEDAL. Bone formation by osteocytes. *The American Journal of Physiology*, 221(3):669–678, 1971. doi:http://ajplegacy.physiology.org/content/221/3/669. (Cited on page 287.)
- W. G. BEAMER, L. R. DONAHUE, C. J. ROSEN, AND D. J. BAYLINK. Genetic variability in adult bone density among inbred strains of mice. *Bone*, 18(5):397–403, 1996. doi:10.1016/8756-3282(96)00047-6. (Cited on pages 259 and 262.)
- T. BEETZ, M. HOWELLS, C. JACOBSEN, C. KAO, J. KIRZ, E. LIMA, T. MENTES, H. MIAO, C. SANCHEZ-HANKE, D. SAYRE, AND D. SHAPIRO. Apparatus for X-ray diffraction microscopy and tomography of cryo specimens. *Nuclear Instruments and Methods in Physics Research Section A*, 545(1-2):459–468, 2005. doi:10.1016/j.nima.2004.12.040. (Cited on page 156.)
- T. BEETZ AND C. JACOBSEN. Soft X-ray radiation-damage studies in PMMA using a cryo-STXM. *Journal of Synchrotron Radiation*, 10(3):280–283, 2002. doi:10.1107/S0909049503003261. (Cited on page 156.)
- L. F. BÉLANGER. Osteocytic osteolysis. *Calcified Tissue Research*, 4(1):1–12, 1969. doi:10.1007/BF02279101. (Cited on page 287.)
- T. BENO, Y.-J. YOON, S. C. COWIN, AND S. P. FRITTON. Estimation of bone permeability using accurate microstructural measurements. *Journal of Biomechanics*, 39(13):2378–87, 2006. doi:10.1016/j.jbiomech.2005.08.005. (Cited on page 264.)

- R. BILTZ AND E. PELLEGRINO. The Composition of Recrystallized Bone Mineral. *Journal of Dental Research*, 62(12):1190–1195, 1983. doi:10.1177/00220345830620120301. (Cited on page 285.)
- P. BLEUET, P. CLOETENS, P. GERGAUD, D. MARIOLLE, N. CHEVALIER, R. TUCOULOU, J. SUSINI, AND A. CHABLI. A hard x-ray nanoprobe for scanning and projection nanotomography. *Review of Scientific Instruments*, 80(5):056101, 2009. doi:10.1063/1.3117489. (Cited on pages 39, 137 and 140.)
- P. BLEUET, A. SIMIONOVICI, L. LEMELLE, T. FERROIR, P. CLOETENS, R. TUCOULOU, AND J. SUSINI. Hard x-rays nanoscale fluorescence imaging of Earth and Planetary science samples. *Applied Physics Letters*, 92(21):213111, 2008. doi:10.1063/1.2927476. (Cited on page 138.)
- R. BLOEBAUM, J. SKEDROS, E. VAJDA, K. BACHUS, AND B. CONSTANTZ. Determining mineral content variations in bone using backscattered electron imaging. *Bone*, 20(5):485–490, 1997. doi:10.1016/S8756-3282(97)00015-X. (Cited on page 304.)
- L. F. BONEWALD. The amazing osteocyte. *Journal of Bone and Mineral Research*, 26(2):229–238, 2011. doi:10.1002/jbmr.320. (Cited on page 287.)
- E. BONUCCI. The osteocyte: the underestimated conductor of the bone orchestra. *Rendiconti Lincei*, 20(3):237–254, 2009. doi:10.1007/s12210-009-0051-y. (Cited on page 287.)
- M. BORN AND E. WOLF. *Principles of optics: electromagnetic theory of propagation, interference and diffraction of light*. Cambridge Univ. Press, Cambridge, 7. edn., 2006. (Cited on pages 17, 19, 25, 46, 47 and 217.)
- Y. BOULIGAND. Twisted fibrous arrangements in biological materials and cholesteric mesophases. *Tissue and Cell*, 4(2):189–217, 1972. doi:10.1016/S0040-8166(72)80042-9. (Cited on pages 307, 308 and 314.)
- W. J. BOYLE, W. S. SIMONET, AND D. L. LACEY. Osteoclast differentiation and activation. *Nature*, 423(6937):337–342, 2003. doi:10.1038/nature01658. (Cited on page 289.)
- R. N. BRACEWELL. *The Fourier transform and its applications*. McGraw-Hill series in electrical engineering : Circuits and systems. McGraw-Hill, New York, 2. edn., 1986. (Cited on pages 337 and 339.)

-
- P. BRAUN. *Probe position refinement in X-ray ptychography*. B.Sc. thesis, Technische Universität München, 2013. (Cited on page 332.)
- Y. BRUCK AND L. SODIN. On the ambiguity of the image reconstruction problem. *Optics Communications*, 30(3):304–308, 1979. doi:10.1016/0030-4018(79)90358-4. (Cited on page 53.)
- O. BUNK, M. BECH, T. H. JENSEN, R. FEIDENHANS’L, T. BINDERUP, A. MENZEL, AND F. PFEIFFER. Multimodal x-ray scatter imaging. *New Journal of Physics*, 11(12):123016, 2009. doi:10.1088/1367-2630/11/12/123016. (Cited on page 42.)
- O. BUNK, M. DIEROLF, S. KYNDE, I. JOHNSON, O. MARTI, AND F. PFEIFFER. Influence of the overlap parameter on the convergence of the ptychographical iterative engine. *Ultramicroscopy*, 108(5):481–487, 2008. doi:10.1016/j.ultramic.2007.08.003. (Cited on page 88.)
- O. BUNK, A. MENZEL, AND A. DIAZ. *cSAXS notes v1.02 (March 18th, 2011)*. Available online (last accessed March 2nd, 2015): http://www.psi.ch/sls/csaxs/ManualsEN/csaxs_notes.pdf, 2011. (Cited on page 125.)
- N. BURDET, G. R. MORRISON, X. HUANG, X. SHI, J. N. CLARK, F. ZHANG, M. CIVITA, R. HARDER, AND I. K. ROBINSON. Observations of artefacts in the x-ray ptychography method. *Optics Express*, 22(9):10294–10303, 2014. doi:10.1364/OE.22.010294. (Cited on page 92.)
- N. BURDET, X. SHI, D. PARKS, J. N. CLARK, X. HUANG, S. D. KEVAN, AND I. K. ROBINSON. Evaluation of partial coherence correction in X-ray ptychography. *Optics Express*, 23(5):5452–5467, 2015. doi:10.1364/OE.23.005452. (Cited on page 331.)
- E. H. BURGER AND J. KLEIN-NULEND. Mechanotransduction in bone—role of the lacuno-canalicular network. *The FASEB Journal*, 13:S101–12, 1999. doi:<http://www.fasebj.org/content/13/9001/101.long>. (Cited on page 264.)
- T. BUTZ. *Fourier Transformation for Pedestrians*. Springer Berlin Heidelberg, Berlin, Heidelberg, 2006. doi:10.1007/978-3-540-31108-9. (Cited on pages 50, 51 and 339.)
- D. C. CHAMPENEY. *Fourier transforms and their physical applications*. Techniques of physics 1. Academic Press, London, 1973. (Cited on pages 21, 338 and 339.)

- W. CHAO, B. D. HARTENECK, J. A. LIDDLE, E. H. ANDERSON, AND D. T. ATTWOOD. Soft X-ray microscopy at a spatial resolution better than 15 nm. *Nature*, 435(7046):1210–1213, 2005. doi:10.1038/nature03719. (Cited on pages 32 and 110.)
- H. N. CHAPMAN. Phase-retrieval X-ray microscopy by Wigner-distribution deconvolution. *Ultramicroscopy*, 66(3-4):153–172, 1996. doi:10.1016/S0304-3991(96)00084-8. (Cited on pages 79, 80, 81, 89 and 90.)
- H. N. CHAPMAN. Phase-Retrieval X-Ray Microscopy by Wigner-Distribution Deconvolution: Signal Processing. *Scanning Microscopy*, 11:67–80, 1997. doi:http://www.ecmjournals.org/journal/smi/pdf/smi97-06.pdf. (Cited on page 80.)
- H. N. CHAPMAN. Focus on x-ray diffraction. *Science*, 321(5887):352–353, 2008. doi:10.1126/science.1161183. (Cited on pages 325 and 327.)
- H. N. CHAPMAN, A. BARTY, M. J. BOGAN, S. BOUTET, M. FRANK, S. P. HAU-RIEGE, S. MARCHESINI, B. W. WOODS, S. BAJT, W. H. BENNER, R. A. LONDON, E. PLÖNJES, M. KUHLMANN, R. TREUSCH, S. DÜSTERER, T. TSCHENTSCHER, J. R. SCHNEIDER, E. SPILLER, T. MÖLLER, C. BOSTEDT, M. HOENER, D. A. SHAPIRO, K. O. HODGSON, D. VAN DER SPOEL, F. BURMEISTER, M. BERGH, C. CALEMAN, G. HULDT, M. M. SEIBERT, F. R. N. C. MAIA, R. W. LEE, A. SZÖKE, N. TIMNEANU, AND J. HAJDU. Femtosecond diffractive imaging with a soft-X-ray free-electron laser. *Nature Physics*, 2(12):839–843, 2006a. doi:10.1038/nphys461. (Cited on pages 69, 70, 88, 112 and 279.)
- H. N. CHAPMAN, A. BARTY, S. MARCHESINI, A. NOY, S. P. HAU-RIEGE, C. CUI, M. R. HOWELLS, R. ROSEN, H. HE, J. C. H. SPENCE, U. WEIERSTALL, T. BEETZ, C. JACOBSEN, AND D. A. SHAPIRO. High-resolution ab initio three-dimensional x-ray diffraction microscopy. *Journal of the Optical Society of America A*, 23(5):1179–1200, 2006b. doi:10.1364/JOSAA.23.001179. (Cited on pages 63, 64, 72, 97, 111 and 112.)
- H. N. CHAPMAN, C. JACOBSEN, AND S. WILLIAMS. Applications of a CCD detector in scanning transmission x-ray microscope. *Review of Scientific Instruments*, 66(2):1332, 1995. doi:10.1063/1.1145967. (Cited on pages 41 and 42.)
- B. CHEN, M. GUIZAR-SICAIROS, G. XIONG, L. SHEMILT, A. DIAZ, J. NUTTER, N. BURDET, S. HUO, J. MANCUSO, A. MONTEITH,

-
- F. VERGEER, A. BURGESS, AND I. ROBINSON. Three-dimensional structure analysis and percolation properties of a barrier marine coating. *Scientific Reports*, 3:1177, 2013. doi:10.1038/srep01177. (Cited on pages 281 and 328.)
- M. CHMEISSANI, C. FROJDH, O. GAL, X. LLOPART, J. LUDWIG, M. MAIORINO, E. MANACH, G. METTIVIER, M. MONTESI, C. PONCHUT, P. RUSSO, L. TLUSTOS, AND A. ZWERGER. First Experimental Tests With a CdTe Photon Counting Pixel Detector Hybridized With a Medipix2 Readout Chip. *IEEE Transactions on Nuclear Science*, 51(5):2379–2385, 2004. doi:10.1109/TNS.2004.832324. (Cited on page 232.)
- P. CLOETENS. *Contribution to Phase Contrast Imaging, Reconstruction and Tomography with Hard Synchrotron Radiation: Principles, Implementation and Applications*. Ph.D. thesis, Vrije Universiteit Brussel, 1999. (Cited on pages 21 and 119.)
- P. CLOETENS. *Upgrade Programme – Phase I, UPBL Conceptual Design Report. UPBL4: Nano-imaging and nano-analysis*. Available online (last accessed March 19th, 2013): http://www.esrf.eu/UsersAndScience/Experiments/Imaging/beamline-portfolio/CDR_UPBL04_future-ID16.pdf, 2009. (Cited on page 232.)
- P. CLOETENS, R. BARRETT, J. BARUCHEL, J. GUIGAY, AND M. SCHLENKER. Phase objects in synchrotron radiation hard x-ray imaging. *Journal of Physics D: Applied Physics*, 29:133–146, 1996. doi:10.1088/0022-3727/29/1/023. (Cited on page 39.)
- P. CLOETENS, W. LUDWIG, J. BARUCHEL, D. VAN DYCK, J. VAN LANDUYT, J. P. GUIGAY, AND M. SCHLENKER. Holotomography: Quantitative phase tomography with micrometer resolution using hard synchrotron radiation x rays. *Applied Physics Letters*, 75(19):2912, 1999. doi:10.1063/1.125225. (Cited on pages 39 and 45.)
- P. COAN, A. PETERZOL, S. FIEDLER, C. PONCHUT, J. C. LABICHE, AND A. BRAVIN. Evaluation of imaging performance of a taper optics CCD 'FReLoN' camera designed for medical imaging. *Journal of Synchrotron Radiation*, 13(3):260–270, 2006. doi:10.1107/S0909049506008983. (Cited on page 141.)
- A. R. CONN, N. I. M. GOULD, AND P. L. TOINT. *Trust-Region Methods*. MPS-SIAM Series on Optimization. Society for Industrial and Applied Mathematics (SIAM), 2000. (Cited on pages 213, 219 and 227.)

- J. W. COOLEY AND J. W. TUKEY. An algorithm for the machine calculation of complex Fourier series. *Mathematics of Computation*, 19(90):297–297, 1965. doi:10.1090/S0025-5718-1965-0178586-1. (Cited on page 340.)
- V. E. COSSLETT AND W. C. NIXON. The X-Ray Shadow Microscope. *Journal of Applied Physics*, 24(5):616, 1953. doi:10.1063/1.1721338. (Cited on page 38.)
- CSAXS WEBSITE. <http://www.psi.ch/sls/csaxs>, last accessed 02. Mar. 2015. (Cited on pages 125 and 127.)
- I. A. CUNNINGHAM AND R. SHAW. Signal-to-noise optimization of medical imaging systems. *Journal of the Optical Society of America A*, 16(3):621–632, 1999. doi:10.1364/JOSAA.16.000621. (Cited on page 35.)
- J. C. DA SILVA, K. MADER, M. HOLLER, D. HABERTHÜR, A. DIAZ, M. GUIZAR-SICAIROS, W.-C. CHENG, Y. SHU, J. RAABE, A. MENZEL, AND J. A. VAN BOKHOVEN. Assessment of the 3 D Pore Structure and Individual Components of Preshaped Catalyst Bodies by X-Ray Imaging. *ChemCatChem*, 7(3):413–416, 2015. doi:10.1002/cctc.201402925. (Cited on page 328.)
- B. J. DAURER. *Advanced Image Processing Algorithms for Coherent X-ray nanoCT*. M.Sc. thesis, Technische Universität München, 2013. (Cited on pages 327 and 333.)
- M. DE JONGE, B. HORNBERGER, C. HOLZNER, D. LEGNINI, D. PATERSON, I. MCNULTY, C. JACOBSEN, AND S. VOGT. Quantitative Phase Imaging with a Scanning Transmission X-Ray Microscope. *Physical Review Letters*, 100(16):163902, 2008. doi:10.1103/PhysRevLett.100.163902. (Cited on pages 41, 43 and 44.)
- J. DENG, Y. S. G. NASHED, S. CHEN, N. W. PHILLIPS, T. PETERKA, R. ROSS, S. VOGT, C. JACOBSEN, AND D. J. VINE. Continuous motion scan ptychography: characterization for increased speed in coherent x-ray imaging. *Optics Express*, 23(5):5438–5451, 2015a. doi:10.1364/OE.23.005438. (Cited on pages 148 and 331.)
- J. DENG, D. J. VINE, S. CHEN, Y. S. G. NASHED, Q. JIN, N. W. PHILLIPS, T. PETERKA, R. ROSS, S. VOGT, AND C. J. JACOBSEN. Simultaneous cryo X-ray ptychographic and fluorescence microscopy of green algae. *Proceedings of the National Academy of Sciences of the United States of America*, 112(8):2314–2319, 2015b. doi:10.1073/pnas.1413003112. (Cited on page 330.)

- A. DIAZ, M. GUIZAR-SICAIROS, A. POEPEL, A. MENZEL, AND O. BUNK. Characterization of carbon fibers using X-ray phase nanotomography. *Carbon*, 67:98–103, 2014. doi:10.1016/j.carbon.2013.09.066. (Cited on pages 281 and 328.)
- M. DIEROLF. *Development of a Lensless Microscopy Technique for Imaging Cellular Structures*. Diplom thesis, Ulm University, 2007. (Cited on pages 25, 48, 49, 56, 60, 75, 84, 88, 89, 90 and 337.)
- M. DIEROLF, A. MENZEL, P. THIBAUT, P. SCHNEIDER, C. M. KEWISH, R. WEPF, O. BUNK, AND F. PFEIFFER. Ptychographic X-ray computed tomography at the nanoscale. *Nature*, 467(7314):436–439, 2010a. doi:10.1038/nature09419. (Cited on pages 143, 239, 240, 241, 242, 244, 246, 248, 249, 250, 252, 256, 257, 261, 263, 269, 316 and 325.)
- M. DIEROLF, P. THIBAUT, A. MENZEL, C. M. KEWISH, K. JEFIMOV, I. SCHLICHTING, K. VON KÖNIG, O. BUNK, AND F. PFEIFFER. Ptychographic coherent diffractive imaging of weakly scattering specimens. *New Journal of Physics*, 12(3):035017, 2010b. doi:10.1088/1367-2630/12/3/035017. (Cited on pages 76, 100, 109, 112, 143, 163, 165, 166, 170, 172, 282 and 326.)
- R. DINAPOLI, A. BERGAMASCHI, B. HENRICH, R. HORISBERGER, I. JOHNSON, A. MOZZANICA, E. SCHMID, B. SCHMITT, A. SCHREIBER, X. SHI, AND G. THEIDEL. EIGER: Next generation single photon counting detector for X-ray applications. *Nuclear Instruments and Methods in Physics Research Section A*, 650(1):79–83, 2011. doi:10.1016/j.nima.2010.12.005. (Cited on pages 145 and 329.)
- S. V. DOROZHUKIN AND M. EPPLE. Biological and medical significance of calcium phosphates. *Angewandte Chemie International Edition*, 41(17):3130–3146, 2002. doi:10.1002/1522-3773(20020902)41:17<3130::AID-ANIE3130>3.0.CO;2-1. (Cited on page 302.)
- J. DUBOCHET, M. ADRIAN, J.-J. CHANG, J.-C. HOMO, J. LEPAULT, A. W. MCDOWALL, AND P. SCHULTZ. Cryo-electron microscopy of vitrified specimens. *Quarterly Reviews of Biophysics*, 21(2):129–228, 1988. doi:10.1017/S0033583500004297. (Cited on page 155.)
- V. ELSER. Phase retrieval by iterated projections. *Journal of the Optical Society of America A*, 20(1):40–55, 2003a. doi:10.1364/JOSAA.20.000040. (Cited on pages 56, 57, 63, 64, 65, 66, 67, 68 and 94.)

- V. ELSER. Random projections and the optimization of an algorithm for phase retrieval. *Journal of Physics A: Mathematical and General*, 36(12):2995–3007, 2003b. doi:10.1088/0305-4470/36/12/309. (Cited on pages 66 and 94.)
- V. ELSER, I. RANKENBURG, AND P. THIBAUT. Searching with iterated maps. *Proceedings of the National Academy of Sciences of the United States of America*, 104(2):418–423, 2007. doi:10.1073/pnas.0606359104. (Cited on pages 60 and 65.)
- B. ENDERS, M. DIEROLF, P. CLOETENS, M. STOCKMAR, F. PFEIFFER, AND P. THIBAUT. Ptychography with broad-bandwidth radiation. *Applied Physics Letters*, 104(17):171104, 2014. doi:10.1063/1.4874304. (Cited on pages 233, 327, 330, 331 and 332.)
- B. ENDERS AND P. THIBAUT. ptypy: Ptychography Reconstruction for Python. *Zenodo*, 2014. doi:10.5281/zenodo.12480. (Cited on page 331.)
- M. ERIKSSON, J. F. VAN DER VEEN, AND C. QUITMANN. Diffraction-limited storage rings – a window to the science of tomorrow. *Journal of Synchrotron Radiation*, 21:837–842, 2014. doi:10.1107/S1600577514019286. (Cited on page 330.)
- O. K. ERSOY. *Diffraction, Fourier Optics and Imaging*. John Wiley & Sons, Hoboken, New Jersey, 1 edn., 2006. (Cited on pages 17, 19 and 20.)
- M. ESMAEILI, J. B. FLØYSTAD, A. DIAZ, K. HØYDALSVIK, M. GUIZAR-SICAIROS, J. W. ANDREASEN, AND D. W. BREIBY. Ptychographic X-ray Tomography of Silk Fiber Hydration. *Macromolecules*, 46(2):434–439, 2013. doi:10.1021/ma3021163. (Cited on pages 281, 328 and 330.)
- M. ESMAEILI, J. B. FLØYSTAD, A. HIPPEL, M. WILLNER, M. BECH, A. DIAZ, A. ROYSET, J. W. ANDREASEN, F. PFEIFFER, AND D. W. BREIBY. Monitoring moisture distribution in textile materials using grating interferometry and ptychographic X-ray imaging. *Textile Research Journal*, 85(1):80–90, 2015. doi:10.1177/0040517514538693. (Cited on pages 328 and 330.)
- ESRF WEBSITE. <http://www.esrf.eu/Accelerators/Performance>, last accessed 02. Mar. 2015. (Cited on page 137.)
- A. FARIDANI, E. L. RITMAN, AND K. T. SMITH. Local Tomography. *SIAM Journal on Applied Mathematics*, 52(2):459, 1992. doi:10.1137/0152026. (Cited on page 266.)

- G. W. FARIS AND R. L. BYER. Three-dimensional beam-deflection optical tomography of a supersonic jet. *Applied Optics*, 27(24):5202, 1988. doi:10.1364/AO.27.005202. (Cited on page 123.)
- H. M. L. FAULKNER AND J. M. RODENBURG. Movable Aperture Lensless Transmission Microscopy: A Novel Phase Retrieval Algorithm. *Physical Review Letters*, 93(2):023903, 2004. doi:10.1103/PhysRevLett.93.023903. (Cited on pages 74, 82, 83, 84 and 87.)
- H. M. L. FAULKNER AND J. M. RODENBURG. Error tolerance of an iterative phase retrieval algorithm for moveable illumination microscopy. *Ultramicroscopy*, 103(2):153–164, 2005. doi:10.1016/j.ultramic.2004.11.006. (Cited on pages 76, 84, 86 and 87.)
- A. FEHRINGER. *Advanced Algorithms for Ptychographic X-Ray Computed Tomography*. Diplom thesis, Technische Universität München, 2011. (Cited on page 293.)
- M. FERNÁNDEZ, J. KEYRILÄINEN, R. SERIMAA, M. TORKKELI, M. L. KARJALAINEN-LINDSBERG, M. TENHUNEN, W. THOMLINSON, V. URBAN, AND P. SUORTTI. Small-angle x-ray scattering studies of human breast tissue samples. *Physics in Medicine and Biology*, 47(4):577–92, 2002. doi:10.1088/0031-9155/47/4/303. (Cited on page 276.)
- M. FESER, J. GELB, H. CHANG, H. CUI, F. DUEWER, S. H. LAU, A. TKACHUK, AND W. YUN. Sub-micron resolution CT for failure analysis and process development. *Measurement Science and Technology*, 19(9):94001, 2008. doi:10.1088/0957-0233/19/9/094001. (Cited on pages 23 and 266.)
- M. FESER, C. JACOBSEN, P. REHAK, AND G. DEGERONIMO. Scanning transmission X-ray microscopy with a segmented detector. *Journal de Physique IV*, 104:529–534, 2003. doi:10.1051/jp4:20030138. (Cited on page 41.)
- J. R. FIENUP. Reconstruction of an object from the modulus of its Fourier transform. *Optics Letters*, 3(1):27–29, 1978. doi:10.1364/OL.3.000027. (Cited on pages 60, 61 and 62.)
- J. R. FIENUP. Phase retrieval algorithms: a comparison. *Applied Optics*, 21(15):2758–2769, 1982. doi:10.1364/AO.21.002758. (Cited on pages 56, 61, 62, 63, 64, 67, 69, 71, 96 and 97.)

- J. R. FIENUP. Reconstruction of a complex-valued object from the modulus of its Fourier transform using a support constraint. *Journal of the Optical Society of America A*, 4(1):118–123, 1987. doi:10.1364/JOSAA.4.000118. (Cited on pages 63, 69 and 71.)
- J. R. FIENUP. Lensless coherent imaging by phase retrieval with an illumination pattern constraint. *Optics Express*, 14(2):498–508, 2006. doi:10.1364/OPEX.14.000498. (Cited on pages 56, 70 and 71.)
- J. R. FIENUP, T. R. CRIMMINS, AND W. HOLSZTYNSKI. Reconstruction of the support of an object from the support of its autocorrelation. *Journal of the Optical Society of America*, 72(5):610–624, 1982. doi:10.1364/JOSA.72.000610. (Cited on page 68.)
- J. R. FIENUP AND C. C. WACKERMAN. Phase-retrieval stagnation problems and solutions. *Journal of the Optical Society of America A*, 3(11):1897–1907, 1986. doi:10.1364/JOSAA.3.001897. (Cited on page 71.)
- J. FRANK AND B. F. MCEWEN. Alignment by Cross-Correlation. In J. FRANK (ed.), *Electron Tomography: Three-Dimensional Imaging with the Transmission Electron Microscope*, chap. 8. Plenum Press, New York, 1992. (Cited on page 250.)
- T. A. FRANZ-ODENDAAL, B. K. HALL, AND P. E. WITTEN. Buried alive: how osteoblasts become osteocytes. *Developmental Dynamics of Anatomists*, 235(1):176–190, 2006. doi:10.1002/dvdy.20603. (Cited on page 264.)
- P. FRATZL, H. S. GUPTA, E. P. PASCHALIS, AND P. ROSCHGER. Structure and mechanical quality of the collagen–mineral nanocomposite in bone. *Journal of Materials Chemistry*, 14(14):2115, 2004. doi:10.1039/b402005g. (Cited on page 285.)
- M. FUCHS, R. WEINGARTNER, A. POPP, Z. MAJOR, S. BECKER, J. OSTERHOFF, I. CORTRIE, B. ZEITLER, R. HÖRLEIN, G. D. TSAKIRIS, U. SCHRAMM, T. P. ROWLANDS-REES, S. M. HOOKER, D. HABS, F. KRAUSZ, S. KARSCH, AND F. GRÜNER. Laser-driven soft-X-ray undulator source. *Nature Physics*, 5(11):826–829, 2009. doi:10.1038/nphys1404. (Cited on page 23.)
- R. W. GERCHBERG AND W. O. SAXTON. A Practical Algorithm for Determination of Phase from Image and Diffraction Plane Pictures. *Optik*, 35(2):237–246, 1972. (Cited on pages 60, 61 and 96.)

- J.-M. GEUSEBROEK, A. W. M. SMEULDERS, AND J. VAN DE WEIJER. Fast anisotropic Gauss filtering. *IEEE Transactions on Image Processing*, 12(8):938–943, 2003. doi:10.1109/TIP.2003.812429. (Cited on page 311.)
- D. GHIGLIA AND M. PRITT. *Two-dimensional phase unwrapping: theory, algorithms, and software*. Wiley New York:, 1998. (Cited on pages 99, 247 and 249.)
- A. GIANONCELLI, G. R. MORRISON, B. KAULICH, D. BACESCU, AND J. KOVAC. Scanning transmission x-ray microscopy with a configurable detector. *Applied Physics Letters*, 89(25):251117, 2006. doi:10.1063/1.2422908. (Cited on page 41.)
- K. GIEWEKEMEYER. *A study on new approaches in coherent x-ray microscopy of biological specimens*. Göttingen Series in X-ray Physics. Universitätsverlag Göttingen, Göttingen, 2011. (Cited on page 28.)
- K. GIEWEKEMEYER, H. T. PHILIPP, R. N. WILKE, A. AQUILA, M. OSTERHOFF, M. W. TATE, K. S. SHANKS, A. V. ZOZULYA, T. SALDITT, S. M. GRUNER, AND A. P. MANCUSO. High-dynamic-range coherent diffractive imaging: ptychography using the mixed-mode pixel array detector. *Journal of Synchrotron Radiation*, 21:1167–1174, 2014. doi:10.1107/S1600577514013411. (Cited on page 329.)
- K. GIEWEKEMEYER, P. THIBAUT, S. KALBFLEISCH, A. BEERLINK, C. M. KEWISH, M. DIEROLF, F. PFEIFFER, AND T. SALDITT. Quantitative biological imaging by ptychographic x-ray diffraction microscopy. *Proceedings of the National Academy of Sciences of the United States of America*, 107(2):529–534, 2010. doi:10.1073/pnas.0905846107. (Cited on pages 76, 97, 110, 143, 165 and 282.)
- M. M. GIRAUD-GUILLE. Twisted plywood architecture of collagen fibrils in human compact bone osteons. *Calcified Tissue International*, 42(3):167–180, 1988. doi:10.1007/BF02556330. (Cited on pages 307, 308 and 314.)
- M. M. GIRAUD-GUILLE. Liquid crystalline order of biopolymers in cuticles and bones. *Microscopy Research and Technique*, 27(5):420–428, 1994. doi:10.1002/jemt.1070270508. (Cited on pages 307, 308 and 314.)
- P. GODARD, G. CARBONE, M. ALLAIN, F. MASTROPIETRO, G. CHEN, L. CAPELLO, A. DIAZ, T. METZGER, J. STANGL, AND V. CHAMARD. Three-dimensional high-resolution quantitative microscopy of extended crystals. *Nature Communications*, 2:568, 2011. doi:10.1038/ncomms1569. (Cited on page 332.)

- J. W. GOODMAN. *Introduction to Fourier Optics*. McGraw-Hill series in electrical and computer engineering. McGraw-Hill, 2 edn., 1996. (Cited on pages [17](#), [19](#), [20](#), [31](#), [36](#), [217](#) and [338](#).)
- H. GRAAFSMA. Requirements for and development of 2 dimensional X-ray detectors for the European X-ray Free Electron Laser in Hamburg. *Journal of Instrumentation*, 4(12):P12011, 2009. doi:[10.1088/1748-0221/4/12/P12011](#). (Cited on page [144](#).)
- S. M. GRUNER, D. BILDERBACK, I. BAZAROV, K. FINKELSTEIN, G. KRAFFT, L. MERMINGA, H. PADAMSEE, Q. SHEN, C. SINCLAIR, AND M. TIGNER. Energy recovery linacs as synchrotron radiation sources (invited). *Review of Scientific Instruments*, 73(3):1402–1406, 2002a. doi:[10.1063/1.1420754](#). (Cited on pages [142](#) and [330](#).)
- S. M. GRUNER, M. W. TATE, AND E. F. EIKENBERRY. Charge-coupled device area x-ray detectors. *Review of Scientific Instruments*, 73(8):2815–2842, 2002b. doi:[10.1063/1.1488674](#). (Cited on pages [21](#), [35](#) and [221](#).)
- M. GUIZAR-SICAIROS, A. DIAZ, M. HOLLER, M. S. LUCAS, A. MENZEL, R. A. WEPF, AND O. BUNK. Phase tomography from x-ray coherent diffractive imaging projections. *Optics Express*, 19(22):21345–21357, 2011. doi:[10.1364/OE.19.021345](#). (Cited on pages [98](#), [121](#), [122](#), [123](#), [243](#), [246](#), [247](#), [250](#), [252](#), [253](#), [273](#), [282](#), [292](#), [293](#), [327](#) and [333](#).)
- M. GUIZAR-SICAIROS AND J. R. FIENUP. Phase retrieval with transverse translation diversity: a nonlinear optimization approach. *Optics Express*, 16(10):7264–7278, 2008. doi:[10.1364/OE.16.007264](#). (Cited on pages [82](#), [91](#), [151](#) and [332](#).)
- M. GUIZAR-SICAIROS AND J. C. GUTIÉRREZ-VEGA. Computation of quasi-discrete Hankel transforms of integer order for propagating optical wave fields. *Journal of the Optical Society of America A*, 21(1):53–58, 2004. doi:[10.1364/JOSAA.21.000053](#). (Cited on page [339](#).)
- M. GUIZAR-SICAIROS, M. HOLLER, A. DIAZ, J. VILA-COMAMALA, O. BUNK, AND A. MENZEL. Role of the illumination spatial-frequency spectrum for ptychography. *Physical Review B*, 86(10):100103, 2012. doi:[10.1103/PhysRevB.86.100103](#). (Cited on pages [74](#), [82](#), [113](#), [143](#) and [156](#).)
- M. GUIZAR-SICAIROS, I. JOHNSON, A. DIAZ, M. HOLLER, P. KARVINEN, H.-C. STADLER, R. DINAPOLI, O. BUNK, AND A. MEN-

- ZEL. High-throughput ptychography using Eiger: scanning X-ray nano-imaging of extended regions. *Optics Express*, 22(12):14859–14870, 2014. doi:10.1364/OE.22.014859. (Cited on pages 145, 326 and 329.)
- M. GUIZAR-SICAIROS, S. T. THURMAN, AND J. R. FIENUP. Efficient sub-pixel image registration algorithms. *Optics Letters*, 33(2):156–158, 2008. doi:10.1364/OL.33.000156. (Cited on page 115.)
- H. S. GUPTA, J. SETO, W. WAGERMAIER, P. ZASLANSKY, P. BOESECKE, AND P. FRATZL. Cooperative deformation of mineral and collagen in bone at the nanoscale. *Proceedings of the National Academy of Sciences of the United States of America*, 103(47):17741–17746, 2006. doi:10.1073/pnas.0604237103. (Cited on page 290.)
- G. HARAUZ AND M. VAN HEEL. Exact filters for general geometry three dimensional reconstruction. *Optik*, 73(4):146–156, 1986. (Cited on page 115.)
- R. HEGERL AND W. HOPPE. Dynamische Theorie der Kristallstrukturanalyse durch Elektronenbeugung im inhomogenen Primärstrahlwellenfeld. *Berichte der Bunsen-Gesellschaft*, 74(11):1148–1154, 1970. doi:10.1002/bbpc.19700741112. (Cited on page 76.)
- R. HEGERL AND W. HOPPE. Influence of electron noise on three-dimensional image reconstruction. *Zeitschrift für Naturforschung Teil A*, 31(12):1717–1721, 1976. doi:10.1515/zna-1976-1241. (Cited on pages 273 and 277.)
- L. HELFEN, T. BAUMBACH, P. MIKULÍK, D. KIEL, P. PERNOT, P. CLOETENS, AND J. BARUCHEL. High-resolution three-dimensional imaging of flat objects by synchrotron-radiation computed laminography. *Applied Physics Letters*, 86(7):71915, 2005. doi:10.1063/1.1854735. (Cited on page 253.)
- S. W. HELL. Far-field optical nanoscopy. *Science*, 316(5828):1153–8, 2007. doi:10.1126/science.1137395. (Cited on pages 268 and 269.)
- R. HENDERSON. Cryo-Protection of Protein Crystals against Radiation Damage in Electron and X-Ray Diffraction. *Proceedings of the Royal Society B: Biological Sciences*, 241(1300):6–8, 1990. doi:10.1098/rspb.1990.0057. (Cited on page 155.)
- B. HENKE, E. GULLIKSON, AND J. DAVIS. X-Ray Interactions: Photoabsorption, Scattering, Transmission, and Reflection at $E = 50\text{--}30,000$ eV, $Z = 1\text{--}92$. *Atomic Data and Nuclear Data Tables*, 54(2):181–342, 1993.

- doi:10.1006/adnd.1993.1013. (Cited on pages 24, 172, 227, 229, 230, 257, 259, 277 and 302.)
- U. HEYEN AND D. SCHÜLER. Growth and magnetosome formation by microaerophilic *Magnetospirillum* strains in an oxygen-controlled fermentor. *Applied Microbiology and Biotechnology*, 61(5-6):536–544, 2003. doi:10.1007/s00253-002-1219-x. (Cited on page 165.)
- O. HIGNETTE, P. CLOETENS, G. ROSTAING, P. BERNARD, AND C. MORAWE. Efficient sub 100 nm focusing of hard x rays. *Review of Scientific Instruments*, 76(6):063709, 2005. doi:10.1063/1.1928191. (Cited on pages 29 and 138.)
- M. HOLLER, A. DIAZ, M. GUIZAR-SICAIROS, P. KARVINEN, E. FÄRM, E. HÄRKÖNEN, M. RITALA, A. MENZEL, J. RAABE, AND O. BUNK. X-ray ptychographic computed tomography at 16 nm isotropic 3D resolution. *Scientific Reports*, 4:3857, 2014. doi:10.1038/srep03857. (Cited on pages 151 and 329.)
- M. HOLLER, J. RAABE, A. DIAZ, M. GUIZAR-SICAIROS, C. QUITMANN, A. MENZEL, AND O. BUNK. An instrument for 3D x-ray nano-imaging. *Review of Scientific Instruments*, 83(7):073703, 2012. doi:10.1063/1.4737624. (Cited on pages 113, 137, 143 and 151.)
- J. M. HOLTON. A beginner’s guide to radiation damage. *Journal of Synchrotron Radiation*, 16(2):133–142, 2009. doi:10.1107/S0909049509004361. (Cited on pages 155 and 179.)
- J. M. HOLTON, C. NIELSEN, AND K. A. FRANKEL. The point-spread function of fiber-coupled area detectors. *Journal of Synchrotron Radiation*, 19(6):1006–1011, 2012. doi:10.1107/S0909049512035571. (Cited on pages 36, 141, 218 and 221.)
- C. HOLZNER, M. FESER, S. VOGT, B. HORNBERGER, S. B. BAINES, AND C. JACOBSEN. Zernike phase contrast in scanning microscopy with X-rays. *Nature Physics*, 6(11):883–887, 2010. doi:10.1038/nphys1765. (Cited on page 41.)
- H. HOPE. Cryocrystallography of biological macromolecules: a generally applicable method. *Acta Crystallographica Section B Structural Science*, 44(1):22–26, 1988. doi:10.1107/S0108768187008632. (Cited on page 155.)

- W. HOPPE. Beugung im inhomogenen Primärstrahlwellenfeld. I. Prinzip einer Phasenmessung von Elektronenbeugungsinterferenzen. *Acta Crystallographica Section A*, 25(4):495–501, 1969a. doi:10.1107/S0567739469001045. (Cited on pages 75 and 76.)
- W. HOPPE. Beugung im inhomogenen Primärstrahlwellenfeld. III. Amplituden- und Phasenbestimmung bei unperiodischen Objekten. *Acta Crystallographica Section A*, 25(4):508–514, 1969b. doi:10.1107/S0567739469001069. (Cited on page 76.)
- W. HOPPE. Trace structure analysis, ptychography, phase tomography. *Ultramicroscopy*, 10(3):187–198, 1982. doi:10.1016/0304-3991(82)90038-9. (Cited on page 76.)
- W. HOPPE AND G. STRUBE. Beugung in inhomogenen Primärstrahlwellenfeld. II. Lichtoptische Analogieversuche zur Phasenmessung von Gitterinterferenzen. *Acta Crystallographica Section A*, 25(4):502–507, 1969. doi:10.1107/S0567739469001057. (Cited on page 76.)
- B. HORNBERGER, M. D. DE JONGE, M. FESER, P. HOLL, C. HOLZNER, C. JACOBSEN, D. LEGNINI, D. PATERSON, P. REHAK, L. STRÜDER, AND S. VOGT. Differential phase contrast with a segmented detector in a scanning X-ray microprobe. *Journal of Synchrotron Radiation*, 15(4):355–362, 2008. doi:10.1107/S0909049508008509. (Cited on page 41.)
- P. HOROWITZ AND J. A. HOWELL. A Scanning X-Ray Microscope Using Synchrotron Radiation. *Science*, 178(4061):608–611, 1972. doi:10.1126/science.178.4061.608. (Cited on page 39.)
- M. HOWELLS, T. BEETZ, H. CHAPMAN, C. CUI, J. HOLTON, C. JACOBSEN, J. KIRZ, E. LIMA, S. MARCHESINI, H. MIAO, D. SAYRE, D. A. SHAPIRO, J. C. H. SPENCE, AND D. STARODUB. An assessment of the resolution limitation due to radiation-damage in x-ray diffraction microscopy. *Journal of Electron Spectroscopy and Related Phenomena*, 170(1-3):4–12, 2009. doi:10.1016/j.elspec.2008.10.008. (Cited on pages 172, 174, 276, 277, 278, 279 and 280.)
- K. HØYDALSVIK, J. B. FLØYSTAD, T. ZHAO, M. ESMAEILI, A. DIAZ, J. W. ANDREASEN, R. H. MATHIESEN, M. RØNNING, AND D. W. BREIBY. In situ X-ray ptychography imaging of high-temperature CO₂ acceptor particle agglomerates. *Applied Physics Letters*, 104(24):241909, 2014. doi:10.1063/1.4884598. (Cited on pages 328 and 330.)

- X. HUANG, J. NELSON, J. KIRZ, E. LIMA, S. MARCHESINI, H. MIAO, A. NEIMAN, D. SHAPIRO, J. STEINBRENER, A. STEWART, J. TURNER, AND C. JACOBSEN. Soft X-Ray Diffraction Microscopy of a Frozen Hydrated Yeast Cell. *Physical Review Letters*, 103(19):198101, 2009. doi:10.1103/PhysRevLett.103.198101. (Cited on pages 112, 156 and 282.)
- X. HUANG, H. YAN, R. HARDER, Y. HWU, I. K. ROBINSON, AND Y. S. CHU. Optimization of overlap uniformness for ptychography. *Optics Express*, 22(10):12634–12644, 2014. doi:10.1364/OE.22.012634. (Cited on page 326.)
- M. HUMPHRY, B. KRAUS, A. HURST, A. MAIDEN, AND J. RODENBURG. Ptychographic electron microscopy using high-angle dark-field scattering for sub-nanometre resolution imaging. *Nature Communications*, 3:730, 2012. doi:10.1038/ncomms1733. (Cited on page 331.)
- ICRU. *Report 44, Tissue Substitutes in Radiation Dosimetry and Measurement*. International Commission on Radiation Units and Measurements, Bethesda, MD, 1989. (Cited on pages 257, 259 and 263.)
- C. JACOBSEN, S. LINDAAS, S. WILLIAMS, AND X. ZHANG. Scanning luminescence X-ray microscopy: Imaging fluorescence dyes at suboptical resolution. *Journal of Microscopy*, 172(2):121–129, 1993. doi:10.1111/j.1365-2818.1993.tb03403.x. (Cited on page 41.)
- B. JÄHNE. *Digital image processing*. Springer-Verlag, Berlin, Heidelberg, New York, 5th rev. a edn., 2002. (Cited on page 17.)
- K. JEFIMOV, O. BUNK, F. PFEIFFER, D. GROLIMUND, J. F. VAN DER VEEN, AND C. DAVID. Fabrication of Fresnel zone plates for hard X-rays. *Microelectronic Engineering*, 84(5-8):1467–1470, 2007a. doi:10.1016/j.mee.2007.01.112. (Cited on page 32.)
- K. JEFIMOV, J. VILA-COMAMALA, T. PILVI, J. RAABE, M. RITALA, AND C. DAVID. Zone-Doubling Technique to Produce Ultrahigh-Resolution X-Ray Optics. *Physical Review Letters*, 99(26):264801, 2007b. doi:10.1103/PhysRevLett.99.264801. (Cited on pages 32 and 188.)
- T. H. JENSEN, M. BECH, O. BUNK, A. MENZEL, A. BOUCHET, G. LE DUC, R. FEIDENHANS'L, AND F. PFEIFFER. Molecular X-ray computed tomography of myelin in a rat brain. *NeuroImage*, 57(1):124–129, 2011. doi:10.1016/j.neuroimage.2011.04.013. (Cited on page 308.)

- K. J. JEPSEN, D. E. PENNINGTON, Y. L. LEE, M. WARMAN, AND J. NADEAU. Bone brittleness varies with genetic background in A/J and C57BL/6J inbred mice. *Journal of Bone and Mineral Research*, 16(10):1854–1862, 2001. doi:10.1359/jbmr.2001.16.10.1854. (Cited on pages 257, 259 and 262.)
- L. JOCHUM AND W. MEYER-ILSE. Partially coherent image formation with x-ray microscopes. *Applied Optics*, 34(22):4944–4950, 1995. doi:10.1364/AO.34.004944. (Cited on page 38.)
- I. JOHNSON, A. BERGAMASCHI, H. BILlich, S. CARTIER, R. DINAPOLI, D. GREIFFENBERG, M. GUIZAR-SICAIROS, B. HENRICH, J. JUNG-MANN, D. MEZZA, A. MOZZANICA, B. SCHMITT, X. SHI, AND G. TINTI. Eiger: a single-photon counting x-ray detector. *Journal of Instrumentation*, 9(05):C05032, 2014. doi:10.1088/1748-0221/9/05/C05032. (Cited on pages 145 and 329.)
- A. C. KAK AND M. SLANEY. *Principles of Computerized Tomographic Imaging*. IEEE Service Center, Piscataway, NJ, 1988. (Cited on pages 21, 117, 118, 119, 121 and 334.)
- H. KAMIOKA, T. HONJO, AND T. TAKANO-YAMAMOTO. A three-dimensional distribution of osteocyte processes revealed by the combination of confocal laser scanning microscopy and differential interference contrast microscopy. *Bone*, 28(2):145–149, 2001. doi:10.1016/S8756-3282(00)00421-X. (Cited on page 268.)
- H. C. KANG, J. MASER, G. B. STEPHENSON, C. LIU, R. CONLEY, A. T. MACRANDER, AND S. VOGT. Nanometer linear focusing of hard x rays by a multilayer Laue lens. *Physical Review Letters*, 96(12):127401, 2006. doi:10.1103/PhysRevLett.96.127401. (Cited on page 32.)
- S. KAPISHNIKOV, T. BERTHING, L. HVIID, M. DIEROLF, A. MENZEL, F. PFEIFFER, J. ALS-NIELSEN, AND L. LEISEROWITZ. Aligned hemozoin crystals in curved clusters in malarial red blood cells revealed by nanoprobe X-ray Fe fluorescence and diffraction. *Proceedings of the National Academy of Sciences of the United States of America*, 109(28):11184–11187, 2012. doi:10.1073/pnas.1118134109. (Cited on page 41.)
- M. KERSCHNITZKI. *Bone Material Characteristics Influenced by Osteocytes*. Ph.D. thesis, Humboldt-Universität, Berlin, 2012. (Cited on page 289.)

- M. KERSCHNITZKI, P. KOLLMANNBERGER, M. BURGHAMMER, G. N. DUDA, R. WEINKAMER, W. WAGERMAIER, AND P. FRATZL. Architecture of the osteocyte network correlates with bone material quality. *Journal of Bone and Mineral Research*, 28(8):1837–1845, 2013. doi:10.1002/jbmr.1927. (Cited on page 295.)
- M. KERSCHNITZKI, W. WAGERMAIER, P. ROSCHGER, J. SETO, R. SHARHAR, G. N. DUDA, S. MUNDLOS, AND P. FRATZL. The organization of the osteocyte network mirrors the extracellular matrix orientation in bone. *Journal of Structural Biology*, 173(2):303–11, 2011. doi:10.1016/j.jsb.2010.11.014. (Cited on pages 264, 268, 285, 289 and 310.)
- C. M. KEWISH, M. GUIZAR-SICAÍROS, C. LIU, J. QIAN, B. SHI, C. BENSON, A. M. KHOUNSARY, J. VILA-COMAMALA, O. BUNK, J. R. FIENUP, A. T. MACRANDER, AND L. ASSOUFID. Reconstruction of an astigmatic hard X-ray beam and alignment of K-B mirrors from ptychographic coherent diffraction data. *Optics Express*, 18(22):23420, 2010a. doi:10.1364/OE.18.023420. (Cited on pages 81, 143, 328 and 330.)
- C. M. KEWISH, P. THIBAUT, O. BUNK, AND F. PFEIFFER. The potential for two-dimensional crystallography of membrane proteins at future x-ray free-electron laser sources. *New Journal of Physics*, 12(3):035005, 2010b. doi:10.1088/1367-2630/12/3/035005. (Cited on pages 88, 142 and 330.)
- C. M. KEWISH, P. THIBAUT, M. DIEROLF, O. BUNK, A. MENZEL, J. VILA-COMAMALA, K. JEFIMOV, AND F. PFEIFFER. Ptychographic characterization of the wavefield in the focus of reflective hard X-ray optics. *Ultramicroscopy*, 110(4):325–329, 2010c. doi:10.1016/j.ultramic.2010.01.004. (Cited on pages 81, 143, 328 and 330.)
- P. KIRKPATRICK AND A. V. BAEZ. Formation of Optical Images by X-Rays. *Journal of the Optical Society of America*, 38(9):766–774, 1948. doi:10.1364/JOSA.38.000766. (Cited on page 29.)
- J. KIRZ, H. ADE, E. ANDERSON, D. ATTWOOD, C. BUCKLEY, S. HELLMAN, M. HOWELLS, C. JACOBSEN, D. KERN, S. LINDAAS, I. MCNULTY, M. OVERSLUIZEN, H. RARBACK, M. RIVERS, S. ROTHMAN, D. SAYRE, AND D. SHU. X-ray Microscopy with the NSLS Soft X-ray Undulator. *Physica Scripta*, T31:12–17, 1990. doi:10.1088/0031-8949/1990/T31/001. (Cited on pages 39, 40 and 325.)
- J. KIRZ AND C. JACOBSEN. The history and future of X-ray microscopy. *Journal of Physics: Conference Series*, 186:012001, 2009. doi:10.1088/1742-6596/186/1/012001. (Cited on page 37.)

- J. KIRZ, C. JACOBSEN, AND M. HOWELLS. Soft X-ray microscopes and their biological applications. *Quarterly Reviews of Biophysics*, 28(01):33–130, 1995. doi:10.1017/S0033583500003139. (Cited on pages 37 and 41.)
- J. KLEIN-NULEND, A. D. BAKKER, R. G. BACABAC, A. VATSA, AND S. WEINBAUM. Mechanosensation and transduction in osteocytes. *Bone*, 54(2):182–190, 2013. doi:10.1016/j.bone.2012.10.013. (Cited on pages 264 and 286.)
- J. KLEIN-NULEND, A. VAN DER PLAS, C. M. SEMEINS, N. E. AJUBI, J. A. FRANGOS, P. J. NIJWEIDE, AND E. H. BURGER. Sensitivity of osteocytes to biomechanical stress in vitro. *The FASEB Journal*, 9(5):441–445, 1995. doi:http://www.fasebj.org/content/9/5/441.abstract. (Cited on page 264.)
- G. F. KNOLL. *Radiation detection and measurement*. Wiley, New York, 3 edn., 2000. (Cited on pages 32, 34 and 130.)
- M. L. KNOTHE TATE, J. R. ADAMSON, A. E. TAMI, AND T. W. BAUER. The osteocyte. *The International Journal of Biochemistry & Cell Biology*, 36(1):1–8, 2004. doi:10.1016/S1357-2725(03)00241-3. (Cited on page 264.)
- C. KOTTLER, C. DAVID, F. PFEIFFER, AND O. BUNK. A two-directional approach for grating based differential phase contrast imaging using hard x-rays. *Optics Express*, 15(3):1175–1181, 2007. doi:10.1364/OE.15.001175. (Cited on page 44.)
- P. KRAFT, A. BERGAMASCHI, C. BROENNIMANN, R. DINAPOLI, E. F. EIKENBERRY, B. HENRICH, I. JOHNSON, A. MOZZANICA, C. M. SCHLEPÜTZ, P. R. WILLMOTT, AND B. SCHMITT. Performance of single-photon-counting PILATUS detector modules. *Journal of Synchrotron Radiation*, 16(3):368–375, 2009a. doi:10.1107/S0909049509009911. (Cited on pages 33, 34, 130, 144 and 146.)
- P. KRAFT, A. BERGAMASCHI, C. BRONNIMANN, R. DINAPOLI, E. F. EIKENBERRY, H. GRAAFSMA, B. HENRICH, I. JOHNSON, M. KOBAS, A. MOZZANICA, C. M. SCHLEPUTZ, AND B. SCHMITT. Characterization and Calibration of PILATUS Detectors. *IEEE Transactions on Nuclear Science*, 56(3):758–764, 2009b. doi:10.1109/TNS.2008.2009448. (Cited on pages 130, 144, 145 and 146.)
- D. KUNDUR AND D. HATZINAKOS. Blind image deconvolution. *IEEE Signal Processing Magazine*, 13(3):43–64, 1996. doi:10.1109/79.489268. (Cited on pages 81 and 224.)

- J.-C. LABICHE, O. MATHON, S. PASCARELLI, M. A. NEWTON, G. G. FERRE, C. CURFS, G. VAUGHAN, A. HOMS, AND D. F. CARREIRAS. Invited article: The fast readout low noise camera as a versatile x-ray detector for time resolved dispersive extended x-ray absorption fine structure and diffraction studies of dynamic problems in materials science, chemistry, and catalysis. *Review of Scientific Instruments*, 78(9):091301, 2007. doi:10.1063/1.2783112. (Cited on pages 141 and 204.)
- J. L. LACLARE. Target Specifications and Performance of the ESRF Source. *Journal of Synchrotron radiation*, 1(1):12–18, 1994. doi:10.1107/S0909049594006564. (Cited on page 137.)
- M. LANGER, A. PACUREANU, H. SUHONEN, Q. GRIMAL, P. CLOETENS, AND F. PEYRIN. X-ray phase nanotomography resolves the 3D human bone ultrastructure. *PloS One*, 7(8):e35691, 2012. doi:10.1371/journal.pone.0035691. (Cited on page 309.)
- C. A. LARABELL AND K. A. NUGENT. Imaging cellular architecture with X-rays. *Current Opinion in Structural Biology*, 20(5):623–631, 2010. doi:10.1016/j.sbi.2010.08.008. (Cited on page 38.)
- W. LAUTERBORN AND T. KURZ. *Coherent Optics: Fundamentals and Applications*. Advanced Texts in Physics. Springer Berlin Heidelberg, Berlin, Heidelberg, 2003. doi:10.1007/978-3-662-05273-0. (Cited on pages 25 and 52.)
- M. C. LAWRENCE. Least-Squares Method for Alignment Using Markers. In J. FRANK (ed.), *Electron Tomography: Three-Dimensional Imaging with the Transmission Electron Microscope*, chap. 8. Plenum Press, New York, 1992. (Cited on page 250.)
- M. A. LE GROS, G. MCDERMOTT, AND C. A. LARABELL. X-ray tomography of whole cells. *Current Opinion in Structural Biology*, 15(5):593–600, 2005. doi:10.1016/j.sbi.2005.08.008. (Cited on page 156.)
- H. LIM, W. XU, AND X. HUANG. Two new practical methods for phase unwrapping. In *1995 International Geoscience and Remote Sensing Symposium IGARSS 95 Quantitative Remote Sensing for Science and Applications*, vol. 1, pp. 196–198. IEEE, 1995. doi:10.1109/IGARSS.1995.519688. (Cited on page 249.)
- E. LIMA, A. DIAZ, M. GUIZAR-SICAIROS, S. GORELICK, P. PERNOT, T. SCHLEIER, AND A. MENZEL. Cryo-scanning x-ray diffraction mi-

- croscopy of frozen-hydrated yeast. *Journal of Microscopy*, 249(1):1–7, 2013. doi:10.1111/j.1365-2818.2012.03682.x. (Cited on page 156.)
- E. LIMA, L. WIEGART, P. PERNOT, M. HOWELLS, J. TIMMINS, F. ZONTONE, AND A. MADSEN. Cryogenic X-Ray Diffraction Microscopy for Biological Samples. *Physical Review Letters*, 103(19):198102, 2009. doi:10.1103/PhysRevLett.103.198102. (Cited on pages 156 and 282.)
- E. H. LINFOOT. *Fourier methods in optical image evaluation*. The Focal library. Focal Press, London, New York, 1964. (Cited on page 85.)
- B. G. LOWE AND R. A. SAREEN. *Semiconductor X-Ray Detectors*. Series in Sensors. CRC Press, Taylor & Francis Group, Boca Raton, 2013. (Cited on page 32.)
- D. R. LUKE. Relaxed averaged alternating reflections for diffraction imaging. *Inverse Problems*, 21(1):37–50, 2005. doi:10.1088/0266-5611/21/1/004. (Cited on pages 64, 67 and 68.)
- D. R. LUKE, J. V. BURKE, AND R. G. LYON. Optical wavefront reconstruction: theory and numerical methods. *SIAM Review*, 44(2):169–224, 2002. doi:10.1137/S003614450139075. (Cited on page 56.)
- F. R. N. C. MAIA, T. EKEBERG, D. VAN DER SPOEL, AND J. HAJDU. Hawk: The image reconstruction package for coherent X-ray diffractive imaging. *Journal of Applied Crystallography*, 43:1535–1539, 2010. doi:10.1107/S0021889810036083. (Cited on page 65.)
- A. M. MAIDEN, M. J. HUMPHRY, AND J. M. RODENBURG. Ptychographic transmission microscopy in three dimensions using a multi-slice approach. *Journal of the Optical Society of America A*, 29(8):1606–1614, 2012a. doi:10.1364/JOSAA.29.001606. (Cited on page 332.)
- A. M. MAIDEN, M. J. HUMPHRY, M. C. SARAHAN, B. KRAUS, AND J. M. RODENBURG. An annealing algorithm to correct positioning errors in ptychography. *Ultramicroscopy*, 120:64–72, 2012b. doi:10.1016/j.ultramic.2012.06.001. (Cited on pages 151 and 332.)
- A. M. MAIDEN, M. J. HUMPHRY, F. ZHANG, AND J. M. RODENBURG. Superresolution imaging via ptychography. *Journal of the Optical Society of America A*, 28(4):604–612, 2011. (Cited on page 332.)
- A. M. MAIDEN AND J. M. RODENBURG. An improved ptychographical phase retrieval algorithm for diffractive imaging. *Ultramicroscopy*,

- 109(10):1256–1262, 2009. doi:10.1016/j.ultramic.2009.05.012. (Cited on pages 82, 90 and 91.)
- L. MANDEL AND E. WOLF. Coherence Properties of Optical Fields. *Reviews of Modern Physics*, 37(2):231–287, 1965. doi:10.1103/RevModPhys.37.231. (Cited on pages 46 and 47.)
- S. MARCHESINI. A unified evaluation of iterative projection algorithms for phase retrieval. *Review of Scientific Instruments*, 78(1):011301, 2007. doi:10.1063/1.2403783. (Cited on pages 56, 64, 65 and 67.)
- S. MARCHESINI, H. N. CHAPMAN, A. BARTY, M. R. HOWELLS, J. C. H. SPENCE, C. CUI, U. WEIERSTALL, AND A. MINOR. Phase aberrations in diffraction microscopy. *Proceedings of the 8th International Conference on X-ray Microscopy, Himeji, Japan: IPAP*, pp. 380–382, 2006. doi:http://arxiv.org/abs/physics/0510033. (Cited on page 164.)
- S. MARCHESINI, H. HE, H. N. CHAPMAN, S. P. HAU-RIEGE, A. NOY, M. R. HOWELLS, U. WEIERSTALL, AND J. C. H. SPENCE. X-ray image reconstruction from a diffraction pattern alone. *Physical Review B*, 68(14):140101, 2003. doi:10.1103/PhysRevB.68.140101. (Cited on pages 63, 69 and 111.)
- G. W. MARSHALL, S. J. MARSHALL, J. H. KINNEY, AND M. BALOOCH. The dentin substrate: structure and properties related to bonding. *Journal of Dentistry*, 25(6):441–458, 1997. doi:10.1016/S0300-5712(96)00065-6. (Cited on pages 307 and 308.)
- G. MARTÍNEZ-CRIADO, R. TUCOULOU, P. CLOETENS, P. BLEUET, S. BOHIC, J. CAUZID, I. KIEFFER, E. KOSIOR, S. LABOURÉ, S. PETITGIRARD, A. RACK, J. A. SANS, J. SEGURA-RUIZ, H. SUHONEN, J. SUSINI, AND J. VILLANOVA. Status of the hard X-ray microprobe beamline ID22 of the European Synchrotron Radiation Facility. *Journal of Synchrotron Radiation*, 19(1):10–18, 2012. doi:10.1107/S090904951104249X. (Cited on pages 30, 39 and 138.)
- J. MASER, A. OSANNA, Y. WANG, C. JACOBSEN, J. KIRZ, S. SPECTOR, B. WINN, AND D. TENNANT. Soft X-ray microscopy with a cryo scanning transmission X-ray microscope: I. Instrumentation, imaging and spectroscopy. *Journal of Microscopy*, 197(1):68–79, 2000. doi:10.1046/j.1365-2818.2000.00630.x. (Cited on page 156.)
- MATLAB. *Image Processing Toolbox Reference R2012b*. The Mathworks Inc., Natick, 2012a. (Cited on pages 121 and 224.)

-
- MATLAB. *Image Processing Toolbox User's Guide R2012b*. The Mathworks Inc., Natick, 2012b. (Cited on pages 121, 122 and 224.)
- MATLAB. *Optimization Toolbox User's Guide R2012b*. The Mathworks Inc., Natick, 2012c. (Cited on pages 213, 219 and 227.)
- B. C. MCCALLUM AND J. M. RODENBURG. Two-dimensional demonstration of Wigner phase-retrieval microscopy in the STEM configuration. *Ultramicroscopy*, 45(3-4):371–380, 1992. doi:10.1016/0304-3991(92)90149-E. (Cited on pages 79 and 80.)
- B. C. MCCALLUM AND J. M. RODENBURG. Simultaneous reconstruction of object and aperture functions from multiple far-field intensity measurements. *Journal of the Optical Society of America A*, 10(2):231–239, 1993. doi:10.1364/JOSAA.10.000231. (Cited on page 81.)
- A. MEENTS, S. GUTMANN, A. WAGNER, AND C. SCHULZE-BRIESE. Origin and temperature dependence of radiation damage in biological samples at cryogenic temperatures. *Proceedings of the National Academy of Sciences of the United States of America*, 107(3):1094–1099, 2010. doi:10.1073/pnas.09054811107. (Cited on page 155.)
- A. MENZEL, C. M. KEWISH, P. KRAFT, B. HENRICH, K. JEFIMOV, J. VILA-COMAMALA, C. DAVID, M. DIEROLF, P. THIBAUT, F. PFEIFFER, AND O. BUNK. Scanning transmission X-ray microscopy with a fast framing pixel detector. *Ultramicroscopy*, 110(9):1143–1147, 2010. doi:10.1016/j.ultramic.2010.04.007. (Cited on pages 41, 44 and 241.)
- K. MEYBERG AND P. VACHENAUER. *Höhere Mathematik*, vol. 2 of *Springer-Lehrbuch*. Springer, Berlin ; Heidelberg [u.a.], 3. rev. edn., 1999. (Cited on pages 18 and 339.)
- J. MIAO, K. O. HODGSON, T. ISHIKAWA, C. A. LARABELL, M. A. LEGROS, AND Y. NISHINO. Imaging whole *Escherichia coli* bacteria by using single-particle x-ray diffraction. *Proceedings of the National Academy of Sciences of the United States of America*, 100(1):110–112, 2003. doi:10.1073/pnas.232691299. (Cited on page 282.)
- J. MIAO AND D. SAYRE. On possible extensions of X-ray crystallography through diffraction-pattern oversampling. *Acta Crystallographica Section A*, 56(6):596–605, 2000. doi:10.1107/S010876730001031X. (Cited on page 55.)

- J. MIAO, D. SAYRE, AND H. N. CHAPMAN. Phase retrieval from the magnitude of the Fourier transforms of nonperiodic objects. *Journal of the Optical Society of America A*, 15(6):1662–1669, 1998. doi:10.1364/JOSAA.15.001662. (Cited on pages 46, 53, 54, 55 and 72.)
- J. W. MIAO, P. CHARALAMBOUS, J. KIRZ, AND D. SAYRE. Extending the methodology of X-ray crystallography to allow imaging of micrometre-sized non-crystalline specimens. *Nature*, 400(6742):342–344, 1999. doi:10.1038/22498. (Cited on pages 52 and 325.)
- H. MIMURA, S. HANDA, T. KIMURA, H. YUMOTO, D. YAMAKAWA, H. YOKOYAMA, S. MATSUYAMA, K. INAGAKI, K. YAMAMURA, Y. SANO, K. TAMASAKU, Y. NISHINO, M. YABASHI, T. ISHIKAWA, AND K. YAMAUCHI. Breaking the 10 nm barrier in hard-X-ray focusing. *Nature Physics*, 6(2):122–125, 2009. doi:10.1038/nphys1457. (Cited on page 30.)
- A. F. J. MOFFAT. A theoretical investigation of focal stellar images in the photographic emulsion and application to photographic photometry. *Astronomy and Astrophysics*, 3(4):455–461, 1969. (Cited on page 218.)
- R. MOKSO, P. CLOETENS, E. MAIRE, W. LUDWIG, AND J.-Y. BUFFIÈRE. Nanoscale zoom tomography with hard x rays using Kirkpatrick-Baez optics. *Applied Physics Letters*, 90(14):144104, 2007. doi:10.1063/1.2719653. (Cited on page 39.)
- J. MORENO AND F. FORRIOL. Effects of preservation on the mechanical strength and chemical composition of cortical bone: an experimental study in sheep femora. *Biomaterials*, 23(12):2615–2619, 2002. doi:10.1016/S0142-9612(01)00402-1. (Cited on page 305.)
- G. MORRISON, W. J. EATON, R. BARRETT, AND P. CHARALAMBOUS. STXM imaging with a configured detector. *Journal de Physique IV France*, 104:547–550, 2003. doi:10.1051/jp4:20030141. (Cited on page 41.)
- G. R. MORRISON AND M. T. BROWNE. Dark-field imaging with the scanning transmission x-ray microscope. *Review of Scientific Instruments*, 63(1):611–614, 1992. doi:10.1063/1.1143820. (Cited on page 42.)
- J. MURPHY, J. BENGTSSON, L. BERMAN, R. BISCARDI, L. CARR, W. CASEY, S. DIERKER, E. HAAS, R. HEESE, S. HULBERT, E. JOHNSON, C.-C. KAO, S. KRAMER, S. KRINSKY, I. PINAYEV, R. PINDAK, S. PJEROV, B. PODOBEDOV, G. RAKOWSKY, J. ROSE, T. SHAFTAN,

-
- B. SHEEHY, P. SIDDON, J. SKARITKA, N. TOWNE, J. M. WANG, X. J. WANG, AND L. H. YU. NSLS II: a Future Source for the NSLS. In *Proceedings of EPAC*, pp. 2457–2459. Lucerne, Switzerland, 2004. (Cited on page 330.)
- I. J. MYUNG. Tutorial on maximum likelihood estimation. *Journal of Mathematical Psychology*, 47(1):90–100, 2003. doi:10.1016/S0022-2496(02)00028-7. (Cited on page 101.)
- Y. S. G. NASHED, D. J. VINE, T. PETERKA, J. DENG, R. ROSS, AND C. JACOBSEN. Parallel ptychographic reconstruction. *Optics Express*, 22(26):32082–32097, 2014. doi:10.1364/OE.22.032082. (Cited on page 331.)
- P. D. NELLIST, B. C. MCCALLUM, AND J. M. RODENBURG. Resolution beyond the ‘information limit’ in transmission electron microscopy. *Nature*, 374(6523):630–632, 1995. doi:10.1038/374630a0. (Cited on pages 76 and 78.)
- J. NELSON, X. HUANG, J. STEINBRENER, D. SHAPIRO, J. KIRZ, S. MARCHESINI, A. M. NEIMAN, J. J. TURNER, AND C. JACOBSEN. High-resolution x-ray diffraction microscopy of specifically labeled yeast cells. *Proceedings of the National Academy of Sciences of the United States of America*, 107(16):7235–7239, 2010. doi:10.1073/pnas.0910874107. (Cited on page 282.)
- U. NEUHÄUSLER, G. SCHNEIDER, W. LUDWIG, M. A. MEYER, E. ZSCHECH, AND D. HAMBACH. X-ray microscopy in Zernike phase contrast mode at 4 keV photon energy with 60 nm resolution. *Journal of Physics D: Applied Physics*, 36(10A):A79–A82, 2003. doi:10.1088/0022-3727/36/10A/316. (Cited on page 38.)
- R. NEUTZE, R. WOUTS, D. VAN DER SPOEL, E. WECKERT, AND J. HAJDU. Potential for biomolecular imaging with femtosecond X-ray pulses. *Nature*, 406(6797):752–7, 2000. doi:10.1038/35021099. (Cited on page 279.)
- S. NICKELL, F. FÖRSTER, A. LINAROUDIS, W. D. NET, F. BECK, R. HEGERL, W. BAUMEISTER, AND J. M. PLITZKO. TOM software toolbox: acquisition and analysis for electron tomography. *Journal of Structural Biology*, 149(3):227–234, 2005. doi:10.1016/j.jsb.2004.10.006. (Cited on page 250.)

- B. NIEMANN, D. RUDOLPH, AND G. SCHMAHL. X-ray microscopy with synchrotron radiation. *Applied Optics*, 15(8):1883–1884, 1976. doi:10.1364/AO.15.001883. (Cited on page 37.)
- Y. NISHINO, Y. TAKAHASHI, N. IMAMOTO, T. ISHIKAWA, AND K. MAESHIMA. Three-dimensional visualization of a human chromosome using coherent x-ray diffraction. *Physical Review Letters*, 102(1):018101, 2009. doi:10.1103/PhysRevLett.102.018101. (Cited on pages 280 and 282.)
- K. A. NUGENT, A. G. PEELE, H. N. CHAPMAN, AND A. P. MANCUSO. Unique phase recovery for nonperiodic objects. *Physical Review Letters*, 91(20):203902, 2003. doi:10.1103/PhysRevLett.91.203902. (Cited on page 73.)
- K. A. NUGENT, A. G. PEELE, H. M. QUINEY, AND H. N. CHAPMAN. Diffraction with wavefront curvature: a path to unique phase recovery. *Acta Crystallographica Section A*, 61(3):373–381, 2005. doi:10.1107/S010876730501055X. (Cited on page 73.)
- T. OMOKANWAYE, O. WILSON, H. IRAVANI, AND P. KARIYAWASAM. Extraction and Characterization of a Soluble Chicken Bone Collagen. In K. E. HEROLD, J. VOSSOUGH, AND W. E. BENTLEY (eds.), *26th Southern Biomedical Engineering Conference 2010 (SBEC 2010)*, vol. 32 of *IFMBE Proceedings*, pp. 520–523. Springer Berlin Heidelberg, 2010. doi:10.1007/978-3-642-14998-6_133. (Cited on pages 277 and 302.)
- E. L. O’NEILL. *Introduction to statistical optics*. Dover Publ., Mineola, N.Y., reissued edn., 2003. (Cited on page 113.)
- T. OVERSLUIZEN, W. STOEBER, AND E. D. JOHNSON. Kinematic mounting systems for National Synchrotron Light Source beamlines and experiments. *Review of Scientific Instruments*, 63(1):1285–1288, 1992. doi:10.1063/1.1143101. (Cited on page 152.)
- R. L. OWEN, A. R. PEARSON, A. MEENTS, P. BOEHLER, V. THOMINET, AND C. SCHULZE-BRIESE. A new on-axis multimode spectrometer for the macromolecular crystallography beamlines of the Swiss Light Source. *Journal of Synchrotron Radiation*, 16(2):173–182, 2009. doi:10.1107/S0909049508040120. (Cited on page 157.)
- A. PACUREANU, M. LANGER, E. BOLLER, P. TAFFOREAU, AND F. PEYRIN. Nanoscale imaging of the bone cell network with synchrotron X-ray tomography: optimization of acquisition setup. *Medical Physics*,

- 39(4):2229–2238, 2012. doi:10.1118/1.3697525. (Cited on pages 266 and 270.)
- D. M. PAGANIN. *Coherent X-Ray Optics*. Oxford Series on Synchrotron Radiation. Oxford University Press, Oxford, 2006. doi:10.1093/acprof:oso/9780198567288.001.0001. (Cited on pages 25, 28 and 32.)
- A. M. PARFITT. The cellular basis of bone turnover and bone loss: a rebuttal of the osteocytic resorption–bone flow theory. *Clinical Orthopaedics and Related Research*, 127:236–247, 1977. (Cited on pages 287 and 288.)
- D. Y. PARKINSON, G. MCDERMOTT, L. D. ETKIN, M. A. LE GROS, AND C. A. LARABELL. Quantitative 3-D imaging of eukaryotic cells using soft X-ray tomography. *Journal of Structural Biology*, 162(3):380–386, 2008. doi:10.1016/j.jsb.2008.02.003. (Cited on page 156.)
- A. I. PEARCE, R. G. RICHARDS, S. MILZ, E. SCHNEIDER, AND S. G. PEARCE. Animal models for implant biomaterial research in bone: a review. *European Cells & Materials*, 13:1–10, 2007. (Cited on page 305.)
- A. G. PEELE, K. A. NUGENT, A. P. MANCUSO, D. PATERSON, I. MCNULTY, AND J. P. HAYES. X-ray phase vortices: theory and experiment. *Journal of the Optical Society of America A*, 21(8):1575–1584, 2004. doi:10.1364/JOSAA.21.001575. (Cited on page 67.)
- P. M. PELZ, M. GUIZAR-SICAIROS, P. THIBAUT, I. JOHNSON, M. HOLLER, AND A. MENZEL. On-the-fly scans for X-ray ptychography. *Applied Physics Letters*, 105(25):251101, 2014. doi:10.1063/1.4904943. (Cited on pages 148 and 331.)
- P. PERONA AND J. MALIK. Scale-space and edge detection using anisotropic diffusion. *IEEE Transactions on Pattern Analysis and Machine Intelligence*, 12(7):629–639, 1990. doi:10.1109/34.56205. (Cited on page 299.)
- F. PEYRIN. Investigation of bone with synchrotron radiation imaging: from micro to nano. *Osteoporosis International*, 20(6):1057–1063, 2009. doi:10.1007/s00198-009-0855-8. (Cited on page 266.)
- F. PFEIFFER, C. KOTTLER, O. BUNK, AND C. DAVID. Hard X-Ray Phase Tomography with Low-Brilliance Sources. *Physical Review Letters*, 98(10):108105, 2007. doi:10.1103/PhysRevLett.98.108105. (Cited on pages 123 and 241.)

- V. PIAZZA, B. WEINHAUSEN, A. DIAZ, C. DAMMANN, C. MAURER, M. REYNOLDS, M. BURGHAMMER, AND S. KÖSTER. Revealing the Structure of Stereociliary Actin by X-ray Nanoimaging. *ACS Nano*, 8(12):12228–12237, 2014. doi:10.1021/nm5041526. (Cited on page 328.)
- T. A. PITTS AND J. F. GREENLEAF. Fresnel transform phase retrieval from magnitude. *IEEE Transactions on Ultrasonics, Ferroelectrics, and Frequency Control*, 50(8):1035–1045, 2003. doi:10.1109/TUFFC.2003.1226547. (Cited on page 73.)
- V. PODRAZKÝ AND V. SEDMEROVÁ. Densities of collagen dehydrated by some organic solvents. *Cellular and Molecular Life Sciences*, 22(12):792, 1966. doi:10.1007/BF01897416. (Cited on pages 277 and 302.)
- C. PONCHUT. Characterization of X-ray area detectors for synchrotron beamlines. *Journal of Synchrotron Radiation*, 13(2):195–203, 2006. doi:10.1107/S0909049505034278. (Cited on pages 141, 145, 208, 215 and 221.)
- C. PONCHUT, J. M. RIGAL, J. CLÉMENT, E. PAPILLON, A. HOMS, AND S. PETITDEMANGE. MAXIPIX, a fast readout photon-counting X-ray area detector for synchrotron applications. *Journal of Instrumentation*, 6(01):C01069–C01069, 2011. doi:10.1088/1748-0221/6/01/C01069. (Cited on pages 144, 146 and 232.)
- G. POROD. Die Röntgenkleinwinkelstreuung von dichtgepackten kolloiden Systemen. *Kolloid-Zeitschrift*, 124(2):83–114, 1951. doi:10.1007/BF01512792. (Cited on page 145.)
- C. T. PUTKUNZ, A. J. D’ALFONSO, A. J. MORGAN, M. WEYLAND, C. DWYER, L. BOURGEOIS, J. ETHERIDGE, A. ROBERTS, R. E. SCHOLTEN, K. A. NUGENT, AND L. J. ALLEN. Atom-Scale Ptychographic Electron Diffractive Imaging of Boron Nitride Cones. *Physical Review Letters*, 108(7):073901, 2012. doi:10.1103/PhysRevLett.108.073901. (Cited on page 331.)
- H. QING, L. ARDESHIRPOUR, P. D. PAJEVIC, V. DUSEVICH, K. JÄHN, S. KATO, J. WYSOLMERSKI, AND L. F. BONEWALD. Demonstration of osteocytic perilacunar/canalicular remodeling in mice during lactation. *Journal of Bone and Mineral Research*, 27(5):1018–1029, 2012. doi:10.1002/jbmr.1567. (Cited on page 288.)

- H. QING AND L. F. BONEWALD. Osteocyte Remodeling of the Perilacunar and Pericanalicular Matrix. *International Journal of Oral Science*, 1(2):59–65, 2009. doi:10.4248/ijos.09019. (Cited on pages 287 and 288.)
- H. M. QUINEY, K. A. NUGENT, AND A. G. PEELE. Iterative image reconstruction algorithms using wave-front intensity and phase variation. *Optics Letters*, 30(13):1638–1640, 2005. doi:10.1364/OL.30.001638. (Cited on pages 56 and 73.)
- H. M. QUINEY, A. G. PEELE, Z. CAI, D. PATERSON, AND K. A. NUGENT. Diffractive imaging of highly focused X-ray fields. *Nature Physics*, 2(2):101–104, 2006. doi:10.1038/nphys218. (Cited on pages 73 and 89.)
- M. RABBANI, R. SHAW, AND R. VAN METTER. Detective quantum efficiency of imaging systems with amplifying and scattering mechanisms. *Journal of the Optical Society of America A*, 4(5):895–901, 1987. doi:10.1364/JOSAA.4.000895. (Cited on page 35.)
- V. RADICCI, A. BERGAMASCHI, R. DINAPOLI, D. GREIFFENBERG, B. HENRICH, I. JOHNSON, A. MOZZANICA, B. SCHMITT, AND X. SHI. EIGER a new single photon counting detector for X-ray applications: performance of the chip. *Journal of Instrumentation*, 7(02):C02019, 2012. doi:10.1088/1748-0221/7/02/C02019. (Cited on pages 144, 145, 146 and 329.)
- H. RARBACK, D. SHU, S. C. FENG, H. ADE, J. KIRZ, I. MCNULTY, D. P. KERN, T. H. P. CHANG, Y. VLADIMIRSKY, N. ISKANDER, D. ATTWOOD, K. MCQUAID, AND S. ROTHMAN. Scanning x-ray microscope with 75-nm resolution. *Review of Scientific Instruments*, 59(1):52–59, 1988. doi:10.1063/1.1139965. (Cited on page 39.)
- C. RAU, V. CRECEA, W. LIU, C.-P. RICHTER, K. PETERSON, P. JEMIAN, U. NEUHÄUSLER, G. SCHNEIDER, X. YU, P. BRAUN, T.-C. CHIANG, AND I. ROBINSON. Synchrotron-based imaging and tomography with hard X-rays. *Nuclear Instruments and Methods in Physics Research Section B*, 261(1-2):850–854, 2007. doi:10.1016/j.nimb.2007.03.053. (Cited on page 202.)
- A. RAVAGLIOLI, A. KRAJEWSKI, G. CELOTTI, A. PIANCASTELLI, B. BACCHINI, L. MONTANARI, G. ZAMA, AND L. PIOMBI. Mineral evolution of bone. *Biomaterials*, 17(6):617–622, 1996. doi:10.1016/0142-9612(96)88712-6. (Cited on page 305.)

- S. REHBEIN, S. HEIM, P. GUTTMANN, S. WERNER, AND G. SCHNEIDER. Ultrahigh-Resolution Soft-X-Ray Microscopy with Zone Plates in High Orders of Diffraction. *Physical Review Letters*, 103(11):110801, 2009. doi:10.1103/PhysRevLett.103.110801. (Cited on page 37.)
- N. REZNIKOV, R. ALMANY-MAGAL, R. SHAHAR, AND S. WEINER. Three-dimensional imaging of collagen fibril organization in rat circumferential lamellar bone using a dual beam electron microscope reveals ordered and disordered sub-lamellar structures. *Bone*, 52(2):676–683, 2013. doi:10.1016/j.bone.2012.10.034. (Cited on pages 308 and 314.)
- N. REZNIKOV, R. SHAHAR, AND S. WEINER. Three-dimensional structure of human lamellar bone: The presence of two different materials and new insights into the hierarchical organization. *Bone*, 59:93–104, 2014. doi:10.1016/j.bone.2013.10.023. (Cited on page 308.)
- J.-Y. RHO, L. KUHN-SPEARING, AND P. ZIOUPOS. Mechanical properties and the hierarchical structure of bone. *Medical Engineering & Physics*, 20(2):92–102, 1998. doi:10.1016/S1350-4533(98)00007-1. (Cited on page 307.)
- A. RIGAL AND W. VIGNAL. Recherches experimentales sur la formation du cal et sur les modifications des tissus dans les pseudoarthroses. *Arch Physiol*, 8:419–458, 1881. (Cited on page 287.)
- S. RINNERTHALER, P. ROSCHGER, H. F. JAKOB, A. NADER, K. KLAUSHOFER, AND P. FRATZL. Scanning Small Angle X-ray Scattering Analysis of Human Bone Sections. *Calcified Tissue International*, 64(5):422–429, 1999. doi:10.1007/PL00005824. (Cited on pages 308 and 310.)
- M. L. RIVERS, S. R. SUTTON, AND K. W. JONES. Synchrotron X-ray fluorescence microscopy. *Synchrotron Radiation News*, 4(2):23–26, 1991. doi:10.1080/08940889108602607. (Cited on page 41.)
- A.-L. ROBISCH AND T. SALDITT. Phase retrieval for object and probe using a series of defocus near-field images. *Optics Express*, 21(20):23345–23357, 2013. doi:10.1364/OE.21.023345. (Cited on page 332.)
- J. M. RODENBURG. Ptychography and related diffractive imaging methods. In P. W. HAWKES (ed.), *Advances in Imaging and Electron Physics*, vol. 150 of *Advances in Imaging and Electron Physics*, pp. 87–184. Elsevier, 2008. doi:10.1016/S1076-5670(07)00003-1. (Cited on pages 75, 76, 77, 78, 79, 81 and 84.)

- J. M. RODENBURG AND R. H. T. BATES. The Theory of Super-Resolution Electron Microscopy Via Wigner-Distribution Deconvolution. *Philosophical Transactions of the Royal Society A*, 339(1655):521–553, 1992. doi:10.1098/rsta.1992.0050. (Cited on pages 78, 79 and 81.)
- J. M. RODENBURG AND H. M. L. FAULKNER. A phase retrieval algorithm for shifting illumination. *Applied Physics Letters*, 85(20):4795–4797, 2004. doi:10.1063/1.1823034. (Cited on pages 84, 86 and 87.)
- J. M. RODENBURG, A. C. HURST, AND A. G. CULLIS. Transmission microscopy without lenses for objects of unlimited size. *Ultramicroscopy*, 107(2-3):227–231, 2007a. doi:10.1016/j.ultramic.2006.07.007. (Cited on pages 84, 85, 86, 88 and 143.)
- J. M. RODENBURG, A. C. HURST, A. G. CULLIS, B. R. DOBSON, F. PFEIFFER, O. BUNK, C. DAVID, K. JEFIMOV, AND I. JOHNSON. Hard-X-Ray Lensless Imaging of Extended Objects. *Physical Review Letters*, 98(3):034801, 2007b. doi:10.1103/PhysRevLett.98.034801. (Cited on pages 83, 88, 143 and 325.)
- J. M. RODENBURG, B. C. MCCALLUM, AND P. D. NELLIST. Experimental tests on double-resolution coherent imaging via STEM. *Ultramicroscopy*, 48(3):304–314, 1993. doi:10.1016/0304-3991(93)90105-7. (Cited on page 80.)
- G. D. ROODMAN. Advances in Bone Biology: The Osteoclast. *Endocrine Reviews*, 17(4):308–332, 1996. doi:10.1210/edrv-17-4-308. (Cited on page 289.)
- P. ROSCHGER, P. FRATZL, J. ESCHBERGER, AND K. KLAUSHOFER. Validation of quantitative backscattered electron imaging for the measurement of mineral density distribution in human bone biopsies. *Bone*, 23(4):319–326, 1998. doi:10.1016/S8756-3282(98)00112-4. (Cited on page 304.)
- P. ROSCHGER, E. P. PASCHALIS, P. FRATZL, AND K. KLAUSHOFER. Bone mineralization density distribution in health and disease. *Bone*, 42(3):456–466, 2008. doi:10.1016/j.bone.2007.10.021. (Cited on page 305.)
- A. ROSE. The sensitivity performance of the human eye on an absolute scale. *Journal of the Optical Society of America*, 38(2):196–208, 1948. doi:10.1364/JOSA.38.000196. (Cited on page 277.)

- A. SAKDINAWAT AND D. ATTWOOD. Nanoscale X-ray imaging. *Nature Photonics*, 4(12):840–848, 2010. doi:10.1038/nphoton.2010.267. (Cited on page 37.)
- A. R. SANDY, L. B. LURIO, S. G. J. MOCHRIE, A. MALIK, G. B. STEPHENSON, J. F. PELLETIER, AND M. SUTTON. Design and characterization of an undulator beamline optimized for small-angle coherent X-ray scattering at the Advanced Photon Source. *Journal of Synchrotron Radiation*, 6(6):1174–1184, 1999. doi:10.1107/S0909049599009590. (Cited on page 48.)
- W. O. SAXTON AND W. BAUMEISTER. The correlation averaging of a regularly arranged bacterial cell envelope protein. *Journal of Microscopy*, 127(2):127–138, 1982. doi:10.1111/j.1365-2818.1982.tb00405.x. (Cited on page 115.)
- D. SAYRE. Some implications of a theorem due to Shannon. *Acta Crystallographica*, 5(6):843–843, 1952. doi:10.1107/S0365110X52002276. (Cited on pages 52 and 54.)
- D. SAYRE. Prospects for long-wavelength X-ray microscopy and diffraction. In M. SCHLENKER, M. FINK, J. P. GOEDGEBUER, C. MALGRANGE, J. C. VIEÉNOT, AND R. H. WADE (eds.), *Imaging Processes and Coherence in Physics*, vol. 112 of *Lecture Notes in Physics*, pp. 229–235. Springer, Berlin, Heidelberg, 1980. doi:10.1007/3-540-09727-9. (Cited on pages 52 and 61.)
- D. SAYRE. X-Ray Crystallography: The Past and Present of the Phase Problem. *Structural Chemistry*, 13(1):81–96, 2002. doi:10.1023/A:1013477415486. (Cited on page 52.)
- D. SAYRE AND H. N. CHAPMAN. X-ray microscopy. *Acta Crystallographica Section A*, 51(3):237–252, 1995. doi:10.1107/S0108767394011803. (Cited on page 52.)
- G. SCHMAHL, D. RUDOLPH, P. GUTTMANN, G. SCHNEIDER, J. THIEME, B. NIEMANN, AND T. WILHEIN. Phase contrast X-ray microscopy. *Synchrotron Radiation News*, 7(4):19–22, 1994. doi:10.1080/08940889408261282. (Cited on page 38.)
- G. SCHNEIDER. Cryo X-ray microscopy with high spatial resolution in amplitude and phase contrast. *Ultramicroscopy*, 75(2):85–104, 1998. doi:10.1016/S0304-3991(98)00054-0. (Cited on page 156.)

- G. SCHNEIDER, P. GUTTMANN, S. REHBEIN, S. WERNER, AND R. FOLLATH. Cryo X-ray microscope with flat sample geometry for correlative fluorescence and nanoscale tomographic imaging. *Journal of Structural Biology*, 177(2):212–223, 2012. doi:10.1016/j.jsb.2011.12.023. (Cited on pages 37 and 155.)
- P. SCHNEIDER, M. MEIER, R. WEPF, AND R. MÜLLER. Towards quantitative 3D imaging of the osteocyte lacuno-canalicular network. *Bone*, 47(5):848–858, 2010. doi:10.1016/j.bone.2010.07.026. (Cited on pages 240, 264, 265 and 267.)
- P. SCHNEIDER, M. MEIER, R. WEPF, AND R. MÜLLER. Serial FIB/SEM imaging for quantitative 3D assessment of the osteocyte lacuno-canalicular network. *Bone*, 49(2):304–311, 2011. doi:10.1016/j.bone.2011.04.005. (Cited on pages 264, 265, 267, 268, 269 and 270.)
- C. G. SCHROER, P. BOYE, J. M. FELDKAMP, J. PATOMMEL, D. SAMBERG, A. SCHROPP, A. SCHWAB, S. STEPHAN, G. FALKENBERG, G. WELLENREUTHER, AND N. REIMERS. Hard X-ray nanoprobe at beamline P06 at PETRA III. *Nuclear Instruments and Methods in Physics Research Section A*, 616(2-3):93–97, 2010. doi:10.1016/j.nima.2009.10.094. (Cited on page 142.)
- C. G. SCHROER, P. BOYE, J. M. FELDKAMP, J. PATOMMEL, A. SCHROPP, A. SCHWAB, S. STEPHAN, M. BURGHAMMER, S. SCHÖDER, AND C. RIEKEL. Coherent X-Ray Diffraction Imaging with Nanofocused Illumination. *Physical Review Letters*, 101(9):090801, 2008. doi:10.1103/PhysRevLett.101.090801. (Cited on page 111.)
- C. G. SCHROER, M. KUHLMANN, U. T. HUNGER, T. F. GÜNZLER, O. KURAPOVA, S. FESTE, F. FREHSE, B. LENGELER, M. DRAKOPOULOS, A. SOMOGYI, A. S. SIMIONOVICI, A. SNIGIREV, I. SNIGIREVA, C. SCHUG, AND W. H. SCHRÖDER. Nanofocusing parabolic refractive x-ray lenses. *Applied Physics Letters*, 82(9):1485–1487, 2003. doi:10.1063/1.1556960. (Cited on page 29.)
- C. G. SCHROER, M. KUHLMANN, S. V. ROTH, R. GEHRKE, N. STRIBECK, A. ALMENDAREZ-CAMARILLO, AND B. LENGELER. Mapping the local nanostructure inside a specimen by tomographic small-angle x-ray scattering. *Applied Physics Letters*, 88(16):164102, 2006. doi:10.1063/1.2196062. (Cited on page 308.)

- C. G. SCHROER AND B. LENGELER. Focusing Hard X Rays to Nanometer Dimensions by Adiabatically Focusing Lenses. *Physical Review Letters*, 94(5):54802, 2005. doi:10.1103/PhysRevLett.94.054802. (Cited on page 29.)
- A. SCHROPP, P. BOYE, J. M. FELDKAMP, R. HOPPE, J. PATOMMEL, D. SAMBERG, S. STEPHAN, K. GIEWEKEMEYER, R. N. WILKE, T. SALDITT, J. GULDEN, A. P. MANCUSO, I. A. VARTANYANTS, E. WECKERT, S. SCHÖDER, M. BURGHAMMER, AND C. G. SCHROER. Hard x-ray nanobeam characterization by coherent diffraction microscopy. *Applied Physics Letters*, 96(9):091102, 2010. doi:10.1063/1.3332591. (Cited on pages 81, 143, 328 and 330.)
- A. SCHROPP, R. HOPPE, V. MEIER, J. PATOMMEL, F. SEIBOTH, H. J. LEE, B. NAGLER, E. C. GALTIER, B. ARNOLD, U. ZASTRAU, J. B. HASTINGS, D. NILSSON, F. UHLEN, U. VOGT, H. M. HERTZ, AND C. G. SCHROER. Full spatial characterization of a nanofocused x-ray free-electron laser beam by ptychographic imaging. *Scientific Reports*, 3:1633, 2013. doi:10.1038/srep01633. (Cited on page 330.)
- M. M. SEIBERT, T. EKEBERG, F. R. N. C. MAIA, M. SVENDA, J. ANDREASSON, O. JÖNSSON, D. ODIĆ, B. IWAN, A. ROCKER, D. WESTPHAL, M. HANTKE, D. P. DEPONTE, A. BARTY, J. SCHULZ, L. GUMPRECHT, N. COPPOLA, A. AQUILA, M. LIANG, T. A. WHITE, A. MARTIN, C. CALEMAN, S. STERN, C. ABERGEL, V. SELTZER, J.-M. CLAVERIE, C. BOSTEDT, J. D. BOZEK, S. BOUTET, A. A. MIAHNAHRI, M. MESSERSCHMIDT, J. KRZYWINSKI, G. WILLIAMS, K. O. HODGSON, M. J. BOGAN, C. Y. HAMPTON, R. G. SIERRA, D. STARODUB, I. ANDERSSON, S. BAJT, M. BARTHELMESS, J. C. H. SPENCE, P. FROMME, U. WEIERSTALL, R. KIRIAN, M. HUNTER, R. B. DOAK, S. MARCHESINI, S. P. HAU-RIEGE, M. FRANK, R. L. SHOEMAN, L. LOMB, S. W. EPP, R. HARTMANN, D. ROLLES, A. RUDENKO, C. SCHMIDT, L. FOUCAR, N. KIMMEL, P. HOLL, B. RUDEK, B. ERK, A. HÖMKE, C. REICH, D. PIETSCHNER, G. WEIDENSPONTNER, L. STRÜDER, G. HAUSER, H. GORKE, J. ULLRICH, I. SCHLICHTING, S. HERRMANN, G. SCHALLER, F. SCHOPPER, H. SOLTAU, K.-U. KÜHNEL, R. ANDRITSCHKE, C.-D. SCHRÖTER, F. KRASNIQI, M. BOTT, S. SCHORB, D. RUPP, M. ADOLPH, T. GORKHOVER, H. HIRSEMANN, G. POTDEVIN, H. GRAAFSMA, B. NILSSON, H. N. CHAPMAN, AND J. HAJDU. Single mimivirus particles intercepted and imaged with an X-ray laser. *Nature*, 470(7332):78–81, 2011. doi:10.1038/nature09748. (Cited on pages 65 and 69.)

- E. W. H. SELWYN. A theory of graininess. *Photographic Journal*, 75:571–580, 1935. doi:<http://archive.rps.org/archive/volume-75/70553>. (Cited on page 113.)
- C. E. SHANNON. A mathematical theory of communication. *Bell System Technical Journal*, 27(July and October):379–423 and 623–656, 1948. (Cited on page 116.)
- C. E. SHANNON. Communication in the Presence of Noise. *Proceedings of the IRE*, 37(1):10–21, 1949. doi:10.1109/JRPROC.1949.232969. (Cited on pages 50 and 51.)
- D. SHAPIRO, P. THIBAUT, T. BEETZ, V. ELSE, M. HOWELLS, C. JACOBSEN, J. KIRZ, E. LIMA, H. MIAO, A. M. NEIMAN, AND D. SAYRE. Biological imaging by soft x-ray diffraction microscopy. *Proceedings of the National Academy of Sciences of the United States of America*, 102(43):15343–15346, 2005. doi:10.1073/pnas.0503305102. (Cited on pages 67, 70, 111 and 282.)
- D. A. SHAPIRO, Y.-S. YU, T. TYLISZCZAK, J. CABANA, R. CELESTRE, W. CHAO, K. KAZNATCHEEV, A. L. D. KILCOYNE, F. MAIA, S. MARCHESINI, Y. S. MENG, T. WARWICK, L. L. YANG, AND H. A. PADMORE. Chemical composition mapping with nanometre resolution by soft X-ray microscopy. *Nature Photonics*, 8(10):765–769, 2014. doi:10.1038/nphoton.2014.207. (Cited on page 330.)
- SHARP CAMERA TEAM. *Sharp Camera Documentation*. Available online (last accessed March 2nd, 2015): <http://sharpcamera.bitbucket.org>, 2014. (Cited on page 331.)
- R. SHAW. Evaluating the efficiency of imaging processes. *Reports on Progress in Physics*, 41(7):1103–1155, 1978. doi:10.1088/0034-4885/41/7/003. (Cited on pages 35 and 36.)
- S. K. SINHA, E. B. SIROTA, S. GAROFF, AND H. STANLEY. X-ray and neutron scattering from rough surfaces. *Physical Review B*, 38(4):2297–2311, 1988. doi:10.1103/PhysRevB.38.2297. (Cited on page 211.)
- J. G. SKEDROS, S. C. SU, AND R. D. BLOEBAUM. Biomechanical implications of mineral content and microstructural variations in cortical bone of horse, elk, and sheep calcanei. *The Anatomical Record*, 249(3):297–316, 1997. doi:10.1002/(SICI)1097-0185(199711)249:3<297::AID-AR1>3.0.CO;2-S. (Cited on page 306.)

- A. SNIGIREV, V. KOHN, I. SNIGIREVA, AND B. LENGELER. A compound refractive lens for focusing high-energy X-rays. *Nature*, 384(6604):49–51, 1996. doi:10.1038/384049a0. (Cited on page 29.)
- B. A. SOBOTT, C. BROENNIMANN, E. F. EIKENBERRY, R. DINAPOLI, P. KRAFT, G. N. TAYLOR, P. R. WILLMOTT, C. M. SCHLEPÜTZ, AND R. P. RASSOOL. Synchrotron radiation hardness studies of PILATUS II. *Journal of Synchrotron Radiation*, 16(4):489–493, 2009. doi:10.1107/S0909049509014733. (Cited on page 144.)
- C. SONG, H. JIANG, A. MANCUSO, B. AMIRBEKIAN, L. PENG, R. SUN, S. SHAH, Z. ZHOU, T. ISHIKAWA, AND J. MIAO. Quantitative imaging of single, unstained viruses with coherent X rays. *Physical Review Letters*, 101(15):158101, 2008. doi:10.1103/PhysRevLett.101.158101. (Cited on page 282.)
- J. C. H. SPENCE, U. WEIERSTALL, AND M. HOWELLS. Phase recovery and lensless imaging by iterative methods in optical, X-ray and electron diffraction. *Philosophical Transactions of the Royal Society A*, 360(1794):875–895, 2002. doi:10.1098/rsta.2001.0972. (Cited on pages 69, 71 and 72.)
- M. STOCKMAR, P. CLOETENS, I. ZANETTE, B. ENDERS, M. DIEROLF, F. PFEIFFER, AND P. THIBAUT. Near-field ptychography: phase retrieval for inline holography using a structured illumination. *Scientific Reports*, 3:1927, 2013. doi:10.1038/srep01927. (Cited on page 330.)
- M. STOCKMAR, I. ZANETTE, M. DIEROLF, B. ENDERS, R. CLARE, F. PFEIFFER, P. CLOETENS, A. BONNIN, AND P. THIBAUT. X-Ray Near-Field Ptychography for Optically Thick Specimens. *Physical Review Applied*, 3(1):014005, 2015. doi:10.1103/PhysRevApplied.3.014005. (Cited on page 330.)
- N. STRIBECK, U. NÖCHEL, S. FAKIROV, J. FELDKAMP, C. SCHROER, A. TIMMANN, AND M. KUHLMANN. SAXS-Fiber Computer Tomography. Method Enhancement and Analysis of Microfibrillar-Reinforced Composite Precursors from PEBA and PET. *Macromolecules*, 41(20):7637–7647, 2008. doi:10.1021/ma8015322. (Cited on page 308.)
- M. SU, H. JIANG, P. ZHANG, Y. LIU, E. WANG, A. HSU, AND H. YOKOTA. Knee-loading modality drives molecular transport in mouse femur. *Annals of Biomedical Engineering*, 34(10):1600–1606, 2006. doi:10.1007/s10439-006-9171-z. (Cited on page 264.)

-
- K. A. TAYLOR AND R. M. GLAESER. Electron Diffraction of Frozen, Hydrated Protein Crystals. *Science*, 186(4168):1036–1037, 1974. doi:10.1126/science.186.4168.1036. (Cited on page 155.)
- A. TETI AND A. ZALLONE. Do osteocytes contribute to bone mineral homeostasis? Osteocytic osteolysis revisited. *Bone*, 44(1):11–16, 2009. doi:10.1016/j.bone.2008.09.017. (Cited on pages 287 and 288.)
- P. THIBAUT. *Algorithmic methods in diffraction microscopy*. Ph.D. thesis, Cornell University, 2007. (Cited on pages 56, 64, 65, 67 and 69.)
- P. THIBAUT, M. DIEROLF, O. BUNK, A. MENZEL, AND F. PFEIFFER. Probe retrieval in ptychographic coherent diffractive imaging. *Ultramicroscopy*, 109(4):338–343, 2009a. doi:10.1016/j.ultramic.2008.12.011. (Cited on pages 82, 90, 91, 92 and 100.)
- P. THIBAUT, M. DIEROLF, C. M. KEWISH, A. MENZEL, O. BUNK, AND F. PFEIFFER. Contrast mechanisms in scanning transmission x-ray microscopy. *Physical Review A*, 80(4):043813, 2009b. doi:10.1103/PhysRevA.80.043813. (Cited on pages 41 and 43.)
- P. THIBAUT, M. DIEROLF, A. MENZEL, O. BUNK, C. DAVID, AND F. PFEIFFER. High-resolution scanning x-ray diffraction microscopy. *Science*, 321(5887):379–382, 2008. doi:10.1126/science.1158573. (Cited on pages 76, 82, 90, 91, 92, 95, 143, 325 and 328.)
- P. THIBAUT, V. ELSER, C. JACOBSEN, D. SHAPIRO, AND D. SAYRE. Reconstruction of a yeast cell from X-ray diffraction data. *Acta Crystallographica Section A*, 62(4):248–261, 2006. doi:10.1107/S0108767306016515. (Cited on pages 65, 66, 67, 68, 69, 70 and 97.)
- P. THIBAUT AND M. GUIZAR-SICAIROS. Maximum-likelihood refinement for coherent diffractive imaging. *New Journal of Physics*, 14(6):063004, 2012. doi:10.1088/1367-2630/14/6/063004. (Cited on pages 91, 101, 102, 103, 104, 105 and 108.)
- P. THIBAUT, M. GUIZAR-SICAIROS, AND A. MENZEL. Coherent imaging at the diffraction limit. *Journal of Synchrotron Radiation*, 21:1011–1018, 2014. doi:10.1107/S1600577514015343. (Cited on page 330.)
- P. THIBAUT AND A. MENZEL. Reconstructing state mixtures from diffraction measurements. *Nature*, 494(7435):68–71, 2013. doi:10.1038/nature11806. (Cited on pages 82, 134, 148, 233, 327, 330 and 331.)

- D. J. THIEL, D. H. BILDERBACK, A. LEWIS, AND E. A. STERN. Submicron concentration and confinement of hard X-rays. *Nuclear Instruments and Methods in Physics Research A*, 317(3):597–600, 1992. doi:10.1016/0168-9002(92)91006-U. (Cited on page 29.)
- P. TRTIK, A. DIAZ, M. GUIZAR-SICAIROS, A. MENZEL, AND O. BUNK. Density mapping of hardened cement paste using ptychographic X-ray computed tomography. *Cement and Concrete Composites*, 36:71–77, 2013. doi:10.1016/j.cemconcomp.2012.06.001. (Cited on pages 281 and 328.)
- P. VAN CITTERT. Die Wahrscheinliche Schwingungsverteilung in Einer von Einer Lichtquelle Direkt Oder Mittels Einer Linse Beleuchteten Ebene. *Physica*, 1(1-6):201–210, 1934. doi:10.1016/S0031-8914(34)90026-4. (Cited on page 46.)
- P. VAN CITTERT. Degree of coherence. *Physica*, 24(1-5):505–507, 1958. doi:10.1016/S0031-8914(58)96209-8. (Cited on page 47.)
- F. VAN DER VEEN AND F. PFEIFFER. Coherent x-ray scattering. *Journal of Physics: Condensed Matter*, 16(28):5003–5030, 2004. doi:10.1088/0953-8984/16/28/020. (Cited on pages 47, 48 and 49.)
- M. VAN HEEL. Similarity measures between images. *Ultramicroscopy*, 21(1):95–100, 1987. doi:10.1016/0304-3991(87)90010-6. (Cited on page 115.)
- M. VAN HEEL, W. KEEGSTRAS, W. SCHUTTER, AND E. J. F. VAN BRUGGEN. Arthropod hemocyanin structures studied by image analysis. In E. J. WOOD (ed.), *Life Chemistry Reports, Suppl. 1, "The Structure and Function of Invertebrate Respiratory Proteins"*, EMBO Workshop, pp. 63–73. Leeds, 1982. (Cited on page 115.)
- M. VAN HEEL AND M. SCHATZ. Fourier shell correlation threshold criteria. *Journal of Structural Biology*, 151(3):250–262, 2005. doi:10.1016/j.jsb.2005.05.009. (Cited on pages 113, 115, 116, 272 and 274.)
- P. VARGA, A. PACUREANU, M. LANGER, H. SUHONEN, B. HESSE, Q. GRIMAL, P. CLOETENS, K. RAUM, AND F. PEYRIN. Investigation of the three-dimensional orientation of mineralized collagen fibrils in human lamellar bone using synchrotron X-ray phase nano-tomography. *Acta Biomaterialia*, 9(9):8118–8127, 2013. doi:10.1016/j.actbio.2013.05.015. (Cited on pages 309, 311, 312 and 314.)

- J. VILA-COMAMALA, A. DIAZ, M. GUIZAR-SICAIROS, A. MANTION, C. M. KEWISH, A. MENZEL, O. BUNK, AND C. DAVID. Characterization of high-resolution diffractive X-ray optics by ptychographic coherent diffractive imaging. *Optics Express*, 19(22):21333–21344, 2011a. doi:10.1364/OE.19.021333. (Cited on pages 81, 113, 143, 328 and 330.)
- J. VILA-COMAMALA, S. GORELICK, E. FÄRM, C. M. KEWISH, A. DIAZ, R. BARRETT, V. A. GUZENKO, M. RITALA, AND C. DAVID. Ultra-high resolution zone-doubled diffractive X-ray optics for the multi-keV regime. *Optics Express*, 19(1):175–184, 2011b. doi:10.1364/OE.19.000175. (Cited on pages 31 and 39.)
- J. VILA-COMAMALA, K. JEFIMOV, J. RAABE, T. PILVI, R. H. FINK, M. SENONER, A. MAASSDORF, M. RITALA, AND C. DAVID. Advanced thin film technology for ultrahigh resolution X-ray microscopy. *Ultramicroscopy*, 109(11):1360–1364, 2009. doi:10.1016/j.ultramic.2009.07.005. (Cited on page 110.)
- D. J. VINE, G. J. WILLIAMS, B. ABBEY, M. A. PFEIFER, J. N. CLARK, M. D. DE JONGE, I. MCNULTY, A. G. PEELE, AND K. A. NUGENT. Ptychographic fresnel coherent diffractive imaging. *Physical Review A*, 80(6):063823, 2009. doi:10.1103/PhysRevA.80.063823. (Cited on page 74.)
- F. VON RECKLINGHAUSEN. *Untersuchungen über Rachitis and Osteomalacia*. Gustav Fischer, Jena, 1910. (Cited on page 287.)
- W. WAGERMAIER, H. S. GUPTA, A. GOURRIER, M. BURGHAMMER, P. ROSCHGER, AND P. FRATZL. Spiral twisting of fiber orientation inside bone lamellae. *Biointerphases*, 1(1):1–5, 2006. doi:10.1116/1.2178386. (Cited on pages 307 and 308.)
- T. WARWICK, K. FRANCK, J. B. KORTRIGHT, G. MEIGS, M. MORONNE, S. MYNENI, E. ROTENBERG, S. SEAL, W. F. STEELE, H. ADE, A. GARCIA, S. CERASARI, J. DENLINGER, S. HAYAKAWA, A. P. HITCHCOCK, T. TYLISZCZAK, J. KIKUMA, E. G. RIGHTOR, H.-J. SHIN, AND B. P. TONNER. A scanning transmission x-ray microscope for materials science spectromicroscopy at the advanced light source. *Review of Scientific Instruments*, 69(8):2964–2973, 1998. doi:10.1063/1.1149041. (Cited on page 152.)
- F. WASSERMANN AND J. A. YAEGER. The matrices of mineralizable tissues. *International Dental Journal*, 19(2):308–343, 1969. (Cited on page 288.)

- S. WEINER AND H. D. WAGNER. THE MATERIAL BONE: Structure-Mechanical Function Relations. *Annual Review of Materials Science*, 28(1):271–298, 1998. doi:10.1146/annurev.matsci.28.1.271. (Cited on pages 285, 286, 306, 307, 308 and 314.)
- L. W. WHITEHEAD, G. J. WILLIAMS, H. M. QUINEY, D. J. VINE, R. A. DILANIAN, S. FLEWETT, K. A. NUGENT, A. G. PEELE, E. BALAUR, AND I. MCNULTY. Diffractive imaging using partially coherent X rays. *Physical Review Letters*, 103(24):243902, 2009. doi:10.1103/PhysRevLett.103.243902. (Cited on pages 72 and 82.)
- S. W. WILKINS, T. E. GUREYEV, D. GAO, A. POGANY, AND A. W. STEVENSON. Phase-contrast imaging using polychromatic hard X-rays. *Nature*, 384(6607):335–338, 1996. doi:10.1038/384335a0. (Cited on page 39.)
- G. J. WILLIAMS, H. M. QUINEY, B. B. DHAL, C. Q. TRAN, K. A. NUGENT, A. G. PEELE, D. PATERSON, AND M. D. DE JONGE. Fresnel coherent diffractive imaging. *Physical Review Letters*, 97(2):025506, 2006. doi:10.1103/PhysRevLett.97.025506. (Cited on page 73.)
- G. J. WILLIAMS, H. M. QUINEY, A. G. PEELE, AND K. A. NUGENT. Coherent diffractive imaging and partial coherence. *Physical Review B*, 75(10):104102, 2007. doi:10.1103/PhysRevB.75.104102. (Cited on pages 72, 73 and 82.)
- M. WOHLSCHLÖGEL, T. U. SCHÜLLI, B. LANTZ, AND U. WELZEL. Application of a single-reflection collimating multilayer optic for X-ray diffraction experiments employing parallel-beam geometry. *Journal of Applied Crystallography*, 41(1):124–133, 2008. doi:10.1107/S0021889807050005. (Cited on page 29.)
- B. WOPENKA AND J. D. PASTERIS. A mineralogical perspective on the apatite in bone. *Materials Science and Engineering: C*, 25(2):131–143, 2005. doi:10.1016/j.msec.2005.01.008. (Cited on page 285.)
- J. J. WYSOLMERSKI. Osteocytes remove and replace perilacunar mineral during reproductive cycles. *Bone*, 54(2):230–236, 2013. doi:10.1016/j.bone.2013.01.025. (Cited on page 288.)
- M. J. YAFFE AND J. A. ROWLANDS. X-ray detectors for digital radiography. *Physics in Medicine and Biology*, 42(1):1–39, 1997. doi:10.1088/0031-9155/42/1/001. (Cited on pages 32 and 34.)

-
- L. YU, M. HUANG, M. CHEN, W. CHEN, W. HUANG, AND Z. ZHU. Quasi-discrete Hankel transform. *Optics Letters*, 23(6):409–411, 1998. doi:10.1364/OL.23.000409. (Cited on page 339.)
- S. ZELENKA AND S. FLECHSIG. Kinematic Couplings for Synchrotron Radiation Instrumentation. In *2nd International Workshop on Mechanical Engineering Design of Synchrotron Radiation Equipment and Instrumentation (MEDSI02) September 5-6, 2002*, pp. 262–270. Advanced Photon Source, Argonne National Laboratory, Argonne, Illinois U.S.A., 2002. (Cited on page 152.)
- X. ZENG, F. DUEWER, M. FESER, C. HUANG, A. LYON, A. TKACHUK, AND W. YUN. Ellipsoidal and parabolic glass capillaries as condensers for x-ray microscopes. *Applied Optics*, 47(13):2376–2381, 2008. doi:10.1364/AO.47.002376. (Cited on page 37.)
- F. ZERNIKE. The concept of degree of coherence and its application to optical problems. *Physica*, 5(8):785–795, 1938. doi:10.1016/S0031-8914(38)80203-2. (Cited on page 46.)
- F. ZERNIKE. Phase contrast, a new method for the microscopic observation of transparent objects. *Physica*, 9(7):686–698, 1942. doi:10.1016/S0031-8914(42)80035-X. (Cited on page 38.)
- F. ZERNIKE. How I Discovered Phase Contrast. *Science*, 121(3141):345–349, 1955. doi:10.1126/science.121.3141.345. (Cited on page 38.)
- F. ZHANG, I. PETERSON, J. VILA-COMAMALA, A. DIAZ, F. BERENQUER, R. BEAN, B. CHEN, A. MENZEL, I. K. ROBINSON, AND J. M. RODENBURG. Translation position determination in ptychographic coherent diffraction imaging. *Optics Express*, 21(11):13592–13606, 2013. doi:10.1364/OE.21.013592. (Cited on page 332.)
- L. ZHANG, R. BAKER, R. BARRETT, P. CLOETENS, AND Y. DABIN. Mirror profile optimization for nano-focusing KB mirror. *AIP Conference Proceedings*, 1234(1):801–804, 2010. doi:10.1063/1.3463335. (Cited on page 138.)
- M. ZHAO, L. HUANG, Q. ZHANG, X. SU, A. ASUNDI, AND Q. KE-MAO. Quality-guided phase unwrapping technique: comparison of quality maps and guiding strategies. *Applied Optics*, 50(33):6214–6224, 2011. doi:10.1364/AO.50.006214. (Cited on page 249.)

Bibliography

List of Figures

1.1	Comparison of δ/β -ratios for four different materials for X-ray energies ranging from 30 eV to 20 keV	24
1.2	Sketch of a Fresnel zone plate.	31
1.3	Sketch of a Scanning Transmission X-ray Microscope with a Fresnel zone plate as focusing device	40
1.4	Analysis of STXM data	42
1.5	Relation of beam deflection angle and phase gradient	43
2.1	Derivation of transverse coherence length.	48
2.2	Derivation of longitudinal coherence length.	49
2.3	Visualization of the Fourier modulus projection	59
2.4	Schematic representation of the Gerchberg-Saxton / error-reduction algorithm	60
2.5	Error-reduction algorithm and projections onto constraint sets	61
3.1	Schematic representation of the PIE algorithm	83
3.2	PIE with probe feedback	90
4.1	Radon transform and Fourier slice theorem.	118
4.2	Filtered backprojection of a simulated phantom.	120
4.3	Frequency response of various filters used in filtered backprojection.	123
5.1	Sketch of cSAXS beamline optics.	127
5.2	Photos of set-up for two-dimensional scanning (diffraction) microscopy at the cSAXS beamline	132
5.3	Photos of the nanotomography set-up at the cSAXS beamline	135
5.4	Effect of a clean-up pinhole on diffraction data quality at ID22NI.	139
5.5	Photos of scanning set-up at ID22NI	140
6.1	Evaluation of scattering power for a weakly interacting biological specimen.	166

6.2	Imaging of a Au Fresnel zone plate structure as a reference for retrieval of the incident probe.	170
6.3	Ptychographic reconstruction of a sample of <i>Magnetospirillum gryphiswaldense</i>	172
7.1	Implementation of ptychographic reconstruction with a shared probe.	175
7.2	Ptychographic reconstruction scheme in which multiple data sets share the same object.	178
7.3	Proposals for sequential implementations of ptychographic reconstruction with a shared object.	180
7.4	Scheme for an application of a hybrid approach for data-set sharing in a ptychographic reconstruction.	181
7.5	Simulation results illustrating the effects of sharing the probe with a flat object.	184
7.6	Reconstruction of two scans with a shared object compared to result obtained from their averaged diffraction data.	186
7.7	Examples of diffraction data used for the high-resolution reconstructions with a shared-probe approach	189
7.8	Reconstruction of multiple data sets with a shared probe (Ir zone plate)	191
7.9	Visible-light micrographs of mouse liver slice used as specimen in the shared-object test experiment.	192
7.10	Comparison of shared-object reconstruction results for an increasing amount of input data.	195
7.11	Dependence of variance in reconstructed shared object on number of data sets used.	197
7.12	Comparison of shared-object results with reconstructions based on averaged diffraction data.	198
8.1	Low-resolution images of Siemens star test object scanned at ID22NI in July 2009.	206
8.2	PCDI reconstruction of test specimen	206
8.3	Manual modelling of ID22NI probe function	211
8.4	Isolation of background-induced artefact in probe by using a least-squares fit.	214
8.5	Least-squares fit to estimate of point-spread-function obtained from background-induced artefact.	219
8.6	Comparison of original and post-processed diffraction patterns	225
8.7	Comparison of ptychographic reconstructions of Siemens star test pattern for different background-correction approaches . .	228

8.8	Reconstruction of Siemens star test pattern with four probe modes.	233
8.9	Line-outs across structures of Siemens star test pattern.	235
9.1	Data collection and online evaluation in demonstration experiment.	241
9.2	Ptychographic reconstruction of tomographic projection	244
9.3	Phase ramp removal and offset correction	246
9.4	Illustration of phase unwrapping using quality-guided path following.	248
9.5	Alignment of PXCT projections	251
9.6	Examples for projections and sinograms serving as input for tomographic reconstructions.	254
9.7	Complex-plane histogram plot encoding the relative frequency of each complex value within the data set	257
9.8	Reconstructed electron densities for murine bone specimen.	261
9.9	3D rendering of reconstructed murine bone specimen	263
9.10	Assessment of spatial resolution by Fourier ring correlation.	272
9.11	Required imaging doses for collagen, a general empirical protein and gold.	278
10.1	Visible light micrographs of ovine bone specimen with mineralization gradient indicating area covered by ptychographic scans	291
10.2	Reconstruction result for ovine bone with mineralization gradient	294
10.3	Slices through ovine bone with mineralization gradient at different heights	296
10.4	Reconstruction result for ovine bone with native mineralization.	298
10.5	Slices through tomographic reconstruction of hydroxyapatite particle	299
10.6	Volumetric rendering of lacuno-canalicular network in reference bone volume	300
10.7	Comparison of the histogram of the bone with a mineralization gradient to the histograms of a reference bone volume and a hydroxyapatite particle.	301
10.8	Conversion of mineral volume fractions or electron density values to mass fractions of hydroxyapatite, calcium and collagen.	305
10.9	Schematic cross-sectional view of a secondary osteon	310
10.10	Analysis procedure employed to visualize the orientations of collagen fibril array patterns	313

10.11	Visualization of collagen fibril array orientations in reference bone sample.	317
10.12	Ptychographically reconstructed phase-contrast projection images of regions on a slice of bone	321
12.1	Illustration of ambiguous position refinement due to lack of translation diversity along one direction	332
12.2	Information sharing via a tomographic volume.	333

Index of cited authors

- AARDEN ET AL. (1994), 287, 341
ABBEY ET AL. (2008), 73, 341
ADE ET AL. (1990), 41, 341
ADE ET AL. (1992), 41, 341
ALS-NIELSEN AND MCMORROW (2011), 30, 37, 50, 128, 201, 211, 338, 341
ANDREWS ET AL. (2010), 266, 267, 341
ATKINS AND FINDLAY (2012), 287, 341
ATTWOOD (2000), 22, 24, 25, 29, 31, 32, 37, 38, 45, 110, 341
BÉLANGER (1969), 287, 343
BAEZ (1961), 30, 342
BALEWSKI ET AL. (2004), 330, 342
BALLABRIGA ET AL. (2011), 330, 342
BANHAM AND KATSAGGELOS (1997), 20, 224, 342
BARRETT (1990), 156, 253, 267, 342
BARTH ET AL. (2010), 276, 342
BATES AND RODENBURG (1989), 78, 79, 342
BATES (1982), 46, 53, 54, 61, 72, 342
BAUMEISTER ET AL. (1999), 155, 342
BAUSCHKE ET AL. (2002), 56–59, 62, 343
BAUSCHKE ET AL. (2003), 64, 343
BAYLINK AND WERGEDAL (1971), 287, 343
BEAMER ET AL. (1996), 259, 262, 343
BEETZ AND JACOBSEN (2002), 156, 343
BEETZ ET AL. (2005), 156, 343
BENO ET AL. (2006), 264, 343
BILTZ AND PELLEGRINO (1983), 285, 343
BLEUET ET AL. (2008), 138, 344
BLEUET ET AL. (2009), 39, 137, 140, 344
BLOEBAUM ET AL. (1997), 304, 344
BONEWALD (2011), 287, 344
BONUCCI (2009), 287, 344
BORN AND WOLF (2006), 17, 19, 25, 46, 47, 217, 344
BOULIGAND (1972), 307, 308, 314, 344
BOYLE ET AL. (2003), 289, 344
BRACEWELL (1986), 337, 339, 344
BRAUN (2013), 332, 344
BRUCK AND SODIN (1979), 53, 345
BUNK ET AL. (2008), 88, 345, 403
BUNK ET AL. (2009), 42, 345
BUNK ET AL. (2011), 125, 345
BURDET ET AL. (2014), 92, 345
BURDET ET AL. (2015), 331, 345
BURGER AND KLEIN-NULEND (1999), 264, 345
BUTZ (2006), 50, 51, 339, 345

- CHAMPENEY (1973), 21, 338, 339, 345
- CHAO ET AL. (2005), 32, 110, 345
- CHAPMAN ET AL. (1995), 41, 42, 346
- CHAPMAN ET AL. (2006a), 69, 70, 87, 88, 112, 279, 346
- CHAPMAN ET AL. (2006b), 63, 64, 72, 97, 111, 112, 346
- CHAPMAN (1996), 79–81, 89, 90, 346
- CHAPMAN (1997), 80, 346
- CHAPMAN (2008), 325, 327, 346
- CHEN ET AL. (2013), 281, 328, 346
- CHMEISSANI ET AL. (2004), 232, 347
- CLOETENS ET AL. (1996), 39, 347
- CLOETENS ET AL. (1999), 39, 45, 347
- CLOETENS (1999), 21, 119, 347
- CLOETENS (2009), 232, 347
- COAN ET AL. (2006), 141, 347
- CONN ET AL. (2000), 213, 219, 227, 347
- COOLEY AND TUKEY (1965), 340, 347
- COSSLETT AND NIXON (1953), 38, 348
- CUNNINGHAM AND SHAW (1999), 35, 348
- DAURER (2013), 327, 333, 348
- DENG ET AL. (2015a), 148, 331, 348
- DENG ET AL. (2015b), 330, 348
- DIAZ ET AL. (2014), 281, 328, 348
- DIEROLF ET AL. (2008), 405
- DIEROLF ET AL. (2009), 403
- DIEROLF ET AL. (2010a), 143, 239–242, 244, 246, 248–250, 252, 256, 257, 261, 263, 269, 316, 325, 349, 403
- DIEROLF ET AL. (2010b), 76, 100, 109, 112, 143, 163, 165, 166, 170, 172, 282, 326, 349, 403
- DIEROLF (2007), 25, 48, 49, 56, 60, 75, 84, 88–90, 337, 349, 405
- DINAPOLI ET AL. (2011), 145, 329, 349
- DOROZHUKIN AND EPPLE (2002), 302, 349
- DUBOCHET ET AL. (1988), 155, 349
- ELSER ET AL. (2007), 60, 65, 350
- ELSER (2003a), 56, 57, 63–68, 94, 349
- ELSER (2003b), 66, 94, 349
- ENDERS AND THIBAUT (2014), 331, 350
- ENDERS ET AL. (2014), 233, 327, 330–332, 350, 403
- ERIKSSON ET AL. (2014), 330, 350
- ERSOY (2006), 17, 19, 20, 350
- ESMAEILI ET AL. (2013), 281, 328, 330, 350
- ESMAEILI ET AL. (2015), 328, 330, 350
- FARIDANI ET AL. (1992), 266, 350
- FARIS AND BYER (1988), 123, 350
- FAULKNER AND RODENBURG (2004), 74, 82–84, 87, 351
- FAULKNER AND RODENBURG (2005), 76, 84, 86, 87, 351
- FEHRINGER (2011), 293, 351
- FERNÁNDEZ ET AL. (2002), 276, 351
- FESER ET AL. (2003), 41, 351
- FESER ET AL. (2008), 23, 266, 351
- FIENUP AND WACKERMAN (1986), 71, 352
- FIENUP ET AL. (1982), 68, 352
- FIENUP (1978), 60–62, 351
- FIENUP (1982), 56, 61–64, 67, 69, 71, 96, 97, 351

- FIENUP (1987), 63, 69, 71, 351
FIENUP (2006), 56, 70, 71, 352
FRANK AND MCEWEN (1992), 250, 352
FRANZ-ODENDAAL ET AL. (2006), 264, 352
FRATZL ET AL. (2004), 285, 352
FUCHS ET AL. (2009), 23, 352
GERCHBERG AND SAXTON (1972), 60, 61, 96, 352
GEUSEBROEK ET AL. (2003), 311, 352
GHIGLIA AND PRITT (1998), 99, 247, 249, 353
GIANONCELLI ET AL. (2006), 41, 353
GIEWEKEMEYER ET AL. (2010), 76, 97, 110, 143, 165, 282, 353, 403
GIEWEKEMEYER ET AL. (2014), 329, 353
GIEWEKEMEYER (2011), 28, 353
GIRAUD-GUILLE (1988), 307, 308, 314, 353
GIRAUD-GUILLE (1994), 307, 308, 314, 353
GODARD ET AL. (2011), 332, 353
GOODMAN (1996), 17, 19, 20, 31, 36, 217, 338, 353
GRÜNZWEIG ET AL. (2008a), 404
GRÜNZWEIG ET AL. (2008b), 404
GRÜNZWEIG ET AL. (2008c), 404
GRAAFSMA (2009), 144, 354
GRUNER ET AL. (2002a), 142, 330, 354
GRUNER ET AL. (2002b), 21, 35, 221, 354
GUIZAR-SICAIROS AND FIENUP (2008), 82, 91, 151, 332, 354
GUIZAR-SICAIROS AND GUTIÉRREZ-VEGA (2004), 339, 354
GUIZAR-SICAIROS ET AL. (2008), 115, 355
GUIZAR-SICAIROS ET AL. (2011), 98, 121–123, 243, 246, 247, 250, 252, 253, 273, 282, 292, 293, 327, 333, 354
GUIZAR-SICAIROS ET AL. (2012), 74, 82, 113, 143, 156, 354
GUIZAR-SICAIROS ET AL. (2014), 145, 326, 329, 354
GUPTA ET AL. (2006), 290, 355
HARAUZ AND VAN HEEL (1986), 115, 355
HEGERL AND HOPPE (1970), 76, 355
HEGERL AND HOPPE (1976), 273, 277, 355
HELFEN ET AL. (2005), 253, 355
HELL (2007), 268, 269, 355
HENDERSON (1990), 155, 355
HENKE ET AL. (1993), 24, 172, 227, 229, 230, 257, 259, 277, 302, 355
HEYEN AND SCHÜLER (2003), 165, 356
HIGNETTE ET AL. (2005), 29, 138, 356
HOLLER ET AL. (2012), 113, 137, 143, 151, 356
HOLLER ET AL. (2014), 151, 329, 356
HOLTON ET AL. (2012), 36, 141, 218, 221, 356
HOLTON (2009), 155, 179, 356
HOLZNER ET AL. (2010), 41, 356
HOPE (1988), 155, 356
HOPPE AND STRUBE (1969), 76, 357
HOPPE (1969a), 75, 76, 356
HOPPE (1969b), 76, 357
HOPPE (1982), 76, 357

- HORNBERGER ET AL. (2008), 41, 357
- HOROWITZ AND HOWELL (1972), 39, 357
- HOWELLS ET AL. (2009), 172, 174, 276–280, 357
- HUANG ET AL. (2009), 112, 156, 282, 357
- HUANG ET AL. (2014), 326, 358
- HUMPHRY ET AL. (2012), 331, 358
- HØYDALSVIK ET AL. (2014), 328, 330, 357
- ICRU (1989), 257, 259, 263, 358
- JÄHNE (2002), 17, 358
- JACOBSEN ET AL. (1993), 41, 358
- JEFIMOV ET AL. (2007a), 32, 358
- JEFIMOV ET AL. (2007b), 32, 188, 358
- JENSEN ET AL. (2011), 308, 358
- JEPSEN ET AL. (2001), 257, 259, 262, 358
- JOCHUM AND MEYER-ILSE (1995), 38, 359
- JOHNSON ET AL. (2008), 404
- JOHNSON ET AL. (2014), 145, 329, 359
- KAK AND SLANEY (1988), 21, 117–119, 121, 334, 359
- KAMIOKA ET AL. (2001), 268, 359
- KANG ET AL. (2006), 32, 359
- KAPISHNIKOV ET AL. (2012), 41, 359, 404
- KERSCHNITZKI ET AL. (2011), 264, 268, 285, 289, 310, 360
- KERSCHNITZKI ET AL. (2013), 295, 359
- KERSCHNITZKI (2012), 289, 359
- KEWISH ET AL. (2010), 404
- KEWISH ET AL. (2010a), 81, 143, 328, 330, 360
- KEWISH ET AL. (2010b), 88, 142, 330, 360
- KEWISH ET AL. (2010c), 81, 143, 328, 330, 360
- KIRKPATRICK AND BAEZ (1948), 29, 360
- KIRZ AND JACOBSEN (2009), 37, 360
- KIRZ ET AL. (1990), 39, 40, 325, 360
- KIRZ ET AL. (1995), 37, 41, 360
- KLEIN-NULEND ET AL. (1995), 264, 361
- KLEIN-NULEND ET AL. (2013), 264, 286, 361
- KNOLL (2000), 32, 34, 130, 361
- KOTTLER ET AL. (2007), 44, 361
- KRAFT ET AL. (2009a), 33, 34, 130, 144, 146, 361
- KRAFT ET AL. (2009b), 130, 144–146, 361
- KUNDUR AND HATZINAKOS (1996), 81, 224, 361
- LABICHE ET AL. (2007), 141, 204, 361
- LACLARE (1994), 137, 362
- LANGER ET AL. (2012), 309, 362
- LARABELL AND NUGENT (2010), 38, 362
- LAUTERBORN AND KURZ (2003), 25, 52, 362
- LAWRENCE (1992), 250, 362
- LIM ET AL. (1995), 249, 362
- LIMA ET AL. (2009), 156, 282, 363
- LIMA ET AL. (2013), 156, 362
- LINFOOT (1964), 85, 363
- LOWE AND SAREEN (2013), 32, 363
- LUKE ET AL. (2002), 56, 363
- LUKE (2005), 64, 67, 68, 363
- MAIA ET AL. (2010), 65, 363

- MAIDEN AND RODENBURG (2009),
82, 90, 91, 363
- MAIDEN ET AL. (2011), 332, 363
- MAIDEN ET AL. (2012a), 332, 363
- MAIDEN ET AL. (2012b), 151, 332,
363
- MANDEL AND WOLF (1965), 46,
47, 364
- MARCHESINI ET AL. (2003), 63, 69,
111, 364
- MARCHESINI ET AL. (2006), 164,
364
- MARCHESINI (2007), 56, 64, 65, 67,
364
- MARSHALL ET AL. (1997), 307, 308,
364
- MARTÍNEZ-CRIADO ET AL. (2012),
30, 39, 138, 364
- MASER ET AL. (2000), 156, 364
- MATLAB (2012a), 121, 224, 364
- MATLAB (2012b), 121, 122, 224,
364
- MATLAB (2012c), 213, 219, 227, 365
- MCCALLUM AND RODENBURG (1992),
79, 80, 365
- MCCALLUM AND RODENBURG (1993),
81, 365
- MEENTS ET AL. (2010), 155, 365
- MENZEL ET AL. (2008), 405
- MENZEL ET AL. (2009), 404, 405
- MENZEL ET AL. (2010), 41, 44, 241,
365, 404
- MEYBERG AND VACHENAUER (1999),
18, 339, 365
- MIAO AND SAYRE (2000), 55, 365
- MIAO ET AL. (1998), 46, 53–55, 72,
365
- MIAO ET AL. (1999), 52, 325, 366
- MIAO ET AL. (2003), 282, 365
- MIMURA ET AL. (2009), 30, 366
- MOFFAT (1969), 218, 366
- MOKSO ET AL. (2007), 39, 366
- MORENO AND FORRIOL (2002), 305,
366
- MORRISON AND BROWNE (1992),
42, 366
- MORRISON ET AL. (2003), 41, 366
- MURPHY ET AL. (2004), 330, 366
- MYUNG (2003), 101, 367
- NASHED ET AL. (2014), 331, 367
- NELLIST ET AL. (1995), 76, 78, 367
- NELSON ET AL. (2010), 282, 367
- NEUHÄUSLER ET AL. (2003), 38,
367
- NEUTZE ET AL. (2000), 279, 367
- NICKELL ET AL. (2005), 250, 367
- NIEMANN ET AL. (1976), 37, 367
- NISHINO ET AL. (2009), 280, 282,
368
- NUGENT ET AL. (2003), 73, 368
- NUGENT ET AL. (2005), 73, 368
- O’NEILL (2003), 113, 368
- OMOKANWAYE ET AL. (2010), 277,
302, 368
- OVERSLUIZEN ET AL. (1992), 152,
368
- OWEN ET AL. (2009), 157, 368
- PACUREANU ET AL. (2012), 266,
270, 368
- PAGANIN (2006), 25, 28, 32, 369
- PARFITT (1977), 287, 288, 369
- PARKINSON ET AL. (2008), 156, 369
- PEARCE ET AL. (2007), 305, 369
- PEELE ET AL. (2004), 67, 369
- PELZ ET AL. (2014), 148, 331, 369
- PERONA AND MALIK (1990), 299,
369
- PEYRIN (2009), 266, 369
- PFEIFFER ET AL. (2007), 123, 241,
369
- PIAZZA ET AL. (2014), 328, 369

- PITTS AND GREENLEAF (2003), 73, 370
- PODRAZKÝ AND SEDMEROVÁ (1966), 277, 302, 370
- PONCHUT ET AL. (2011), 144, 146, 232, 370
- PONCHUT (2006), 141, 145, 208, 215, 221, 370
- POROD (1951), 145, 370
- PUTKUNZ ET AL. (2012), 331, 370
- QING AND BONEWALD (2009), 287, 288, 370
- QING ET AL. (2012), 288, 370
- QUINEY ET AL. (2005), 56, 73, 371
- QUINEY ET AL. (2006), 73, 89, 371
- RABBANI ET AL. (1987), 35, 371
- RADICCI ET AL. (2012), 144–146, 329, 371
- RARBACK ET AL. (1988), 39, 371
- RAU ET AL. (2007), 202, 371
- RAVAGLIOLI ET AL. (1996), 305, 371
- REHBEIN ET AL. (2009), 37, 371
- REZNIKOV ET AL. (2013), 308, 314, 372
- REZNIKOV ET AL. (2014), 308, 372
- RHO ET AL. (1998), 307, 372
- RIGAL AND VIGNAL (1881), 287, 372
- RINNERTHALER ET AL. (1999), 308, 310, 372
- RIVERS ET AL. (1991), 41, 372
- ROBISCH AND SALDITT (2013), 332, 372
- RODENBURG AND BATES (1992), 78, 79, 81, 372
- RODENBURG AND FAULKNER (2004), 84, 86, 87, 373
- RODENBURG ET AL. (1993), 80, 373
- RODENBURG ET AL. (2007a), 84–86, 88, 143, 373
- RODENBURG ET AL. (2007b), 83, 88, 143, 325, 373
- RODENBURG (2008), 75–79, 81, 84, 372
- ROODMAN (1996), 289, 373
- ROSCHGER ET AL. (1998), 304, 373
- ROSCHGER ET AL. (2008), 305, 373
- ROSE (1948), 277, 373
- SAKDINAWAT AND ATTWOOD (2010), 37, 373
- SANDY ET AL. (1999), 48, 374
- SAXTON AND BAUMEISTER (1982), 115, 374
- SAYRE AND CHAPMAN (1995), 52, 374
- SAYRE (1952), 52, 54, 374
- SAYRE (1980), 52, 61, 374
- SAYRE (2002), 52, 374
- SCHMAHL ET AL. (1994), 38, 374
- SCHNEIDER ET AL. (2010), 240, 264, 265, 267, 375
- SCHNEIDER ET AL. (2011), 264, 265, 267–270, 375
- SCHNEIDER ET AL. (2012), 37, 155, 374
- SCHNEIDER (1998), 156, 374
- SCHROER AND LENGELER (2005), 29, 375
- SCHROER ET AL. (2003), 29, 375
- SCHROER ET AL. (2006), 308, 375
- SCHROER ET AL. (2008), 111, 375
- SCHROER ET AL. (2010), 142, 375
- SCHROPP ET AL. (2010), 81, 143, 328, 330, 376
- SCHROPP ET AL. (2013), 330, 376
- SEIBERT ET AL. (2011), 65, 69, 376
- SELWYN (1935), 113, 376
- SHANNON (1948), 116, 377
- SHANNON (1949), 50, 51, 377
- SHAPIRO ET AL. (2005), 67, 70, 111, 282, 377

- SHAPIRO ET AL. (2014), 330, 377
SHAW (1978), 35, 36, 377
SINHA ET AL. (1988), 211, 377
SKEDROS ET AL. (1997), 306, 377
SNIGIREV ET AL. (1996), 29, 377
SOBOTT ET AL. (2009), 144, 378
SONG ET AL. (2008), 282, 378
SPENCE ET AL. (2002), 69, 71, 72, 378
STOCKMAR ET AL. (2013), 330, 378, 405
STOCKMAR ET AL. (2015), 330, 378, 405
STRIBECK ET AL. (2008), 308, 378
SU ET AL. (2006), 264, 378
TAYLOR AND GLAESER (1974), 155, 378
TETI AND ZALLONE (2009), 287, 288, 379
THIBAUT AND GUIZAR-SICAIROS (2012), 91, 101–105, 108, 379
THIBAUT AND MENZEL (2013), 82, 134, 148, 233, 327, 330, 331, 379
THIBAUT ET AL. (2006), 65–70, 97, 379
THIBAUT ET AL. (2008), 76, 82, 90–92, 95, 143, 325, 328, 379, 405
THIBAUT ET AL. (2009a), 82, 90–92, 100, 379, 405
THIBAUT ET AL. (2009b), 41, 43, 379, 405
THIBAUT ET AL. (2014), 330, 379
THIBAUT (2007), 56, 64, 65, 67, 69, 379
THIEL ET AL. (1992), 29, 379
TRTIK ET AL. (2013), 281, 328, 380
VARGA ET AL. (2013), 309, 311, 312, 314, 380
VILA-COMAMALA ET AL. (2009), 110, 381
VILA-COMAMALA ET AL. (2010), 406
VILA-COMAMALA ET AL. (2011a), 81, 113, 143, 328, 330, 380
VILA-COMAMALA ET AL. (2011b), 31, 39, 381
VINE ET AL. (2009), 74, 381
WAGERMAIER ET AL. (2006), 307, 308, 381
WARWICK ET AL. (1998), 152, 381
WASSERMANN AND YAEGER (1969), 288, 381
WEINER AND WAGNER (1998), 285, 286, 306–308, 314, 381
WHITEHEAD ET AL. (2009), 72, 82, 382
WILKINS ET AL. (1996), 39, 382
WILLIAMS ET AL. (2006), 73, 382
WILLIAMS ET AL. (2007), 72, 73, 82, 382
WOHLSCHLÖGEL ET AL. (2008), 29, 382
WOPENKA AND PASTERIS (2005), 285, 382
WYSOLMERSKI (2013), 288, 382
YAFFE AND ROWLANDS (1997), 32, 34, 382
YU ET AL. (1998), 339, 382
ZELENKA AND FLECHSIG (2002), 152, 383
ZENG ET AL. (2008), 37, 383
ZERNIKE (1938), 46, 383
ZERNIKE (1942), 38, 383
ZERNIKE (1955), 38, 383
ZHANG ET AL. (2010), 138, 383
ZHANG ET AL. (2013), 332, 383
ZHAO ET AL. (2011), 249, 383
DA SILVA ET AL. (2015), 328, 348

- DE JONGE ET AL. (2008), 41, 43,
44, 348
- VAN CITTERT (1934), 46, 380
- VAN CITTERT (1958), 47, 380
- VAN HEEL AND SCHATZ (2005),
113, 115, 116, 272, 274, 380
- VAN HEEL ET AL. (1982), 115, 380
- VAN HEEL (1987), 115, 380
- VAN DER VEEN AND PFEIFFER (2004),
47–49, 380
- VON RECKLINGHAUSEN (1910), 287,
381
- KNOTHE TATE ET AL. (2004), 264,
361
- LE GROS ET AL. (2005), 156, 362
- SHARP CAMERA TEAM (2014), 331,
377
- ESRF WEBSITE (2015), 137, 350
- CSAXS WEBSITE (2015), 125, 127,
348

Subject index

- aliasing, 51
- amplitude transfer function, 20
- amplitude-spread function, 19
- autocorrelation, 338
- blind deconvolution, 81, *see* deconvolution
- bone
 - bone flow theory, 287
 - cells
 - osteoblast, 286
 - osteoclast, 287
 - hierarchical levels, 285, 286
- Bragg's law, 30
- canaliculi, 264
- coastal crystals, 288
- coherence
 - coherence length
 - longitudinal, 48, 49
 - transverse, 47, 48
 - complex coherence factor, 46
 - longitudinal, 48
 - mutual coherence function, 46
 - transverse, 47
- coherent transfer function, *see* amplitude transfer function
- complex object transmission function, 23
- constraints in PCDDI
 - Fourier, 91
 - overlap, 91
- convex set, 57
- convolution, 338
- critical angle, 29
- cross-correlation, 338
- dark noise, 34
- deconvolution
 - blind, 224
- difference map (DM), 65
- difference map error, 67
- edge-spread function, 21
- electron density, 22
- error-reduction algorithm (ER), 61
- far-field condition, 27
- Filtered backprojection, 119–123
 - filter definitions, 121
 - from derivatives, 122
- flat field, 34
- Fourier constraint
 - for ptychography, 91
- Fourier projection, 93
 - relaxed, 97
- Fourier ring correlation, 113
- Fourier shell correlation, 113
- Fourier slice theorem, 21, 118
- Fourier transform
 - circular symmetric system, *see* Hankel transform
 - continuous, 337
 - convolution theorem, 338
 - discrete, 339
 - fast, 340

- real-valued function, 338
 - similarity theorem, 338
- Fraunhofer approximation, 27
- Fresnel approximation, 26
- Fresnel coherent diffractive imaging (FCDI), 73
- Fresnel number, 27
- Fresnel propagator
 - in Fourier space, 28
 - in real space, 26
- Fresnel zone plate, 30
- Fresnel-Kirchhoff integral, 25
- Friedel's law, 338
- gain map, 34
- Gerchberg-Saxton algorithm, 60
- Goldstein's algorithm, *see* phase unwrapping
- Hamming filter, 121
- Hankel transform, 339
- Hann filter, 121
- Huygens-Fresnel principle, 25
- hybrid input-output algorithm (HIO), 63
- hybrid projection reflection algorithm (HPR), 64
- idempotent mapping, 58
- input-output algorithms, 62
- intensity, 45
- keyhole imaging, 73
- Kirkpatrick-Baez mirrors, 29
- lacunae, 264
- lacuno-canalicular network, 264
- linear (imaging) system, 17
 - impulse response of, 18
 - shift-invariant, 18
 - space-invariant, 18
- multilayer Laue lens, 32
- nonconvex set, 57
- Nyquist frequency, 36, 51
- optical transfer function, 20
- osteoblast, 264, 286
- osteoclast, 287
- osteocyte, 264
- osteocytic osteolysis, 287
- overlap constraint, 91
- oversampling ratio, 55
- Parseval's theorem, 338
- Patterson function, 52
- perilacunar bone, *see* perilacunar matrix
- perilacunar matrix, 288
- phase problem, 45
- phase ramp, 98
- phase retrieval algorithm
 - basic input-output, 62
 - difference map (DM), 65
 - error-reduction (ER), 61
 - Gerchberg-Saxton, 60
 - hybrid input-output (HIO), 63
 - hybrid projection reflection (HPR), 64
 - output-output, 63
 - relaxed averaged alternating reflection (RAAR), 64
- phase retrieval transfer function, 111
- phase unwrapping, 247–250
 - Goldstein's algorithm, 247
 - quality-guided path following, 249
- phase vortex, 67
- phase wrapping, 99
- PIE, 82
- point-spread function, 19
- Poisson noise, 34
- Porod's law, 145
- Poynting vector, 45

-
- projection
 - onto constraint set, 58
 - projection approximation, 22
 - projections
 - multi-valued, 59
 - ptychographical iterative engine (PIE), 82
 - ptychography
 - ePIE, 90
 - generalized definition, 77
 - original concept, 75
 - PCDI, 89
 - PIE, 82
 - Wigner-distribution deconvolution, 78
 - partial coherence, 81
 - probe reconstruction, 81
 - reconstruction procedure, 78
 - resolution, 80
 - quality-guided path following, *see* phase unwrapping
 - quantum efficiency, 33
 - Radon transform, 117
 - Ram-Lak filter, 121
 - raster grid pathology, 99
 - Rayleigh criterion, 31
 - read-out noise, 34
 - refractive index, 22
 - β , 22
 - δ , 22
 - relaxed averaged alternating reflection algorithm (RAAR), 64
 - round scan, 100
 - sampling theorem, 51
 - Shannon, 51
 - set
 - convex, 57
 - nonconvex, 57
 - shift-invariant linear system, 18
 - shot noise, *see* Poisson noise
 - Shrinkwrap algorithm, 69
 - Siemens star, 110
 - signal-to-noise ratio, 35
 - space-invariant linear system, 18
 - support
 - shrink wrap algorithm, 69
 - transfer function, 19
 - twin image, 46
 - twisted plywood structure (in bone), 314
 - undulator, 23, 25
 - unitary transform, 57
 - visibility of interference fringes, 47
 - Wiener-Khinchin theorem, 36
 - wiggler, 25
 - Wigner distribution function, 79
 - Wigner-distribution deconvolution, *see* ptychography
 - X-ray microscope
 - scanning, 39
 - transmission, 37

Nomenclature

ASF	Amplitude Spread Function, page 19
CDI	Coherent Diffractive Imaging, page 45
CLSM	Confocal Laser Scanning Microscopy, page 268
cSAXS	coherent Small-Angle X-ray Scattering beamline at the Swiss Light Source, page 125
DFT	Discrete Fourier Transform, page 339
DM	Difference Map, page 65
DPC	Differential Phase Contrast, page 41
DQE	Detective Quantum Efficiency, page 35
ePIE	extended Ptychographical Iterative Engine, page 90
ER	Error-Reduction algorithm, page 61
ESF	Edge-Spread Function, page 21
ESRF	European Synchrotron Radiation Facility, page 137
FCDI	Fresnel Coherent Diffractive Imaging, page 73
FFT	Fast Fourier Transform, page 340
FIB	Focused Ion Beam, page 240
FRC	Fourier Ring Correlation, page 113
FSC	Fourier Shell Correlation, page 113
FWHM	Full Width at Half Maximum, page 48

- FZP **F**resnel **Z**one **P**late, page 30
- GPU **G**raphics **P**rocessing **U**nit, page 71
- HIO **H**ybrid **I**nput-**O**utput algorithm, page 63
- HPR **H**ybrid **P**rojection **R**eflection algorithm, page 64
- ID22NI **N**ano-**I**maging endstation of beamline **ID22** at the ESRF, page 137
- KB **K**irkpatrick-**B**aez X-ray focusing mirrors, page 29
- ML **M**aximum **L**ikelihood, page 91
- MTF **M**odulation **T**ransfer **F**unction, page 111
- OSA **O**rdersorting **A**perture (in a X-ray scanning transmission microscope using zone plate optics), page 40
- OTF **O**ptical **T**ransfer **F**unction, page 20
- PCDI **P**tychographic **C**oherent **D**iffractive **I**maging, page 89
- PIE **P**tychographical **I**terative **E**ngine, page 82
- PRTF **P**hase **R**etrieval **T**ransfer **F**unction, page 111
- PSF **P**oint **S**pread **F**unction, page 19
- PXCT **P**tychographic **X**-ray **C**omputed **T**omography, page 239
- qBSE **q**uantitative **B**ackscattered **E**lectron **I**maging, page 304
- RAAR **R**elaxed **A**veraged **A**lternating **R**eflection algorithm, page 64
- SEM **S**canning **E**lectron **M**icroscope, page 267
- SLS **S**wiss **L**ight **S**ource, page 125
- SNR **S**ignal-to-**N**oise **R**atio, page 35
- STXM **S**canning **T**ransmission **X**-ray **M**icroscope, page 39
- TXM **T**ransmission **X**-ray **M**icroscope, page 37

List of publications

Peer-reviewed publications as first author

M. DIEROLF, A. MENZEL, P. THIBAUT, P. SCHNEIDER, C. M. KEWISH, R. WEPF, O. BUNK, AND F. PFEIFFER. Ptychographic X-ray computed tomography at the nanoscale. *Nature*, 467(7314):436–439, 2010a. doi:[10.1038/nature09419](https://doi.org/10.1038/nature09419).

M. DIEROLF, P. THIBAUT, A. MENZEL, C. M. KEWISH, K. JEFIMOV, I. SCHLICHTING, K. VON KÖNIG, O. BUNK, AND F. PFEIFFER. Ptychographic coherent diffractive imaging of weakly scattering specimens. *New Journal of Physics*, 12(3):035017, 2010b. doi:[10.1088/1367-2630/12/3/035017](https://doi.org/10.1088/1367-2630/12/3/035017).

M. DIEROLF, P. THIBAUT, C. M. KEWISH, A. MENZEL, O. BUNK, AND F. PFEIFFER. Coherent laser scanning diffraction microscopy. *Journal of Physics: Conference Series*, 186:012052, 2009. doi:[10.1088/1742-6596/186/1/012052](https://doi.org/10.1088/1742-6596/186/1/012052).

Peer-reviewed publications as co-author

O. BUNK, M. DIEROLF, S. KYNDE, I. JOHNSON, O. MARTI, AND F. PFEIFFER. Influence of the overlap parameter on the convergence of the ptychographical iterative engine. *Ultramicroscopy*, 108(5):481–487, 2008. doi:[10.1016/j.ultramic.2007.08.003](https://doi.org/10.1016/j.ultramic.2007.08.003).

B. ENDERS, M. DIEROLF, P. CLOETENS, M. STOCKMAR, F. PFEIFFER, AND P. THIBAUT. Ptychography with broad-bandwidth radiation. *Applied Physics Letters*, 104(17):171104, 2014. doi:[10.1063/1.4874304](https://doi.org/10.1063/1.4874304).

K. GIEWEKEMEYER, P. THIBAUT, S. KALBFLEISCH, A. BEERLINK, C. M. KEWISH, M. DIEROLF, F. PFEIFFER, AND T. SالدITT. Quantitative biological imaging by ptychographic x-ray diffraction microscopy.

Proceedings of the National Academy of Sciences of the United States of America, 107(2):529–534, 2010. doi:[10.1073/pnas.0905846107](https://doi.org/10.1073/pnas.0905846107).

C. GRÜNZWEIG, C. DAVID, O. BUNK, M. DIEROLF, G. FREI, G. KÜHNE, J. KOHLBRECHER, R. SCHÄFER, P. LEJCEK, H. RØNNOW, AND F. PFEIFFER. Neutron Decoherence Imaging for Visualizing Bulk Magnetic Domain Structures. *Physical Review Letters*, 101(2):025504, 2008a. doi:[10.1103/PhysRevLett.101.025504](https://doi.org/10.1103/PhysRevLett.101.025504).

C. GRÜNZWEIG, C. DAVID, O. BUNK, M. DIEROLF, G. FREI, G. KÜHNE, R. SCHÄFER, S. POFAHL, H. M. R. RØNNOW, AND F. PFEIFFER. Bulk magnetic domain structures visualized by neutron dark-field imaging. *Applied Physics Letters*, 93(11):112504, 2008b. doi:[10.1063/1.2975848](https://doi.org/10.1063/1.2975848).

C. GRÜNZWEIG, F. PFEIFFER, O. BUNK, T. DONATH, G. KÜHNE, G. FREI, M. DIEROLF, AND C. DAVID. Design, fabrication, and characterization of diffraction gratings for neutron phase contrast imaging. *Review of Scientific Instruments*, 79(5):053703, 2008c. doi:[10.1063/1.2930866](https://doi.org/10.1063/1.2930866).

I. JOHNSON, K. JEFIMOV, O. BUNK, C. DAVID, M. DIEROLF, J. GRAY, D. RENKER, AND F. PFEIFFER. Coherent diffractive imaging using phase front modifications. *Physical Review Letters*, 100(15):155503, 2008. doi:[10.1103/PhysRevLett.100.155503](https://doi.org/10.1103/PhysRevLett.100.155503).

S. KAPISHNIKOV, T. BERTHING, L. HVIID, M. DIEROLF, A. MENZEL, F. PFEIFFER, J. ALS-NIELSEN, AND L. LEISEROWITZ. Aligned hemozoin crystals in curved clusters in malarial red blood cells revealed by nanoprobe X-ray Fe fluorescence and diffraction. *Proceedings of the National Academy of Sciences of the United States of America*, 109(28):11184–11187, 2012. doi:[10.1073/pnas.1118134109](https://doi.org/10.1073/pnas.1118134109).

C. M. KEWISH, P. THIBAUT, M. DIEROLF, O. BUNK, A. MENZEL, J. VILA-COMAMALA, K. JEFIMOV, AND F. PFEIFFER. Ptychographic characterization of the wavefield in the focus of reflective hard X-ray optics. *Ultramicroscopy*, 110(4):325–329, 2010. doi:[10.1016/j.ultramic.2010.01.004](https://doi.org/10.1016/j.ultramic.2010.01.004).

A. MENZEL, C. M. KEWISH, M. DIEROLF, P. THIBAUT, P. KRAFT, O. BUNK, K. JEFIMOV, C. DAVID, AND F. PFEIFFER. Hard X-ray scanning transmission microscopy with a 2D pixel array detector. *Journal of Physics: Conference Series*, 186:012054, 2009. doi:[10.1088/1742-6596/186/1/012054](https://doi.org/10.1088/1742-6596/186/1/012054).

A. MENZEL, C. M. KEWISH, P. KRAFT, B. HENRICH, K. JEFIMOV, J. VILA-COMAMALA, C. DAVID, M. DIEROLF, P. THIBAUT, F. PFEIFFER, AND O. BUNK. Scanning transmission X-ray microscopy with a fast framing pixel detector. *Ultramicroscopy*, 110(9):1143–1147, 2010. doi:10.1016/j.ultramic.2010.04.007.

M. STOCKMAR, P. CLOETENS, I. ZANETTE, B. ENDERS, M. DIEROLF, F. PFEIFFER, AND P. THIBAUT. Near-field ptychography: phase retrieval for inline holography using a structured illumination. *Scientific Reports*, 3:1927, 2013. doi:10.1038/srep01927.

M. STOCKMAR, I. ZANETTE, M. DIEROLF, B. ENDERS, R. CLARE, F. PFEIFFER, P. CLOETENS, A. BONNIN, AND P. THIBAUT. X-Ray Near-Field Ptychography for Optically Thick Specimens. *Physical Review Applied*, 3(1):014005, 2015. doi:10.1103/PhysRevApplied.3.014005.

P. THIBAUT, M. DIEROLF, O. BUNK, A. MENZEL, AND F. PFEIFFER. Probe retrieval in ptychographic coherent diffractive imaging. *Ultramicroscopy*, 109(4):338–343, 2009a. doi:10.1016/j.ultramic.2008.12.011.

P. THIBAUT, M. DIEROLF, C. M. KEWISH, A. MENZEL, O. BUNK, AND F. PFEIFFER. Contrast mechanisms in scanning transmission x-ray microscopy. *Physical Review A*, 80(4):43813, 2009b. doi:10.1103/PhysRevA.80.043813.

P. THIBAUT, M. DIEROLF, A. MENZEL, O. BUNK, C. DAVID, AND F. PFEIFFER. High-resolution scanning x-ray diffraction microscopy. *Science*, 321(5887):379–382, 2008. doi:10.1126/science.1158573.

Other publications

M. DIEROLF. *Development of a Lensless Microscopy Technique for Imaging Cellular Structures*. Diplom thesis, Ulm University, 2007.

M. DIEROLF, O. BUNK, S. R. KYNDE, P. THIBAUT, I. JOHNSON, A. MENZEL, K. JEFIMOV, C. DAVID, O. MARTI, AND F. PFEIFFER. Ptychography & lensless X-ray imaging. *Europhysicis News*, 39:22–24, 2008. doi:10.1051/eprn:2008003.

A. MENZEL, M. DIEROLF, C. KEWISH, AND P. THIBAUT. Advanced methods in scanning x-ray microscopy. In M. T. POSTEK, D. E. NEWBURY, S. F. PLATEK, AND D. C. JOY (eds.), *Proceedings of SPIE, Scanning Microscopy 2009*, vol. 7378, p. 73780O. 2009. doi:10.1117/12.821823.

A. MENZEL, P. THIBAUT, M. DIEROLF, C. M. KEWISH, O. BUNK, C. DAVID, W. LEITENBERGER, AND F. PFEIFFER. Advances in ptychographical coherent diffractive imaging. In P. J. BONES, M. A. FIDDY, AND R. P. MILLANE (eds.), *Proceedings of SPIE, Image Reconstruction from Incomplete Data V*, vol. 7076, p. 707609. 2008. doi:[10.1117/12.794186](https://doi.org/10.1117/12.794186).

J. VILA-COMAMALA, M. DIEROLF, C. M. KEWISH, P. THIBAUT, T. PILVI, E. FÄRM, V. GUZENKO, S. GORELICK, A. MENZEL, O. BUNK, M. RITALA, F. PFEIFFER, AND C. DAVID. High Spatial Resolution STXM at 6.2 keV Photon Energy. In M. DENECKE AND C. T. WALKER (eds.), *X-RAY OPTICS AND MICROANALYSIS: Proceedings of the 20th International Congress*, vol. 1221, pp. 80–84. AIP, Karlsruhe (Germany), 2010. doi:[10.1063/1.3399261](https://doi.org/10.1063/1.3399261).